Francesco Sottile

Theoretical Spectroscopy :: Developments and Applications

Jury

C. Brouder	
T. Deutsch	*Referee*
E.K.U. Gross	*Referee*
M. Marsi	
E. Molinari	*Referee*
O. Stephan	
E. Suraud	

Habilitation à Diriger la Recherche

Laboratoire des Solides Irradiés UMR 7642
École POLYTECHNIQUE, F-91128 Palaiseau, France

Francesco Sottile `francesco.sottile@polytechnique.fr`

2015

This manuscript has been conceived only using free software: LaTeX, Memoir class, Garamond and Linux Libertine fonts.
Figures and graphs were created with Inkscape, The Gimp, XMGrace,VESTA and GNUPlot.

Contents

Preface

This document is a shell. Those who believe it could represent a summary of many years of work are indeed mistaken. If it is true, in fact, that a collection of papers can be easily put together, even with a nice story, pretending to see *a posteriori* a unique and precise long-term strategy (instead of the more realistic crazy jumping among subjects, according to mood, grant (un)acceptance, students availability, etc.), how can this efficiently summarize years of real work (most of which un-accounted for in terms of publications), how can it report the so many wrong (and still enriching) directions taken, how can this witness the constant sewing of human relationships well beyond the professional level? Well, it can't. And how about the (too many) deadlines approached with awe and agony, the (too few) jubilance from accepted grants, the (great) satisfactions of successful students and post-docs, that underpin the researcher life ? Again it is impossible to account for it. So let's not.

What I did instead is to report, beside some lines of research (and the associated articles), a perspective of future challenges and promising topics. The discussion will focus especially on two points: the exciton dispersion and the bootstrap kernel. These are in fact the (chronologically) last two topics of my research and those that, I hope, will lead fun and enriching discussions in the next-future. For what concerns the first part, I wanted at all cost to spare the reader from the n-th description of GW+BSE and TDDFT (after all, any PhD thesis in the electronic excitations community has it, mine included). However one point, most often unaccounted for, is the relation between the experiments and theory, between the macroscopic and microscopic word. I have often discussed this matter (but helas, not as much as I would have wanted) with Rodolfo Del Sole. He was the first one, and among the few, who understood the importance (and the limits, the approximations, the incoherences) of such a connection and managed to explain it (instead of simply and inappropriately citing papers from the '60s), and I owe him a lot for this.

I take at this point the occasion to thank all the people I work(ed) with. I can safely say I have learnt from every collaborator (from Master students to retired professors) a great deal, not only in the Theoretical Spectroscopy group, but in a much larger circle of collaborations (both with theoreticians and experimentalists) thanks to our network, the European Theoretical Spectroscopy Facility. It was indeed thanks to the ETSF (and to Lucia who godfathered this application, and to whom goes my everlasting gratitude) that I got the position I have today in the École Polytechnique.

Let me end on a more personal note, thanking my precious family. Not really supportive (no proofreading, no figure preparing, no latex-typing), not in the least interested in spectroscopy, nor with knowledge in solid state or quantum mechanics, they nonetheless undermine any temptation of mine to go to relativistic problems, avoiding me useless pains and headaches. They have in fact falsified the basic principles of relativity, giving me a unique frame of existence, for which I couldn't be more grateful. So thanks to Daniella, Adriano e Atena.

Brief Curriculum Vitae

Personal Information

· Francesco Sottile (born 4 February 1976 in Messina-Italy)
· Website :: `http://etsf.polytechnique.fr/people/francesco`
· Email :: `francesco.sottile@polytechnique.edu`
· RESEARCHERID :: A-4910-2012

Research Position

Director of the unit GDR3675 at the CNRS (France)	*2015-2019*
Ingénieur de Recherche École Polytechnique	*2007-present*
Post-Doc - Universidad del País Vasco (Spain)	*2005-2006*
Post-Doc - École Polytechnique	*2004*
PhD Thesis École Polytechnique	*2000-2003*
Research Contract at the SISSA-Trieste (Italie)	*2000*

Studies

· **PhD Thesis (Physics)**	École Polytechnique (Très honorable avec félicitations du jury)	*2003*
· **Master ("Laurea") in Physics**	University of Messina - Italy (110/110 cum laude)	*1999*

Awards and Fellowship

· **Prix de thèse** of the École Polytechnique, obtained 6 July 2004
· **Prix Paristech** Finalist (9 thesis selected out of 462) in 2004
· **Fellowship** ("Borsa di Studio") Fondazione Angelo della Riccia, obtained in 2001

Tutoring and Supervision

Tetiana Khotiaintseva PhD (100%) *2015-2018 École Polytechnique*

Ab initio description of singlet fission for photovoltaics.

Matteo Guzzo PhD (100%) *2009-2012 École Polytechnique*

New ideas for photoemission. **Prix de Thèse de l'École Polytechnique in 2013.** Today post-doc in Berlin.

Lucia Caramella PhD (30%) *2007 University of Milan, École Polytechnique*

Developement and implementation of the Hilbert transform for the calculation of polarizabilities

Margherita Marsili PhD (30%) *2004 University of Rome, École Polytechnique*

Numerical implementation of the Haydock recursive scheme in the calculation of spectra

Fabiana Da Pieve Post-doc (100%) *2014-2016* ***Marie-Curie Fellowship***

Development of an ab initio description of Resonant Inelastic X-ray scattering (RIXS)

Giorgia Fugallo Post-doc (100%) *2013-2015 École Polytechnique*

Exciton Dispersion in bulk and 2D systems. **Giorgia is applying for a CNRS research position**

Linda Hung (100%) *2010-2013* ***Eurotalent*** *and CEA*

Theory and application on photocatalytic systems **Linda won the Eurotalent grant**

Claudia Rödl Post-doc (50%) *2010-2013* ***Eurotalent*** *and CEA*

Towards an accurate description of strongly correlated systems. **Claudia won the Eurotalent grant**

Jan Adriaan Berger Post-doc (100%) *2007-2009 Triangle de la Physique, École Polytechnique*

Improving GW: the EET method. **Today Assistant Professor at the University of Toulouse**

Alberto Zobelli Post-doc (100%) *2008 École Polytechnique*

Electron energy loss of HfO_2. **Today Assistant Professor at the University of Paris XI Orsay**

Margherita Marsili Post-doc (100%) *2006 CNRS*

Putting together Many-Body and Density theories. **Today post-doc in Modena, Italy**

Conference Organization (7 international events organised)

Green's function methods: the next generation II *Lausanne (Switzerland). 2015*

Main organiser. 50 participants foreseen.

ETSF Conference on Electronic excitations *Berlin (Germany). 2010*

Main organiser. 114 participants.

ETSF Conference on Electronic excitations *Evora (Portugal). 2009*

Scientific Committee. 97 participants.

NANOQUANTA Conference on Electronic excitations *Vieste (Italy). 2008*

Main organiser. 113 participants.

NANOQUANTA Conference on Electronic excitations *Aussois (France). 2007*

Main organiser. 120 participants.

NANOQUANTA Conference on Electronic excitations *Houffalize (Belgium). 2006*

Main organiser. 115 participants.

NANOPHASE Young Researchers' Meeting *Palaiseau (France). 2004*

Main organiser of this first (of a still-standing series) workshop organised by and for young researchers

School Organization (14 international schools organised)

- **CECAM School :: Theoretical Spectroscopy Lectures** (6 events: Lyon 2006, Lyon 2007, Zurich 2009, Lausanne 2011, Lausanne 2013, Lausanne 2015). Average of 25 students for 5 full days.

- **Spectroscopy Lectures :: Theory and codes** École Polytechnique, Palaiseau. 2 events: February 2012 and May 2014
- **ETSF Theory Day for experimentalists**, 20 attendees for a full day of lecures (2 events at the École Polytechnique, Palaiseau in November 2009 and October 2010, 1 event at the Synchrotron SOLEIL, Gif-sur-Ivette in January 2014).
- **CECAM School :: Basic techniques and tools for development and maintenance of atomic-scale software**. (3 events organised: Lyon 2008, Zaragoza 2010, Lausanne 2014). Average of 25 students for 5 full days.

Trusts and Responsabilities

Director of the CNRS unit GDR3675 *2015-2019*

Director of the Groupement de Recherche REST, which gathers groups (more than 100 permanent researchers) involved in theoretical spectroscopy from 23 French institutions and universities.

Editor for Frontiers *2014-present*

Invited to cover the role of Review Editor, to control the quality of articles published in Frontiers.

Referee for international journals *2004-present*

Physical Reviev B and Letters, Nanotechnology, New Journal of Chemistry, Journal of Chemical Physics, Chemical Physics, Journal of the American Chemical Society, Journal of Physical Chemistry Letter, etc.

Reviewer for Innovational Research Incentives Scheme Veni *2012*

Funding Scheme to select outstanding researchers for granting.

Steering Committee Member *2012-present*

The European Theoretical Spectroscopy Facility (ETSF) is a European Network, involving more than 200 researchers, that develops theory and codes for describing spectroscopic properties through a collaborative approach.

ETSF Beamline Coordinator *2008-present*

Coordinator of the “Loss Spectroscopy” beamline of the ETSF.

Codes coordinator *2006-present*

Coordinator of two open-source projects: DP (dp license) is a Time-Dependent Density Functional Theory code and EXC (GPL license) solves the Bethe-Salpeter equation (and is at the core of the present project).

Teaching

Frequently invited to give lectures in international schools devoted mainly to electronic structure theory, theoretical spectroscopy and software development. Responsible for a course (Master level) of Theoretical Spectroscopy at the École Polytechnique.

Languages

Italian (mother tongue), French and English (fluent), Spanish (good level).

Part I

Setting the ground

Chapter 1

From Spectroscopy to Theoretical Spectroscopy

If we want to know something about a system, let alone to analyse its properties in details, we have to interact with it. Tipically, the system is submitted to an external perturbation, it reacts to such a perturbation and we measure this reaction. Often this measure comes as a spectrum (as a function of energy, or mass, or states, etc.), that's why we call it **spectroscopy**. When we look at a system, for instance, we perform an optical spectroscopy experiment: the system is exposed to light (the perturbation), it reacts to this (by experiencing all sort of electronic excitations) and we measure its reaction (the reflected beam). This permits us to know position, color and shape of the (macroscopic) system.

Even if we limit ourselves to valence electrons (nonetheless responsible for chemical, electrical, optical, mechanical properties) excitations, we still have a wide range of different spectroscopies. A separation is very often made among the different spectroscopies, on the basis of the final state of the system: i) if the system is left (after perturbation) with the very same number of electrons we talk about neutral excitations spectroscopies; it is the case of *optical absorption*, *electron energy loss spectroscopy* (EELS) or *inelastic X-ray scattering* (either in its resonant (RIXS) or non-resonant (NIXS) variety)); ii) if the system is instead left in a charged state (plus or minus one electron, for instance), we talk about charged excitations spectroscopies, like *photo-emission* (PES) and *inverse photo-emission spectroscopy* (IPES). This distinction is of course purely fictitious, but can be very useful when deciding the theoretical approach one might use to tackle this or the other spectroscopy.

1.1 Photoemission Spectroscopy

In (direct) photo-emission, a photon of energy E_{ph} and momentum $\mathbf{k}_{\text{ph}}$ impinges on the system, removing[1] one electron. The *photo-electron* leaves the system (which is now in an excited state, i.e. presenting a *hole*) and impinges on an electron-detector that measure its kinetic energy E_{kin}.

Energy conservation makes that the removal energy of the electron is

$$E_{\text{be}} = E_{\text{ph}} - E_{\text{kin}} = E(N) - E(N-1, s), \tag{1.1}$$

also called the electron binding energy E_{be}, which corresponds to a difference of the energy of the system with N electrons (before the perturbation) and the energy of the system with $N-1$ electrons (in the excited states s). This is why it is called a charged excitation.

---

[1] The energy required to do so is normally quite high, for the electron has to reach a scattering state, in the continuum. Ultra-violet lamp or synchrotron radiations are normally used as sources for PES.

The knowledge of the two angles involved in the PES geometry (from Fig.1.1), θ and ϕ permits also to infer about momentum of the electron inside the material. This technique is called Angle-Resolved photo-emission (ARPES). It is clear then, that ARPES is able to experimentally investigate the band structure of a system. But the interpretation of PES and ARPES is not so straightforward, and we will see why.

From the historical point of view, the origin of PES goes back to 1887, when the photoelectric effect was discovered by Hertz [1]; we might want to remark that this was anterior even to the discovery of the electron itself. It was in fact Thomson who interpret this effect as electron emission [2], at the same time of Lenard [3]. Finally Einstein gave his famous quantum theory interpretation of the photoelectric effect [4], which opened him the way to the Nobel prize in 1921. Today the PES and ARPES are widely used to *see* the electronic distribution in energy-momentum space, and the experimental details, together with the capabilities of such approaches, can be found in well established books [5] or reviews [6, 7]. However, it has to be underlined that *to see* does not automatically imply *to understand*, and the physical interpretation of an experimental spectrum (not only PES) is far from trivial. To be aware of these difficulties, it is enough to look at Fig.1.1: in a naïve interpretation, the energy difference between the incoming photon and the kinetic energy of the electron simply gives the binding energy of the electron. This should be seen in a PES spectrum as a sharp (delta-like) peak, as shown in Fig.1.2 in red. However in reality, we rather have a spectrum that looks like the black curve in Fig.1.2: the peak is shifted at lower energy (for convention we consider the electron removal as negative energies) and is broadened; in addition at higher energy a new structure appears, which is called satellite. This is because in reality many things happen when an electron is removed from the system.

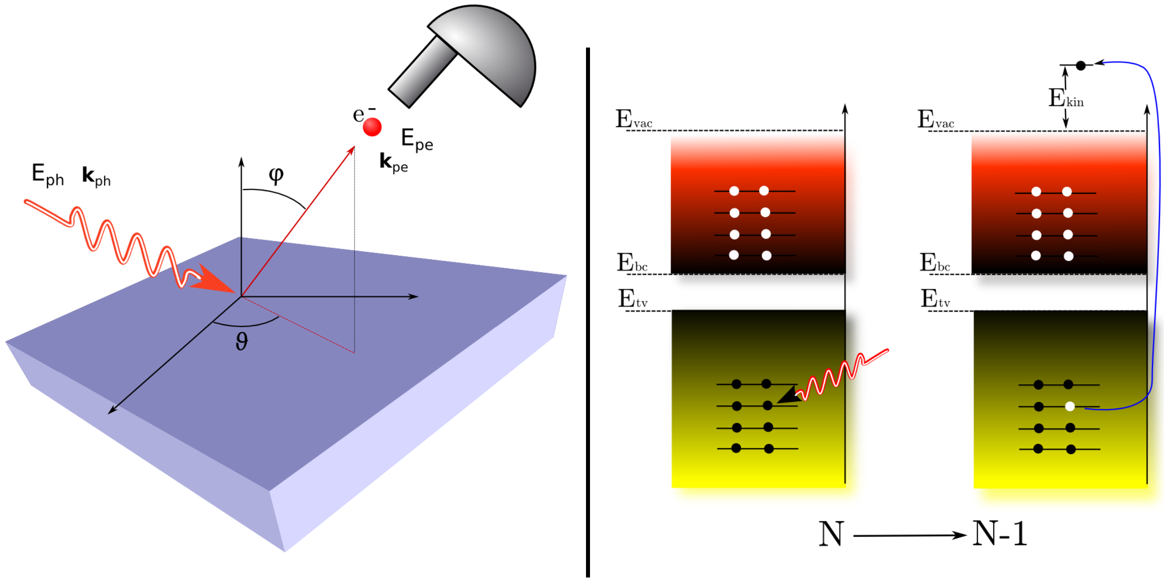

Figure 1.1: Schematic representation of the (AR)PES, from an experimental point of view (left panel), and from a theoretical one (right panel).

Even if this is not the place to review the theory of photoemission, we would like to mention, roughly, the different events that take place in a PES (or ARPES) experiment (and the different questions arised):

1. a photon impinges on the system and it is absorbed. where? at the surface or in the bulk? in the latter case, the penetrated electro-magnetic field is modified, following the Maxwell-Fresnel equation, which however apply only on ideally sharp vacuum-solid interface, far from the physical reality.

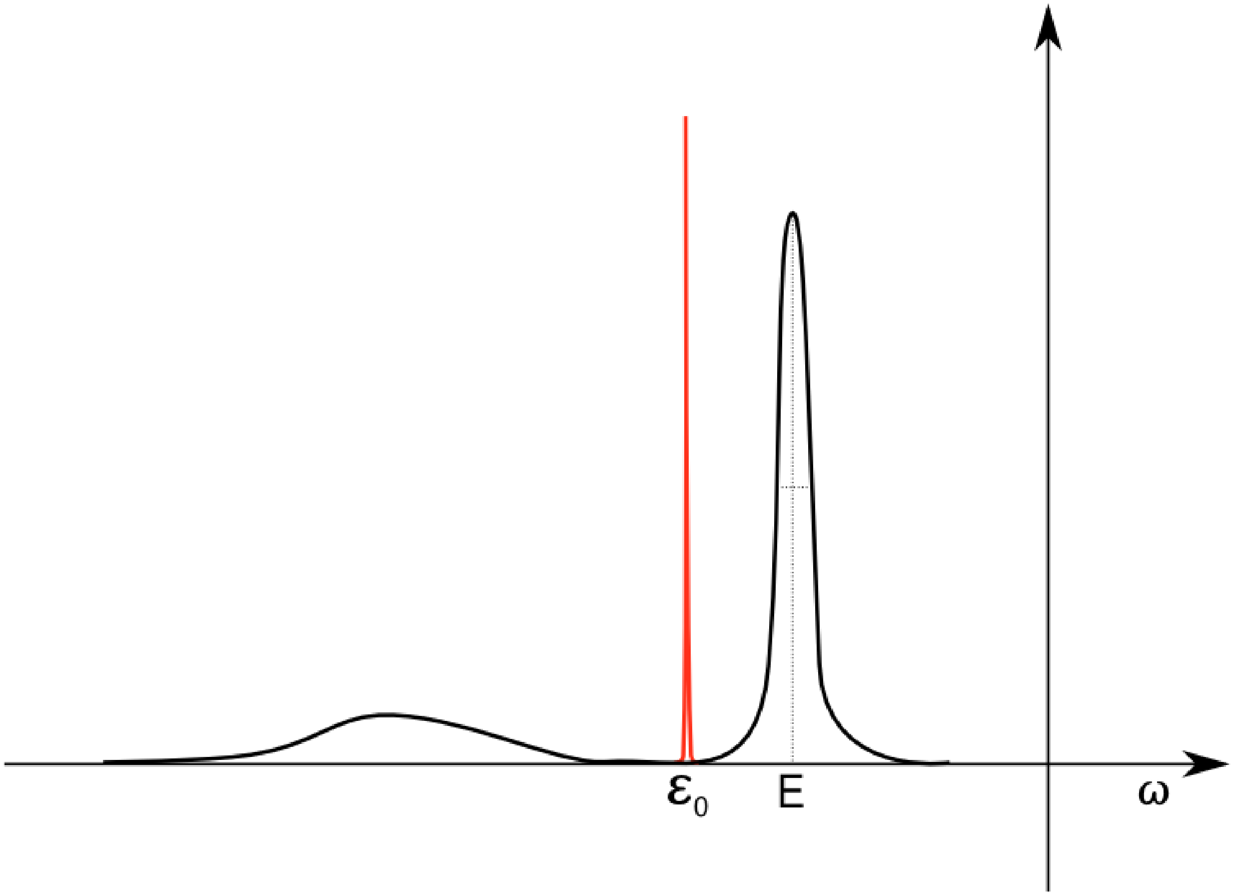

Figure 1.2: Schematic representation of a PES spectrum. The red curve shows the naïve picture of a delta-peak given by the difference between the incoming photon and the kinetic energy of the detected electron. The black curve is more similar to reality. The binding energy is considered to be negative (see Eq.(1.1)).

2. an electron is excited (selection rules applies) and travels inside the bulk, creating a lot of additional (though higher order) excitations. which ones?
3. when the photo-electron reaches the surface, it can bounce back in the bulk, or escape in the vacuum, if its energy and momentum permit. what are such conditions?
4. with a certain delay (how much?) also the hole just created will start exciting additional excitations. which ones? one particle, collective, structural ?
5. the photo-electron that has left the system still interacts with the solid behind: electron-hole interaction.

It is better to state immediately this: **there is no a rigorous treatment of PES that permits to take all these effects into account**, on the same ground, in one step. To have an idea about how important are the approximations involved, we write the photo-emission current (the measured quantity) in terms of the Fermi golden rule, between the initial state (system in its ground state and an incoming photon of energy ω) and the final state (a photo-electron of kinetic energy $\mathbf{p}^2/2$ and the $N-1$ electron system in the excited state s)

$$J_{\mathbf{p}}(\omega) = \sum_s |\langle \Psi_{\mathbf{p},s} | \Delta | \psi_i \rangle|^2 \, \delta(\omega - \frac{\mathbf{p}^2}{2} + \epsilon_s), \tag{1.2}$$

with $\epsilon_s = E_N - E_{N-1,s}$ and the transition operator (first order in the vector potential) $\Delta = \sum_{ij} \langle i|\mathbf{A}\mathbf{p} + \mathbf{p}\mathbf{A}|j\rangle\, c_i^\dagger c_j = \Delta_{ij} c_i^\dagger c_j$ (where $c_i^\dagger$ and c_j are creation and annihilation operators, respectively). So far nothing can be said about the final state, that concerns the system with a hole plus the photo-electron, still interacting with the rest of the system. And this is more or less as far as we can go with the whole theory, which is sometimes called the one-step approach [8].

Here comes the first, and most important, approximation: we assume that i) the photo-electron is istantenously removed from the system and ii) it goes to the detector as a free electron, without interaction with the rest of the system. This is called the *sudden* approximation, and the final state is "simply" $|\Psi_{\mathbf{p},s}\rangle = c_{\mathbf{p}}^\dagger |N-1, s>$, i.e. a free electron of momentum $\mathbf{p}$ and a system with $N-1$ electron in the excited state s. What are we missing here? It seems quite a lot, for all steps 1 to 5 enumerated above are neglected totally or partially: we do not have any electro-magnetic propagation (step 1 gone), we do not have the propagation of the electron inside the bulk (step 2 partially gone), nor it ever crosses the surface (no step 3) and there's no interaction between the photo-electron and the system (no step 5). All these effects have been called extrinsic effects [5, 6, 8, 9]. We have of course the creation of the hole and its effects (step 4) that are by contrast called intrinsic. From a pictorial point of view, instead of Fig. 1.1 we should rather look at Fig. 1.3. From a mathematical point of view, let's see where it leads in the photocurrent formula. If we try with a system of non-interacting electrons, the many-body wavefunction can be written like a Slater determinant $\Psi_i = |N>$ and the final state reads $|\Psi_{\mathbf{p},s}\rangle = c_{\mathbf{p}}^\dagger |N-1, s>= c_{\mathbf{p}}^\dagger c_s |N>$, where s now labels a (occupied) one-electron state.

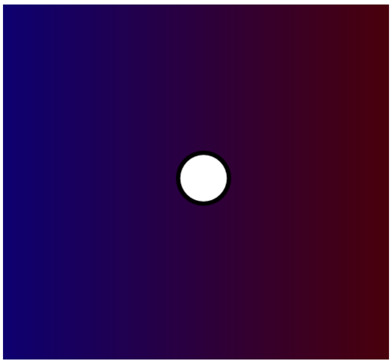

Figure 1.3: sudden approximation (quite simplified) scheme: a hole is suddenly created in a many-electron system.

$$\begin{aligned}
J_{\mathbf{p}}(\omega) &= \sum_s^{occ} \left| \left\langle N | c_s^\dagger c_{\mathbf{p}} \sum_{ij} \Delta_{ij} c_i^\dagger c_j | N \right\rangle \right|^2 \delta(\omega - \frac{\mathbf{p}^2}{2} + \epsilon_s) \\
&= \sum_s^{occ} \left| \sum_{ij} \Delta_{ij} \left\langle N | c_s^\dagger c_{\mathbf{p}} c_i^\dagger c_j | N \right\rangle \right|^2 \delta(\omega - \frac{\mathbf{p}^2}{2} + \epsilon_s) \\
&= \sum_s^{occ} |\Delta_{s\mathbf{p}}|^2\, \delta(\omega - \frac{\mathbf{p}^2}{2} + \epsilon_s)
\end{aligned} \tag{1.3}$$

where we have assumed that $c_{\mathbf{p}}|N>= 0$ (no interaction between the photoelectron and the system) and $c_s^\dagger|N>= 0$ (it is not possible to create an electron in an occupied state). Here we recover our naïve image of the one-particle peak-like PES spectrum depicted in red in Fig. 1.2.

Let's now consider an interacting system, where the many-body wavefunction is not a Slater determinant any longer. In this case the photo-current reads

$$\begin{aligned}
J_{\mathbf{p}}(\omega) &= \sum_s \langle N-1, s|\, c_{\mathbf{p}} \sum_{ij} \Delta_{ij} c_i^\dagger c_j \,|N\rangle \langle N| \sum_{ij} \Delta_{ij} c_j c_i^\dagger c_{\mathbf{p}}^\dagger \,|N-1, s\rangle\, \delta(\omega - \frac{\mathbf{p}^2}{2} + \epsilon_s) \\
&= \sum_s \sum_j \Delta_{\mathbf{p}j} \langle N-1, s|\, c_j \,|N\rangle \sum_i \Delta_{i\mathbf{p}} \langle N|\, c_i^\dagger \,|N-1, s\rangle\, \delta(\omega - \frac{\mathbf{p}^2}{2} + \epsilon_s) \\
&= \sum_{ij} \Delta_{\mathbf{p}j} A_{ij}(\frac{\mathbf{p}^2}{2} - \omega) \Delta_{i\mathbf{p}},
\end{aligned} \tag{1.4}$$

where again we have used (in the spirit of the sudden approximation) $c_{\mathbf{p}}|N>= 0$. Eq.(1.4) permits us also to define the **spectral function**, which represents then the **intrinsic part of the photo-**

current.

$$A_{ij}(\omega) = \sum_s \langle N| c_i^\dagger |N-1,s\rangle \langle N-1,s| c_j |N\rangle \, \delta(\omega - \epsilon_s). \tag{1.5}$$

The spectral function reduces to the simple delta-peak form for independent particle $A_{ij}(\omega) = \sum_i \delta(\omega - \epsilon_i)$ which is clearly diagonal. It might be worth notice that even if in general the spectral function is non-diagonal, in practice this function is very often considered diagonal, for example within the GW approximation [10, 11]. But, what is the shape (and content) of the spectral function in the interacting case? To answer this question, we have to notice that the spectral function is strongly connected to the one-particle Green's function G. The Green's function being exactly the propagator of an electron (or in the specific case of photoemission, of a hole), its relation with the spectral function is quite simply via its imaginary part

$$\begin{aligned} G_{ij}^{\text{hole}}(t-t') &= i\theta(t-t') \langle N| c_i^\dagger e^{-i\hat{H}t} c_j e^{i\hat{H}t'} |N\rangle \\ G_{ij}^{\text{hole}}(\omega) &= i \sum_s \frac{\langle N| c_i^\dagger |N-1,s\rangle \langle N-1,s| c_j |N\rangle}{\omega - \epsilon_s - i\eta} \end{aligned} \tag{1.6}$$

so

$$A_{ij}(\omega) = \frac{1}{\pi} \text{Im}\left[G_{ij}^{\text{hole}}(\omega)\right]. \tag{1.7}$$

The latter is a very important relation, because it opens the way to operative (at least in principle) evaluation of the spectral function. The Green's function is in fact calculated (very often) through the self-energy Σ, related to G via

$$[\omega - \epsilon_i]\, G_{ij}(\omega) = \delta_{ij} + \sum_k \Sigma_{ik}(\omega) G_{kj}(\omega) \tag{1.8}$$

where ϵ_i are one-particle energies, like in the Hartree potential (in this case Σ take care of all exchange and correlation effects, beyond Hartree). With this definition, the spectral function is related to the self-energy via

$$A_{ij}(\omega) = \frac{1}{\pi} \frac{|\text{Im}\Sigma_{ij}(\omega)|}{(\omega - \epsilon_i - \text{Re}\Sigma_{ij}(\omega))^2 + (\text{Im}\Sigma_{ij}(\omega))^2}. \tag{1.9}$$

We can now interpret the black curve of Fig.1.4 in a direct way, through the real and imaginary part of the self-energy. We have a peak in the spectral function, either when the denominator is zero or when the numerator is big (and the denominator not too big). When the ImΣ is small the zeros of $(\omega - \epsilon_i - \text{Re}\Sigma_{ij}(\omega))$ define the main peak of the spectral function, which is called the quasi-particle peak:[2] its position is shifted with respect to the single-particle position ϵ_i (for example evaluated at the Hartree level) by an amount related to the real part of the self-energy. The imaginary part of Σ instead can be seen in first approximation as the width of the broadened quasi-particle peak (and is related to the inverse lifetime of the quasi-particle). Also when the ImΣ is big the spectral function can have a peak: it is called a satellite. Let's summarize these findings: in a non-interacting system we would have just a peak at the energy ϵ_i, for example calculated within the Hartree approximation. For an interacting system the quasi-particle peak is shifted and broadened (by virtue of the real and imaginary part of Σ) and a satellite appears. Why? Simply because, when we have created the hole, the (now interacting) system tends to screen the hole, with auxiliary excitations that take place, like, for instance, plasmons. These are called the intrinsic losses and are in principle contained in the spectral function, even within the sudden approximation. It is of course of crucial importance to decide how to calculate the Green's function. In fact, even

---

[2] This feature is not always present in a PES experiment. For certain materials, exhibiting strong correlation among electrons, this part of the spectrum is partially or completely damped and the whole weight of the spectrum is tranferred to the satellite part, also called the incoherent part of the spectrum.

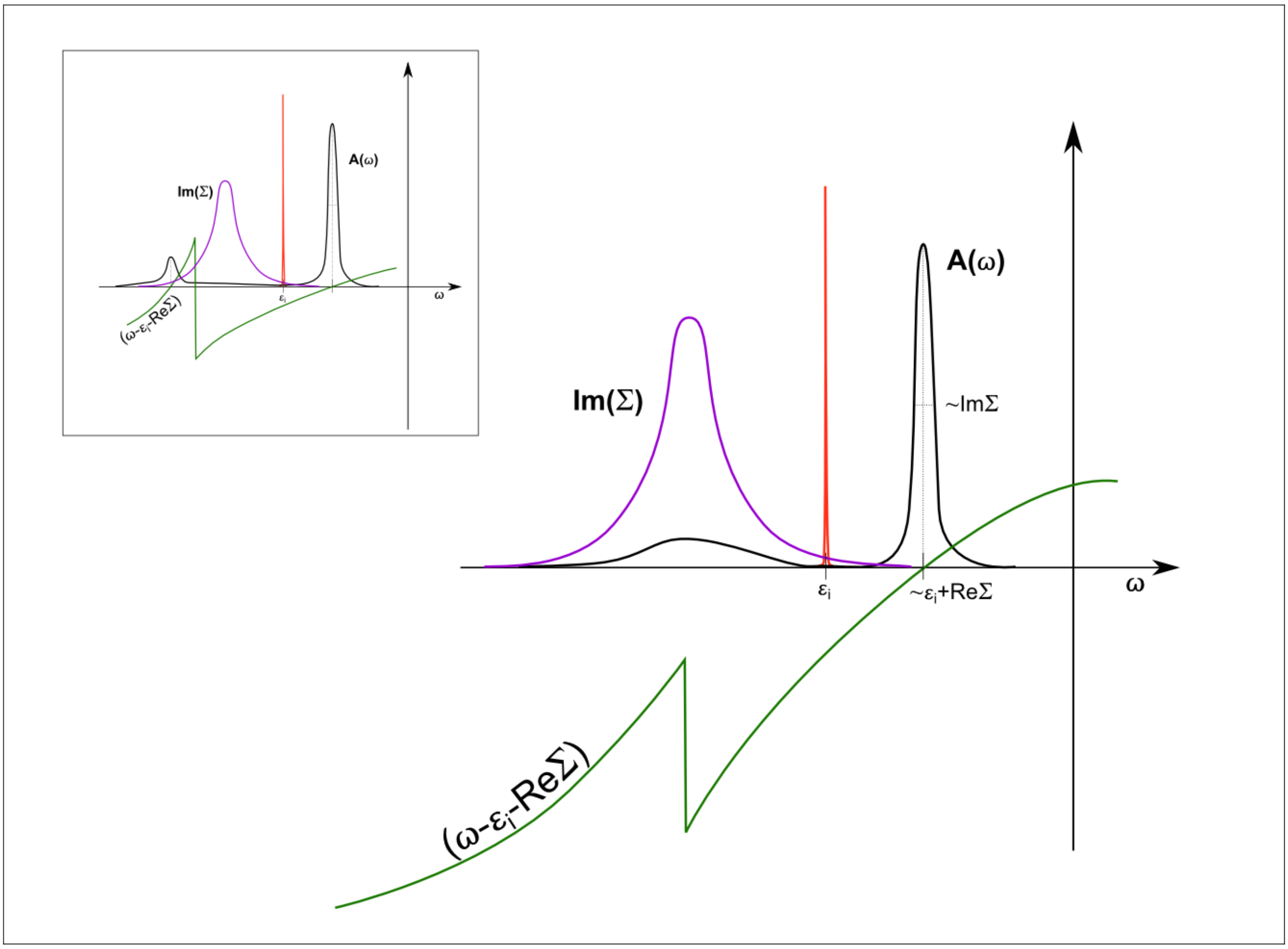

Figure 1.4: Spectral function $A(\omega)$ (black curve) together with real (green line) and imaginary (violet line) part of Σ for an ideal system. In the inset a more anomalous situation in which a spurious satellite appears.

small error in the latter can lead to completely wrong interpretation of the spectral function. An example can be seen in the inset of Fig. 1.4: here the real part of Σ crosses the real axis giving rise of an additional peak in the spectral function (completely different from the previous case, given by ImΣ), that might be due solely to an uncorrect evaluation of the Green's function. This schematic example finds in the PES spectrum of bulk Silicon its realistic situation [12]. This point will be analised in more details in the next chapter (and more precisely in Matteo Guzzo's thesis [13] and in [12]).

The correct evaluation of the Green's function is then of paramount importance for the description and anaysis of PES experiments. Several approaches can be cited, both model-based, like LDA+U [14] or Dynamical Mean Field Theory (DMFT) [15, 16], or ab-initio within the Many-Body Perturbation Theory (MBPT), like the GW approximation [17–20]. We, in particular, follow the latter approach. For further details, we can suggest the numerous thesis of our group on the subject [21–23] and in particular Matteo Guzzo's thesis for everything beyond spectral function [13].

Inverse Photoemission

As well as the PES permits one to investigate the filled bands of a system, the inverse technique, called Inverse Photo-Emission Spectroscopy (IPES), permits to investigate the empty states. The process is the following: an electron of kinetic energy E_i makes a transition (it is captured) to a final bound state E_f, emitting a photon of energy $E_i - E_f$. The latter is detected. Knowing the kinetic energy of the incoming electron and the emitted photon energy, one infers about the empty states of the system. Again this process can be described by a Green's function G^e and the theoretical investigation proceeds like above for the description of PES. In recent years, IPES (and its angle-resolved version, called ARIPES or KRIPES) has gained in importance, performance and efficiency, still remaining a difficult technique, without the "big instrument approach" (most IPES experimental setup are lab-scale ad-hoc setup) and suffering from lower resolution than direct PES [5, 24]. Very often, and also to obtain a wider angle recollection, an isochromat detector is used. So, if the outcoming photon has always the same energy, the incoming electron must varies its energy: this variation of IPES is called Bremsstrahlung Isochromat Spectroscopy (BIS) [25, 26].

1.2 Electron Energy Loss Spectroscopy

Scattering experimental techniques are very useful to investigate the property of matter, in light of the wide range of energy loss and momentum transfer they incur in such experiments. In Electron Energy Loss Spectroscopy (EELS), a fast electron is scattered by the system and later detected (see Fig.1.5). The difference in energy (kinetic energy before and after the scattering) is called energy loss. This energy has been given to the system to produce some excitations. We can in this way study the neutral excitations of a system. The different in momentum (again before and after the scattering) is called the momentum transfer and (contrary, for instance to photo-absorption), can be very big (the order of the Brillouin zone size). The developments of EELS are intimately related with the developements of the electron microscope. This is not place for an historical overview of the electron microscope, nonetheless we would like to mention a anecdote involving the first father (rarely accredited) of the electron microscope, Leo Szilard (who also patented his electron-microscope idea). In a bar in Berlin, this was the discussion between Szilard and Gabor (later nobel price for the invention of holography) *Szilard: "Busch has shown that one can make electron lenses, de Broglie has shown that they have sub-Angström wave lengths. Why don't you make an electron microscope, one could see atoms with it!" Gabor: "Yes, I know. But one cannot put living matter into a vacuum and everything will burn anyway to a cinder under an electron beam."* [27]. The electron microscope, immediately after invented by Ruska (awarded with the Nobel prize after more than 50 years [28]), has known important progress in the last decades, especially in the domain of the aberration correction and the spatial resolution. Also the development of the EELS itself dates back quite far in time, in the mid-1940s (by Hillier and Baker [29]), but its golden age starts only in the 1990s [30, 31]. Today EELS is one of the best techniques to investigate the properties of matter, thanks also to the wide range of energy involved in the scattering process (as can be schematically represented in Fig.1.6), that permits one to scan out a large variety of electronic (and structural) excitations. Let's now figure out how to connect EELS with theory. Ideally, one should treat everything at the (highest) quantum mechanical level,

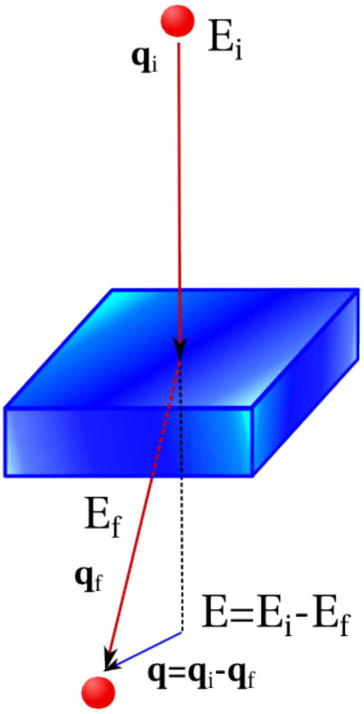

Figure 1.5: Schematic representation of EELS.

$$\frac{d^2\sigma}{d\Omega d\omega} \propto |\langle\psi_f|H_{\text{int}}|\psi_i\rangle|^2\,\delta(E_i - E_f + \omega) \tag{1.10}$$

with a quantum mechanical initial and final state (both containing the in and out electron). If

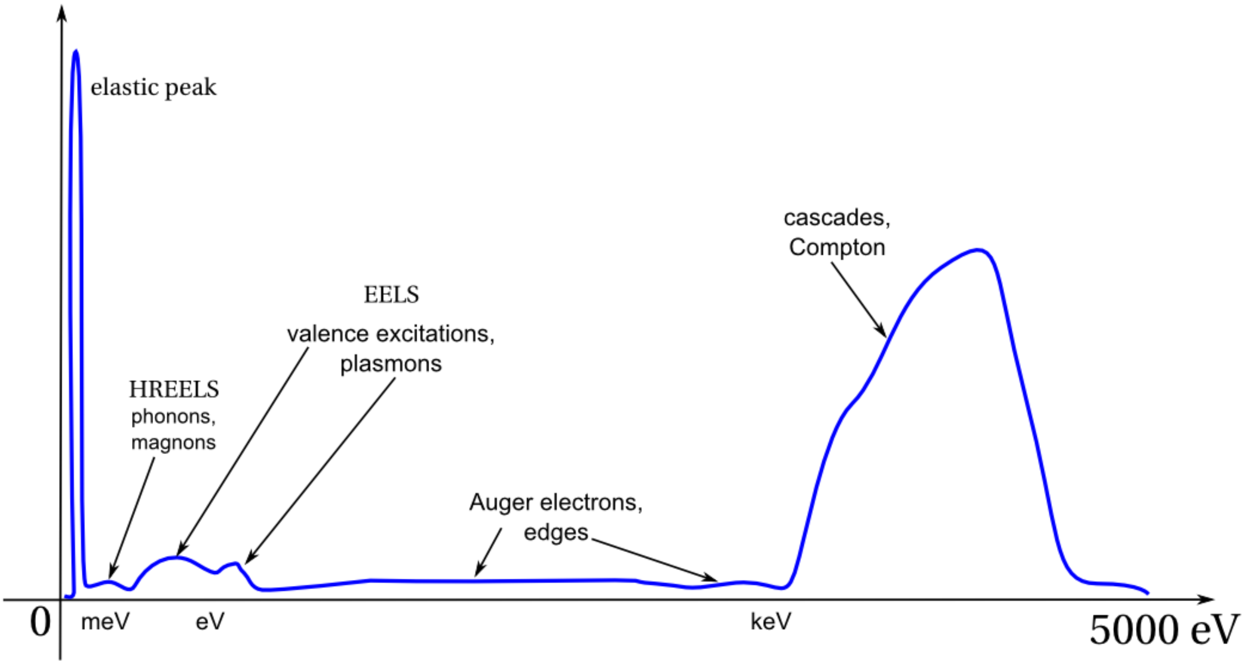

Figure 1.6: Loss function (as a function of the energy loss in eV) in a wide range of energy. After the elestic peak, we can have losses in the meV region (magnons and phonons), in the eV region (valence electrons interband transitions, excitons and plasmons), and so on (going through Auger electrons, edges of core electrons) up to the keV regime, where Compton scattering takes place.

the scattering electron is a fast particle, we can distinguish between the probe (the electron) and the target (the system in study). Still we should ideally treat both quantum mechanically, the fast particle and the target. Also, retardation effects should be taken into account, when treating the electron-electron interaction (contained in H_{int}). Let's tackle here the first issue: in order to get the local characteristics of the systems (in solids these are called crystal local fields) and/or to be able to describe excitonic effects, a quantum mechanical treatment of the target is mandatory. For what concerns the fast electron, a very important and powerful result has been obtained by Ritchie and Howie [32]: whenever one does not search for high spatial resolution the probe electron can be considered classical; when instead we push to the limit of spatial resolution, in order for the electron to be considered semi-classical (and the Poisson equation used as below), the whole collection angle has to be integrated over. We will then stick to this limit and consider the fast electron as a semi-classical particle. Other considerations, like the quantum treatment of the beam aperture and the collection angle, are definitely considered for our purposes minor corrections on the prefactor [32].

Let's then specify as the external perturbation ρ_{ext} the charge density of an electron moving with velocity $\mathbf{v}$:

$$\rho_{ext}(\mathbf{r},t) = e\delta(\mathbf{r}-\mathbf{v}t)$$
$$\rho_{ext}(\mathbf{k},\omega) = \delta(\omega-\mathbf{k}\cdot\mathbf{v})$$

For the Poisson equation, the external potential associate is $\delta(\omega-\mathbf{k}\cdot\mathbf{v})/k^2$. Such a perturbation will induce a total electric field E which is associated to the external field, via the material relations to the Maxwell equation ($\mathsf{E} = \varepsilon^{-1}\mathsf{D}$ in linear response). It is here important to well define the left quantity (the total electric field) and the right external quantity (the electric displacement D).

Fields and potential are related via the spatial gradient $\mathsf{E} = -\nabla V$.[3] The material relation linking D with E also defines the linear response function ε^{-1}, called inverse dielectric function.

The energy loss by an electron in unit time is defined [34] as

$$\frac{dW}{dt} = \int d\mathbf{r}\; \mathbf{j} \cdot \mathsf{E} \tag{1.11}$$

where the current density is $\mathbf{j} = -\mathbf{v}\delta(\mathbf{r} - \mathbf{v}t)$. We have then to fill in all the ingredients

$$\begin{aligned} \frac{dW}{dt} &= \int d\mathbf{r}\; \mathbf{v}\delta(\mathbf{r} - \mathbf{v}t) \int d\mathbf{k}d\mathbf{k}' \int d\omega\; e^{i(\mathbf{k}\cdot\mathbf{r}-\omega t)} \frac{\mathbf{k}'}{k'^2} \varepsilon^{-1}(\mathbf{k}, \mathbf{k}', \omega)\delta(\omega - \mathbf{k}' \cdot \mathbf{v}) \\ &= \int d\mathbf{k}d\mathbf{k}' \int d\omega\; \mathbf{v} \cdot \mathbf{k}'\, \frac{1}{k'^2}\, e^{i(\mathbf{v}\cdot\mathbf{k}-\omega)t} \varepsilon^{-1}(\mathbf{k}, \mathbf{k}', \omega)\delta(\omega - \mathbf{k}' \cdot \mathbf{v}) \\ &= -\int \frac{d\mathbf{k}d\mathbf{k}'}{k'^2}\; \omega \mathrm{Im}\left\{\varepsilon^{-1}(\mathbf{k}, \mathbf{k}', \omega)\right\}, \end{aligned} \tag{1.12}$$

to find[4] the final *electron energy loss rate per unit time*, for a given energy ω. The quantity -Im$\{\varepsilon^{-1}\}$ is called the **loss function**, while the term (whose imaginary part appears in Eq.(1.12)) $W = \varepsilon^{-1}v = \frac{\varepsilon^{-1}}{k^2}$ is the **screened Coulomb interaction**. The electron energy-loss per unit time can still be expressed in terms of a Fermi-golden-rule formula [35], like in Eq.(1.10), remembering that, within this semi-classical approach, the probe (which is the same of the detected) electron is a plane wave $e^{i\mathbf{q}_i\cdot\mathbf{r}}$:

$$\begin{aligned} \frac{d^2\sigma}{d\Omega d\omega} &\propto |\langle\psi_f|H_{\text{int}}|\psi_i\rangle|^2\, \delta(E_i - E_f + \omega) \\ &\propto \frac{1}{q^2} \left|\left\langle\psi_f|e^{i\mathbf{q}\cdot\mathbf{r}}|\psi_i\right\rangle\right|^2 \delta(E_i - E_f + \omega) \\ &\propto \frac{1}{q^2} \mathrm{Im}\varepsilon^{-1}(\mathbf{q}, \omega) \end{aligned} \tag{1.13}$$

In order to compare with the measured loss function, several approaches in theory have been established to give an accurate description of the inverse dielectric function. Here we mention the two most important approaches: Time Dependent Density Functional Theory (TDDFT) [36–38] for the density-based formalism and the Bethe-Salpeter Equation (BSE) [39–41] within MBPT. Again, many thesis [21, 23, 42] show the details of such methods, for both the specific case of finite and infinite systems. Independently of how the inverse dielectric function is evaluated, we have to make the connection between the microscopic (calculation) and macroscopic (experiment) word.

Microscopic-macroscopic connection

The inverse dielectric function is, by definition, and in the most general case, a frequence (or time) dependent matrix $\varepsilon^{-1}(\mathbf{r}, \mathbf{r}', \omega)$, because it connects a perturbation in $\mathbf{r}$ with the total field in $\mathbf{r}'$ (it should also be noted that, since it connects two vectors, the dielectric matrix should also be a 2-rank tensor - we ignore this fact for the purpose of the present discussion). When the system to deal with is a solid, it is more convenient to work in reciprocal space and to speak about the microscopic inverse dielectric function $\epsilon^{-1}_{\mathbf{G}\mathbf{G}'}(\mathbf{q}, \omega)$, with the wave vector $\mathbf{q}$ contained in the first Brillouin zone and $\mathbf{G}$ a reciprocal lattice vector. Of course, in order to make a connection between

---

[3] This is the second important issue: especially in the case of very fast particle (in a 200 keV TEM, the electron travels so fast that the Lorentz contraction factor is 1.4) retardation effects might be important. In this case, the electric and magnetic fields are not decoupled, the electric field is not only the gradient of the potential and a more complicate version of Eq.(1.11) should be used. However for what concerns bulk systems very often these retardation effects can be neglected (or removed *a posteriori* [33]) and we will not focus on that.

[4] In the last step we have made use of the causality condition of the inverse dielectric function.

the microscopic quantity that is calculated and a macroscopic quantity like the measured spectrum (which is essentially one number per frequency), an average operation is involved. The target quantity is something that depends only on the energy (the energy loss) and on the momentum tranfer (the $\mathbf{q}$ vector),[5] other than being easy to integrate. To find this quantity, we expand in Fourier space the inverse dielectric function

$$\begin{aligned}\varepsilon^{-1}(\mathbf{r},\mathbf{r}',\omega) &= \int d\mathbf{q} \sum_{\mathbf{G},\mathbf{G}'} e^{-i(\mathbf{q}+\mathbf{G})\cdot\mathbf{r}} \varepsilon^{-1}_{\mathbf{G}\mathbf{G}'}(\mathbf{q},\omega) e^{i(\mathbf{q}+\mathbf{G}')\cdot\mathbf{r}'} \\ &= \int d\mathbf{q} e^{-i\mathbf{q}\cdot(\mathbf{r}-\mathbf{r}')} \sum_{\mathbf{G},\mathbf{G}'} e^{-i\mathbf{G}\cdot\mathbf{r}} \varepsilon^{-1}_{\mathbf{G}\mathbf{G}'}(\mathbf{q},\omega) e^{i\mathbf{G}'\cdot\mathbf{r}'} \\ &= \int d\mathbf{q} e^{-i\mathbf{q}\cdot(\mathbf{r}-\mathbf{r}')} \varepsilon^{-1}(\mathbf{q},\mathbf{r},\mathbf{r}',\omega).\end{aligned} \tag{1.14}$$

We now have found the interested quantity $\varepsilon^{-1}(\mathbf{q},\mathbf{r},\mathbf{r}',\omega)$, that is also easy to integrate,[6] and so we define the macroscopic inverse dielectric function

$$\begin{aligned}\varepsilon^{-1}_M &= \int d\mathbf{r} d\mathbf{r}' \varepsilon^{-1}(\mathbf{q},\mathbf{r},\mathbf{r}',\omega) \\ &= \int d\mathbf{r} d\mathbf{r}' \sum_{\mathbf{G},\mathbf{G}'} e^{-i\mathbf{G}\cdot\mathbf{r}} \varepsilon^{-1}_{\mathbf{G}\mathbf{G}'}(\mathbf{q},\omega) e^{i\mathbf{G}'\cdot\mathbf{r}'} \\ &= \varepsilon^{-1}_{00}(\mathbf{q},\omega).\end{aligned} \tag{1.15}$$

The macroscopic inverse dielectric function is then given by the head ($\mathbf{G} = \mathbf{G}' = 0$ component) of the inverse dielectric matrix. Eq.(1.15) gives on the operative way to compare directly with EELS experiments (to compare for instance with Eq.(1.13)). Let's finally notice that the momentum transfer in a scattering experiment can be very big. This is not always the case for EELS, but we'll see that, in the case of Inelastic X-ray scattering, the momentum transfer can be bigger than the first Brillouin zone. We have mentioned though that $\mathbf{q}$ is contained in the first BZ, so how is this going to work for $\mathbf{q}$ outside the BZ? If we call $\mathbf{Q}$ the momentum transfer, this can be always written as $\mathbf{Q} = \mathbf{q} + \tilde{\mathbf{G}}$, i.e. the sum of a vector within the BZ plus a reciprocal lattice vector. In this case the macroscopic loss function would be

$$\varepsilon^{-1}_M = \varepsilon^{-1}_{\tilde{\mathbf{G}}\tilde{\mathbf{G}}'}(\mathbf{q},\omega) \tag{1.16}$$

where we have taken (instead of the head) the diagonal element of ε^{-1} corresponding to the vector $\tilde{\mathbf{G}}$.

1.3 Inelastic X-ray Scattering

Scattering experiments do not concern only electrons, but also visible and infrared light (like in Raman spectroscopy [43]), neutrons [44] or, for the purpose of this chapter, X-rays [45]. In an experiment very similar to EELS, Inelastic X-ray scattering (IXS) is another useful tool to investigate electronic excitations. Fig.1.5 still applies, provided one substitutes the fast electron with an X-ray photon. In case of a photon probe, we can specify the perturbation Hamiltonian $H_{\text{int}} = -\mathbf{A} \cdot \mathbf{q} + \frac{1}{2}\mathbf{A}^2 + \ldots$, where the vector potential can be expanded in terms of creation and annihilation operators (representing the quantized electro-magnetif field). This leads to a very complicate scattering expression, called generalized Kramers-Heisenberg formula. Details of the mathematical foundation can be found either in the original articles about scattering of photons by

---

[5] And, in the most general case, also on the Cartesian index i,j, because we are talking about a tensor. But we omit these indeces to unburden the notation.

[6] It is enough to integrate over the Bravais cell, because the function is periodic.

electrons [46, 47], later revised for magnetic scattering [48], or in a more recent approach by Blume [49]. The generalised Kramers-Heisenberg equation for the double scattering cross section contains many terms, and can be summarized here (in the non-relativistic approximation):

$$\frac{d^2\sigma}{d\Omega d\omega} \propto \Bigg| \left\langle \psi_f | e^{i\mathbf{q}\cdot\mathbf{r}} | \psi_i \right\rangle (\boldsymbol{\epsilon}_1 \cdot \boldsymbol{\epsilon}_2) + \tag{1.17}$$

$$- \frac{1}{c^2} \left\langle \psi_f | e^{i\mathbf{q}\cdot\mathbf{r}} \boldsymbol{\sigma} | \psi_i \right\rangle (\boldsymbol{\epsilon}_2^* \times \boldsymbol{\epsilon}_1) + \tag{1.18}$$

$$\begin{aligned} &+ \sum_n \frac{\langle \psi_f | \left[\boldsymbol{\epsilon}_2^* \cdot \mathbf{p} - i(\mathbf{q}_f \times \boldsymbol{\epsilon}_2) \cdot \boldsymbol{\sigma} \right] e^{i\mathbf{q}_f\cdot\mathbf{r}} | \psi_n \rangle}{E_i - E_n + \omega_i - i\eta_n} \\ &\qquad \times \left\langle \psi_n | \left[\boldsymbol{\epsilon}_1 \cdot \mathbf{p} + i(\mathbf{q}_i \times \boldsymbol{\epsilon}_1) \cdot \boldsymbol{\sigma} \right] e^{i\mathbf{q}_i\cdot\mathbf{r}} | \psi_i \right\rangle \end{aligned} \tag{1.19}$$

$$\begin{aligned} &+ \sum_n \frac{\langle \psi_f | \left[\boldsymbol{\epsilon}_1 \cdot \mathbf{p} + i(\mathbf{q}_i \times \boldsymbol{\epsilon}_1) \cdot \boldsymbol{\sigma} \right] e^{i\mathbf{q}_i\cdot\mathbf{r}} | \psi_n \rangle}{E_i - E_n - \omega_f} \\ &\qquad \times \left\langle \psi_n | \left[\boldsymbol{\epsilon}_2^* \cdot \mathbf{p} + i(\mathbf{q}_f \times \boldsymbol{\epsilon}_2) \cdot \boldsymbol{\sigma} \right] e^{i\mathbf{q}_f\cdot\mathbf{r}} | \psi_i \right\rangle \Bigg|^2 \delta(E_i - E_f + \omega). \end{aligned} \tag{1.20}$$

Many regimes enter in the previous formula. We will neglect here the spin ($\boldsymbol{\sigma}$) dependent contribution (given by the term (1.18),[7] and the magnetic scattering (given by the sum of the term (1.19) - when out of resonance - and term (1.20)), for they are smaller terms (in the $1/c$ expansion [49]). We are left with the first term, (1.17), and the third term, (1.19), (when in resonance, i.e. when the incoming photon energy ω_i coincides with an excitation energy of a (most often) core electron). The former constitutes the measurement of the non-resonant inelastic X-ray scattering (NIXS), the latter of the resonant inelastic X-ray scattering (RIXS). From now on, we will consider the first case, so the term IXS will be a synonimous of NIXS. In this (non-resonant) regime, the experimental scattering techniques will give information about the so called Dynamical Structure Factor (DSF), defined as

$$\begin{aligned} \frac{d^2\sigma}{d\Omega d\omega} &\propto \left| \left\langle \psi_f | e^{i\mathbf{q}\cdot\mathbf{r}} | \psi_i \right\rangle (\boldsymbol{\epsilon}_1 \cdot \boldsymbol{\epsilon}_2) \right|^2 \delta(E_i - E_f + \omega) \\ &= (\boldsymbol{\epsilon}_1 \cdot \boldsymbol{\epsilon}_2)^2 S(\mathbf{q}, \omega), \end{aligned} \tag{1.21}$$

in which $\boldsymbol{\epsilon}_1, \boldsymbol{\epsilon}_2$ are the polarization vectors of the incoming and scattered photons, respectively. It is then evident the similarity between IXS and EELS. They share the same intrinsic contribution: the loss function. In a scattering experiment like depicted in Fig. 1.5, it doesn't matter if the scattered particle is a photon or an electron. We are probing the inverse dielectric function of the system. The kinematic prefactor changes, of course, leading to a q^2 difference, between the two cases. It has to be underlined that, from the experimental point of view, the two techniques are quite different both in terms of experimental setup (in one case one needs a source of electrons, which is normally achieved with an electron microscope, in the other synchrotron radiation facility is required) and in resolution (EELS has much better energy resolution at low $\mathbf{q}$, IXS can achieve high $\mathbf{q}$ inaccessible to EELS, which in contrast can perform better spatial resolution, etc.).

Because of the intrinsic similarities between IXS and EELS, the micro-macro connection explained at page 19 still holds.

---

[7] Even if a.u. are used throughout the document, here we want to explicitly underline the $1/c^2$ behaviour of this term.

1.4 Optical Spectroscopy

From the Maxwell's equations (in presence of matter) [50–52]

$$\begin{aligned} \nabla \times \mathsf{H} &= \frac{1}{c}\frac{\partial \mathsf{D}}{\partial t} + \frac{4\pi}{c}\mathbf{j}_{ext} \\ \nabla \times \mathsf{E} &= -\frac{1}{c}\frac{\partial \mathsf{B}}{\partial t} \\ \nabla \cdot \mathsf{D} &= 4\pi\rho_{ext} \\ \nabla \cdot \mathsf{B} &= 0 \end{aligned} \tag{1.22}$$

we can get the total electric field in a medium as a damped wave

$$\mathsf{E} = \mathsf{E}_0 e^{i(\mathbf{K}\cdot\mathbf{r}-\omega t)}$$

with

$$|\mathbf{K}|^2 = \frac{\omega^2}{c^2}\mu\varepsilon$$

and we have used the linear material equations $\mathsf{D} = \varepsilon\ \mathsf{E}$ and $\mathsf{B} = \mu\ \mathsf{H}$. If we neglect for a moment the magnetic properties,[8] setting $\mu = 1$, we define the complex refractive index $\mathcal{N}$ as

$$\mathcal{N} = \sqrt{\varepsilon} = \nu + i\kappa \tag{1.23}$$

whose real and imaginary parts are called the *refraction index* and the *extinction coefficient*, respectively, and they are related to the real ε_1 and the imaginary part ε_2 of ε, as

$$\begin{aligned} \varepsilon_1 &= \nu^2 - \kappa^2 \\ \varepsilon_2 &= 2\nu\kappa \end{aligned}$$

ν and κ being not independent, since ε_1 and ε_2 are related by the Kramers Kronig relations. We will see now how important this simple linear relation is for a variety of quantities.

We can define the the *optical skin depth* δ as the distance where the amplitude of the field is reduced by $1/e$, and the *absorption coefficient* α as the inverse distance where the intensity[9] of the field is reduced by $1/e$:

$$\delta = \frac{c}{\omega\kappa} \tag{1.24}$$

$$\alpha = \frac{2\omega\kappa}{c} = \frac{\omega\varepsilon_2}{\nu c} \tag{1.25}$$

the latter giving a linear relation between the absorption coefficient and the imaginary part of the dielectric function. All these quantities are, in the most general case, frequency dependent rank-2 tensors.

In experiments concerning optical properties of solids often the *normal incidence reflectivity* is involved. Following Fig. 1.7, one can see an incident beam which impinges normally at the surface of a solid, with an amplitude given by E_i, and a reflected beam, with the same frequency but an amplitude $E_r < E_i$. So in the vacuum the wave is:

$$E_z = E_i e^{i\left(\frac{\omega x}{c}-\omega t\right)} + E_r e^{-i\left(\frac{\omega x}{c}+\omega t\right)} \qquad x < 0,$$

---

[8] This is not strictly necessary. Due to the ambiguity of D and H that could be changed without changing the Maxwell's equation, we can always define an $\tilde{\varepsilon}$ such as $\mathsf{D} = \tilde{\varepsilon}\mathsf{E}$ and $\mathsf{H} = \mathsf{B}$ so $\mu = 1$. In this case all magnetic properties would be included in $\tilde{\varepsilon}$ but this choice is not always convenient.

[9] The intensity of an electromagnetic field is proportional to $|\mathsf{E}(x)|^2$, i.e. $I(x) = I_0 e^{-2\frac{\omega}{c}\kappa x}$ if we consider one dimension.

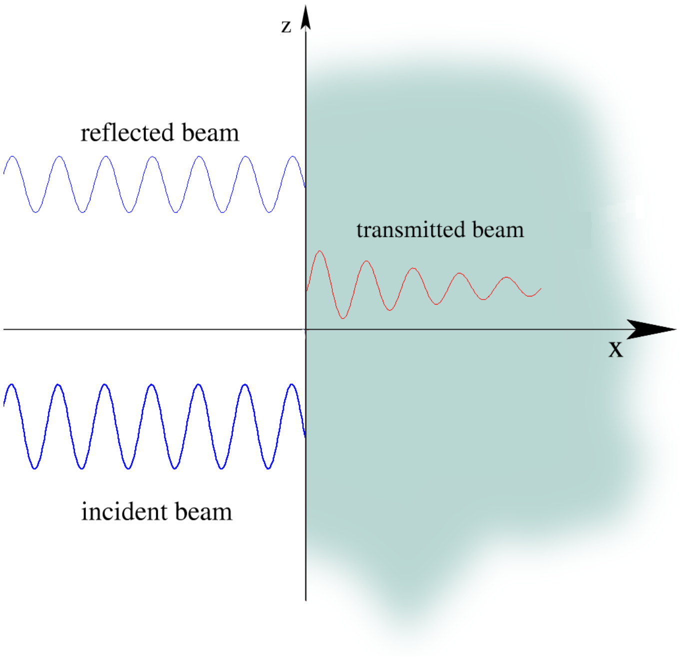

Figure 1.7: Schematic diagram of incident, reflected and transmitted electromagnetic wave at the surface.

where we imagine the beam polarised along z; inside the solid, one can see the transmitted wave

$$E_z = E_t e^{i(kx-\omega t)} \qquad x > 0.$$

Imposing the boundary condition to the tangential component of the electric field[10]

$$E_z(x \to 0^+) = E_z(x \to 0^-)$$

we have

$$E_i + E_r = E_t.$$

The second boundary condition has to be applied to the tangential component of the magnetic field H_y:

$$-\partial_x E_z = \frac{i\omega\mu}{c} H_y$$

$$q\,(E_i - E_r) = kE_t = q\mathcal{N}E_t \Rightarrow E_i - E_r = \mathcal{N}E_t.$$

We define the *normal incidence reflectivity* $\mathcal{R}$ as

$$\mathcal{R} = \left|\frac{E_r}{E_i}\right|^2 < 1$$

which becomes

$$\mathcal{R} = \left|\frac{(1-\nu)^2 + \kappa^2}{(1+\nu)^2 + \kappa^2}\right| < 1.$$

The knowledge of the optical constants implies hence the knowledge of the reflectivity, which can be compared, e.g., with the experiment (in a very recent paper, just accepted [53], we do a careful

---

[10] Let $\hat{\mathbf{n}}$ be a normal (unit) vector to the surface separating the two materials. We have, for the normal components, the two relations: $(\mathsf{D}_2 - \mathsf{D}_1)\cdot\hat{\mathbf{n}} = 4\pi\rho_s$ and $(\mathsf{B}_2 - \mathsf{B}_1)\cdot\hat{\mathbf{n}} = 0$; while for the tangential components: $\hat{\mathbf{n}} \times (\mathsf{E}_2 - \mathsf{E}_1) = 0$ and $\hat{\mathbf{n}} \times (\mathsf{H}_2 - \mathsf{H}_1) = \frac{4\pi}{c}\mathbf{j}_s$, with ρ_s and $\mathbf{j}_s$ the surface density and surface current respectively [52].

comparison between calculated and experimental reflectivity for VO_2). But the opposite procedure is more interesting, because we can measure the reflectivity, and then deduce the optical constants. Since there are two optical constants involved (ν and κ), we need two reflectivity experiments or just one experiment, but in a very large frequency range, in order to exploit the Kramers-Kronig relation between ν and κ.

Another measurable quantity, useful in the description of a surface, is the *surface impedance* $\mathcal{Z}$ defined as

$$\mathcal{Z} = \frac{4\pi}{c}\frac{\mathsf{E}(0)}{\mathsf{B}(0)}$$

which can also be related to the optical refractive index $\mathcal{N}$ by $\mathcal{Z} = \frac{4\pi}{c\mathcal{N}}$.

Today, one frequently applied technique to probe the optical properties of a sample is the optical *ellipsometry*. Ellipsometry deals with measurements of polarised light undergoing oblique reflection (or transmission) from a sample surface. The quantities measured are the ellipsometric angles φ and δ related to the complex ratio of Fresnel reflection (or refraction) coefficient R_p and R_n for light polarised parallel (p-component) and normal (n-component) to the plane of incidence

$$\zeta = \frac{R_p}{R_n} = \mathrm{tg}\varphi\, e^{i\delta}$$

characterizing the different changes in amplitude and phase. Ellipsometry experiments [54–57] can be carried out at multiple frequency (spectroscopic ellipsometry) and also at different angles of incidence (variable angle spectroscopic ellipsometry, V.A.S.E). In Fig. 1.8 a schematic example of reflection ellipsometry is reported. Knowing the ratio ζ and the incidence angle θ the complex dielectric function is

$$\varepsilon = \sin^2\theta + \sin^2\theta\tan^2\theta\left(\frac{1-\zeta}{1+\zeta}\right)^2 . \qquad (1.26)$$

It is important to notice two things: i) only the ellipsometry quantities φ and δ are the real mea-

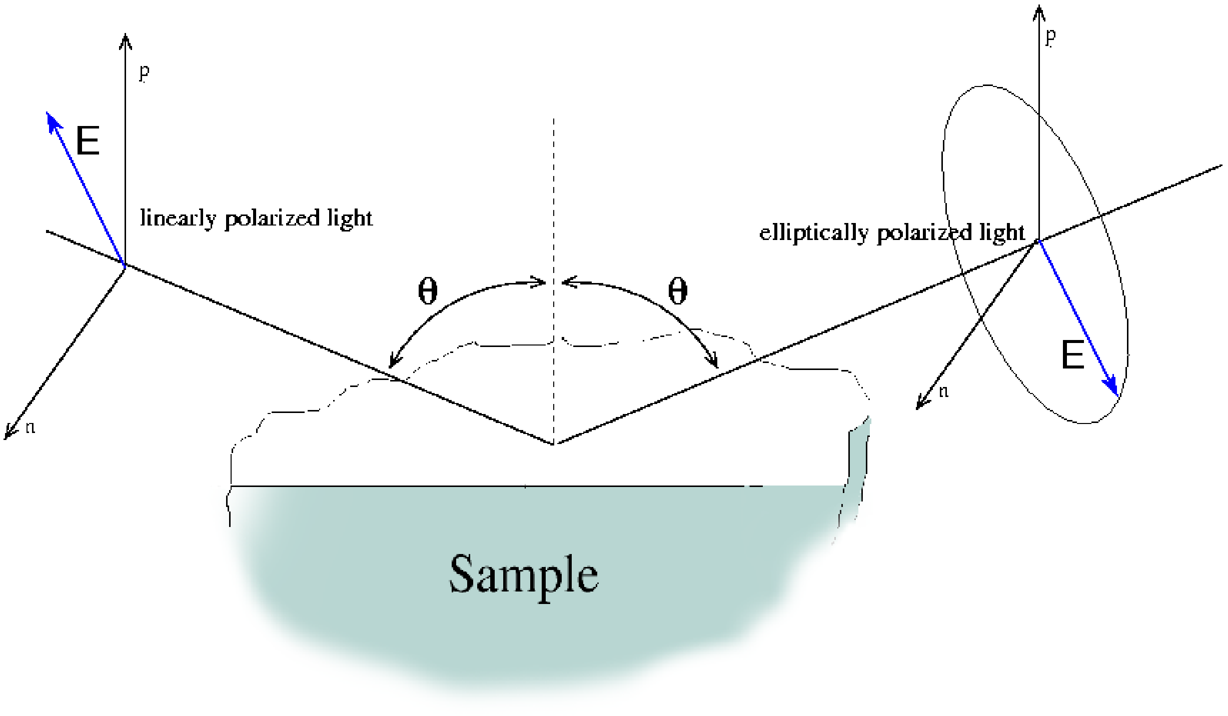

Figure 1.8: Schematic representation of a reflection ellipsometry experiment.

surable quantities, so the connection to the dielectric function is based on analytical calculation (involving certain assumptions and models); ii) both real and imaginary parts of ε are evaluated in an ellipsometry experiment, this not requiring any Kramers-Kronig analysis and post-processing. As we have said in the previous section, TDDFT and BSE are currently used to evaluate, from first principles, the dielectric function. It has to be said, however, that even though current approximations to TDDFT manage to give a good description of the loss function, this is not necessarily the case for the absorption spectroscopy. Especially in solids, where excitonic and local field effects come out from a competition between short and long range correlations, the use of state-of-the-art BSE approach is needed. We have detailed elsewhere this issue [21].

Microscopic-macroscopic connection

Even in the case of optical spectroscopy we have to make a link between what is measured, a spectrum, and the microscopic quantities that are calculated, $\varepsilon(\mathbf{r}, \mathbf{r}', \omega)$. First of all, we have to correctly consider the response function in these two worlds, microscopic and macroscopic, and then make the connection between the two. Let's start from the first one. In the microscopic world the relation in which the dielectric function appears has to be written as

$$\mathsf{E}(\mathbf{r}, \omega) = \int d\mathbf{r}' \varepsilon^{-1}(\mathbf{r}, \mathbf{r}', \omega) \mathsf{D}(\mathbf{r}', \omega) \tag{1.27}$$

because D is the external field (as can be seen from the Maxwell's Eq.(1.22), D is related to the external charge). Again, we are omitting the tensorial character of the response function and, since we consider a solid system, it is better to work in reciprocal space

$$\mathsf{E}_{\mathbf{G}}(\mathbf{q}, \omega) = \sum_{\mathbf{G}'} \varepsilon^{-1}_{\mathbf{G}\mathbf{G}'}(\mathbf{q}, \omega) \mathsf{D}_{\mathbf{G}'}(\mathbf{q}, \omega) \tag{1.28}$$

We have seen previously that in order to get the macroscopic quantity for the loss function we simply have to get the head of the matrix. This was for the loss function. Here we have to describe what is our macroscopic quantity. The incoming photon in an ellipsometry experiment (whose range spans from infrared to ultraviolet light) carries a very small $\mathbf{q}$, which is normally considered zero. That's why the dipole approximation is used in the oscillator strength term

$$\left\langle \psi_f | e^{i\mathbf{q}\cdot\mathbf{r}} | \psi_i \right\rangle = \langle \psi_f | 1 + i\mathbf{q} \cdot \mathbf{r} + ... | \psi_i \rangle = i\mathbf{q} \cdot \langle \psi_f | \mathbf{r} | \psi_i \rangle$$

when one considers the absorption of a photon.[11] Now, the wavelength associated to this $\mathbf{q} \to 0$ is very big and normally contains the system for which we want to study the response. In this particular case, it is crucial to pay attention in defining correctly the *perturbing* quantity, the one that can be changed at will. It turns out that this is not the macroscopic external potential (or field $\mathsf{D}(\mathbf{G} = 0, \omega)$) but an effective (or total) potential. The mathematical derivation of this is reported in details in two (nice and difficult) articles [59, 60]. We would like nonetheless give the physical reasons for this. In the case of a perturbation which has a wavelength bigger than the system, like an optical photon, we can consider the perturbation itself as a macroscopic electric field (and magnetic field) applied to the system: this can be schematically represented by a condensator. Looking at Fig. 1.9, we see that the potential that can be changed at will (and so representing the truly pertubing potential in the linear response approach, as mentioned in Appendix A) is a total potential given by the sum of the external (battery) plus the macroscopic polarization potential. It is not possible in this case to talk about external measurable potential: the measurable quantity in the voltimeter will be a total potential. The same reasonement could be done for the magnetic field:

---

[11] In practical cases, the dipole approximation is used even in the case of X-ray absorption. Electric quadrupole and magnetic dipole intervene as very small adjustement [58].

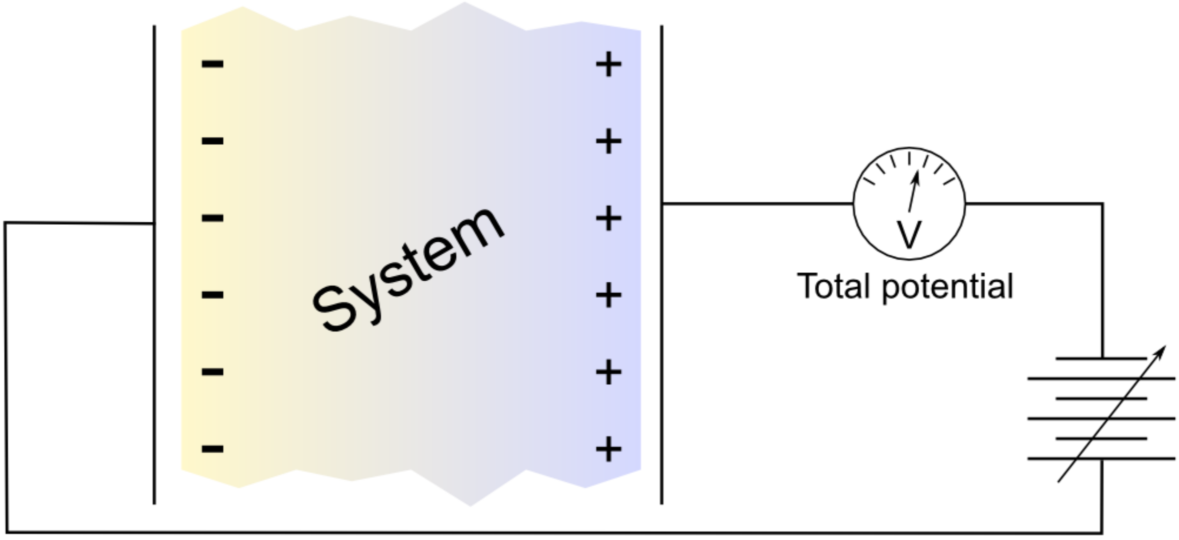

Figure 1.9: The measurable potential on the voltimeter is a total potential given by the sum of the external potential given by the battery plus the macroscopic polarization of the system. This total potential is the one that can be changed at will.

we might insert the system into a solenoid and measuring a given effective (or total) current on the solenoid coils. So, from a macroscopic point of view (for this specific case of a long wave-length perturbation like a visible or ultraviolet photon) the perturbing field is the total one. That is way we often write (see the excellent Jackson book [52], for instance) $\mathsf{D} = \varepsilon_M \mathsf{E}$. This is correct in a macroscopic world. This is sometimes referred to the widely used (but rarely explained) sentence: "Optical absorption is the response to a total potential, contrary, for instance, to EELS that is the response to an external potential". It comes now the second issue: creating the connection between the microscopic response function and the macroscopic ones. We have to put together the two equations (let's put the momentum back, considered to be small)

$$\mathsf{E}_{\mathbf{G}}(\mathbf{q},\omega) = \varepsilon^{-1}_{\mathbf{G},\mathbf{G}'}(\mathbf{q},\omega)\mathsf{D}_{\mathbf{G}'}(\mathbf{q},\omega) \tag{1.29}$$

$$\mathsf{D}(\mathbf{q},\omega) = \varepsilon_M(\mathbf{q},\omega)\mathsf{E}(\mathbf{q},\omega). \tag{1.30}$$

Since the macroscopic average of the first equation is just (as we have seen in the previous section) $\mathsf{E}(\mathbf{q},\omega) = \varepsilon^{-1}_{00}(\mathbf{q},\omega)\mathsf{D}(\mathbf{q},\omega)$, we have the final connection

$$\varepsilon_M(\mathbf{q},\omega) = \frac{1}{\varepsilon^{-1}_{00}(\mathbf{q},\omega)}, \tag{1.31}$$

which defines the *macroscopic dielectric function* as the inverse of the macroscopically averaged inverse dielectric function. There are two reference articles that are normally cited for this formula, though they not fully explain why the formula has to be written like it is, in rigorous mathematical terms [61, 62]. What it is instead very well explained is what is instead the value ε_{00}. It is a macroscopic quantity, of course, but not the macroscopic dielectric function. To answer that, one can indeed read Refs.[61, 62], but also ask the simple question: when do ε_{00} can be considered the macroscopic dielectric function? Or, in other terms, when $\varepsilon_{00} = \frac{1}{\varepsilon^{-1}_{00}}$, i.e. when the inverse of a matrix is composed by the inverted elements of the original matrix? Only when the matrix is diagonal. If we neglect the non-diagonal components $\mathbf{G} \neq \mathbf{G}'$ of ε^{-1}, we are considering $\varepsilon^{-1} = \varepsilon^{-1}(|\mathbf{r} - \mathbf{r}'|)$, like if the system were homogeneous. So ε_{00} is nothing else than the macroscopic dielectric function without local fields.

Chapter 2

From Theory to Code

We have seen the crucial role played by the inverse dielectric function, either directly, in the description of optical and loss spectroscopy, or indirectly, in photoemission (through the screened Coulomb interaction entering the self-energy). This is why lot of effort has been carried out, in the electronic structure community, to efficiently describe, in an *ab initio* way, this function.

As mentioned before, two opposed theoretical approaches have been devised to describe the calculate (among other things) the dielectric function: the TDDFT, in the density functional formalism, and the BSE, within the Green's function theory. In both cases the answer comes through the evaluation of another response function:[1] the polarizability.

$$\varepsilon^{-1}(\mathbf{r},\mathbf{r}',\omega) = \delta(\mathbf{r}-\mathbf{r}') + \int d\mathbf{r}'' v(\mathbf{r}-\mathbf{r}'')\chi(\mathbf{r}'',\mathbf{r}',\omega) \tag{2.1}$$

The full polarizability function is another response function, defined as

$$\delta\rho(\mathbf{r},\omega) = \int d\mathbf{r}'' \chi(\mathbf{r}'',\mathbf{r}',\omega)\delta V_{\text{ext}}(\mathbf{r}',\omega) \tag{2.2}$$

with $\rho(\mathbf{r},\omega)$ defining the induced density and $V_{\text{ext}}(\mathbf{r},\omega)$ the external perturbation potential. Again here we are considering only the scalar dielectric function (related to the observables and experiments mentioned in the previous chapter), which connects to the so-called density-density response, defined in Eq.(A.2), and to the full rank-2 tensor via $\varepsilon^{-1} = \sum_{ij} \boldsymbol{\epsilon}_i \varepsilon^{-1}_{ij} \boldsymbol{\epsilon}_j$. Finding χ is of course equivalent to find ε^{-1}. The advantage of the former is that can be expressed as a modification of the independent particle polarizability, for which an analytical expression exists [63–65].

2.1 TDDFT and the DP code

Within TDDFT the polarizability can be written, in reciprocal space, as a Dyson equation [21, 36–38]

$$\chi_{\mathbf{G}\mathbf{G}'}(\mathbf{q},\omega) = \chi^0_{\mathbf{G}\mathbf{G}'}(\mathbf{q},\omega) + \chi^0_{\mathbf{G}\mathbf{G}''}(\mathbf{q},\omega)\left[v_{\mathbf{G}''\mathbf{G}'''}(\mathbf{q}) + f^{\text{xc}}_{\mathbf{G}''\mathbf{G}'''}(\mathbf{q},\omega)\right]\chi_{\mathbf{G}'''\mathbf{G}'}(\mathbf{q},\omega), \tag{2.3}$$

with χ^0 being the independent-particle polarizability and f^{xc} the unknown exchange-correlation kernel. Here and after, an implicit sum over repeated indeces should be considered. Eq.(2.3) is

---

[1] We talk here about the *linear* response function, because it enters in the optical absorption, in the loss function and in photoemission. However other spectroscopies, like harmonic generation for instance, or the reponse to intense laser fields, do not fall into the linear regime. The linear polarizability (or the dielectric function as defined in the material relation) is only one observable of the Green's function theory or TDDFT, that are indeed exact to all regimes, not restricted to linear response.

implemented in the DP code [66], a plane-wave code, working in reciprocal space and frequency domain. The language of the code is Fortran, with some insertion of C (parser, utilities) and perl scripts for tests. The releases are tested for several platforms, thanks to a buildbot testfarm (`http://http://dev.abinit.org/environment/buildbot`). Several linear algebra libraries can be linked, thanks to an adaptive interface, either free, like lapack+blas, atlas, or proprietor, like cxml, asl, imsl or essl. The FFTW3 are the preferable fft libraries, but interface with cxml, asl, goedecker-fft are also provided. The goedecker-fft library itself is provided as well. The DP code was born in Rome, during V.Olevano's PhD with Rodolfo Del Sole. The development then moved to Palaiseau, where Valerio did his post-doc, before being hired by the CNRS. At that time (2000), I was starting my PhD with Lucia Reining and Valerio. In the last 15 years many things have changed in the code: several approximations for the exchange-correlation kernel have been added (to the original RPA and ALDA [21]), the code has been parallelized, the interface with other codes improved, etc. However the basic structure stay the same. In short, two main tasks have to be carried out:

1. Creation of the independent particle polarizability

   $$\chi^0_{\mathbf{GG}'}(\mathbf{q},\omega) = \sum_{nm\mathbf{k}} \frac{\tilde{\rho}_{nm\mathbf{k}}(\mathbf{q}+\mathbf{G})\tilde{\rho}^*_{nm\mathbf{k}}(\mathbf{q}+\mathbf{G}')\,(f_{n\mathbf{k}-\mathbf{q}} - f_{m\mathbf{k}})}{\omega - (\epsilon_{m\mathbf{k}} - \epsilon_{n\mathbf{k}-\mathbf{q}}) + i\eta} \tag{2.4}$$

   where $nm\mathbf{k}$ is a transition from a band n (at $\mathbf{k}-\mathbf{q}$) to a band m (at $\mathbf{k}$), $\tilde{\rho}_{nm\mathbf{k}}(\mathbf{q}+\mathbf{G}) = \int d\mathbf{r}\psi_{n\mathbf{k}-\mathbf{q}}(\mathbf{r})e^{i(\mathbf{q}+\mathbf{G})\cdot\mathbf{r}}\psi^*_{m\mathbf{k}}(\mathbf{r})$ is the oscillator strength of the transition (built with Kohn-Sham orbitals) and $\epsilon_{m\mathbf{k}} - \epsilon_{n\mathbf{k}-\mathbf{q}}$ is the energy transition. The transition is possible only if the occupation number condition is fulfilled $(f_{n\mathbf{k}-\mathbf{q}} - f_{m\mathbf{k}})$. All this implies that the DP code needs the output (eigenvalues, wavefunctions and occupation numbers) of a ground-state DFT code. At today, we have interfaces with the Abinit [67] and Quantum Expresso [68] projects. The evaluation of χ^0 is the most expensive part (with one exception: the Nanoquanta kernel) of the calculation. The scaling is $o(\mathrm{N_{at}})^4$, so quite bad, but with a very small prefactor. In addition, this procedure is very simple to parallelize. We have in fact adopted for DP, a triple possible parallelization strategy: both MPI or OpenMP can be used to parallelize the loop over transitions (the big sum in Eq.(2.4)); very recently, thanks to a PRACE project carried out in collaboration with the Maison de la Simulation,[2], this loop has been ported over GPU (following the CUDA directives) [69]. Since the transitions are decided at the very beginning, the memory distribution over processors is very effective, making it possible to calculate even systems with thousand of electrons.

2. Once the independent particle polarizability evaluated, the full polarizability is the result of the Dyson equation

   $$\chi_{\mathbf{GG}'}(\mathbf{q},\omega) = \left[\delta_{\tilde{\mathbf{G}}\tilde{\mathbf{G}}'} - \chi^0_{\tilde{\mathbf{G}}\tilde{\mathbf{G}}''}(\mathbf{q},\omega)\left(v_{\tilde{\mathbf{G}}''\tilde{\mathbf{G}}'}(\mathbf{q}) + f^{\mathrm{xc}}_{\tilde{\mathbf{G}}''\tilde{\mathbf{G}}'}(\mathbf{q},\omega)\right)\right]^{-1}_{\mathbf{GG}''}\chi^0_{\mathbf{G}''\mathbf{G}'}(\mathbf{q},\omega) \tag{2.5}$$

   which again can be easily parallelized (over energies ω). This part of the calculation, which is indeed responsible for the local field effects, excitonic effects, confinement, polarization, etc. does not alter significantly the computational time of a typical run. Several approximations are possible for f^{xc}: RPA (indeed $f^{\mathrm{xc}} = 0$), ALDA, the long-range kernel [70], the Nanoquanta kernel [71–73] (derived from a BSE-like formula[3] and, since recently, the bootstrap kernel [74–76].

All TDDFT-related results shown in the summary of research are obtained with the DP code.

---

[2] The Maison de la Simulation is one of the PRACE Advanced Training Centres (PATC) in Europe, and is located in the new University Paris-Saclay site. Main objective is to help researchers in developing very high level parallel computing. `http://www.maisondelasimulation.fr/`

[3] This constitute also the only exception in the evaluation of the run time: being BSE-like, this term is very difficult to calculate and takes much more time than the evaluation of χ^0. See details in [21].

2.2 BSE and the EXC code

Analogously to TDDFT, also within Many-body theory we can define an in principle exact equation for the linear response function χ, that we call L following the historical term [39]: the Bethe-Salpeter equation.

$$L(1,2,3,4) = L^0(1,2,3,4) + L^0(1,2,5,6)\left(v(5,7)\delta(56)\delta(78) + \frac{\delta\Sigma(5,6)}{\delta G(7,8)}\right) L(7,8,3,4), \quad (2.6)$$

where we have used the convention $(1) = (\mathbf{r}_1, t_1)$. We can immediately see the similarities between Eq.(2.7) and Eq.(2.3). Both are Dyson equations in which the full polarizability is expressed as: i) an indipendent particle term, χ^0 for TDDFT, $L^0 = GG$ for the BSE;[4] ii) plus something else, related to the variation of the potentials (v and f^{xc} for TDDFT, as variation of the Hartree and exchange-correlation potential; v and $\delta\Sigma/\delta G$ for the BSE as the variation of the Hartree potential and self-energy). But there are also important differences: first of all, the BSE is a four-point equation, contrary to the two-point character of TDDFT (this is related to the mathematical tools involved in the two approaches: in one case, TDDFT, we have propagation of density, in the other propagation of two particles, the electron and the hole, for instance). And the kernel of the Dyson equation is different: instead of the completely unknown f^{xc}, we have the variation of the self-energy, for which reliable approximations exist. Making use of the so-called GW approximation for the self-energy [77], we have the well-known formula

$$\begin{aligned} L(\mathbf{r}_1,\mathbf{r}_2,\mathbf{r}_3,\mathbf{r}_4,\omega) &= L^0(\mathbf{r}_1,\mathbf{r}_2,\mathbf{r}_3,\mathbf{r}_4,\omega) + \\ & L^0(\mathbf{r}_1,\mathbf{r}_2,\mathbf{r}_5,\mathbf{r}_6,\omega)\left(v(\mathbf{r}_5,\mathbf{r}_7)\delta(56)\delta(78) - W(\mathbf{r}_5,\mathbf{r}_6)\delta(57)\delta(68)\right) L(\mathbf{r}_7,\mathbf{r}_8,\mathbf{r}_3,\mathbf{r}_4,\omega), \quad (2.7)\end{aligned}$$

where several approximations have been used ($\frac{\delta W}{\delta G} = 0$, static W, istantaneous creation of the electron-hole pairs) [21]. The crucial point here is the static $W = \varepsilon^{-1}(\omega = 0)v$,[5] that permits one to have a frequency-independent kernel and so to transform the 4-point inversion problem in Eq.(2.7), into a matrix inversion in transition space

$$L_{tt'} = \frac{1}{H^{\text{exc}}_{tt'} - I\omega} \quad (2.8)$$

where H^{exc} is the excitonic hamitonian, containing all the information about L^0, v, W, and having defined the polarizability in the transition space (t transition between band n (at $\mathbf{k}-\mathbf{q}$) to a band m (at $\mathbf{k}$))

$$L_{tt'} = \int d\mathbf{r}_1 d\mathbf{r}_2 d\mathbf{r}_3 d\mathbf{r}_4 L(1,2,3,4)\phi_{n\mathbf{k}-\mathbf{q}}(\mathbf{r}_1)\phi^*_{m\mathbf{k}}(\mathbf{r}_2)\phi^*_{n'\mathbf{k}'-\mathbf{q}}(\mathbf{r}_3)\phi_{m'\mathbf{k}'}(\mathbf{r}_4). \quad (2.9)$$

Now Eq.(2.8) can be solved in many ways:

i) The most direct one is to diagonalise the excitonic matrix $H^{\text{exc}}_{tt'}A^{t'}_\lambda = E_\lambda A^t_\lambda$, in order to have the polarizability thanks to the spectral representation of the inverse of an operator, like

$$L_{tt'} = \frac{1}{H^{\text{exc}}_{tt'} - I\omega} = \sum_{\lambda\lambda'} \frac{A^t_\lambda \, \mathsf{S}^{-1}_{\lambda\lambda'} \, A^{*t'}_{\lambda'}}{E_\lambda - \omega}, \quad (2.10)$$

---

[4] This is not strictly speaking a non-interacting term, because the function G is a fully interacting one-particle Green's function. However this term constitutes the decoupled (hence the 0 exponent) propagation of two particles, like the electron and the hole.

[5] Even though attempts to relax this contraint have been made in the past [78–81], no practical implementation for real material has been developed. Lorenzo Sponza, in his PhD thesis [82], has investigated a convenient approach where the dynamical effects can be introduced both in the one-particle *and* in the two-particle Green's function on the same footing. At today this looks the most promising direction for dynamical effects in the BSE, though not finalised yet.

(here $\mathsf{S}^{-1}_{\lambda\lambda'}$ is the overlapping matrix, due to the fact that $H^{\text{exc}}_{tt'}$ is not Hermitian, so it has left and right eigenvectors). This method offers clear advantages (full spectrum automatically obtained, powerful analysis possible), but also some drawbacks (the full diagonalisation is a N^3 problem (with $N =$ number of transitions), the whole Hamiltonian have to be kept in memory, the parallelization of the diagonalization problem is never simple).

ii) The conjugate-gradient method can be used [83] to select few lower-energies eigenvalues and eigenvectors for the formula Eq.(2.10). Even few eigenvectors are enough to have an optical spectrum, of course, at the onset of the inter-band transitions. However, as in any conjugated-gradient approach, the method only works if the matrix is not ill-conditioned and there's a clear separation among the eigenvalues [84]. Since the excitonic matrix is dense, especially in solid systems, this method can be applied only in cases where one wants to study bound excitons. The scaling of the method is N^2.

iii) The eigenvalue problem can be transformed into an initial value problem, in which a starting vector can be evoluted in (imaginary) time, via successive application of matrix-vector moltiplication (the matrix is the excitonic matrix), as described in Ref.[85, 86]. Also this method scales as N^2, but one obtains directly the spectrum, not eigenvalues and eigenvectors. Analysis of the different features of a spectrum is then difficult, if not impossible.

iv) Another iterative scheme is the Haydock inversion scheme [87, 88], which, similarly to the previous method, is based on a ripetitive matrix-vector multiplication. The great advantage of these iterative schemes, besides the reduced scaling (also Haydock scales as N^2), is the memory occupation and parallelization scheme. A matrix-vector multiplication can be carried out by stripes, so that a processor can deal with only a part of the problem, with a virtual perfect memory distribution. The intercommunication which results from this approach is very low.

The EXC code [89] is an open-source project, which implement indeed the BSE, in transition space and frequency domain. Like DP, the language of the code is Fortran, with some insertion of C (parser, utilities) and perl scripts for tests. The releases are tested for several platforms, thanks to a buildbot testfarm (`http://http://dev.abinit.org/environment/buildbot`). Several linear algebra libraries can be linked, thanks to an adaptive interface, either free, like lapack+blas, atlas, or proprietor, like cxml, asl, imsl or essl. The FFTW3 are the preferable fft libraries, but interface with cxml, asl, goedecker-fft are also provided. The goedecker-fft library itself is provided as well. This code has to be used on top of: (1) a ground state calculation; (2) a gw calculation for the quasi-particle energies (this step can be avoided, if a scissor operator approximation is adopted); (3) rpa calculation for the statiscally screened Coulomb interaction. For what concerns the excitonic hamiltonian solver, methods i) and iv) are implemented. For detailed explanation, see Ref.[21] for the full diagonalization, and Ref.[90] for the implementation of the Haydock method.

Part II

Summary of Research

Chapter 3

Theoretical Developments

3.1 Quest for a better TDDFT kernels

THE most used approach for the electronic excitations in solids is represented by time dependent density functional theory (TDDFT) [36, 91]. The problem of TDDFT is that its (by far) most used approximations, the Adiabatic Local Density approximation (ALDA) [91] or the Generalized Gradient corrected (GGA) [92] approximation fail in describing the optical properties of solids. More sophisticated approaches, derived from many-body perturbation theory (MBPT), have been able to reproduce, ab initio, the effect of the electron-hole interaction in extended systems, not least thanks to an explicit long-range contribution [70, 73, 79, 93, 94]. This long-range interaction strongly influences spectra like optical absorption or energy loss spectroscopy, especially (but not only) for relatively small momentum transfer (where the value $1/|\mathbf{q}|^2$ can be very big).

In a work conducted in collaboration with Margherita Marsili (my post-doc at the time), we have shown that this kind of kernel is even able to reproduce the hydrogen-like excitonic series in the photoemission gap of a rare gas solid. This provided for the first time a formulation, though cumbersome, for the description of optical properties of solids. The main article with this outcomes [95] has been followed by many other articles and this implementation is known to work in at least 4 widely distributed codes: DP (`http://www.dp-code.org`)[66], YAMBO (`http://www.yambo-code.org`) [96], EXCITING (`http://exciting-code.org`) [97], and VASP (`https://www.vasp.at/`) [98].
PLEASE REFER TO THE ATTACHED ARTICLE

The question of a parameter-free, but quick TDDFT calculation of excitonic effects in solids is still however an unsolved problem. Most recently we have developed a new, much simpler, formulation for the exchange correlation kernel working within TDDFT, able to describe the optical properities of semi-conductors in a very efficient way. Though the spectrum of wide-gap insulators is not yet well-described, this method permits at least to have a very good prediction of the exciton binding energies. It has just been published on PRL [76]. Actually the first spark in this direction came from a recent paper published by Sharma and co-workers [74], that stirred up a lot of attention in the electronic excitations community with very good results for optical absorption of solids. Unfortunately, after a careful investigation, the promising results had to be revisited, but the value of an ab initio description of excitonic effects is semiconductors is still very important. Also, without that first work, we wouldn't have come out with our guided iterative scheme.
PLEASE REFER TO THE ATTACHED ARTICLE

PHYSICAL REVIEW B **76**, 161103(R) (2007)

Efficient *ab initio* calculations of bound and continuum excitons in the absorption spectra of semiconductors and insulators

Francesco Sottile,[1,2] Margherita Marsili,[1,2,3] Valerio Olevano,[1,4] and Lucia Reining[1,2]
[1]*European Theoretical Spectroscopy Facility (ETSF), ETSF-France, F-91128 Palaiseau, France*
[2]*Laboratoire des Solides Irradiés UMR 7642, CNRS-CEA/DSM, École Polytechnique, F-91128 Palaiseau, France*
[3]*INFM-CNR-CNISM Dipartimento di Fisica, Università di Roma "Tor Vergata," Italy*
[4]*LEPES, Boîte Postale 166-25, avenue des Martyrs, 38042 Grenoble, France*

(Received 11 September 2007; published 22 October 2007)

We present calculations of the absorption spectrum of semiconductors and insulators comparing various approaches: (i) the two-particle Bethe-Salpeter equation of many-body perturbation theory; (ii) time-dependent density-functional theory using a recently developed kernel that was derived from the Bethe-Salpeter equation; and (iii) a mapping scheme that we propose in the present work and that allows one to derive different parameter-free approximations to (ii). We show that all methods reproduce the series of bound excitons in the gap of solid argon, as well as continuum excitons in semiconductors. This is even true for the simplest static approximation, which allows us to reformulate the equations in a way such that the scaling of the calculations with the number of atoms equals the one of the random phase approximation.

DOI: 10.1103/PhysRevB.76.161103 PACS number(s): 71.10.−w, 71.15.Qe, 71.35.−y, 78.20.Bh

Time-dependent density-functional theory (TDDFT)[1] is more and more considered to be a promising approach for the calculation of neutral electronic excitations, even in extended systems.[2,3] In linear response, spectra are described by the Kohn-Sham independent-particle polarizability χ_0^{KS} and the frequency-dependent exchange-correlation (XC) kernel f_{xc}. The widely used adiabatic local-density approximation[4,5] (TDLDA), with its static and short-ranged kernel, often yields good results in clusters but fails for absorption spectra of solids. Instead, more sophisticated approaches derived from many-body perturbation theory (MBPT)[6–10] have been able to reproduce, *ab initio*, the effect of the electron-hole interaction in extended systems, not least thanks to an explicit long-range contribution.[6,11,12] The latter strongly influences spectra like optical absorption or energy loss, especially for relatively small momentum transfer.

Here we show that this kernel is even able to reproduce the hydrogenlike excitonic series in the photoemission gap of a rare gas solid. However, the kernel has a strong spatial and frequency dependence, and its evaluation requires a significant amount of computer time. We therefore tackle the question of a parameter-free, but quick TDDFT calculation of excitonic effects in solids, which has been so far an unsolved problem, and show that a much more efficient formulation can indeed be achieved. In particular we demonstrate how it is possible for a wide range of materials to obtain good absorption spectra including excitonic effects with a *static* kernel leading in principle to a random phase approximation (RPA)-like scaling of the calculation with the number of atoms of the system.

Atomic units are used throughout the paper. The vectorial character of the quantities r,k,G,q (where k and q are vectors in the Brillouin zone, and G is a reciprocal lattice vector) is implicit. Only transitions of positive frequency (i.e., resonant contributions), which dominate absorption spectra, are considered throughout.

Let us first concentrate on the absorption spectrum of solid argon. The low band dispersion, together with the small polarizability of the solid, conjures a picture where the electron-hole interaction is very strong and gives rise to a whole series of bound excitons below the interband threshold. As in the optical spectra of other rare gas solids, the first exciton is strongly bound (in argon by ~2 eV), falling in the class of localized Frenkel[13] excitons. Closer to the continuum onset at 14.2 eV, one finds more weakly bound Mott-Wannier[14] type excitons in a hydrogenlike series. In the *ab initio* framework, such a complex spectrum is typically described by the solution of the four-point (electron-hole) Bethe-Salpeter equation (BSE).[2,15,16] In Fig. 1 we show the optical spectrum of solid argon calculated within the BSE approach, and within TDDFT both using TDLDA[17] and the MBPT-derived kernel.[7] The agreement of the BSE curve with experiment (line-circles)[20] (and with previous BSE calculations[19]) is good, concerning both position and relative intensity of the first two peaks. It should be noted that the experiment shows double peaks due to spin-orbit splitting, which is not taken into account in our calculations. The latter yields the singlet excitons that should essentially relate to the hole with $j=1/2$ and be compared with the n' peaks. Besides the spin-orbit splitting, the pseudopotential approximation as well as the construction of a static W from LDA ingredients contribute to the remaining discrepancy with experiment. In spite of these limitations, the $n'=3$ peak can also be detected, although the 2048 k points used to calculate the spectrum are not sufficient to discuss it quantitatively, nor to describe the higher peaks. Instead, the first two peaks require less k points and, as can be seen in the inset, are already well-reproduced with 256 k points. In the following we therefore concentrate on these two structures and perform all calculations with 256 k points.

The BSE definitely improves upon the TDLDA (dotted line), which shows a structureless broad curve, clearly missing the bound excitons. Instead, the kernel of Ref. 7 (full curve in Fig. 1) leads to the same accuracy as the BSE, both for the Frenkel exciton and for the following structures. This demonstrates the potential of the method and shows that the MBPT-derived kernel can be used to quantitatively predict the absorption spectra of a wide range of materials, including the insulating rare-gas solids.

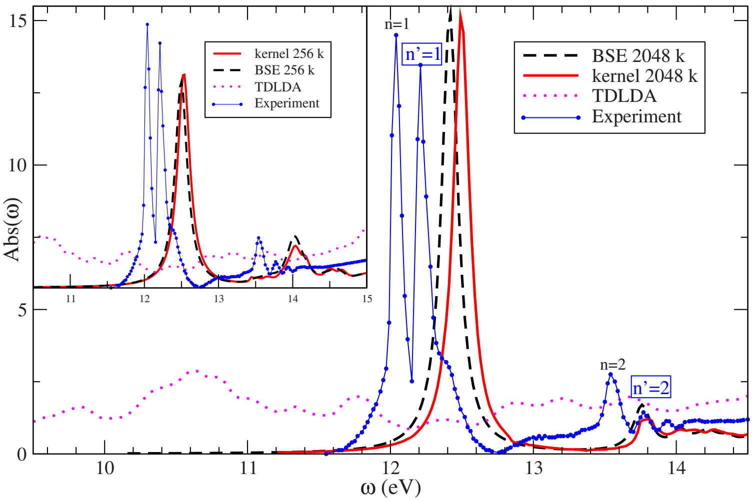

FIG. 1. (Color online) Absorption spectrum of solid Ar. The BSE (dashed) and TDDFT using the kernel of Ref. 7 (solid) are compared (only the n' singlet exciton series) with experiment.[20] TDLDA is given by the points. Main panel: calculation with 2048 k points. Inset: 256 k points.

However, the method is still computationally demanding. Indeed in the MBPT-derived TDDFT approach, the same as for the BSE two-particle Hamiltonian, one has to evaluate the matrix elements $F_{tt'}^{\mathrm{BSE}}$ of the statically screened electron-hole Coulomb interaction W,

$$F_{tt'}^{\mathrm{BSE}} = -2\pi\alpha \int dr_1 dr_2 \widetilde{\Phi}_t^*(r_1,r_2) W(r_1,r_2) \widetilde{\Phi}_{t'}(r_1,r_2), \quad (1)$$

where the product $\widetilde{\Phi}_t(r_1,r_2)=\phi_{vk}(r_1)\phi_{ck+q}^*(r_2)$ of two KS wave functions ϕ is a generalized nonlocal transition term; here t is an index of transition with momentum transfer q, i.e., $t=\{vckq\}$, from valence vk to conduction $ck+q$ states. $\alpha=2/(N_k\Omega_0)$ with N_k the number of k points and Ω_0 the volume of the unit cell. The calculation of $F_{tt'}^{\mathrm{BSE}}$ scales with the number of atoms N_{at} as $N_r N_t^2 \sim N_{at}^5$, where N_r is the number of points in real space, and N_t is the total number of transitions. Following Ref. 7, one then constructs an approximate kernel $f_{xc}^{\mathrm{eff},\mathcal{A}}=\chi_0^{-1}T_{\mathcal{A}}^{\mathrm{eff}}\chi_0^{-1}$ with

$$T_{\mathcal{A}}^{\mathrm{eff}}(r,r',\omega) = \alpha\sum_{tt'} \frac{\Phi_t(r)}{(\omega+i\eta-\Delta E_t)} F_{tt'}^{\mathrm{BSE}} \frac{\Phi_{t'}^*(r')}{(\omega+i\eta-\Delta E_{t'})},$$

where $\Phi_t(r_1)=\widetilde{\Phi}_t(r_1,r_1)$ and ΔE_t are differences between quasiparticle (QP) eigenvalues. $f_{xc}^{\mathrm{eff},\mathcal{A}}$ is an approximation to the "many-body" kernel f_{xc}^{mb} that has to be used in conjunction with an independent particle response function χ_0 built with QP energies instead of Kohn-Sham (KS) ones as in pure TDDFT. This kernel simulates hence to good approximation the electron-hole interaction that is described by the BSE.[7] Even though this construction can be optimized,[9] the method is at least an order of magnitude slower than an RPA calculation. In the following we show how this problem can be overcome.

We concentrate on the irreducible polarizability P that yields via the bare Coulomb interaction v the reducible polarizability χ from the matrix equation $\chi=P+Pv\chi$, and the inverse dielectric matrix $\epsilon^{-1}=1+v\chi$. All quantities are functions of q and frequency ω, and matrices in G,G'. Absorption spectra are then obtained from $\mathrm{Abs}(\omega) =\lim_{q\to 0} \mathrm{Im}\{1/\epsilon_{00}^{-1}(q,\omega)\}$. The polarizability P is determined from the screening equation $P=\chi_0+\chi_0 f_{xc}^{\mathrm{mb}}P$. In this equation we can now insert to the left and right of f_{xc}^{mb} the identity $1 =XX^{-1}=X^{-1}X$, providing that X is a nonsingular function. This yields

$$P = \chi_0 + \chi_0 X^{-1} T X^{-1} P, \quad (2)$$

where $T=Xf_{xc}^{\mathrm{mb}}X$. We choose a matrix of the form $X =\alpha\Sigma_t g_t(\omega)\Phi_t(r)\Phi_t^*(r')$, where $g_t(\omega)$ is an arbitrary function. The term T contains an explicit sum over matrix elements $F_{tt'}^{\mathrm{TDDFT}}=4\pi\alpha\int dr_1 dr_2 \Phi_t^*(r_1) f_{xc}^{\mathrm{mb}}(r_1,r_2,\omega)\Phi_t(r_2)$ in a basis of transitions Φ_t, namely

$$T(r,r',\omega) = \alpha\sum_{tt'} g_t(\omega)\Phi_t(r) F_{tt'}^{\mathrm{TDDFT}} g_{t'}(\omega)\Phi_{t'}^*(r'). \quad (3)$$

The exact $F_{tt'}^{\mathrm{TDDFT}}$ is of course not known. However, in the spirit of Refs. 6 and 7 we now replace the unknown matrix elements $F_{tt'}^{\mathrm{TDDFT}}$ with the BSE ones, given by Eq. (1). With this *mapping*, T is approximated as

$$\begin{aligned} T \to T^{\mathrm{eff}} = \alpha\sum_{tt'} & g_t(\omega)\Phi_t(r) \\ & \times\left[\int dr_1 dr_2 \widetilde{\Phi}_t^*(r_1,r_2) W(r_1,r_2) \widetilde{\Phi}_{t'}(r_1,r_2)\right] \\ & \times\Phi_{t'}^*(r') g_{t'}(\omega) = X^{(3)} W^{(3)} X, \end{aligned} \quad (4)$$

where we have defined a three-point right and left X operator as $X^{(3)}(r_1;r_2r_{2'};\omega)=\alpha\Sigma_t g_t(\omega)\Phi_t(r_1)\widetilde{\Phi}_t^*(r_2,r_{2'})$ and ${}^{(3)}X(r_1r_{1'};r_2;\omega)=\alpha\Sigma_t g_t(\omega)\widetilde{\Phi}_{t'}(r_1,r_{1'})\Phi_{t'}^*(r_2)$. Here it is important to underline that $F_{tt'}^{\mathrm{TDDFT}}$ are constructed as matrix elements of the *local* $\Phi_t(r)$, whereas $F_{tt'}^{\mathrm{BSE}}$ are matrix elements of the *nonlocal* $\widetilde{\Phi}_t(r,r')$. In fact the *mapping* (4) is not an exact operation because $F_{tt'}^{\mathrm{BSE}}$ cannot be expressed as a matrix element (between Φ_t and $\Phi_{t'}$) of a single f_{xc}^{mb} for all t,t'.[6,7,21] Therefore $f_{xc}^{\mathrm{eff}}=X^{-1}T^{\mathrm{eff}}X^{-1}$ can be different from f_{xc}^{mb}, and the quality of the resulting spectra will depend on the choice of X. If a certain freedom in the choice of g_t can be exploited, one may find approaches that boost the computational efficiency with respect to $f_{xc}^{\mathrm{eff},\mathcal{A}}$, i.e., the expression of Ref. 7

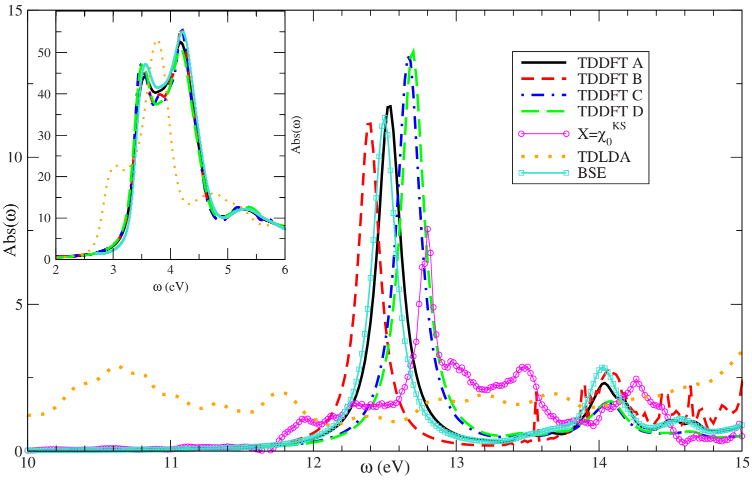

FIG. 2. (Color online) Absorption spectrum on solid argon: illustration of the different choices for Eq. (5). Inset: same choices for the absorption spectrum of Si. (Experiment from Ref. 27.)

In the following we will first illustrate, with the example of bulk silicon and solid argon, how different choices for $g_t(\omega)$ can lead to very similar spectra.

We label with calligraphic letters the different choices $\mathcal{A}$, $\mathcal{B}$, $\mathcal{C}$, and $\mathcal{D}$ that stand for

$$(\mathcal{A})\ g_t(\omega) = 1/(\omega - \Delta E_t + i\eta) \quad (\text{i.e., } X = \chi_0),$$
$$(\mathcal{B})\ g_t(\omega) = \text{Im}\{1/(\omega - \Delta E_t + i\eta)\},$$
$$(\mathcal{C})\ g_t(\omega) = 1/\Delta E_t, \quad (\mathcal{D})\ g_t(\omega) = 1. \tag{5}$$

The first choice $(\mathcal{A})$ defines nothing but the case $X=\chi_0$, as proposed in Ref. 7 and leading to $f_{xc}^{\text{eff},\mathcal{A}}$ above; in the second case $(\mathcal{B})$ only the imaginary part is taken from the denominator of the independent particle polarizability (very localized function in frequency); the cases $(\mathcal{C})$ and $(\mathcal{D})$ describe simple static choices for $g_t(\omega)$.

The inset of Fig. 2 shows the optical absorption of bulk silicon calculated with the BSE and within TDDFT, using these mapping kernels $(\mathcal{A},\mathcal{B},\mathcal{C},\mathcal{D})$; the TDLDA result is also shown in order to emphasize the little differences among the mapping kernels, compared to the huge improvements of $(\mathcal{A},\mathcal{B},\mathcal{C},\mathcal{D})$ with respect to TDLDA. The description of the optical absorption of Argon is a much more stringent test. In Fig. 2 we see that all the different kernels [$(\mathcal{A})$ being slightly better than the others] are able to well reproduce the excitonic series and to strongly improve upon the TDLDA result (dotted curve). This is especially surprising for choices $(\mathcal{C})$ and $(\mathcal{D})$: bound excitons have up to now only been obtained using either the full, strong frequency dependent kernel[9] or a frequency dependent long-range model $(\alpha+\beta\omega^2)/q^2$,[22] whereas a *static scalar* model can at best yield one single bound exciton, with largely overestimated intensity, by tuning appropriately two model parameters.[21] Our excellent results of Fig. 1 show that even a *static* parameter-free two-point kernel is able to reproduce a series of strongly bound excitons.

It is now crucial to understand and hence predict the performance of the various choices, and to elucidate whether one can choose any possible X. To this aim we start from the four-point Bethe-Salpeter equation ${}^{(4)}P={}^{(4)}\chi_0+{}^{(4)}\chi_0 W^{(4)}P$, and contract the left and right indices. We obtain hence $P=\chi_0+\chi_0^{(3)}W^{(3)}P$, where we have defined a three-point right χ_0 as $\chi_0^{(3)}={}^{(4)}\chi_0(r_1,r_1;r_2,r_{2'};\omega)$ and a three-point left polarizability ${}^{(3)}P={}^{(4)}P(r_1,r_{1'};r_2,r_2;\omega)$. Now, inserting the identity $1=\chi_0\chi_0^{-1}$, we obtain

$$P = \chi_0 + \chi_0\chi_0^{-1}\chi_0^{(3)}W^{(3)}P. \tag{6}$$

On the other hand using the *mapping* (4) in Eq. (2), we obtain the approximate polarizability

$$P^{\text{eff}} = \chi_0 + \chi_0 X^{-1}X^{(3)}W^{(3)}XX^{-1}P^{\text{eff}}. \tag{7}$$

If TDDFT is to reproduce the BSE results, P^{eff} resulting from Eq. (7) must be equal to P of Eq. (6).

It should be noted that in principle the matrix X can be chosen differently for the left and for the right side of W in Eqs. (7) and (2). Concentrating first on the left side, the choice $X=\chi_0$, i.e., $g_t(\omega)=1/(\omega+i\eta-\Delta E_t)$ recovers exactly the left side of W in Eq. (6). The right side is still to be optimized. The comparison between Eqs. (6) and (7) suggests to choose $X=P$. Of course this is not the solution of the problem, since (i) P is the quantity we are looking for and (ii) P cannot be expressed as a sum over KS transitions respecting the *ansatz* for X. Hence one can only try to find a good guess. Again, $\mathcal{A}$, with $X=\chi_0$ seems a good choice. In fact, in a solid the joint density of states calculated in GW is very close to the density of transition energies calculated from the BSE; i.e., χ_0 from GW and P from the BSE have a very similar distribution of poles.[23] Concerning the other choices, it is useful to note that $P^{(3)}$ and P have the same poles; the same statement holds for $X^{(3)}$ and X. If, in Eq. (7) the poles of $X^{(3)}$ canceled with the zeroes of X^{-1}, and no new poles were introduced, one would just find the poles of P^{eff} in the right side of W in Eq. (7), right as for P in Eq. (6). However, X^{-1} has poles that lie between the poles of X. These new poles are not problematic for energies in the continuum, but they can lead to spurious structures when they appear isolated, i.e., in the band gap. It turns out that this effect is particularly strong when the poles of X are in the vicinity of the bound excitons. This is for example the case when one chooses $X=\chi_0^{KS}$ [i.e., $g_t(\omega)=1/(\omega+i\eta-\Delta E_t^{KS})$, ΔE_t^{KS} being the difference between KS eigenvalues]: indeed, the pink circles in Fig. 2 show the bad performance of that choice.

We have, in fact, verified that the spectra are generally very stable as long as we choose an X that (i) either does not have *any* poles (static choices); or (ii) has poles in the continuum (like χ_0); or (iii) has poles at very low energies, much lower than all poles of P^{eff}. This confirms that a *wide range of choices for X is indeed possible*. Moreover, this observation is valid for a wide range of materials: we have performed the same test calculations for the prototype materials diamond and SiC, with similar conclusions.

As pointed out above, the aim is to avoid the unfavorable scaling of the calculations, determined essentially by the evaluation of F_{tt}^{BSE} via Eq. (1). Choice $(\mathcal{D})$ is of course particularly simple and promising. In fact even when it is used as it is in Eq. (4), the static choice $(\mathcal{D})$ leads to a speedup with respect to choice $(\mathcal{A})$.[7] More importantly, it allows one to recombine the sums and integrals in Eq. (4) in a more convenient way. The latter equation, once $(\mathcal{D})$ is chosen, can in fact be written as

$$
\begin{aligned}
T^{\mathrm{eff}}(q,G,G') = -4\pi\alpha^2 \sum_{k\tilde{q}\tilde{G}\tilde{G}'} W_{\tilde{G},\tilde{G}'}(\tilde{q}) \int_{\Omega_0} dr\,dr'\,d\tilde{r}\,d\tilde{r}'\, e^{-\iota G r} \\
\times e^{\iota G' r'} A_k(r,\tilde{r}) B_{k-q}(\tilde{r}',r) A_{k+\tilde{q}}(\tilde{r},r') \\
\times B_{k+\tilde{q}-q}(r',\tilde{r}') e^{\iota \tilde{G}\tilde{r}} e^{-\iota \tilde{G}'\tilde{r}'}, \qquad (8)
\end{aligned}
$$

where $A_k(r,r') = \Sigma_v u_{vk}^*(r) u_{vk}(r')$ and $B_k(r,r') = \Sigma_c u_{ck}^*(r) u_{ck}(r')$, with the u's representing the periodic part of the KS wave function $\phi_{vk}(r) = e^{-\iota k r} u_{vk}(r)$. $W_{G,\tilde{G}'(\tilde{q})}$ is the reciprocal space Fourier transform of the statically screened Coulomb interaction, with $\tilde{q}$ the difference between two k points in the Brillouin zone. For $q \rightarrow 0$ we have the special case of vanishing momentum transfer q (e.g., for optical absorption); Eq. (8) is the general formula valid for any q in order to treat also, e.g., electron energy loss or inelastic x-ray scattering.

The scaling of Eq. (8) is in principle N_{at}^4, but with a clearly dominant contribution given by the spatial integrals, which scales as $N_r^3 \ln(N_r) < N_{at}^4$.[24] Note that N_{at}^4 is the scaling of the construction of χ_0 itself.[25] In other words, this formulation offers the possibility to determine absorption spectra including excitonic effects with a workload comparable to the RPA.

In conclusion, we have calculated the absorption spectra of solid argon, both by solving the Bethe-Salpeter equation and by time-dependent density functional theory using a MBPT-derived *mapping* kernel. Both methods yield results in good agreement with experiment and reproduce well positions and relative intensities of the peaks, with a drastic improvement over TDLDA results. We have then introduced a method that allows one to derive a variety of approximations for the TDDFT kernel; these can be used to tune computational efficiency while maintaining most of the precision of the original formulation. The method has been tested for solid argon, silicon, diamond, and silicon carbide. The good results, in turn, have allowed us to propose a reformulation of the kernel [Eq. (8)] that leads to a TDDFT calculation with the same quality of the BSE, but with an RPA-like scaling $< N_{at}^4$, rather than N_{at}^5. This, we believe, can constitute a real breakthrough for practical applications where a low computational effort, that characterizes TDDFT, and a precise description of many-body effects, like in the BSE, are required.[27]

We are grateful for discussions with R. Del Sole and O. Pulci. This work was partially supported by the EU 6th Framework Programme through the NANOQUANTA Network of Excellence (NMP4-CT-2004-500198), ANR project XNT05-3_43900, and by the Fondazione Italiana "Angelo Della Riccia." Computer time was granted by IDRIS (Project No. 544).

---

[1] E. Runge and E. K. U. Gross, Phys. Rev. Lett. **52**, 997 (1984).

[2] G. Onida *et al.*, Rev. Mod. Phys. **74**, 601 (2002).

[3] *Time-Dependent Density Functional Theory*, edited by M. A. L. Marques *et al.* (Springer, New York, 2006).

[4] A. Zangwill and P. Soven, Phys. Rev. A **21**, 1561 (1980).

[5] E. K. U. Gross and W. Kohn, Phys. Rev. Lett. **55**, 2850 (1985).

[6] L. Reining *et al.*, Phys. Rev. Lett. **88**, 066404 (2002).

[7] F. Sottile *et al.*, Phys. Rev. Lett. **91**, 056402 (2003).

[8] G. Adragna *et al.*, Phys. Rev. B **68**, 165108 (2003).

[9] A. Marini *et al.*, Phys. Rev. Lett. **91**, 256402 (2003).

[10] R. Stubner *et al.*, Phys. Rev. B **70**, 245119 (2004).

[11] P. de Boeij *et al.*, J. Chem. Phys. **115**, 1995 (2001).

[12] S. Botti *et al.*, Phys. Rev. B **69**, 155112 (2004).

[13] J. Frenkel, Phys. Rev. **37**, 17 (1931).

[14] G. H. Wannier, Phys. Rev. **52**, 191 (1937).

[15] G. Strinati, Riv. Nuovo Cimento **11**, 1 (1988).

[16] W. Hanke and L. J. Sham, Phys. Rev. Lett. **43**, 387 (1979).

[17] We use a set of 256 (2048) shifted k points,[18] three valence and three conduction bands, and 307 G vectors. QP eigenvalues that reproduce the experimental band gap are simulated by a scissor operator of 6.6 eV with respect to the KS-LDA eigenvalues. This mainly explains the difference with respect to the results of Ref. 19; this difference is not relevant for the purpose of the present work. For silicon the same parameters have been used, except the scissor energy (0.71 eV) and G vectors [Eq. (59)]. Calculations are carried out with the EXC code (http://www.bethe-salpeter.org) and DP code (http://theory.polytechnique.fr/codes/dp).

[18] L. X. Benedict *et al.*, Phys. Rev. B **57**, R9385 (1998).

[19] S. Galamić-Mulaomerović and C. H. Patterson, Phys. Rev. B **72**, 035127 (2005).

[20] V. Saile *et al.*, Phys. Rev. Lett. **37**, 305 (1976).

[21] F. Sottile *et al.*, Phys. Rev. B **68**, 205112 (2003).

[22] S. Botti *et al.*, Phys. Rev. B **72**, 125203 (2005).

[23] M. Rohlfing and S. G. Louie, Phys. Rev. Lett. **82**, 1959 (1999).

[24] The approximation $W_{GG'} = W_{GG}\delta_{GG'}$, that is very often used in solids, moreover, completely eliminates the N_{at}^4 terms leaving a pure $N_r^{(3)} \ln(N_r)$ scaling.

[25] More efficient methods are available[26] if one is interested only in one element of $\chi_{G,G'}$, and not in the whole matrix.

[26] B. Walker *et al.*, Phys. Rev. Lett. **96**, 113001 (2006).

[27] P. Lautenschlager *et al.*, Phys. Rev. B **36**, 4821 (1987).

Estimating Excitonic Effects in the Absorption Spectra of Solids: Problems and Insight from a Guided Iteration Scheme

Santiago Rigamonti,[1,2,*] Silvana Botti,[3,4,2] Valérie Veniard,[5,2] Claudia Draxl,[1,2] Lucia Reining,[5,2,†] and Francesco Sottile[5,2]
[1]Humboldt-Universität zu Berlin, Institut für Physik and IRIS Adlershof, 12489 Berlin, Germany
[2]European Theoretical Spectroscopy Facility (ETSF)
[3]Institut Lumière Matière, UMR5306 Université Lyon 1-CNRS, Université de Lyon, F-69622 Villeurbanne Cedex, France
[4]Friedrich-Schiller Universität Jena, Institut für Festkörpertheorie und -optik, Max-Wien-Platz 1, 07743 Jena, Germany
[5]Laboratoire des Solides Irradiés, École Polytechnique, CNRS, CEA-DSM, F-91128 Palaiseau, France

(Received 28 November 2014; published 7 April 2015)

A major obstacle for computing optical spectra of solids is the lack of reliable approximations for capturing excitonic effects within time-dependent density functional theory. We show that the accurate prediction of strongly bound electron-hole pairs within this framework using simple approximations is still a challenge and that available promising results have to be revisited. Deriving a set of analytical formulas we analyze and explain the difficulties. We deduce an alternative approximation from an iterative scheme guided by previously available knowledge, significantly improving the description of exciton binding energies. Finally, we show how one can "read" exciton binding energies from spectra determined in the random phase approximation, without any further calculation.

DOI: 10.1103/PhysRevLett.114.146402 PACS numbers: 71.15.Qe, 71.10.-w, 71.35.-y, 78.20.Ci

The response of materials to an electromagnetic field is a key to many properties and applications. In the frequency range from infrared to ultraviolet, the optical properties determine the color of materials, their ability to absorb sunlight, and much more. They lay the ground for nondestructive spectroscopies, such as ellipsometry, that can tell us much about the electronic or atomic structure of materials. However, theoretical tools are needed that allow one to analyze, understand, and predict measured results and desired or undesired properties. These tools should be reliable and versatile, but simple enough to be applicable to systems of fundamental or technological interest, which are often rather complex. One of the major challenges is to design approximations for the *ab initio* calculation of optical spectra of extended systems such as solids and liquids [1].

The state-of-the-art approach for the *ab initio* calculation of optical spectra consists in using the Kohn-Sham electronic structure coming from a density functional theory calculation as the starting point for a quasiparticle band structure calculation in the *GW* approximation, and the subsequent solution of the Bethe-Salpeter equation (BSE) to account for the electron-hole interaction [1–5]. The scheme is successful; in particular, excitonic effects are well described. However, the calculations are computationally demanding, because of the two-particle (electron and hole) nature of the problem. Alternatively, time-dependent density functional theory (TDDFT) [1,6,7] formulates the response in terms of variations of local potentials that are functionals of the time-dependent density. This reduces the size of the problem, but raises the question of how to find a good approximation for the time-dependent exchange-correlation (xc) potential v_{xc} and its first derivative, the xc kernel $f_{\mathrm{xc}}(\mathbf{r},\mathbf{r}',t-t')=\delta v_{\mathrm{xc}}(\mathbf{r},t)/\delta n(\mathbf{r}',t')$, where n is the time-dependent electron density. Some simple but widely used approximations such as the adiabatic local density approximation [8,9], which are often successful for finite systems and for electron energy-loss spectra, yield disappointing results similar to the random phase approximation ($f_{\mathrm{xc}}=0$) [7,10] for absorption spectra of solids.

Many works, e.g., Refs. [11–16], try to overcome this problem. A class of successful kernels has been derived from the BSE [17–22]. The nanoquanta kernel [20–23] gives results close to BSE ones, but with a comparable computational cost, although suggestions for speedups have been made [24]. The long-range corrected (LRC) kernel [23,25] $f_{\mathrm{xc}}^{\mathrm{LRC}}=-\alpha/q^2$ with the correct divergence for small wave vectors q is a simple scalar approximation of the nanoquanta kernel. $f_{\mathrm{xc}}^{\mathrm{LRC}}$, with α empirically determined from the static dielectric constant of the crystal [25], works well for continuum excitons in semiconductors [26–28]. However, it fails to reproduce bound excitons, unless α is set *ad hoc* to a much higher value than in Ref. [25]. In this case, a transition may appear within the quasiparticle gap [29–31], but with too high oscillator strength [29].

Alternatively, the so-called bootstrap (BO) kernel [32] also has the correct $1/q^2$ behavior; the prefactor is determined self-consistently, and it goes beyond the scalar version. Promising results have been published [32,33] for continuum and bound excitons, and the exciton binding energies of a range of small- and large-gap semiconductors have been calculated [34,35]. However, the BO expression has not been derived, but rather justified by observations, and the predictive power of the approach has not yet been demonstrated. Indeed, as we will show below, the BO does not lead to reliable absorption spectra, sometimes not even qualitatively.

The aim of this work is to elucidate the origin of the BO and of its shortcomings, in order to go beyond. We show that a BO-like expression can indeed be derived, but it is slightly different from the *ad hoc* (i.e., without derivation) one of Ref. [32] and it leads to improvements, in particular for exciton binding energies. The computational cost can be further significantly reduced thanks to simple analytical formulas. In particular one can "read" exciton binding energies from results obtained in the random-phase approximation (RPA), without any further calculation.

Optical spectra of solids are obtained from the imaginary part of the macroscopic dielectric function $\epsilon_M(\omega)$, which can be calculated from

$$\epsilon_M(\omega) = \frac{1}{\epsilon^{-1}_{00}(\omega)} = 1 - v_0\bar{\chi}_{00}(\omega), \tag{1}$$

where $\epsilon_{\mathbf{G}\mathbf{G}'}(\omega)$ is the $\mathbf{q} \to 0$ limit of the microscopic dielectric matrix $\epsilon_{\mathbf{G}\mathbf{G}'}(\mathbf{q},\omega)$ in a basis of reciprocal lattice vectors. 00 indicates the head ($\mathbf{G} = \mathbf{G}' = 0$) element of the matrix, v_0 is the long-range ($\mathbf{G} = 0, \mathbf{q} \to 0$) part of the Coulomb interaction, and $\bar{\chi}$, the linear density response to the total macroscopic classical potential [1], is obtained from the matrix (in $\mathbf{G}, \mathbf{G}'$) Dyson equation

$$\bar{\chi}(\omega) = \bar{\chi}^{\mathrm{RPA}}(\omega) + \bar{\chi}^{\mathrm{RPA}}(\omega) f_{\mathrm{xc}}(\omega)\bar{\chi}(\omega), \tag{2}$$

$$\bar{\chi}^{\mathrm{RPA}}(\omega) = \chi^0(\omega) + \chi^0(\omega)\bar{v}\bar{\chi}^{\mathrm{RPA}}(\omega) \tag{3}$$

with $\bar{v}$ the Coulomb interaction without the $\mathbf{G} = 0$ component v_0, and χ^0 the independent-particle response function. The RPA solution $\bar{\chi}^{\mathrm{RPA}}(\omega)$ includes crystal local field effects (LFE) through $\bar{v}$. Note that χ^0 is in principle the Kohn-Sham independent-particle response function. However, here we build χ^0 with quasiparticle energies, e.g., from a *GW* calculation (see the Supplemental Material for details [36]). Hence f_{xc} does not have to simulate the gap opening with respect to the Kohn-Sham gap. This often adopted strategy for TDDFT in solids allows one to simplify the kernel significantly, and is used also for the BO kernel [32]. The latter is a static matrix (middle term below)

$$f^{\mathrm{BO}}_{\mathrm{xc},\mathbf{G}\mathbf{G}'} = \frac{\epsilon^{-1}_{\mathbf{G}\mathbf{G}'}(0)v_{\mathbf{G}'}}{1 - \epsilon^{\mathrm{RPA}}_{00}(0)} \to \frac{1}{\epsilon_M(0)\chi^0_{00}(0)}. \tag{4}$$

Often one can consider just the head element $f_{\mathrm{xc},00}$ without altering results significantly. The BO kernel is then the last term of Eq. (4), and Eq. (2) for $\bar{\chi}_{00}$ is scalar [53]. For clarity, in the following we will work with scalar equations unless stated. We have performed a detailed study for a family of matrix kernels [54] and found that results for the full matrix $f^{\mathrm{BO}}_{\mathrm{xc}}$ are similar to the present scalar version. We hence drop the subscripts 0 and consider the head of $\bar{\chi}^{\mathrm{RPA}}$ and f_{xc}.

In Ref. [32] the equivalent of Eqs. (1), (2), and (4) were iterated numerically to self-consistency. However, this can easily be avoided since Eqs. (1), (2), and (4) combine to a quadratic equation for $\epsilon_M(0)$ with two solutions

$$\epsilon_M(0) = \frac{1}{2}\left(1 + \frac{\bar{\chi}^{\mathrm{RPA}}}{\chi^0} - v\bar{\chi}^{\mathrm{RPA}}\right) \pm \sqrt{\frac{1}{4}\left(1 + \frac{\bar{\chi}^{\mathrm{RPA}}}{\chi^0} - v\bar{\chi}^{\mathrm{RPA}}\right)^2 - \frac{\bar{\chi}^{\mathrm{RPA}}}{\chi^0}}, \tag{5}$$

where all quantities are static. Only the solution with the plus (+) sign is meaningful, since in the limit of strong screening and neglecting LFE it leads to the RPA solution $\epsilon^{\mathrm{RPA}}_M \to 1 - v\chi^0_{00}$ as expected. The minus sign would lead to $\epsilon_M \to 1$. Given χ^0 and $\bar{\chi}^{\mathrm{RPA}}$, the static $\epsilon_M(\omega = 0)$ from Eq. (5) and hence $f^{\mathrm{BO}}_{\mathrm{xc}}$ from Eq. (4) are numbers that can be determined on a pocket calculator and then used in Eq. (2) to correct a given RPA spectrum for excitonic effects. We have checked that the converged iterative results and those of Eq. (5) are indistinguishable. The next order in the strong screening expansion of Eq. (5) yields $\epsilon_M(\omega = 0) = \epsilon^{\mathrm{RPA}}_M(\omega = 0) + 1$, which agrees with the typical magnitude of excitonic effects on the dielectric constant of semiconductors (see, for example, Table I of Ref. [25]).

Bound excitons occur when $\mathrm{Im}\epsilon_M(\omega_0)$, and hence $\mathrm{Im}\bar{\chi}(\omega_0)$, is nonvanishing at energies ω_0 within the quasiparticle gap, where χ^0 and $\bar{\chi}^{\mathrm{RPA}}$ are real. Since the scalar f_{xc} in Eq. (4) is real, the imaginary part of Eq. (2) is [29]

$$f_{\mathrm{xc}} = \frac{1}{\bar{\chi}^{\mathrm{RPA}}(\omega_0)}. \tag{6}$$

With Eq. (4), the position ω_0 of the first excitonic peak inside the gap is then the implicit solution of

$$\bar{\chi}^{\mathrm{RPA}}(\omega_0) = \epsilon_M(0)\chi^0(0). \tag{7}$$

By plotting $\mathrm{Re}\epsilon^{\mathrm{RPA}}_M(\omega)$ and comparing to the static $1 - v\epsilon_M\chi^0$ with ϵ_M from Eq. (5), one can hence read exciton binding energies from a RPA spectrum. For illustration, we show bulk silicon, LiF, and solid argon. The black solid lines in Fig. 1 show the real part of $\epsilon^{\mathrm{RPA}}_M(\omega)$ for the three materials (for computational details, see the Supplemental Material [36]); it is monotonically increasing within the quasiparticle gap. The value $[1 - \epsilon_M(0)v\chi^0(0)]$ with ϵ_M calculated with Eq. (5) is given by the horizontal red dashed lines, and the red vertical lines indicate intersections, hence bound excitons.

In silicon no bound exciton is found because $\epsilon_M(0)$ is large. LiF and argon have a low dielectric constant and therefore exhibit a crossing below the gap. However, the exciton binding energies, given by the difference between the energy of the fundamental quasiparticle gap and the exciton peak, are only 0.05 eV in LiF and 0.0 eV in Ar, much smaller than the experimental results (about 1.4 and 2.0 eV, respectively [55,56]), and in apparent contrast to Ref. [32]. The latter discrepancy cannot be explained with the use of Eq. (7), which is exact when the BO kernel is used. Let us therefore look at the spectra. Figure 2 shows our results of BO calculations for the imaginary parts of the macroscopic dielectric function for Si, LiF, and Ar.

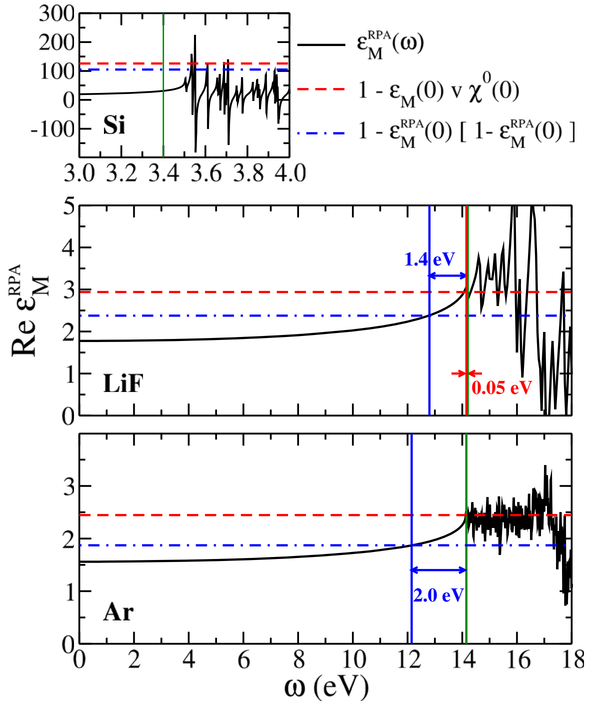

FIG. 1 (color online). Real part of $\epsilon_M^{\mathrm{RPA}}(\omega)$ for Si, LiF, and Ar (black solid line). Its crossing with the red dashed [blue dot-dashed] horizontal lines gives the exciton binding energy ω_0 from Eq. (7) [Eq. (11)]. The green vertical line indicates the quasiparticle gap.

Red dashed curves stem from our TDDFT calculations with the BO kernel [Eq. (4)]. In silicon, like in Ref. [32], the kernel improves the spectrum with respect to quasiparticle RPA (QP-RPA) [57] by enhancing the first peak and inducing an overall transfer of oscillator strength to lower energies. However, the effect appears underestimated when compared to experiment [58] and to BSE results [25]. For silicon, the simple long-range $f_{\mathrm{xc}}^{\mathrm{LRC}} = \alpha/q^2$ is sufficient [23]. However, the prefactor α_{BO} from the BO kernel defined in Eq. (4) is only $\alpha = -0.1$, too weak compared to the optimal value $\alpha = -0.2$ [25], which explains why the effect is not strong enough.

In LiF and Ar, our BO spectra confirm the weak exciton binding energies obtained from Eq. (7). The spectral shapes look similar to the ones of Ref. [32]; however, the positions of the exciton peak differ and, for argon, the peak height from our BO is about half of that in Ref. [32]. As regards the peak position, we are not in contradiction with Ref. [32] since our quasiparticle gaps are close to experimental photoemission gaps. Instead, the quasiparticle gaps used in Ref. [32] are much smaller. This compensates the too small exciton binding energy and leads to seemingly good agreement with experimental optical spectra. We elaborate on this point in the Supplemental Material [36]. Additionally, it is important to note that the exciton binding energy is very sensitive to details, especially for strongly bound excitons. The reason is that the latter lie in a region where the real part of $\epsilon^{\mathrm{RPA}}(\omega)$ is very flat (see Fig. 1). A small change in $\chi^0(0)$ leads then to a large shift in the crossing point, and hence in the exciton binding energy. Such a small change in $\chi^0(0)$ can be due to a small change of the structure, or of computational ingredients like a pseudopotential or convergence parameters, and it can be amplified since the static dielectric constant enters the BO self-consistently. Indeed, the calculations for the BO kernel show a notable slow convergence with respect to both the LFE (i.e., number N_G of $\mathbf{G}$ vectors) and the number of empty bands. The second issue is exemplified in Fig. 2 for the case of Ar: the brown double dot–dashed curve has been obtained with only 8 bands, versus 20 in the converged calculation (red dashed curve). The unconverged calculation exhibits a bound exciton with a binding energy of more than half an eV. Similarly, poorly converged calculations with respect to N_G give also, for the case of argon, a BO spectrum with a slightly higher binding energy and a higher peak height than the converged result [54], much more similar to Ref. [32]. More generally, this explains why for argon or LiF one can easily obtain results that differ by an eV or more from others in the literature [34].

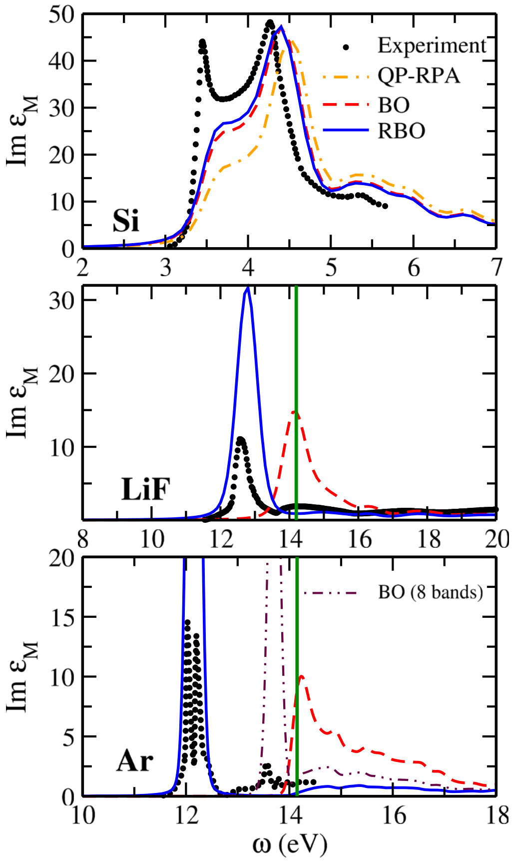

FIG. 2 (color online). Imaginary part of $\epsilon_M^{\mathrm{RPA}}(\omega)$ for Si, LiF, and Ar computed in various approximations. Experimental spectra are taken from Ref. [58] for Si, Ref. [55] for LiF, and Ref. [56] for Ar. The green vertical lines indicate the quasiparticle gap.

Once the calculations are settled, the results of the BO are hence disappointing. Let us therefore finally elucidate the origin of this kernel and indicate a possible improvement. We start from three assumptions: (A) We can take a static $f_{\rm xc}(\omega = 0)$ in the optical range. (B) The static dielectric constant is larger than 1. (C) The static dielectric constant is not too different from the RPA one. These assumptions are based on previous knowledge from theory and experiment [assumption (B)], numerical results, e.g., of Bethe-Salpeter calculations [assumption (C)], and, most importantly [assumption (A)], insight from previous studies of long-range corrected kernels, e.g., Refs. [23,24,59]. The fact that $f_{\rm xc}$ should be proportional to the inverse dielectric constant [23,25,60,61] has also been useful to guide the derivation, which we start by combining Eqs. (1) and (2):

$$f_{\rm xc} = \frac{1}{\bar{\chi}^{\rm RPA}} - \frac{1}{\bar{\chi}} = \frac{1}{\bar{\chi}^{\rm RPA}} - \frac{v}{1 - \epsilon_M}. \qquad (8)$$

If one had to make a guess for $f_{\rm xc}$ and iterate Eqs. (1), (2), and (8), one would of course get the same $f_{\rm xc}$ back, however absurd it might be. The trick of a BO-like approach is to make an approximation in one of the equations, such that they are no longer equivalent. At first sight this should not lead to any advantage: how could an approximation be better than the exact formula? However, by choosing the approximation carefully one can feed information. In that case, iteration of the (now no longer equivalent) equations may indeed define the three unknowns $f_{\rm xc}, \bar{\chi}$, and ϵ_M. We will call this procedure "guided iteration." We will first use condition (A) to this aim: a static kernel can be determined from the equations at $\omega = 0$ alone. In that limit, hypothesis (B) is generally valid, and we can use it to expand the $1/\bar{\chi}$ term in Eq. (8) to leading order in $1/\epsilon_M$

$$\frac{1}{\bar{\chi}} = \frac{v}{1 - \epsilon_M} \approx -\frac{v}{\epsilon_M} \approx -\frac{v}{\epsilon_M^{\rm RPA}}, \qquad (9)$$

where we have used hypothesis (C) in order to obtain the last expression. This finally leads to

$$f_{\rm xc}^{\rm RBO} \approx \frac{1}{\epsilon_M^{\rm RPA} \bar{\chi}^{\rm RPA}}, \qquad (10)$$

which we call the RBO (RPA bootstrap). The RBO is close to BO which appears in Eq. (4), but there is no self-consistency condition. The blue curves in Fig. 2 are obtained using Eq. (10). In silicon, the improvement with respect to the RPA result is close to that of the original BO (red dashed curve). Changes are noticeable in LiF and argon, where now the peak position is close to the experimental one [62]. Compared to experiment there is still too much spectral weight on these peaks. This is to be expected, because the two kernels behave like the LRC kernel. It is indeed known [29] that one can tune α to reproduce the exciton binding energy, but at the price of too much oscillator strength. To cure this problem, one may have to introduce a frequency dependence that is able to distribute spectral weight over the whole Rydberg series; this is however beyond the scope of the present work. Here, we focus on the exciton binding energy, which can now again be obtained from $\epsilon_M^{\rm RPA}(\omega)$ alone, using the modified prescription

$$\bar{\chi}^{\rm RPA}(\omega_0) = \epsilon_M^{\rm RPA}(\omega = 0)\bar{\chi}^{\rm RPA}(\omega = 0). \qquad (11)$$

This corresponds to the use of the blue horizontal dot-dashed line in Fig. 1. The exciton binding energies that we can read in this way, and which correspond of course to the peak positions given by the RBO in Fig. 2, are 2.0 eV for argon and 1.4 eV for LiF, in excellent agreement with the experimental values of 2.0 and 1.43 eV, respectively.

In conclusion, starting from the so-called bootstrap kernel of TDDFT [32], we have derived very simple approaches to determine absorption spectra and to estimate exciton binding energies from RPA calculations alone. We have however shown that the boostrap kernel is not reliable for the determination of exciton binding energies, and that promising results in the literature are partially misleading. We have therefore derived a related kernel starting from a few physically meaningful assumptions. Numerical results confirm that the new kernel is more reliable. One may expect that this first derivation of a boostrap-like kernel could trigger new developments, but caution is called for: our guided iteration is not a systematic expansion that one might continue to obtain better and better results, since it intrinsically relies on the fact that an approximation is made by feeding knowledge. We stress again the importance of this approximation: Eqs. (1) and (2), and Eq. (8) are equivalent, though written in a different way; however, making an approximation on the second term of Eq. (8) [as in Eq. (9)] leads to a new formula, so breaking the otherwise tautological sequence Eqs. (1) and (2), and Eq. (8). The choice of a reasonable approximation (in this case the RBO) makes the method very effective in the description of the spectrum and, above all, for estimates of exciton binding energies. As we have shown and explained, these estimates are very sensitive, and a numerically precise agreement should not be overemphasized. Most importantly, we have shown that exciton binding energies can be obtained at literally zero cost, since we have introduced a way to read binding energies from RPA dielectric functions alone. This may be interesting especially for scientists outside the community of *ab initio* calculations, including experimentalists, since it allows one to use the numerous already published RPA results, without the need of new calculations.

We are grateful for helpful discussions with S. Sharma and C. Ullrich. We acknowledge support by the French ANR (projects NT09-610745 and ANR-12-BS04-0001-02), the Einstein Foundation Berlin, and the DFG (Deutsche Forschungsgemeinschaft). Computer time was granted by GENCI (544).

---

[*] srigamonti@physik.hu-berlin.de
[†] lucia.reining@polytechnique.edu

[1] G. Onida, L. Reining, and A. Rubio, Rev. Mod. Phys. **74**, 601 (2002).

[2] W. Hanke and L. J. Sham, Phys. Rev. B **21**, 4656 (1980).

[3] S. Albrecht, L. Reining, R. Del Sole, and G. Onida, Phys. Rev. Lett. **80**, 4510 (1998).
[4] L. X. Benedict, E. L. Shirley, and R. B. Bohn, Phys. Rev. Lett. **80**, 4514 (1998).
[5] M. Rohlfing and S. G. Louie, Phys. Rev. Lett. **81**, 2312 (1998).
[6] E. Runge and E. K. U. Gross, Phys. Rev. Lett. **52**, 997 (1984).
[7] S. Botti, A. Schindlmayr, R. Del Sole, and L. Reining, Rep. Prog. Phys. **70**, 357 (2007).
[8] E. Gross, J. Dobson, and M. Petersilka, in *Density Functional Theory II*, Topics in Current Chemistry, Vol. 181, edited by R. Nalewajski (Springer, Berlin, 1996), pp. 81–172.
[9] E. K. U. Gross and W. Kohn, Phys. Rev. Lett. **55**, 2850 (1985).
[10] V. I. Gavrilenko and F. Bechstedt, Phys. Rev. B **55**, 4343 (1997).
[11] V. U. Nazarov, G. Vignale, and Y.-C. Chang, Phys. Rev. Lett. **102**, 113001 (2009).
[12] V. U. Nazarov and G. Vignale, Phys. Rev. Lett. **107**, 216402 (2011).
[13] P. E. Trevisanutto, A. Terentjevs, L. A. Constantin, V. Olevano, and F. D. Sala, Phys. Rev. B **87**, 205143 (2013).
[14] M. Hellgren and E. K. U. Gross, Phys. Rev. A **88**, 052507 (2013).
[15] J. Paier, M. Marsman, and G. Kresse, Phys. Rev. B **78**, 121201 (2008).
[16] P. Ghosez, X. Gonze, and R. W. Godby, Phys. Rev. B **56**, 12811 (1997).
[17] R. Stubner, I. V. Tokatly, and O. Pankratov, Phys. Rev. B **70**, 245119 (2004).
[18] U. von Barth, N. E. Dahlen, R. van Leeuwen, and G. Stefanucci, Phys. Rev. B **72**, 235109 (2005).
[19] F. Bruneval, F. Sottile, V. Olevano, R. Del Sole, and L. Reining, Phys. Rev. Lett. **94**, 186402 (2005).
[20] F. Sottile, V. Olevano, and L. Reining, Phys. Rev. Lett. **91**, 056402 (2003).
[21] G. Adragna, R. Del Sole, and A. Marini, Phys. Rev. B **68**, 165108 (2003).
[22] A. Marini, R. Del Sole, and A. Rubio, Phys. Rev. Lett. **91**, 256402 (2003).
[23] L. Reining, V. Olevano, A. Rubio, and G. Onida, Phys. Rev. Lett. **88**, 066404 (2002).
[24] F. Sottile, M. Marsili, V. Olevano, and L. Reining, Phys. Rev. B **76**, 161103 (2007).
[25] S. Botti, F. Sottile, N. Vast, V. Olevano, L. Reining, H.-C. Weissker, A. Rubio, G. Onida, R. Del Sole, and R. W. Godby, Phys. Rev. B **69**, 155112 (2004).
[26] W. Wełnic, S. Botti, L. Reining, and M. Wuttig, Phys. Rev. Lett. **98**, 236403 (2007).
[27] G.-X. Zhang, A. Tkatchenko, J. Paier, H. Appel, and M. Scheffler, Phys. Rev. Lett. **107**, 245501 (2011).
[28] H. Hübener, E. Luppi, and V. Véniard, Phys. Rev. B **83**, 115205 (2011).
[29] F. Sottile, K. Karlsson, L. Reining, and F. Aryasetiawan, Phys. Rev. B **68**, 205112 (2003).
[30] V. Turkowski and C. A. Ullrich, Phys. Rev. B **77**, 075204 (2008).
[31] V. Turkowski, A. Leonardo, and C. A. Ullrich, Phys. Rev. B **79**, 233201 (2009).
[32] S. Sharma, J. K. Dewhurst, A. Sanna, and E. K. U. Gross, Phys. Rev. Lett. **107**, 186401 (2011).
[33] S. Sharma, J. K. Dewhurst, A. Sanna, A. Rubio, and E. K. U. Gross, New J. Phys. **14**, 053052 (2012).
[34] Z.-h. Yang and C. A. Ullrich, Phys. Rev. B **87**, 195204 (2013).
[35] Z.-h. Yang, Y. Li, and C. A. Ullrich, J. Chem. Phys. **137**, 014513 (2012).
[36] See Supplemental Material at http://link.aps.org/supplemental/10.1103/PhysRevLett.114.146402, for the computational details and an analysis of the influence of the quasiparticle gap in the optical spectra, which includes Refs. [37–52].
[37] P. Hohenberg and W. Kohn, Phys. Rev. **136**, B864 (1964).
[38] W. Kohn and L. J. Sham, Phys. Rev. **140**, A1133 (1965).
[39] N. Troullier and J. L. Martins, Phys. Rev. B **43**, 1993 (1991).
[40] Pseudopotentials for the ABINIT code, http://www.abinit.org/downloads/psp-links/psp-links/lda_tm.
[41] A. Gulans, S. Kontur, C. Meisenbichler, D. Nabok, P. Pavone, S. Rigamonti, S. Sagmeister, U. Werner, and C. Draxl, J. Phys. Condens. Matter **26**, 363202 (2014).
[42] OPIUM pseudopotential generation program. http://opium.sourceforge.net/.
[43] J. P. Perdew and Y. Wang, Phys. Rev. B **33**, 8800 (1986).
[44] G. B. Bachelet, D. R. Hamann, and M. Schlüter, Phys. Rev. B **26**, 4199 (1982).
[45] J. A. Soininen and E. L. Shirley, Phys. Rev. B **61**, 16423 (2000).
[46] H. J. Monkhorst and J. D. Pack, Phys. Rev. B **13**, 5188 (1976).
[47] *Numerical Data and Functional Relationships in Science and Technology*, edited by K. H. Hellwege and O. Madelung (Springer, Berlin, 1982).
[48] M. Piacentini, D. W. Lynch, and C. G. Olson, Phys. Rev. B **13**, 5530 (1976).
[49] M. Runne and G. Zimmerer, Nucl. Instrum. Methods Phys. Res., Sect. B **101**, 156 (1995).
[50] L. Reining, V. Olevano, F. Sottile, S. Albrecht, and G. Onida, “The exc code” (unpublished).
[51] X. Gonze, J.-M. Beuken, R. Caracas, F. Detraux, M. Fuchs, G.-M. Rignanese, L. Sindic, M. Verstraete, G. Zerah, F. Jollet, M. Torrent, A. Roy, M. Mikami, P. Ghosez, J.-Y. Raty, and D. Allan, Comput. Mater. Sci. **25**, 478 (2002).
[52] V. Olevano, L. Reining, and F. Sottile, “The dp code” (unpublished).
[53] Note that $\bar{\chi}_{00}^{\mathrm{RPA}}$ still results from a matrix Eq. (3).
[54] S. Rigamonti, S. Botti, V. Véniard, C. Draxl, L. Reining, and F. Sottile (to be published).
[55] D. M. Roessler and W. C. Walker, J. Opt. Soc. Am. **57**, 835 (1967).
[56] V. Saile, M. Skibowski, W. Steinmann, P. Gürtler, E. E. Koch, and A. Kozevnikov, Phys. Rev. Lett. **37**, 305 (1976).
[57] QP-RPA stands for a RPA calculation with χ_0 built with quasiparticle energies.
[58] P. Lautenschlager, M. Garriga, L. Vina, and M. Cardona, Phys. Rev. B **36**, 4821 (1987).
[59] R. Del Sole, G. Adragna, V. Olevano, and L. Reining, Phys. Rev. B **67**, 045207 (2003).
[60] E. G. Maksimov, I. I. Maxin, S. Y. Savrasov, and Y. A. Uspenski, J. Phys. Condens. Matter **1**, 2493 (1989).
[61] M. A. L. Marques, J. Vidal, M. J. T. Oliveira, L. Reining, and S. Botti, Phys. Rev. B **83**, 035119 (2011).
[62] Note that our calculations do not include the spin-orbit coupling, which is experimentally observed in Ar.

3.2 Simplified BSE

The TDDFT approach being anyway so difficult to tackle (at least to find reliable and universal exchange-correlation kernels), the development of a simplified version of the BSE is still an important option. I have recently started a collaboration with Carsten Ullrich, from University of Missouri, in occasion of his sabbatical leave in our group in 2014. In this occasion we have worked on a many-body approach to screen the long-range Coulomb interaction. The result can be viewed as a simplified BSE approach. We show that this screened exact-exchange (SXX) approach we propose outperforms all TDDFT approaches currently on the market, retaining most of the accuracy of the BSE over a wide range of materials, but at a lower computational cost. Here the key of the game is to completely skip the calculation of the screening function, and substitute this with a number, evaluated ab initio from the self-energy. The aim of the work is not however to substitute the BSE as is, but rather to build a bridge between TDDFT and many-body theories, and opens up new directions towards the development of hybrid functionals for the optical properties of crystal systems. The work is still at the beginning. We have submitted and article to PRL [99].
PLEASE REFER TO THE ATTACHED ARTICLE

arXiv:1501.05631v1 [cond-mat.mtrl-sci] 22 Jan 2015

A simple screened exact-exchange approach for excitonic properties in solids

Zeng-hui Yang,[1, 2] Francesco Sottile,[3, 4] and Carsten A. Ullrich[2]
[1]Department of Physics, Temple University, Philadelphia, PA 19122, USA
[2]Department of Physics and Astronomy, University of Missouri, Columbia, MO 65211, USA
[3]Laboratoire des Solides Irradiés, École Polytechnique, CNRS, CEA-DSM, F-91128 Palaiseau, France
[4]European Theoretical Spectroscopy Facility (ETSF)

(Dated: January 23, 2015)

We present a screened exact-exchange (SXX) method for the efficient and accurate calculation of the optical properties of solids, where the screening is achieved through the zero-wavevector limit of the inverse dielectric function. The SXX approach can be viewed as a simplification of the Bethe-Salpeter equation (BSE) or, in the context of time-dependent density-functional theory, as a first step towards a new class of hybrid functionals for the optical properties of solids. SXX performs well for bound excitons and continuum spectra in both small-gap semiconductors and large-gap insulators, with a computational cost much lower than that of the BSE.

PACS numbers: 31.15.ee, 71.15.Qe, 71.35.Cc, 78.20.Bh

The Bethe-Salpeter equation (BSE) [1, 2] is considered the gold standard for calculating the optical properties of periodic solids and many other materials. The nonempirical nature of the BSE guarantees its wide applicability and high degree of accuracy, but its computational cost becomes prohibitive beyond the simplest systems. Time-dependent density-functional theory (TDDFT) [3–5] is computationally much less expensive, and is therefore a popular alternative for the calculation of optical properties. TDDFT calculations can be orders of magnitude faster than the BSE, but none of the existing empirical or nonempirical exchange-correlation (xc) kernels for solids [6–10] can achieve the same level of accuracy for both small-gap and wide-gap solids. The exception is the so-called "nanoquanta" xc kernel [2, 11–14], which is as accurate as the BSE, but equally expensive.

Recent TDDFT studies for solids have identified the crucial importance of the long-range part of the xc kernel [15, 16]. Exact-exchange TDDFT [17, 18] successfully produces excitonic properties, but the Coulomb singularity needs to be cut off, which is equivalent to using a screened Coulomb interaction [19]. Hybrid xc functionals are defined as a mixture of semilocal (gradient-corrected) xc functionals with a fraction of nonlocal exact exchange. The B3LYP hybrid functional [20] has been used to calculate optical spectra in semiconductors [21, 22], with a generally good description of optical gaps, despite the fact that the 0.2 mixing parameter of B3LYP is optimized for finite systems. The HSE functional [23, 24] uses exact exchange for short-range interactions only; this produces very good quasiparticle gaps [25–27], but HSE cannot yield bound excitons, although it may still give decent continuum spectra [28].

In this paper we propose a simple, nonempirical and material-dependent way of screening the long-range Coulomb exchange, which can be viewed as a simplified BSE approach. We show that this screened exact-exchange (SXX) approach outperforms all TDDFT approaches currently on the market, retaining most of the accuracy of the BSE over a wide range of materials, but at a much lower computational cost. This builds a bridge between TDDFT and many-body theories, and opens up new directions towards the development of hybrid functionals for the optical properties of insulating solids.

Although TDDFT and BSE are very different theories, the excitation spectra in solids are in both cases obtained through an eigenvalue equation [2, 29] (atomic units [$e = \hbar = m_e = 1/4\pi\epsilon_0 = 1$] are used throughout):

$$\sum_{(m\mathbf{k}_m n\mathbf{k}_n)} \Big[\delta_{i\mathbf{k}_i,m\mathbf{k}_m}\delta_{j\mathbf{k}_j,n\mathbf{k}_n}(\epsilon_{j\mathbf{k}_j}-\epsilon_{i\mathbf{k}_i}) + F_{\mathrm{Hxc}}^{(i\mathbf{k}_i j\mathbf{k}_j)(m\mathbf{k}_m n\mathbf{k}_n)}\Big]\rho_\lambda^{(m\mathbf{k}_m n\mathbf{k}_n)} = \omega_\lambda \rho_\lambda^{(i\mathbf{k}_i j\mathbf{k}_j)} \quad (1)$$

where i and m denote occupied bands, j and n denote unoccupied bands, the ϵ's are single-particle energies (either quasiparticle or Kohn-Sham), and ω is the excitation frequency. The main difference lies in the coupling matrix $F_{\mathrm{Hxc}} = F_{\mathrm{H}} + F_{\mathrm{xc}}$. For optical properties, only vertical excitations are considered, so that $\mathbf{k}_i = \mathbf{k}_j$ and $\mathbf{k}_m = \mathbf{k}_n$ in Eq. (1). The Hartree part of the coupling matrix is the same in the two methods, and is given by

$$F_{\mathrm{H}}^{(ij\mathbf{k})(mn\mathbf{k}')} = \frac{2}{V_{\mathrm{crys}}}\sum_{\mathbf{G}\neq 0}\frac{4\pi}{|\mathbf{G}|^2}\left\langle j\mathbf{k}\left|e^{i\mathbf{G}\cdot\mathbf{r}}\right|i\mathbf{k}\right\rangle \times \left\langle m\mathbf{k}'\left|e^{-i\mathbf{G}\cdot\mathbf{r}}\right|n\mathbf{k}'\right\rangle. \quad (2)$$

The long-range part ($\mathbf{G} = 0$) of the Coulomb interaction is omitted so that the eigenvalues of Eq. (1) correspond to poles in the macroscopic dielectric function [2, 30].

For the BSE, as well as for our SXX method, the xc part of the coupling matrix can be written as

$$F_{\mathrm{xc}}^{(ij\mathbf{k})(mn\mathbf{k}')} = \frac{1}{V_{\mathrm{crys}}}\sum_{\mathbf{G}\mathbf{G}'} g_{\mathbf{G}\mathbf{G}'}(\mathbf{q}) \times \left\langle j\mathbf{k}\left|e^{i(\mathbf{q}+\mathbf{G})\cdot\mathbf{r}}\right|n\mathbf{k}'\right\rangle\left\langle m\mathbf{k}'\left|e^{-i(\mathbf{q}+\mathbf{G})\cdot\mathbf{r}}\right|i\mathbf{k}\right\rangle\delta_{\mathbf{q},\mathbf{k}-\mathbf{k}'} \quad (3)$$

Here, $g_{\mathbf{GG}'}(\mathbf{q}) = -4\pi\gamma\delta_{\mathbf{GG}'}/|\mathbf{q}+\mathbf{G}|^2$ for SXX (γ is a screening parameter, to be further specified below), and $g_{\mathbf{GG}'}(\mathbf{q}) = -4\pi\epsilon^{-1}_{\mathbf{GG}'}(\mathbf{q},\omega=0)/|\mathbf{q}+\mathbf{G}'|^2$ for the BSE. ϵ^{-1} is the inverse dielectric function, obtained within the random phase approximation (RPA) as

$$\epsilon^{-1}_{\mathbf{GG}'}(\mathbf{q},\omega) = \delta_{\mathbf{GG}'} + \frac{4\pi}{|\mathbf{q}+\mathbf{G}|^2}\chi^{\rm RPA}_{\mathbf{GG}'}(\mathbf{q},\omega), \qquad (4)$$

with the RPA response function defined as $\chi^{\rm RPA} = \chi_0 + \chi_0 v \chi^{\rm RPA}$ (χ_0 is the quasiparticle response function [5]).

In TDDFT, the xc part of the coupling matrix is

$$F_{\rm xc}^{(ij\mathbf{k})(mn\mathbf{k}')} = \frac{2}{V_{\rm crys}}\sum_{\mathbf{GG}'} f_{{\rm xc},\mathbf{GG}'}(\mathbf{q}=0) \times \left\langle j\mathbf{k}\left|e^{i\mathbf{G}\cdot\mathbf{r}}\right| i\mathbf{k}\right\rangle \left\langle m\mathbf{k}'\left|e^{-i\mathbf{G}'\cdot\mathbf{r}}\right| n\mathbf{k}'\right\rangle, \qquad (5)$$

where $f_{\rm xc}(\mathbf{r},\mathbf{r}') = \delta v_{\rm xc}(\mathbf{r})/\delta n(\mathbf{r}')$ is the adiabatic xc kernel of TDDFT. The structure of Eq. (5) is similar to Eq. (2), but different from Eq. (3): only the $\mathbf{q}=0$ part of $f_{\rm xc}$ enters in the expression, so the head ($\mathbf{G}=\mathbf{G}'=0$) at $\mathbf{q}=0$ of the xc kernel plays a much more important role in TDDFT than $g_{00}(0)$ in the BSE.

To illustrate the difficulty in developing a universally applicable nonempirical xc kernel, we consider the long-range corrected (LRC) kernel [7, 15, 31]

$$f^{\rm LRC}_{{\rm xc},\mathbf{GG}'}(\mathbf{q}) = -\frac{\alpha}{|\mathbf{q}+\mathbf{G}|^2}\,\delta_{\mathbf{GG}'}, \qquad (6)$$

which represents the long-range part of the exact xc kernel in insulators. The empirical parameter α acts as a rough approximation to the dielectric screening effects within the BSE, but has no clear justification in the TDDFT framework, besides giving the correct asymptotic behavior. In Ref. [7], the relation $\alpha = 4.615\,\epsilon^{-1}_\infty - 0.213$ was proposed, which works quite well for the optical spectra of semiconductors, but fails for insulators.

In Ref. [32], α was fitted against experimental exciton binding energies for various materials. It was found that the value of α spans a wide numerical range, from 0.595 (GaAs) to 96.5 (solid Ne). For small-gap materials, the relative change in the exciton binding energy caused by a change in α is substantial; for large-gap materials, the exciton binding energies are not as sensitive. This shows how difficult it is to develop a widely applicable nonempirical xc kernel within the TDDFT framework [33].

The situation is different in SXX. Unscreened time-dependent Hartree-Fock (TDHF) always overbinds excitons, so γ has to be in the $[0,1]$ range for the correction to be in the right direction. Therefore, it is a much easier task to develop nonempirical approximations for γ than for the TDDFT parameter α.

To derive the SXX screening parameter γ, we start from the self-energy Σ:

$$\Sigma(\mathbf{r},\mathbf{r}',\omega) = \frac{i}{2\pi}G(\mathbf{r},\mathbf{r}',\omega)W(\mathbf{r},\mathbf{r}',0) = \frac{i}{2\pi}G(\mathbf{r},\mathbf{r}',\omega)\int d^3r''\;\epsilon^{-1}(\mathbf{r},\mathbf{r}'',0)v(\mathbf{r}''-\mathbf{r}'), \qquad (7)$$

where G is the quasiparticle Green's function. ϵ^{-1} in Eq. (7) is the full dielectric screening of the BSE, and we want to find a way to average its effect and motivate replacing it with a constant. Assuming that we can replace the static nonlocal screening $\epsilon^{-1}(\mathbf{r},\mathbf{r}')$ with a frequency-dependent uniform screening $\epsilon^{-1}_{\rm uni}(\mathbf{r}-\mathbf{r}',\omega)$, we write

$$\Sigma(\mathbf{r},\mathbf{r}',\omega) = \frac{i}{2\pi}\tilde{G}(\mathbf{r},\mathbf{r}',\omega)\int d^3r''\;\epsilon^{-1}_{\rm uni}(\mathbf{r}-\mathbf{r}'',\omega)v(\mathbf{r}''-\mathbf{r}'), \qquad (8)$$

which defines the function $\tilde{G}$. Combining Eqs. (7) and (8) in reciprocal space leads to

$$\sum_{\mathbf{G}_2}\epsilon^{-1}_{\mathbf{G}_2\mathbf{G}_1}(\mathbf{q}',0)G_{\mathbf{G}-\mathbf{G}_2,\mathbf{G}-\mathbf{G}_1}(\mathbf{q}-\mathbf{q}',\omega) \equiv \epsilon^{-1}_{{\rm uni},\mathbf{G}_1}(\mathbf{q}',\omega)\tilde{G}_{\mathbf{G}-\mathbf{G}_1,\mathbf{G}'-\mathbf{G}_1}(\mathbf{q}-\mathbf{q}',\omega). \qquad (9)$$

Eq. (9) holds for any $\mathbf{q},\mathbf{G},\mathbf{G}'$. Setting these to zero and assuming the functions G and $\tilde{G}$ to be real, we have

$$\epsilon^{-1}_{{\rm uni},\mathbf{G}}(\mathbf{q},\omega) = \frac{\sum_{\mathbf{G}'}G_{\mathbf{GG}'}(\mathbf{q},\omega)\epsilon^{-1}_{\mathbf{G}'\mathbf{G}}(\mathbf{q},0)}{\tilde{G}_{\mathbf{GG}}(\mathbf{q},\omega)}. \qquad (10)$$

In the $q\to 0$ limit, Eq. (10) becomes

$$\lim_{q\to 0}\epsilon^{-1}_{{\rm uni},\mathbf{G}}(\mathbf{q},\omega) = \frac{G_{\mathbf{G}0}(\mathbf{q},\omega)\epsilon^{-1}_{0\mathbf{G}}(\mathbf{q},0)}{\tilde{G}_{\mathbf{GG}}(\mathbf{q},\omega)}. \qquad (11)$$

For $\mathbf{G}\neq 0$, Eq. (11) behaves like $O(1/q)$, so it is impossible to derive a general uniform screening as an average of the nonlocal screening of the BSE. However, the head ($\mathbf{G}=\mathbf{G}'=0$) of Eq. (11) has the correct $q\to 0$ behavior, and can be used to approximate the BSE. Assuming that $\tilde{G}=G$, we obtain

$$\epsilon^{-1}_{{\rm uni},0}(\mathbf{q},\omega) = \epsilon^{-1}_{00}(\mathbf{q},0). \qquad (12)$$

Now we make a rather drastic approximation by setting $\mathbf{q}=0$, since the long-range interaction dominates in solids. The screening parameter γ then becomes

$$\gamma = \epsilon^{-1}_{00}(0,0), \qquad (13)$$

which is also the inverse of the infinite-frequency dielectric constant, ϵ^{-1}_∞, since phonon effects are not included. A similar simplified screening was proposed in Ref. [34] for the nonlocal exchange part of a hybrid xc functional in order to obtain good band structures; by contrast, the purpose of our SXX is to yield good optical properties. We use the RPA for $\epsilon^{-1}_{00}(0,0)$ in actual calculations. Since $\epsilon = 1 - v\chi$, and the static χ at zero wave vector is negative, γ of Eq. (13) is bounded in the $[0,1]$ range.

Let us now compare the SXX approach with the BSE. The main difference is that in BSE the exchange is screened by the full inverse dielectric function ϵ^{-1}, which makes it much more costly than SXX, where the screening parameter γ is just a constant. In practice, a BSE calculation is a four-step procedure: (i) ground-state calculation with a diagonalization over the selected k-points

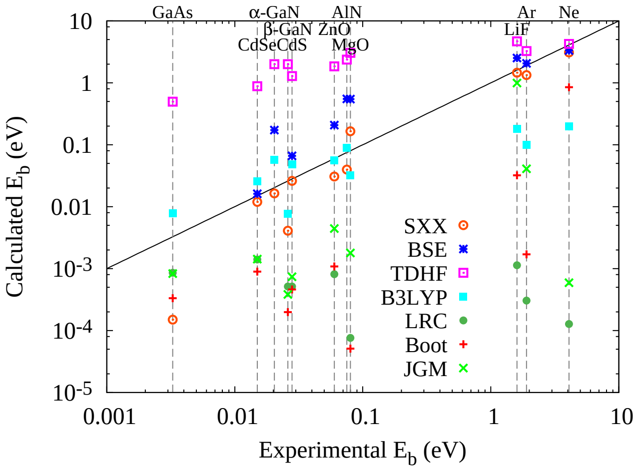

FIG. 1. (Color online) Comparison of calculated and experimental exciton binding energies E_b in various materials (see Table I for further details). The solid line indicates where the calculated and experimental values of E_b coincide.

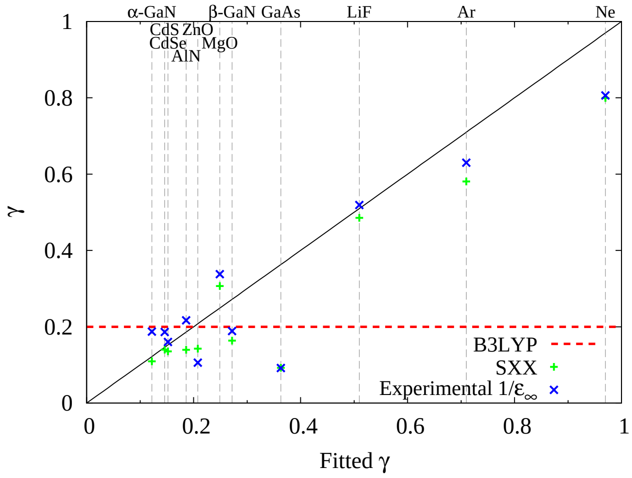

FIG. 2. (Color online) SXX screening parameter γ [Eq. (13)] and experimental value of ϵ_∞^{-1} versus the fitted γ reproducing the first exciton, for various materials. B3LYP corresponds to a constant value of $\gamma = 0.2$.

grid (often shifted [35] for optical properties); (ii) quasiparticle correction, typically within the GW approximation [36], but substituted with a simple scissor correction step in this work since we focus on the excitonic effects; (iii) generation of static screening $\epsilon^{-1}_{\mathbf{G}\mathbf{G}'}(\mathbf{q}, \omega = 0)$ within the RPA; (iv) construction and diagonalization of the excitonic Hamiltonian [i.e., Eq. (1)] containing the ingredients listed above.

Regarding the computational workload, even though step (iv) has the worst scaling, step (iii) is often the most cumbersome part of the whole procedure, especially when one is interested in the small energy region of the spectrum and uses the scissor operator procedure: the number of q-vectors in the screening is proportional to the number of k-points (since $\mathbf{q} = \mathbf{k} - \mathbf{k}'$) even for optical properties. This can become very demanding when many k-points have to be used together with many $\mathbf{G}$-vectors, as is the case for lower-dimensional systems, in particular 2D [37]. In addition, the numerical evaluation of $\epsilon^{-1}_{\mathbf{G}\mathbf{G}'}(\mathbf{q}, 0)$ has a much worse convergence with the empty bands than the evaluation of the spectrum (for instance, the screening for LiF requires 20 empty bands, while the first exciton peak requires only one empty band). Our SXX approach bypasses this step and thus avoids a severe computational bottleneck in the description of optical properties at BSE-level for complex materials.

We have calculated the exciton binding energies E_b of various semiconductors and insulators with SXX and other methods; the results are collected in Table I and in Fig. 1. Clearly, SXX produces a much better overall agreement with experiment than all TDDFT methods (except for GaAs), and yields an accuracy that is comparable to BSE across the board.

The calculations of E_b were done with the method described in Ref. [32]. We use a scissor-corrected LDA ground state (calculated with ABINIT [38]) as starting point. All calculations use three valence bands and one conduction band for Eq. (1), which is sufficient when only the exciton binding energies are of interest (but is, generally, insufficient for the continuum part). We use an 18 × 18 × 18 Monkhorst-Pack grid [39] for GaAs and β-GaN, a 15 × 15 × 15 grid for MgO, a 10 × 10 × 10 grid for Ar, Ne, and LiF, and a 20 × 20 × 20 grid for other materials. To speed up the calculation, we only use the head of the xc kernel when calculating the coupling matrices [i.e., we neglect local-field effects by not taking the $\mathbf{G}$ and $\mathbf{G}'$ sums in Eq. (3) and (5)]. Including local-field effects generally changes E_b very little (at most ∼10%). Since the E_b are already small numbers, the results without local-field effects are sufficiently accurate for our purposes. For the calculation of $\epsilon^{-1}_{00}(0, 0)$, we use 60 bands for GaAs, β-GaN and MgO, and 30 bands for all other materials. 59 $\mathbf{G}$-vectors are used for ϵ^{-1}, and the error for the convergence of $\epsilon^{-1}_{00}(0, 0)$ is less than 1%.

Figure 2 compares γ from Eq. (13) with values of γ fitted to reproduce the lowest experimental exciton binding energies. Aside from a few outliers (such as GaAs), the calculated and the fitted values of γ are very close, which explains the good performance for exciton binding energies in Table I. The experimental ϵ_∞^{-1} values are also plotted in Fig. 2, showing that $\epsilon^{-1}_{00}(0, 0)$ at the RPA level is already a good approximation to ϵ_∞^{-1}. It should be noticed that the B3LYP hybrid kernel [20] (only the long-range part, which corresponds to $\gamma = 0.2$, since the calculation only uses the head of the xc kernel) also performs well for semiconductors: Fig. 2 shows that $\gamma = 0.2$ is roughly the average of the semiconductor screening parameters. The B3LYP functional was designed with

	GaAs	β-GaN	α-GaN	CdS	CdSe	Ar	Ne	LiF	AlN	ZnO	MgO
Exp.	3.27	26.0	20.4	28.0	15.0	1.90×10^3	4.08×10^3	1.6×10^3	75	60	80
BSE	—	—	172	66.0	16.2	2.07×10^3	3.32×10^3	2.51×10^3	552	208	546
TDHF	497	1.99×10^3	2.00×10^3	1.28×10^3	879	3.27×10^3	4.26×10^3	4.68×10^3	2.37×10^3	1.84×10^3	3.04×10^3
B3LYP[a]	0.792	7.71	57.4	48.1	25.8	100	197	180	89.4	55.8	31.9
SXX	0.151	4.08	16.4	26.0	11.9	1.33×10^3	3.08×10^3	1.46×10^3	39.9	30.8	165
LRC[b]	0.858	0.514	0	0.513	1.40	0.304	0.127	1.14	0	0.810	0.076
Boot[c]	0.332	0.199	0	0.461	0.895	1.70[d]	852[d]	32.2[d]	0	1.09	0.051
JGM[e]	0.833	0.382	0	0.741	1.42	41.0	0.593	993	0	4.45	1.79

TABLE I. Exciton binding energies calculated with Eq. (1), compared with experimental values (all numbers in meV). All calculations are head-only; see text for other technical details. The BSE results for GaAs and β-GaN were not calculated. The estimated error due to the head-only approximation is $< 10\%$ for all many-body calculations, and $< 5\%$ for TDDFT.

[a] Head-only calculation, equivalent to SXX with $\gamma = 0.2$ independent of the material.

[b] With the empirical formula of Ref. [7].

[c] The bootstrap kernel of Ref. [8].

[d] The convergence of the bootstrap kernel strongly depends on the number of bands included in the iterative calculation of the kernel. These results are obtained by evaluating the bootstrap kernel with 30 bands. The results reported in Ref. [32] were not fully converged.

[e] The jellium-with-gap model of Ref. [9].

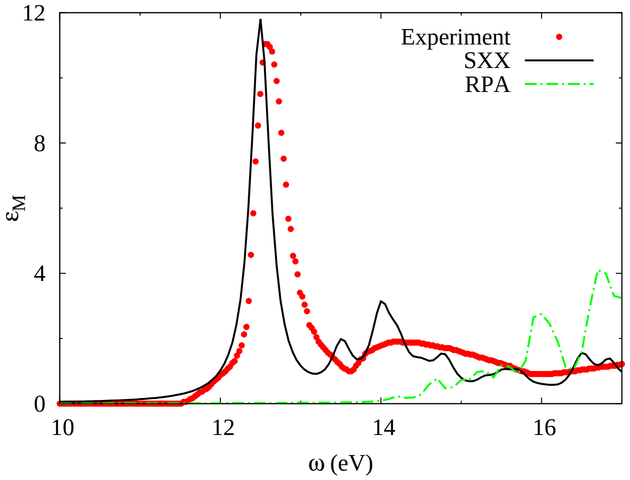

FIG. 3. (Color online) Absorption spectrum of LiF calculated with SXX and RPA, compared with experiment [40].

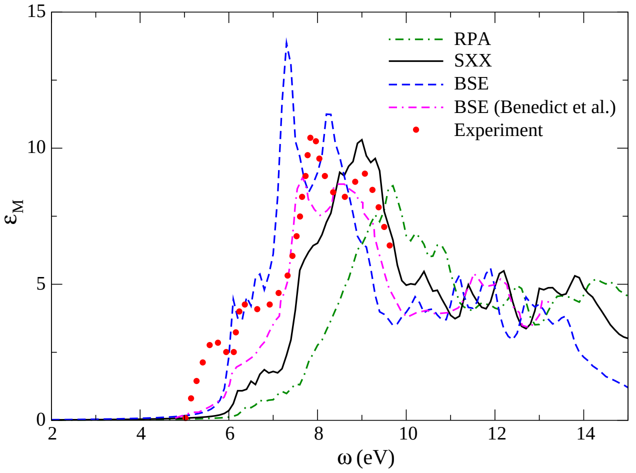

FIG. 4. (Color online) Absorption spectrum of AlN calculated with SXX, RPA, and BSE, compared with experiment [41]. The BSE spectrum of Benedict *et al.* [42] is also shown.

small molecules in mind, so its good performance for bound excitons in semiconductors seems fortuitous.

To demonstrate that our method yields good results not only for the exciton binding energies, we present the optical spectra of LiF (Fig. 3), AlN (Fig. 4), and Si (Fig. 5). The spectra are obtained in a standard manner via the imaginary part of the macroscopic dielectric function [2]. We use 20 bands and 256 k-points for LiF, 10 bands and 256 k-points for AlN and Si. All calculations include local field effects. We obtain a very good agreement of the position and strength of the strong bound-exciton peak in LiF compared to experiment, which is also evident from the good agreement between the calculated and fitted screening parameters shown in Fig. 2. For the smaller-gap materials AlN and Si, the excitonic enhancement of the band-edge spectrum is somewhat underestimated (the bound excitons are not shown in Figs. 4 and 5 since E_b is smaller than the frequency resolution). Here, the excitonic enhancement effects in the BSE and experimental spectra are due to continuum excitons. Compared to RPA, the SXX spectra in Figs. 4 and 5 give a much better description of the excitonic enhancement effects.

In conclusion, we propose a very simple nonempirical screening factor for nonlocal exchange, derived as a simplification of BSE. We show that it is easier to derive a good approximation in the many-body framework than

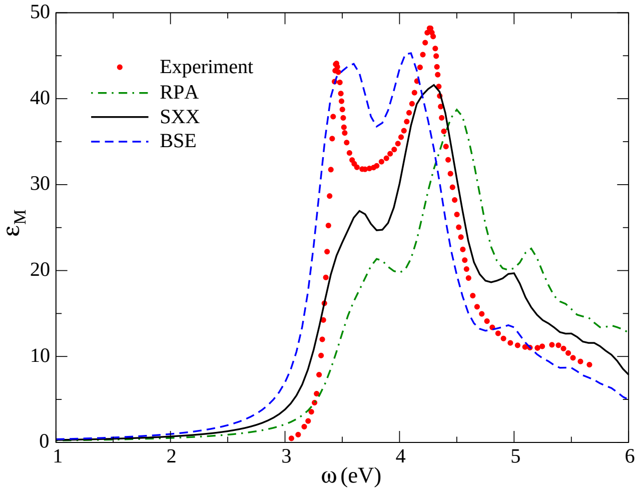

FIG. 5. (Color online) Absorption spectrum of Si calculated with SXX, RPA, and BSE, compared with experiment [43].

developing a better long-ranged xc kernel for TDDFT. Our SXX approach yields exciton binding energies of a wide range of semiconductors and insulators in good agreement with experiment; the performance is consistently better than currently available TDDFT methods. The SXX method works well for the optical spectra of wide-gap materials, and captures continuum excitonic effects in small-gap materials to some extent, although there is still some room for improvement.

The SXX approach constitutes a first step towards a hybrid xc kernel specifically designed for optical properties in periodic insulators and semiconductors. In this paper we have focused on the long-range behavior of the xc kernel; the next step will be to match the SXX approach with suitable xc functionals for the short range to capture local-field effects. This should have minor effects on strongly bound excitons, but is likely to lead to an improvement of the continuum part of the optical spectrum. Work along these lines is in progress.

We thank Lucia Reining for very helpful discussions. C.U. thanks the ETSF-Palaiseau group for its hospitality and the Ecole Polytechnique for its support during an extended visit in 2014. Z.-h.Y. and C.U. are supported by NSF grant DMR-1408904. F. S. thanks GENCI for computer time (project 0544).

[1] W. Hanke and L. J. Sham, Phys. Rev. B **21**, 4656 (1980).
[2] G. Onida, L. Reining, and A. Rubio, Rev. Mod. Phys. **74**, 601 (2002).
[3] E. Runge and E. K. U. Gross, Phys. Rev. Lett. **52**, 997 (1984).
[4] M. A. L. Marques, N. T. Maitra, F. M. S. Nogueira, E. K. U. Gross, and A. Rubio, eds., *Fundamentals of time-dependent density functional theory*, Lecture notes in physics (Springer, Berlin, 2012).
[5] C. A. Ullrich, *Time-dependent density-functional theory: concepts and applications* (Oxford University Press, Oxford, 2012).
[6] F. Sottile, K. Karlsson, L. Reining, and F. Aryasetiawan, Phys. Rev. B **68**, 205112 (2003).
[7] S. Botti, F. Sottile, N. Vast, V. Olevano, L. Reining, H.-C. Weissker, A. Rubio, G. Onida, R. Del Sole, and R. W. Godby, Phys. Rev. B **69**, 155112 (2004).
[8] S. Sharma, J. K. Dewhurst, A. Sanna, and E. K. U. Gross, Phys. Rev. Lett. **107**, 186401 (2011).
[9] P. E. Trevisanutto, A. Terentjevs, L. A. Constantin, V. Olevano, and F. Della Sala, Phys. Rev. B **87**, 205143 (2013).
[10] P. L. de Boeij, F. Kootstra, J. A. Berger, R. van Leeuwen, and J. G. Snijders, J. Chem. Phys. **115**, 1995 (2001).
[11] L. Reining, V. Olevano, A. Rubio, and G. Onida, Phys. Rev. Lett. **88**, 066404 (2002).
[12] F. Sottile, V. Olevano, and L. Reining, Phys. Rev. Lett. **91**, 056402 (2003).
[13] G. Adragna, R. Del Sole, and A. Marini, Phys. Rev. B **68**, 165108 (2003).
[14] A. Marini, R. Del Sole, and A. Rubio, Phys. Rev. Lett. **91**, 256402 (2003).
[15] P. Ghosez, X. Gonze, and R. W. Godby, Phys. Rev. B **56**, 12811 (1997).
[16] S. Botti, A. Schindlmayr, R. Del Sole, and L. Reining, Rep. Prog. Phys. **70**, 357 (2007).
[17] Y.-H. Kim and A. Görling, Phys. Rev. Lett. **89**, 096402 (2002).
[18] Y.-H. Kim and A. Görling, Phys. Rev. B **66**, 035114 (2002).
[19] F. Bruneval, F. Sottile, V. Olevano, and L. Reining, J. Chem. Phys. **124**, 144113 (2006).
[20] P. J. Stephens, F. J. Devlin, C. F. Chabalowski, and M. J. Frisch, J. Phys. Chem. **98**, 11623 (1994).
[21] L. Bernasconi, S. Tomić, M. Ferrero, M. Rérat, R. Orlando, R. Dovesi, and N. M. Harrison, Phys. Rev. B **83**, 195325 (2011).
[22] S. Tomić, L. Bernasconi, B. G. Searle, and N. M. Harrison, J. Phys. Chem. C **118**, 14478 (2014).
[23] J. Heyd, G. E. Scuseria, and M. Ernzerhof, J. Chem. Phys. **118**, 8207 (2003).
[24] J. Heyd, G. E. Scuseria, and M. Ernzerhof, J. Chem. Phys. **124**, 219906 (2006).
[25] J. Heyd, J. E. Peralta, G. E. Scuseria, and R. L. Martin, J. Chem. Phys. **123**, 174101 (2005).
[26] L. Schimka, J. Harl, and G. Kresse, J. Chem. Phys. **134**, 024116 (2011).
[27] J. E. Moussa, P. A. Schultz, and J. R. Chelikowsky, J. Chem. Phys. **136**, 204117 (2012).
[28] J. Paier, M. Marsman, and G. Kresse, Phys. Rev. B **78**, 121201 (2008).
[29] M. E. Casida, in *Recent developments and applications in density functional theory*, edited by J. M. Seminario (Elsevier, Amsterdam, 1996).
[30] C. A. Ullrich and Z.-H. Yang, Brazilian J. Phys. **44**, 154 (2014).
[31] F. Bruneval, F. Sottile, V. Olevano, and L. Reining, J. Chem. Phys. **124**, 144113 (2006).
[32] Z.-H. Yang and C. A. Ullrich, Phys. Rev. B **87**, 195204 (2013).
[33] Z.-H. Yang, Y. Li, and C. A. Ullrich, J. Chem. Phys. **137**, 014513 (2012).

[34] M. A. L. Marques, J. Vidal, M. J. T. Oliveira, L. Reining, and S. Botti, Phys. Rev. B **83**, 035119 (2011).

[35] L. X. Benedict, E. L. Shirley, and R. B. Bohn, Phys. Rev. B **57**, R9385 (1998).

[36] L. Hedin, Phys. Rev. **139**, 796 (1965).

[37] P. Cudazzo, I. V. Tokatly, and A. Rubio, Phys. Rev. B **84**, 085406 (2011).

[38] X. Gonze, B. Amadon, P.-M. Anglade, J.-M. Beuken, F. Bottin, P. Boulanger, F. Bruneval, D. Caliste, R. Caracas, M. Côté, T. Deutsch, L. Genovese, P. Ghosez, M. Giantomassi, S. Goedecker, D. R. Hamann, P. Hermet, F. Jollet, G. Jomard, S. Leroux, M. Mancini, S. Mazevet, M. J. T. Oliveira, G. Onida, Y. Pouillon, T. Rangel, G.-M. Rignanese, D. Sangalli, R. Shaltaf, M. Torrent, M. J. Verstraete, G. Zerah, and J. W. Zwanziger, Computer Phys. Comm. **180**, 2582 (2009).

[39] H. J. Monkhorst and J. D. Pack, Phys. Rev. B **13**, 5188 (1976).

[40] D. M. Roessler and W. C. Walker, J. Opt. Soc. Am. **57**, 835 (1967).

[41] V. Cimalla, V. Lebedev, U. Kaiser, R. Goldhahn, C. Foerster, J. Pezoldt, and O. Ambacher, Phys. Status Solidi C **2**, 2199 (2005).

[42] L. X. Benedict, T. Wethkamp, K. Wilmers, C. Cobet, N. Esser, E. L. Shirley, W. Richter, and M. Cardona, Solid State Comm. **112**, 129 (1999).

[43] P. Lautenschlager, M. Garriga, L. Viña, and M. Cardona, Phys. Rev. B **36**, 4821 (1987).

Chapter 4

Numerical Developments

DEVELOPMENTS of theory are of course crucial in our domain, to understand the behaviour of matter, to anayse in details the different ingredients entering in a given phenomena, or to predict a new feature or a new experiment. However we have to remember that an important part of the work is represented by *obtaining* the results out of a simulation job. This is not always the case, but most of the time is. It is then also crucial to try to obtain those results as more efficiently as possible. I shall not mention here the technical details about optimization and parallelization of the simulation codes.[1] But, since part of my reseach activity is invested on code and algorithm developments, I report here a couple of examples in which a new numerical scheme, once implemented, allowed us to tackle a bigger problem (or a bigger system)

4.1 Lanczos algorithm for the BSE

Within Green's function theory, the dielectric function is written in terms of eigenvalues and eigenvectors of an excitonic matrix, the so-called Bethe-Salpeter equation (BSE). This procedure, beside of being time consuming, also requires huge amount of memory to be stored and diagonalised. R. Haydock has developed, in 1980, a recursive method for dynamical problems. Margherita Marsili, during her PhD work (University of Rome Tor Vergata), within her 4-months leave under my supervision at Polytechnique, implemented the algorithm for the specific problem of the BSE into the EXC code [89]. The outcome of this work was the first publication of her PhD thesis [100]. Today the method is currently used by all users of the EXC code and, thanks to a recent porting, also into the ABINIT project [67]. The details of the method can be found in the original article from Haydock [87, 88], which extend the Lanczos iterative technique, and in the appendix of M.Marsili thesis [90].

4.2 Hilbert transform

Polarizability is a key ingredient for ab initio calculations in the framework of the Time Dependent Density Functional Theory. The first step, the evaluation of the independent-particle polarizability (see Eq.(2.4)), is also the most cumbersome, as we have seen in Section 2.1. During her Master thesis, Lucia Caramella had a 3-moths leave in our group, under my supervision, to implement and quantitatively analyse the performances of an Hilbert transform based approach in speeding up the calculations of this quantity. The conclusions, wrapped up in an article [101], show that the method

---

[1] The only exception being the section about porting DP, our TDDFT code, over GPU. Since it consists of quite a new paradigm for numerical simulations, it deserves, in my view, mention here. It is however reported only in the Appendix.

is particularly advantageous for systems presenting strong anisotropies for which the crystal local-field effects are important, and when many frequencies have to be evaluated (for example a wide range energy-loss spectrum). The method is today implemented in the DP code (http://www.dp-code.org) [66], as well as in the Abinit code (http://www.abinit.org) [67]. The details of the method can be found in L.Caramella's thesis [102].
PLEASE REFER TO THE ATTACHED ARTICLE

PHYSICAL REVIEW B **75**, 205405 (2007)

Optical properties of real surfaces: Local-field effects at oxidized Si(100)(2×2) computed with an efficient numerical scheme

L. Caramella,[1] G. Onida,[1] F. Finocchi,[2] L. Reining,[3] and F. Sottile[3]
[1]*European Theoretical Spectroscopy Facility (ETSF)*
and Dipartimento di Fisica dell' Università degli Studi di Milano and CNISM, via Celoria 16, I-20133 Milano, Italy
[2]*European Theoretical Spectroscopy Facility (ETSF)*
and Institut des Nanosciences de Paris (INSP), Université Pierre et Marie Curie-Paris 6, Université Denis Diderot-Paris 7
and CNRS (UMR 7588), 140, rue de Lourmel, F-75015 Paris, France
[3]*European Theoretical Spectroscopy Facility (ETSF)*
and Laboratoire des Solides Irradiées, UMR 7462 CNRS/CEA, Ecole Polytechnique, F-91128 Palaiseau, France
(Received 20 November 2006; revised manuscript received 7 February 2007; published 3 May 2007)

We show the application of an efficient numerical scheme to obtain the independent-particle dynamic polarizability matrix $\chi^{(0)}(\mathbf{r},\mathbf{r}',\omega)$, a key quantity in modern *ab initio* excited-state calculations. The method has been applied to the study of the optical response of a realistic oxidized silicon surface, including the effects of crystal local fields. The latter are shown to substantially increase the surface optical anisotropy in the energy range below the bulk band gap. Our implementation in a large-scale *ab initio* computational code allows us to make a quantitative study of the CPU time scaling with respect to the system size, and demonstrates the real potential of the method for the study of excited states in large systems.

DOI: 10.1103/PhysRevB.75.205405 PACS number(s): 71.15.Qe, 78.68.+m, 78.40.−q, 71.15.Mb

INTRODUCTION

The recent developments of experimental techniques for the nondestructive study of solid surfaces call for a simultaneous improvement of the theoretical tools: the interpretation and prediction of optical and dielectric properties of surfaces require more and more quantitative and reliable *ab initio* calculations, possibly including many-body effects. Such an improvement of the theoretical description can be achieved, for example, by lifting some of the usual approximations adopted in the calculation of the optical response. However, making less approximations increases the computational heaviness and is only possible if efficient numerical algorithms can be adopted. A good example is given by the calculation of the independent-particle dynamical polarizability matrix $\chi^{(0)}(\mathbf{r},\mathbf{r}',\omega)$, which is often required as the starting point in time-dependent density-functional theory[1] (TDDFT) and in many-body perturbation-theory-based calculations, such as in the GW (Ref. 2) or GW+Bethe-Salpeter schemes (for a review, see, e.g., Ref. 3). Evaluating the full response matrix for realistic, many-atom systems can be a major computational bottleneck, since it requires a computational effort growing as the fourth power of the number of atoms, and the availability of efficient numerical schemes becomes a key issue. Recently, schemes allowing to decouple the sum over states and the frequency dependence have been presented. Miyake and Aryasetiawan[4] and Shishkin and Kresse[5] have shown that methods based on the Hilbert transform can substantially reduce the computational cost of frequency-dependent response functions, making it comparable to that of the static case. In particular, the approach presented in Ref. 4 has been applied to a linear-muffin-tin-orbital calculation of the spectral function of bulk copper, while in Ref. 5, a work focused on the GW implementation using the projector augmented-wave method,[6] a similar approach is used to compute the spectral function of bulk silicon and materials with *d* electrons (GaAs and CdS). Another recent work by Foerster[7] is focused on the same issue and demonstrates how the use of a basis of local orbitals can reduce the scaling of a susceptibility calculation for an *N*-atom system from N^4 to N^3 operations for each frequency, but at the cost of disk space. However, as a matter of fact, application of such nontraditional methods to large supercells, such as those involved in real surface calculations, has not been presented so far.

It may be stressed that for a given application, the computational burden is determined not only by general scaling law but also by prefactors. In particular, prefactors determine the crossover where one method becomes more convenient than the other. This crossover has not yet been discussed for the Hilbert-transform methods.

In the present work, we demonstrate the application of a scheme—similar to that introduced in Refs. 4 and 5—based on the efficient use of the Hilbert transforms by performing the calculation of the optical properties of a realistic, reconstructed surface: Si(100)(2×2):O, covered with 1 ML (monolayer) of oxygen.

We provide a *quantitative* evaluation of the computational gain for this calculation of the full dynamical independent-particle polarizability. The latter is constructed from Kohn-Sham eigenvalues and eigenvectors and is then used to compute surface optical spectra, including the local-field (LF) effects on reflectance anisotropy (RAS) and surface differential reflectivity (SDR) spectra of this surface.

The impact of local fields on surface optical spectra has been a controversial issue for decades, especially concerning the so-called intrinsic or bulk-originated effects. The latter have been measured for energies above the bulk band gap, since the seminal works by Aspnes and Studna[8] showed that the normal incidence optical reflectivity of natural Si(110) and Ge(110) surfaces displays an anisotropy on the order of 10^{-3}. The effect was called intrinsic, since it is not due to the existence of surface states nor to surface reconstruction. Early model calculations by Mochán and Barrera[9] performed for a lattice of polarizable entities and exploiting the Clausius-Mossotti relation pointed out that intrinsic anisotropies could be due to LF effects. A subsequent work by Del Sole *et al.*[10] based on tight binding has shown that the RAS spectra calculated for Si(110):H within this semiempirical scheme did not reproduce well the experimental data, despite the inclusion of surface LF effects. However, more recent calculations based on realistic band structures [within density-functional-theory–local-density-approximation (DFT-LDA) with GW-corrected band gap][11] have suggested that intrinsic anisotropies at the bulk critical points for the (almost ideally terminated) Si (110):H surface could arise as a consequence of surface perturbation of bulk states, without invoking LF effects. Other tight-binding calculations (see, e.g., Ref. 12) suggested the existence of intrinsic surface optical anisotropies not due to surface local fields.

A substantial improvement in clarifying the role of local fields has been achieved only recently by Bechstedt and coworkers, who carried out a calculation of the RAS spectra of Si(110):H (Ref. 13) and monohydride Si(100)(2×1) (Ref. 14) including self-energy, crystal local fields, and excitonic effects from a fully *ab initio* point of view. In both the considered surfaces, which have no surface states within the bulk band gap, the LFs were found to cause a slight decrease of the optical reflectivity; however, the effect was found to cancel to a large extent in the RAS spectra, being almost identical for the two polarizations of the incident light. The situation may be different in the case of extrinsic optical anisotropies, i.e., those directly related to surface states and surface reconstruction and appearing below the bulk band gap. In at least one case, substantial effects due to LF have been reported.[15] However, further calculations for a wider class of surfaces are necessary in order to assess this point more precisely.

The system we consider here belongs to a widely studied family of surfaces, because of their importance in the understanding of silicon–silicon-dioxide interfaces in semiconductor technology. Despite the many experimental[16–22] and theoretical[23–28] works that appeared in recent years, the debate on the oxidation mechanism of Si(100) is still open. However, the most favorable oxygen adsorption sites in the first stages of (room-temperature) oxidation process have been identified as the dimer-bridge position, and a bridge position on the backbond corresponding to the lower atom of the dimer. This remark is supported by scanning tunneling microscopy experiments[22] and by a first-principles molecular-dynamics calculation.[28] From the theoretical point of view, ground- and excited-state properties of Si(100)(2×2):O at 0.5 and 1 ML coverages have been recently studied by some of the authors;[29] however, computational limits prevented until now the inclusion of the local-field effects in the *ab initio* calculation of optical properties.

This work is organized as follows: in Sec. I, we summarize the theoretical framework and the expression for $\chi^{(0)}$ usually employed in plane-wave based calculations. We then show how the Hilbert-transform (HT) technique can be applied, as a generalization of the Kramers-Kronig relations, in order to decouple the sum over states and the frequency dependence in $\chi^{(0)}$. Estimates of the accuracy and of the possible computational gain are presented for a model system. In the following section, we use our implementation of the HT scheme in the *ab initio* DP (Ref. 30) code to study a real reconstructed surface, oxidized Si(100)(2×2), for which we present the calculation of its optical reflectivity spectra (RAS and SDR) with the inclusion of local-field effects. Finally, we carefully compare the numerical performance of the DP code with and without the use of HTs, and we draw our conclusions.

I. THEORY

The starting point of our work is a DFT-LDA ground-state calculation performed with the ABINIT code[31] yielding independent-particle eigenvalues and eigenvectors within the Kohn-Sham scheme.[32] Besides the occupied ones, empty (conduction) states up to an energy of several eV above the Fermi level are obtained by means of iterative diagonalization techniques.

However, in order to study the optical and dielectric response, the level of theory must be brought beyond the ground-state one, using, e.g., many-body perturbation theory or TDDFT.[1] The latter is particularly suited for the study of neutral excitations, as those involved in optical reflectivity and electron energy loss. Within TDDFT, it is possible to obtain the retarded density-density response function $\chi(\mathbf{r},\mathbf{r}',\omega)$ from its noninteracting Kohn-Sham counterpart $\chi^{(0)}(\mathbf{r},\mathbf{r}',\omega)$ through a Dyson-type equation:

$$\chi = \chi^{(0)} + \chi^{(0)} K \chi, \tag{1}$$

where the kernel K contains two terms: the Coulomb potential v_c and the exchange-correlation kernel $f_{xc}(\mathbf{r},\mathbf{r}',\omega)$. An explicit expression for χ is then given by

$$\chi = \chi^{(0)}[1 - (v_c + f_{xc})\chi^{(0)}]^{-1}. \tag{2}$$

Equations (1) and (2) are matrix equations, involving two-point functions such as χ and $\chi^{(0)}$. In the present case, working within a plane-wave expansion, $\chi_{\mathbf{GG}'}(\mathbf{q},\omega)$ and $\chi^{(0)}_{\mathbf{GG}'}(\mathbf{q},\omega)$ are matrices in reciprocal space, and

$$v_c(\mathbf{q}+\mathbf{G}) = \frac{4\pi}{|\mathbf{q}+\mathbf{G}|^2} \tag{3}$$

is the Coulomb potential. The exchange-correlation contribution f_{xc} is not exactly known. It can be included in an approximate form, e.g., using the LDA functional[33] in the adiabatic approximation, or in a more sophisticated approximation such as those described in Refs. 34–39. In order to compare with optical experiments, the macroscopic dielectric function $\varepsilon_M(\omega)$ must be calculated. The latter is defined as

$$\varepsilon_M(\omega) = \lim_{\mathbf{q}\to\mathbf{0}} \frac{1}{\varepsilon^{-1}_{\mathbf{G}=\mathbf{G}'=0}(\mathbf{q},\omega)}, \tag{4}$$

where the inverse dielectric function $\varepsilon^{-1}_{\mathbf{G},\mathbf{G}'}(\mathbf{q},\omega)$ is linked to the response function χ by

$$\varepsilon^{-1}_{\mathbf{G},\mathbf{G}'}(\mathbf{q},\omega) = 1 + v_c(\mathbf{q}+\mathbf{G})\chi_{\mathbf{G},\mathbf{G}'}(\mathbf{q},\omega). \tag{5}$$

When only v_c is included in the kernel K of Eq. (1), exchange and correlation effects in the response are neglected, while the use of the correct expression [Eq. (4)] still considers the LF effects.[40] Already at this level, the calculations can become very heavy from the computational point of view when the full $\chi^{(0)}_{\mathbf{G},\mathbf{G}'}(\omega)$ matrix has to be obtained. In complex systems with large unit cells, the only tractable way to proceed is often to neglect local fields by assuming that $\varepsilon_M(\omega)$ is well approximated by the average of the microscopic dielectric function:

$$\varepsilon^{NLF}_M(\omega) = \lim_{\mathbf{q}\to 0} \varepsilon_{\mathbf{0},\mathbf{0}}(\mathbf{q},\omega). \tag{6}$$

This corresponds to neglecting the off-diagonal elements of ε in reciprocal space.[41] Moreover, when exchange and correlation effects are neglected [independent-quasiparticle approximation or independent-particle random-phase approximation (IP-RPA)], the imaginary part of the macroscopic dielectric function ε^{NLF}_M takes the following simple Ehrenreich–Cohen[42] form:

$$\operatorname{Im} \varepsilon^{NLF}_M(\omega) = \frac{16\pi}{\omega^2}\sum_{ij} |\langle\psi_i|\mathbf{v}|\psi_j\rangle|^2 \delta(\epsilon_j - \epsilon_i - \omega), \tag{7}$$

where $\mathbf{v}$ is the velocity operator and i and j stand for occupied and unoccupied states respectively. The substantial simplification obtained in this case explains why most of the calculations of the optical properties of real surfaces are done within the independent-quasiparticle approach, neglecting local-field effects. On the other hand, a fast and efficient scheme to compute the full matrix $\chi^{(0)}$ represents a key issue in order to be able to go beyond this approximation, e.g., by including the local fields, as we do in the present work. Moreover, an efficient method giving access to the full $\chi^{(0)}$ is of paramount importance when the screened Coulomb interaction $W_{\mathbf{GG}'}(\mathbf{q})$ is needed, such as in *ab initio* GW calculations. In the following, we hence concentrate on the expression of $\chi^{(0)}$ itself, i.e., assuming time reversal,

$$\chi^{(0)}(\mathbf{r},\mathbf{r}',\omega) = 2\sum_{ij} f_i(1-f_j)\psi^*_i(\mathbf{r})\psi_j(\mathbf{r})\psi^*_j(\mathbf{r}')\psi_i(\mathbf{r}') \times\left[\frac{1}{\omega-(\epsilon_j-\epsilon_i)+i\eta} - \frac{1}{\omega+(\epsilon_j-\epsilon_i)+i\eta}\right], \tag{8}$$

where f_i are occupation numbers (f_j=0 and f_i=1 in the present case), η is an infinitesimal, and the factor of 2 is due to the spin degeneracy. Switching to reciprocal space and focusing on the case of semiconductors, we make valence (v) and conduction (c) bands appear explicitly, and rewrite this equation as

$$\chi^{(0)}_{\mathbf{G},\mathbf{G}'}(\mathbf{q},\omega) = \frac{2}{\Omega_0 N_k}\sum_{\mathbf{k}}\sum_{c,v}\left[\frac{\tilde{\rho}_{vc\mathbf{k}}(\mathbf{q}+\mathbf{G})\tilde{\rho}^*_{vc\mathbf{k}}(\mathbf{q}+\mathbf{G}')}{\omega-(\epsilon_{c\mathbf{k}}-\epsilon_{v\mathbf{k}})+i\eta} - \frac{\tilde{\rho}_{cv\mathbf{k}}(\mathbf{q}+\mathbf{G})\tilde{\rho}^*_{cv\mathbf{k}}(\mathbf{q}+\mathbf{G}')}{\omega+(\epsilon_{c\mathbf{k}}-\epsilon_{v\mathbf{k}})+i\eta}\right], \tag{9}$$

where Ω_0 is the volume of the unit cell and we have also introduced the notation $\tilde{\rho}_{vc\mathbf{k}}(\mathbf{q}+\mathbf{G})$ to indicate the Fourier transform of $\phi^*_{v\mathbf{k}+\mathbf{q}}(\mathbf{r})\phi_{c\mathbf{k}}(\mathbf{r})$. From the numerical point of view, the evaluation of these sums for each frequency ω can become very heavy. Indeed, for a realistic system, the evaluation of Eq. (9) involves, for each frequency, the summation over a large number of terms, which for a system of 50 atoms is typically on the order of 10^8.

The Hilbert-transform approach

Since in this paper we consider the case of the $\mathbf{q}\to 0$ limit to study optical properties, in the following the label $\mathbf{q}$ will be omitted to simplify the notation. The generalization to the case of finite $\mathbf{q}$ is straightforward. Introducing a simplified notation for band and $\mathbf{k}$-point indices, we define a single index of transition t to represent the triplet $\{v,c,\mathbf{k}\}$. In this way, ω_t indicates an (always positive) energy difference $(\varepsilon_{c,\mathbf{k}}-\varepsilon_{v,\mathbf{k}})$. We also introduce the two complex quantities

$$Z_{1,t} = \frac{2}{\Omega_0 N_k}\tilde{\rho}_{vc\mathbf{k}}(\mathbf{G})\tilde{\rho}^*_{vc\mathbf{k}}(\mathbf{G}'), \tag{10}$$

$$Z_{2,t} = -\frac{2}{\Omega_0 N_k}\tilde{\rho}_{cv\mathbf{k}}(\mathbf{G})\tilde{\rho}^*_{cv\mathbf{k}}(\mathbf{G}'), \tag{11}$$

such that

$$\chi^{(0)}_{\mathbf{GG}'}(\omega) = \sum_t\left(\frac{Z_{1,t}}{\omega-\omega_t+i\eta} + \frac{Z_{2,t}}{\omega+\omega_t+i\eta}\right). \tag{12}$$

When $\mathbf{G}=\mathbf{G}'$ (diagonal elements), the $Z_{i,t}$ are real and $Z_1 = -Z_2$. Using

$$\lim_{\eta\to 0^+}\frac{1}{x\pm i\eta} = \mathcal{P}\left(\frac{1}{x}\right) \mp i\pi\delta(x), \tag{13}$$

one can rewrite the $\eta\to 0^+$ limit of Eq. (12) as the sum of the following four terms:

$$\chi^{R1}_{\mathbf{GG}'}(\omega) = \mathcal{P}\sum_t \frac{Z_{1,t}}{\omega-\omega_t}, \tag{14}$$

$$\chi^{R2}_{\mathbf{GG}'}(\omega) = -i\pi\sum_t Z_{1,t}\delta(\omega-\omega_t), \tag{15}$$

$$\chi^{A1}_{\mathbf{GG}'}(\omega) = \mathcal{P}\sum_t \frac{Z_{2,t}}{\omega+\omega_t}, \tag{16}$$

$$\chi^{A2}_{\mathbf{GG}'}(\omega) = -i\pi\sum_t Z_{2,t}\delta(\omega+\omega_t). \tag{17}$$

R and A label resonant and antiresonant contributions, respectively, and the four terms are in general complex quan-

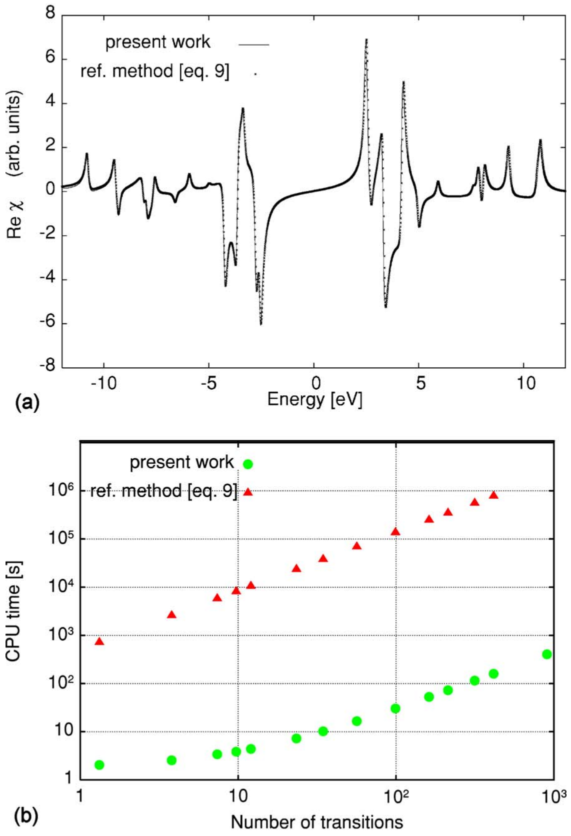

FIG. 1. (Color online) (a) Accuracy test for the HT-based algorithm, shown for the real part of $\chi^{(0)}_{\mathbf{GG}'}(\omega)$ of a model system (see text). The two curves turn out to be indistinguishable on the scale of the plot (maximum error less than 0.5%). (b) Computational load requested to evaluate $\chi^{(0)}_{\mathbf{GG}'}(\omega)$ on a model system, as a function of the number of transitions, for both the traditional and the HT-based methods.

ties. In $\chi^{R2}(\omega)$ and $\chi^{A2}(\omega)$, each term Z_t contributes to the function χ only at $\omega=\omega_t$, and has no effect elsewhere. By discretizing the frequency axis, the sums over t appearing in χ^{R2} and χ^{A2} can hence be performed once and for all, at difference with those labeled by $R1$ and $A1$ for which the sums should be calculated for each ω. Thanks to the linearity of the Hilbert transform, defined as

$$H[f(t)] = \frac{1}{\pi}\mathcal{P}\int_{-\infty}^{+\infty}\frac{f(x)}{t-x}dx, \tag{18}$$

one can, however, directly obtain χ^{A1} and χ^{R1} from χ^{A2} and χ^{R2}:

$$\chi^{A1} = iH[\chi^{A2}], \tag{19}$$

$$\chi^{R1} = iH[\chi^{R2}]. \tag{20}$$

In such a way,[43] it is possible to recover the complete $\chi^{(0)}_{\mathbf{G},\mathbf{G}'}(\omega)$ in the spectral range of interest from the knowledge of a single sum performed over the poles ω_t. In other words, one can avoid the explicit summation over $t=\{c,v,\mathbf{k}\}$ to be repeated for each frequency. The present procedure for the calculation of the frequency-dependent polarizability matrices is similar to the method of Miyake and Aryasetiawan,[4] with the difference that these authors represented δ functions using Gaussians, instead of bare rectangular functions as in our case.[44]

Our scheme has first been tested on a model system[45] in order to check both the accuracy and the efficiency of the algorithm. Figure 1 shows the results of the test, comparing $\chi^{(0)}(\omega)$ (real part) as obtained in the traditional way [i.e., by evaluating expression (9) for several frequencies] and by the HT algorithm. The results are practically indistinguishable on the scale of the plot. The same figure shows the growth of the required CPU time as a function of the number of transitions (number of $\{v,c,\mathbf{k}\}$ triplets), simulating an increasing system size.

The possibility to achieve such a large gain, at least in principle and for a simple system, was also noticed in the previous works describing efficient algorithms for the calculation of $\chi^{(0)}$.[4,5] Alternative approaches for efficient TDDFT calculations have also been suggested. In particular, another promising scheme based on a superoperator approach and allowing to access TDDFT *spectra* in a numerically efficient way has recently been introduced by Walker *et al.*[46] This approach is, however, not designed for the calculation of the whole matrix $\chi^{(0)}$, contrary to the method studied here.

In order to know the actual CPU requirements for the calculation of $\chi^{(0)}$, and to explore the possibilities in studying complex systems, such as the impurity levels and band offsets mentioned in Ref. 5, in practice, one has to take into account the time used to compute the matrix elements [numerators in Eq. (12)] and the time used to perform the Hilbert transforms, which was not explicitly evaluated in previous works. In the following, we hence applied our approach, similar in its essence to that used in Refs. 4 and 5, to a large system investigating the actual numerical performances of the algorithm. As it will be shown below, substantial improvements can actually be achieved in such realistic calculations.

II. APPLICATIONS

The method has been implemented into the large-scale, plane-wave *ab initio* TDDFT code named DP,[30] developed by the French node of ETSF.[47] We have then applied it to the study of the optical properties of the Si(100)(2×2):O surface as mentioned in the Introduction. We adopt the equilibrium structure for 1 ML coverage shown in Fig. 2, which is representative of a situation in which dimer and backbond sites are both occupied by an oxygen atom (structure c3 in Ref. 48). The surface is simulated with a slab composed by six layers, containing 48 Si and 8 O atoms, in a repeated supercell approach. Our structural results agree well with those of previous calculations.[24,48,49] We use standard norm conserving pseudopotentials of the Hamann type[50] and an energy cutoff of 30 Ry, yielding 15 000 plane waves in our unit cell. Eight special (Monkhorst-Pack[51]) **k** points in the irreducible Brillouin zone are used for the self-consistent ground-state calculation, while a 7×7 grid is used in the evaluation of $\chi^{(0)}_{\mathbf{GG}'}(\omega)$. Kohn-Sham eigenvalues and eigen-

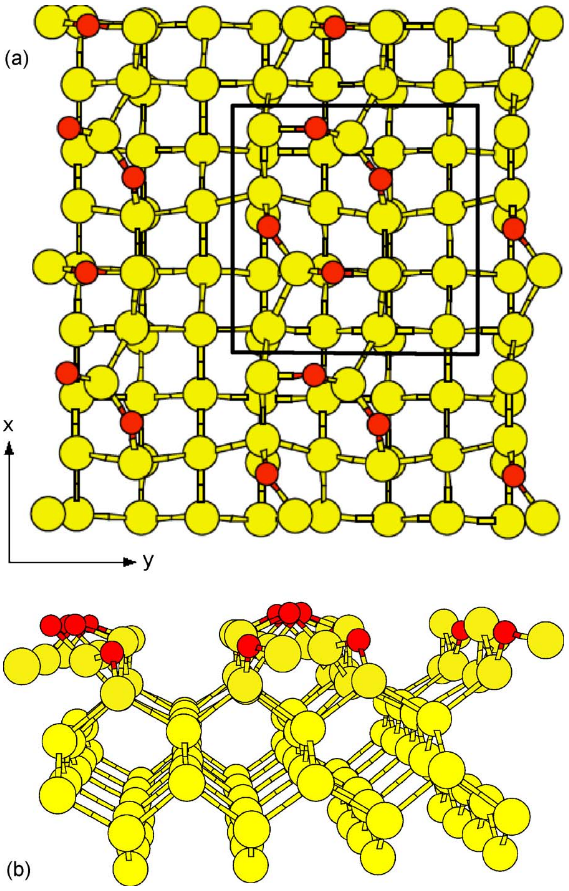

FIG. 2. (Color online) Surface structure of Si(100)(2×2):O at 1 ML coverage with oxidation of Si dimers and backbonds. Oxygen atoms are depicted in dark gray (red), while light gray (yellow) circles represent bulk and surface Si atoms. Dimer chains are oriented along the *x* direction. (a) Top view of the surface (*xy* plane), with the surface unit cell; (b) lateral view of the half slab (*yz* plane).

vectors are obtained for all occupied states (120) and for empty states up to 15 eV above the highest occupied state (top valence). Optical properties are computed through the evaluation of the macroscopic dielectric function with and without the inclusion of local-field effects.

Figure 3 shows the imaginary part of the slab dielectric function as a function of the energy. Local-field effects are shown to be quite important in the low-energy region 0–2 eV, enhancing ε_M for light polarized along the direction of the dimer chains (*x* direction, see Fig. 2) and suppressing it for light polarized along the dimers axis (*y* direction). This goes in the direction of a better description of themicroscopic inhomogeneities of the system. In the present case, the extrinsic surface optical anisotropy, as defined in the Introduction, is hence found to be visibly affected by LF. In the case of the third polarization, i.e., the one perpendicular to the surface (not experimentally relevant in the case of normally incident light), local-field effects are huge and introduce a blueshift of the absorption edge as large as 5 eV. This can be explained by the strong inhomogeneity of the charge distribution in passing from the slab to the vacuum, leading to a classical depolarization effect. Similar behaviors have been found, for example, in GaAs/AlAs superlattices,[52] graphite,[53] and nanowires.[54]

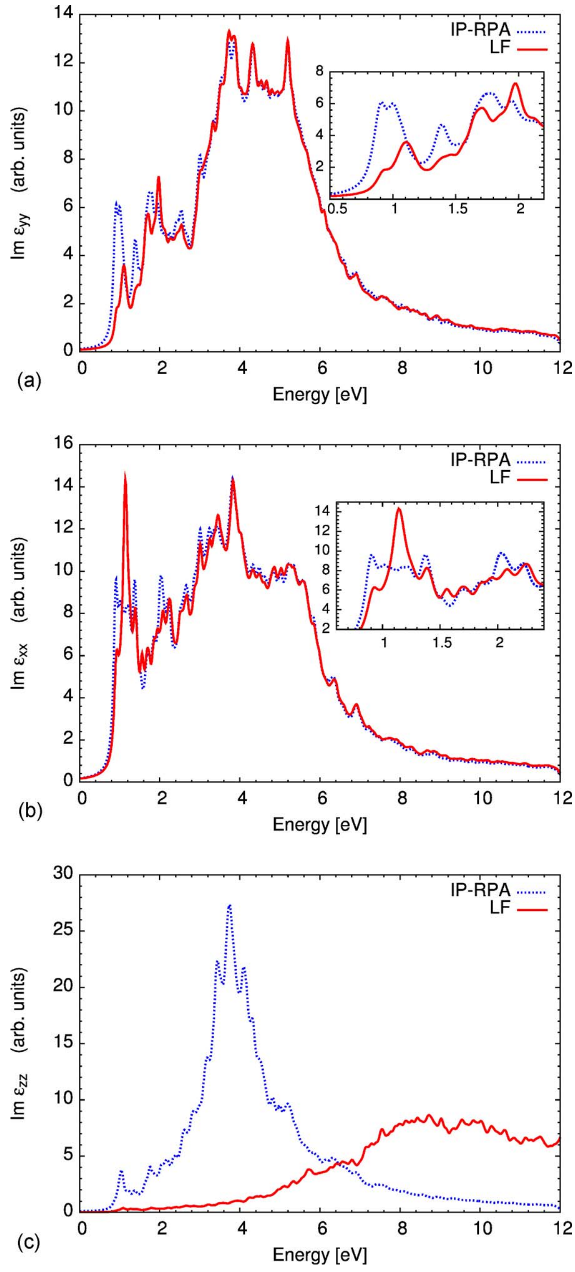

FIG. 3. (Color online) Imaginary part of the diagonal components of the slab dielectric tensor, calculated with (LF) and without (IP-RPA) local-field effects, for the three polarizations: (a) parallel to the surface, along the dimer axis; (b) parallel to the surface, along the dimer chains; and (c) perpendicular to the surface. The spectra presented in this figure are not fully converged in the **k**-point sampling.

Starting from the slab dielectric function, we computed RAS and SDR spectra,[55] with and without inclusion of LF effects. A RAS spectrum is defined as

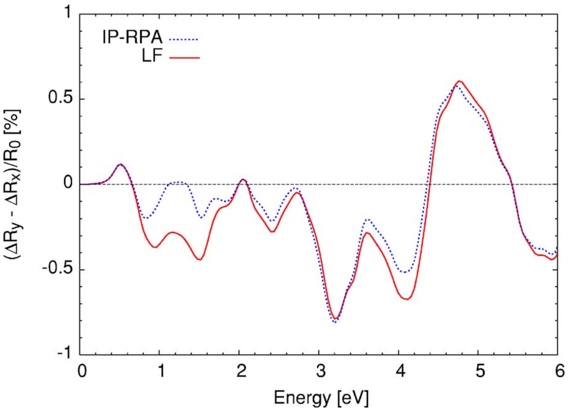

FIG. 4. (Color online) Calculated RAS spectrum of Si(100)(2 $\times$ 2):O at convergence, for the structural model shown in Fig. 2. Results including (LF) or neglecting (IP-RPA) the local-field effects are very similar, except for the region between 0.8 and 1.8 eV, where the LF effects strongly enhance the RAS signal. The energy scale has been shifted by 0.6 eV to compensate for the neglect of self-energy effects.

$$\mathrm{RAS} = \frac{\Delta R_y - \Delta R_x}{R_0}, \tag{21}$$

where R_i is the reflectivity for light polarized parallel to the $i$direction, and R_0 is the Fresnel reflectivity. Similarly, SDR is defined as the difference in the reflectivity measured on a clean surface and the one measured after passivation (e.g., by adsorbing atoms or molecules on the surface). Passivation [oxidation in the present Si(100) case] removes the surface states, but does not affect bulk contributions. One hence obtains, for the optical response specific to the surface,

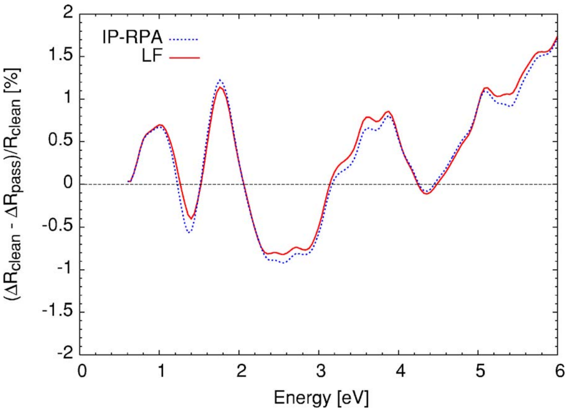

FIG. 5. (Color online) Calculated SDR spectrum (unpolarized light) of Si(100)(2 $\times$ 2):O, for the structural model shown in Fig. 2. Results including (LF) or neglecting (IP-RPA) the local fields are almost indistinguishable, showing that the effects visible in the low-energy part of Fig. 3 are canceling each other in the SDR spectrum. The same energy shift as in Fig. 4 has been applied. In *polarized* SDR, the local-field effects would be of the same size as for the RAS spectra.

$$\mathrm{SDR} = \frac{\Delta R_{\mathrm{Si}} - \Delta R_{\mathrm{Si:O}}}{R_{\mathrm{Si}}}. \tag{22}$$

Theoretical models[56] link the RAS and SDR spectra to the dielectric functions evaluated for the bulk crystal (ε_b) and for the slab (ε_{ii}) through the relation

$$\frac{\Delta R_i}{R_0} = \frac{4\omega}{c}\,\mathrm{Im}\left[\frac{\varepsilon_{yy}(\omega) - \varepsilon_{xx}(\omega)}{\varepsilon_b(\omega)}\right], \tag{23}$$

where ε_{xx} and ε_{yy} are the diagonal components of the surface dielectric tensor. We show our results for RAS and SDR in Figs. 4 and 5, respectively.

We first discuss the case of RAS. The effects of local fields on the imaginary part of the dielectric tensor are most evident in the low-energy region of the spectrum (below 2 eV), as shown in the inset of Figs. 3(a) and 3(b). In particular, LFs are found to enhance and sharpen the strong ε_2 peak at about 1.2 eV for light polarized along the dimer chains [Fig. 3(b)] and to reduce the first three peaks for light polarized along the dimer axis. As a result, LFs induce a strong enhancement in the surface optical anisotropy (on the order of 100%) in the region between 0.8 and 2 eV, as displayed in Fig. 4. This low-energy region (below the direct gap of bulk Si) corresponds to surface-localized states, which are expected to carry the surface anisotropy. The fact that LFs evidentiate this anisotropy is consistent with the fact that dimer chains realize a structure which is strongly inhomogeneous in the direction perpendicular to the dimer chains (see Fig. 2). At higher energies (above 2 eV), bulk contributions dominate ε_2, and the resulting RAS is mainly due to surface perturbed bulk states. The latter appear to be less affected by local fields than the true surface states, and lead to a RAS spectrum which, above 2.0 eV, is almost insensitive to the inclusion of local-field effects. This picture is confirmed by the analysis of SDR results. The latter are, in fact, calculated for unpolarized light, i.e., by averaging ε_{xx} and ε_{yy}. Since LFs enlarge ε_{yy} and reduce ε_{xx}, their effects almost completely cancel out when the average is taken. Our calculated (unpolarized) SDR spectrum, displayed in Fig. 5, appears, in fact, to be very little affected by the local fields in the whole energy range between 0 and 6 eV. However, if a polarized SDR spectrum is computed, then local fields are found to influence the low-energy region ($\leqslant$2 eV) in a way which is very similar to the behavior of the RAS.

Unfortunately, it is not possible to perform here a comprehensive comparison with RAS and SDR experimental data, since this would require the calculation of several possible reconstructions and geometries. In fact, the oxidation mechanism of Si(100) has been shown to be exceedingly complex, with different mechanisms playing their role depending on the oxidation temperature: a barrierless oxidation of the first Si layer[28] or an "active oxidation" involving etching of the surface and penetration of oxygen in a layer-by-layer manner at higher temperature.[57] Recently, the Si(100)(2 $\times$ 1):O surface optical anisotropy has been shown to be sensitive to the structural details of the oxygen adsorption by *ab initio* calculations of the atomic geometries and optical response of a large number of Si(110):O structures.[58,59] A highly structured potential-energy surface has been found, with minima at the backbonds of the "down" atoms in Si-Si dimers.[59] Moreover, an appreciable amount of disorder is probably present after oxidation of the first Si monolayer, and the local strain induced by oxygen adsorption is expected to have a sizable impact on the optical anisotropy spectra.[58]

However, our findings for LF effects in the single case studied here suggest an important general remark about surface optical spectroscopies. In fact, it is well known that, due to the large penetration depth of visible and UV photons, the surface-specific optical reflectivity signal is very small with respect to the bulk contribution. For materials with an isotropic bulk, the RAS spectroscopy has indeed been developed in order to extract the surface signal, by exploiting its anisotropy. A correct evaluation of the latter hence has the highest priority in theoretical calculations of surface optical spectra. The fact that crystal local fields are potentially able to alter significantly the surface optical anisotropy, at least below the bulk band gap, should hence be kept in mind, particularly when the anisotropy of electronic states is associated with a large structural anisotropy at the surface, such as in the case of dimer chains on Si(100)(2×1).

III. COMPUTATIONAL SCALING AND PERFORMANCES

In this section, we present a quantitative analysis of the numerical performance of the HT-based approach, as implemented in the large-scale code DP,[30] with respect to the traditional approach. Several calculations have been done by varying the three main convergence parameters: (i) the number of valence-conduction transitions ($N_t = N_{\mathbf{k}} \times N_v \times N_c$); (ii) the number of frequency intervals considered in the spectrum, i.e., the spectral resolution (number of frequencies N_ω); and (iii) the number of plane waves considered in the response matrix ($N_{\mathbf{G}}$). Optical properties usually converge at an $N_{\mathbf{G}}$ value which can be substantially smaller than the total number of plane waves N_g used to describe the wave functions.

The calculation of $\chi^{(0)}$ is expected to scale, in the case of the reference approach, as[60]

$$T_{ref} = N_{\mathbf{k}}(\alpha N_v N_c N_g \log N_g + \beta N_v N_c N_{\mathbf{G}}^2 N_\omega) + A, \qquad (24)$$

where $N_{\mathbf{k}}$ is the number of **k** points, and α and β are prefactors which are independent of N_v, N_c, $N_{\mathbf{G}}$, $N_{\mathbf{k}}$, N_g, and N_ω. The first term in Eq. (24) is due to the evaluation of the numerators Z_n in Eqs. (15) and (17) by using fast Fourier transform, and is present in both the reference and Hilbert approaches. The second term stems from the evaluation of Eq. (12) in the traditional way. The remaining term A takes into account residual parts of the calculation, as the matrix inversions, which contribute much less to the CPU time than the first two terms.

The expected scaling in the case of the Hilbert-based scheme is instead

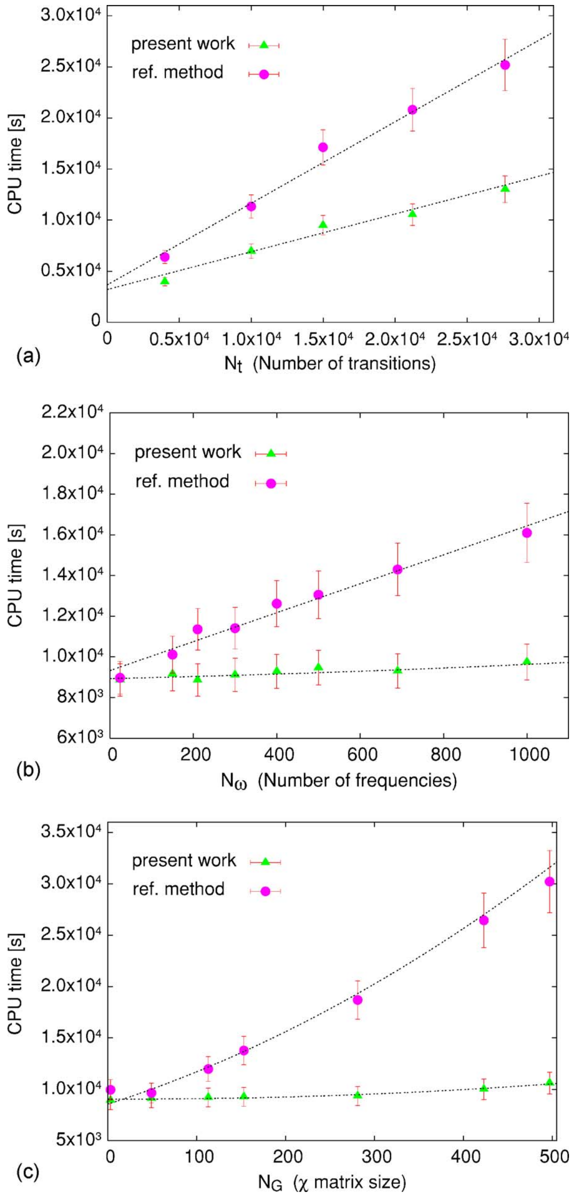

FIG. 6. (Color online) Quantitative study of the computational load required to evaluate the $\chi^{(0)}$ matrix for the 56-atom slab representing a Si(100)(2×2):O surface. The effects of the three main parameters determining the numerical convergence of the theoretical spectra are studied separately. (a) Number of valence-conduction transitions, determined by the energy cutoff on the empty (conduction) bands included in Eq. (9), the number of occupied bands being fixed; (b) number of frequency intervals taken on the ω axis, determined by the requested spectral resolution; and (c) size of the $\chi^{(0)}$ matrix in reciprocal space, roughly proportional to the system size (for a fixed real-space resolution).

$$T_{new} = N_{\mathbf{k}}(\alpha N_v N_c N_g \log N_g + \beta' N_v N_c N_{\mathbf{G}}^2) + \gamma N_{\mathbf{G}}^2 N_\omega^2 + A'. \qquad (25)$$

In this case, the second term does not contain the factor N_ω anymore, and its prefactor becomes β', due to the calculation of χ^{A2} and χ^{R2} [Eqs. (15) and (17)]. The calculation becomes, in this sense, comparable to a static one.

However, the actual evaluation of the Hilbert transforms [Eqs. (19) and (20)] introduces a new term scaling as $N_{\mathbf{G}}^2 N_\omega^2$. Due to the small prefactor γ, the latter term can often be neglected (see, e.g., Fig. 3 of Ref. 4). In the present work, we found that the CPU time spent inside the Hilbert transform itself can be made negligible by an optimized algorithm.[61]

Considering an N-atom unit cell, the number of transitions N_t is clearly the parameter growing fastest with the system size, since it is proportional to N^2. About 22 000 transitions per **k** point, corresponding to the inclusion of about 200 empty bands, are requested to converge the dielectric tensor of the Si(100)(2×2):O slab up to 12 eV. The number of frequency intervals N_ω is instead independent of N, but it grows linearly with the required spectral resolution. In the present case, 300 frequencies are necessary in order to achieve a 40 meV resolution over a spectral range of 12 eV. Finally, $N_{\mathbf{G}}$, i.e., the size of $\chi^{(0)}$ in reciprocal space, depends on the requested real-space resolution needed in the description of the induced density variations. This means that larger $N_{\mathbf{G}}$ will be necessary to describe systems with smaller interatomic distances, or with larger polarizability. The real-space resolution is independent of the system size; however, for a fixed resolution, $N_{\mathbf{G}}$ will grow linearly with the volume of the unit cell in direct space. $N_{\mathbf{G}}$ is hence proportional to the number of atoms (in a bulk system) or to the volume of the supercell (for a finite or semi-infinite system). In our slab calculation, converging the spectra with local-field effects requires considering at least 113×113 matrices (incidentally, we stress that the IP-RPA spectra, requiring just the $\mathbf{G}=0$, $\mathbf{G}'=0$ matrix element of $\chi^{(0)}$, do not depend on $N_{\mathbf{G}}$).

The HT algorithm turns out to be clearly advantageous with respect to N_t and $N_{\mathbf{G}}$, as shown in the first and last panels of Fig. 6. Concerning N_ω, despite an unfavorable scaling in the limit of infinite spectral resolution (the CPU time grows quadratically with the number of frequency intervals), one must notice that, due to the small prefactor γ, the HT method is largely convenient in the whole range of interest ($N_\omega \simeq 10^3$).

CONCLUSIONS

Two classes of conclusions can be drawn from the presented results. First is the physics: the study of Si(100)(2×2):O has shown that local-field effects, although playing only a minor role in the surface optical properties above the bulk band gap, are able to enhance substantially the surface optical anisotropy in the low-energy end of the spectra. A similar effect can be expected for other surfaces, when the anisotropy of electronic states is associated with a large structural anisotropy, such as in the case of the dimer chains on Si(100)(2×2). Moreover, large local-field effects are found for light polarized normally to the surface. Second is the numerics: the computational gain achievable by using the Hilbert-transform-based algorithm has been shown to be substantial, both in a model system *and* in a real, physical application. A successful implementation of the Hilbert-transform method in the large-scale plane-wave *ab initio* computer code DP (Ref. 30) allows us to locate the crossover (starting from which the Hilbert-transform algorithm becomes convenient) already at medium size systems (less than 50 atoms).

ACKNOWLEDGMENTS

This work was supported by the EU's 6th Framework Programme through the NANOQUANTA Network of Excellence (NMP4-CT-2004-500198), the Consorzio Nazionale Interuniversitario per le Scienze fisiche della Materia (CNISM-Progetto Innesco), and the ERASMUS project. We thank the Institut des Nanoscience de Paris (INSP) for the computer facilities.

---

[1] E. Runge and E. K. U. Gross, Phys. Rev. Lett. **52**, 997 (1984); *Time-Dependent Density Functional Theory*, edited by M. A. L. Marques, C. A. Ullrich, F. Nogueira, A. Rubio, K. Burke, and E. K. U. Gross, Lecture Notes in Physics Vol. 706 (Springer-Verlag, Berlin, 2006).

[2] L. Hedin, Phys. Rev. **139**, A796 (1965).

[3] G. Onida, L. Reining, and A. Rubio, Rev. Mod. Phys. **74**, 601 (2002).

[4] T. Miyake and F. Aryasetiawan, Phys. Rev. B **61**, 7172 (2000).

[5] M. Shishkin and G. Kresse, Phys. Rev. B **74**, 035101 (2006).

[6] P. E. Blöchl, Phys. Rev. B **50**, 17953 (1994).

[7] D. Foerster, Phys. Rev. B **72**, 073106 (2005).

[8] D. E. Aspnes and A. A. Studna, Phys. Rev. Lett. **54**, 1956 (1985).

[9] W. L. Mochán and R. G. Barrera, Phys. Rev. Lett. **55**, 1192 (1985).

[10] R. Del Sole, W. L. Mochan, and R. G. Barrera, Phys. Rev. B **43**, 2136 (1991).

[11] W. G. Schmidt and J. Bernholc, Phys. Rev. B **61**, 7604 (2000).

[12] R. Del Sole and G. Onida, Phys. Rev. B **60**, 5523 (1999).

[13] P. H. Hahn, W. G. Schmidt, and F. Bechstedt, Phys. Rev. Lett. **88**, 016402 (2002).

[14] W. G. Schmidt, S. Glutsch, P. H. Hahn, and F. Bechstedt, Phys. Rev. B **67**, 085307 (2003).

[15] M. Palummo, O. Pulci, R. Del Sole, A. Marini, M. Schwitters, S. R. Haines, K. H. Williams, D. S. Martin, P. Weightman, and J. E. Butler, Phys. Rev. Lett. **94**, 087404 (2005); see also Figs. 2 and 3 in M. Palummo, O. Pulci, A. Marini, L. Reining, and R. Del Sole, Phys. Rev. B **74**, 235431 (2006).

[16] H. Watanabe, K. Kato, T. Uda, K. Fujita, M. Ichikawa, T. Kawamura, and K. Terakura, Phys. Rev. Lett. **80**, 345 (1998).

[17] K. Nakajima, Y. Okazaki, and K. Kimura, Phys. Rev. B **63**, 113314 (2001).

[18] S. Dreiner, M. Schürmann, and C. Westphal, Phys. Rev. Lett. **93**, 126101 (2004).

[19] T.-W. Pi, J.-F. Wen, C.-P. Ouyang, R.-T. Wu, and G. K. Wertheim, Surf. Sci. **478**, L333 (2001).

[20] A. Yoshigoe and Y. Teraoka, Surf. Sci. **32**, 690 (2003).

[21] H. Ikegami, K. Ohmori, H. Ikeda, H. Iwano, S. Zaima, and Y.

Yasuda, Jpn. J. Appl. Phys., Part 1 **35**, 1593 (1996).

[22] H. Itoh, K. Nakamura, A. Kurokawa, and S. Ichimura, Surf. Sci. **482**, 114 (2001).

[23] T. Uchiyama, T. Uda, and K. Terakura, Surf. Sci. **433**, 896 (1999).

[24] K. Kato and T. Uda, Phys. Rev. B **62**, 15978 (2000).

[25] N. Richard, A. Estève, and M. Djafari-Rouhani, Comput. Mater. Sci. **33**, 26 (2005).

[26] Y. J. Chabal, K. Raghavachari, X. Zhang, and E. Garfunkel, Phys. Rev. B **66**, 161315(R) (2002).

[27] Y. Widjaja and C. B. Musgrave, J. Chem. Phys. **116**, 5774 (2002).

[28] L. C. Ciacchi and M. C. Payne, Phys. Rev. Lett. **95**, 196101 (2005).

[29] A. Incze, R. Del Sole, and G. Onida, Phys. Rev. B **71**, 035350 (2005).

[30] http://www.dp-code.org

[31] X. Gonze *et al.*, Comput. Mater. Sci. **25**, 478 (2002); http://www.abinit.org

[32] W. Kohn and L. J. Sham, Phys. Rev. **140**, A1113 (1965); P. Hohenberg and W. Kohn, *ibid.* **136**, B864 (1964).

[33] D. M. Ceperley and B. J. Alder, Phys. Rev. Lett. **45**, 566 (1980); J. P. Perdew and A. Zunger, Phys. Rev. B **23**, 5048 (1981).

[34] L. Reining, V. Olevano, A. Rubio, and G. Onida, Phys. Rev. Lett. **88**, 066404 (2002).

[35] F. Bruneval, F. Sottile, V. Olevano, R. Del Sole, and L. Reining, Phys. Rev. Lett. **94**, 186402 (2005).

[36] G. Adragna, R. Del Sole, and A. Marini, Phys. Rev. B **68**, 165108 (2003).

[37] R. Del Sole, G. Adragna, V. Olevano, and L. Reining, Phys. Rev. B **67**, 045207 (2003).

[38] R. Stubner, I. V. Tokatly, and O. Pankratov, Phys. Rev. B **70**, 245119 (2004).

[39] F. Sottile, K. Karlsson, L. Reining, and F. Aryasetiawan, Phys. Rev. B **68**, 205112 (2003).

[40] See, e.g., S. Baroni and R. Resta, Phys. Rev. B **33**, 7017 (1986), and references therein.

[41] In real space, this corresponds to assuming a dependence of $\varepsilon_M(\mathbf{r},\mathbf{r}',\omega)$ only on the difference $(\mathbf{r}-\mathbf{r}')$.

[42] H. Ehrenreich and H. M. Cohen, Phys. Rev. **115**, 786 (1959).

[43] In the case of real matrix elements, $Z_{i,n} \in \mathbb{R}$, one recovers the Kramers-Kronig relations linking real and imaginary parts of the response.

[44] Similarly, Shishkin and Kresse (Ref. 5) used triangular functions.

[45] We considered bulk silicon Kohn-Sham energies, increasing the number of transitions to build $\chi^{(0)}$ and randomly redefining the transition matrix elements.

[46] B. Walker, A. M. Saitta, R. Gebauer, and S. Baroni, Phys. Rev. Lett. **96**, 113001 (2006).

[47] See http://www.etsf.eu

[48] A. Incze, G. Onida, R. Del Sole, and M. Fuchs (unpublished).

[49] T. Nakayama and M. Murayama, Appl. Phys. Lett. **77**, 4286 (2000); T. Yasuda, S. Yamasaki, M. Nishizawa, N. Miyata, A. Shklyaev, M. Ichikawa, T. Matsudo, and T. Ohta, Phys. Rev. Lett. **87**, 037403 (2001).

[50] D. R. Hamann, Phys. Rev. B **40**, 2980 (1989).

[51] H. J. Monkhorst and J. D. Pack, Phys. Rev. B **13**, 5188 (1976).

[52] S. Botti, N. Vast, L. Reining, V. Olevano, and L. C. Andreani, Phys. Rev. Lett. **89**, 216803 (2002).

[53] A. G. Marinopoulos, L. Reining, V. Olevano, A. Rubio, T. Pichler, X. Liu, M. Knupfer, and J. Fink, Phys. Rev. Lett. **89**, 076402 (2002).

[54] F. Sottile *et al.*, Int. J. Quantum Chem. **102**, 684 (2005); F. Bruneval, S. Botti, and L. Reining, Phys. Rev. Lett. **94**, 219701 (2005).

[55] See, e.g., Y. Borensztein, Phys. Status Solidi A **202**, 1313 (2005).

[56] R. Del Sole, in *Photonic Probes of Surfaces*, edited by P. Halevi (Elsevier Science, New York, 1995).

[57] T. Yasuda, S. Yamasaki, M. Nishizawa, N. Miyata, A. Shklyaev, M. Ichikawa, T. Matsudo, and T. Ohta, Phys. Rev. Lett. **87**, 037403 (2001); T. Yasuda, N. Kumagai, M. Nishizawa, S. Yamasaki, H. Oheda, and K. Yamabe, Phys. Rev. B **67**, 195338 (2003); M. A. Albao, Da-Jiang Liu, Cheol H. Choi, Mark S. Gordon, and J. W. Evans, Surf. Sci. **555**, 51 (2004).

[58] F. Fuchs, W. G. Schmidt, and F. Bechstedt, Phys. Rev. B **72**, 075353 (2005).

[59] F. Fuchs, W. G. Schmidt, and F. Bechstedt, J. Phys. Chem. B **109**, 17649 (2005).

[60] $N_t N_{\mathbf{G}}^2$ leads to the N_{at}^4 scaling mentioned in the Introduction.

[61] Exploiting the fact that the principal value numerical integration routine has to be called $N_{\mathbf{G}}^2$ times, always on the same energy intervals, a substantial gain could be achieved by tabulating the (about 10^6) required values of the complex logarithm once and for all at the beginning of the double loop over **G** vectors in the construction of $\chi^{(0)}$.

4.3 Effective-Energy technique

Another case in which the evaluation of the independent-particle polarizability is very cumbersome is when lots of empty states have to be included. Contrary to the previous case (many frequencies), in problems like the GW approximation,[2] the number of empty states (quickly able to reach values such as many hundreds) can make the evalution of the spectrum impossible. During his post-doc under my supervision, Arjan Berger has developed a very efficient method by completely eliminating the empty states from the calculation (of both the independent-particle polarizability and the self-energy $\Sigma = GW$). This has been explained in a seminal article in PRB [103], later proposed in a simplified version [104], and applied to a very complex system, like rubrene [105], a system for which the standard approach would have not been viable. The method is implemented and widely used in the DP code (http://www.dp-code.org) [66], as well as in the Abinit code (http://www.abinit.org) [67].

PLEASE REFER TO THE ATTACHED ARTICLE

---

[2] Here only few frequencies (even only 1 - $\omega = 0$ - in the case of static approximation or COHSEX) are to evaluated.

RAPID COMMUNICATIONS

PHYSICAL REVIEW B **82**, 041103(R) (2010)

Ab initio calculations of electronic excitations: Collapsing spectral sums

J. A. Berger,[1,2,*] Lucia Reining,[1,2] and Francesco Sottile[1,2]
[1]*Laboratoire des Solides Irradiés, École Polytechnique, CNRS, CEA-DSM, 91128 Palaiseau, France*
[2]*European Theoretical Spectroscopy Facility (ETSF)*

(Received 24 June 2010; published 14 July 2010)

We present a method for the evaluation of electronic excitations of advanced materials by reformulating spectral sum-over-states expressions such that only occupied states appear. All empty states are accounted for by one effective energy. Thus we keep the simplicity and precision of the sum-over-states approach while speeding up calculations by more than an order of magnitude. We demonstrate its power by applying it to the *GW* method, where a huge summation over empty states appears twice (screening and self-energy). The precision is shown for bulk Si and solid and atomic Ar. We then use it to determine the band gap of the technologically important oxide SnO_2.

DOI: 10.1103/PhysRevB.82.041103 PACS number(s): 71.10.−w, 71.15.Qe, 71.20.−b

Many crucial physical quantities, e.g., electron spectral functions, optical response, or total energies, can be expressed in terms of one- or two-particle Green's functions that contain information about the propagation of an electron and/or hole in the system. This physics is directly reflected in their spectral representations in terms of amplitudes and energies. In practice, calculations are often performed using this relatively simple sum-over-states (SOS) formulation in an independent-particle or quasiparticle (QP) approximation. However, the SOS approach suffers from two main drawbacks. First, it does not scale well with the size of the system. Second, one has to sum over an, in principle, infinite, and, in practice, (at convergence) huge number of empty states. This is especially true for large unit cells (dense bands) or for materials with localized states (high-energy cutoff). Prototype examples are, e.g., the transparent conducting oxides (TCOs) based on SnO_2 and ZnO, for which calculations of many-body Green's functions are close to prohibitive. However, for these technologically important materials it is particularly desirable to predict electronic properties and first of all a reliable QP band structure. QP energies can be obtained from many-body perturbation theory; the state-of-the-art approach is the *GW* approximation.[1] However, in a standard *GW* calculation two SOS expressions appear since the self-energy Σ, which accounts for all the many-body effects beyond the Hartree potential, is given by the following convolution:

$$\Sigma(\mathbf{r},\mathbf{r}',\omega) = i\int \frac{d\omega'}{2\pi} e^{i\delta\omega'} G(\mathbf{r},\mathbf{r}',\omega+\omega') W(\mathbf{r},\mathbf{r}',\omega'), \quad (1)$$

where G is the single-particle Green's function and $W=\epsilon^{-1}v_c$ is the screened Coulomb potential in which ϵ is the dielectric function in the random-phase approximation (RPA): $\epsilon = 1 - v_c\chi^0$, where χ^0 is the time-ordered independent-particle polarizability.[2] Most often both χ^0 and Σ are evaluated using a slowly converging[3–5] SOS expression. Several methods have been proposed to decrease or avoid completely the summation over empty states,[1,6–10] ranging from a static Coulomb-hole plus screened exchange (COHSEX) approximation[1] which eliminates empty states in Σ only and at the price of a crude description of QP energies, to methods using a Sternheimer type of approach[7,11] that are, in principle, exact. When applied in a straightforward manner the latter approach does not speed up with respect to the standard SOS formulation[7] but it can be improved by using efficient algorithms[8,9] and by introducing an optimal polarizability basis.[8] The latter methods are promising but require a profound restructuring of the *GW* method and detailed comparisons, in particular, concerning the prefactor and hence the crossover, with the SOS approach are still missing.[12]

In this work, we present a very efficient method which retains all advantages of the SOS approach, namely, simplicity, a good prefactor, and systematic and controlled accuracy but *completely* eliminates empty states from the entire calculation, leading to an *immediate* speedup for *all* system sizes, as well as an improved scaling. Here we calculate *GW* QP energies to demonstrate the power of our approach but the method is general and can be applied to other spectral quantities.

In the calculation of the *GW* self-energy, the main numerical effort lies in the calculation of the matrix elements of Σ_c, the correlation part of the self-energy. For simplicity, we will focus here on the diagonal matrix elements. The extension to off-diagonal elements is straightforward. In its spectral representation, the diagonal matrix elements Σ_c^n are given by

$$\Sigma_c^n(\omega) = \sum_i \sum_{j\neq 0} \frac{|\langle n|V^j|i\rangle|^2}{\omega + \omega_j \,\mathrm{sgn}(\mu - \varepsilon_i) - \varepsilon_i}. \quad (2)$$

Here $|i\rangle$ and ε_i are the QP states and energies, respectively, $\omega_j = E(N,j) - E(N,0) - i\eta$ are the excitation energies of the N-electron system minus an infinitesimal η which ensures the correct time ordering, μ is the chemical potential, and $V^j(\mathbf{r})$ are fluctuation potentials[13] which, together with ω_j represent W. Although the method that we will describe in this work is valid for both finite and extended systems we will focus here on the latter. Therefore, i and n should be considered multi-indices composed of the band index and the Bloch vector. The summation over i in Eq. (2) can be split into a summation over v with $\varepsilon_v < \mu$ and a summation over c with $\varepsilon_c > \mu$. In the following, we will focus on the latter since it is the bottleneck in the calculation of Σ_c^n as it sums over the, in principle, infinite, empty states of the system. Introducing the

Fourier transforms of the fluctuation potentials, we can rewrite this part as

$$\Sigma_c^{n,emp}(\omega) = \sum_{j\neq 0}\sum_{\mathbf{q},\mathbf{G},\mathbf{G}'} V^j_{\mathbf{G}}(\mathbf{q}) V^{j*}_{\mathbf{G}'}(\mathbf{q}) S^n_j(\mathbf{q},\mathbf{G},\mathbf{G}',\omega), \tag{3}$$

where we defined

$$S^n_j(\mathbf{q},\mathbf{G},\mathbf{G}',\omega) = \sum_c \frac{\tilde{\rho}^*_{cn}(\mathbf{q}+\mathbf{G})\tilde{\rho}_{cn}(\mathbf{q}+\mathbf{G}')}{\omega-\omega_j-\varepsilon_c} \tag{4}$$

in which $\tilde{\rho}_{cn}(\mathbf{q}+\mathbf{G})=\langle c|e^{-i(\mathbf{q}+\mathbf{G})\cdot\mathbf{r}}|n\rangle$. It is the above summation over empty states that we want to eliminate. One can always find a function $\delta_{nj}(\mathbf{q},\mathbf{G},\mathbf{G}',\omega)$ such that the following equality holds:

$$S^n_j(\mathbf{q},\mathbf{G},\mathbf{G}',\omega) = \frac{\sum_c \tilde{\rho}^*_{cn}(\mathbf{q}+\mathbf{G})\tilde{\rho}_{cn}(\mathbf{q}+\mathbf{G}')}{\omega-\omega_j-\varepsilon_n-\delta_{nj}(\mathbf{q},\mathbf{G},\mathbf{G}',\omega)} \tag{5}$$

since $\delta_{nj}(\mathbf{q},\mathbf{G},\mathbf{G}',\omega)$ has sufficient degrees of freedom. Using the closure relation $\Sigma_c|c\rangle\langle c|=1-\Sigma_v|v\rangle\langle v|$, we obtain an expression for S^n_j which contains a sum over occupied states only. At variance with related ideas,[6,10] the relation in Eq. (5) is exact; the effective energy $\varepsilon_n+\delta_{nj}(\mathbf{q},\mathbf{G},\mathbf{G}',\omega)$ takes into account the contributions of all the empty states to $S^n_j(\mathbf{q},\mathbf{G},\mathbf{G}',\omega)$. For this reason we will refer to this approach as the effective-energy technique (EET). It now remains to transform the expression for $\delta_{nj}(\mathbf{q},\mathbf{G},\mathbf{G}',\omega)$ such that no empty states appear. Subtracting Eq. (5) from Eq. (4) and making use of the fact that the ε_i are eigenvalues of the Hamiltonian $\hat{H}(\mathbf{r})$ with eigenstates $|i\rangle$ (Ref. 6), we obtain

$$\delta_{nj}(\mathbf{q},\mathbf{G},\mathbf{G}',\omega)S^n_j(\mathbf{q},\mathbf{G},\mathbf{G}',\omega) = \sum_c \frac{\tilde{\rho}^*_{cn}(\mathbf{q}+\mathbf{G})\langle c|[\hat{H}(\mathbf{r}'),e^{-i(\mathbf{q}+\mathbf{G}')\cdot\mathbf{r}'}]|n\rangle}{[\omega-\omega_j-\varepsilon_c]}. \tag{6}$$

For notational convenience, we consider a Hamiltonian that contains only a local potential. The derivation can be easily generalized to include Hamiltonians with nonlocal potentials. Working out the commutator and dividing both sides by S^n_j, we obtain

$$\delta_{nj}(\mathbf{q},\mathbf{G},\mathbf{G}',\omega) = \frac{|\mathbf{q}+\mathbf{G}'|^2}{2} + \frac{\tilde{S}^n_j(\mathbf{q},\mathbf{G},\mathbf{G}',\omega)}{S^n_j(\mathbf{q},\mathbf{G},\mathbf{G}',\omega)}, \tag{7}$$

where we defined

$$\tilde{S}^n_j(\mathbf{q},\mathbf{G},\mathbf{G}',\omega) = \sum_c \frac{\tilde{\rho}^*_{cn}(\mathbf{q}+\mathbf{G})\tilde{j}_{cn}(\mathbf{q}+\mathbf{G}')}{[\omega-\omega_j-\varepsilon_c]} \tag{8}$$

in which

$$\tilde{j}_{cn}(\mathbf{q}+\mathbf{G}) = \langle c|e^{-i(\mathbf{q}+\mathbf{G})\cdot\mathbf{r}}[i\nabla_{\mathbf{r}}]|n\rangle\cdot(\mathbf{q}+\mathbf{G}). \tag{9}$$

In Eq. (7), δ_{nj} is expressed in terms of itself through S^n_j. Since $\tilde{S}^n_j$ depends on a summation over the empty states solving for δ_{nj} will not lead to the desired result. However, in view of the similarity of Eqs. (4) and (8), we can also rewrite Eq. (8) in terms of only occupied states in an equivalent manner as Eq. (5) using a modified δ_{nj}. In principle, this procedure could be continued *ad infinitum*. However, one wishes to truncate the expression for δ_{nj} since, in practice, one would like to use simple expressions. In the following, we will show that these simple expressions already lead to excellent results. Here we give explicitly the first three approximations for δ_{nj} that we obtain

$$\delta^{(0)}(\mathbf{q},\mathbf{G}') = \frac{|\mathbf{q}+\mathbf{G}'|^2}{2}, \tag{10}$$

$$\delta^{(1)}_n(\mathbf{q},\mathbf{G},\mathbf{G}') = \frac{|\mathbf{q}+\mathbf{G}'|^2}{2} + \frac{f^{\rho j}_n(\mathbf{q},\mathbf{G},\mathbf{G}')}{f^{\rho\rho}_n(\mathbf{q},\mathbf{G},\mathbf{G}')}, \tag{11}$$

$$\delta^{(2)}_{nj}(\mathbf{q},\mathbf{G},\mathbf{G}',\omega) = \frac{|\mathbf{q}+\mathbf{G}'|^2}{2} + \frac{f^{\rho j}_n(\mathbf{q},\mathbf{G},\mathbf{G}')}{f^{\rho\rho}_n(\mathbf{q},\mathbf{G},\mathbf{G}')} \times \left[\frac{\omega_{nj}-\dfrac{|\mathbf{q}+\mathbf{G}'|^2}{2}-\dfrac{f^{\rho j}_n(\mathbf{q},\mathbf{G},\mathbf{G}')}{f^{\rho\rho}_n(\mathbf{q},\mathbf{G},\mathbf{G}')}}{\omega_{nj}-\dfrac{|\mathbf{q}+\mathbf{G}|^2}{2}-\dfrac{f^{jj}_n(\mathbf{q},\mathbf{G},\mathbf{G}')}{f^{\rho j}_n(\mathbf{q},\mathbf{G},\mathbf{G}')}}\right], \tag{12}$$

where $\omega_{nj}=\omega-\omega_j-\varepsilon_n$ and

$$f^{ab}_n(\mathbf{q},\mathbf{G},\mathbf{G}') = \sum_c \tilde{a}^*_{cn}(\mathbf{q}+\mathbf{G})\tilde{b}_{cn}(\mathbf{q}+\mathbf{G}'), \tag{13}$$

where a and b can be either ρ or j.[14] We use the closure relation to get rid of the sum over empty states in f^{ab}_n. Note that, in particular, the expression for $\delta^{(2)}_{nj}$ is simple but highly nontrivial due to its frequency dependence. Higher-order expressions for δ_{nj} will contain terms with higher-order derivatives of the valence wave functions as well as derivatives of the potential. Our results show that these terms can be safely neglected. We note that the EET is exact in the limit of a homogeneous electron gas starting at order $\delta^{(1)}_n$.[15] The approximations for δ_{nj} in Eqs. (10)–(12) are asymmetric with respect to $\mathbf{G}$ and $\mathbf{G}'$. This is due to the freedom in choosing whether the Hamiltonian in Eq. (6) is applied inside the left or right matrix element. Since the exact δ_{nj} is Hermitian, we symmetrize the above results such that this exact constraint is met at each level of approximation.

In practice, the excitation energies ω_j that enter Σ^n_c are not known and as a first step ϵ has to be calculated. This ϵ relies on the calculation of χ^0 which in its spectral representation is given by

$$\chi^0_{\mathbf{G}\mathbf{G}'}(\mathbf{q},\omega) = \sum_{s=\pm 1}\sum_{v,c} \frac{\tilde{\rho}^*_{cv}(\mathbf{q}+\mathbf{G})\tilde{\rho}_{cv}(\mathbf{q}+\mathbf{G}')}{s\omega-(\varepsilon_c-\varepsilon_v)+i\eta}. \tag{14}$$

Since χ^0 has a similar structure as Σ^n_c, we can also apply the EET here to obtain an expression that does not contain any empty states. The result is given by

$$\chi^0_{\mathbf{G}\mathbf{G}'}(\mathbf{q},\omega) = \sum_{s=\pm 1}\sum_{v} \frac{f^{\rho\rho}_v(\mathbf{q},\mathbf{G},\mathbf{G}')}{s\omega-\delta'_v(\mathbf{q},\mathbf{G},\mathbf{G}',s\omega)+i\eta}. \tag{15}$$

The approximations for δ' equal those for δ given in Eqs. (10)–(12) with the difference that ω_{nj} has to be replaced by

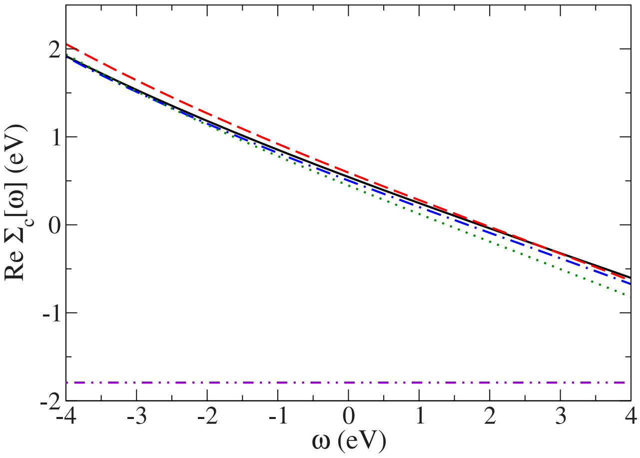

FIG. 1. (Color online) The real part of $\Sigma_c(\omega)$ for the highest occupied band at Γ for Si around the LDA orbital energy (set to 0 eV). Solid line (black): G^0W^0 (SOS); dotted line (green): G^0W^0 (EET: $\delta'^{(2)}$ and $\delta^{(0)}$); dashed line (red): G^0W^0 (EET: $\delta'^{(2)}$ and $\delta^{(2)}$); dotted-dashed line (blue): G^0W^0 (EET: $\delta'^{(4)}$ and $\delta^{(4)}$); double-dotted-dashed line (violet): COHSEX.

ω. We have thus arrived at a simple *GW* method without summations over empty states. Moreover, once the f_n^{ab} are determined the calculation of Σ_c^{emp} (χ^0) scales as $N_n N_{\mathbf{G}}^2$ ($N_v N_{\mathbf{G}}^2$) versus $N_c N_n N_{\mathbf{G}}^2$ ($N_c N_v N_{\mathbf{G}}^2$) for the SOS approach, where N_n is the number of diagonal matrix elements of Σ_c, N_v and N_c are the number of occupied and empty states, respectively, and $N_{\mathbf{G}}$ is the number of plane waves. The calculation of the f_n^{ab} can be done straightforwardly from $\tilde{\rho}$ and $\tilde{j}$ for an immediate overall speedup for any system on the order of N_c/N_v with respect to the SOS approach or one can improve the scaling using fast-Fourier transforms.[16] We note that since Eqs. (4) and (5) are similar and also Eqs. (14) and (15), if desired, the EET can be combined with the ideas of Refs. 8 and 9, e.g., basis design, to get further speedups.

To illustrate the EET, we have implemented it in the ABINIT software package[17] and performed G^0W^0 calculations for some materials with zero-order energies and wave functions obtained from Kohn-Sham density-functional theory within the local-density approximation (LDA).[18] We used a generalized plasmon-pole model fitting ϵ^{-1} at imaginary frequencies.[19] In Fig. 1, we plot the real part of Σ_c for the highest occupied band of bulk silicon at the Γ point as a function of the frequency around the LDA orbital energy. We compare our EET results using various approximations for δ and δ' with the converged SOS results (200 empty bands) and those obtained with the static COHSEX approximation. Using $\delta'^{(2)}$ in χ^0 and $\delta^{(0)}$ in Σ, we already obtain results that are in excellent agreement with the SOS result over the whole frequency range of interest, thereby largely improving on the COHSEX self-energy (using $\delta'^{(0)}$ in χ^0 we obtain self-energies which are, in general, not sufficiently accurate). With higher-order approximations, we can improve the results further. Since, in general, $\delta^{(2)}$ and $\delta'^{(2)}$ lead to G^0W^0 results that are in good agreement with the exact SOS results and since the difference with results obtained using higher-order approximations is small, we will use $\delta^{(2)}$ and $\delta'^{(2)}$ in the remainder unless stated otherwise.

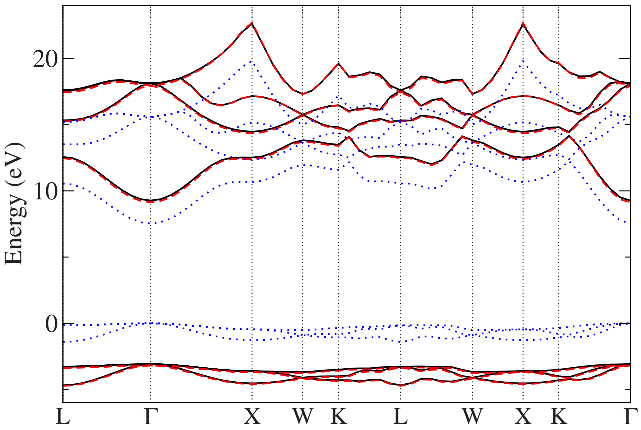

FIG. 2. (Color online) Band structure of solid argon. Solid line (black): G^0W^0 (SOS); dashed line (red): G^0W^0 (EET); dotted line (blue): LDA.

We also applied the EET to solid and atomic argon because they provide good test cases for two reasons: first, they are very inhomogeneous systems and therefore very different from the homogeneous systems for which our expressions become exact and, second, the G^0W^0 QP energies lie far from the LDA energies. In Fig. 2, we plot the G^0W^0 band structure of solid argon for the three highest occupied bands and four lowest empty bands using the standard SOS approach and the EET. The two band structures are almost indistinguishable. We also reported the LDA band structure to show the large difference between LDA and G^0W^0 energies. In Table I, we summarize our EET results for the fundamental gaps of silicon and solid argon, the direct band gap at Γ of silicon and the highest occupied molecular orbital (HOMO)-lowest unoccupied molecular orbital (LUMO) gap of atomic argon. We obtain a large improvement with respect to the COHSEX results which largely overestimate the G^0W^0 band gaps and a very good agreement with the SOS approach. Moreover, the accuracy of the *absolute* COHSEX energies is in the order of 1 eV while the accuracy of the *absolute* EET energies is in the order of 0.1 eV. This means that accurate calculations of, for example, band off-sets with the EET can be performed since, contrary to COHSEX, it does not rely on error cancellation.

In Table I, we also report the G^0W^0 band gap of SnO_2 obtained using the SOS approach and the EET which again agree well. We note that the χ^0 and Σ SOS calculations for SnO_2 required 1000 and 1600 bands, respectively, while the

TABLE I. Fundamental gaps (E_g) of silicon, solid argon, and SnO_2, the direct band gap at Γ ($\Gamma^v-\Gamma^c$) of silicon and the HOMO-LUMO gap of atomic argon (*H*-*L*).

	LDA	G^0W^0 (SOS)	G^0W^0 (EET)	COHSEX
Silicon (E_g)	0.52	1.20	1.19	1.75
Silicon ($\Gamma^v-\Gamma^c$)	2.56	3.23	3.22	3.76
Solid argon (E_g)	7.53	12.4	12.3	14.6
Atomic argon (*H*-*L*)	9.81	14.6	14.5	15.8
SnO_2 (E_g)	0.91	2.88	2.94	4.61

TABLE II. Fundamental gap (E_g) of SnO_2 obtained with self-consistent COHSEX+G^0W^0 (GW) using the EET.

	LDA	GW	Experiment (Ref. 20)
SnO_2 (E_g) [a]	0.9	3.8	3.6

[a] Reference 22.

EET calculations just required 34 occupied bands. The G^0W^0 band gap of SnO_2 is not in good agreement with the experimental band gap of 3.6 eV.[20] This is due to the fact that the LDA energies and wave functions do not provide a good starting point for the G^0W^0 calculation. However, within the GW method, we can recalculate the screening and self-energy using updated energies and wave functions by including some form of self-consistency. Using the SOS approach, even the simplest GW method involving self-consistency, the self-consistent COHSEX+G^0W^0 approach[21] is computationally quite demanding because χ^0 has to be recalculated. This means that the energies and wave functions have to be updated during self-consistency. This bottleneck can now be reduced by applying the EET to the calculation of both the static χ^0 in the self-consistent COHSEX calculation and the subsequent G^0W^0 self-energy. We can thus include self-consistency effects using occupied states only. Using the EET, we were now able to determine the GW band gap of SnO_2 to be 3.8 eV which is in good agreement with experiment. This result, which is summarized in Table II, confirms that the EET could indeed be the method of choice for the study of, e.g., TCOs.

In conclusion, we have introduced the effective-energy technique which permits a simple and efficient evaluation of spectral representations without summing over the infinite number of empty states. Moreover, the EET speeds up calculations by more than an order of magnitude for systems of any size. We have illustrated our approach by applying it to the G^0W^0 method and shown that the results perfectly reproduce the SOS results. Furthermore, by combining the EET with the self-consistent COHSEX+G^0W^0 approach, we demonstrated its power by calculating the band gap of SnO_2. The band gap thus obtained is in good agreement with that found in experiment. Large speedups of more advanced self-consistent GW approaches[23] are also expected when combined with the EET since only QP wave functions and energies of occupied states need to be updated. Other potential applications of the EET include the calculation of RPA total energies,[24] optimized effective potentials[25] and kernels,[26] and the modeling of self-energies.

We acknowledge funding from Triangle de la Physique under Contract No. 2007-71, Saint-Gobain R&D under Contract No. 091986, and the European Community's FP7 under grant agreement No. 211956.

---

*arjan.berger@polytechnique.edu

[1] L. Hedin, Phys. Rev. **139**, A796 (1965).

[2] We use atomic units throughout.

[3] W. G. Aulbur, L. Jönsson, and J. W. Wilkins, *Solid State Physics* (Academic, New York, 2000), Vol. 54, p. 1.

[4] M. L. Tiago, S. Ismail-Beigi, and S. G. Louie, Phys. Rev. B **69**, 125212 (2004).

[5] M. van Schilfgaarde, T. Kotani, and S. V. Faleev, Phys. Rev. B **74**, 245125 (2006).

[6] F. Bechstedt, R. Del Sole, G. Cappellini, and L. Reining, Solid State Commun. **84**, 765 (1992).

[7] L. Reining, G. Onida, and R. W. Godby, Phys. Rev. B **56**, R4301 (1997).

[8] P. Umari, G. Stenuit, and S. Baroni, Phys. Rev. B **79**, 201104(R) (2009); **81**, 115104 (2010).

[9] F. Giustino, M. L. Cohen, and S. G. Louie, Phys. Rev. B **81**, 115105 (2010).

[10] F. Bruneval and X. Gonze, Phys. Rev. B **78**, 085125 (2008).

[11] S. Baroni and A. Quattropani, Nuovo Cimento D **5**, 89 (1985); S. Baroni, P. Giannozzi, and A. Testa, Phys. Rev. Lett. **58**, 1861 (1987).

[12] In Ref. 9, it is explicitly stated that for the calculation of the screening their Sternheimer approach is only convenient for extremely large systems (~1650 empty states).

[13] L. Hedin, J. Phys.: Condens. Matter **11**, R489 (1999).

[14] Note that Eq. (5) has poles and that an approximate δ could lead to spurious poles. In practice, we avoid this by constraining our approximations using integral mean-value theorems.

[15] Instead, simply replacing δ_{nj} with its homogeneous electron-gas expression does, in general, not lead to sufficiently accurate results.

[16] The part of $\Sigma_c^n(\omega)$ in Eq. (2) for which $\epsilon_i < \mu$ scales as $N_n N_v N_{\mathbf{G}}^2$ but the total number of operations is small.

[17] X. Gonze *et al.*, Z. Kristallogr. **220**, 558 (2005).

[18] P. Hohenberg and W. Kohn, Phys. Rev. **136**, B864 (1964); W. Kohn and L. J. Sham, *ibid.* **140**, A1133 (1965).

[19] R. W. Godby and R. J. Needs, Phys. Rev. Lett. **62**, 1169 (1989).

[20] K. Reimann and M. Steube, Solid State Commun. **105**, 649 (1998).

[21] F. Bruneval, N. Vast, and L. Reining, Phys. Rev. B **74**, 045102 (2006).

[22] We have neglected the effect of the commutator with the nonlocal part of the Hamiltonian in the calculation of χ^0. In the self-consistent COHSEX+G^0W^0 calculation, we used $\delta^{(0)}$ for the G^0W^0 self-energy.

[23] S. V. Faleev, M. van Schilfgaarde, and T. Kotani, Phys. Rev. Lett. **93**, 126406 (2004).

[24] D. C. Langreth and J. P. Perdew, Solid State Commun. **17**, 1425 (1975).

[25] T. Grabo *et al.*, *Strong Coulomb Correlations in Electronic Structure: Beyond the Local Density Approximation* (Gordon and Breach, Amsterdam, 2000), p. 203.

[26] F. Sottile, V. Olevano, and L. Reining, Phys. Rev. Lett. **91**, 056402 (2003).

Eur. Phys. J. B (2012) 85: 326
DOI: 10.1140/epjb/e2012-30237-5

THE EUROPEAN
PHYSICAL JOURNAL B

Regular Article

Efficient calculation of the polarizability: a simplified effective-energy technique

J.A. Berger[1,a,b], L. Reining[2,b], and F. Sottile[2,b]

[1] Laboratoire de Chimie et Physique Quantiques, (UMR 5626 du CNRS), IRSAMC, Université P. Sabatier, 118 route de Narbonne, 31062 Toulouse Cedex, France
[2] Laboratoire des Solides Irradiés, École Polytechnique, CNRS, CEA-DSM, 91128 Palaiseau, France

Received 16 March 2012

Abstract. In a recent publication [J.A. Berger, L. Reining, F. Sottile, Phys. Rev. B **82**, 041103(R) (2010)] we introduced the effective-energy technique to calculate in an accurate and numerically efficient manner the *GW* self-energy as well as the polarizability, which is required to evaluate the screened Coulomb interaction W. In this work we show that the effective-energy technique can be used to further simplify the expression for the polarizability without a significant loss of accuracy. In contrast to standard sum-over-state methods where huge summations over empty states are required, our approach only requires summations over occupied states. The three simplest approximations we obtain for the polarizability are explicit functionals of an independent- or quasi-particle one-body reduced density matrix. We provide evidence of the numerical accuracy of this simplified effective-energy technique as well as an analysis of our method.

1 Introduction

The polarizability of a system is an important physical quantity because it describes how the density of a system responds to a perturbation. Therefore, this quantity plays an important role in many condensed-matter theories, such as many-body perturbation theory (MBPT) [1], time-dependent density-functional theory [2], and also in certain areas of ground-state density-functional theory [3,4], e.g., the optimized-potential method [5,6] and the generalized random-phase approximation (RPA) [7]. In almost all cases, as the first step, an independent-particle polarizability is calculated. Traditionally, this quantity is calculated by performing a sum over states (SOS) which includes a summation over the occupied states and a summation over all the, in principle infinitely many, empty states. In practice the latter summation is truncated but a large number of empty states is required to reach numerical convergence [8–12].

Recently several approaches have been proposed in the literature to overcome this problem [9,13–16]. The incentive to resolve this problem is largely due to the recent increased popularity of Hedin's *GW* method [17] which is the state-of-the-art MBPT approximation for the calculation of quasiparticle energies of many-electron systems because it takes into account in an accurate and efficient manner the fact that each electron is screened by its Coulomb hole. The polarizability is an important quantity within *GW* since it is required for the calculation of the screened Coulomb interaction. Another important quantity within MBPT is the self-energy because it is the quantity that takes into account all the many-body effects beyond the Hartree potential. Within its standard sum-over-states representation the *GW* approximation to the self-energy also contains a summation over all the empty states that is cumbersome to converge.

In recent years, many advances have been made to eliminate or reduce the number of empty states in the calculation of the polarizability and the self-energy [9,13–16,18]. In particular, many efforts have been made to improve the Sternheimer [19–21] approach for the calculation of the polarizability and the self-energy by introducing efficient iterative techniques [14–16] and a self-consistent Sternheimer equation [13]. Other recent proposals to speed up *GW* calculations involve the design of efficient bases [22–24] or the use of simple approximate physical orbitals [25].

Recently, we presented the effective-energy technique [26,27] (EET) to reformulate SOS expressions in terms of occupied states only. Within the EET all the empty states are accounted for by a single effective energy. Moreover, we demonstrated that this effective energy can be obtained from first principles. In recent works we successfully applied this approach to calculate both the polarizability and the *GW* self-energy in an accurate

---

[a] e-mail: `arjan.berger@irsamc.ups-tlse.fr`

[b] European Theoretical Spectroscopy Facility (ETSF), `http://www.etsf.eu`

and numerically efficient manner for a large variety of systems [26,27].

However, often one is interested in the calculation of only a few quasiparticle energies, e.g., the calculation of a band gap. In these cases the main bottleneck of the standard G^0W^0 method [28,29] is the calculation of the polarizability. While, within the SOS approach, the evaluation of the self-energy scales as N_{at}^3 for each desired quasiparticle energy, the calculation of the polarizability scales as N_{at}^4, where N_{at} is the number of atoms. We recently showed that with the EET the scaling of the calculation of the polarizability can be reduced to $N_{at}^3 \log N_{at}$ [26,27]. In this work we use the EET to further simplify the expression for the polarizability and thus reduce this scaling to N_{at}^3. We will show that the first three approximations that we obtain with this simplified EET are explicit functionals of an independent- or quasi-particle one-body reduced density matrix.

The paper is organized as follows. In Section 2 we give a detailed account of the theory behind this simplified effective-energy technique for the polarizability. In Section 3 we discuss some details of our implementation. In Section 4 we show results of this simplified EET for quasiparticle energies and band gaps of several kinds of materials. We compare these results to those of standard SOS and EET calculations. Finally, in Section 5 we draw our conclusions.

2 Theory

In the following we describe in detail how our simplified effective-energy technique is used to obtain expressions for the independent-particle polarizability that contain occupied states only and scale as N_{at}^3. We use atomic units everywhere unless stated otherwise and time-reversal symmetry is assumed to hold throughout.

2.1 The independent-particle polarizability

In reciprocal space the time-ordered independent-particle polarizability is defined as

$$\chi^0_{\mathbf{GG}'}(\mathbf{q},\omega) = \sum_{s=\pm1} X(\mathbf{q},\mathbf{G},\mathbf{G}',s\omega) + \sum_{v,v'}^{occ}(n_v - n_{v'})\frac{\tilde\rho^*_{vv'}(\mathbf{q}+\mathbf{G})\tilde\rho_{v'v}(\mathbf{q}+\mathbf{G}')}{\omega-(\varepsilon_{v'}-\varepsilon_v)+i\eta\,\mathrm{sgn}(\varepsilon_{v'}-\varepsilon_v)}, \qquad (1)$$

in which $\tilde\rho_{cn}(\mathbf{q}+\mathbf{G}) = \langle c|e^{-i(\mathbf{q}+\mathbf{G})\cdot\mathbf{r}}|n\rangle$. Here n_v, ε_v, and $|v\rangle$ are Kohn-Sham or quasi-particle occupation numbers, energies, and states, respectively, and η is an infinitesimal which ensure the correct time ordering. Furthermore, we defined

$$X(\mathbf{q},\mathbf{G},\mathbf{G}',\omega) = \sum_v^{occ} n_v \sum_c^{empty} \frac{\tilde\rho^*_{cv}(\mathbf{q}+\mathbf{G})\tilde\rho_{cv}(\mathbf{q}+\mathbf{G}')}{\omega-(\varepsilon_c-\varepsilon_v)+i\eta}. \qquad (2)$$

We note that the second term on the right-hand side of equation (1) leads to nonzero contributions in the case of systems with partially occupied bands only. It is the summation over empty states that appears in equation (2) that we eliminate. Although the method that we describe in this work is valid for both finite and extended systems described by periodic boundary conditions we focus here on the latter. Therefore the indices v, v', and c in equations (1) and (2) should be considered multi-indices composed of the band index, the spin and the Bloch vector.

We now introduce a function $\Delta(\mathbf{q},\mathbf{G},\mathbf{G}',\omega)$ which is defined by the following equation:

$$X(\mathbf{q},\mathbf{G},\mathbf{G}',\omega) = \frac{\sum_{v,c} n_v\tilde\rho^*_{cv}(\mathbf{q}+\mathbf{G})\tilde\rho_{cv}(\mathbf{q}+\mathbf{G}')}{\omega-\Delta(\mathbf{q},\mathbf{G},\mathbf{G}',\omega)+i\eta}. \qquad (3)$$

Such a function can always be found since $\Delta(\mathbf{q},\mathbf{G},\mathbf{G}',\omega)$ has the same degrees of freedom as the left-hand side of equation (3). With the introduction of this function we can use the closure relation, $\sum_c |c\rangle\langle c| = 1 - \sum_v |v\rangle\langle v|$ to obtain an expression for $X(\mathbf{q},\mathbf{G},\mathbf{G}',\omega)$ which contains a summation over occupied states only. The relation in equation (3) is exact; the effective energy $\Delta(\mathbf{q},\mathbf{G},\mathbf{G}',\omega)$ takes into account the contributions of all the empty states to $X(\mathbf{q},\mathbf{G},\mathbf{G}',\omega)$.

Contrary to the effective energy in the original EET (see, for example, Eq. (15) of Ref. [26]), the effective energy $\Delta(\omega)$ in our simplified EET is independent of the occupied state v. It is this simplification that allows us to further reduce the scaling for the calculation of $\chi^0(\omega)$ from $N_{at}^3\log N_{at}$ to N_{at}^3.

It now remains to find accurate approximations to $\Delta(\mathbf{q},\mathbf{G},\mathbf{G}',\omega)$ that do not contain any summations over empty states. Following the strategy of references [26,27] we will show that such approximations can be obtained from first principles. Subtracting equation (3) from equation (2), and putting the right-hand side over a common denominator, we obtain

$$0 = \sum_{v,c} n_v\left[\frac{\tilde\rho^*_{cv}(\mathbf{q}+\mathbf{G})\tilde\rho_{cv}(\mathbf{q}+\mathbf{G}')}{\omega-(\varepsilon_c-\varepsilon_v)+i\eta} \times\frac{(\varepsilon_c-\varepsilon_v-\Delta(\mathbf{q},\mathbf{G},\mathbf{G}',\omega))}{\omega-\Delta(\mathbf{q},\mathbf{G},\mathbf{G}',\omega)+i\eta}\right]. \qquad (4)$$

Multiplying the above equation by $[\omega-\Delta(\omega)+i\eta]$ and rearranging we arrive at

$$\Delta(\mathbf{q},\mathbf{G},\mathbf{G}',\omega)X(\mathbf{q},\mathbf{G},\mathbf{G}',\omega) = \sum_{v,c} n_v\frac{\tilde\rho^*_{cv}(\mathbf{q}+\mathbf{G})\tilde\rho_{cv}(\mathbf{q}+\mathbf{G}')(\varepsilon_c-\varepsilon_v)}{\omega-(\varepsilon_c-\varepsilon_v)+i\eta} \qquad (5)$$

$$= \frac{1}{2}\sum_{v,c} n_v\frac{\tilde\rho^*_{cv}(\mathbf{q}+\mathbf{G})\langle c|[\hat H(\mathbf{r}'),e^{-i(\mathbf{q}+\mathbf{G}')\cdot\mathbf{r}'}]|v\rangle + h.c.}{\omega-(\varepsilon_c-\varepsilon_v)+i\eta}, \qquad (6)$$

where *h.c.* denotes the Hermitian conjugate. In the last step, we made use of the fact that the ε_i are eigenvalues of the Hamiltonian $\hat H(\mathbf{r})$ with eigenstates $|i\rangle$ [30]. Here we consider a Hamiltonian that contains only a local potential, i.e., $\hat{H}(\mathbf{r}) = -\nabla_{\mathbf{r}}^2/2 + v(\mathbf{r})$. The derivation that follows can be easily generalized to include Hamiltonians with additional nonlocal potentials [27]. We note that the symmetrization we carried out in the numerator of equation (6) ensures that the approximations for $\Delta(\omega)$ that we will derive in the following have the correct symmetry.

Working out the commutator in equation (6) and dividing both sides by $X(\omega)$ we obtain

$$\Delta(\mathbf{q},\mathbf{G},\mathbf{G}',\omega) = Q(\mathbf{q},\mathbf{G},\mathbf{G}') + \frac{\tilde{X}(\mathbf{q},\mathbf{G},\mathbf{G}',\omega)}{X(\mathbf{q},\mathbf{G},\mathbf{G}',\omega)}, \tag{7}$$

where we defined

$$Q(\mathbf{q},\mathbf{G},\mathbf{G}') = \frac{1}{2}\left[\frac{|\mathbf{q}+\mathbf{G}|^2}{2} + \frac{|\mathbf{q}+\mathbf{G}'|^2}{2}\right] \tag{8}$$

$$\tilde{X}(\mathbf{q},\mathbf{G},\mathbf{G}',\omega) = \frac{1}{2}\sum_{v,c} n_v \frac{\tilde{\rho}^*_{cv}(\mathbf{q}+\mathbf{G})\tilde{j}_{cv}(\mathbf{q}+\mathbf{G}') + h.c.}{[\omega - (\varepsilon_c - \varepsilon_v) + i\eta]}, \tag{9}$$

in which

$$\tilde{j}_{cv}(\mathbf{q}+\mathbf{G}) = \langle c|e^{-i(\mathbf{q}+\mathbf{G})\cdot\mathbf{r}}[i\nabla_{\mathbf{r}}]|v\rangle\cdot(\mathbf{q}+\mathbf{G}). \tag{10}$$

In equation (7) $\Delta(\omega)$ is expressed in terms of itself through $X(\omega)$. Since $\tilde{X}(\omega)$ depends on a summation over the empty states solving for $\Delta(\omega)$ will not lead to the desired result. However, in view of the similarity of equations (9) and (2) we can also rewrite equation (9) in terms of occupied states only in an equivalent manner as equation (3) by defining a modified effective energy $\tilde{\Delta}(\omega)$ such that

$$\tilde{X}(\mathbf{q},\mathbf{G},\mathbf{G}',\omega) = \frac{1}{2}\frac{\sum_{v,c} n_v\tilde{\rho}^*_{cv}(\mathbf{q}+\mathbf{G})\tilde{j}_{cv}(\mathbf{q}+\mathbf{G}')+h.c.}{\omega-\tilde{\Delta}(\mathbf{q},\mathbf{G},\mathbf{G}',\omega)+i\eta}. \tag{11}$$

Combining the above equation with equations (3) and (7) leads to the following (exact) expression for $\Delta(\omega)$:

$$\Delta(\mathbf{q},\mathbf{G},\mathbf{G}',\omega) = Q(\mathbf{q},\mathbf{G},\mathbf{G}') + \frac{F^{\rho j}(\mathbf{q},\mathbf{G},\mathbf{G}')}{F^{\rho\rho}(\mathbf{q},\mathbf{G},\mathbf{G}')} \times \frac{\omega - \Delta(\mathbf{q},\mathbf{G},\mathbf{G}',\omega) + i\eta}{\omega - \tilde{\Delta}(\mathbf{q},\mathbf{G},\mathbf{G}',\omega) + i\eta}, \tag{12}$$

where

$$F^{\rho\rho}(\mathbf{q},\mathbf{G},\mathbf{G}') = \rho(\mathbf{G}'-\mathbf{G}) - \int d\mathbf{r}d\mathbf{r}' e^{i(\mathbf{q}+\mathbf{G})\cdot\mathbf{r}} e^{-i(\mathbf{q}+\mathbf{G}')\cdot\mathbf{r}'}|\rho(\mathbf{r},\mathbf{r}')|^2 \tag{13}$$

$$F^{\rho j}(\mathbf{q},\mathbf{G},\mathbf{G}') = \frac{i}{2}P(\mathbf{q},\mathbf{G},\mathbf{G}')\cdot(\mathbf{q}+\mathbf{G}') + h.c. \tag{14}$$

$$F^{jj}(\mathbf{q},\mathbf{G},\mathbf{G}') = (\mathbf{q}+\mathbf{G})\cdot\tilde{P}(\mathbf{q},\mathbf{G},\mathbf{G}')\cdot(\mathbf{q}+\mathbf{G}') \tag{15}$$

in which

$$P(\mathbf{q},\mathbf{G},\mathbf{G}') = \int d\mathbf{r} e^{i(\mathbf{G}-\mathbf{G}')\cdot\mathbf{r}}\nabla_{\mathbf{r}}\rho(\mathbf{r}) - \int d\mathbf{r}d\mathbf{r}' e^{i(\mathbf{q}+\mathbf{G})\cdot\mathbf{r}} e^{-i(\mathbf{q}+\mathbf{G}')\cdot\mathbf{r}'}\nabla_{\mathbf{r}'}|\rho(\mathbf{r},\mathbf{r}')|^2 \tag{16}$$

$$\tilde{P}(\mathbf{q},\mathbf{G},\mathbf{G}') = \int d\mathbf{r} e^{i(\mathbf{G}-\mathbf{G}')\cdot\mathbf{r}}\nabla_{\mathbf{r}}\nabla_{\mathbf{r}}\rho(\mathbf{r}) - \int d\mathbf{r}d\mathbf{r}' e^{i(\mathbf{q}+\mathbf{G})\cdot\mathbf{r}} e^{-i(\mathbf{q}+\mathbf{G}')\cdot\mathbf{r}'}\rho(\mathbf{r},\mathbf{r}')\nabla_{\mathbf{r}}\nabla_{\mathbf{r}'}\rho(\mathbf{r},\mathbf{r}'). \tag{17}$$

The expression for F^{jj} in equation (15) has been added for future reference.

In analogy with the original EET [26,27] we obtain the first-order approximation for $\Delta(\omega)$ by setting $\Delta(\omega) = \tilde{\Delta}(\omega)$ in equation (12). We obtain

$$\Delta^{(1)}(\mathbf{q},\mathbf{G},\mathbf{G}') = Q(\mathbf{q},\mathbf{G},\mathbf{G}') + \frac{F^{\rho j}(\mathbf{q},\mathbf{G},\mathbf{G}')}{F^{\rho\rho}(\mathbf{q},\mathbf{G},\mathbf{G}')} \tag{18}$$

which is independent of the frequency. We note that, contrary to the equivalent approximation in the original EET [26,27], the above expression is not exact for a homogeneous electron gas. Further details are given in the next section.

We continue the above iteritave procedure by expressing $\tilde{\Delta}(\omega)$ in equation (12) in terms of another effective energy $\tilde{\tilde{\Delta}}(\omega)$, etc. This second iteration then leads to

$$\Delta(\mathbf{q},\mathbf{G},\mathbf{G}',\omega) = Q(\mathbf{q},\mathbf{G},\mathbf{G}') + \frac{F^{\rho j}(\mathbf{q},\mathbf{G},\mathbf{G}')}{F^{\rho\rho}(\mathbf{q},\mathbf{G},\mathbf{G}')} \times \left[\frac{\omega - Q(\mathbf{q},\mathbf{G},\mathbf{G}') - \frac{F^{\rho j}(\mathbf{q},\mathbf{G},\mathbf{G}')}{F^{\rho\rho}(\mathbf{q},\mathbf{G},\mathbf{G}')}\frac{\omega-\Delta(\mathbf{q},\mathbf{G},\mathbf{G}',\omega)}{\omega-\tilde{\Delta}(\mathbf{q},\mathbf{G},\mathbf{G}',\omega)}}{\omega - Q(\mathbf{q},\mathbf{G},\mathbf{G}') - \frac{F^{jj}(\mathbf{q},\mathbf{G},\mathbf{G}')}{F^{\rho j}(\mathbf{q},\mathbf{G},\mathbf{G}')}\frac{\omega-\tilde{\Delta}(\mathbf{q},\mathbf{G},\mathbf{G}',\omega)}{\omega-\tilde{\tilde{\Delta}}(\mathbf{q},\mathbf{G},\mathbf{G}',\omega)}}\right] \tag{19}$$

where F^{jj} is given in equation (15). Our second-order approximation for $\Delta(\omega)$ is then obtained by setting $\tilde{\tilde{\Delta}}(\omega) = \tilde{\Delta}(\omega) = \Delta(\omega)$. Let us now summarize our first three approximations for $\Delta(\omega)$. We obtain

$$\Delta^{(0)}(\mathbf{q},\mathbf{G},\mathbf{G}') = Q(\mathbf{q},\mathbf{G},\mathbf{G}') \tag{20}$$

$$\Delta^{(1)}(\mathbf{q},\mathbf{G},\mathbf{G}') = Q(\mathbf{q},\mathbf{G},\mathbf{G}') + \frac{F^{\rho j}(\mathbf{q},\mathbf{G},\mathbf{G}')}{F^{\rho\rho}(\mathbf{q},\mathbf{G},\mathbf{G}')} \tag{21}$$

$$\Delta^{(2)}(\mathbf{q},\mathbf{G},\mathbf{G}',\omega) = Q(\mathbf{q},\mathbf{G},\mathbf{G}') + \frac{F^{\rho j}(\mathbf{q},\mathbf{G},\mathbf{G}')}{F^{\rho\rho}(\mathbf{q},\mathbf{G},\mathbf{G}')} \times \left[\frac{\omega - Q(\mathbf{q},\mathbf{G},\mathbf{G}') - \frac{F^{\rho j}(\mathbf{q},\mathbf{G},\mathbf{G}')}{F^{\rho\rho}(\mathbf{q},\mathbf{G},\mathbf{G}')}}{\omega - Q(\mathbf{q},\mathbf{G},\mathbf{G}') - \frac{F^{jj}(\mathbf{q},\mathbf{G},\mathbf{G}')}{F^{\rho j}(\mathbf{q},\mathbf{G},\mathbf{G}')}}\right]. \tag{22}$$

Here we added a simple zero-order approximation which neglects the second term on the right-hand side of equation (7). With the second-order expression $\Delta^{(2)}(\omega)$ we have obtained an approximation which is frequency dependent. The expression for $\Delta^{(2)}(\omega)$ is therefore nontrivial despite its simple form. Higher order expressions for Δ will contain terms with higher order derivatives of the valence wave functions as well as derivatives of the potential.

The above approximations for $\Delta(\omega)$ as well as the corresponding approximations for $\chi^0(\omega)$ (for systems with a gap) are explicit functionals of a one-body reduced density matrix. Therefore, these effective energies could also be useful in the modeling of density-matrix functionals [31]. Furthermore, the polarizabilities obtained using these effective energies could be used to calculate efficiently RPA total energies [7], or to obtain optimized effective potentials [5,6].

2.2 Homogeneous electron gas

As can be seen by comparing equations (12) and (21), for the approximation $\Delta^{(1)}$ given in equation (21) to be exact for a homogeneous electron gas it is required that $\tilde{\Delta}^{hom}(\mathbf{G},\omega) = \Delta^{hom}(\mathbf{G},\omega)$. We now show that, in general, this is not the case.

Combining equations (2) and (3) and making use of the fact that the wave functions can be expressed in terms of a single plane wave, i.e., $\phi_{i\mathbf{k}}(\mathbf{r}) = e^{i(\mathbf{k}+\mathbf{G}_i)\cdot\mathbf{r}}$ (we made the $\mathbf{k}$ dependence explicit) we obtain

$$\Delta^{hom}(\mathbf{G},\omega) = \omega - \sum_{vc\mathbf{k}} \delta(\mathbf{G}_v - \mathbf{G} - \mathbf{G}_c) \times \left[\sum_{v'c'\mathbf{k}'} \frac{\delta(\mathbf{G}_{v'} - \mathbf{G} - \mathbf{G}_{c'})}{\omega - (\varepsilon_{c'\mathbf{k}'} - \varepsilon_{v'\mathbf{k}'}) + i\eta}\right]^{-1}. \tag{23}$$

In a similar manner by combining equations (9) and (11) we get

$$\tilde{\Delta}^{hom}(\mathbf{G},\omega) = \omega - \sum_{vc\mathbf{k}} \delta(\mathbf{G}_v - \mathbf{G} - \mathbf{G}_c)[(\mathbf{k}+\mathbf{G}_v)\cdot(\mathbf{q}+\mathbf{G})] \times \left[\sum_{v'c'\mathbf{k}'} \frac{\delta(\mathbf{G}_{v'} - \mathbf{G} - \mathbf{G}_{c'})[(\mathbf{k}'+\mathbf{G}_{v'})\cdot(\mathbf{q}+\mathbf{G})]}{\omega - (\varepsilon_{c'\mathbf{k}'} - \varepsilon_{v'\mathbf{k}'}) + i\eta}\right]^{-1}. \tag{24}$$

Contrary to the original EET, the factors $[(\mathbf{k}+\mathbf{G}_v)\cdot(\mathbf{q}+\mathbf{G})]$ in the numerator and denominator of the second term on the right-hand side of equation (24) do not cancel out due to the summations over v and $\mathbf{k}$ in both the numerator and denominator. Therefore $\tilde{\Delta}^{hom}(\mathbf{G},\omega) \neq \Delta^{hom}(\mathbf{G},\omega)$. Similarly one can show that $\tilde{\tilde{\Delta}}^{hom}(\mathbf{G},\omega) \neq \Delta^{hom}(\mathbf{G},\omega)$, etc.

Despite the fact that the approximation in equation (21) is not exact for the homogeneous electron gas, we show in the next section that both the high-frequency limit and the f-sum rule are satisfied.

2.3 Exact constraints

It is known that the RPA polarizability satisfies several sum rules and exact constraints such as the high-frequency limit and the f-sum rule. These constraints allow us to obtain more insights in the approximations given by equations (20)–(22). In Section 2.3.1 we show that any approximation $\Delta^{(k)}(\omega)$ with $k > 0$ satisfies the high-frequency limit. However, the same is not true for the f-sum rule. While we can show that the first-order approximation $\Delta^{(1)}$ satisfies the f-sum rule for its diagonal elements (see Sect. 2.3.2), we cannot do the same for higher-order approximations, such as $\Delta^{(2)}(\omega)$. This opens a possible route to construct improved approximations for $\Delta(\omega)$. For example, one could constrain higher-order approximations to satisfy the f-sum rule.

2.3.1 The high-frequency limit

The high frequency limit of $\chi^0(\omega)$ is given by [32]

$$\lim_{\omega\to\infty} \omega^2 \chi^0_{\mathbf{GG}'}(\mathbf{q},\omega) = (\mathbf{q}+\mathbf{G})\cdot(\mathbf{q}+\mathbf{G}')\rho(\mathbf{G}'-\mathbf{G}). \tag{25}$$

We will now show that this exact constraint remains satisfied when we express $\chi^0(\omega)$ in terms of an effective energy for all approximations $\Delta^{(k)}(\mathbf{q},\mathbf{G},\mathbf{G}',\omega)$ with $k > 0$.

Performing a Taylor expansion of $\chi^0_{\mathbf{GG}'}(\omega)$ around $\omega = \infty$ yields for any $k > 0$

$$\chi^0_{\mathbf{GG}'}(\mathbf{q},\omega) = \frac{1}{\omega^2}\left[2\left[F^{\rho\rho}Q(\mathbf{q},\mathbf{G},\mathbf{G}') + F^{\rho j}\right] + \sum_{v,v'}(n_v - n_{v'})\tilde{\rho}^*_{v'v}(\mathbf{G})\tilde{\rho}_{v'v}(\mathbf{G}')(\varepsilon_{v'} - \varepsilon_v)\right] + O\left(\frac{1}{\omega^4}\right). \tag{26}$$

For notational convenience, we have suppressed the dependence of $F^{\rho\rho}$ and $F^{\rho j}$ on $\mathbf{q}, \mathbf{G}$ and $\mathbf{G}'$ as well as the dependence of $\tilde{\rho}_{v'v}$ on $\mathbf{q}$. Using the following relation

$$F^{\rho\rho}Q(\mathbf{q},\mathbf{G},\mathbf{G}') + F^{\rho j} = \sum_{v,c} n_v \tilde{\rho}^*_{cv}(\mathbf{G})\tilde{\rho}_{cv}(\mathbf{G}')(\varepsilon_c - \varepsilon_v), \tag{27}$$

which can be verified by substitution of equations (13) and (14), we obtain

$$\chi^0_{\mathbf{GG}'}(\mathbf{q},\omega) = \frac{1}{\omega^2}\sum_{n,n'}(n_n - n_{n'}) \times \tilde{\rho}^*_{n'n}(\mathbf{G})\tilde{\rho}_{n'n}(\mathbf{G}')(\varepsilon_{n'} - \varepsilon_n) + O\left(\frac{1}{\omega^4}\right) \tag{28}$$

$$= \frac{1}{\omega^2}\sum_n n_n \langle n| \left[e^{i(\mathbf{q}+\mathbf{G})\cdot\mathbf{r}}, \left[\hat{H}(\mathbf{r}), e^{-i(\mathbf{q}+\mathbf{G}')\cdot\mathbf{r}}\right]\right] |n\rangle + O\left(\frac{1}{\omega^4}\right) \tag{29}$$

$$= \frac{1}{\omega^2}(\mathbf{q}+\mathbf{G})\cdot(\mathbf{q}+\mathbf{G}')\rho(\mathbf{G}'-\mathbf{G}) + O\left(\frac{1}{\omega^4}\right). \tag{30}$$

We therefore obtain

$$\lim_{\omega\to\infty} \omega^2 \chi^0_{\mathbf{GG}'}(\mathbf{q},\omega) = (\mathbf{q}+\mathbf{G})\cdot(\mathbf{q}+\mathbf{G}')\rho(\mathbf{G}'-\mathbf{G}) \tag{31}$$

which proves that the high-frequency limit is satisfied for all $\Delta^{(k)}(\mathbf{q},\mathbf{G},\mathbf{G}',\omega)$ with $k > 0$.

2.3.2 The f-sum rule

The generalized f-sum rule is given by [32]

$$\int_0^\infty d\omega\omega \mathrm{Im}\chi^0_{\mathbf{G}\mathbf{G}'}(\mathbf{q},\omega) = -\frac{\pi}{2}(\mathbf{q}+\mathbf{G})\cdot(\mathbf{q}+\mathbf{G}')\rho(\mathbf{G}'-\mathbf{G}). \tag{32}$$

We will now show that this exact constraint also holds for $\chi^0(\omega)$ when it is expressed in terms of an effective energy using $\Delta^{(1)}$ if we assume that $\Delta^{(1)}(\mathbf{q},\mathbf{G},\mathbf{G}')$ is both real and non-negative. This assumption holds true for the diagonal elements $\Delta^{(1)}(\mathbf{q},\mathbf{G},\mathbf{G})$ as can be verified from equation (21). We can now use the following relation

$$\lim_{\eta\to 0^+}\frac{1}{x\pm i\eta} = \mathcal{P}\frac{1}{x} \mp i\pi\delta(x), \tag{33}$$

where $\mathcal{P}$ denotes the principal value, to write

$$\begin{aligned}\int_0^\infty d\omega\omega \mathrm{Im}\chi^0_{\mathbf{G}\mathbf{G}'}(\mathbf{q},\omega) &= -\pi F^{\rho\rho}\\ &\times \int_0^\infty d\omega\omega\left[\delta(\omega-\Delta^{(1)})+\delta(\omega+\Delta^{(1)})\right]\\ -\pi\sum_{v.v'}(n_v-n_{v'})\tilde{\rho}^*_{v'v}(\mathbf{G})\tilde{\rho}_{v'v}(\mathbf{G}')&\int_0^\infty d\omega\omega\delta(\omega-(\varepsilon_{v'}-\varepsilon_v)).\end{aligned} \tag{34}$$

For notational convenience, we have suppressed the dependence of $\Delta^{(1)}$ and $F^{\rho\rho}$ on $\mathbf{q},\mathbf{G}$ and $\mathbf{G}'$ as well as the dependence of $\tilde{\rho}_{v'v}$ on $\mathbf{q}$. Since, thanks to time-reversal symmetry,

$$\begin{aligned}\sum_{v.v'}(n_v-n_{v'})\tilde{\rho}^*_{v'v}(\mathbf{G})\tilde{\rho}_{v'v}(\mathbf{G}')\int_0^\infty d\omega\omega\delta(\omega-(\varepsilon_{v'}-\varepsilon_v)) =\\ \sum_{v.v'}(n_v-n_{v'})\tilde{\rho}^*_{v'v}(\mathbf{G})\tilde{\rho}_{v'v}(\mathbf{G}')\int_{-\infty}^0 d\omega\omega\delta(\omega-(\varepsilon_{v'}-\varepsilon_v))\end{aligned} \tag{35}$$

we can write

$$\begin{aligned}\int_0^\infty d\omega\omega \mathrm{Im}\chi^0_{\mathbf{G}\mathbf{G}'}(\mathbf{q},\omega) &= -\pi F^{\rho\rho}\Delta^{(1)}\\ &-\frac{\pi}{2}\sum_{v.v'}(n_v-n_{v'})\tilde{\rho}^*_{v'v}(\mathbf{G})\tilde{\rho}_{v'v}(\mathbf{G}')(\varepsilon_{v'}-\varepsilon_v) && (36)\\ &= -\frac{\pi}{2}\sum_{n.n'}(n_n-n_{n'})\tilde{\rho}^*_{n'n}(\mathbf{G})\tilde{\rho}_{n'n}(\mathbf{G}')(\varepsilon_{n'}-\varepsilon_n) && (37)\\ &= -\frac{\pi}{2}(\mathbf{q}+\mathbf{G})\cdot(\mathbf{q}+\mathbf{G}')\rho(\mathbf{G}'-\mathbf{G}) && (38)\end{aligned}$$

where we used equation (27). Therefore, the f-sum rule is satisfied for $\Delta^{(1)}(\mathbf{q},\mathbf{G},\mathbf{G}')$. With the same procedure we cannot show that the f-sum rule is satisfied for $\Delta^{(0)}(\mathbf{q},\mathbf{G},\mathbf{G}')$ and $\Delta^{(2)}(\mathbf{q},\mathbf{G},\mathbf{G}',\omega)$.

2.4 $\mathbf{G^0W^0}$

In this work we focus on the efficient calculation of the polarizability and, in particular, on how it can be used to calculate efficiently the screened Coulomb potential $W(\omega) = \epsilon^{-1}(\omega)v_c$ for GW calculations of quasi-particle energies. Here $\epsilon(\omega)$ is the dielectric function and v_c is the Coulomb potential. Within the standard G^0W^0 method [28,29], $\epsilon(\omega)$ is evaluated in the random-phase approximation (RPA). Within the RPA $\epsilon(\omega)$ is directly related to $\chi^0(\omega)$: $\epsilon(\omega) = 1 - v_c\chi^0(\omega)$. Therefore the calculation of $W(\omega)$ immediately benefits from the efficient EET described above.

In order to obtain GW quasi-particle energies we also have to calculate the GW self-energy $\Sigma(\omega)$. It is given by the following convolution of $G(\omega)$, the single-particle Green's function, and $W(\omega)$,

$$\Sigma(\mathbf{r},\mathbf{r}',\omega) = i\int_{-\infty}^{\infty}\frac{d\omega'}{2\pi}e^{i\eta\omega'}G(\mathbf{r},\mathbf{r}',\omega+\omega')W(\mathbf{r},\mathbf{r}',\omega'), \tag{39}$$

where the infinitesimal η is to be taken in the limit to zero after the frequency integration.

In standard G^0W^0 calculations the quasi-particle energies are obtained from first-order perturbation theory where the perturbation is given by the difference of the GW Hamiltonian and the Kohn-Sham (KS) Hamiltonian of density-functional theory (DFT) [3,4], i.e., $\Sigma(\mathbf{r},\mathbf{r}',\omega) - v_{xc}(\mathbf{r})$, with $v_{xc}(\mathbf{r})$ the exchange-correlation potential of DFT:

$$\varepsilon_n = \varepsilon_n^{KS} + Z_n\langle\phi_n^{KS}|\Sigma(\varepsilon_n^{KS}) - v_{xc}|\phi_n^{KS}\rangle \tag{40}$$

where the renormalization factor Z_n is given by

$$Z_n = \left[1 - \left.\frac{\partial\langle\phi_n^{KS}|\Sigma(\omega)|\phi_n^{KS}\rangle}{\partial\omega}\right|_{\omega=\varepsilon_n^{KS}}\right]^{-1}. \tag{41}$$

In previous works we have discussed how the GW self-energy can be calculated accurately and efficiently without summations over empty states using the EET [26,27]. We refer the reader to those works for details.

2.5 Converging $\mathbf{G^0W^0}$ calculations

Inserting the approximations derived in equations (20)–(22) into the expression for $\chi^0(\omega)$ in equation (3) leads to approximations for $\chi^0(\omega)$ which do not contain empty states. In the following we will show that the approximation for $\chi^0(\omega)$ using the effective energy given in equation (22) leads to accurate G^0W^0 results. However, one might wish to converge to the numerically exact G^0W^0 result. Such numerically exact results can be obtained efficiently and in a systematic way by combining the EET and the SOS approach. In the following we illustrate how we achieve this goal. We first split the expression in equation (2) into two parts according to

$$X(\mathbf{q},\mathbf{G},\mathbf{G}',\omega)=\sum_v n_v\left[\sum_{c=N_v+1}^{M}\frac{\tilde{\rho}^*_{cv}(\mathbf{q}+\mathbf{G})\tilde{\rho}_{cv}(\mathbf{q}+\mathbf{G}')}{\omega-(\varepsilon_c-\varepsilon_v)+i\eta}\right.$$
$$\left.+\sum_{c=M+1}^{\infty}\frac{\tilde{\rho}^*_{cv}(\mathbf{q}+\mathbf{G})\tilde{\rho}_{cv}(\mathbf{q}+\mathbf{G}')}{\omega-\Delta(\mathbf{q},\mathbf{G},\mathbf{G}',\omega)+i\eta}\right] \quad (42)$$

where N_v is the number of occupied bands. Here we used the simplified EET only in the second term on the right-hand side which contains a summation over all the empty states starting from $M+1$. If we choose $M=N_v$ we retrieve equation (3). However, if we choose $M>N_v$ the part that needs to be approximated with the EET becomes smaller as M increases. In this way we have obtained an efficient way to converge $X(\omega)$, and therefore $\chi^0(\omega)$, with respect to the number of empty states. We note that this procedure is similar to the one proposed by Bruneval and Gonze [9] with the important difference that our approach generally converges more rapidly and, most importantly, is parameter free.

2.6 Range of applicability

In this section we will briefly discuss the range of applicability of the simplified EET. As mentioned before, in principle, the EET can be used to rewrite any SOS expression in terms of occupied states only, namely by the introduction of an effective energy with sufficient degrees of freedom. However, we do not expect that in all cases simple approximations to this effective energy will lead to accurate results.

Let us consider, for example, the imaginary part of the head of the polarizability tensor $\chi^0_{\mathbf{GG}'}(\omega)$. The SOS expression for this element is given by

$$\mathrm{Im}\chi^0_{\mathbf{00}}(\mathbf{q},\omega)=\sum_{v,c}\int d\mathbf{r}\int d\mathbf{r}'\phi^*_v(\mathbf{r})\phi_c(\mathbf{r})\phi^*_c(\mathbf{r}')\phi_v(\mathbf{r}')$$
$$\times\, e^{i\mathbf{q}\cdot(\mathbf{r}-\mathbf{r}')}\delta(\omega-(\varepsilon_c-\varepsilon_v)) \quad (43)$$

where, for simplicity, we assumed a material with a gap and $\omega>0$. If we compare this to the EET result using $\Delta^{(0)}$ and $\Delta^{(1)}$ we obtain

$$\mathrm{Im}\chi^0_{\mathbf{00}}(\mathbf{q},\omega)=F^{\rho\rho}(\mathbf{q},\mathbf{0},\mathbf{0})\delta(\omega-\Delta^{(0)}(\mathbf{q},\mathbf{0},\mathbf{0})) \quad (44)$$
$$\mathrm{Im}\chi^0_{\mathbf{00}}(\mathbf{q},\omega)=F^{\rho\rho}(\mathbf{q},\mathbf{0},\mathbf{0})\delta(\omega-\Delta^{(1)}(\mathbf{q},\mathbf{0},\mathbf{0})). \quad (45)$$

While equation (43) consists of a summation over a number of poles equal to N_vN_c, equations (44) and (45) contain only a single pole. Therefore, with the simple frequency-independent approximations $\Delta^{(0)}_v$ and $\Delta^{(1)}$ we will, in general, not be able to describe $\mathrm{Im}\chi^0_{\mathbf{00}}(\omega)$ in an accurate way. Hence, we expect that the calculation of an accurate absorption spectrum, which is closely related to $\mathrm{Im}\chi^0_{\mathbf{00}}(\omega)$, would require complicated frequency-dependent effective energies far beyond $\Delta^{(1)}$. We note that, nevertheless, $\chi^0_{\mathbf{00}}(\omega)$ expressed in terms of $\Delta^{(1)}$ satisfies the high-frequency limit and the generalized f-sum rule (see Sects. 2.3.1 and 2.3.2).

On the other hand, we expect that quantities which depend on frequency integrals over $\chi^0(\omega)$, such as the GW self-energy, can be accurately reproduced with simple approximations to $\Delta(\omega)$, precisely because exact constraints such as the generalized f-sum rule and the high-frequency limit are satisfied.

3 Implementation

We implemented the EET described above in the ABINIT software package [33]. In this section we would like to discuss two technical details of our implementation.

First, as can be verified from equation (2), $X(\omega)$ does not have poles in the energy range $[-\infty,\varepsilon_L-\varepsilon_H]$ where ε_H is the eigenvalue of the highest occupied state and ε_L is the eigenvalue of the lowest empty state. In practice, however, the approximations for $\Delta(\omega)$ given in equations (20)–(22), might lead to spurious poles in this energy range. In standard GW calculations the independent-particle polarizability is evaluated on the imaginary-frequency axis, where it has no poles (excepting metals at $\omega=0$), and then fitted to a plasmon-pole model (PPM) [29,34]. Therefore, numerical instabilities can only occur at $\omega=0$, where there should be no pole. To avoid these instabilities we constrain the effective energy $\Delta(\omega)$ in equation (3) to the range $[\varepsilon_L-\varepsilon_H,\infty]$, i.e., $\Delta(\omega)$ is set to $\varepsilon_L-\varepsilon_H$ in the case that the effective energy $\Delta(\omega)$ obtained using the approximations in equations (20)–(22) results in $\Delta(\omega)<\varepsilon_L-\varepsilon_H$. Using the first mean-value theorem for integration [35] one can show that this constraint is exact for all diagonal elements $\Delta(\mathbf{q},\mathbf{G},\mathbf{G},\omega)$ since in this case the numerator on the right-hand side of equation (2) is non-negative for every v and c.

Second, as within the SOS approach, the calculation of the head and wings of the dielectric matrix for $\mathbf{q}\to 0$ requires special attention since for these elements one can not simply set $\mathbf{q}=0$. One usually employs $\mathbf{k}\cdot\mathbf{p}$ perturbation theory to evaluate the limit $\mathbf{q}\to 0$ for these elements. However, $\mathbf{k}\cdot\mathbf{p}$ perturbation theory introduces an additional summation over empty states. This can, for example, be avoided by using a small but finite $\mathbf{q}$ or by numerically expanding the wave functions around $\mathbf{q}=0$ [36]. However, since the calculation of the head and wings is an order of magnitude smaller than the body and the number of empty states required to reach convergence for these elements is small, we found it more efficient to simply use the SOS approach for the head and wings when $\mathbf{q}\to 0$. The extra computational cost is negligible.

4 Results

4.1 Computational details

All our calculations were performed using separable norm-conserving pseudopotentials [37,38]. For Sn, the semicore

Table 1. Fundamental gaps (E_g) of silicon, solid argon, SnO$_2$, and ZnO, the direct band gap at Γ ($\Gamma^v - \Gamma^c$) of silicon and the HOMO-LUMO gap of atomic argon ($H - L$).

	LDA	G^0W^0 (SOS)	G^0W^0 (EET)	G^0W^0 (sEET)
Silicon (E_g)	0.52	1.21	1.10	0.98
Silicon ($\Gamma^v - \Gamma^c$)	2.56	3.24	3.17	3.11
Solid argon (E_g)	7.53	12.4	12.3	12.3
Atomic argon ($H - L$)	9.81	14.6	14.5	14.5
SnO$_2$ (E_g)	0.94	2.89	2.86	2.88
ZnO (E_g)	0.82	2.56	2.39	2.50

electrons of the $4s$, $4p$, and $4d$ states were considered as valence electrons. Similarly, for Zn, the semicore electrons of the $3s$, $3p$, and $3d$ states were considered as valence electrons. For Si and Ar we did not include the semicore electrons in the valence. In the case of O the $2s$ and $2p$ states were considered as valence.

For SnO$_2$ we used calculcated lattice parameters and atomic positions which we obtained from a density-functional calculation using the local-density approximation (LDA), while for all the other materials we used experimental values.

The k-point sampling of the Brillouin zone was carried out using a Monkhorst-Pack (MP) grid [39]. In the cases of SnO$_2$ and ZnO we used a $4 \times 4 \times 6$ and $6 \times 6 \times 4$ MP grid, respectively, while for Si and solid Ar we used a $4 \times 4 \times 4$ MP grid. For the calculation of the self-energy these grids were shifted such that they contain the Γ-point while for the calculation of the dielectric matrix they were shifted such that they do not include the Γ-point. In the cases of Si and solid Ar four such shifts were applied to increase the number of **k**-points to 256. The ground-state cut-off energies we used were 40 Ry (Si, Ar), 240 Ry (SnO$_2$), and 350 Ry (ZnO). The cut-off energies we used for the dielectric matrix were 16 Ry (Si), 17.2 Ry (solid Ar), 3.3 Ry (atomic Ar), 48 Ry (SnO$_2$), and 80 Ry (ZnO). We used the generalized plasmon-pole model of Godby and Needs [34] to fit $\epsilon^{-1}(\omega)$.

4.2 Band gaps

In Table 1 we report the calculated band gaps of several materials using the simplified EET (sEET) proposed in this work to calculate the polarizability. We used $\Delta^{(2)}(\omega)$ given in equation (22) to approximate the effective energy. The calculation of the polarizability is combined with an EET calculation of the self-energy using $\delta^{(2)}(\omega)$. We refer the reader to references [26,27] for the approximations to the effective energy of the original EET, $\delta(\omega)$ and $\delta'(\omega)$, which are the effective energies for the self-energy and polarizability, respectively. For comparison we also report in Table 1 the band gaps obtained with the standard SOS approach as well as those obtained with the original EET using $\delta^{(2)}(\omega)$ and $\delta'^{(2)}(\omega)$ as approximations for the effective energies in the calculation of the self-energy and polarizability, respectively. For all materials except silicon the band gaps obtained using the simplified EET to calculate the polarizability are in very good agreement with those obtained using the original EET. The calculated band gaps are very close to the numerically converged values given in the second column of Table 1. However, in the case of silicon the band gaps come out too small in comparison to both the SOS and the original EET[1]. For silicon we can now use the SOS + EET approach discussed in Section 2.5 to arrive at numerically converged G^0W^0 band gaps.

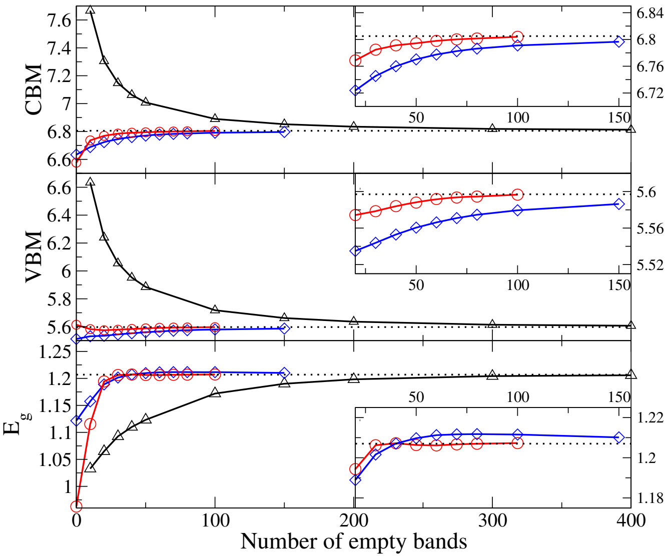

Fig. 1. (Color online) Convergence behavior of the calculate energies (in eV) of the VBM, CBM, and fundamental gap (E_g) of Si with the number of empty states in both the screening and self-energy calculcations. Triangles (black): SOS approach; circles (red): SOS + EET approach using $\Delta^{(2)}$ and $\delta^{(0)}$; diamonds (blue): SOS + EET approach using $\delta'^{(0)}$ and $\delta^{(0)}$. The insets focus on the difference between the SOS + EET approach using $\Delta^{(2)}$ and $\delta^{(0)}$ and the SOS + EET approach using $\delta'^{(0)}$ and $\delta^{(0)}$.

Contrary to the original EET the approximations given in equations (20)–(22) all lead to the same N_{at}^3 scaling for $\chi^0(\omega)$. Therefore, we can now use $\Delta^{(2)}(\omega)$ as the effective energy in the EET part of the polarizability calculation. For the EET part of the calculation of the self-energy we use $\delta^{(0)}$ to approximate the effective energy since it is simple and accurate [26,27]. In Figure 1 we report the convergence behavior of the calculated energies of the VBM, CBM and band gap of Si with the number of empty states using the standard SOS approach and the SOS + EET approach using $\Delta^{(2)}(\omega)$. We also compare to results obtained with the original EET using $\delta'^{(0)}$ [26,27] since with this approximation the calculation of $\chi^{(0)}(\omega)$ has the same scaling as with $\Delta^{(2)}(\omega)$. We see that with the SOS + EET approach using $\Delta^{(2)}(\omega)$ numerical

---

[1] The differences of the EET band gaps of Si reported in this work and those reported in a previous work (Ref. [26]) are due to a different choice of the symmetrization of the effective energy in the self-energy.

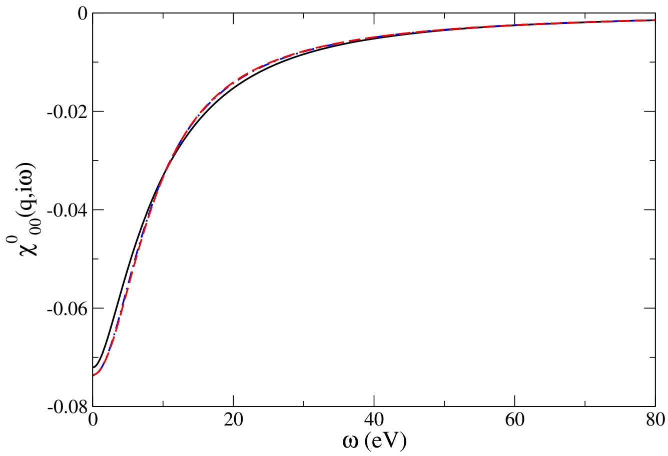

Fig. 2. (Color online) $\chi^0_{\mathbf{00}}(\mathbf{q},i\omega)$ of silicon as a function of ω for $\mathbf{q}=(-0.375,-0.25,0.375)$. Continuous (black) line: SOS; dashed (red) line: EET using $\Delta^{(2)}(\omega)$; dot-dashed (blue) line: EET using $\delta_v'^{(2)}(\omega)$.

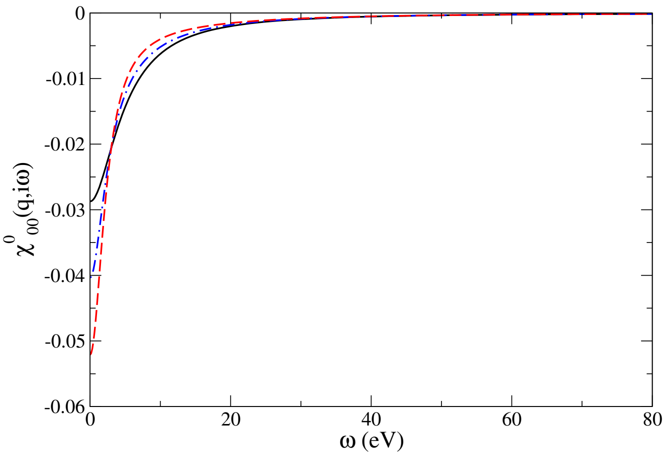

Fig. 3. (Color online) $\chi^0_{\mathbf{00}}(\mathbf{q},i\omega)$ of silicon as a function of ω for $\mathbf{q}=(-0.125,0.125,0.0)$. Continuous (black) line: SOS; dashed (red) line: EET using $\Delta^{(2)}(\omega)$; dot-dashed (blue) line: EET using $\delta_v'^{(2)}(\omega)$.

convergence of 10 meV is reached with about 20 empty bands for the band gap and about 40 empty bands for the VBM and CBM energies. Within the standard SOS approach one has to use at least 10 times as much empty states to reach the same level of convergence. The original EET using $\delta'^{(0)}$ also leads to results that converge much quicker than the SOS method but not as fast as the SOS + EET approach using $\Delta^{(2)}(\omega)$.

We note that although the approximation $\Delta^{(0)}$ given in equation (20) is the same as the approximation $\delta'^{(0)}$ described in references [26,27], the corresponding $\chi^0(\omega)$ is not necessarily the same. The difference is due to the different constraints put on $\delta'^{(0)}$ and $\Delta^{(0)}$ in the calculation of $\chi^0(\omega)$ at $\omega=0$. As described in Section 3 every $\Delta^{(0)}$ is constrained to lie within a certain range for this frequency. This check is performed for every $\mathbf{q}$, $\mathbf{G}$, and $\mathbf{G}'$. However, in the case of $\delta'^{(0)}$ this check is done for every $\mathbf{q}$, $\mathbf{G}$, $\mathbf{G}'$, and v. This also explains why the simple approximation $\delta'^{(0)}$ is doing relatively well compared to $\Delta^{(2)}(\omega)$ since the latter is checked for every $\mathbf{q}$, $\mathbf{G}$, and $\mathbf{G}'$ but not v. The calculation of $\chi^0(\omega)$ using $\Delta^{(2)}(\omega)$ therefore truly scales as N_{at}^3.

4.3 Analysis

Let us inspect more closely some elements of $\chi^0_{\mathbf{GG}'}(\mathbf{q},\omega)$. In Figure 2 we plot $\chi^0_{\mathbf{00}}(\mathbf{q},\omega)$ for Si at $\mathbf{q}=(-0.375,-0.25,0.375)$ obtained with the SOS approach, with the EET using $\delta_v'^{(2)}(\omega)$ [26,27], and with the simplified EET using $\Delta^{(2)}(\omega)$. We see that for this element we obtain a very good agreement between the two EET's and the SOS approach over the whole frequency range. The good agreement for high frequency is guaranteed by the fulfillment of the high-frequency limit by $\delta_v'^{(2)}(\omega)$ and $\Delta^{(2)}(\omega)$. In Figure 3 we plot $\chi^0_{\mathbf{00}}(\mathbf{q},\omega)$ for Si at $\mathbf{q}=(-0.125,0.125,0.0)$ obtained with the SOS approach, with the EET using $\delta_v'^{(2)}(\omega)$, and with the simplified EET using $\Delta^{(2)}(\omega)$. Again, the coincidence of the three curves at high frequency is guaranteed by the fulfillment of the high-frequency limit. However, for this element the agreement between the two EET's and the SOS approach is not very good in the low-frequency range, with the EET using $\delta_v'^{(2)}(\omega)$ being slightly better than the EET using $\Delta^{(2)}(\omega)$.

Interestingly, a numerical integration of the three curves over the positive frequency range shows that the f-sum rule is satisfied by the EET using $\delta_v'^{(2)}(\omega)$ and $\Delta^{(2)}(\omega)$. The same is true for the curves in Figure 2. This is interesting because we were not able to show the fulfillment of this sum rule analytically. It might, therefore, not be necessary to improve the EET by imposing the f-sum rule. A better strategy would probably be to try to impose some constraints for the low-frequency range. We note that this can be partially achieved by constraining $\delta_v'^{(2)}(\omega)$ and $\Delta^{(2)}(\omega)$ with mean-value theorems for integration as discussed in Section 3. For example, in the cases of the element of the polarizability plotted in Figure 3 this leads to a reduction of the absolute value of $\chi^0_{\mathbf{00}}(\mathbf{q},\omega)$ at $\omega=0$ of 15% in the case of $\delta_v'^{(2)}(\omega)$. In the case of $\Delta^{(2)}(\omega)$ the effect is negligible. Therefore, other constraints have to be found to improve $\Delta(\omega)$ in the low-frequency range.

Let us now look more closely at the effective energy $\Delta(\omega)$ itself. From equation (3) we obtain an expression for the exact $\Delta(\omega)$:

$$\Delta(\mathbf{q},\mathbf{G},\mathbf{G}',\omega)=\omega-\frac{F^{\rho\rho}(\mathbf{q},\mathbf{G},\mathbf{G}')}{X(\mathbf{q},\mathbf{G},\mathbf{G}',\omega)}, \qquad (46)$$

where $X(\omega)$ can be calculated exactly from equation (2). We can now compare the approximate $\Delta^{(2)}(\omega)$ to the exact $\Delta(\omega)$. Therefore, in Figures 4 and 5 we report $\Delta(\mathbf{q},\mathbf{0},\mathbf{0},i\omega)$ and $\Delta^{(2)}(\mathbf{q},\mathbf{0},\mathbf{0},i\omega)$ as a function of the frequency for the two $\mathbf{q}$ vectors that correspond to the $\chi^0_{\mathbf{00}}(\mathbf{q},i\omega)$ shown in Figures 2 and 3.

We see that for high frequencies $\Delta^{(2)}(\mathbf{q},\mathbf{G},\mathbf{G}',\omega)$ is tending to the exact $\Delta(\mathbf{q},\mathbf{0},\mathbf{0},\omega)$. In the limit

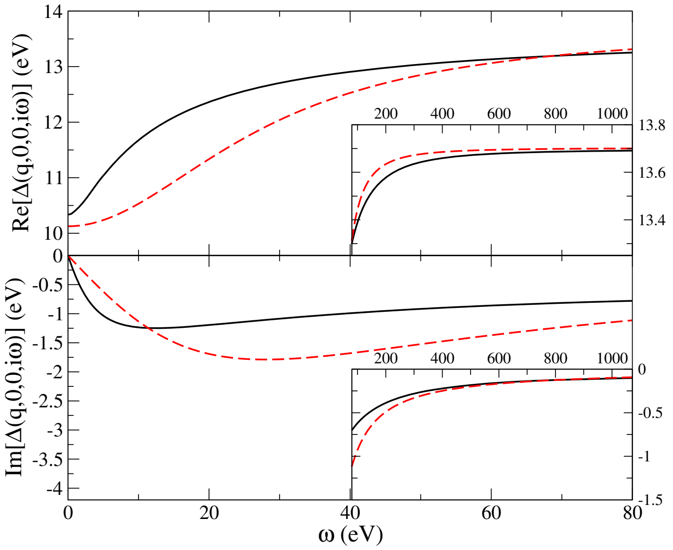

Fig. 4. (Color online) Real and imaginary part of $\Delta(\mathbf{q},\mathbf{0},\mathbf{0},i\omega)$ for silicon as a function of ω for $\mathbf{q} = (-0.375, -0.25, 0.375)$. Continuous (black) line: SOS; dashed (red) line: $\Delta^{(2)}(\omega)$. The insets show the real and imaginary part of $\Delta(\mathbf{q},\mathbf{0},\mathbf{0},i\omega)$ at high frequency.

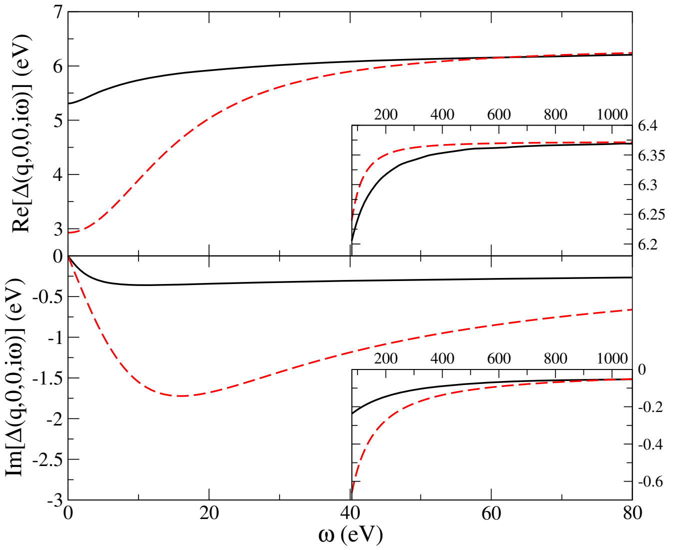

Fig. 5. (Color online) Real and imaginary part of $\Delta(\mathbf{q},\mathbf{0},\mathbf{0},i\omega)$ for silicon as a function of ω for $\mathbf{q} = (-0.125, 0.125, 0.0)$. Continuous (black) line: SOS; dashed (red) line: $\Delta^{(2)}(\omega)$. The insets show the real and imaginary part of $\Delta(\mathbf{q},\mathbf{0},\mathbf{0},i\omega)$ at high frequency.

$\omega \to \infty$ we obtain the same value for both, namely $|\mathbf{q}|^2\rho(\mathbf{0})/F^{\rho\rho}(\mathbf{q},\mathbf{0},\mathbf{0})$. In general, the high-frequency limit of both the exact $\Delta(\mathbf{q},\mathbf{G},\mathbf{G}',\omega)$ and an approximate $\Delta^{(k)}(\mathbf{q},\mathbf{G},\mathbf{G}',\omega)$ with $k > 0$ is $(\mathbf{q}+\mathbf{G})\cdot(\mathbf{q}+\mathbf{G}')\rho(\mathbf{G}'-\mathbf{G})/F^{\rho\rho}(\mathbf{q},\mathbf{G},\mathbf{G}')$. This result can be obtained in a similar way as was done to obtain the high-frequency limit of $\chi^{(0)}(\omega)$ in Section 2.3.1.

5 Conclusions

In this work we derived efficient approximations to the polarizability that scale as N_{at}^3 using a simplified effective-energy technique. We used the polarizabilities thus obtained for the calculation of G^0W^0 band gaps and showed that there is, in general, no significant loss of accuracy with respect to the standard effective-energy technique. The three simplest approximations we obtain for the polarizability with this simplified EET are explicit functionals of an independent- or quasi-particle one-body reduced density matrix. Therefore, the results of this work could be used to develop functionals in the framework of density-matrix-functional theory [31], to derive optimized-effective potentials [5,6], and to calculate total energies using the random-phase approximation [7].

We acknowledge funding from Triangle de la Physique under Contract No. 2007-71, Saint-Gobain R&D under Contract No. 091986, the European Community's FP7 under Grant agreement No. 211956, and ANR under project No. NT09-610745. We thank Julien Vidal for providing us with the pseudopotential of Zn.

References

1. A.L. Fetter, J.D. Walecka, *Quantum Theory of Many-Particle Systems* (Dover publications, 2003)
2. E. Runge, E.K.U. Gross, Phys. Rev. Lett. **52**, 997 (1984)
3. P. Hohenberg, W. Kohn, Phys. Rev. **136**, B864 (1964)
4. W. Kohn, L.J. Sham, Phys. Rev. **140**, A1133 (1965)
5. R.T. Sharp, G.K. Horton, Phys. Rev. **90**, 317 (1953)
6. J.D. Talman, W.F. Shadwick, Phys. Rev. A **14**, 36 (1976)
7. D.C. Langreth, J.P. Perdew, Solid State Commun. **17**, 1425 (1975)
8. W.G. Aulbur, L Jönsson, J.W. Wilkins, Quasiparticle calculations in solids, in *Solid State Physics* (Academic, New York, 2000), Vol. 54, p. 1
9. F. Bruneval, X. Gonze, Phys. Rev. B **78**, 085125 (2008)
10. L. Steinbeck, A. Rubio, L. Reining, M. Torrent, I.D. White, R.W. Godby, Comput. Phys. Commun. **125**, 105 (2000)
11. M.L. Tiago, S. Ismail-Beigi, S.G. Louie, Phys. Rev. B **69**, 125212 (2004)
12. M. van Schilfgaarde, T. Kotani, S.V. Faleev, Phys. Rev. B **74**, 245125 (2006)
13. F. Giustino, M.L. Cohen, S.G. Louie, Phys. Rev. B **81**, 115105 (2010)
14. P. Umari, G. Stenuit, S. Baroni, Phys. Rev. B **81**, 115104 (2010)
15. H.F. Wilson, F. Gygi, G. Galli, Phys. Rev. B **78**, 113303 (2008)
16. H.F. Wilson, D. Lu, F. Gygi, G. Galli, Phys. Rev. B **79**, 245106 (2009)
17. L. Hedin, Phys. Rev. **139**, A796 (1965)
18. W. Kang, M.S. Hybertsen, Phys. Rev. B **82**, 195108 (2010)
19. S. Baroni, A. Quattropani, Nuovo Cimento D **5**, 89 (1985)
20. S. Baroni, P. Giannozzi, A. Testa, Phys. Rev. Lett. **58**, 1861 (1987)

21. L. Reining, G. Onida, R.W. Godby, Phys. Rev. B **56**, R4301 (1997)
22. X. Blase, C. Attaccalite, V. Olevano, Phys. Rev. B **83**, 115103 (2011)
23. D. Foerster, P. Koval, D. Sánchez-Portal, J. Chem. Phys. **135**, 074105 (2011)
24. P. Umari, G. Stenuit, S. Baroni, Phys. Rev. B **79**, 201104(R) (2009)
25. G. Samsonidze, M. Jain, J. Deslippe, M.L. Cohen, S.G. Louie, Phys. Rev. Lett. **107**, 186404 (2011)
26. J.A. Berger, L. Reining, F. Sottile, Phys. Rev. B **82**, 041103R (2010)
27. J.A. Berger, L. Reining, F. Sottile, Phys. Rev. B **85**, 085126 (2012)
28. R.W. Godby, M. Schlüter, L.J. Sham, Phys. Rev. B **37**, 10159 (1988)
29. M.S. Hybertsen, S.G. Louie, Phys. Rev. B **34**, 5390 (1986)
30. F. Bechstedt, R. Del Sole, G. Cappellini, L. Reining, Solid State Commun. **84**, 765 (1992)
31. T.L. Gilbert, Phys. Rev. B **12**, 2111 (1975)
32. D.L. Johnson, Phys. Rev. B **9**, 4475 (1974)
33. X. Gonze, G.M. Rignanese, M. Verstraete, J.M. Beuken, Y. Pouillon, R. Caracas, F. Jollet, M. Torrent, G. Zerah, M. Mikami, P. Ghosez, M. Veithen, J.Y. Raty, V. Olevano, F. Bruneval, L. Reining, R. Godby, G. Onida, D.R. Hamann, D.C. Allan, Z. Kristallogr. **220**, 558 (2005)
34. R.W. Godby, R.J. Needs, Phys. Rev. Lett. **62**, 1169 (1989)
35. H. von Mangoldt, K. Knopp, *Einführung in die höhere Mathematik* (S. Hirzel Verlag, Stuttgart, 1948)
36. X. Gonze, Phys. Rev. B **55**, 10337 (1997)
37. L. Kleinman, D.M. Bylander, Phys. Rev. Lett. **48**, 1425 (1982)
38. N. Troullier, J.L. Martins, Phys. Rev. B **43**, 1993 (1991)
39. H.J. Monkhorst, J.D. Pack, Phys. Rev. B **13**, 5188 (1976)

PHYSICAL REVIEW B **85**, 085126 (2012)

Efficient *GW* calculations for $\mathrm{SnO_2}$, ZnO, and rubrene: The effective-energy technique

J. A. Berger,[1,3,*] Lucia Reining,[2,3] and Francesco Sottile[2,3]

[1]*Laboratoire de Chimie et Physique Quantiques (UMR 5626 du CNRS), IRSAMC, Université P. Sabatier, 118 Route de Narbonne, F-31062 Toulouse Cedex, France*

[2]*Laboratoire des Solides Irradiés, École Polytechnique, CNRS, CEA-DSM, F-91128 Palaiseau, France*

[3]*European Theoretical Spectroscopy Facility (ETSF)*

(Received 22 December 2011; published 27 February 2012)

In a recent Rapid Communication [J. A. Berger, L. Reining, and F. Sottile, Phys. Rev. B **82**, 041103(R) (2010)], we presented the effective-energy technique to evaluate, in an accurate and numerically efficient manner, electronic excitations by reformulating spectral sum-over-states expressions such that only occupied states appear. In our approach all the empty states are accounted for by a single effective energy that can be obtained from first principles. In this work we provide further details of the effective-energy technique, in particular, when combined with the *GW* method, in which a huge summation over empty states appears in the calculation of both the screened Coulomb interaction and the self-energy. We also give further evidence of the numerical accuracy of the effective-energy technique by applying it to the technological important materials $\mathrm{SnO_2}$ and ZnO. Finally, we use this technique to predict the band gap of bulk rubrene, an organic molecular crystal with a 140-atom unit cell.

DOI: 10.1103/PhysRevB.85.085126 PACS number(s): 71.10.−w, 71.15.Qe, 71.20.−b

I. INTRODUCTION

Many-body perturbation theory (MBPT) has become the standard tool for the calculation of quasiparticle energies. The fundamental quantity of MBPT is the single-particle Green's function, the poles of which are the electron removal and addition energies of the system. For the study of many-electron systems, such as solids and macromolecules, the state-of-the-art MBPT approximation is Hedin's *GW*[1] method because it takes into account in an accurate and efficient manner the fact that each electron is screened by its Coulomb hole.

However, the *GW* approach is a computationally demanding method, which limits its application to relatively simple systems. The main reason for this shortcoming is related to the simple but slowly converging sum-over-states (SOS) approach used in standard *GW* implementations to calculate both the screened Coulomb interaction and the self-energy. The self-energy is the quantity within MBPT that takes into account all the many-body effects beyond the Hartree potential. The SOS approach requires the summation of an, in principle, infinite number of empty states. In practice, this summation is truncated but a huge number of empty states is required to reach numerical convergence.[2–6]

In the past, several approaches have been proposed to overcome this problem of *GW*, beginning with the Coulomb hole plus screened exchange (COHSEX) approximation.[1] The COHSEX self-energy is a static approximation to the *GW* self-energy which eliminates empty states in the self-energy only, and at the price of a crude description of the quasiparticle energies. The omitted dynamical part can be approximately accounted for by a linear expansion of the *GW* self-energy with respect to the frequency.[7,8] Alternatively, one can use a Sternheimer type of approach,[9–11] that is in principle exact, for both the screened interaction and the self-energy. However, in its straightforward application, an approximate Taylor expansion around a set of reference energies is necessary to improve on the standard SOS formulation.[11]

In recent years, thanks to an increased interest in the *GW* method, many advances have been made to eliminate or reduce the number of empty states in *GW* calculations.[6,12–16] In particular, many efforts have been made to improve the Sternheimer approach for *GW* calculations by introducing efficient iterative techniques[12–14] and a self-consistent Sternheimer equation.[15] Other recent proposals to speed up *GW* calculations involve the design of efficient bases[17–19] or the use of simple approximate physical orbitals.[20]

Recently, we presented the effective-energy technique[21] (EET) to reformulate SOS expressions in terms of occupied states only. Within the EET all the empty states are accounted for by a single effective energy. Moreover, we demonstrated that this effective energy can be obtained from first principles and that already simple approximations to the effective energy lead to excellent results.[21] Therefore, the EET is an efficient method that retains the advantages of the SOS approach, such as simplicity and a good prefactor, but eliminates empty states from the calculation, leading to an immediate speedup for all system sizes. In principle, the EET could be used to speed up the calculation of many spectral quantities. The *GW* method, in particular, benefits from this approach, as an SOS is encountered twice, once for the calculation of the screening and once for the calculation of the self-energy.

The paper is organized as follows. In Sec. II we give a detailed account of the theory behind the EET. In particular, we focus on its application to the efficient calculation of the polarizability and the *GW* self-energy. In Sec. III we discuss some details of our implementation of the EET. In Sec. IV we show results of the EET for quasiparticle energies and band gaps of $\mathrm{SnO_2}$ and ZnO, two materials with interesting electronic applications, in particular, in the field of transparent conducting oxides. We compare these results to those of standard SOS calculations. We then use the EET to predict the band gap of a large molecular crystal, namely, bulk rubrene. Finally, in Sec. V we draw our conclusions.

II. THEORY

In the following we describe in detail how the EET can be used to reformulate both the GW self-energy and the polarizability in terms of occupied states only. We use atomic units everywhere unless stated otherwise and time-reversal symmetry is assumed to hold throughout.

A. The GW self-energy

The GW self-energy Σ is given by the convolution

$$\Sigma(\mathbf{r},\mathbf{r}',\omega) = i\int_{-\infty}^{\infty}\frac{d\omega'}{2\pi}e^{i\eta\omega'}G(\mathbf{r},\mathbf{r}',\omega+\omega')W(\mathbf{r},\mathbf{r}',\omega'), \quad (1)$$

where the infinitesimal η is to be taken in the limit to 0 after the frequency integration. In the above expression $G(\omega)$ is the single-particle Green's function and $W(\omega)$ is the dynamically screened Coulomb potential given by

$$W(\mathbf{r},\mathbf{r}',\omega) = \int d\mathbf{r}''\frac{\epsilon^{-1}(\mathbf{r},\mathbf{r}'',\omega)}{|\mathbf{r}''-\mathbf{r}'|}, \quad (2)$$

where the inverse dielectric function $\epsilon^{-1}(\omega)$ is defined as

$$\epsilon^{-1}(\mathbf{r},\mathbf{r}',\omega) = \delta(\mathbf{r}-\mathbf{r}') + \int d\mathbf{r}''\frac{\chi(\mathbf{r}'',\mathbf{r}',\omega)}{|\mathbf{r}-\mathbf{r}''|}. \quad (3)$$

The reducible time-ordered polarizability $\chi(\omega)$ is given by

$$\chi(\mathbf{r},\mathbf{r}',\omega) = \sum_{g=1}^{\infty}\frac{2\omega_g n_g(\mathbf{r})n_g(\mathbf{r}')}{\omega^2-\omega_g^2}, \quad (4)$$

where $\omega_g = E(N,g) - E(N,0) - i\eta$ are the neutral excitation energies of the N-electron system minus an infinitesimal $i\eta$, which ensures the correct time ordering, and n_g are the corresponding oscillator strengths. To keep our formalism general we do not yet make any assumptions on the excitation energies and oscillator strengths and, therefore, on the dielectric function. From Sec. II C onward we employ the usual random-phase approximation (RPA) for the dielectric function, which is generally associated with the GW approximation. In standard GW calculations the Green's function in Eq. (1) is replaced by a zero-order or independent-particle Green's function $G_0(\omega)$ which, in its spectral representation, reads

$$G_0(\mathbf{r},\mathbf{r}',\omega) = \sum_{i=1}^{\infty}\frac{\phi_i(\mathbf{r})\phi_i^*(\mathbf{r}')}{\omega-\varepsilon_i-i\eta\mathrm{sgn}(\mu-\varepsilon_i)}, \quad (5)$$

where $\phi_i(\mathbf{r})$ and ε_i are quasiparticle wave functions and energies, respectively, and μ is the chemical potential. Although the method that we describe in this work is valid for both finite systems and extended systems described by periodic boundary conditions, we focus here on the latter. Therefore the index i in Eq. (5) should be considered a multi-index composed of the band index, the spin, and the Bloch vector. The substitution of $G_0(\omega)$ for $G(\omega)$ in Eq. (1) permits us to carry out analytically the frequency integration in Eq. (1), giving[22]

$$\Sigma(\mathbf{r},\mathbf{r}',\omega) = \Sigma_x(\mathbf{r},\mathbf{r}'\omega) + \Sigma_c(\mathbf{r},\mathbf{r}'\omega), \quad (6)$$

$$\Sigma_x(\mathbf{r},\mathbf{r}',\omega) = \sum_{i=1}^{\infty}\theta(\mu-\varepsilon_i)\frac{\phi_i(\mathbf{r})\phi_i^*(\mathbf{r}')}{|\mathbf{r}-\mathbf{r}'|}, \quad (7)$$

$$\Sigma_c(\mathbf{r},\mathbf{r}',\omega) = \sum_{i=1}^{\infty}\sum_{g=1}^{\infty}\frac{V^g(\mathbf{r})V^g(\mathbf{r}')\phi_i(\mathbf{r})\phi_i^*(\mathbf{r}')}{\omega+\omega_g\,\mathrm{sgn}(\mu-\varepsilon_i)-\varepsilon_i}, \quad (8)$$

where we divided the self-energy into an exchange (Σ_x) and a correlation (Σ_c) part and where $V^g(\mathbf{r}) = \int d\mathbf{r}'n_g(\mathbf{r}')/|\mathbf{r}-\mathbf{r}'|$ are fluctuation potentials. Only the correlation part of the self-energy implies a summation over all the empty states, and therefore we only consider this part of the self-energy in the following.

In standard GW calculations[23,24] the quasiparticle energies are obtained from first-order perturbation theory, where the perturbation is given by the difference between the GW Hamiltonian and the Kohn-Sham (KS) Hamiltonian of density-functional theory (DFT),[25,26] i.e., $\Sigma(\mathbf{r},\mathbf{r}',\omega) - v_{\mathrm{xc}}(\mathbf{r})$, with $v_{\mathrm{xc}}(\mathbf{r})$ the exchange-correlation potential of DFT:

$$\varepsilon_n = \varepsilon_n^{\mathrm{KS}} + Z_n\langle\phi_n^{\mathrm{KS}}|\Sigma(\varepsilon_n^{\mathrm{KS}}) - v_{\mathrm{xc}}|\phi_n^{\mathrm{KS}}\rangle, \quad (9)$$

where the renormalization factor Z_n is given by

$$Z_n = \left[1 - \left.\frac{\partial\langle\phi_n^{\mathrm{KS}}|\Sigma(\omega)|\phi_n^{\mathrm{KS}}\rangle}{\partial\omega}\right|_{\omega=\varepsilon_n^{\mathrm{KS}}}\right]^{-1}. \quad (10)$$

Therefore in standard GW calculations one does not require the full knowledge of the spatial dependence of the self-energy but only has to evaluate its diagonal matrix elements. In Eqs. (9) and (10), these matrix elements involve KS wave functions. However, to keep our formulation general, in the following we consider matrix elements of general wave functions which can be the eigenfunctions either of a KS Hamiltonian or of a general static nonlocal Hamiltonian.

B. The effective-energy technique

The matrix elements of the correlation part $\Sigma_c^n(\omega) \equiv \langle n|\Sigma_c(\omega)|n\rangle$ are given by

$$\Sigma_c^n(\omega) = \sum_{i=1}^{\infty}\sum_{g=1}^{\infty}\frac{|\langle n|V^g|i\rangle|^2}{\omega+\omega_g\,\mathrm{sgn}(\mu-\varepsilon_i)-\varepsilon_i}. \quad (11)$$

The summation over i in Eq. (11) can be split into a summation over occupied states v with $\varepsilon_v < \mu$ and a summation over empty states c with $\varepsilon_c > \mu$. In the following we focus on the latter summation since it is the bottleneck in the calculation of Σ_c^n as it sums over the, in principle infinite, empty states of the system. Introducing the Fourier transforms of the fluctuation potentials,

$$V^g(\mathbf{r}) = \sum_{\mathbf{q},\mathbf{G}}V_{\mathbf{G}}^g(\mathbf{q})e^{i(\mathbf{q}+\mathbf{G})\cdot\mathbf{r}}, \quad (12)$$

$$V_{\mathbf{G}}^g(\mathbf{q}) = \frac{1}{\Omega}\int d\mathbf{r}V^g(\mathbf{r})e^{-i(\mathbf{q}+\mathbf{G})\cdot\mathbf{r}}, \quad (13)$$

with Ω the volume of the system, we can rewrite this part as

$$\Sigma_c^{n,\mathrm{emp}}(\omega) = \sum_{g=1}^{\infty}\sum_{\mathbf{q},\mathbf{G},\mathbf{G}'}V_{\mathbf{G}}^g(\mathbf{q})V_{\mathbf{G}'}^{g*}(\mathbf{q})S_g^n(\mathbf{q},\mathbf{G},\mathbf{G}',\omega), \quad (14)$$

where we defined

$$S_g^n(\mathbf{q},\mathbf{G},\mathbf{G}',\omega) = \sum_c\frac{\tilde{\rho}_{cn}^*(\mathbf{q}+\mathbf{G})\tilde{\rho}_{cn}(\mathbf{q}+\mathbf{G}')}{\omega-\omega_g-\varepsilon_c}, \quad (15)$$

in which $\tilde{\rho}_{cn}(\mathbf{q}+\mathbf{G}) = \langle c|e^{-i(\mathbf{q}+\mathbf{G})\cdot\mathbf{r}}|n\rangle$. It is the above summation over empty states that we eliminate. We now introduce a function $\delta_{ng}(\mathbf{q},\mathbf{G},\mathbf{G}',\omega)$, which is defined by the following equation:

$$S_g^n(\mathbf{q},\mathbf{G},\mathbf{G}',\omega) = \frac{\sum_c \tilde{\rho}^*_{cn}(\mathbf{q}+\mathbf{G})\tilde{\rho}_{cn}(\mathbf{q}+\mathbf{G}')}{\omega-\omega_g-\varepsilon_n-\delta_{ng}(\mathbf{q},\mathbf{G},\mathbf{G}',\omega)}. \tag{16}$$

Such a function can always be found since $\delta_{ng}(\mathbf{q},\mathbf{G},\mathbf{G}',\omega)$ has the same degrees of freedom as the left-hand side of Eq. (16). With the introduction of this function we can use the closure relation, $\sum_c |c\rangle\langle c| = 1 - \sum_v |v\rangle\langle v|$, and we obtain an expression for S_g^n which contains a summation over occupied states only. The relation in Eq. (16) is exact; the effective energy $\varepsilon_n + \delta_{ng}(\mathbf{q},\mathbf{G},\mathbf{G}',\omega)$ takes into account the contributions of all the empty states to $S_g^n(\mathbf{q},\mathbf{G},\mathbf{G}',\omega)$. For this reason we have named this approach the effective-energy technique (cf. the common-energy denominator approximation).[27] It now remains to find accurate approximations to $\delta_{ng}(\mathbf{q},\mathbf{G},\mathbf{G}',\omega)$ that do not contain any summations over empty states. In the following we show that such approximations can be obtained from first principles. Subtracting Eq. (16) from Eq. (15), and putting the right-hand side over a common denominator, we obtain

$$0 = \sum_c \left[\frac{\tilde{\rho}^*_{cn}(\mathbf{q}+\mathbf{G})\tilde{\rho}_{cn}(\mathbf{q}+\mathbf{G}')}{[\omega-\omega_g-\varepsilon_c]}\,\frac{(\varepsilon_c-\varepsilon_n-\delta_{ng}(\mathbf{q},\mathbf{G},\mathbf{G}',\omega))}{[\omega-\omega_g-\varepsilon_n-\delta_{ng}(\mathbf{q},\mathbf{G},\mathbf{G}',\omega)]}\right]. \tag{17}$$

Multiplying the above equation by $[\omega-\omega_g-\varepsilon_n-\delta_{ng}(\omega)]$ and rearranging, we arrive at

$$\begin{aligned}\delta_{ng}&(\mathbf{q},\mathbf{G},\mathbf{G}',\omega)S_g^n(\mathbf{q},\mathbf{G},\mathbf{G}',\omega)\\ &= \sum_c \frac{\tilde{\rho}^*_{cn}(\mathbf{q}+\mathbf{G})\tilde{\rho}_{cn}(\mathbf{q}+\mathbf{G}')(\varepsilon_c-\varepsilon_n)}{\omega-\omega_g-\varepsilon_c} &(18)\\ &= \frac{1}{2}\sum_c \frac{\tilde{\rho}^*_{cn}(\mathbf{q}+\mathbf{G})\langle c|[\hat{H}(\mathbf{r}'),e^{-i(\mathbf{q}+\mathbf{G}')\cdot\mathbf{r}'}]|n\rangle + \text{H.c.}}{\omega-\omega_g-\varepsilon_c}, &(19)\end{aligned}$$

where H.c. denotes the Hermitian conjugate. In the last step, we made use of the fact that the ε_i are eigenvalues of the Hamiltonian $\hat{H}(\mathbf{r})$ with eigenstates $|i\rangle$.[8] Here we consider a Hamiltonian that contains only a local potential, i.e., $\hat{H}(\mathbf{r}) = -\nabla^2_{\mathbf{r}}/2 + v(\mathbf{r})$. The derivation that follows can be easily generalized to include Hamiltonians with additional nonlocal potentials (see Appendix A for further details). We note that the symmetrization we carried out in the numerator of Eq. (19) ensures that the approximations for $\delta_{ng}(\omega)$ that we derive in the following have the correct symmetry.

Working out the commutator in Eq. (19) and dividing both sides by S_g^n, we obtain

$$\delta_{ng}(\mathbf{q},\mathbf{G},\mathbf{G}',\omega) = Q(\mathbf{q},\mathbf{G},\mathbf{G}') + \frac{\tilde{S}_g^n(\mathbf{q},\mathbf{G},\mathbf{G}',\omega)}{S_g^n(\mathbf{q},\mathbf{G},\mathbf{G}',\omega)}, \tag{20}$$

where we have defined

$$Q(\mathbf{q},\mathbf{G},\mathbf{G}') = \frac{1}{2}\left[\frac{|\mathbf{q}+\mathbf{G}|^2}{2} + \frac{|\mathbf{q}+\mathbf{G}'|^2}{2}\right], \tag{21}$$

$$\tilde{S}_g^n(\mathbf{q},\mathbf{G},\mathbf{G}',\omega) = \frac{1}{2}\sum_c \frac{\tilde{\rho}^*_{cn}(\mathbf{q}+\mathbf{G})\tilde{j}_{cn}(\mathbf{q}+\mathbf{G}') + \text{H.c.}}{[\omega-\omega_g-\varepsilon_c]}, \tag{22}$$

in which

$$\tilde{j}_{cn}(\mathbf{q}+\mathbf{G}) = \langle c|e^{-i(\mathbf{q}+\mathbf{G})\cdot\mathbf{r}}[i\nabla_{\mathbf{r}}]|n\rangle \cdot (\mathbf{q}+\mathbf{G}). \tag{23}$$

In the case where the Hamiltonian in Eq. (19) contains an additional nonlocal potential $v_{nl}(\mathbf{r},\mathbf{r}')$, the expression for $\tilde{j}_{cn}$ in Eq. (23) has an additional term. This generalized expression for $\tilde{j}_{cn}$ is shown in Eq. (A1). In Eq. (20) δ_{ng} is expressed in terms of itself through S_g^n. Since $\tilde{S}_g^n$ depends on a summation over the empty states, solving for δ_{ng} will not lead to the desired result. However, in view of the similarity of Eqs. (22) and (15), we can also rewrite Eq. (22) in terms of occupied states only in an equivalent manner to Eq. (16) by defining a modified effective energy $\epsilon_n + \tilde{\delta}_{ng}$ such that

$$\tilde{S}_g^n(\mathbf{q},\mathbf{G},\mathbf{G}',\omega) = \frac{1}{2}\,\frac{\sum_c \tilde{\rho}^*_{cn}(\mathbf{q}+\mathbf{G})\tilde{j}_{cn}(\mathbf{q}+\mathbf{G}') + \text{H.c.}}{\omega-\omega_g-\varepsilon_n-\tilde{\delta}_{ng}(\mathbf{q},\mathbf{G},\mathbf{G}',\omega)}. \tag{24}$$

Combining the above equation with Eqs. (16) and (20) leads to the following (exact) expression for $\delta_{ng}(\omega)$:

$$\begin{aligned}\delta_{ng}(\mathbf{q},\mathbf{G},\mathbf{G}',\omega) = {}& Q(\mathbf{q},\mathbf{G},\mathbf{G}')\\ &+ \frac{f_n^{\rho j}(\mathbf{q},\mathbf{G},\mathbf{G}')}{f_n^{\rho\rho}(\mathbf{q},\mathbf{G},\mathbf{G}')}\,\frac{\omega_{ng}-\delta_{ng}(\mathbf{q},\mathbf{G},\mathbf{G}',\omega)}{\omega_{ng}-\tilde{\delta}_{ng}(\mathbf{q},\mathbf{G},\mathbf{G}',\omega)},\end{aligned} \tag{25}$$

in which $\omega_{ng} = \omega - \omega_g - \varepsilon_n$ and where

$$\begin{aligned}f_n^{\rho\rho}(\mathbf{q},\mathbf{G},\mathbf{G}') = {}& -\sum_v \tilde{\rho}^*_{vn}(\mathbf{q}+\mathbf{G})\tilde{\rho}_{vn}(\mathbf{q}+\mathbf{G}')\\ &+ \tilde{\rho}_{nn}(\mathbf{G}'-\mathbf{G}),\end{aligned} \tag{26}$$

$$\begin{aligned}f_n^{\rho j}(\mathbf{q},\mathbf{G},\mathbf{G}') = {}& \frac{1}{2}\Bigg[-\sum_v \tilde{\rho}^*_{vn}(\mathbf{q}+\mathbf{G})\tilde{j}_{vn}(\mathbf{q}+\mathbf{G}')\\ &+ \langle n|e^{i(\mathbf{G}-\mathbf{G}')\cdot\mathbf{r}}(i\nabla_{\mathbf{r}})|n\rangle \cdot (\mathbf{q}+\mathbf{G}')\Bigg] + \text{H.c.}\end{aligned} \tag{27}$$

$$\begin{aligned}f_n^{jj}(\mathbf{q},\mathbf{G},\mathbf{G}') = {}& -\sum_v \tilde{j}^*_{vn}(\mathbf{q}+\mathbf{G})\tilde{j}_{vn}(\mathbf{q}+\mathbf{G}')\\ &+ (\mathbf{q}+\mathbf{G}) \cdot \langle \nabla_{\mathbf{r}} n|e^{i(\mathbf{G}-\mathbf{G}')\cdot\mathbf{r}}|\nabla_{\mathbf{r}} n\rangle \cdot (\mathbf{q}+\mathbf{G}').\end{aligned} \tag{28}$$

The expression for f_n^{jj} in Eq. (28) has been added for future reference. In principle, the above procedure could be continued *ad infinitum* by expressing $\tilde{\delta}_{ng}(\omega)$ in Eq. (25) in terms of another effective energy $\epsilon_n + \tilde{\tilde{\delta}}_{ng}(\omega)$, etc. However, one wishes to truncate the expression for δ_{ng} since, in practice, one would like to use simple expressions. In Ref. 21 we showed that simple expressions already lead to excellent results. To truncate this expression we make use of the fact that, for a homogeneous electron gas, $\delta_{ng} = \tilde{\delta}_{ng}$ (see Appendix B for further details). This motivates our first-order approximation for $\delta_{ng}(\omega)$:

$$\delta_n^{(1)}(\mathbf{q},\mathbf{G},\mathbf{G}') = Q(\mathbf{q},\mathbf{G},\mathbf{G}') + \frac{f_n^{\rho j}(\mathbf{q},\mathbf{G},\mathbf{G}')}{f_n^{\rho\rho}(\mathbf{q},\mathbf{G},\mathbf{G}')}, \tag{29}$$

which is independent of both g and ω. Higher order approximations for $\delta_{ng}(\omega)$ are obtained by continuing the iterative procedure described above and truncating the remaining expression in such a way that the approximate expression remains exact for a homogeneous electron gas. For example, a second iteration [which introduces $\tilde{\tilde{\delta}}_{ng}(\omega)$] leads to

$$\delta_{ng}(\mathbf{q},\mathbf{G},\mathbf{G}',\omega) = Q(\mathbf{q},\mathbf{G},\mathbf{G}') + \frac{f_n^{\rho j}(\mathbf{q},\mathbf{G},\mathbf{G}')}{f_n^{\rho\rho}(\mathbf{q},\mathbf{G},\mathbf{G}')} \times \left[\frac{\omega_{ng} - Q(\mathbf{q},\mathbf{G},\mathbf{G}') - \frac{f_n^{\rho j}(\mathbf{q},\mathbf{G},\mathbf{G}')}{f_n^{\rho\rho}(\mathbf{q},\mathbf{G},\mathbf{G}')} \frac{\omega_{ng} - \delta_{ng}(\mathbf{q},\mathbf{G},\mathbf{G}',\omega)}{\omega_{ng} - \tilde{\delta}_{ng}(\mathbf{q},\mathbf{G},\mathbf{G}',\omega)}}{\omega_{ng} - Q(\mathbf{q},\mathbf{G},\mathbf{G}') - \frac{f_n^{jj}(\mathbf{q},\mathbf{G},\mathbf{G}')}{f_n^{\rho j}(\mathbf{q},\mathbf{G},\mathbf{G}')} \frac{\omega_{ng} - \tilde{\delta}_{ng}(\mathbf{q},\mathbf{G},\mathbf{G}',\omega)}{\omega_{ng} - \tilde{\tilde{\delta}}_{ng}(\mathbf{q},\mathbf{G},\mathbf{G}',\omega)}} \right], \tag{30}$$

where f_n^{jj} is given in Eq. (28). Our second-order approximation for $\delta_{ng}(\omega)$ is then motivated by the fact that, for a homogeneous electron gas, $\tilde{\tilde{\delta}}_{ng}(\omega) = \tilde{\delta}_{ng}(\omega) = \delta_{ng}(\omega)$. We now summarize the first three approximations for δ_{ng} that we obtain:

$$\delta^{(0)}(\mathbf{q},\mathbf{G},\mathbf{G}') = Q(\mathbf{q},\mathbf{G},\mathbf{G}'), \tag{31}$$

$$\delta_n^{(1)}(\mathbf{q},\mathbf{G},\mathbf{G}') = Q(\mathbf{q},\mathbf{G},\mathbf{G}') + \frac{f_n^{\rho j}(\mathbf{q},\mathbf{G},\mathbf{G}')}{f_n^{\rho\rho}(\mathbf{q},\mathbf{G},\mathbf{G}')}, \tag{32}$$

$$\delta_{ng}^{(2)}(\mathbf{q},\mathbf{G},\mathbf{G}',\omega) = Q(\mathbf{q},\mathbf{G},\mathbf{G}') + \frac{f_n^{\rho j}(\mathbf{q},\mathbf{G},\mathbf{G}')}{f_n^{\rho\rho}(\mathbf{q},\mathbf{G},\mathbf{G}')} \times \left[\frac{\omega_{ng} - Q(\mathbf{q},\mathbf{G},\mathbf{G}') - \frac{f_n^{\rho j}(\mathbf{q},\mathbf{G},\mathbf{G}')}{f_n^{\rho\rho}(\mathbf{q},\mathbf{G},\mathbf{G}')}}{\omega_{ng} - Q(\mathbf{q},\mathbf{G},\mathbf{G}') - \frac{f_n^{jj}(\mathbf{q},\mathbf{G},\mathbf{G}')}{f_n^{\rho j}(\mathbf{q},\mathbf{G},\mathbf{G}')}} \right]. \tag{33}$$

Here we added a simple zero-order approximation which neglects the second term on the right-hand side of Eq. (20). With the second-order expression $\delta_{ng}^{(2)}(\omega)$, we have obtained an approximation which is frequency dependent. The expression for $\delta_{ng}^{(2)}(\omega)$ is therefore nontrivial despite its simple form. Higher order expressions for δ_{ng} will contain terms with higher order derivatives of the valence wave functions as well as derivatives of the potential. Also, these expressions are, by construction, exact for the homogeneous electron gas. Our results have shown that for inhomogeneous systems these terms can be safely neglected.[21]

C. The polarizability

In practice, the neutral excitation energies ω_g and fluctuation potentials $V_{\mathbf{G}}^g(\mathbf{q})$ that enter $\Sigma_c^n(\omega)$ are not known, and as the first step, $\epsilon(\omega)$ has to be calculated. The dielectric function can be expressed in terms of the time-ordered irreducible polarizability $\tilde{\chi}(\omega)$ according to

$$\epsilon(\mathbf{r},\mathbf{r}',\omega) = \delta(\mathbf{r}-\mathbf{r}') - \int d\mathbf{r}'' \frac{\tilde{\chi}(\mathbf{r}'',\mathbf{r}',\omega)}{|\mathbf{r}-\mathbf{r}''|}. \tag{34}$$

Within an approximation that is consistent with the GW approximation for the self-energy, $\tilde{\chi}(\omega)$ is given by a convolution of two Green's functions:

$$\tilde{\chi}(\mathbf{r},\mathbf{r}',\omega) = -i \int d\omega' G(\mathbf{r},\mathbf{r}',\omega+\omega') G(\mathbf{r}',\mathbf{r},\omega'). \tag{35}$$

In standard calculations the Green's functions are replaced by zero-order Green's functions [see Eq. (5)], which leads to $\chi^0(\omega)$, the irreducible polarizability in the RPA. The frequency integral can then be evaluated analytically, which, in reciprocal space, leads to the expression

$$\chi^0_{\mathbf{G}\mathbf{G}'}(\mathbf{q},\omega) = \sum_{s=\pm 1} \sum_{v} n_v X_v(\mathbf{q},\mathbf{G},\mathbf{G}',s\omega) + \sum_{v,v'}^{\text{occ}} (n_v - n_{v'}) \times \frac{\tilde{\rho}^*_{vv'}(\mathbf{q}+\mathbf{G})\tilde{\rho}_{v'v}(\mathbf{q}+\mathbf{G}')}{\omega - (\varepsilon_{v'} - \varepsilon_v) + i\eta \,\mathrm{sgn}(\epsilon_{v'} - \varepsilon_v)}, \tag{36}$$

in which n_v are occupation numbers and where we have defined

$$X_v(\mathbf{q},\mathbf{G},\mathbf{G}',\omega) = \sum_c \frac{\tilde{\rho}^*_{cv}(\mathbf{q}+\mathbf{G})\tilde{\rho}_{cv}(\mathbf{q}+\mathbf{G}')}{\omega - (\varepsilon_c - \varepsilon_v) + i\eta}. \tag{37}$$

We note that the second term on the right-hand side of Eq. (36) only leads to nonzero contributions in the case of systems with partially occupied bands. Since $X_v(\omega)$ has a structure similar to that of $S_g^n(\omega)$ in Eq. (15), we can also apply the EET to $X_v(\omega)$ and thus obtain an expression for $\chi^0(\omega)$ that does not contain any summations over empty states. Introducing the effective energy $\epsilon_v + \delta'_v(\omega)$, we can rewrite $X_v(\omega)$ as

$$X_v(\mathbf{q},\mathbf{G},\mathbf{G}',\omega) = \frac{f_v^{\rho\rho}(\mathbf{q},\mathbf{G},\mathbf{G}')}{\omega - \delta'_v(\mathbf{q},\mathbf{G},\mathbf{G}',\omega) + i\eta}. \tag{38}$$

To obtain approximations for $\delta'_v(\omega)$ we can follow a strategy similar to that for $\delta_{ng}(\omega)$. The first three approximations that we obtain are

$$\delta'^{(0)}(\mathbf{q},\mathbf{G},\mathbf{G}') = Q(\mathbf{q},\mathbf{G},\mathbf{G}'), \tag{39}$$

$$\delta_v'^{(1)}(\mathbf{q},\mathbf{G},\mathbf{G}') = Q(\mathbf{q},\mathbf{G},\mathbf{G}') + \frac{f_v^{\rho j}(\mathbf{q},\mathbf{G},\mathbf{G}')}{f_v^{\rho\rho}(\mathbf{q},\mathbf{G},\mathbf{G}')}, \tag{40}$$

$$\delta_v'^{(2)}(\mathbf{q},\mathbf{G},\mathbf{G}',\omega) = Q(\mathbf{q},\mathbf{G},\mathbf{G}') + \frac{f_v^{\rho j}(\mathbf{q},\mathbf{G},\mathbf{G}')}{f_v^{\rho\rho}(\mathbf{q},\mathbf{G},\mathbf{G}')} \times \left[\frac{\omega - Q(\mathbf{q},\mathbf{G},\mathbf{G}') - \frac{f_v^{\rho j}(\mathbf{q},\mathbf{G},\mathbf{G}')}{f_v^{\rho\rho}(\mathbf{q},\mathbf{G},\mathbf{G}')}}{\omega - Q(\mathbf{q},\mathbf{G},\mathbf{G}') - \frac{f_v^{jj}(\mathbf{q},\mathbf{G},\mathbf{G}')}{f_v^{\rho j}(\mathbf{q},\mathbf{G},\mathbf{G}')}} \right]. \tag{41}$$

We note that the zero- and first-order approximations for $\delta'(\omega)$ are identical in form to those for $\delta(\omega)$.

Finally, we note that the expression for $\chi_0(\omega)$ could be further simplified if, instead of approximating $X_v(\omega)$, we approximate $\sum_v n_v X_v(\omega)$. Further details of this simplified EET are given in Appendix C.

D. Exact constraints

It is known that the RPA polarizability satisfies several sum rules and exact constraints such as the high-frequency limit and the f-sum rule. These constraints allow us to obtain more insights in the approximations given by Eqs. (39)–(41). In Sec. II D 1 we show that any approximation $\delta_v'^{(k)}$ with $k > 0$ satisfies the high-frequency limit. However, the same is not true for the f-sum rule. While we can show that the first-order approximation $\delta_v'^{(1)}$ satisfies the f-sum rule for its diagonal elements (see Sec. II D 2), we cannot do the same for higher order approximations, such as $\delta_v'^{(2)}$. This opens a possible route to construct improved approximations for $\delta'_v(\omega)$. One could either constrain higher-order approximations to satisfy the f-sum rule or find an alternative or additional motivation to the electron-gas argument to truncate $\delta_v'(\omega)$ such that the f-sum rule is satisfied. Other exact constraints could be used in a similar way to improve approximations to $\delta_v'(\omega)$ and $\delta_{ng}(\omega)$.[6]

1. *The high-frequency limit*

The high-frequency limit of $\chi^0(\omega)$ is given by[28]

$$\lim_{\omega\to\infty}\omega^2\chi^0_{\mathbf{GG}'}(\mathbf{q},\omega) = (\mathbf{q}+\mathbf{G})\cdot(\mathbf{q}+\mathbf{G}')\rho(\mathbf{G}'-\mathbf{G}). \tag{42}$$

We now show that this exact constraint remains satisfied when we express $\chi^0(\omega)$ in terms of an effective energy for all approximations $\delta_v'^{(k)}(\mathbf{q},\mathbf{G},\mathbf{G}',\omega)$ with $k > 0$.

Performing a Taylor expansion of $\chi^0_{\mathbf{GG}'}(\omega)$ around $\omega = \infty$ yields, for any $k > 0$,

$$\chi^0_{\mathbf{GG}'}(\mathbf{q},\omega) = \frac{1}{\omega^2}\Bigg[2\sum_v n_v\left[f_v^{\rho\rho}Q(\mathbf{q},\mathbf{G},\mathbf{G}') + f_v^{\rho j}\right] + \sum_{v,v'}(n_v - n_{v'})\tilde{\rho}^*_{v'v}(\mathbf{G})\tilde{\rho}_{v'v}(\mathbf{G}')(\varepsilon_{v'}-\varepsilon_v)\Bigg] + O\left(\frac{1}{\omega^4}\right). \tag{43}$$

For notational convenience, we have suppressed the dependence of $f_v^{\rho\rho}$ and $f_v^{\rho j}$ on $\mathbf{q}$, $\mathbf{G}$, and $\mathbf{G}'$ as well as the dependence of $\tilde{\rho}_{v'v}$ on $\mathbf{q}$. Using the relation

$$f_v^{\rho\rho}Q(\mathbf{q},\mathbf{G},\mathbf{G}') + f_v^{\rho j} = \sum_c \tilde{\rho}^*_{cv}(\mathbf{G})\tilde{\rho}_{cv}(\mathbf{G}')(\varepsilon_c - \varepsilon_v), \tag{44}$$

which can be verified by substitution of Eqs. (26) and (27), we obtain

$$\begin{aligned}\chi^0_{\mathbf{GG}'}(\mathbf{q},\omega) &= \frac{1}{\omega^2}\sum_{n,n'}(n_n - n_{n'})\tilde{\rho}^*_{n'n}(\mathbf{G})\tilde{\rho}_{n'n}(\mathbf{G}')(\varepsilon_{n'}-\varepsilon_n) + O\left(\frac{1}{\omega^4}\right) &(45)\\ &= \frac{1}{\omega^2}\sum_n n_n\langle n|[e^{i(\mathbf{q}+\mathbf{G})\cdot\mathbf{r}},[\hat{H}(\mathbf{r}),e^{-i(\mathbf{q}+\mathbf{G}')\cdot\mathbf{r}}]]|n\rangle + O\left(\frac{1}{\omega^4}\right) &(46)\\ &= \frac{1}{\omega^2}(\mathbf{q}+\mathbf{G})\cdot(\mathbf{q}+\mathbf{G}')\rho(\mathbf{G}'-\mathbf{G}) + O\left(\frac{1}{\omega^4}\right). &(47)\end{aligned}$$

We therefore obtain

$$\lim_{\omega\to\infty}\omega^2\chi^0_{\mathbf{GG}'}(\mathbf{q},\omega) = (\mathbf{q}+\mathbf{G})\cdot(\mathbf{q}+\mathbf{G}')\rho(\mathbf{G}'-\mathbf{G}), \tag{48}$$

which proves that the high-frequency limit is satisfied for all $\delta_v'^{(k)}(\mathbf{q},\mathbf{G},\mathbf{G}',\omega)$ with $k > 0$.

2. *The f-sum rule*

The generalized f-sum rule is given by[28]

$$\int_0^\infty d\omega\omega\mathrm{Im}\chi^0_{\mathbf{GG}'}(\mathbf{q},\omega) = -\frac{\pi}{2}(\mathbf{q}+\mathbf{G})\cdot(\mathbf{q}+\mathbf{G}')\rho(\mathbf{G}'-\mathbf{G}). \tag{49}$$

We now show that this exact constraint also holds for $\chi^0(\omega)$ when it is expressed in terms of an effective energy using $\delta_v'^{(1)}$ if we assume that $\delta_v'^{(1)}(\mathbf{q},\mathbf{G},\mathbf{G}')$ is both real and nonnegative. This assumption holds true for the diagonal elements $\delta_v'^{(1)}(\mathbf{q},\mathbf{G},\mathbf{G})$, as can be verified from Eq. (40). We can now use the relation

$$\lim_{\eta\to 0^+}\frac{1}{x\pm i\eta} = \mathcal{P}\frac{1}{x} \mp i\pi\delta(x), \tag{50}$$

where $\mathcal{P}$ denotes the principal value, to write

$$\begin{aligned}\int_0^\infty d\omega\omega\mathrm{Im}\chi^0_{\mathbf{GG}'}(\mathbf{q},\omega) &= -\pi\sum_v n_v f_v^{\rho\rho}\int_0^\infty d\omega\omega\left[\delta\left(\omega-\delta_v'^{(1)}\right)+\delta\left(\omega+\delta_v'^{(1)}\right)\right]\\ &\quad -\pi\sum_{v.v'}(n_v-n_{v'})\tilde{\rho}^*_{v'v}(\mathbf{G})\tilde{\rho}_{v'v}(\mathbf{G}')\\ &\quad\times\int_0^\infty d\omega\omega\delta(\omega-(\varepsilon_{v'}-\varepsilon_v)).\end{aligned} \tag{51}$$

For notational convenience, we have suppressed the dependence of $\delta_v'^{(1)}$ and $f_v^{\rho\rho}$ on $\mathbf{q}$, $\mathbf{G}$, and $\mathbf{G}'$ as well as the dependence of $\tilde{\rho}_{v'v}$ on $\mathbf{q}$. Since, thanks to time-reversal symmetry,

$$\begin{aligned}&\sum_{v.v'}(n_v-n_{v'})\tilde{\rho}^*_{v'v}(\mathbf{G})\tilde{\rho}_{v'v}(\mathbf{G}')\int_0^\infty d\omega\omega\delta(\omega-(\varepsilon_{v'}-\varepsilon_v))\\ &\quad=\sum_{v.v'}(n_v-n_{v'})\tilde{\rho}^*_{v'v}(\mathbf{G})\tilde{\rho}_{v'v}(\mathbf{G}')\int_{-\infty}^0 d\omega\omega\delta(\omega-(\varepsilon_{v'}-\varepsilon_v)),\end{aligned} \tag{52}$$

we can write

$$\begin{aligned}\int_0^\infty d\omega\omega\mathrm{Im}\chi^0_{\mathbf{GG}'}(\mathbf{q},\omega) &= -\pi\sum_v n_v f_v^{\rho\rho}\delta_v'^{(1)} - \frac{\pi}{2}\sum_{v.v'}(n_v-n_{v'})\tilde{\rho}^*_{v'v}(\mathbf{G})\\ &\quad\times\tilde{\rho}_{v'v}(\mathbf{G}')(\varepsilon_{v'}-\varepsilon_v) &(53)\\ &= -\frac{\pi}{2}\sum_{n.n'}(n_n-n_{n'})\tilde{\rho}^*_{n'n}(\mathbf{G})\tilde{\rho}_{n'n}(\mathbf{G}')(\varepsilon_{n'}-\varepsilon_n) &(54)\\ &= -\frac{\pi}{2}(\mathbf{q}+\mathbf{G})\cdot(\mathbf{q}+\mathbf{G}')\rho(\mathbf{G}'-\mathbf{G}), &(55)\end{aligned}$$

where we used Eq. (44). Therefore, the f-sum rule is satisfied for $\delta_v'^{(1)}(\mathbf{q},\mathbf{G},\mathbf{G}')$. Using the same procedure we cannot show that the f-sum rule is satisfied for $\delta'^{(0)}(\mathbf{q},\mathbf{G},\mathbf{G}')$ and $\delta_v'^{(2)}(\mathbf{q},\mathbf{G},\mathbf{G}',\omega)$

E. Converging GW calculations

In Ref. 21 we used the EET to obtain approximations to the GW self-energy and the independent-particle polarizability which do not contain summations over empty states. We showed there that simple approximations, such as $\delta^{(2)}(\omega) + \delta'^{(2)}(\omega)$, are accurate and numerically efficient. However, one might wish to converge to the numerically exact GW result. Such numerically exact results can be obtained efficiently and in a systematic way by combining the EET and the SOS approach. Let us illustrate how we achieve this goal for the self-energy. We first split the expression in Eq. (15) into two parts according to

$$S^n_g(\mathbf{q},\mathbf{G},\mathbf{G}',\omega) = \sum_{c=N_v+1}^{M} \frac{\tilde{\rho}^*_{cn}(\mathbf{q}+\mathbf{G})\tilde{\rho}_{cn}(\mathbf{q}+\mathbf{G}')}{\omega-\omega_g-\varepsilon_c} + \sum_{c=M+1}^{\infty} \frac{\tilde{\rho}^*_{cn}(\mathbf{q}+\mathbf{G})\tilde{\rho}_{cn}(\mathbf{q}+\mathbf{G}')}{\omega_{ng}-\delta_{ng}(\mathbf{q},\mathbf{G},\mathbf{G}',\omega)}, \quad (56)$$

where N_v is the number of occupied states. Here we used the EET only in the second term on the right-hand side, which contains a summation over all the empty states starting from $M+1$. If we choose $M = N_v$, we retrieve Eq. (16). However, if we choose $M > N_v$, the part that needs to be approximated with the EET becomes smaller as M increases. In this way we have obtained an efficient way to converge $S^n_g(\omega)$ with respect to the number of empty states. In a similar way, one can efficiently converge $\chi_0(\omega)$. We note that this procedure is similar to the one proposed by Bruneval and Gonze,[6] with the important difference that our approach generally converges more rapidly and, most importantly, is parameter free.

F. Range of applicability

In this section we briefly discuss the range of applicability of the EET. As mentioned before, in principle, the EET can be used to rewrite any SOS expression in terms of occupied states only, namely, by the introduction of an effective energy with sufficient degrees of freedom. However, we do not expect that simple approximations to this effective energy will lead to accurate results in all cases.

Let us consider, for example, the imaginary part of the head of the polarizability tensor $\chi^0_{\mathbf{GG}'}(\omega)$. The SOS expression for this element is given by

$$\mathrm{Im}\chi^0_{\mathbf{00}}(\mathbf{q},\omega) = \sum_{v,c}\int d\mathbf{r}\int d\mathbf{r}'\phi^*_v(\mathbf{r})\phi_v(\mathbf{r})\phi^*_c(\mathbf{r}')\phi_v(\mathbf{r}') \times e^{i\mathbf{q}\cdot(\mathbf{r}-\mathbf{r}')}\delta\big(\omega-(\epsilon_c-\epsilon_v)\big), \quad (57)$$

where, for simplicity, we assumed a material with a gap and $\omega > 0$. If we compare this to the EET result using $\delta'^{(0)}$ and $\delta'^{(1)}_v$, we obtain

$$\mathrm{Im}\chi^0_{\mathbf{00}}(\mathbf{q},\omega) = \sum_v f^{\rho\rho}_v(\mathbf{q},\mathbf{0},\mathbf{0})\delta\big(\omega-\delta'^{(0)}(\mathbf{q},\mathbf{0},\mathbf{0})\big), \quad (58)$$

$$\mathrm{Im}\chi^0_{\mathbf{00}}(\mathbf{q},\omega) = \sum_v f^{\rho\rho}_v(\mathbf{q},\mathbf{0},\mathbf{0})\delta\big(\omega-\delta'^{(1)}_v(\mathbf{q},\mathbf{0},\mathbf{0})\big). \quad (59)$$

While Eq. (57) consists of a summation over a number of poles equal to N_vN_c, Eq. (58) contains only a single pole while Eq. (59) contains N_v poles. Therefore, with the simple frequency-independent approximations $\delta'^{(0)}$ and $\delta'^{(1)}_v$, we will, in general, not be able to describe $\mathrm{Im}\chi^0_{\mathbf{00}}(\omega)$ in an accurate way. Hence, we expect that the calculation of an accurate absorption spectrum, which is closely related to $\mathrm{Im}\chi^0_{\mathbf{00}}(\omega)$, would require complicated frequency-dependent effective energies far beyond $\delta^{(1)}_v$. We note that, nevertheless, $\chi^0_{\mathbf{00}}(\omega)$ expressed in terms of $\delta^{(1)}_v$ satisfies the high-frequency limit and the generalized f-sum rule (see Secs. II D 1 and II D 2).

On the other hand, we expect that quantities which depend on frequency integrals over $\chi^0(\omega)$, such as the GW self-energy, can be accurately reproduced with simple approximations to $\delta'_v(\omega)$, precisely because exact constraints such as the generalized f-sum rule and the high-frequency limit are satisfied. Similarly, we expect that summations over $\mathbf{q}$, $\mathbf{G}$, and $\mathbf{G}'$, such as those that occur in the calculation of the self-energy matrix elements, allow us to use relatively simple approximations for $\delta_v(\omega)$.

III. IMPLEMENTATION

We implemented the EET described above in the ABINIT software package.[29] In this section we would like to discuss two technical details of our implementation.

First, as can be verified from Eqs. (14) and (15), $\Sigma^{n,\mathrm{emp}}_c(\omega)$ does not have poles in the energy range $[-\infty,\epsilon_L+\omega_1]$, where ϵ_L is the eigenvalue of the lowest empty state and ω_1 is the first neutral excitation energy. In practice, however, the approximations for $\delta_{ng}(\omega)$ given in Eqs. (31)–(33), might lead to spurious poles in this energy range. Therefore, to avoid numerical instabilities, we constrain the effective energy $\epsilon_n+\delta_{ng}(\omega)$ in Eq. (16) to the range $[\epsilon_L,\infty]$; i.e., $\delta_{ng}(\omega)$ is set to $\epsilon_L-\epsilon_n$ in the case that the effective energy $\epsilon_n+\delta_{ng}(\omega)$ obtained using the approximations in Eqs. (39)–(41) results in $\epsilon_n+\delta_{ng}(\omega)<\epsilon_L$. Using the first mean-value theorem for integration,[30] one can show that this constraint is exact for all diagonal elements $\delta_{ng}(\mathbf{q},\mathbf{G},\mathbf{G},\omega)$ since in this case the numerator on the right-hand side of Eq. (15) is non-negative for every c.

In standard GW calculations the independent-particle polarizability is evaluated on the imaginary-frequency axis, where it has no poles (excepting metals at $\omega = 0$), and then fitted to a plasmon-pole model (PPM).[23,31] Therefore, similar numerical instabilities as described above might only occur in the evaluation of $\chi^0(i\omega)$ at $\omega = 0$. Since there should be no pole at $\omega = 0$ (for systems with a gap), we constrain $\epsilon_v+\delta'_v(\omega)$ in Eq. (38) to the range $[\epsilon_L,\infty]$ for this frequency in a manner similar to that explained above for $\epsilon_n+\delta_{ng}(\omega)$.

Second, as within the SOS approach, the calculation of the head and wings of the dielectric matrix for $\mathbf{q}\to 0$ requires special attention since for these elements one cannot simply set $\mathbf{q} = 0$. One usually employs $\mathbf{k}\cdot\mathbf{p}$ perturbation theory to evaluate the limit $\mathbf{q}\to 0$ for these elements. However, $\mathbf{k}\cdot\mathbf{p}$ perturbation theory introduces an additional summation over empty states. This can, for example, be avoided by using a small but finite $\mathbf{q}$ or by numerically expanding the wave functions around $\mathbf{q} = 0$.[32] However, since the calculation of the head and wings is an order of magnitude smaller than that of the body and the number of empty states required to reach convergence for these elements is small, we found it more efficient to simply use the SOS approach for the head and wings when $\mathbf{q}\to 0$. The extra computational cost is negligible.

IV. RESULTS

A. Computational details

All our calculations were performed using separable norm-conserving pseudopotentials.[33,34] For Sn, the semicore electrons of the 4s, 4p, and 4d states were considered as

TABLE I. Calculated energies (in eV) for the VBM, CBM, and fundamental gap (E_g) of SnO_2. The last column contains numerically converged G^0W^0 quasiparticle energies. See the text for further details.

		G^0W^0	
	LDA	EET	SOS + EET
CBM	8.20	8.73	8.74
VBM	7.26	5.87	5.85
E_g	0.94	2.86	2.89

valence electrons. Similarly, for Zn, the semicore electrons of the $3s$, $3p$, and $3d$ states were considered as valence electrons.

In the case of SnO_2 we used calculcated lattice parameters and atomic positions which we obtained from a density-functional calculation using the local-density approximation (LDA), while in the cases of ZnO and bulk rubrene we used experimental values. To compare with the work of Sai *et al.*,[35] we also performed calculations for the model geometry of bulk rubrene that they introduced. More details are given below.

The k-point sampling of the Brillouin zone was carried out with a Monkhorst-Pack (MP) grid.[36] For SnO_2 and ZnO we used a $4 \times 4 \times 6$ and $6 \times 6 \times 4$ MP grid, respectively. In the case of bulk rubrene we used a $2 \times 2 \times 2$ and $2 \times 4 \times 2$ MP grid, for the experimental and model geometry, respectively. For the calculation of the self-energy these grids were shifted such that they contain the Γ point, while for the calculation of the dielectric matrix they were shifted such that they do not include the Γ point. The ground-state cutoff energies for SnO_2, ZnO, and bulk rubrene were 240, 350, and 100 Ry, respectively. The cutoff energies for the dielectric matrix for SnO_2, ZnO, and bulk rubrene were 48, 80, and 13 Ry, respectively. We used the generalized PPM of Godby and Needs[31] to fit $\epsilon^{-1}(\omega)$.

B. SnO_2

SnO_2 has a rutile crystal structure with lattice parameters $a = 4.726$ Å and $c = 3.191$ Å, which we obtained from a DFT-LDA calculation and which agrees well with the experimental values $a = 4.737$ Å and $c = 3.186$ Å.[37] We calculated the G^0W^0 quasiparticle energies at the valence band maximum (VBM) and conduction band minimum (CBM) of SnO_2, both located at the Γ point, with our EET using $\delta'^{(2)}$ and $\delta^{(2)}$ in the calculation of the screening and self-energy, respectively. These values for the VBM and CBM as well as the resulting band gap are reported in Table I.

We would like to compare these values to the quasiparticle energies obtained within the standard SOS approach. However, to obtain numerically converged absolute quasiparticle energies is even more difficult than to obtain numerically converged quasiparticle energy differences such as band gaps. While 1600 empty bands (corresponding to a 32.2-Ry energy cutoff)[38] included in the self-energy calculation were sufficient to reach convergence for the band gap, convergence for the quasiparticle energies at the VBM and CBM was still not reached. Therefore, in order to compare our approximate EET results to numerically converged values, we employed the strategy outlined in Sec. II E to combine the SOS aproach with the EET.

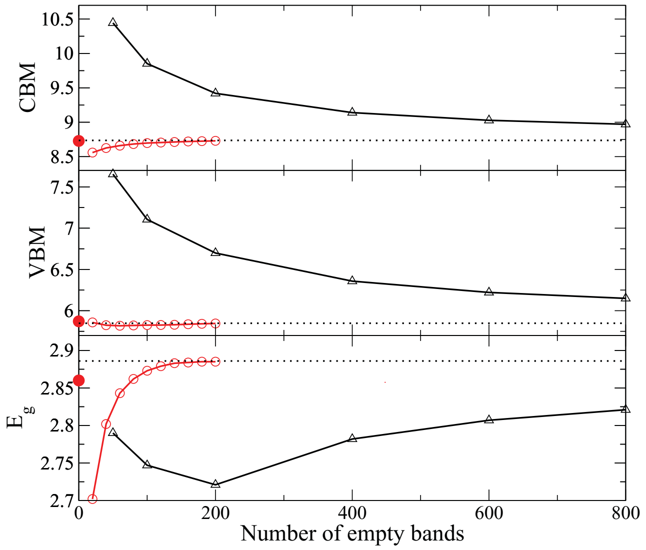

FIG. 1. (Color online) Convergence behavior of the calculated energies (in eV) of the VBM, CBM, and fundamental gap (E_g) of SnO_2 with the number of empty states in both the screening and the self-energy calculcations. Triangles (black), SOS approach; open (red) circles, SOS + EET approach using $\delta'^{(0)}$ and $\delta^{(0)}$; filled (red) circles, EET using $\delta'^{(2)}$ and $\delta^{(2)}$ without empty states.

As an alternative to the accurate high-order approximations for δ' and δ, this SOS + EET approach allows us to combine the slightly less accurate but very simple approximations $\delta^{(0)}$ and $\delta'^{(0)}$ given in Eqs. (31) and (39) with the SOS approach using only very few empty states. In Fig. 1 we report the convergence behavior of the calculated energies of the VBM, CBM and band gap of SnO_2 with the number of empty states using the standard SOS approach and the SOS+EET approach. We see that using the SOS + EET approach, numerical convergence of 10 meV is reached with slightly more than 100 empty bands (corresponding to a 3.5-Ry energy cutoff).[38] This is true, not only for the band gap, but also for the absolute quasiparticle energies at the VBM and CBM. By contrast, the SOS approach has not reached convergence for any of these quantities with as many as 800 empty bands (corresponding to a 19.6-Ry energy cutoff).[38]

We are now also able to compare the converged SOS + EET results with those obtained with our approximate EET scheme using no empty states. This comparison is reported in Table I. We conclude that the values we obtained with our EET using $\delta'^{(2)}$ and $\delta^{(2)}$ are in excellent agreement with the numerically exact values.[39]

C. ZnO

Recently there has been much debate about the numerically exact value of the G^0W^0 band gap of ZnO. This discussion started with the publication of the work by Shih *et al.*[40] in which the authors claimed that the G^0W^0 band gap of ZnO is at least 3.4 eV. This value is significantly larger than previously reported values, which were in the range of 2.1–2.6 eV.[41–44] The explanation by Shih *et al.* is an extremely slow convergence of the band gap with the number of empty states included in the calculation of the self-energy. To obtain a band

TABLE II. Calculated energies (in eV) for the VBM, CBM, and fundamental gap (E_g) of ZnO. The last column contains numerically converged G^0W^0 quasiparticle energies. See the text for further details.

		G^0W^0	
	LDA	EET	SOS + EET
VBM	6.38	5.04	4.97
CBM	7.19	7.43	7.53
E_g	0.82	2.39	2.56

gap of 3.4 eV they had to include 3000 empty bands in their self-energy calculation. Subsequent calculations using the full-potential linear augmented-plane-wave (FLAPW) method[45] performed by Friedrich *et al.*[46] confirmed the extremely slow convergence of the ZnO band gap with the number of empty states. However, the band gap of 2.83 eV that they obtained by extrapolating to an infinite number of empty states was substantially lower than the 3.4 eV found by Shih *et al.* Recently it was shown by Stankovski *et al.*[47] that the main reason for the large discrepancy between the band gap obtained by Shih *et al.* and those obtained in the other works is due to the PPM of Hybertsen and Louie,[23] which was adopted by Shih *et al.* but not by the others. Stankovski *et al.* showed that the use of the Hybertsen-Louie PPM leads to a large overestimation of the G^0W^0 band gap of ZnO. They also showed that the ZnO band gap obtained using the Godby-Needs PPM[31] agrees very well with the band gap obtained from a calculation which avoids the use of a PPM. Nevertheless, also the band gaps obtained without a PPM and with the Godby-Needs PPM show a very slow convergence with the number of empty states. These works motivated us to study ZnO with the EET, in which the summation over empty states can be avoided.

ZnO has a wurtzite crystal structure with lattice parameters $a = 3.249$ Å and $c = 5.207$ Å.[48] In Table II we report the G^0W^0 band gap of ZnO as well as the absolute G^0W^0 quasiparticle energies at the VBM and CBM, which are both located at the Γ point obtained with the EET using $\delta'^{(2)}$ and $\delta^{(2)}$ in the calculation of W and Σ, respectively. To compare these values to numerically converged G^0W^0 energies, once again, we use the SOS + EET approach since also for ZnO the SOS approach alone converges extremely slowly with respect to the number of empty bands. In Fig. 2 we report the convergence behavior of the calculated energies of the VBM, CBM, and band gap of ZnO with the number of empty states using the standard SOS approach and the SOS + EET approach. We see that the band gap using the SOS + EET approach does not converge as quickly as was the case for SnO$_2$ but convergence is still reached much faster than with the SOS approach alone. We conclude that the converged G^0W^0 band gap of ZnO is 2.56 eV. The difference with respect to the extrapolated FLAPW result of Friedrich *et al.* is less than 0.3 eV.

We can now compare the converged SOS + EET results with those obtained with our approximate EET scheme using no empty states. We report this comparison in Table II. We conclude that the absolute quasiparticle energies at the VBM and CBM that we obtained with our EET using $\delta'^{(2)}$ and $\delta^{(2)}$ are in very good agreement with the numerically exact values.

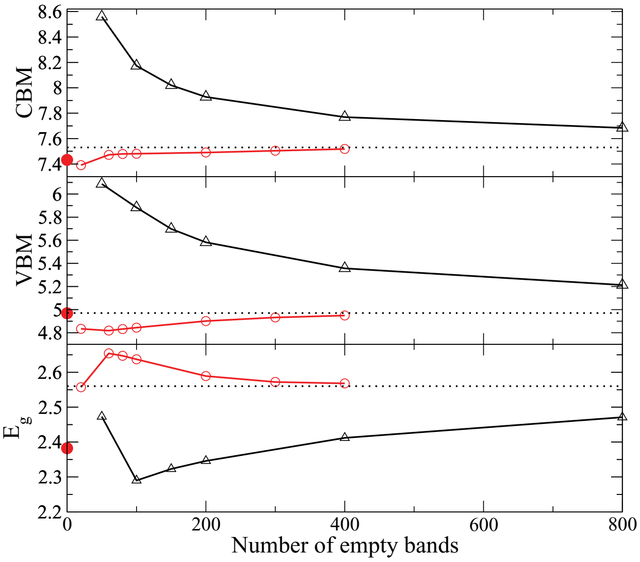

FIG. 2. (Color online) Convergence behavior of the calculated energies (in eV) of the VBM, CBM, and fundamental gap (E_g) of ZnO with the number of empty states in both the screening and the self-energy calculations. Triangles (black), SOS approach; open (red) circles, SOS + EET approach using $\delta'^{(0)}$ and $\delta^{(0)}$; filled (red) circles, EET using $\delta'^{(2)}$ and $\delta^{(2)}$ without empty states.

Due to the fact that the VBM energy is slightly underestimated while the CBM energy is slightly overestimated, the difference between the resulting EET band gap and the numerically exact G^0W^0 gap is slightly larger for ZnO than for SnO$_2$ and the other materials we have studied in a previous work.[21] However, with $\sim$5% deviation, we can still consider the agreement good.

D. Bulk rubrene

Now that we have verified the accuracy of the EET we can safely apply it to predict the band gaps of larger systems, which are cumbersome to treat with the standard SOS approach. Here we study bulk rubrene, an organic molecular crystal. Rubrene is an interesting material with many technological applications, for example, in organic light-emitting diodes and organic field-effect transistors to create flexible electronics,[49] but is computationally challenging due to the large number of atoms involved.

Crystalline rubrene has an orthorhombic unit cell with lattice parameters $a = 14.4$ Å, $b = 7.2$ Å, and $c = 26.8$ Å.[50] Each unit cell contains two identical *ab* planes separated by $c/2$, with a relative shift between the planes of $b/2$. Therefore, the unit cell of bulk rubrene contains two rubrene molecules, for a total of 140 atoms per unit cell. To the best of our knowledge, the only *GW* calculation on bulk rubrene was carried out by Sai *et al.*[35] However, to reduce the cost of their calculations, the authors used a model geometry for the rubrene unit cell in which they neglected the relative shift of the two *ab* planes. This allowed them to use a reduced unit cell with lattice parameters $a = 14.4$ Å, $b = 7.2$ Å, and $c = 14.4$ Å. They expected that the interactions between rubrene molecules in adjacent *ab* planes is weak and therefore relatively insensitive to the relative shift of the two planes. They then further justified this approximation by showing that the band gap

TABLE III. Fundamental gap (E_g; in eV) of bulk rubrene within G^0W^0. Details of the model are explained in the text.

	EET	EET (model)	Ref. 35 (model)
E_g	2.5	2.9	2.8

they obtain for the model geometry (1.20 eV) is only slightly larger than the band gap of the experimental geometry (1.14 eV) when calculated within DFT using a generalized-gradient approximation (GGA).

In this work the DFT ground-state calculcations are performed within the LDA. However, the DFT-LDA band gaps that we obtain, i.e., 1.13 and 1.20 eV for the experimental and model geometry, respectively, are in very close agreement with the DFT-GGA band gaps reported by Sai *et al.*, i.e., 1.14 and 1.20 eV. We therefore assume that a comparison between our G^0W^0 results and those of Sai *et al.* will not be hindered by this difference in the ground-state calculation.

In Table III we report the G^0W^0 band gaps of bulk rubrene that we obtained with the EET, using $\delta'^{(2)}$ and $\delta^{(2)}$, for the experimental and model geometry as well as the G^0W^0 band gap obtained by Sai *et al.* for the model geometry. We see that the band gap we obtain for the model geometry is in good agreement with that found by Sai *et al.* With the EET we can now also calculate the band gap for the unit cell with the experimental geometry containing 140 atoms. This results in a band gap of 2.5 eV, which is 0.4 eV smaller than that for the model geometry. This indicates that the interactions between adjacent *ab* planes are not weak and therefore the relative shift of these planes cannot be neglected.

V. CONCLUSIONS

The scope of this work is multifold. First, we have given further details of the EET, a simple method we introduced recently[21] to evaluate spectral representations in an accurate and efficient manner without summing over empty states as is done in the standard SOS approach. In particular, we showed how the EET can be applied to reformulate the expressions for the *GW* self-energy and the independent-particle polarizability in terms of occupied states only by introducing a single effective energy which takes into account all the empty states. Second, we provided further evidence of the accuracy of the EET by showing that quasiparticle energies and band gaps obtained with *GW* using the EET agree well with those obtained using the standard SOS approach. Third, with the EET we were able to resolve the problem of the slow convergence of the ZnO band gap with the number of empty states in a *GW* calculation. Fourth, thanks to the EET, we could predict the band gap of bulk rubrene, a technologically interesting material for inorganic devices with a 140-atom unit cell.

Finally, the results obtained in this and a previous work[21] have shown that, with the EET, we obtain accurate results for a large variety of systems: an *sp* semiconductor (Si), a wide-gap insulator (solid Ar), an atom (Ar), *d*-band semiconductors ($\mathrm{SnO_2}$, ZnO), and an organic molecular crystal (rubrene).

ACKNOWLEDGMENTS

We thank János Ángyán, Friedhelm Bechstedt, Christoph Friedrich, Matteo Giantomassi, Xavier Gonze, John Rehr, Andreas Savin, and Martin Stankovski for helpful discussions. We thank Julien Vidal for providing us with the pseudopotential of Zn. We acknowledge funding from Triangle de la Physique under Contract No. 2007-71, Saint-Gobain R&D under Contract No. 091986, the European Community's FP7 under Grant No. 211956, and the ANR under Project No. NT09-610745.

APPENDIX A: NONLOCAL POTENTIALS

In the case where the Hamiltonian in Eq. (19) contains an additional nonlocal potential $v_{nl}(\mathbf{r},\mathbf{r}')$, the expression for $\tilde{j}_{cn}$ in Eq. (23) is slightly modified:

$$\begin{aligned}\tilde{j}_{cn}(\mathbf{q}+\mathbf{G}) = {}& \langle c|e^{-i(\mathbf{q}+\mathbf{G})\cdot\mathbf{r}}[i\nabla_{\mathbf{r}}]|n\rangle \cdot (\mathbf{q}+\mathbf{G}) \\ & + \int d\mathbf{r}d\mathbf{r}'\phi_c^*(\mathbf{r})v_{nl}(\mathbf{r},\mathbf{r}') \\ & \times [e^{-i(\mathbf{q}+\mathbf{G})\cdot\mathbf{r}'} - e^{-i(\mathbf{q}+\mathbf{G})\cdot\mathbf{r}}]\phi_n(\mathbf{r}'). \quad \text{(A1)}\end{aligned}$$

If v_{nl} refers to the nonlocal part of a separable pseudopotential, i.e., $v_{nl}(\mathbf{r},\mathbf{r}') = \sum_s \tilde{v}_s(\mathbf{r})\tilde{v}_s(\mathbf{r}')$, the last term on the right-hand side of Eq. (A1) can be written as

$$\begin{aligned}&\int d\mathbf{r}d\mathbf{r}'\phi_c^*(\mathbf{r})v_{nl}(\mathbf{r},\mathbf{r}')[e^{-i(\mathbf{q}+\mathbf{G})\cdot\mathbf{r}'} - e^{-i(\mathbf{q}+\mathbf{G})\cdot\mathbf{r}}]\phi_n(\mathbf{r}') \\ &= \sum_s \int d\mathbf{r}\phi_c^*(\mathbf{r})\tilde{v}_s(\mathbf{r}) \int d\mathbf{r}'\tilde{v}_s(\mathbf{r}')e^{-i(\mathbf{q}+\mathbf{G})\cdot\mathbf{r}'}\phi_n(\mathbf{r}') \\ &\quad - \sum_s \int d\mathbf{r}\phi_c^*(\mathbf{r})e^{-i(\mathbf{q}+\mathbf{G})\cdot\mathbf{r}}\tilde{v}_s(\mathbf{r}) \int d\mathbf{r}'\tilde{v}_s(\mathbf{r}')\phi_n(\mathbf{r}'),\end{aligned}$$

$$\text{(A2)}$$

which can be rapidly calculated in practice. In the case of pseudopotentials of the Kleinman-Bylander type,[33] the index s in the above expression is the multi-index $s = nlm$, where n is the number of the atom, l is the orbital angular momentum quantum number, and m is the magnetic quantum number.

APPENDIX B: A HOMOGENEOUS ELECTRON GAS

Here we show that $\delta_{ng}(\omega)$ and $\tilde{\delta}_{ng}(\omega)$ as defined in Eqs. (16) and (24), respectively, are equal in the case of a homogeneous electron gas. Combining Eqs. (15) and (16) and making use of the fact that the wave functions can be expressed in terms of a single plane wave, i.e., $\phi_{i\mathbf{k}}(\mathbf{r}) = e^{i(\mathbf{k}+\mathbf{G}_i)\cdot\mathbf{r}}$ (we made the $\mathbf{k}$ dependence explicit), we obtain

$$\begin{aligned}&\delta_{ng}^{\mathrm{hom}}(\mathbf{G},\omega) \\ &\quad = \omega_{ng} - \sum_c \delta(\mathbf{G}_n - \mathbf{G} - \mathbf{G}_c)\left[\sum_{c'} \frac{\delta(\mathbf{G}_n - \mathbf{G} - \mathbf{G}_{c'})}{\omega_{c'g}}\right]^{-1}. \quad \text{(B1)}\end{aligned}$$

In a similar manner, by combining Eqs. (22) and (24) we get

$$\tilde{\delta}_{ng}^{\mathrm{hom}}(\mathbf{G},\omega) = \omega_{ng} - \sum_{c} \delta(\mathbf{G}_n - \mathbf{G} - \mathbf{G}_c) \left[\sum_{c'} \frac{\delta(\mathbf{G}_n - \mathbf{G} - \mathbf{G}_{c'})}{\omega_{c'g}} \right]^{-1}. \tag{B2}$$

Therefore $\delta_{ng}^{\mathrm{hom}}(\mathbf{G},\omega) = \tilde{\delta}_{ng}^{\mathrm{hom}}(\mathbf{G},\omega)$. Similarly, one can show that $\delta_{ng}^{\mathrm{hom}}(\mathbf{G},\omega) = \tilde{\tilde{\delta}}_{ng}^{\mathrm{hom}}(\mathbf{G},\omega)$, etc. This also proves that the approximations given in Eqs. (32) and (33) are exact in the limit of a homogeneous electron gas. The same properties can be shown to hold for $\delta'_v(\omega)$ and $\tilde{\delta}'_v(\omega)$, etc.

APPENDIX C: A SIMPLIFIED EET FOR $\chi^0(\omega)$

One can obtain an even simpler expression for $\chi^0(\omega)$ if, instead of approximating $X_v(\omega)$, as is done in the EET, we approximate $\sum_v n_v X_v(\omega)$. We can rewrite this term according to

$$\sum_v n_v X_v(\mathbf{q},\mathbf{G},\mathbf{G}',\omega) = \frac{\sum_v n_v f_v^{\rho\rho}(\mathbf{q},\mathbf{G},\mathbf{G}')}{\omega - \Delta'(\mathbf{q},\mathbf{G},\mathbf{G}',\omega) + i\eta}, \tag{C1}$$

which defines $\Delta'(\mathbf{q},\mathbf{G},\mathbf{G}',\omega)$. We note that such a function can always be found since $\Delta(\mathbf{q},\mathbf{G},\mathbf{G}',\omega)$ has the same degrees of freedom as the left-hand side of Eq. (C1). The quantity $\Delta'(\omega)$ fulfills the same purpose as $\delta'_v(\omega)$ in Eq. (38) but is simpler since it is independent of v. Following a derivation similar to the one that led to Eqs. (39)–(41), we obtain the following approximations for $\Delta'(\omega)$:

$$\Delta'^{(0)}(\mathbf{q},\mathbf{G},\mathbf{G}') = Q(\mathbf{q},\mathbf{G},\mathbf{G}'), \tag{C2}$$

$$\Delta'^{(1)}(\mathbf{q},\mathbf{G},\mathbf{G}') = Q(\mathbf{q},\mathbf{G},\mathbf{G}') + \frac{F^{\rho j}(\mathbf{q},\mathbf{G},\mathbf{G}')}{F^{\rho\rho}(\mathbf{q},\mathbf{G},\mathbf{G}')}, \tag{C3}$$

$$\begin{aligned}\Delta'^{(2)}(\mathbf{q},\mathbf{G},\mathbf{G}',\omega) = {} & Q(\mathbf{q},\mathbf{G},\mathbf{G}') + \frac{F^{\rho j}(\mathbf{q},\mathbf{G},\mathbf{G}')}{F^{\rho\rho}(\mathbf{q},\mathbf{G},\mathbf{G}')} \\ & \times \left[\frac{\omega - Q(\mathbf{q},\mathbf{G},\mathbf{G}') - \frac{F^{\rho j}(\mathbf{q},\mathbf{G},\mathbf{G}')}{F^{\rho\rho}(\mathbf{q},\mathbf{G},\mathbf{G}')}}{\omega - Q(\mathbf{q},\mathbf{G},\mathbf{G}') - \frac{F^{jj}(\mathbf{q},\mathbf{G},\mathbf{G}')}{F^{\rho j}(\mathbf{q},\mathbf{G},\mathbf{G}')}} \right],\end{aligned} \tag{C4}$$

where $F^{\rho\rho} = \sum_v n_v f_v^{\rho\rho}$, etc. The quantities $F^{\rho\rho}$, $F^{\rho j}$, and F^{jj}, which appear in the above equations as well as in the numerator of Eq. (C1), just depend on (Fourier transforms of) the density and the KS or (noninteracting) quasiparticle one-body reduced density matrix:

$$\begin{aligned}F^{\rho\rho}&(\mathbf{q},\mathbf{G},\mathbf{G}') \\ &= \rho(\mathbf{G}' - \mathbf{G}) - \int d\mathbf{r}d\mathbf{r}' e^{i(\mathbf{q}+\mathbf{G})\cdot\mathbf{r}} e^{-i(\mathbf{q}+\mathbf{G}')\cdot\mathbf{r}'} |\rho(\mathbf{r},\mathbf{r}')|^2,\end{aligned} \tag{C5}$$

$$F^{\rho j}(\mathbf{q},\mathbf{G},\mathbf{G}') = \frac{i}{2} P(\mathbf{q},\mathbf{G},\mathbf{G}') \cdot (\mathbf{q} + \mathbf{G}') + \mathrm{H.c.}, \tag{C6}$$

$$F^{jj}(\mathbf{q},\mathbf{G},\mathbf{G}') = (\mathbf{q} + \mathbf{G}) \cdot \tilde{P}(\mathbf{q},\mathbf{G},\mathbf{G}') \cdot (\mathbf{q} + \mathbf{G}'), \tag{C7}$$

where

$$\begin{aligned}P(\mathbf{q},\mathbf{G},\mathbf{G}') = {} & \int d\mathbf{r} e^{i(\mathbf{G}-\mathbf{G}')\cdot\mathbf{r}} \nabla_{\mathbf{r}} \rho(\mathbf{r}) \\ & - \int d\mathbf{r}d\mathbf{r}' e^{i(\mathbf{q}+\mathbf{G})\cdot\mathbf{r}} e^{-i(\mathbf{q}+\mathbf{G}')\cdot\mathbf{r}'} \nabla_{\mathbf{r}'} |\rho(\mathbf{r},\mathbf{r}')|^2,\end{aligned} \tag{C8}$$

$$\begin{aligned}\tilde{P}&(\mathbf{q},\mathbf{G},\mathbf{G}') \\ &= \int d\mathbf{r} e^{i(\mathbf{G}-\mathbf{G}')\cdot\mathbf{r}} \nabla_{\mathbf{r}} \nabla_{\mathbf{r}} \rho(\mathbf{r}) \\ &\quad - \int d\mathbf{r}d\mathbf{r}' e^{i(\mathbf{q}+\mathbf{G})\cdot\mathbf{r}} e^{-i(\mathbf{q}+\mathbf{G}')\cdot\mathbf{r}'} \rho(\mathbf{r},\mathbf{r}') \nabla_{\mathbf{r}} \nabla_{\mathbf{r}'} \rho(\mathbf{r},\mathbf{r}').\end{aligned} \tag{C9}$$

The above approximations for $\Delta'(\omega)$ as well as the corresponding approximations for $\chi^0(\omega)$ (for systems with a gap) are explicit functionals of a one-body reduced density matrix. Therefore, they could also be useful in the modeling of density-matrix functionals or polarizabilities. The latter could then be used to calculate efficiently total energies.[51]

We note that the $\chi^0(\omega)$ that result from using the EET with $\delta'^{(0)}$ and $\Delta'^{(0)}$ are identical. While the overall scaling of the EET approach presented in the previous sections is, in general, $N_{\mathrm{at}}^3 \log N_{\mathrm{at}}$,[21] the scaling of this simplified EET scheme is N_{at}^3, where N_{at} is the number of atoms. This scaling is an order of magnitude smaller than the N_{at}^4 scaling of the standard SOS approach.

---

[*] arjan.berger@irsamc.ups-tlse.fr

[1] L. Hedin, Phys. Rev. A **139**, 796 (1965).
[2] W. G. Aulbur, L. Jönsson, and J. W. Wilkins, in *Solid State Physics* (Academic, New York, 2000), Vol. 54, p. 1.
[3] L. Steinbeck, A. Rubio, L. Reining, M. Torrent, I. White, and R. Godby, Comput. Phys. Commun. **125**, 105 (2000).
[4] M. L. Tiago, S. Ismail-Beigi, and S. G. Louie, Phys. Rev. B **69**, 125212 (2004).
[5] M. van Schilfgaarde, T. Kotani, and S. V. Faleev, Phys. Rev. B **74**, 245125 (2006).
[6] F. Bruneval and X. Gonze, Phys. Rev. B **78**, 085125 (2008).
[7] M. E. Casida and D. P. Chong, Phys. Rev. A **40**, 4837 (1989); **44**, 6151 (1991).
[8] F. Bechstedt, R. Del Sole, G. Cappellini, and L. Reining, Solid State Commun. **84**, 765 (1992).
[9] S. Baroni and A. Quattropani, Nuovo Cimento D **5**, 89 (1985).
[10] S. Baroni, P. Giannozzi, and A. Testa, Phys. Rev. Lett. **58**, 1861 (1987).
[11] L. Reining, G. Onida, and R. W. Godby, Phys. Rev. B **56**, R4301 (1997).
[12] H. F. Wilson, F. Gygi, and G. Galli, Phys. Rev. B **78**, 113303 (2008).
[13] H. F. Wilson, D. Lu, F. Gygi, and G. Galli, Phys. Rev. B **79**, 245106 (2009).
[14] P. Umari, G. Stenuit, and S. Baroni, Phys. Rev. B **81**, 115104 (2010).
[15] F. Giustino, M. L. Cohen, and S. G. Louie, Phys. Rev. B **81**, 115105 (2010).

[16] W. Kang and M. S. Hybertsen, Phys. Rev. B **82**, 195108 (2010).

[17] P. Umari, G. Stenuit, and S. Baroni, Phys. Rev. B **79**, 201104(R) (2009).

[18] X. Blase, C. Attaccalite, and V. Olevano, Phys. Rev. B **83**, 115103 (2011).

[19] D. Foerster, P. Koval, and D. Sánchez-Portal, J. Chem. Phys. **135**, 074105 (2011).

[20] G. Samsonidze, M. Jain, J. Deslippe, M. L. Cohen, and S. G. Louie, Phys. Rev. Lett. **107**, 186404 (2011).

[21] J. A. Berger, L. Reining, and F. Sottile, Phys. Rev. B **82**, 041103(R) (2010).

[22] L. Hedin, J. Phys. Condensed Matter **11**, R489 (1999).

[23] M. S. Hybertsen and S. G. Louie, Phys. Rev. B **34**, 5390 (1986).

[24] R. W. Godby, M. Schlüter, and L. J. Sham, Phys. Rev. B **37**, 10159 (1988).

[25] P. Hohenberg and W. Kohn, Phys. Rev. **136**, B864 (1964).

[26] W. Kohn and L. J. Sham, Phys. Rev. **140**, A1133 (1965).

[27] O. V. Gritsenko and E. J. Baerends, Phys. Rev. A **64**, 042506 (2001).

[28] D. L. Johnson, Phys. Rev. B **9**, 4475 (1974).

[29] X. Gonze, G. Rignanese, M. Verstraete, J. Beuken, Y. Pouillon, R. Caracas, F. Jollet, M. Torrent, G. Zerah, M. Mikami *et al.*, Z. Kristallogr. **220**, 558 (2005).

[30] H. von Mangoldt and K. Knopp, *Einführung in die höhere Mathematik* (S. Hirzel Verlag, Stuttgart, 1948).

[31] R. W. Godby and R. J. Needs, Phys. Rev. Lett. **62**, 1169 (1989).

[32] X. Gonze, Phys. Rev. B **55**, 10337 (1997).

[33] L. Kleinman and D. M. Bylander, Phys. Rev. Lett. **48**, 1425 (1982).

[34] N. Troullier and J. L. Martins, Phys. Rev. B **43**, 1993 (1991).

[35] N. Sai, M. L. Tiago, J. R. Chelikowsky, and F. A. Reboredo, Phys. Rev. B **77**, 161306 (2008).

[36] H. J. Monkhorst and J. D. Pack, Phys. Rev. B **13**, 5188 (1976).

[37] R. W. G. Wyckoff, *Crystal Structures 1* (Interscience, New York, 1963).

[38] The reported energy cut-off is relative to the CBM.

[39] The small differences in the band gaps of SnO_2 reported in this work and those reported in a previous work (Ref. 21) are due to a denser **k**-space sampling of the Brillouin zone in the present work.

[40] B.-C. Shih, Y. Xue, P. Zhang, M. L. Cohen, and S. G. Louie, Phys. Rev. Lett. **105**, 146401 (2010).

[41] M. Usuda, N. Hamada, T. Kotani, and M. van Schilfgaarde, Phys. Rev. B **66**, 125101 (2002).

[42] M. Shishkin and G. Kresse, Phys. Rev. B **75**, 235102 (2007).

[43] F. Fuchs, J. Furthmüller, F. Bechstedt, M. Shishkin, and G. Kresse, Phys. Rev. B **76**, 115109 (2007).

[44] P. Gori, M. Rakel, C. Cobet, W. Richter, N. Esser, A. Hoffmann, R. Del Sole, A. Cricenti, and O. Pulci, Phys. Rev. B **81**, 125207 (2010).

[45] E. Wimmer, H. Krakauer, M. Weinert, and A. J. Freeman, Phys. Rev. B **24**, 864 (1981).

[46] C. Friedrich, M. C. Müller, and S. Blügel, Phys. Rev. B **83**, 081101(R) (2011); **84**, 039906(E) (2011).

[47] M. Stankovski, G. Antonius, D. Waroquiers, A. Miglio, H. Dixit, K. Sankaran, M. Giantomassi, X. Gonze, M. Côté, and G.-M. Rignanese, Phys. Rev. B **84**, 241201(R) (2011).

[48] Y.-N. Xu and W. Y. Ching, Phys. Rev. B **48**, 4335 (1993).

[49] T. Hasegawa and J. Takeya, Sci. Technol. Adv. Mater. **10**, 024314 (2009).

[50] O. D. Jurchescu, A. Meetsma, and T. T. M. Palstra, Acta Crystallogr. B **62**, 330 (2006).

[51] D. C. Langreth and J. P. Perdew, Solid State Commun. **17**, 1425 (1975).

Chapter 5

Applications of different spectroscopies to a variety of systems

NEW theoretical and/or numerical developments, once established, needs to be tested against realistic situation. The general character of a method, and so its applicability to different systems, with different dimensionality and purposes needs to be assessed and proven. Alongside with the development activity, I (try to) maintain a strong link with real applications, being them materials for high-k electronic devices, organic LED or biological systems.

5.1 Excitations of Bio-molecules

During my post-doc in San Sebastián, I worked on ab initio simulation of molecules of biological interest. The understanding of the absorption and emission of light processes from biomolecules is crucial for the understanding of life. Typical examples are the photosynthesis, vision, bioluminescence, DNA damage. A first-principle theoretical description of the interaction of biomolecules with time-dependent electromagnetic radiation is then of paramount importance. This challenge was tackled in the last two decades by Time Dependent Density Functional Theory. In an invited article, we have shown how TDDFT can be successfully applied in predicting optical properties of biomolecules, being fluorescent proteins (biological markers also used in bio-medicine), porphyrins (the base element of chlorophyll), or DNA basis [106]. In another work, we have provided some reference benchmark results for a prototypical system of a wide class of bio-molecules, the porphyrin, using state-of-the-art GW+BSE methods [107]. The latter work has also been very educative for us: before being accepted for publication (also getting the cover page), in fact, we fought a lot (but also understood a lot) with the chemist reviewer of our paper. We wonder about publishing "The Struggle for the Soul of Physics under a chemist Referee", before finally let it go.

PLEASE REFER TO THE ATTACHED ARTICLE

Available online at www.sciencedirect.com
ScienceDirect
ELSEVIER
C. R. Physique 10 (2009) 469–490
COMPTES RENDUS
PHYSIQUE
http://france.elsevier.com/direct/COMREN/

Theoretical spectroscopy / Spectroscopie théorique

The challenge of predicting optical properties of biomolecules: What can we learn from time-dependent density-functional theory?

Alberto Castro [a,b], Miguel A.L. Marques [c,d,b], Daniele Varsano [e,b], Francesco Sottile [f,b],
Angel Rubio [g,h,b,*]

[a] Institut für Theoretische Physik, Fachbereich Physik, Freie Universität Berlin, 14195 Berlin, Germany
[b] European Theoretical Spectroscopy Facility (ETSF)
[c] Laboratoire de physique de la matière condensée et nanostructures, Université Lyon I, CNRS, UMR 5586, domaine scientifique de la Doua, 69622 Villeurbanne cedex, France
[d] Centre for Computational Physics, Department of Physics, University of Coimbra, 3004-516 Coimbra, Portugal
[e] National Center on nanoStructures and bioSystems at Surfaces (S3) of INFM-CNR, c/o Dipartimento di Fisica, Università di Modena e Reggio Emilia, Via Campi 213/A, 41100 Modena, Italy
[f] Laboratoire des solides irradies, École polytechnique, 91128 Palaiseau cedex, France
[g] Departamento de Fisica de Materiales, Universidad del País Vasco, Edificio Korta, 20018 San Sebastián, Spain
[h] Centro Mixto CSIC-UPV/EHU and DIPC, Universidad del País Vasco, 20018 San Sebastián, Spain

---

Abstract

The suitability of the time-dependent density-functional theory (TDDFT) approach for the theoretical study of the optical properties of biomolecules is demonstrated by several examples. We critically discuss the limitations of available TDDFT implementations to address some of the present open questions in the description of the excited-state dynamics of biological complexes. The key objective of the present work is to address the performance of TDDFT in the linear response regime of the bio-molecular systems to the visible or near UV radiation – measured by, e.g. optical absorption or optical dichroism spectra. Although these spectra are essentially determined by the electronic degrees of freedom of small, optically active regions within the usually large biological systems, they can also be strongly influenced by environment effects (solvent, hosting protein, temperature, etc.). Moreover, many key biological processes consist of photo-induced dynamics (photoisomerisation, etc.), and their description requires a coupled treatment of electronic and nuclear degrees of freedom. We illustrate these aspects with a selection of paradigmatic biomolecular systems: chromophores in fluorescent proteins, porphyrins, DNA basis, the azobenzene dye, etc. ***To cite this article: A. Castro et al., C. R. Physique 10 (2009).***

Résumé

Le défi de la prédiction des propriétés optiques des bio-molécules : Que peut nous apprendre la théorie de la fonctionnelle de la densité dépendante du temps ? L'utilité de la théorie de la fonctionnelle de la densité dépendante du temps (TDDFT) pour l'étude théorique des propriétés optiques de biomolécules a été largement démontrée. Nous discutons les limites des implémentations actuelles de la TDDFT, afin de répondre à certaines questions sur la description des états excités des systèmes biologiques complexes. L'objectif principal de ce travail est d'évaluer les performances de la TDDFT, en régime linéaire, pour les systèmes bio-moléculaires, dans le spectre visible ou UV proche – mesuré, par exemple, avec l'absorption optique ou le dichroïsme optique.

---

[*] Corresponding author at: Departamento de Fisica de Materiales, Universidad del País Vasco, Edificio Korta, 20018 San Sebastián, Spain.
E-mail address: angel.rubio@ehu.es (A. Rubio).

1631-0705/$ – see front matter
doi:10.1016/j.crhy.2008.09.001

Bien que ces spectres soient essentiellement déterminés par les degrées de liberté électroniques, les régions optiquement actives des grands systèmes biologiques peuvent être fortement influencés par les effets dus à l'environnement (solvant, entourage de la protéine, température, etc.). De plus, de nombreux processus biologiques essentiels sont des processus dynamiques photo-induits (photoisomérisation, etc.), et leur description a besoin d'un traitement conjoint des degrés de liberté électroniques et nucléaires. Nous illustrons ces aspects avec une sélection de systèmes bio-moléculaires paradigmatiques : chromophores des protéines fluorescentes, porphyrines, ADN, azobenzène, etc. ***Pour citer cet article : A. Castro et al., C. R. Physique 10 (2009).***

Keywords: Biomolecules; Excitations; TDDFT

Mots-clés : Biomolécules ; Excitations ; TDDFT

1. Introduction

Absorption or emission of light from biomolecules are crucial processes to understand the machinery of life [1]. Photosynthesis [2], vision [3], bioluminescence [4] or DNA damage are paradigmatic examples. A sound theoretical understanding of the photo-chemistry of biological molecules is not only needed to describe the mechanisms of Biology, but also because some of the key molecules can be employed for technological purposes at the nanoscale [5]. However, despite the tremendous effort focused on this field, the first-principles theoretical description of the interaction of these molecules with time-dependent electromagnetic fields is still a challenging problem, lacking a definitive and systematic methodology, capable of bridging the different spatial and time scales that are relevant for the description of light-induced biological processes with predictive power.

Time-dependent density-functional theory (TDDFT) [6] has repeatedly shown in the last decade its usefulness when attempting this challenge. The reason is the unparallelled balance between the computational load that it requires and the accuracy that it provides. In the past few years, we have performed a number of theoretical studies on the photo-response of organic and biological molecules by making use of TDDFT. It is the purpose of this article to overview, by showing several of these examples, some of the capabilities of this approach and highlight the deficiencies of present approximations for the unknown frequency-dependent exchange-correlation kernel that enters the TDDFT equations.

The visible and near ultraviolet (UV) range of the spectrum is, of course, specially relevant – and it is indeed the visible and UV spectroscopy the main applicability niche of TDDFT. We will therefore concentrate on this area. Most organic molecules, however, are completely transparent to visible light, and begin to absorb in the UV region. Upon absorption of a photon, a molecule undergoes a transition between two molecular states. The most common transitions are of the σ to σ^*, π to π^* and π to $n\pi$ kind, and correspond to absorption of light in the UV. In molecular chains with alternate bonds, however, absorption can be shifted to longer wavelengths. In these so-called conjugated molecules, electrons are delocalised over the whole system. Therefore, by increasing the length of the molecule, π-electrons become more delocalised, and the HOMO-LUMO energy gap decreases. If the system is long enough, optical absorption may lie in the visible region. Chromophores are those organic molecules with long conjugated bonds, resulting in very efficient absorption in the visible or near-UV regions of the spectrum. Sections 2 and 3 are dedicated to some examples of this large family of molecules.

Section 4 is dedicated to the optical properties of DNA basis and compounds. TDDFT may help in this case to analyse how the response of the nucleobases is altered by their mutual interaction, either in their natural environment (where the bases are paired in the Watson–Crick (WC) scheme, and covalently bound to a sugar-phosphate backbone), or in synthesised arrangements. The favourable scaling properties of TDDFT with respect to traditional Quantum Chemistry approaches is in this case crucial to be able to study the evolution of excited state properties as the size of the DNA compounds grows. We also show calculations of the circular dichroism of the adenine molecule and dimer, where it is highlighted the relevance of the circular dichroism spectra to address the properties of stacked bases (including the chirality of molecules).

TDDFT, in principle, addresses the electronic problem of a molecular system; the study of the nuclear movement requires some form of molecular dynamics. Section 5 is dedicated to some approaches to this coupling between TDDFT and molecular dynamics. The systems chosen for this purpose are the azobenzene chromophore (whose fast isomerisation has a large potential for technological applications), and formaldimine, which also illustrates the double-bond rotation that underlies many biological dynamical processes. As a somehow exotic excursion, Subsection 5.3

displays a particularly intuitive way of monitoring the chemical bonds during a dynamical molecular process: the time-dependent electron-localisation function (TDELF), which can be effectively extracted from a TDDFT calculation.

Most of the calculations reported in this Article have been performed with our own TDDFT implementation, the `octopus` code. We refer the reader to Refs. [7] and [8] for technical details regarding the algorithms. Moreover, we focus here on the results of the applications, rather than on the description of the theory itself. References [6,9–12] are some possibles sources to get acquainted with the foundations of TDDFT.

2. Chromophores in proteins

Biochromophores are never isolated in nature, but are typically covalently bound to a protein. For instance, retinol, present in our eyes and responsible for capturing the photons in the first stage of the vision process, is always a part of some protein – of any in the so called "opsin" family. The proteic surroundings may have a strong influence on the response of a chromophore to light. Following with the retinol example, the absorption maximum of the chromophore in the protein red-shifts by about 120 nm with respect to the chromophore in solution. It is clear that any successful theoretical treatment of the optical response of a chromophore must include consistently the effect of its environment.

The photoactive region, however, is usually constituted by a relatively small active centre – the chromophore, and the surrounding medium – and the rest of the molecule plus the environment can be considered as a perturbation. The environment can be a solution, or even a solid-state device. Optical processes related, for instance, to vision and photosynthesis, rely on a subtle interplay between optical absorption by the photoactive centre and its decay mechanism through the coupling to the internal vibrational modes of the molecule, including isomerisation processes, as well as the coupling to the environment (the supporting protein and the solvent). In the following, we supply some recent examples of application of TDDFT to the calculation of absorption spectra of biomolecules, namely of the so called fluorescent proteins. These constitute a set of molecules with a wide range of applications as biological markers [13] – and now are also being used to form hybrid devices for nano-optic applications [14].

2.1. *The green fluorescent protein (GFP)*

A complex and appealing photoactive molecule is the green flourescent protein (GFP). This molecule has been studied experimentally in various environments, in solution as well as *in vacuo*, and has been found to exhibit a rich and complex behaviour that is the subject of much current debate. The measured optical absorption spectrum of the wild type (wt) GFP shows two main resonances at 2.63 and 3.05 eV [15,16] (see Fig. 1), that are attributed to two different thermodynamically stable protonation states of the chromophore, the neutral and the negative configurations of the chromophore, respectively. So far, ab-initio quantum chemistry has not been able to provide satisfactory agreement with the spectroscopic data, and has not contributed much to confirm or rule out various possible scenarios of photo-dynamics in the GFP. A good description of the optical properties of the GFP photoreceptor has been achieved [17] by using an approach that combines (a) a hybrid quantum mechanics-molecular mechanics (QM-MM) method to obtain the structure, with (b) time-dependent density functional theory to treat the electronic excitations.

The structures were first optimised using a QM-MM method [18–20] with a semiempirical Hamiltonian [21] to describe the quantum subsystem. The quantum mechanical (QM) region included a sequence of three amino-acids that form the chromophore: Ser65, Tyr66 and Gly67. The optimised structure of the chromophore, with the most important neighbour residues, is shown in Fig. 1. On the other hand, the anionic form of the chromophore was obtained by deprotonation of Tyr66 and protonation of Glu222. The calculated photoabsorption spectra of the GFP neutral and anionic chromophores, shown also in Fig. 1, are in excellent agreement with experiment assuming the presence of the two forms of the photo-receptor, protonated and deprotonated respectively, in an approximate 4:1 ratio. Furthermore, it can be seen in the inset of Fig. 1 that light polarised along the x-direction is responsible for the lowest optical transition in the neutral chromophore. The molecule is nearly transparent to visible light polarised along the other two orthogonal directions. The GFP turns out to be a rather anisotropic molecule in the visible region, a property that could be used to enhance the photo-dynamical processes in well oriented GFP samples for opto-electronic devices. It should be emphasised that good agreement is obtained because the breaking of the planarity of the biochromopeptide caused by the protein surrounding has been taken into account. Notice also that the measured peaks can be clearly assigned to either the neutral or anionic forms of the GFP.

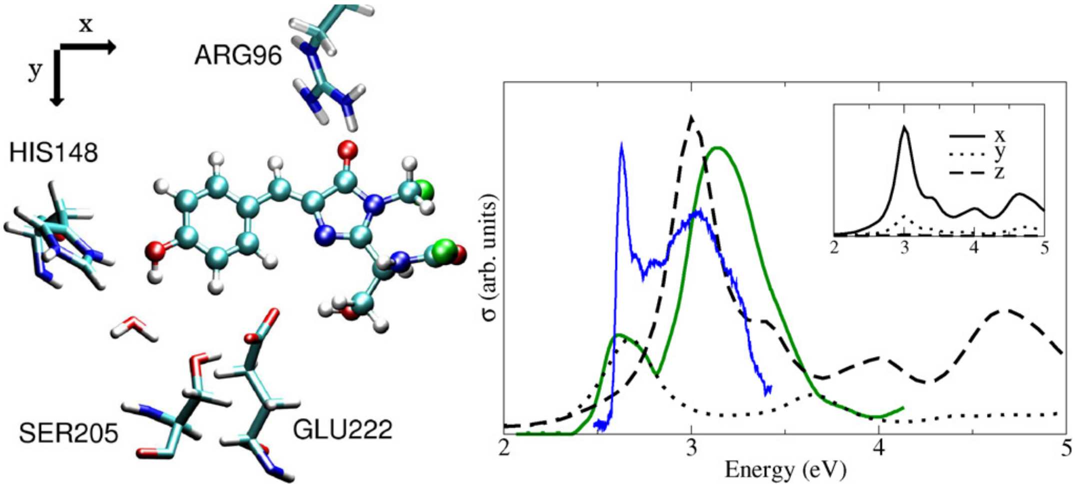

Fig. 1. Left panel: Optimised structure of the neutral chromophore and its closest charged residues inside the green fluorescent protein (GFP): His148, Arg96 (positive) and Glu222 (negative). Right panel: Computed photoabsorption cross section of the neutral (dashed line) and anionic (dotted line) chromophores. For comparative purposes the anionic results have been divided by 4. Experimental results at 1.6 K (blue) [15] and room temperature (green) [16] are also given. The insert gives a decomposition of the calculated spectrum of the neutral chromophore in the three directions, showing the inherent anisotropy of the GPF molecule.

2.2. *The blue mutant of the GFP*

In the past years there has been an increasing demand for the ability to visualise different proteins in vivo that require multicolour mode imaging. For this reason, several groups set forth to develop GFP-mutant forms with different optical responses. A mutant of the GFP of particular interest is the Y66H variant, in which the aminoacid Tyr66 of the GFP is mutated to a Histidine [22,23]. The resultant protein exhibits fluorescence shifted to the blue range, and is for that reason often referred to as the blue emission variant of the GFP, or the blue fluorescent protein (BFP). The BFP chromophore is considerably more complicated than the GFP. It has four possible protonation states: one anionic (named HSA), two neutral (HSD and HSE), and one cationic (HSP). Each one of them, in turn, has two possible stable conformations, one cis and one trans, joined by a transition state. The optical spectra of all these configurations, as obtained by means of TDLDA, is shown in Fig. 2.

The main candidate to explain the experimental spectrum of the BFP turns out to be a neutral-cis configuration. However, in contrast to the wt-GFP where the response of the anionic and of neutral states occurs at distinct frequency ranges [24–26], in the BFP both anionic and neutral configurations have very similar spectra, with only minor differences in the fine structure close to the main peak. On the other hand, even if the absorption spectrum is not conclusive, the acid dissociation constant (pK_a) analysis seems to rule out the existence of the anionic state in vivo. Furthermore, other protonation states (such as the cationic) cannot be present in the BFP protein as their spectral features are outside the measured absorption spectra.

Like in the GFP, it is quite important to take into account the role of the chromophore environment. This role is 2-fold: (i) it induces structural modifications of the gas phase chromophore, the most important being the breaking of the planarity of the imida rings; and (ii) it makes a local-field modification of the external electromagnetic field. To study these effects, QM/MM simulations of the chromopeptide embedded inside the BFP were performed (see Ref. [26] for computational details). We will discuss here the cis-HSD case, since it is the lowest energy structure for the neutral chromophore, and X-ray data indicate a cis conformation, therefore making it the most likely candidate to be present in the experiments.

Regarding the structure, the protein induces the breaking of planarity (around 18°) of the otherwise planar gas-phase structure. Then, in order to determine the role played by the protein intra-media in the optical spectroscopy properties of the chromopeptide, the authors selected several structures from the QM/MM minimisation and performed TDDFT calculations. These calculations are summarised in Fig. 3, along with the calculated gas phase result (named "Gas-phase" in the figure), and the experimental spectrum. The spectrum of the bare chromophore, but as distorted by the protein environment, is denoted "Distorted". The other two curves correspond to the chromopeptide plus a selection of some the closest residues (the *environment*): "Env I" includes His148, Glu222, and Arg96, which are

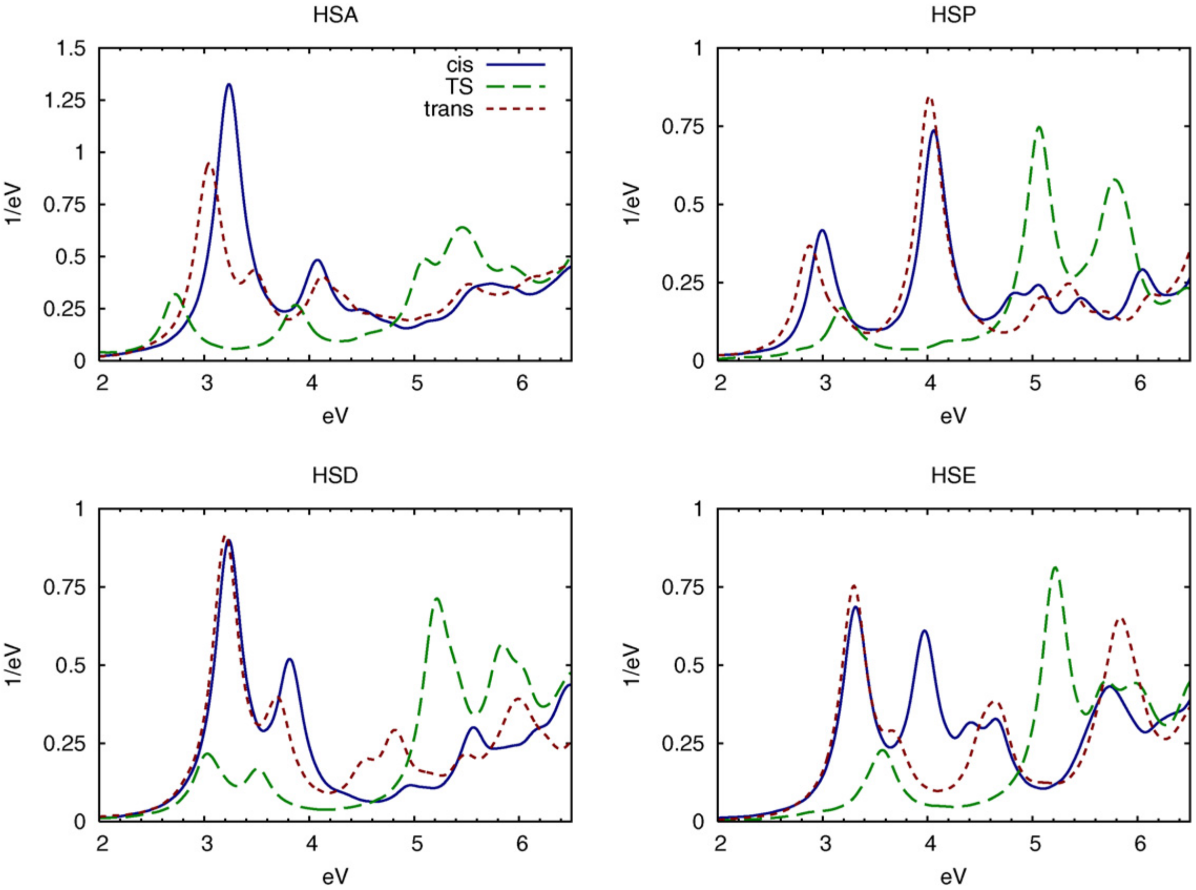

Fig. 2. Calculated TDLDA optical absorption spectrum in the range 2–5 eV for the various protonation states and conformers of the chromopeptide in the gas phase (cis: solid line; TS: dashed line; and trans: dotted line).

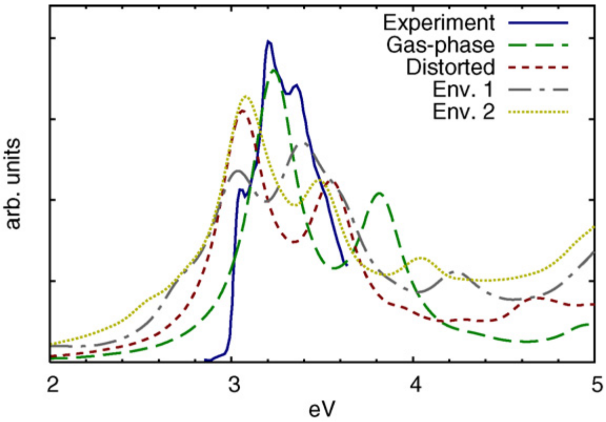

Fig. 3. Calculated TDLDA optical absorption spectrum for the cis-HSD state of the chromophore in the gas phase and distorted by the BFP protein environment, compared with the experimental spectrum of the BFP.

the charged residues in the vicinity of the chromophore (His148 and Arg96 positive; Glu222 negative). As such, it is reasonable to expect that they will have a greater influence in polarising the electronic cloud of the chromopeptide. “Env II” is made of “Env. II” plus Ser205, a buried water molecule, and Gln94. All of these are polar residues that are within 2.5 Å of the chromophore.

It can be seen how the induced non-planarity has a sizable effect in the spectrum. It causes a considerable red-shift of the gas-phase cis-HSD peaks. Thus, the optical spectrum is sensitive to the ≈ 20° torsion. On the other hand, the effect of the polarisation of the electronic cloud by neighbour residues is less important. The inclusion of the residues

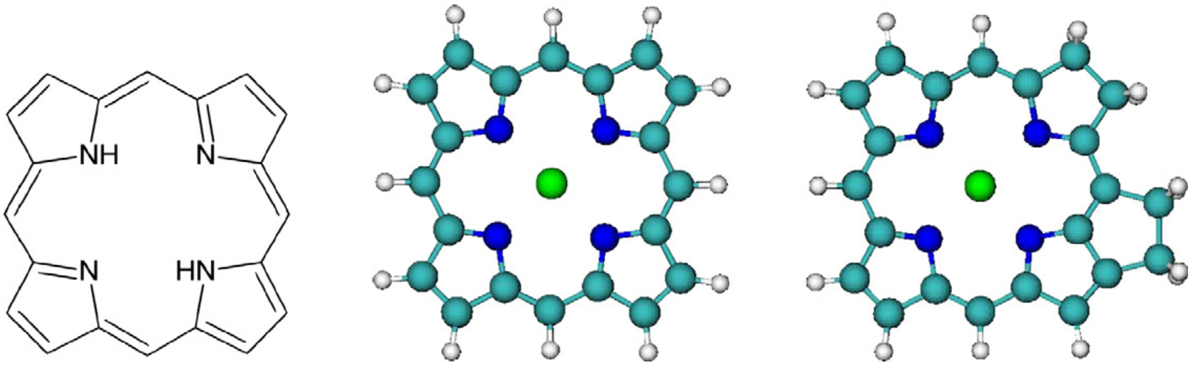

Fig. 4. Left: basic porphyrine structure. Centre and right: symmetric and asymmetric magnesium porphyrine-like molecules (the asymmetry was introduced by closing a pentagonal ring close to the bottom right amida ring).

in "Env I" in the TDLDA calculation causes a further red-shift of the second peak, but leaves the first peak almost unchanged. However, when enlarging the environment to "Env II", we find a spectrum with a shape similar to the one of the twisted chromopeptide with two well-defined peaks at similar positions. It seems that "Env I" provides an inhomogeneous surrounding, which leads to an over-polarisation, and this artifact is corrected by the inclusion of a larger environment.

In summary, the optical absorption inside the BFP exhibits a red shift of about 0.15 eV, which has mainly a structural origin – a breakdown of planarity. This could be responsible for the 0.13 eV red-shift observed between folded and unfolded conformations of the BFP protein [22]. Furthermore, there is a subtle cancellation between the shielding of the electromagnetic field acting on the chromophore due to its closest residues. This cancellation effect makes that the calculated spectra for the isolated (twisted) chromophore and for the chromophore in the protein are nearly identical. Another aspect that we have shown to be relevant is the inclusion of temperature [26] that is important to bring more quantitative agreement between the calculated BFP spectra and the measured one. Temperature introduces fluctuations in the dihedral angle related to the breaking of planarity in the BFP chromophore (floppy torsional motion of the two imida-rings are included), and consequently to a broadening and shift of the calculated spectra. We note this breaking of planarity plays a fundamental role in the description of the optical properties of other GFP-mutants also studied by our group [27].

3. Porphyrins

The porphyrin family [28] is perhaps the paradigm of coloured organic molecules existing in nature ("porphura" meaning "purple pigment" in Greek). The basic constituent of all the members of the family is the porphyne; it consists of four pyrrole units linked by four methine bridges (see Fig. 4). It is an aromatic molecule containing 22 π electrons – which is already an indication of its potential to be active in the visible range of the spectrum. Substitutions and small modifications of this basic structure produce the porphyrin molecules. Usually, a metal is inserted in the canter of the molecule; for example, if it is iron, the porphyrins are called "hemes"; the well known hemoglobin is a protein whose active canter is a heme group (an *hemoprotein*). There is a vast range of different natural and man-made metallo-porphyrin based compounds that evidence the huge field of research that this set of molecules form.

Chlorins are "almost" porphyrins and we can consider them members of this family: the only defining difference is that one of the four pyrroles is reduced and therefore the structure is not aromatic across the full molecular ring. If the chlorin hosts one magnesium atom at its centre, then it constitutes the basic tetrapyrrole of chlorophyll, the well known light harvester present in most plants and algae. This molecule has a characteristic absorption pattern in the visible range of the spectrum: strongly in the red and blue areas, weakly in the green.

More than 50 different types of chlorophylls have been found in living photosynthetic organisms. There exists, in fact, a large variety of additional structural elements to the tetrapyrrole, all giving rise to different vis-UV spectra, one of the most characteristic (important for both structural and electronic properties) being the pythol chain, that normally anchors the pigment to the protein structure.

Since the chlorophylls are derivatives of the porphyrin family, the main features of their optical properties can be understood, from a theoretical point of view, from a study of the latter. However, as we show in Fig. 5, the plain,

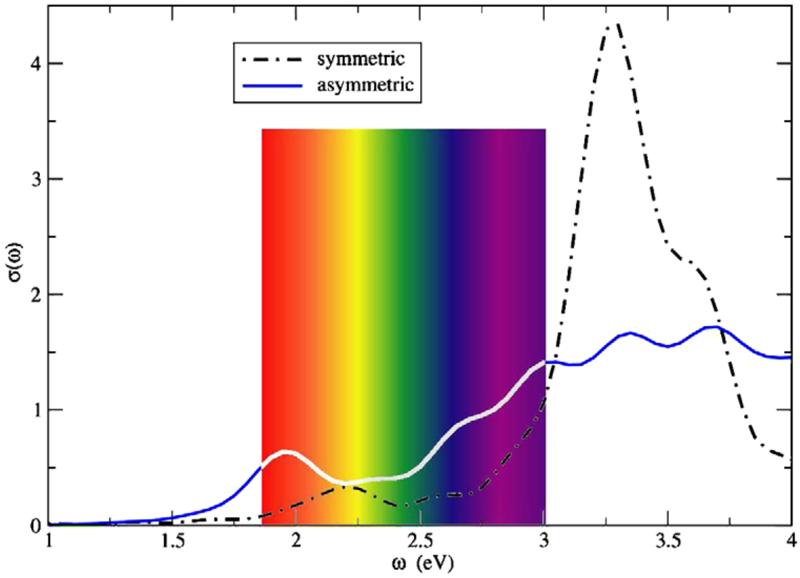

Fig. 5. Calculated TDLDA photoabsorption spectrum of the symmetric and asymmetric forms of the Mg-porphyrin depicted in Fig. 4 (see text for details). The visible part of the spectrum is highlighted as a guide for the eye.

symmetric, flat Mg porphyrin (Fig. 4, centre) cannot on its own give rise to the double-peak absorption typical of chlorophylls. In fact, the smallest representative of chlorophyll is not the plain, symmetric porphyrin structure presented in the left, but the more asymmetric one presented on the right (Fig. 4), and characterised by a fifth isocyclic ring. In this 5-ring porphyrin, the pyrrole ring IV is saturated and as a consequence some transitions shift towards the red and gain oscillator strength. The more asymmetric the π-electron distribution is, the more emphasised the double-peak shape will be (the structure at the centre of Fig. 4 is too symmetric, leading to HOMO's degeneracy, and is then not capable to reproduce the richer chlorophyll spectrum shape). Other details of the chlorophyll structure, like bending, protonation, addition and/or distortion of other elements, might further shift and vary the optical peaks: still the most significant effect stems from the breaking of the square symmetry of the basic porphyrine structure. These ab initio results support the simple exciton-model (4-band model [29]) that has been used in the last two decades to describe experimental results and, at the same time, underline the pertinence and the usefulness of TDDFT, already at the very basic approximations (here LDA/GGA), for a global understanding of the process of light absorption. Still, in the photosynthetic units, besides the absorption process, the conversion of energy also depends on charge-transfer excitation mechanisms that are poorly described by present LDA/GGA functionals (see Section 6 below). On the other hand, the promising results found in this sections open the way towards the description of hybrid devices made of porphyrins and nanowires for either photovoltaic-energy conversion and/or volatile memory devices [30].

4. Optical response of DNA bases and base pairs

In order to characterise either the structural or the response properties of biomolecular systems, it is crucial to be able to distinguish the intrinsic molecular properties from the effects induced by the environment (e.g. the solvent). The optical absorption spectrum may be able to properly discriminate those effects, hence its success as a characterisation tool. This fact is specially important for DNA and DNA-based compounds [32,33].

In addition to the obvious relevance of scientific investigations of DNA molecules for medical and biological purposes, we have witnessed lately how DNA compounds and DNA-like derivatives, are studied for their potential applications for nanotechnological purposes. The reasons are its stability (in solution), its one-dimensional character, along with the unique properties of self-assembly and recognition. However, in order to advance farther this technological line of research, the determination and interpretation of the electronic properties of nucleobases and of DNA helical arrangements is an extremely valuable foreword, and notable multidisciplinary efforts are currently devoted to such goals [34–39]. Furthermore, knowledge of the electronic properties, excited-state lifetimes, and ultraviolet (UV) absorption spectra is of paramount importance for our understanding of, e.g., the crucial phenomenon of UV radiation-induced DNA damage.

To relate the optical properties of nucleic acids to their structure, spatial conformation, and type of intra-molecular interactions, a valuable preliminary step is to gain insight into the excited-state properties of their building blocks, namely the monomeric bases, and to understand the role of hydrogen-bonding and stacking when these monomeric units form complex assemblies. In their natural environment, the DNA bases are paired via hydrogen-bonds in the WC scheme [44], and are covalently bonded to the sugar-phosphate backbone. The hydrogen-bonded base pairs interact with each other in the typical helical arrangement by inter-plane Van der Waals forces. To disentangle how the different interactions control the DNA dynamics upon light absorption, it is important to infer how the spectrum of a given isolated nucleobase is modified by mutual interactions in the different spatial conformations of DNA assemblies. TDDFT certainly is an appropriate tool for attempting this task.

In Ref. [31] a complete study of the optical absorption spectra of the five isolated gas-phase nucleobases and some of their assemblies is reported: simple WC pairs, simple π-stacks of two bases and more complex π-stacks of WC guanine–cytosine (GC) pairs. These calculations of isolated simple nucleobase-assemblies are a remarkable playground to prove the reliability of TDDFT for DNA-based materials. For the first time, the optical properties for a helical conformation of two stacked GC pairs [d(GC)] were computed by an ab-initio method. For such a conformation, H-bonding (which leads to the formation of WC pairs) and π-stacking effects are active simultaneously and can be distinguished.

The results discussed below and in Ref. [31] can be summarised as follows. For the isolated bases we obtained absorption spectra in rather good agreement with previous theoretical works and (qualitatively) with experiments (see Tables 1 to 6 of Ref. [31] for a detailed comparison between TDDFT excitation energies and experiments, and Tables 4 to 6 of Ref. [33] for comparison with quantum chemical calculations). The proper ordering of the $\pi\pi^*$ excitations is well reproduced, namely the excitation energy increases in going from cytosine to guanine to adenine. Moreover, the LUMO state has always a π-like character whereas the HOMO is π-like for the purines and σ-like for the pyrimidines.

Regarding the base assemblies (WC H-bond pairs and stacked configurations), the shape of the spectrum is not much altered by the π-stacking or H-bond interactions. However, hypochromicity (intensity decrease) is observed in the high energy range of the spectrum. The hypochromicity induced by π-stacking is larger than that induced by H-bonding. In the case of H-bonded basis, for light polarised perpendicular to the bases there is a blue-shift of the spectra compared to the spectra of the isolated bases. The photoabsorption cross section along this direction is mainly due to the contribution of $n\pi^*$ excitations and turns out to be orders of magnitude less intense than the spectrum for light polarised along the plane, due to $\pi\pi^*$ excitations. In the stacked case, the HOMO and LUMO states are distributed both on the purine and pyrimidine bases, whereas in the H-bonded configuration the HOMO is in the purine and the LUMO in the pyrimidine (charge transfer-type excitation). When combining both H-bonding and π-stacking, the two effects add independently, and the hypochromicity in the UV is enhanced.

Fig. 6 demonstrates some of these aspects, namely the effect of the H-bonding and π-stacking in the optical absorption. It displays the spectra for the H-bonded GC ("GC_H") and AT ("AT_H") pairs. In order to characterise the effect of the bonding, the spectra of the pairs (solid lines) is compared with the linear combination of the spectra of the isolated basis (dashed lines). The features evidenced by the figure are: (i) a small shift found for the lowest frequency peaks; (ii) the hypochromicity at high frequencies; and (iii) an overall blue-shift of the spectrum for light polarised perpendicular to the pair (not shown). In addition to the above features that originate from the individual bases, new features appear in the spectra because the purine and the pyramidine coexist in the WC arrangement. This coexistence changes the nature of the frontier orbitals: the HOMO is purine-localised, the LUMO is pyramidine-localised (bottom part of Fig. 6), and the value of the HOMO-LUMO gap is smaller than in the isolated bases. Consequently, peaks at lower energies with oscillation strengths orders of magnitude smaller than the $\pi\pi^*$ peaks, or totally dark, emerge in the spectra. These excitations, as for instances the HOMO-LUMO excitation are, consequently, of charge-transfer type.

The role of these charge-transfer excitations needs to be analysed more in detail in order to understand their impact in the excited state dynamics of DNA-based complexes (note that those states are very likely to be dark, or with very low oscillator strength for light-induced electronic excitations). In particular it is important to address which level of exchange-correlation functionals work well to describe properly this effects (see Section 6).

In the second row of Fig. 6 are shown the absorption spectra for the stacked GC_S dimer (left) and for two stacked GC_H stacked pairs. As in the case of hydrogen bonding, the shape of the spectrum is not strongly altered, but important differences are encountered in the oscillator strength, which turns out to be substantially reduced (hypochromism). In particular, looking at the spectrum of the two stacked GC_S dimers d(GC), we find the shape of the spectrum very

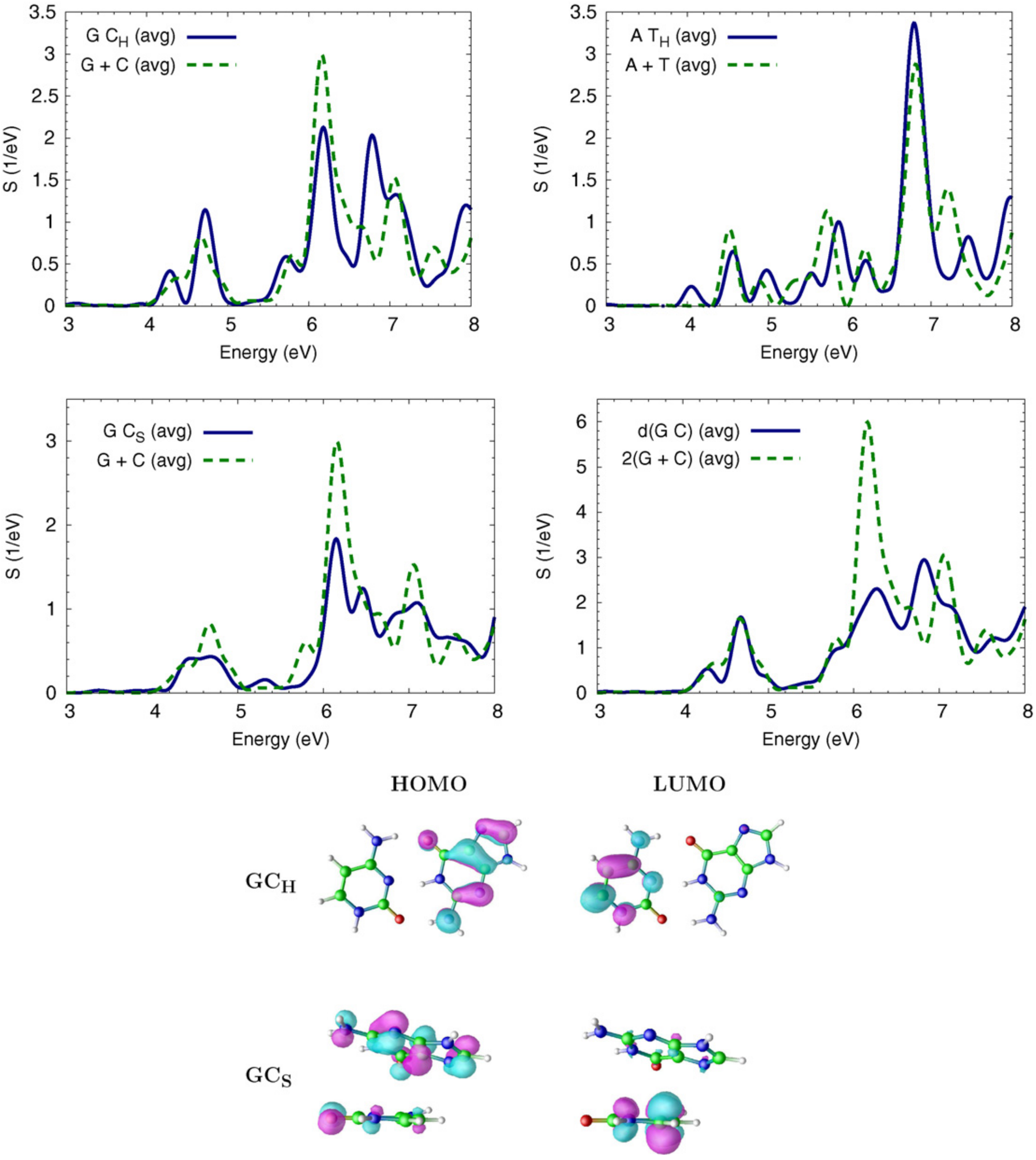

Fig. 6. Average photoabsorption cross section of the GC_H and AT_H base pairs (solid blue, top), and averaged spectra of stacked guanine and cytosine GC_S and of two stacked WC GC_H pairs d(GC) (solid blue, bottom). The linear combination of the spectra of the isolated purine and corresponding pyrimidine (G + C and A + T; dashed lines) are also shown for comparison. Below the spectra, the structures of the GC_H pairs and d(GC) assembly are shown, along with the HOMO and LUMO KS wave functions.

similar to the GC_H pair, but again strongly reduced in intensity because of the stacking. This feature indicates that the two kinds of base couplings seem to act separately and independently, in the sense that on does not affect the other in the optical response. The major effect of the stacking is the hypochromicity, which is very useful because the intensity change can be used to follow the melting of the secondary structure of nucleic acids when varying the temperature or environmental parameters.

Hypochromicity gives us a direct measure of the stacking interaction between bases for different systems, as for instances different DNA-like double helices, obtained modifying the base heterocycles or changing the backbone [45–47], that may be exploited for nano-electronics applications. Among these systems, particularly interesting is the expanded DNA (XDNA), obtained by Kool's group [48], where each DNA base is expanded with a benzene ring that

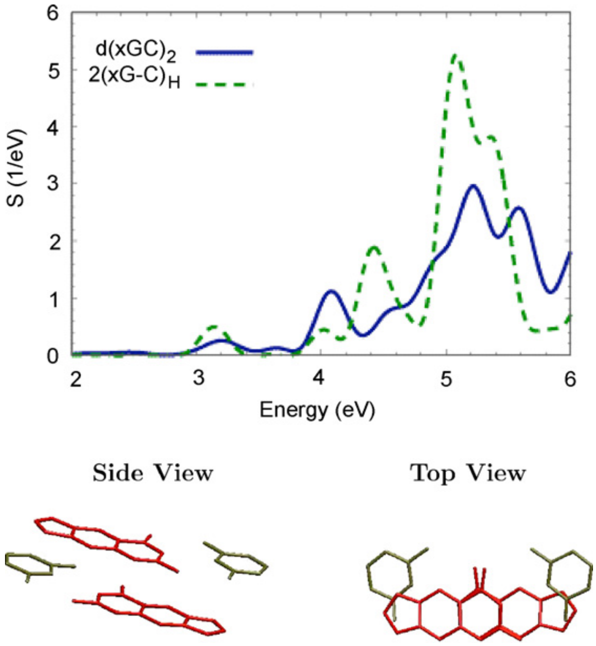

Fig. 7. Calculated dipole strength function for two stacked xG–C pairs with the expanded guanine in different strands [d(xGC)$_2$], in gas phase (solid line). The double of the absorption spectrum of the H-bonded xG–C is also shown with the green dotted line. In the bottom part of the figure the atomic structure from the top view and side view for the [d(xGC)$_2$], constructed from NMR average parameters is shown. Different bases are indicated with different colours: xG(red), C(green). Note the quite perfect overlap between the terminal part of the xG in the opposite strands.

is covalently bonded to the base and co-planar with it. Such expanded bases are able to pair with natural DNA bases by H-bonding, forming base pairs of expanded size, that stacks with each other and with natural bases, assembling helical motifs. Double helices of this kind are more stable than natural DNA, and this enhanced stability was interpreted as a consequence of enhanced stacking whether within each strand or across the strands [49]. A stacked pair of expanded guanine (xG) and cytosine (C) is sketched in Fig. 7. In Ref. [50] a detailed study of the optical properties for all the isolated expanded bases, the xGC$_H$, the xAT$_H$ and some stacked configurations is reported. TDDFT, as in the case of natural DNA bases, gives satisfactory results when compared with the available experiments [51,52] for all the benzo-fused bases, in particular for the appearance of the onset of absorption at a smaller energy (around 3.5 eV) than in any natural nucleobase: this onset peak is the novel feature induced by the benzene-base fusion. Moreover, also the more intense peaks above 4 eV are well reproduced by TDDFT calculations (see Figs. 2 and 3 in Ref. [50]). In Fig. 7 the optical spectrum for two stacked xG–C pairs with the expanded guanine in different strands [d(xGC)$_2$] is shown and is compared with the double of the absorption spectrum of the H-bonded xG–C pair. Similar effects found for natural DNA assemblies are observed also for the expanded analogues. In particular for all the studied stacked complexes the main trait is the pronounced hypochromicity, which is largest for the planar structures where the stacking interaction are mostly favoured, as in the case of d(xGC)$_2$ shown in the figure. For this case, where an enhanced interplane overlap is present, the hypochromicity is more pronounced than in natural DNA. The enhanced stacking interaction between base pairs could have consequences on the conductance and rates of electron/hole transfer, making xDNA helices very appealing for future nanoelectronics applications.

Besides optical absorption, another optical technique that is even more widely used for the characterisation of chiral biomolecules is circular dichroism. TDDFT, in its real-time propagation scheme, allows for a straightforward calculation of the rotatory power or circular dichroism spectra (see Ref. [53] for the details). The implementation and computation of circular dichroism spectra by TDDFT in real-time is in progress and will be the topic of a self-standing investigation [54], that should allow the identification of helical fingerprints in the optical characteristics, and more direct interpretation of standard post-synthesis experimental data. Just as an example, we show in Fig. 8 the calculated optical absorption, and circular dichroism spectra for an isolated adenine base (A) and a stacked dimer made of two adenines (dA$_2$) having interplane distance of 3.4 Å and a twist angle of 36°.

The absorption spectra of the isolated adenine and the dimer (top panel) have practically the same shape and the hyphocromicity induced by the stacking interaction discussed above is observed, and the excitation energies at 182,

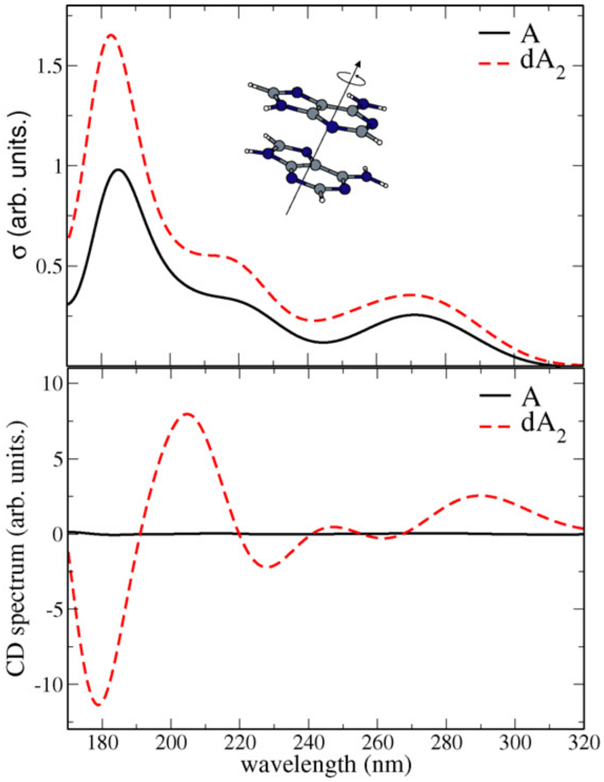

Fig. 8. Calculated dipole strength function (top) and circular dichroism (bottom) for an isolated adenine base (solid line) and for a stacked dimer of two adenines (dashed line). The structure of the stacked dimer is also shown in the insert.

215, and 270 nm (6.9, 5.76 and 4.59 eV) and the shape of the spectrum are in very good agreement with recent experiments [55]. Totally different is the circular dichroism signal: while the optical rotatory power of an isolated adenine is very small in the considered range of energies, we observe a strong signal for the dimer induced by the helical motif, with strong negative and positive bands at 180 nm and 200 nm (6.9 and 6.2 eV, respectively), in satisfactory agreement with recent experimental data where the negative and positive peaks are measured respectively at 182 nm and 194 nm [55].

5. Dynamics of biological molecules and TDDFT

Upon absorption of light, the associated electronic transition may trigger a subsequent nuclear dynamics: photodissociation, photo-isomerisation, etc. These relaxation processes are crucial to the understanding of many biomolecular processes, such as, e.g., the isomerisation of retinol. TDDFT is solely concerned with the electronic structure and in order to study the coupled electron-ion dynamics we need to either extend it or couple it with some flavour of molecular dynamics (MD).

Ideally, one could make use of multi-component TDDFT [56], which treats both electrons and nuclei quantum-mechanically, and on the same footing. This approach, however, is still immature and the computational resources that it would require are still out of reach. MD, on the other hand, assumes classical nuclei, which is sufficient for many purposes, although its formulation involves addressing the difficult problem of non-adiabaticity.

MD can be used in conjunction with TDDFT in various different ways, depending on the purpose and of the computational requirements of the particular system that is addressed. For example, one may perform classical, Born–Oppenheimer MD on the ground state energy surface making use of DFT, and use TDDFT to obtain the time-resolved absorption spectrum – simply performing one TDDFT calculation at sampled points in the molecular trajectory. One example of this approach is given below – applied to the azobenzene dye. This approach, however, does not address the electronic excited states (and therefore, the photon absorption processes) nor the possibility of non-adiabaticity.

In order to allow for electronic transitions, one can use, among others: Ehrenfest dynamics, and surface hopping [70,71]. In the former case, the forces on the (classical, point particle) nuclei are calculated "on the fly" by making use

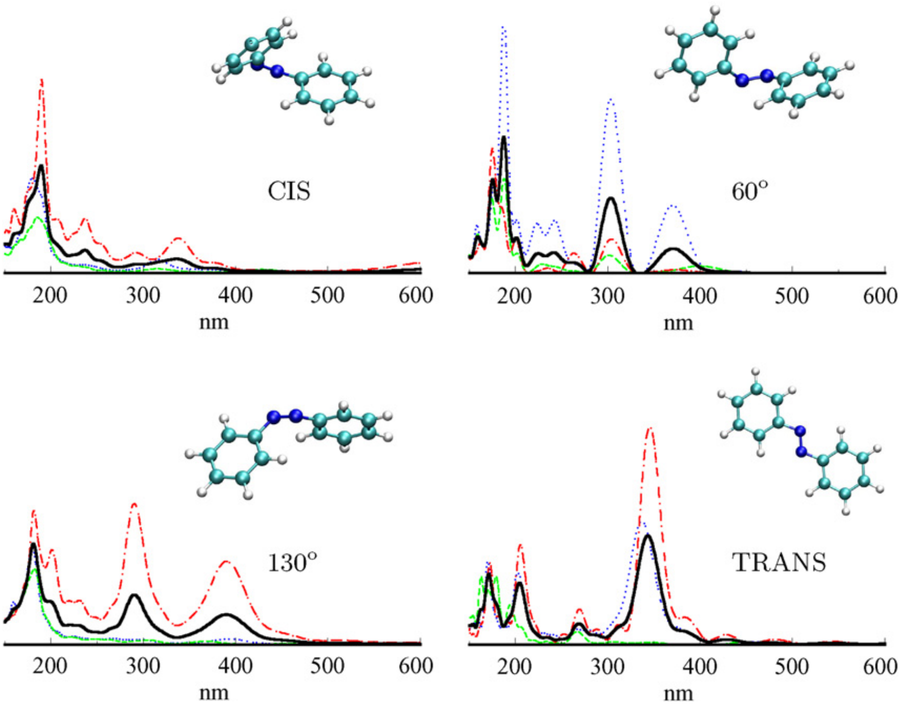

Fig. 9. Calculated photoabsorption spectra of the isolated azobenzene chromophore, at four points along an approximate isomerisation path connecting the cis and the trans conformations. The black curve represents the average absorption; the coloured lines are the decomposition of the spectra into different spatial directions, showing the anisotropy.

of the Ehrenfest theorem (i.e., the force on a nucleus is the expectation value of the partial derivative of the electronic Hamiltonian with respect to the nuclear coordinate). The electronic equations incorporate the nuclear positions as time-varying parameters, and an external, classical, electromagnetic field may also be included. In the surface-hopping scheme, one performs classical adiabatic MD on ground or excited state surfaces, and a stochastic algorithm permits to "hop" between them. We will illustrate below the TDDFT-based Ehrenfest approach. Another example, and the theoretical and computational details of our approach are given in Refs. [73,74]. We also refer the reader to the last section of this article (Section 6) for a brief discussion of the problems related to the combination of classical ion dynamics with quantum electron dynamics (for a nice review on this topic see, for example, Ref. [75]).

5.1. The azobenzene dye

The azobenzene molecule is formed by two phenyl rings joined by an azo group (see Fig. 9 where it is depicted in various conformations). It undergoes very rapid (below the picosecond) cis/trans isomerisation around the N=N bond with very high efficiency [40]. This isomerisation implies an increase of 3 Å and a change in the dipole moment from 6 to 9 Debye. This property has arised great interest on azobenzene-related systems for nanoscale opto-mechanical devices. Furthermore this structural change goes together with a change in dipole moment that can be used to act as a optical-gate in, for example, nanotube-based transistors [41,42]. More relevant for the present work, in Ref. [43], Spörlein et al. have performed femtosecond time-resolved optical spectroscopy on a certain small peptide (APB), which acts as an optical trigger due to the presence of azobenzene. Their results demonstrate how the absorbance is strongly red-shifted upon cis/trans isomerisation. This pronounced spectral difference permits both a selective light-induced interconversion and easy spectroscopical differentiation. We have addressed this problem within our TDDFT formulation: Fig. 9 depicts our calculated photoabsorption spectra for four selected nuclear conformations selected along one predefined approximate isomerisation path joining the cis and trans positions. It must be noted that the peptide backbone has been only used to relax the nuclear conformations – the isomerisation path has been obtained by minimisation using a semiempirical QM/MM approach. Later the peptide backbone has been cut, and TDDFT calculations have been performed only on the azobenzene molecule. The results, nevertheless, show a redshift of most

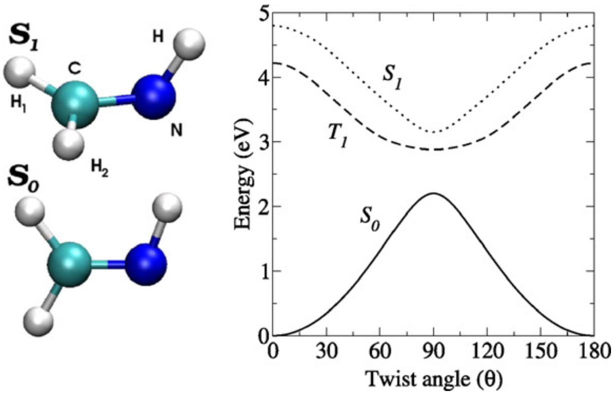

Fig. 10. Left: Geometries of the ground (S_0) – below – and S_1 – above – states of the formaldimine molecule. Right: Energy surfaces of the ground and first excited singlet and triplet states, as a function of the twist angle of the C=N bond – which is simultaneously elongated, see text.

of the spectral weight, in the same manner than the experiment. The position of the main peak does not coincide, which may be due to neglecting the influence of the peptide.

5.2. *Formaldimine*

Imines are those compounds of structure $RN{=}CR_2$, where R may be hydrogen or any hydrocarbyl group. Relatedly, Schiff's bases are those imines bearing a hydrocarbyl group on the nitrogen atom: $R'N{=}CR_2$ (R' not equal to H). Formaldimine ($HN{=}CH_2$, see Fig. 10), also known as methanimine, is the smallest imine, and sometimes is also referred as the smallest Schiff base. In Fig. 10 we have depicted the geometries of the ground state (S_0) and first singlet excited state (S_1). The former is planar, whereas in the latter the hydrogen associated to nitrogen is rotated 90 degrees with respect to the plane of the rest of the molecule. The molecule presents a hetero double bond, C=N, which is one of the most important photoreceptors in organic chemistry: Photo-induced rotation around double bonds are processes of primary interest in Biochemistry (the paradigmatic case being the rotation of the molecular trigger of the human vision process).

Due to this relevance, formaldimine and its protonated counterpart, formaldiminium or methaniminium, has already been studied as a prototypical case-study. Bonačić–Koutecký and others [57,58,66,67] have performed multireference configuration interaction calculations of the electronic structure and geometrical conformations of the lowest singlet and triplet states. The focus was placed on the implications on photochemistry, by regarding the potential energy surfaces along possible isomerisation paths: the *cis* ↔ *trans* rearrangement may proceed via two different paths: in plane – by moving H along the H_1H_2CN plane – or out of plane – by transversing the S_1 geometry depicted in Fig. 10. Note that in the case of formaldimine the *cis* or *trans* character of a conformation is ambiguous. Moreover, the discussed isomerisation leaves the molecule unchanged. More interesting cases in Biochemistry (e.g. the isomerisation of retinal in the vision process) also imply double bond rotations, although in these cases the product and the reactant are not identical. The out-of-plane route for the formaldimine isomerisation seemed to be favoured energetically. Moreover, the surface energy curves demonstrate the existence of a conical intersection between the first two electronic singlet states in this latter path, leading to the necessity of a truly non-adiabatic treatment.

More recently, Parrinello and others [68,69] have addressed the topic in the framework of DFT. In a former publication [68], they translated restricted open-shell Hartree–Fock (ROHF) to the Kohn–Sham formalism (restricted open-shell Kohn–Sham, ROKS), and studied the geometry of excited singlet states of several molecules, including formaldimine. They also used this technique to perform Car–Parrinello adiabatic molecular dynamics on the first excited singlet step. In the latter work [69] they extended the formalism to allow for non-adiabatic transitions via the surface-hopping algorithm [70,71]. Both works suggest the out-of-plane isomerisation.

In organic photochemistry, usually the only relevant excited states are the low lying ones. Of special relevance are the first singlet S_1 and the first triplet T_1. Since the latter is the lowest one with triplet spin symmetry, ground state DFT theory may be used to investigate it, in contrast to the S_1 state, which requires other approaches. However, following Frank and others [68], we may utilise Ziegler's sum method [72] and calculate the singlet excitation energy by making use only of standard DFT, in the following manner: Let us call Φ^{GS} the ground state of a closed shell system such as the formaldimine molecule, which in DFT is built from the Slater determinant of a set of Kohn–Sham orbitals: $\Phi^{\mathrm{GS}} = \mathrm{Slater}\{\psi_1\bar{\psi}_1, \ldots, \psi_n\bar{\psi}_n\}$, where the overlined orbitals are spin up. The first triplet states may be obtained by minimising a set of KS orbitals with the following fixed spin symmetry: $\Phi^{\mathrm{t}_1} = \mathrm{Slater}\{\psi_1\bar{\psi}_1, \ldots, \bar{\psi}_n\bar{\psi}_{n+1}\}$. Another of the three degenerate triplet states is obtained by using spin down for the last two orbitals. Unfortunately, the first excited singlet state cannot be obtained from a single Slater determinant. We may define the "mixed states", m_1 and m_2, as $\Phi^{\mathrm{m}_1} = \mathrm{Slater}\{\psi_1\bar{\psi}_1, \ldots, \psi_n\bar{\psi}_{n+1}\}$ and $\Phi^{\mathrm{m}_2} = \mathrm{Slater}\{\psi_1\bar{\psi}_1, \ldots, \bar{\psi}_n\psi_{n+1}\}$. The remaining triplet and the singlet may then be obtained by combining them:

$$\Phi^{t_3} = \frac{1}{\sqrt{2}}\left(\Phi^{m_1} - \Phi^{m_2}\right) \tag{1}$$

$$\Phi^{s} = \frac{1}{\sqrt{2}}\left(\Phi^{m_1} + \Phi^{m_2}\right) \tag{2}$$

The singlet energy may then be obtained from the energies of the m and t states, as in:

$$E(s) = 2E(m) - E(t) \tag{3}$$

For the S_0 geometrical configuration (planar, lower part of Fig. 10, this procedure yields a singlet excitation energy of 4.8 eV, in agreement with the LDA work of Ref. [68]. This scheme also allows us to obtain a minimised geometry for the S_1 subspace. However, we have not made a fully unrestricted seek: to alleviate the calculational burden, we have assumed the shape depicted the upper part of Fig. 10: The HCN plane is assumed to be perpendicular to the $\mathrm{H_1H_2CN}$ plane. All geometrical parameters are then fixed to the values they have in the S_0 configuration, except for the C=N bond length which is then allowed to relax. The elongation of the bond in the singlet state thus obtained is 0.102 Å, in good agreement with the 0.085 Å of Ref. [68].

We then consider the rotation between the S_0 and S_1 geometries. For that purpose, we define a given path joining both geometries in configuration space: defining θ to be the twist angle around the C=N bond, the C=N bond length $l(\theta)$ is continuously elongated as $l(\theta) = \sin^2(\theta)l(0) + \cos^2(\theta)l(\pi/2)$. Along these geometries, we may sample a given number of configurations and study the excited states energies by calculating the linear response optical spectrum. We may utilise the two methods that we dispose of: linear response in the frequency domain, and time propagation. For the first singlet and triplet states energy, we may also use again previous sum rule.

The results when using Eq. (3) (i.e., still ground state DFT) are displayed in Fig. 10 (right side). The figure is in agreement with Fig. 7 in Ref. [57], where a CI method was employed. Note that for this line in configuration space we do not observe a conical intersection, but an avoided crossing. However, the surfaces do cross [58], although a different path should have been chosen to manifest it. In any case, note how the ground and excited states approach, which involves a non-negligible jump probability, and signal this isomerisation process as an intrinsically non-adiabatic one.

The photoabsorption cross sections calculated at seven points in configuration space linking the S_0 and S_1 geometries are shown in Fig. 11. It displays results obtained with two common formulations of the linear-response TDDFT equations: Casida's approach [59,60] in the frequency domain, and the real-time propagation scheme [61–65]. The red curves are the result of the scheme in the time-domain, whereas the black curves are the result for the scheme in the frequency domain (in this latter case, the lines have been broadened with a Lorentzian curve for comparison purposes). In principle, both methods are mathematically equivalent: the results, specially for the lowest excitations, are indeed very similar. The differences, whose importance increases with the excitation energy, must be assigned to the distinct numerical convergence issues arising in both methods (number of considered virtual orbitals, simulation box size, etc.), which affect the results in an inequivalent way. At full convergence, both curves should overlap.

The excitation to the first triplet configuration T_1 is dark, but the excitation to the first singlet S_0 is present in the graphs (at 4.8 eV for the geometry at $\theta = 0°$, top panel), albeit its small oscillator strength makes it difficult to see it. The insert in the top panel exposes it more clearly. The potential energy surfaces such as the one presented in Fig. 10 may also be reproduced from this figure – moreover, including, if desired, higher lying energy surfaces. The agreement for the S_0 state between these linear response calculations, and those presented in Fig. 10 is almost perfect.

As mentioned above, the molecular dynamics on the S_1 excited state have been investigated already in Ref. [68], as well as non-adiabatic dynamics [69], mixing the ground and the excited state by making use of the surface-hopping idea. Our approach to the simulation of photo-induced geometrical re-organisation is different: we make use of TDDFT to couple the ionic and electronic subsystems to a time-dependent, arbitrarily shaped, classically described, electromagnetic field. A significant laser induced population of an electronic excited state may lead to geometrical

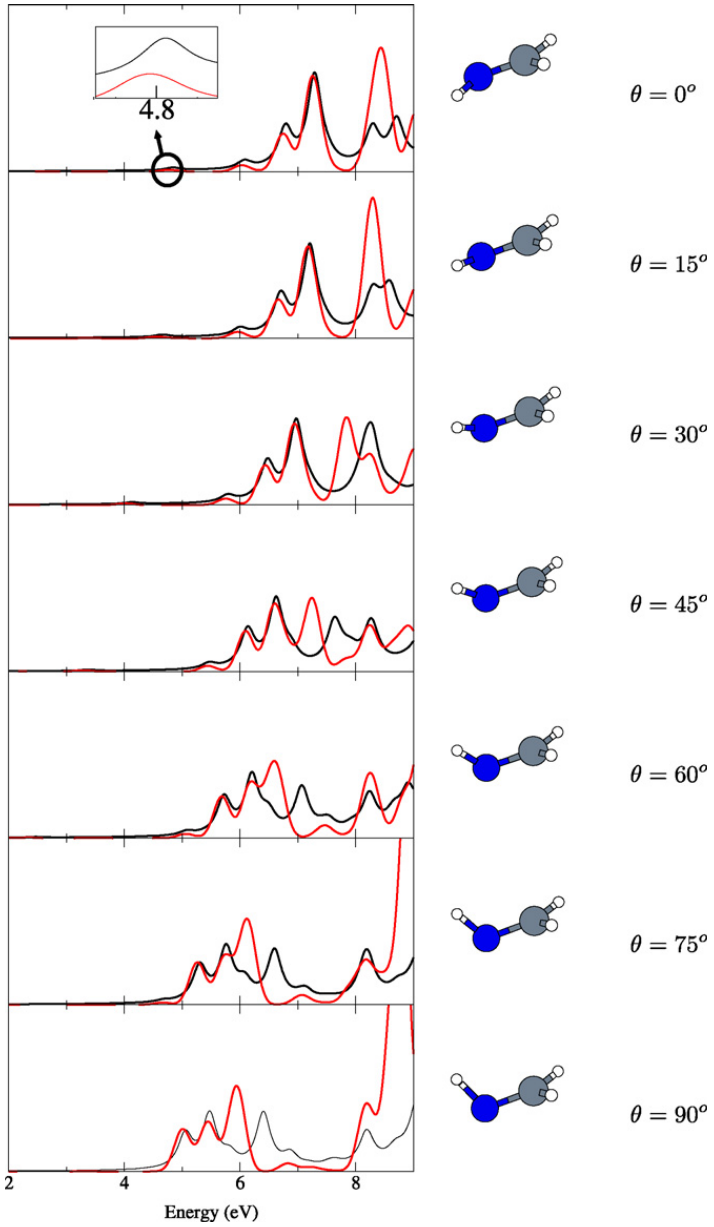

Fig. 11. Photoabsorption cross section of the formaldimine molecule, calculated at some sampled points along an isomerisation path linking the predicted S_0 and S_1 geometries (see text for details). Red: time-propagation method; Black: frequency domain line response method. The insert in the upper panel details the S_0 excitation, of very low oscillator strength, at 4.8 eV.

re-organisation, which means processes such as photo-fragmentation or photo-isomerisation. Some examples of this approach to photo-dissociation are described in Ref. [73]. In the present case, however, we have tried populating the S_1 state, which should lead to an atomic rearrangement leading to the minimum energy conformation for that state, i.e. the upper model in Fig. 10. However, we have not yet been able of observing this process. One of the explanations for this failure is the very low oscillator strength of the pursued transition, which renders difficult its population, even though we performed the simulations modelling high-intensity lasers. Another more fundamental open question is ascertaining to which extent the classical treatment of the electromagnetic fields may be suitable for these purposes.

The simulations depicted in Figs. 12 and 13 are different examples. In both cases, we have used a more traditional approach, which consists of artificially preparing the system in an excited state by populating the LUMO orbital with one electron. Thereafter, TDDFT is used to propagate the electronic state, whereas the nuclei are also propagated governed by Newton's equations of motion, according to the Ehrenfest-path methodology. In the first example (Fig. 12), the ions are initially static, and the resulting dynamics consist of an in-plane isomerisation: the hydrogen atom at-

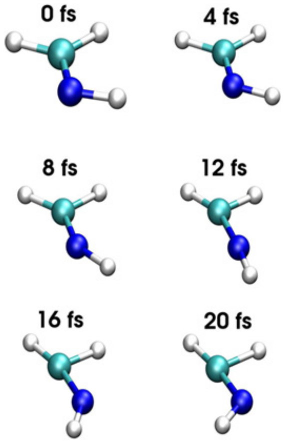

Fig. 12. Snapshots of a simulation performed on the formaldimine molecule. The system is initially prepared by putting one electron of the HOMO on the LUMO orbital. The ionic system is initially frozen.

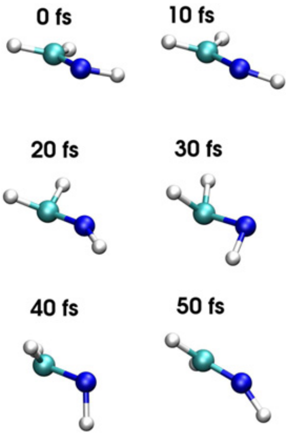

Fig. 13. Snapshots of one of the simulations performed on the formaldimine molecule. The system is initially prepared by putting one electron of the HOMO on the LUMO orbital. The ionic system is initially given a random distribution of velocities corresponding to 300 K.

tached to nitrogen pendulates from one side to the other, without leaving the original molecular plane. The movement is very rapid; the isomerisation needs only 20 fs. If the simulation is allowed to continue, the process is repeated in the same manner. In the second example (Fig. 13) the ionic system is given an initial random velocity distribution corresponding to a temperature of 300 K. The result is rather different: the molecule is rather distorted, and after an oscillation of the hydrogen atom from one molecular side to the other (which lasts only 20 fs), it goes back to its original position but following the out-of-plane route.

5.3. The time-dependent electron localisation function

The real-time dynamics calculations based on TDDFT, such as the ones presented in the previous section, permit us to observe organic chemistry "in action", and in principle should allow us to see how bonds are born and die during chemical reactions, or how they are altered by the presence of an external field. The concept of "bond", however, is an elusive one, and we wish to finish this section on applications of TDDFT with an excursion to a topic that may help to gain intuition about this concept: the electron localisation function (ELF), and the time-dependent ELF (TDELF).

The concept of bond is based on that of electron pair, and was already systematised by G.N. Lewis [76] in 1916. Electrons form pairs due to their $1/2$ spin and Pauli's exclusion principle, and close "shells" – of eight electrons in many atoms due to their spherical symmetry. The preference for pairing and closing shells seemed to explain most bonding in Chemistry. This simple picture of Lewis is still in use today, and the reason is that electrons do indeed "localise" in pairs when forming molecules, and a big amount of the basic machinery of Chemistry is rather well explained with Lewis arguments. We speak of "localised" groups of electrons, either pairs of electrons shared between atoms ("bonds"), non-bonding pairs of electrons ("lone pairs"), and also larger groups – double, triple bonds –, atomic inner shells, π electronic systems, etc.

How can one transfer these concepts to mathematical terms? It is not easy to "define" bonds from electronic densities and wave functions. In order to shed light into this problem, the concept of "electron localisation function" (ELF) was tailored by Becke and Edgecombe [77]; a concept that was later extended for time-dependent phenomena thanks to the time-dependent ELF function (TDELF) [78]. The ELF has repeatedly been used to obtain intuitive pictures of bonding properties in molecules in the ground state; the TDELF, in turn, monitored during a TDDFT-based simulation, helps to visualise time-dependent molecular processes.

We briefly recall the definitions: [77,79,80,78,81,82]

$$\eta(\mathbf{r};t) = \frac{1}{1 + [C(\mathbf{r};t)/C^{\mathrm{HEG}}(\mathbf{r};t)]^2} \tag{4}$$

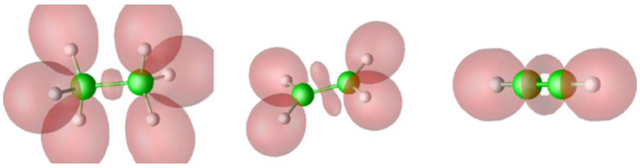

Fig. 14. ELF isosurfaces ($\eta = 0.85$) of ethane (left), ethene (center) and ethyne (right). The single bond of ethane shows as a convex ELF basin between the carbon atoms; the double bond of ethene originates two bond attractos, which in turn imply an eight-shaped ELF isosurface between the carbons), whereas the triple bond of the linear ethyne shows as a ring.

$$C(\mathbf{r};t) = \sum_{\sigma=\uparrow,\downarrow} \left\{ \tau_\sigma(\mathbf{r};t) - \frac{1}{4}\frac{[\nabla n_\sigma(\mathbf{r};t)]^2}{n_\sigma(\mathbf{r};t)} - \frac{j_\sigma^2(\mathbf{r};t)}{n_\sigma(\mathbf{r};t)} \right\} \tag{5}$$

where η is the (TD)ELF function, τ_σ is the kinetic energy density, and j_σ^2 is the squared modulus of the current density. $C^{\mathrm{HEG}}(\mathbf{r};t)$ is the value of the C function for a homogeneous electron gas whose density coincides with the density at point $\mathbf{r}$. This expression is valid only for one-determinantal wave functions, and therefore lends itself to be used within the context of Hartree–Fock or (TD)DFT. An exact definition, in terms of the one-reduced density matrix, can be found, for example, in the seminal Ref. [77]. We should note that the last term of Eq. (5), depending on the current, is, however, neglected in that original derivation, which assumed real-valued wave functions. That term is necessary in the time-dependent case [78].

One may then relate the topology of the ELF to the electron localisation properties of the molecules – which in turn are related to their bonding properties. The ELF takes values between 0 and 1 – high values correspond with high localisation (bonds, lone pairs), whereas low values correspond with delocalised electrons. As a scalar bounded function, it will have attractors and basins; these basins may be *core* basins (their domain contains one nucleus), bonding (located between core attractors) and non-bonding (the rest, that contain the lone-pairs of electrons). In this way, the ELF basins show us the bonds and the lone pairs of the molecules.

We plot in Fig. 14 a classical illustration of the ELF ability to mark bonds: the single, double and triple bond ethane, ethene, and ethyne, respectively. However, our main goal here is to show the TDELF in a dynamical process. We have chosen for that purpose the collision of the acetylene and oxygen molecules, which for the particular chosen initial conditions, leads to the creation of two carbon monoxide molecules (i.e. combustion).

The simulation is performed with the non-adiabatic molecular dynamics based on TDDFT described in the previous section; for this particular example we have used the simple-minded local density approximation (LDA) to the exchange and correlation functional. Some snapshots taken during the simulation are show in Fig. 15. The initial orientation and placement of the molecules is the one depicted in the first snapshot. Their relative initial velocity is 7×10^{-3} a.u. The plot shows, besides the atomic positions (carbon in green, oxygen in red, hydrogen in white), one isosurface of the ELF ($\eta = 0.8$), which contours regions of high electron localisation. The isosurface is coloured: redder areas correspond to higher electron density, whereas whitish areas correspond to regions of almost negligible density. We have done this in order to make apparent one of the less intuitive features of the ELF: it may have large values in regions of low electronic density.

Initially, the acetylene molecule displays its characteristic toroidal ELF isosurface, typical of triple bonds. After 20 fs, the two molecules collide, and a strong link is created between the hydrogen atom of acetylene and one oxygen. The oxygen molecule is rapidly broken due to the collision; at $t = 40$ fs we can see how one oxygen atom starts moving towards the other side of the acetylene molecule, and one of the hydrogen atoms is ejected. The triple bond between the two carbon atoms is already strongly distorted; note how this is already visible in the ELF isosurface. In the next snapshots, we start to see the lone pairs characteristic of CO molecules and the remaining hydrogen atom is also ejected, carrying away one electron.

6. Summary and perspectives

It is clear that the use of TDDFT in the area of photochemistry has been growing in the past decade [6]. The keys for this success are clear: First of all, TDDFT is a simple theory, easy to implement, and leads to very efficient numerical implementations. Furthermore, TDDFT is quite reliable and can be used to obtain useful information: which is evident

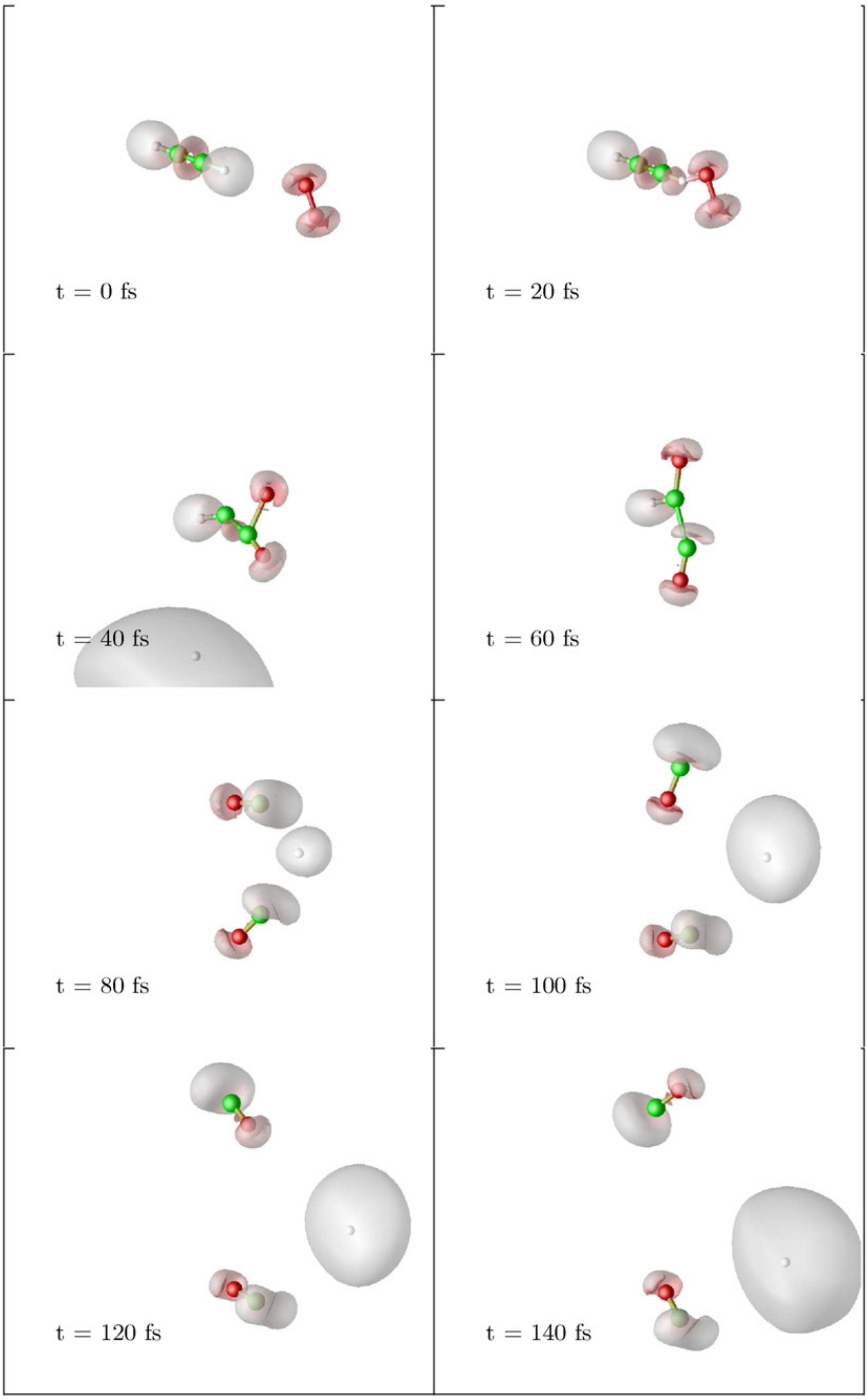

Fig. 15. Snapshots of the TDELF function (isosurface of the ELF ($\eta = 0.8$), taken during the simulation of the acetylene combustion, at the indicated times. Redder areas of the isosurface correspond to higher electron density, whereas whitish areas correspond to regions of almost negligible density.

from the examples presented in this Article. In fact, TDDFT in many cases outperforms other quantum chemical methods, especially for medium and large systems [6,11,12].

However, and in spite of its many successes, TDDFT has its shortcomings. Note that these problems are not inherent to the theory itself – which is an *exact* reformulation of time-dependent quantum-mechanics, but to the approximate functionals that are used in practical applications, or to the specific implementation of the combined electron-ion dynamics to address non-adiabatic effects in the excited-state dynamics.

One of the most important problems is related to the asymptotic behaviour of the LDA xc potential: For neutral finite systems, the exact xc potential decays as $-1/r$, whereas the LDA xc potential falls off exponentially. Note that most of the generalised-gradient approximations (GGAs), or even the newest meta-GGAs have asymptotic behaviours similar to the LDA. This problem gains particular relevance when calculating ionisation yields (the ionisation potential calculated with the ALDA is always too small), in situations where the electrons are pushed to regions far away from the nuclei (e.g., by a strong laser) and feel the incorrect tail of the potential, or in excitations that involve Rydberg states. There are several ways to correct this problem, either by directly modelling the xc potential [83], or by using orbital functionals with the right asymptotic behaviour, like the exact exchange [84] or the self-interaction corrected [85] functionals. Along those lines it is important to mention that present local and semilocal functionals fail dramatically in describing dispersion forces (e.g., in Van der Waals complexes). At present the impact of those failures in the optical spectra of biomolecules has not been discussed in detail, and most of the cure-schemes address the problem for ground-state calculations either as a post-DFT correction [86,87], or by the use of TDDFT in the adiabatic connection/fluctuation-dissipation scheme [88,89]. Clearly there is a lot of work to be done in this context to describe the role of dispersion forces in the combined excited-state dynamics of complex biomolecules (for example to describe light-induced proton transfer and H-bond breaking/formation).

Another noteworthy problem is the absence of true multiple excitations in the TDDFT response functions. This is due to the use of the adiabatic approximation in the construction of time-dependent xc functionals. There have been some attempts at the construction of functionals including memory effects [90–96] or by including the effect of doubles excitations perturbatively [97,98].

Next, we would like to refer to charge-transfer excitations. TDDFT often predicts charge-transfer states of substantially lower energy and below optical states [99]. This is further complicated by the mismatch between the ionisation potentials of the donor and acceptor parts of the molecule, due to the absence of a derivative discontinuity in the common functionals [100]. Thus, charge-transfer excitations are severely underestimated, sometimes by as much as 1 eV. Several correction schemes have been proposed [101] for this problem. However there is not yet a good functional incorporating those processes both at the static as well as at the dynamical level. Thus, the dynamics of many biological processes that are mediated by that type of intermediate states, may not be properly accounted for by present TDDFT implementations. (Kernels based on many-body perturbation theory, as the ones derived to describe the optical properties of solids [12] could account for those excitations. However, it is still not known to which degree of accuracy.)

However, perhaps the largest failure of TDDFT is in the calculations of the optical spectra of solids [102,12]. In fact, the lack of a long-range component of the xc kernel leads to TDDFT spectra of very poor quality, only marginally different from simple RPA calculations. Again, several possible alternatives to correct this problem have been proposed, from orbital functionals that include this long-range component [103–107], to empirical correction terms to the xc kernel [108–110]. Those functionals might have implications in the description of multiple excitations, charge-transfer processes and photo-induced molecular dissociation.

Another important aspect of the specific examples discussed in this article is related to the fact that electron dynamics are usually determined quantum mechanically but the nuclear motion is treated within the framework of classical mechanics. Despite a large difference in the general time scales of electronic and nuclear motions, electronic wavepackets quite often couple with the dynamics of nuclear motion. The proper incorporation of the electronic response is crucial for describing a host of dynamical processes, including laser-induced chemistry, dynamics at metal or semiconductor surfaces, and electron transfer in molecular, biological, interfacial, or electrochemical systems (in particular it is crucial also for describing light-induced processes in biomolecules, and many other photochemical reactions). The two most widely used approaches to account for non-adiabatic effects are the surface-hopping method and the Ehrenfest method implemented here. The surface-hopping approach extends the Born–Oppenheimer framework to the non-adiabatic regime by allowing stochastic electronic transitions subject to a time- and momenta-dependent hopping probability. On the other hand Ehrenfest successfully adds some non-adiabatic features to molecular dynamics but it is rather incomplete. This approximation can fail either when the nuclei have to be treated as quantum particles (e.g. tunnelling) or when the nuclei respond to the microscopic fluctuations in the electron charge density (heating) not reproducing the correct thermal equilibrium between electrons and nuclei (which constitutes a fundamental failure when simulating the vibrational relaxation of biomolecules in solution). However there have been some proposals in the literature to include some of those effects in a modified Ehrenfest scheme [111,112] or beyond it (see, e.g. Ref. [113]).

On a more practical level, the possibility of simulating dynamics on electronic excited states requires the capability of computing forces on those states. On the electronic ground state, the computation of the force is a trivial task within the DFT formalism because the force on an ion is an explicit functional of the ground state density (the Hellman–Feynman expression). In the Ehrenfest dynamics approach, the same expression can be used – the forces are again trivially dependent on the time-dependent density. However, if we attempt to use the same idea to perform dynamics on a given "pure" excited state, we are confronted with the problem of obtaining the corresponding excited state density – not at all a trivial task. Fortunately, one can use linear-response TDDFT in order to obtain suitable expressions (see. e.g. Refs. [114] and [115]).

In conclusion, TDDFT has become a standard tool to calculate excitation energies, and is by now incorporated in all of the major quantum-chemistry codes. There are many examples of successful applications of this theory in the literature, and its usefulness for the study of large, complex systems is unique. Clearly, there are some cases where TDDFT does not perform well. However, in our opinion, we should not dismiss these problems as failures of TDDFT, but as a challenge to the next generation of "density-functionalists", in their quest for better approximations to the elusive xc potential.

Acknowledgements

We acknowledge the fruitful collaboration with X. López, Y. Pouillon, X. Andrade, S. Botti, M. Gruning, R. Di Felice, C. Attacalite, A. Marini, L. Wirtz, J.M. García-Lastra, F. Nogueira, M. Oliveira, F. Lorenzen, C. Rozzi, Steen B. Nielsen, and E.K.U. Gross in many parts of the work presented here. We benefited from discussions with R. Bitl, E. Molinari, and S.G. Louie. The development of this project benefited from many informal discussions with the NANOQUANTA/ETSF members as well as with the Editors and contributors to the TDDFT book [6], the outcome of the series of schools and workshops organised by some of the authors on "Time-Dependent Density-Functional Theory: Prospects and Applications", held in Benasque Spain since 2004 (see http://nano-bio.ehu.es).

We acknowledge funding by the Deutsche Forschungsgemeinschaft through SPP 1093 and SFB 658, Spanish MEC (FIS2007-65702-C02-01) and Grupos Consolidados UPV/EHU of the Basque Country Government (2007), by the European Community through NoE Nanoquanta (NMP4-CT-2004-500198), SANES (NMP4-CT-2006-017310), ANR (Project NT0S-3_43900), DNA-NANODEVICES (IST-2006-029192) and NANO-ERA Chemistry projects, UPV/EHU (SGIker Arina) and the European Community through e-I3 ETSF project (Contract Number 211956). M.A.L.M. acknowledges partial support by the Portuguese FCT through the project PTDC/FIS/73578/2006. The authors thankfully acknowledge the computer resources provided by the Barcelona Supercomputing Center, the Basque Country University UPV/EHU (SGIker Arina) and the Laboratório de Computação Avançada of the University of Coimbra, CPU time from CINECA through INFM-CNR.

References

[1] P.N. Prasad, Introduction to Biophotonics, John Wiley & Sons, Hoboken, 2003.
[2] K. Bacon, Photosynthesis. Photobiochemistry and Photobiophysics, Springer, Berlin, 1999.
[3] C. Musio (Ed.), Vision: The Approach of Biophysics and Neurosciences, World Scientific, Singapore, 2001.
[4] O. Shimomura, Biolumnescence: Chemical Principles and Methods, World Scientific, Singapore, 2006.
[5] O. Shoseyov, I. Levy (Eds.), NanoBioTechnology: BioInspired Devices and Materials of the Future, Humana Press, 2007.
[6] M.A.L. Marques, C. Ullrich, F. Nogueira, A. Rubio, E.K.U. Gross (Eds.), Time-Dependent Density-Functional Theory, Lecture Notes in Physics, vol. 706, Springer-Verlag, Berlin, 2006.
[7] M.A.L. Marques, A. Castro, G.F. Bertsch, A. Rubio, Comput. Phys. Commun. 151 (2003) 60.
[8] A. Castro, H. Appel, M. Oliveira, C.A. Rozzi, X. Andrade, F. Lorenzen, E.K.U. Gross, M.A.L. Marques, A. Rubio, Phys. Status Solidi B 243 (2006) 2465.
[9] E. Runge, E.K.U. Gross, Phys. Rev. Lett. 52 (1984) 997.
[10] E.K.U. Gross, W. Kohn, Adv. Quantum. Chem. 21 (1990) 255.
[11] M.A.L. Marques, E.K.U. Gross, Annu. Rev. Phys. Chem. 55 (2004) 427.
[12] G. Onida, L. Reinig, A. Rubio, Rev. Mod. Phys. 74 (2002) 601.
[13] See, for example, J. Livet, et al., Nature 450 (2007) 56.
[14] S. Takeda, N. Kamiya, Teruyuki Nagamune, Biotechnology Lett. 26 (2004) 121.
[15] T.M.H. Creemers, A.J. Lock, V. Subramaniam, T.M. Jovin, S. Völker, Proc. Natl. Acad. Sci. USA 97 (2000) 2974;
T.M.H. Creemers, A.J. Lock, V. Subramaniam, T.M. Jovin, S. Völker, Nature Struct. Biol. 6 (1999) 557.
[16] S.B. Nielsen, A. Lapierre, J.U. Andersen, U.V. Pedersen, S. Tomita, L.H. Andersen, Phys. Rev. Lett. 87 (2001) 228102.
[17] M.A.L. Marques, X. López, D. Varsano, A. Castro, A. Rubio, Phys. Rev. Lett. 90 (2003) 258101.
[18] B.R. Brooks, R.E. Bruccoleri, B.D. Olafson, D.J. States, S. Swaminathan, M. Karplus, J. Comput. Chem. 2 (1983) 187.
[19] M.J. Field, P.A. Bash, M. Karplus, J. Comput. Chem. 11 (1990) 700.

[20] J. Gao, in: K.B. Lipkowitz, D.B. Boyd (Eds.), Reviews in Computational Chemistry, vol. 7, Wiley VCH, New York, 1995, p. 119.
[21] M.J.S. Dewar, E. Zoebisch, E.F. Healy, J.J.P. Stewart, J. Am. Chem. Soc. 107 (1995) 3902.
[22] R. Wachter, B. King, R. Heim, K. Kallio, R. Tsien, S. Boxer, S. Remington, Biochemistry 36 (1997) 36.
[23] B.G. Bublitz, B. King, S. Boxer, J. Am. Chem. Soc. 120 (1998) 9370.
[24] M. Zimmer, Chem. Rev. 102 (2002) 759, and references therein.
[25] M. Chattoraj, B. King, G. Bublitz, S. Boxer, Proc. Natl. Acad. Sci. USA 93 (1996) 8362.
[26] X. López, M.A.L. Marques, A. Castro, A. Rubio, J. Am. Chem. Soc. 127 (2005) 12329.
[27] M.A.L. Marques, X. Löpez, A. Castro, A. Rubio, in press.
[28] K. Kadish, K.M. Smith, R. Guilard (Eds.), The Porphyrin Handbook, Academic Press, London, 1999.
[29] M. Gouterman, in: D. Dolphin (Ed.), The Porphyrins, vol. 3, Academic Press, New York, 1973.
[30] F. Sottile, C. Hogan, M. Palummo, A. Rubio, in preparation.
[31] D. Varsano, R. Di Felice, M.A.L. Marques, A. Rubio, J. Phys. Chem. B 110 (2006) 7129.
[32] M. Daniels, in: S.Y. Yang (Ed.), Photochemistry and Photobiology of Nucleic Acids, Academic Press, New York, 1976, p. 23.
[33] C.E.C. Hernández, B. Cohen, P.M. Hare, B. Kohler, Chem. Rev. 104 (2004) 1977.
[34] D. Porath, G. Cuniberti, R.D. Felice, in: G. Schuster (Ed.), Topics in Current Chemistry, Springer-Verlag, Heidelberg, 2004, p. 183.
[35] M. Di Ventra, M. Zwolak, in: H.S. Nalwa (Ed.), Encyclopedia of Nanoscience and Nanotechnology and Handbook of Nanostructured Biomaterials and their Application in Nanotechnology, APS, College Park, MD, 2004, p. 475.
[36] R.G. Endres, D. Cox, R. Singh, Rev. Mod. Phys. 76 (2004) 195.
[37] H. Coehn, C. Nogues, R. Naaman, D. Porath, Proc. Natl. Acad. Sci. USA 102 (2005) 11589.
[38] R. Di Felice, A. Calzolari, E. Molinari, A. Garbesi, Phys. Rev. B 65 (2002) 045104.
[39] R. Di Felice, A. Calzolari, in: E.B. Starikov, S. Tanaka, J.P. Lewis (Eds.), Modern Methods for Theoretical Physical Chemistry of Biopolymers, Elsevier, Amsterdam, 2005.
[40] T. Nägele, R. Hoche, W. Zinth, J. Wachtveitl, Chem. Phys. Lett. 272 (1997) 489.
[41] J.M. Simmons, V.E. Campbell, T.J. Mark, F. Léonard, P. Gopalan, M.A. Eriksson, Phys. Rev. Lett. 98 (2007) 086802.
[42] J.M. García-Lastra, K. Thygesen, A. Rubio, Phys. Rev. Lett. 101 (2008) 13302.
[43] S. Spörlein, H. Carstens, H. Satzger, C. Renner, R. Behrendt, L. Moroder, P. Tavan, W. Zinth, J. Wachtveitl, Proc. Natl. Acad. Sci. USA 99 (2002) 7998.
[44] J.H. Watson, F.H. Crick, Nature 171 (1953) 737.
[45] A.A. Henry, F.E. Romesbergi, Curr. Opin. Chem. Biol. 7 (2003) 727.
[46] A.T. Krueger, H. Lu, A.H. Lee, E.T. Kool, Acc. Chem. Res. 40 (2007) 141.
[47] I. Hirao, Curr. Opin. Chem. Biol. 10 (2006) 622.
[48] J. Gao, H. Liu, E.T. Kool, Angew. Chem. Int. Ed. 44 (2005) 3118.
[49] H. Liu, J. Gao, S.R. Lynch, E.T. Kool, Science 302 (2003) 868.
[50] D. Varsano, A. Garbesi, R. Di Felice, J. Phys. Chem. B 111 (2007) 14012.
[51] H. Liu, J. Gao, L. Maynard, Y.D. Saito, E.T. Kool, J. Am. Chem. Soc. 126 (2004) 1102.
[52] H. Liu, J. Gao, E.T. Kool, J. Org. Chem. 70 (2005) 639.
[53] K. Yabana, G.F. Bertsch, Phys. Rev. A 60 (1999) 1271.
[54] D. Varsano, A. Castro, M.A.L. Marques, R. Di Felice, A. Rubio, in preparation.
[55] U. Kadhane, A.I.S. Holm, S.V. Hoffmann, S.B. Nielsen, Phys. Rev. E 77 (2008) 021901.
[56] T. Kreibich, E.K.U. Gross, Phys. Rev. Lett. 86 (2001) 2984.
[57] V. Bonačić-Koutecký, M. Persico, J. Am. Chem. Soc. 105 (1983) 3388.
[58] V. Bonačić-Koutecký, J. Köhler, J. Michl, Chem. Phys. Lett. 104 (1984) 440.
[59] M.E. Casida, in: D.P. Chong (Ed.), Recent Advances in Density Functional Methods, Part I, World Scientific, Singapore, 1995, p. 155.
[60] M. Casida, in: J. Seminario (Ed.), Recent Developments and Applications in Density Functional Theory, Elsevier, Amsterdam, 1996, p. 391.
[61] K. Yabana, G.F. Bertsch, Phys. Rev. B 54 (1996) 4484.
[62] K. Yabana, G.F. Bertsch, Z. Phys. D 42 (1997) 219.
[63] K. Yabana, G.F. Bertsch, Phys. Rev. A 58 (1999) 2604.
[64] K. Yabana, G.F. Bertsch, Phys. Rev. A 60 (1999) 3809.
[65] M.A.L. Marques, A. Castro, A. Rubio, J. Chem. Phys. 115 (2001) 3006.
[66] V. Bonačić-Koutecký, J. Michl, Theor. Chim. Acta 68 (1985) 45.
[67] V. Bonačić-Koutecký, K. Schöffel, J. Michl, Theor. Chim. Acta 72 (1987) 459.
[68] I. Frank, J. Hütter, D. Marx, M. Parrinello, J. Chem. Phys. 108 (1998) 4060.
[69] N.L. Doltsinis, D. Marx, Phys. Rev. Lett. 88 (2002) 166402.
[70] J.C. Tully, R.K. Preston, J. Chem. Phys. 55 (1971) 562.
[71] J.C. Tully, J. Chem. Phys. 93 (1990) 1061.
[72] T. Ziegler, A. Rauk, E.J. Baerends, Theor. Chim. Acta 43 (1977) 261.
[73] A. Castro, M.A.L. Marques, J.A. Alonso, G.F. Bertsch, A. Rubio, Eur. Phys. J. D 28 (2004) 211.
[74] A. Castro, A first-principles time-dependent density functional theory scheme for the computation of the electromagnetic response of nanostructures, PhD. Thesis, University of Valladolid, 2004. The thesis can be downloaded from http://nano-bio.ehu.es/files/acastro_phd.pdf.
[75] A.P. Horsfield, D.R. Bowler, A.J. Fisher, T.N. Todorov, C.G. Sanchez, J. Phys. Cond. Matt. 16 (2004) 8521.
[76] G.N. Lewis, J. Am. Chem. Soc. 38 (1916) 762.
[77] A.D. Becke, K.E. Edgecombe, J. Chem. Phys. 92 (1990) 5397.

[78] T. Burnus, M.A.L. Marques, E.K.U. Gross, Phys. Rev. A 71 (2005) 010501.
[79] R.F.W. Bader, S. Johnson, T.-H. Tang, P.L.A. Popelier, J. Phys. Chem. 100 (1996) 15398.
[80] J.F. Dobson, J. Chem. Phys. 98 (1993) 8870.
[81] B. Silvi, A. Savin, Nature 371 (1994) 683.
[82] A. Savin, R. Nesper, S. Wengert, T.F. Fässler, Angew. Chem. Int. Ed. Engl. 36 (1997) 1808.
[83] R. van Leeuwen, E.J. Baerends, Phys. Rev. B 49 (1994) 2421.
[84] F. Della Sala, Andreas Grling, Int. J. Quantum Chem. 91 (2003) 131.
[85] J.P. Perdew, A. Zunger, Phys. Rev. B 23 (1981) 5408.
[86] E. Hult, Y. Andersson, B.I. Lundqvist, Phys. Rev. Lett. 77 (1996) 202.
[87] H. Rydberg, M. Dion, N. Jacobson, E. Schröder, P. Hyldgaard, S.I. Simak, D.C. Langreth, B.I. Lundqvist, Phys. Rev. Lett. 91 (2003) 126402.
[88] W. Kohn, Y. Meir, D.E. Makarov, Phys. Rev. Lett. 80 (1998) 4153.
[89] J.F. Dobson, A. White, A. Rubio, Phys. Rev. Lett. 96 (2006) 073201.
[90] E. Orestes, K. Capelle, J. Chem. Phys. 127 (2007) 124101.
[91] G. Vignale, W. Kohn, Phys. Rev. Lett. 77 (1996) 2037.
[92] M.J. Bünner, E.K.U. Gross, Phys. Rev. Lett. 79 (1997) 1905.
[93] G. Vignale, C.A. Ullrich, S. Conti, Phys. Rev. Lett. 79 (1997) 4878.
[94] C.A. Ullrich, G. Vignale, Phys. Rev. B 65 (2002) 245102;
C.A. Ullrich, G. Vignale, Phys. Rev. B 70 (2004) 239903(E).
[95] Y. Kurzweil, R. Baer, J. Chem. Phys. 121 (2004) 8731.
[96] I.V. Tokatly, Phys. Rev. B 71 (2005) 165104;
I.V. Tokatly, Phys. Rev. B 71 (2005) 165105.
[97] N. Maitra, F. Zhang, R. Cave, J. Chem. Phys. 120 (2004) 5932.
[98] M. Casida, J. Chem. Phys. 122 (2004) 054111.
[99] A. Dreuw, J.L. Weisman, M. Head-Gordon, J. Chem. Phys. 119 (2003) 2943.
[100] D.J. Tozer, J. Chem. Phys. 119 (2003) 12697.
[101] D.J. Tozer, M. Head-Gordon, J. Am. Chem. Soc. 126 (2004) 4007.
[102] S. Botti, A. Schindlmayr, R. Del Sole, L. Reining, Rep. Prog. Phys. 70 (2007) 357.
[103] E.K.U. Gross, J. Dobson, M. Petersilka, in: R.F. Nalewajski (Ed.), Density Functional Theory II, in: Topics in Current Chemistry, vol. 18, Springer, Berlin, 1996.
[104] A. Görling, Phys. Rev. A 55 (1997) 2630.
[105] A. Görling, Phys. Rev. A 57 (1998) 3433.
[106] A. Görling, Int. J. Quantum Chem. 69 (1998) 265.
[107] Y.H. Kim, A. Görling, Phys. Rev. B 66 (2002) 035114.
[108] S. Botti, A. Fourreau, F. Nguyen, Y.-O. Renault, F. Sottile, L. Reining, Phys. Rev. B 72 (2005) 125203.
[109] S. Botti, F. Sottile, N. Vast, V. Olevano, L. Reining, H.-C. Weissker, A. Rubio, G. Onida, R. Del Sole, R.W. Godby, Phys. Rev. B 69 (2004) 155112.
[110] L. Reining, V. Olevano, A. Rubio, G. Onida, Phys. Rev. Lett. 88 (2002) 066404.
[111] A. Bastida, C. Cruz, J. Zúñiga, A. Requena, B. Miguel, J. Chem. Phys. 126 (2007) 014503.
[112] K. Takatsuka, J. Phys. Chem. A 111 (2007) 10196.
[113] A.P. Horsfield, D.R. Bowler, H. Ness, C.G. Sánchez, T.N. Todorov, A.J. Fisher, Rep. Prog. Phys. 69 (2006) 1195.
[114] F. Furche, R. Ahlrichs, J. Chem. Phys. 117 (2002) 7433.
[115] I. Tavernelli, U.F. Röhrig, U. Rothlisberger, Mol. Phys. 103 (2005) 963.

THE JOURNAL OF CHEMICAL PHYSICS **131**, 084102 (2009)

Ab initio electronic and optical spectra of free-base porphyrins: The role of electronic correlation

Maurizia Palummo,[1,2,a)] Conor Hogan,[1,2,3] Francesco Sottile,[1,4] Paolo Bagalá,[2] and Angel Rubio[5]
[1]*European Theoretical Spectroscopy Facility (ETSF)*
[2]*Department of Physics, University of Rome "Tor Vergata", Via della Ricerca Scientifica 1, 00133 Roma, Italy*
[3]*CNR-INFM-SMC, University of Rome "Tor Vergata", Via della Ricerca Scientifica 1, 00133 Roma, Italy*
[4]*Laboratoire des Solides Irradies, Ecole Polytechnique, CEA/DSM, CNRS, 91128 Palaiseau, France*
[5]*Nano-Bio Spectroscopy Group and ETSF Scientific Development Centre, Dpto. Física de Materiales, Universidad del País Vasco, Centro de Física de Materiales CSIC-UPV/EHU-MPC, Spain; DIPC, Av. Tolosa 72, E-20018 San Sebastián, Spain; and Fritz-Haber-Institut der Max-Planck-Gesellschaft, D-14195 Berlin-Dahlem, Germany*

(Received 10 April 2009; accepted 24 July 2009; published online 24 August 2009)

We present a theoretical investigation of electronic and optical properties of free-base porphyrins based on density functional theory and many-body perturbation theory. The electronic levels of free-base porphine (H_2P) and its phenyl derivative, free-base tetraphenylporphyrin (H_2TPP) are calculated using the *ab initio* GW approximation for the self-energy. The approach is found to yield results that compare favorably with the available photoemission spectra. The excitonic nature of the optical peaks is revealed by solving the Bethe–Salpeter equation, which provides an accurate description of the experimental absorption spectra. The lowest triplet transition energies are in good agreement with the measured values. © *2009 American Institute of Physics*.
[DOI: 10.1063/1.3204938]

I. INTRODUCTION

Porphyrins constitute an important class of π conjugated organic chromophores that play a fundamental role in numerous biological and chemical processes[1–3] and have recently found wide application in developing technologies. Promising memory devices have recently been demonstrated in which porphyrins were used to functionalize nanowires.[4–6] Their oligomers and solid aggregates are of growing interest for optoelectronic devices, solar cells, and light-harvesting devices, as well as having applications in nonlinear optics.[7–12] It is not surprising therefore that, in addition to the numerous experimental studies appearing in the literature, several semiempirical and *ab initio* theoretical studies, based on time-dependent density functional theory (TDDFT) and quantum chemistry techniques, have been carried out in order to characterize the fundamental electronic and optical properties of these molecules.[13–17]

The UV/optical spectra of all porphryins are generally quite similar, being characterized by a number of weak bands or peaks in the optical range (the *Q* bands), and a relatively strong band in the UV region (the Soret or *B* band).[18] The simplest interpretation of porphyrin spectra is given by the Gouterman four-orbital model, a semiempirical configuration interaction scheme involving excitations from the two highest occupied molecular orbitals (HOMOs) to the two lowest unoccupied orbitals (LUMOs).[19] In spite of its success, however, not all spectral features can be explained by the model. In fact, *ab initio* quantum-mechanical approaches are required to gain a thorough knowledge of the excited state and photophysical properties of these molecules, which, despite the numerous technological applications, are not completely understood.

Previous quantum-chemical studies of the porphyrin class of molecules illustrated the important role played by electronic correlation in describing their excited state properties. Excitation energies of free-base porphine have been reported using a variety of techniques, including multiconfigurational second-order perturbation theory (CASPT2),[15] multireference second-order perturbation theory,[20] symmetry adapted cluster-configuration interaction (SAC-CI),[21–24] and similarity transformed equation-of-motion coupled-cluster (STEOM-CC) approaches,[25] generally obtaining a precision of the order of 0.1–0.3 eV.

In the present work, we use an analogous approach based on many-body perturbation theory (MBPT) (Ref. 26) [namely the so-called GW method and the Bethe–Salpeter equation (BSE)], which achieved much success over recent years within the domain of solid-state physics, frequently yielding excitation energies within 0.1–0.3 eV of the experimental values when applied to systems ranging from bulk to zero dimensional.[27–33] The GW/BSE method has not been widely applied, however, to the study of π-conjugated low dimensional and molecular systems. Work carried out in this direction[34–39] furthermore illustrated that some of the usual assumptions made in the application of the method, such as the use of LDA/GGA wave functions as a starting point[37] or the Tamm–Dancoff approximation,[40] are not always valid for

---

[a)] Electronic mail: maurizia.palummo@roma2.infn.it.

molecular systems.[41] The applicability to the porphyrin class of molecules is therefore far from obvious and the present study aims to further knowledge in this direction.

Besides being of general academic interest, the technique should prove to be important for investigating the excitonic character in extended porphyrin oligomers or solid aggregates, for which the use of the less computationally demanding TDDFT approach has been questioned,[42] but which is naturally accessible within GW/BSE. In this work we concentrate on the electronic and optical properties of two such porphryins, namely, free-base porphine (H_2P), the basic building block of all porphryins, and a phenyl derivative, tetraphenylporphyrin (H_2TPP). This study aims, therefore, to be a first step toward a complete *ab initio* analysis of the exciton character in porphyrin systems and in particular for understanding how this character changes when moving from isolated porphyrins to their oligomers or solid aggregates.

II. METHODOLOGY

In the present MBPT scheme, the DFT Kohn–Sham (KS) eigenvalues and eigenfunctions are used as a starting point for constructing the one-particle and two-particle Green's functions including all relevant aspects of electronic interaction and correlation. The key quantity is the electron self-energy operator, which can be evaluated very accurately for many materials in the GW approximation.[27] The one-particle Green's function describes quasiparticle (QP) excitations (i.e., the individual excitation of electrons and holes) while the two-particle Green's function describes coupled electron-hole excitations and is thus required for describing the optical spectrum.[28]

Results presented in this work are based on the following three-stage approach. As a first step, the geometrical structures of the two isolated molecules (H_2P and H_2TPP) are relaxed using DFT (Ref. 43) within the general gradient approximation (DFT-GGA) in the Perdew–Burke–Ernzerhof PBE parametrization functional.[44] We use a plane-wave approach, as implemented in the QUANTUM- ESPRESSO package,[45] with norm-conserving pseudopotentials and a kinetic energy cutoff of 70 Ry. Fictitious molecule-molecule interactions occurring in the repeated cell approach are eliminated by using, after convergence tests, a vacuum thickness of more than 10 Å. The relaxed geometries compare well with other similar calculations found in the literature and with the experimental data.[46,47] In particular, the external phenyl groups of H_2TPP cause an in-plane distortion of the porphyrin ring, without any appreciable out-of-plane distortion, in agreement with Ref. 48. We then calculate, at the optimized geometries, all the KS eigenvalues and eigenvectors up to 15 eV above the HOMO energy using LDA,[49] in order to reach a good convergence in the excited-state calculations. The GGA and LDA eigenvalues, for the same fixed geometry, were found to be very similar, within the order of 0.02–0.03 eV.

In a second step, we perform GW calculations using the YAMBO code[50] in order to obtain the real QP energies E_i^{QP} as corrections to the KS eigenvalues E_i^{KS} using the following well known expression:[27]

$$E_i^{\mathrm{QP}} = E_i^{\mathrm{KS}} + \frac{1}{1-\beta_i}\langle \varphi_i^{\mathrm{KS}}|\Sigma(E_i^{\mathrm{KS}}) - V_{xc}|\varphi_i^{\mathrm{KS}}\rangle, \tag{1}$$

where the index i runs over the occupied (holes h) and unoccupied (electrons e) states. $|\varphi_i^{\mathrm{KS}}\rangle$ are the KS eigenfunctions, β_i is given by

$$\beta_i = \langle \varphi_i^{\mathrm{KS}}| d\Sigma/dE|_{E_i^{\mathrm{KS}}}|\varphi_i^{\mathrm{KS}}\rangle, \tag{2}$$

i.e., the linear coefficient in the energy expansion of the self-energy Σ, which is itself the product of the KS Green's function G times the screened Coulomb interaction W obtained within the random phase approximation (RPA).[51] V_{xc} is the usual DFT exchange-correlation potential. A boxlike cutoff in the long-range Coulomb potential is used at this stage in order to simulate truly isolated molecular excited states. This technique is essential[52] for reaching good convergence (below 0.1 eV) in the self-energy calculations.

In the final step of our approach, we calculate the optical spectra including excitonic effects and self-energy corrections by means of solving the BSE. By expanding the states over the KS basis, the solution of the BSE can be mapped onto an eigenvalue problem for the excitonic Hamiltonian:[28,53]

$$H_{\mathrm{exc}} = \begin{pmatrix} H^{\mathrm{res}} & H^{\mathrm{coupl}} \\ -(H^{\mathrm{coupl}})^* & -(H^{\mathrm{res}})^* \end{pmatrix}, \tag{3}$$

where the resonant part,

$$H^{\mathrm{res}} = (E_e^{\mathrm{QP}} - E_h^{\mathrm{QP}})\delta_{e,e'}\delta_{h,h'} + \langle eh|K|e'h'\rangle, \tag{4}$$

is Hermitian. The part in the lower right is denoted antiresonant. $K = W - 2v$ is the excitonic kernel, with W and v being the screened and bare Coulomb interaction, where the factor 2 comes from the spin degeneracy.[53] The coupling part

$$H^{\mathrm{coupl}} = \langle eh|K|\overline{e'h'}\rangle \tag{5}$$

is symmetric and describes the interaction between the resonant and antiresonant parts, or in other words, between the e-h pairs at positive and negative (antipairs) energies (see Ref. 41 for a more detailed description of the notation). Here electron-hole antipairs are denoted by $\overline{e'h'}$, while $E_h^{\mathrm{QP}}, |h\rangle$ and $E_e^{\mathrm{QP}}, |e\rangle$ refer to the QP energies and eigenstates of the occupied and unoccupied states, respectively. As is often done in this framework, we replace the QP eigenfunctions $|e\rangle, |h\rangle$ with the KS ones $|\varphi_h^{\mathrm{KS}}\rangle, |\varphi_e^{\mathrm{KS}}\rangle$. While several works have shown that this approximation may not work well in highly anisotropic systems[37] or strongly correlated materials,[54] the results presented below demonstrate that it is reasonable for describing the low lying excitations of systems such as the studied porphyrins, as was also illustrated elsewhere for azobenzene.[41]

Once the eigenvectors and eigenvalues E_λ of the excitonic Hamiltonian H_{exc} are obtained, the photoabsorption cross section is obtained from

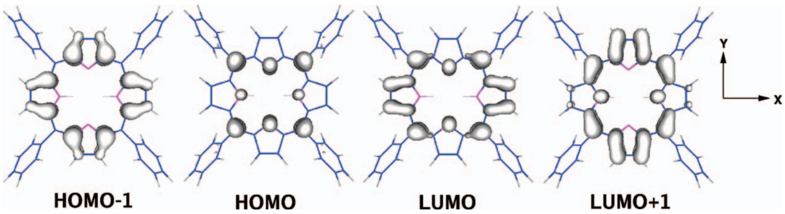

FIG. 1. Plots of $|\psi|^2$ of the four levels that mainly participate in the optical response of H_2TPP, as obtained at the DFT-LDA level of approximation. From left to right are reported the two highest occupied and the two lowest unoccupied states. The x axis coincides with the direction of the central N–H bonds.

$$\sigma(\omega) \propto \sum_{\lambda} |D_\lambda|^2 \delta(\omega - E_\lambda), \tag{6}$$

where $D_\lambda = \langle \lambda | i \vec{\eta} \cdot \vec{r} | 0 \rangle$ are the electron-hole optical strengths, η is the light polarization direction, $|0\rangle$ is the ground state, and $|\lambda\rangle$ is the generic excited state expanded in term of electron-hole pairs and antipairs. If the electron-hole interaction is neglected, the excitations are given by vertical transitions between independent electron and hole states with $D_\lambda = \langle h | i \vec{\eta} \cdot \vec{r} | e \rangle$, so that Eq. (6) reduces to the well known independent-particle Fermi golden rule expression.

Although the above approach is based on a local or semilocal DFT ground state calculation, it is important to realize that it does not inherit all the associated pathologies. In particular, the short-range exchange-correlation potential appearing in LDA and GGA is not present in the self-energy or, more importantly, the BSE. In these methods, the screened Coulomb interaction is used instead, yielding a correct description of the long-range $1/r$ behavior. Thus, the BSE can in principle describe charge transfer as well as Rydberg states.[55–57]

III. RESULTS

According to the Gouterman model, the HOMO (b_{1u}), HOMO−1(a_u), LUMO(b_{2g}), and LUMO+1(b_{3g}) states are the most important ones involved in the Q and B optical peaks. In Fig. 1 we report probability distribution isosurfaces for each of these four states as they occur for the H_2TPP molecule. The inclusion of phenyl rings does not change their character with respect to free-base porphine. We confirmed that the orbital character and ordering are consistent with other DFT-LDA calculations,[46] an observation that does not change if local or semilocal exchange-correlation potentials are used. All these findings attest to the robustness of the Gouterman model in describing the order and character of these energy levels based on the symmetry of the porphyrin molecular orbitals. Nevertheless, we will show below how a proper description of the optical response and photoemission spectra requires a more sophisticated theoretical treatment beyond this simple empirical model.

In Fig. 2 we show the optical spectrum of the H_2TPP molecule obtained at the independent-particle level (or equivalently, within the RPA), where a sum over the KS transitions, according to a Fermi golden rule description, is considered. Two strong peaks are visible at 1.75 and 2.15 eV. The former peak derives from $b_{1u} \leftrightarrow b_{2g}$ and $b_{1u} \leftrightarrow b_{3g}$ transitions, while the latter derives from $a_{1u} \leftrightarrow b_{2g}$ and $a_u \leftrightarrow b_{3g}$ transitions. The RPA optical spectrum of H_2P, not reported here, appears very similar with a small blueshift of the two peaks (of about 0.2 eV). As expected, the optical spectra obtained at this level of approximation are in complete disagreement with the experimental data, which feature almost forbidden Q bands in the visible region and very intense B bands in the near-UV region.

These results stress the need to overcome the single-particle scheme and mix the single-particle transitions. Such mixing can be achieved by means of configuration interaction techniques, the TDDFT approach, or the present GW+BSE approach. As we will see below, the four-level mixing scheme proposed in the Gouterman model appears valid for accounting for the Q bands and, to a lesser extent, the B bands, in agreement with published results based on quantum-chemical or TDDFT schemes.[16,58]

The computed QP energies for the isolated H_2P and H_2TPP molecules are compared with the KS (DFT-LDA) energies in Fig. 3. The typical linear relation that is often found between the two sets of eigenvalues in many semiconductor and insulating materials (both in bulk and in low dimensional systems) is only partially reproduced in the present molecular systems. The GW calculation opens the electronic HOMO-LUMO gap in H_2P to 5 eV (1.97 eV is the corresponding DFT-LDA gap), while a QP gap of 4.39 eV is obtained in H_2TPP (the DFT-LDA gap being 1.75 eV in this case). In Fig. 4 we compare the levels of the H_2P, obtained using the GW method, with experimental UV photoemission spectroscopy (UPS) data found in the literature.[59]

For comparison, we also report KS eigenvalues as obtained using a local (LDA), a semilocal (GGA), and a hybrid exchange-correlation functional [B3LYP (Ref. 60)]. As these methods do not satisfy Koopman's theorem, their eigenvalues should not be directly interpreted as electron removal/addition energies. Nevertheless, a comparison with the GW

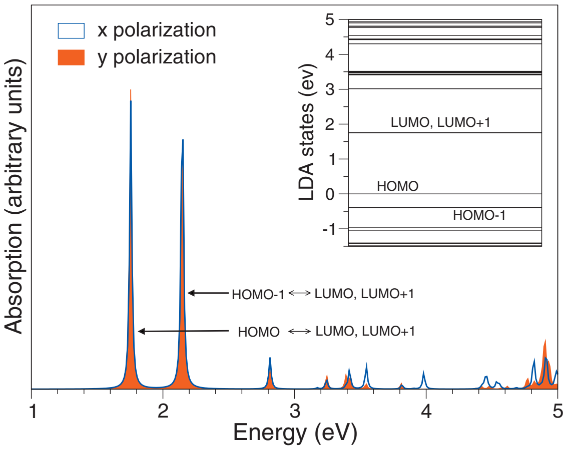

FIG. 2. Absorption spectrum of the H_2TPP molecule as obtained at the independent-particle level (RPA). Spectra according to x and y polarizations are almost identical. An artificial Lorenztian broadening of 10 meV has been used. Inset: DFT-LDA energy levels.

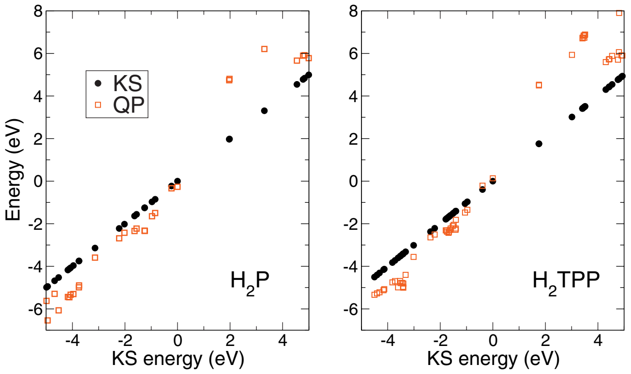

FIG. 3. Quasiparticle levels (open red squares) plotted as a function of the KS levels of the H_2P (left panel) and the H_2TPP molecules (right panel). The KS eigenvalues (filled black dots) are also reported for comparison.

eigenvalues illustrates the importance and magnitude of the self-energy corrections to the starting DFT eigenvalues (that could then be considered as an order 0 approximation to the QP energies). The theoretical description of the experimental UPS peaks is clearly much improved when QP energies are considered. It is interesting that the hybrid functional scheme also gives a very good description of the occupied states. This finding is in agreement with recent studies of porphyrins[61] and of other extended carbon-based molecules.[62,63]

Optical spectra of the H_2P and H_2TPP molecules, computed at the GW+BSE level of approximation, are presented in the top panels of Figs. 5(a) and 5(b), respectively. The theoretical spectra are compared with the corresponding experimental data from Ref. 18 reproduced in the bottom panels. Since the computed absorption for light polarized perpendicular to the central ring is found to be negligible, we report only the in-plane (x and y) components. Note that vibrational coupling effects are not included in the present calculation and hence the $Q_x(0,1)$ and $Q_y(0,1)$ replicas, present in the experimental curves, are always absent in the theoretical spectra.

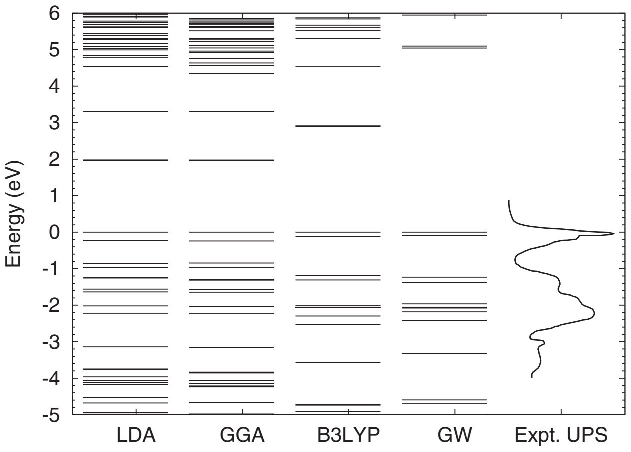

FIG. 4. Electronic states (in eV) obtained within DFT and quasiparticle schemes, compared with experimental UPS experimental data from Ref. 59. The highest occupied orbital has been aligned to zero eV in each case.

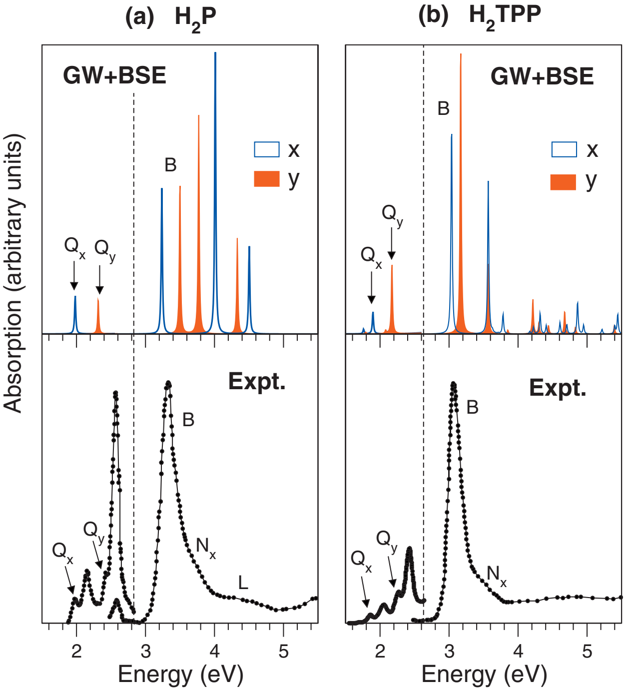

FIG. 5. Absorption spectra of the H_2P (left) and H_2TPP (right) molecules. The top panels show theoretical spectra obtained at the GW+BSE level of approximation for x (blue) and y (red, shaded) light polarizations. Experimental gas phase spectra, as reported in Ref. 18, appear in the bottom panels. Left of the vertical dashed line, the intensity of each spectrum has been multiplied by a factor of 10 for clarity. An artificial Lorenztian broadening of 10 meV has been used.

Inspection of Fig. 5(a) shows a reasonably good agreement between theory and experiment for the H_2P molecule. The $Q_x(0,0)$ and $Q_y(0,0)$ peaks appear at 1.98 and 2.3 eV, respectively, in good agreement with the experimental excitation energies reported at 1.98–2.02 and 2.33–2.42 eV.[18] Very intense optical peaks are obtained in the UV range around 3.3 eV. Their position and shape are in reasonable agreement with the experimentally observed Soret bands at 3.13–3.33 eV.[18] The level of accuracy reached for these low energy transitions is similar to that obtained in other *ab initio* approaches. Some previously computed excitation energies are reported in Table I for comparison with the GW+BSE and experimental data. Other very intense transitions are found near 4.0 eV, which may correspond to the experimentally observed N_x and L bands at 3.65 and 4.25 eV. However, the assignment is not clear in this case, as their intensities are overestimated with respect to the lower energy peaks. This may be due to a lack of convergence in the present GW calculations for states lying close to the continuum of molecular states: By underestimating their lifetime, the calculations yield sharper resonances that those seen experimentally. Large oscillator strengths have also been reported for the N band in Ref. 21, although the accuracy of that work has been questioned.[25]

The comparison with experiment further improves for the H_2TPP case, where the experimental absorption spectrum of H_2TPP, shown in Fig. 5(b), is very well reproduced by the theoretical Bethe–Salpeter calculation. The $Q_x(0,0)$ and $Q_y(0,0)$ peaks appear at 1.88 and 2.15 eV, nicely reproducing the experimental transitions reported at 1.86 and 2.27 eV.[18] The experimentally observed Soret band is located at

TABLE I. Excitation energies (in eV) of the H_2P molecule obtained using different theoretical approaches and compared with the experimental peak positions.

Method	Reference	Q_x	Q_y	B_x	B_y
Expt.	18	1.98–2.02	2.33–2.42	3.13–3.33	3.13–3.33
GW+BSE	This work	1.98	2.3	3.3	3.5
TDDFT (LDA)	This work	1.97	2.1	3.0	3.0
CASPT2	15	1.63	2.11	3.08	3.12
NEVPT2	24	2.04	2.51	3.22	3.30
SAC-CI	22	1.81	2.10	3.47	3.69
STEOM-CC	25	1.70	2.59	3.63	3.74
TDDFT (B3LYP)	17	2.27	2.44	3.33	3.41

3.08 eV, slightly redshifted with respect to the free-base porphine, and is in very good agreement with theoretical prediction. Finally, we note that the BSE absorption curves show an optical anisotropy splitting in the *B* band of about 0.3 and 0.15 eV for the H_2P and H_2TPP molecules, respectively.

From the calculated values of the electronic gaps (5.0 and 4.3 eV, for the H_2P and H_2TPP molecules, respectively) it is clear that the optical spectra feature strong excitonic effects, with estimated exciton binding energies of about 3.0 and 2.5 eV. This is further illustrated in Fig. 6, where we compare a GW+RPA calculation of the H_2TPP absorption spectrum with the result of the full GW+BSE calculation, for the *x*-polarization. It is interesting, therefore, that the excitonic transitions associated with the *Q* bands are found to derive from a mixing of the single particle transitions from the HOMO−1 to LUMO+1 and from the HOMO−1 to LUMO states, in agreement with the Gouterman model. For the *B* and *N* bands, however, single-particle transitions from the HOMO−2 to LUMO+1 also contribute, and hence involve states beyond the standard four involved in the Gouterman picture.

Often (and especially in extended systems) it is found that the resonant part of the excitonic Hamiltonian, H^{res}, is adequate for describing the optical excitations correctly. This corresponds to the so-called Tamm–Dancoff approximation[40] and is equivalent to neglecting the interaction between the *e*-*h* pairs and antipairs. In Fig. 6 we illustrate the influence of the coupling term H^{coupl} on the final optical spectrum of H_2TPP. The effect is found to be quite large, both in the energetic peak positions and in the spectral lineshape. These findings are consistent with the conclusions of Grüning *et al.*[41] for other carbon-based molecules and similar observations in other molecular systems.[64] For this reason we have chosen to include the coupling term in all GW+BSE spectra appearing in this work.

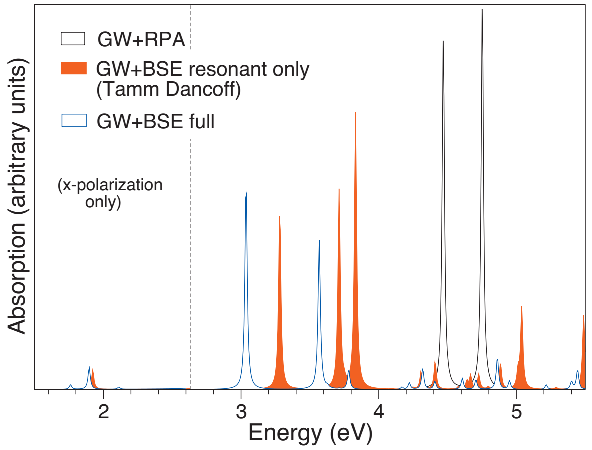

FIG. 6. Absorption spectra of the H_2TPP molecule (*x*-polarization only) computed at various levels of approximation: GW+RPA, resonant only (Tamm–Dancoff approximation), and full GW+BSE as reported previously. An artificial Lorenztian broadening of 10 meV has been used.

Due to their importance in emission processes and in photobiology or medical applications such as photodynamic therapy, it is also interesting to investigate how the present approach is able to reproduce the characteristics of the *triplet* excitons. Within the BSE approach, triplet excitons can be calculated by simply considering $K_{eh}=W$. In Table II we compare our results for the lowest triplet excitons in both molecules with the experimental values and some of the theoretical ones as taken from the literature.

We find that the energetic position of the lowest triplet excitons appears in very good agreement with the available experimental data and with other theoretical approaches for the H_2P and H_2TPP molecules. Spatial analysis of the excitonic wave function reveals that the lowest singlet and triplet excitons have different character: This is illustrated in Fig. 7 for the H_2P molecule. While the lowest singlet exciton results from a mixing of the four Gouterman states (HOMO, HOMO−1, LUMO, LUMO+1), the triplet exciton is instead a pure mixing of the HOMO and LUMO states. From our previous discussion and the results shown in Tables I and II, we can conclude that the present solid-state based scheme (GW+BSE) provides singlet and triplet excitations of porphyrins to within 0.2 eV of experiment, therefore having the very same range of accuracy as the best QC approaches discussed in the introduction.

TABLE II. Theoretical energetic positions (in eV) of the first triplet (*T*) exciton for the H_2P and H_2TPP molecules. The experimental data are also reported for comparison.

Method	Reference	H_2P	H_2TPP
Expt.	65–67	1.56–1.58	1.45
GW+BSE	This work	1.6	1.5
TDDFT (B3LYP)	17	1.46	
CASPT2	15	1.52	
STEOM-CC	25	1.19	
QMC	68	1.6	

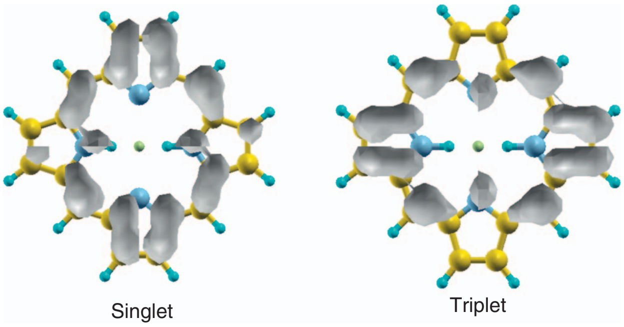

FIG. 7. Excitonic wave function of the lowest energy singlet and triplet states in the isolated H_2P molecule. The green dot in the center of the molecule indicates the position of the hole.

It is useful to compare the GW+BSE results with a complementary approach. We performed a TDDFT calculation[69] for the H_2TPP molecule, within the adiabatic local density approximation. The results, shown in Fig. 8 (see also Tables I and II), illustrate a reasonable agreement between the two methods for both *Q* and Soret bands, in particular with regard to the peak positions. The relative intensities of the *x* and *y* polarizations are also fairly consistent between the two approaches, although we note that the TDDFT calculations appear to overestimate the relative intensity of the *Q* and Soret bands in comparison with the experimental data.

IV. CONCLUDING REMARKS

In conclusion, we calculated by means of *first-principles* MBPT the charged and neutral electronic excitations of the isolated H_2P and H_2TPP molecules. The available photoemission and optical absorption measurements are well described by this approach, which also naturally provides a complete picture of the *e-h* coupling, the singlet and triplet excitations and the real space extension of the excitonic wave functions. The character and energy of the singlet and triplet lowest energy excitons turn out to be in good agreement with experiment and other *ab initio* calculations, with accuracy comparable to quantum chemical methods. As a byproduct, we performed TDDFT calculations. The results show that a simple approximation such as ALDA can already give important insights about the optical spectrum of such molecules. The present study should represent the first step toward a complete *ab initio* analysis of the change in exciton character when moving from isolated porphyrins to their oligomers or to solid aggregates.

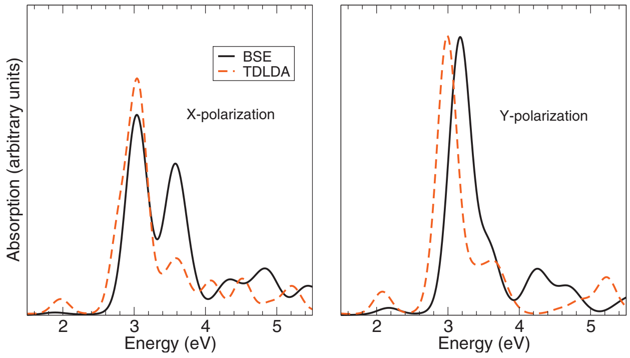

FIG. 8. Comparison of absorption spectra computed within TDDFT and BSE for the H_2TPP molecule. An artificial Lorenztian broadening of 200 meV has been used.

Note added in proof. In a recently published work,[71] the GW method was also used to calculate the ionization potential of the H_2TPP molecule. The work provides further evidence that the MBPT scheme can be applied with success to the study of these molecular systems.

ACKNOWLEDGMENTS

The authors are grateful to Dr. Simona Silaghi and Dr. Norbert Esser for useful discussions, as part of the ETSF pilot user project n. 12. We acknowledge funding by the European Community through e-I3 ETSF project (INFRA-2007-1.2.2: Grant Agreement No. 211956) and by the Spanish MEC (Grant No. FIS2007-65702-C02-01), "Grupos Consolidados UPV/EHU del Gobierno Vasco" (Grant No. IT-319-07), CSIC and by MIUR-PRIN2007. Supercomputing support is acknowledged from The Barcelona Supercomputing Center, "Red Espanola de Supercomputacion" and SGIker ARINA (UPV/EHU), and the CINECA Supercomputing Center through CNR-INFM projects (accounts cne0fm2h and cne0fm2v).

[1] M. Gouterman, in *The Porphyrins*, edited by D. Dolphin (Academic, New York, 1977).
[2] L. K. Hanson, Photochem. Photobiol. **47**, 903 (1988).
[3] L. K. Hanson, in *Chlorophylls*, edited by H. Scheer (CRC, Boca Raton, 1991).
[4] C. Li, J. Ly, B. Lei, W. Fan, D. Zhang, J. Han, M. Mayyappan, C. Thompson, and M. Zhou, J. Phys. Chem. B **108**, 9646 (2004).
[5] K. S. Kwok, Mater. Today **6**, 20 (2003).
[6] X. Duan, Y. Huang, and C. M. Lieber, Nano Lett. **2**, 487 (2002).
[7] F. J. Kampas, K. Yamashita, and J. Fajer, Nature (London) **40**, 284 (1980).
[8] J. M. Tour, Chem. Rev. (Washington, D.C.) **96**, 537 (1996).
[9] L. Jones II, J. S. Schumm, and J. M. Tour, J. Org. Chem. **62**, 1388 (1997).
[10] A. Tsuda and A. Osuka, Science **293**, 79 (2001).
[11] T. Hasobe, H. Imahori, H. Yamada, T. Sato, K. Ohkubo, and S. Fukuzumi, Nano Lett. **3**, 409 (2003).
[12] C. B. Winkelmann, I. Ionica, X. Chevalier, G. Royal, C. Bucher, and V. Bouchiat, Nano Lett. **7**, 1454 (2007).
[13] J. D. Baker and M. C. Zerner, Chem. Phys. Lett. **175**, 192 (1990).
[14] I. Baraldi, A. Carnevali, G. Ponterini, and D. Vanossi, J. Mol. Struct.: THEOCHEM **333**, 121 (1995).
[15] L. Serrano-Andrés, M. Merchán, M. Rubio, and B. O. Roos, Chem. Phys. Lett. **295**, 195 (1998).
[16] D. Sundholm, Phys. Chem. Chem. Phys. **2**, 2275 (2000).
[17] B. Minaev and H. Ågren, Chem. Phys. **315**, 215 (2005).
[18] L. Edwards, D. H. Dolphin, M. Gouterman, and A. D. Adler, J. Mol. Spectrosc. **38**, 16 (1971).
[19] M. Gouterman, J. Chem. Phys. **30**, 1139 (1959).
[20] P. Celani and H.-J. Werner, J. Chem. Phys. **112**, 5546 (2000).
[21] H. Nakatsuji, J. Hasegawa, and M. Hada, J. Chem. Phys. **104**, 2321 (1996).
[22] O. Kitao, H. Ushiyama, and N. Miura, J. Chem. Phys. **110**, 2936 (1999).
[23] J. Hasegawa, K. Takata, T. Miyahara, S. Neya, M. J. Frisch, and H. Nakatsuji, J. Phys. Chem. A **109**, 3187 (2005).
[24] C. Angeli, M. Pastore, and R. Cimiraglia, Theor. Chem. Acc. **117**, 743 (2007).
[25] S. R. Gwaltney and R. J. Bartlett, J. Chem. Phys. **108**, 6790 (1998).
[26] In using the term "MBPT" we do not intend the quantum-chemistry approaches that take into account the electronic correlation as a perturbation of Hartree–Fock, but only a subclass of many-body techniques

developed using a Green's function method in solid state physics, which treat the electron-electron interaction as a perturbation to the homogeneous electron gas.

[27] F. Aryasetiawan and O. Gunnarsson, Rep. Prog. Phys. **61**, 237 (1998); W. G. Aulbur, L. W. Jönsson, and J. W. Wilkins, Solid State Phys. **54**, 1 (1999) (and references therein).

[28] G. Onida, L. Reining, and A. Rubio, Rev. Mod. Phys. **74**, 601 (2002) (and references therein).

[29] *Time Dependent Density Functional Theory*, Lecture Notes in Physics Vol. 706, edited by M. A. L. Marques, C. A. Ullrich, F. Nogueira, A. Rubio, K. Burke, E. K. U. Gross (Springer, Berlin, Heidelberg, 2006), Chaps. 16–23; Phys. Chem. Chem. Phys. **11**, Issue (22) (2009).

[30] J. C. Grossman, M. Rohlfing, L. Mitas, S. G. Louie, and M. L. Cohen, Phys. Rev. Lett. **86**, 472 (2001).

[31] M. Rohlfing and S. G. Louie, Phys. Rev. Lett. **80**, 3320 (1998).

[32] M. Bruno, M. Palummo, A. Marini, R. Del Sole, and S. Ossicini, Phys. Rev. Lett. **98**, 036807 (2007).

[33] P. H. Hahn, W. G. Schmidt, and F. Bechstedt, Phys. Rev. B **72**, 245425 (2005).

[34] M. Rohlfing and S. G. Louie, Phys. Rev. Lett. **82**, 1959 (1999).

[35] A. Ruini, M. J. Caldas, G. Bussi, and E. Molinari, Phys. Rev. Lett. **88**, 206403 (2002).

[36] K. Hummer and C. Ambrosch-Draxl, Phys. Rev. B **71**, 081202 (2005).

[37] D. Varsano, A. Marini, and A. Rubio, Phys. Rev. Lett. **101**, 133002 (2008).

[38] D. Prezzi, D. Varsano, A. Ruini, A. Marini, and E. Molinari, Phys. Rev. B **77**, 041404(R) (2008).

[39] N. Sai, M. L. Tiago, J. R. Chelikowsky, and F. A. Reboredo, Phys. Rev. B **77**, 161306 (2008).

[40] A. L. Fetter and J. D. Walecka, *Quantum Theory of Many-Particle Systems* (Dover, New York, 2003), Chap. 15, p. 565.

[41] M. Grüning, A. Marini, and X. Gonze, "Exciton-Plasmon States in Nanoscale Materials: Breakdown of the Tamm-Dancoff Approximation," Nano Lett. (in press) (e-print arXiv:0909.3389).

[42] Z.-L. Cai, K. Sendt, and J. R. Reimers, J. Chem. Phys. **117**, 5543 (2002).

[43] P. Hohenberg and W. Kohn, Phys. Rev. **136**, B864 (1964); W. Kohn and L. J. Sham, *ibid.* **140**, A1133 (1965).

[44] J. P. Perdew, K. Burke, and M. Ernzerhof, Phys. Rev. Lett. **77**, 3865 (1996).

[45] QUANTUM-ESPRESSO is a community project for high-quality quantum-simulation software, based on density-functional theory, and coordinated by P. Giannozzi. See http://www.quantum-espresso.org and http://www.pwscf.org.

[46] D. Lamoen and M. Parrinello, Chem. Phys. Lett. **248**, 309 (1996).

[47] G. G. Gurzadyan, T.-H. Tran-Thi, and T. Gustavsson, J. Chem. Phys. **108**, 385 (1998).

[48] Y.-H. Zhang, W.-J. Ruan, Z.-Y. Li, Y. Wu, and J.-Y. Zheng, Chem. Phys. **315**, 201 (2005).

[49] J. P. Perdew and A. Zunger, Phys. Rev. B **23**, 5048 (1981).

[50] A. Marini, C. Hogan, M. Grüning, and D. Varsano, Comput. Phys. Commun. **180**, 1392 (2009) (the code is freely available from http://www.yambo-code.org).

[51] S. L. Adler, Phys. Rev. **126**, 413 (1962); N. Wiser, *ibid.* **129**, 62 (1963).

[52] C. A. Rozzi, D. Varsano, A. Marini, E. K. U. Gross, and A. Rubio, Phys. Rev. B **73**, 205119 (2006).

[53] M. Rohlfing and S. G. Louie, Phys. Rev. B **62**, 4927 (2000).

[54] M. Gatti, F. Bruneval, V. Olevano, and L. Reining, Phys. Rev. Lett. **99**, 266402 (2007).

[55] S. Galamic-Mulaomerovic and C. H. Patterson, Phys. Rev. B **72**, 035127 (2005).

[56] F. Sottile, M. Marsili, V. Olevano, L. Reining, Phys. Rev. B **76**, 161103 (2007).

[57] N. P. Wang, M. Rohfing, P. Kruger, and J. Pollman, Phys. Rev. B **71**, 045407 (2005).

[58] J. Seda, J. V. Burda, and J. Leszczynski, J. Comput. Chem. **26**, 294 (2005).

[59] P. Dupuis, R. Roberge, and C. Sandorfy, Chem. Phys. Lett. **75**, 434 (1980).

[60] A. Becke, J. Chem. Phys. **98**, 5648 (1993).

[61] A. Ghosh and T. Vangberg, Theor. Chem. Acc. **97**, 143 (1997).

[62] N. Dori, M. Menon, L. Kilian, M. Sokolowski, L. Kronik, and E. Umbach, Phys. Rev. B **73**, 195208 (2006).

[63] N. Marom, O. Hod, G. E. Scuseria, and L. Kronik, J. Chem. Phys. **128**, 164107 (2008).

[64] M. Casida, J. Chem. Phys. **122**, 054111 (2005).

[65] M. Gouterman and G. E. Khalil, J. Mol. Spectrosc. **53**, 88 (1974).

[66] J. G. Radziszewski, J. Waluk, M. Nepras, and J. Michl, J. Phys. Chem. **95**, 1963 (1991).

[67] H. Gratz and A. Penzkofer, Chem. Phys. **254**, 363 (2000).

[68] A. Aspuru-Guzik, O. El Akramine, J. C. Grossman, and W. A. Lester, Jr., J. Chem. Phys. **120**, 3049 (2004).

[69] Real space-real time calculation, using the code OCTOPUS (Ref. 70), within the LDA (GGA gives very similar results, however). BSE and TDDFT spectra were compared using $\sigma(\omega)=\omega/c\ \mathrm{Im}\{\varepsilon^{-1}(\mathbf{q}=0,\omega)\}$, where σ, the photoabsorption cross section, is the quantity calculated by OCTOPUS (real-space approach), and $\varepsilon^{-1}(\mathbf{q}=0,\omega)$ is the quantity calculated by YAMBO (plane wave approach). We scaled the BSE spectra such that the y component intensity was equal to that of the TDDFT spectrum.

[70] M. A. L. Marques, A. Castro, G. F. Bertsch, and A. Rubio, Comput. Phys. Commun. **151**, 60 (2003).

[71] P. Umari, G. Stenuit, and S. Baroni, Phys. Rev. B **79**, 201104 (2009).

5.2 Layered systems

New generation synchrotron light sources and aberration-corrected electron microscopes made the loss spectroscopies explodes in the last two decades. The range of excitations is very wide, scanning lattice vibrations to core electron excitations, from interband transitions to collective plasmon excitations. For the latter in particular, the two experimental techniques are able to give the same response function, with an unparalelled resolution (in space, energy, momentum, etc.), crucially asking for the theoretical counterpart. In addition, the possibility to explore a wide range in momentum transfer, also means probing local features (especially for large $\mathbf{q}$), called, in the language of solid state, crystal local field effects. Graphite, for instance, with its well separated graphene sheets, is a remarkable prototype for local fields-induced phenomena. Graphite was also the system Ralf Hambach was studying during his thesis: he came at a certain moment talking to me about a possible bug in the DP code, in light of the very weird results he was obtaining, with strong anisotropy effects and really bizarre momentum dispersion. After a deep check, we (sure by then of the numerical results) tried to propose to several experimental groups the task to measure the plasmon dispersion of graphite fo specific momenta and to prove (or disprove) the wild change of the loss function for tiny variation of $\mathbf{q}$. A group in Japan finally proved Ralf's theoretical prediction, with astonishing precision, and the results have been published on PRL [108]. Further details are available in Ralf's thesis [42]. Since then, this behaviour has been also found in transition metal dichalcogenides [109], and we are curently studying this effects on hexagonal BN and MoS_2 [110].

Please Refer to the attached Article

Anomalous Angular Dependence of the Dynamic Structure Factor near Bragg Reflections: Graphite

R. Hambach,[1,2,3] C. Giorgetti,[1,2] N. Hiraoka,[4] Y. Q. Cai,[4,*] F. Sottile,[1,2] A. G. Marinopoulos,[5]
F. Bechstedt,[3,2] and Lucia Reining[1,2]

[1]*Laboratoire des Solides Irradiés, Ecole Polytechnique, CEA/DSM, CNRS, 91128 Palaiseau, France*
[2]*European Theoretical Spectroscopy Facility (ETSF)*
[3]*Institut für Festkörpertheorie und -optik, Friedrich-Schiller-Universität Jena, 07743 Jena, Germany*
[4]*National Synchrotron Radiation Research Center, Hsinchu 30076, Taiwan*
[5]*CEMDRX, Department of Physics, University of Coimbra, P-3004-516 Coimbra, Portugal*

(Received 8 February 2008; published 31 December 2008)

The electron energy-loss function of graphite is studied for momentum transfers **q** beyond the first Brillouin zone. We find that near Bragg reflections the spectra can change drastically for very small variations in **q**. The effect is investigated by means of first principle calculations in the random phase approximation and confirmed by inelastic x-ray scattering measurements of the dynamic structure factor $S(\mathbf{q}, \omega)$. We demonstrate that this effect is governed by crystal local field effects and the stacking of graphite. It is traced back to a strong coupling between excitations at small and large momentum transfers.

DOI: 10.1103/PhysRevLett.101.266406 PACS numbers: 71.45.Gm, 73.21.Ac, 78.70.Ck, 81.05.Uw

The momentum-resolved and frequency-dependent dynamic structure factor $S(\mathbf{q}, \omega)$ is a fundamental quantity in plasma physics, nuclear physics, particle physics, and condensed matter physics. It is important for the understanding of many problems like, e.g., electronic correlation, and it links the theory of many-body systems to scattering experiments like electron energy-loss spectroscopy (EELS) or inelastic x-ray scattering (IXS).

EELS measurements are particularly efficient for moderate momentum transfer, i.e. when **q** is shorter than a reciprocal-lattice vector and multiple scattering effects remain secondary. Recently, modern synchrotron radiation sources have opened the way to study electronic excitations at large momentum transfer using IXS [1,2]. New phenomena can be observed in this range, such as a periodic plasmon dispersion in magnesium diboride MgB_2 [2] or plasmon-bands in Silicon [3]. Crystal local field effects (LFE) [4,5], namely, the fact that an external perturbation can induce a response on the length scale of the structure of the material, become increasingly important for large **q** [6]. They acquire particular importance for layered systems, such as graphite [7], or superlattices [8].

Graphite, with its well separated and polarizable graphene sheets, is a very good candidate for the exploration of LFE-induced phenomena. EELS and IXS measurements (see, e.g., [1,9–11]) have determined the energy-loss spectra and plasmon dispersion for a wide range of momentum transfer **q**. Calculations of the energy-loss function that are based on the homogeneous electron gas (see, e.g., [12–14]) or the tight-binding model (see, e.g., [15,16]) have been used extensively to study in-plane properties of graphite. *Ab initio* calculations based on Density-Functional Theory (DFT) in its time-dependent extension (TDDFT) [17], either in the adiabatic local density approximation (TDLDA) or even in the Random Phase Approximation (RPA), reproduce experimental plasmon spectra with very good precision [7,11] and show a continuous angular dependence of the dynamic structure factor for relatively moderate momentum transfer **q**. The range of larger **q**, instead, is much less explored.

In the present Letter, we demonstrate that this range offers access to striking phenomena. In particular, our *ab initio* calculations and IXS measurements reveal an anomaly in the angular dependence of the dynamic structure factor: For a momentum transfer close to certain reciprocal-lattice vectors, we observe drastic changes in the spectra upon small variations in **q**. This discontinuous behavior should have important implications for the interpretation of measurements close to Bragg reflections in any strongly inhomogeneous system.

We performed first principle RPA calculations of the momentum-resolved and frequency-dependent dynamic structure factor $S(\mathbf{q}, \omega)$, which is directly related to the energy-loss function. The electronic ground state of graphite (Bernal stacking) was calculated in DFT-LDA (local density approximation) with ABINIT [18], using a plane-wave basis set [19] and norm-conserving pseudopotentials [20]. The Kohn-Sham band structure was used to compute the independent particle polarizability χ^0 with the DP-code [21]. In RPA, the longitudinal dielectric function ϵ and its inverse ϵ^{-1}, that links the total to the external potential in linear response $\varphi_{\text{tot}} = \epsilon^{-1}\varphi_{\text{ext}}$ is given by $\epsilon = 1 - v\chi^0$, where v denotes the Coulomb interaction. For a solid, ϵ is a *matrix* in reciprocal-lattice vectors $(\mathbf{G}, \mathbf{G}')$ and a function of the reduced momentum transfer $\mathbf{q}_r$ inside the first Brillouin zone and of frequency ω. The dynamic structure factor for a given momentum transfer $\mathbf{q} = \mathbf{q}_r + \mathbf{G}_0$ and frequency ω is then

$$S(\mathbf{q},\omega) = -\frac{q^2}{4\pi^2 n_0}\,\mathrm{Im}[\epsilon^{-1}_{\mathbf{G}_0\mathbf{G}_0}(\mathbf{q}_r,\omega)];$$

where $\mathbf{G}_0$ is a reciprocal-lattice vector and n_0 denotes the average electron density. Hence, only diagonal elements of ϵ^{-1} are needed. However, as ϵ is *not* diagonal for an inhomogeneous material, its inversion will mix all matrix elements. One can understand the physics of this mathematical fact by expanding $\epsilon^{-1} = (1 - v\chi^0)^{-1}$:

$$\epsilon^{-1}_{\mathbf{G}_0\mathbf{G}_0}(\mathbf{q}_r,\omega) = 1 + v_{\mathbf{G}_0}\chi^0_{\mathbf{G}_0\mathbf{G}_0}(\mathbf{q}_r,\omega) + \sum_{\mathbf{G}} v_{\mathbf{G}_0}\chi^0_{\mathbf{G}_0\mathbf{G}}(\mathbf{q}_r,\omega)v_{\mathbf{G}}\chi^0_{\mathbf{G}\mathbf{G}_0}(\mathbf{q}_r,\omega) + \ldots.$$

The first order term gives the response of the independent particles to the external potential. The second term is the response to the Hartree potential that is induced by the first order response. This self-consistent process is then continued to infinite order. As χ_0 is a matrix, an external potential with momentum $\mathbf{q}_r + \mathbf{G}_0$ can induce spatial charge fluctuations, whose momentum $\mathbf{q}_r + \mathbf{G}$ differs by any reciprocal-lattice vector, and to which the system will *also* respond; these are the (crystal) LFE.

When $\mathbf{q} = \mathbf{q}_r$ is small, all induced potentials are of shorter wavelength, i.e., $|\mathbf{G}| > |\mathbf{G}_0|$. However, for large $\mathbf{q} = \mathbf{q}_r + \mathbf{G}_0$ beyond the first Brillouin zone, long wavelength fluctuations with $|\mathbf{G}| < |\mathbf{G}_0|$ may be induced, too. They have been found to cause a Fano resonance in silicon [22] and lithium [23] and a periodic plasmon dispersion in magnesium diboride MgB_2 [2]. We will now show that the situation is particularly striking for graphite, where the long wavelength fluctuations give rise to an unexpected discontinuity in the dynamic structure factor.

Figure 1(a) shows the calculated dynamic structure factor $S(\mathbf{q},\omega)$ of graphite for a sequence of $\mathbf{q} = (0, 0, q_3)$ that are chosen exactly perpendicular to the planes [Note that $(q_1, q_2, q_3) = q_1\mathbf{b}_1 + q_2\mathbf{b}_2 + q_3\mathbf{b}_3$ where the $\mathbf{b}_n$ are primitive reciprocal-lattice vectors; see Fig. 3(b)]. The structures that can be seen in this low-energy range are due to the very weak interaction between the graphene sheets; the intensity of the spectrum is therefore quite low and the dispersion small, contrary to the case of MgB_2 [2] where the coupling between layers is much stronger.

Instead, Fig. 1(b) shows calculations for momentum transfers $\mathbf{q} = (\frac{1}{8}, 0, q_3)$ where the in-plane component $q_1 = \frac{1}{8}$ is kept fixed and the perpendicular component q_3 is varied. Although for large q_3 the direction of $\mathbf{q}$ deviates only slightly from the c-axis, we observe a striking difference compared to the on-axis results: First, the intensity is significantly increased for most of the spectra—when q_3 is zero, we simply see the in-plane π-plasmon. Second, there is a strong dispersion in the peak positions; the main peak shifts between 7.6 eV at $q_3 = 0$ and 6 eV at $q_3 = 1$. The most striking observation, however, is the disappearance of the peak at $q_3 = 2$: for that value, the dynamic structure factor abruptly becomes completely flat below 8 eV. There is hence a *significant* change of the spectra for a *small* change of $\mathbf{q}$. Even more important, these results remain valid for arbitrarily small in-plane components q_1, as we will see in the following.

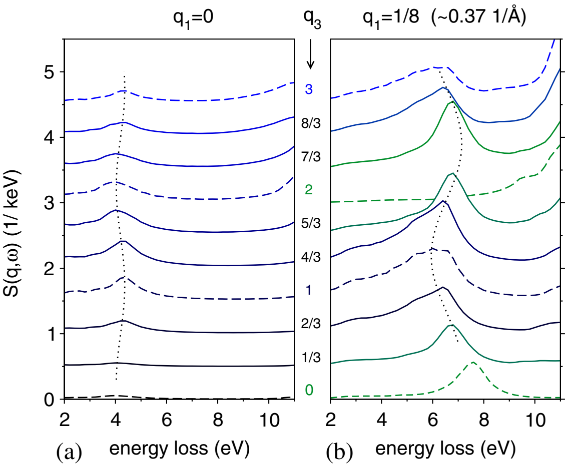

FIG. 1 (color online). Calculated dynamic structure factor $S(\mathbf{q},\omega)$ of graphite for different momentum transfers $\mathbf{q} = (q_1, 0, q_3)$ (a) exactly perpendicular to the planes ($q_1 = 0$) and (b) with a small in-plane component ($q_1 = \frac{1}{8}$). Dashed lines indicate spectra for integer q_3. All spectra have been shifted equidistantly in the y-direction for better visibility. Dotted lines are guides to the eye.

The bottom panel of Fig. 2(a) shows $S(\mathbf{q},\omega)$ calculated with and without LFE (solid and dashed lines, respectively) for momentum transfers $\mathbf{q} = \boldsymbol{\eta}$ that are vanishingly small ($|\boldsymbol{\eta}| = 5 \times 10^{-5}$ Å^{-1}) and differ only in the angle α to the c-axis. For in-plane momentum transfers ($\alpha = 90°$), we find a pronounced π-plasmon peak at 7 eV, whereas in the perpendicular direction ($\alpha = 0°$), a peak, although of much lower intensity, is found at 4 eV. For intermediate directions of $\boldsymbol{\eta}$, one finds a continuous behavior when the angle α is changed, as one would expect. LFE contribute only marginally; i.e., the anisotropy simply stems from the anisotropy of the head element $\epsilon_{\mathbf{00}}(\boldsymbol{\eta},\omega)$ of the dielectric matrix. These results are consistent with earlier calculations on graphite [7].

Moving on to large momentum transfers, the next higher panel displays the results for $\mathbf{q} = (0, 0, 1) + \boldsymbol{\eta}$. A change in $\boldsymbol{\eta}$ corresponds now to an infinitesimal change in $\mathbf{q}$ [see Fig. 2(b)]. Only one spectrum is shown as it does not change with $\boldsymbol{\eta}$. It should be noted however that LFE start to become significant because of the larger $\mathbf{q}$.

This picture changes completely when we reach momentum transfers $\mathbf{q} = (0, 0, 2) + \boldsymbol{\eta}$ near the second reciprocal-lattice vector, shown in the top panel of Fig. 2(a): whereas the spectrum *without* LFE is completely flat and remains stable while $\boldsymbol{\eta}$ is changed, we find that LFE lead to drastic modifications of the spectra for infinitesimal variations of the total momentum transfer $\mathbf{q}$. A direct comparison between spectra for momentum transfers $\mathbf{q} = (0, 0, 2) + \boldsymbol{\eta}$ and the corresponding reduced mo-

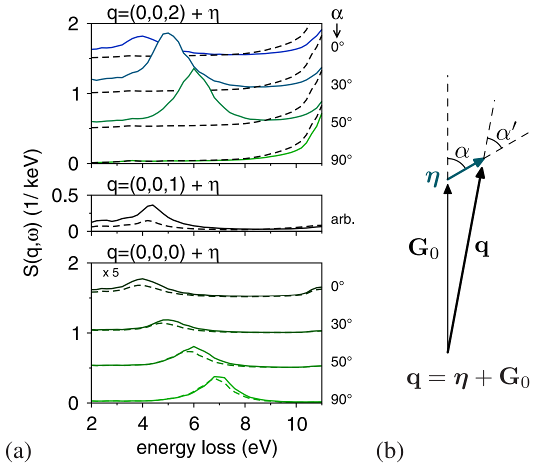

FIG. 2 (color online). (a) Dynamic structure factor $S(\boldsymbol{\eta} + \mathbf{G}_0, \omega)$ for small deviations $|\boldsymbol{\eta}| = 5 \times 10^{-5}$ Å^{-1} from reciprocal-lattice vectors $\mathbf{G}_0$ calculated with (solid line) or without (dashed line) LFE. (Bottom) For $\mathbf{G}_0 = (0, 0, 0)$, $S(\boldsymbol{\eta}, \omega)$ depends on the direction of $\boldsymbol{\eta}$. (Middle) For $\mathbf{G}_0 = (0, 0, 1)$, arbitrary $\boldsymbol{\eta}$ lead to the same spectrum. (Top) For $\mathbf{G}_0 = (0, 0, 2)$, $S(\boldsymbol{\eta} + \mathbf{G}_0, \omega)$ again changes with $\boldsymbol{\eta}$, but only when LFE are included. (b) Definition of the angles α and α'.

mentum transfer $\boldsymbol{\eta}$ (top vs bottom panel) shows that they are very similar up to a scaling factor, whenever $\boldsymbol{\eta}$ is not exactly in-plane. In other words, near the reciprocal-lattice vector (0, 0, 2), LFE lead to the reappearance of spectra of lower Brillouin zones [2,22], and the dynamic structure factor is determined by the direction of the *reduced* momentum transfer $\mathbf{q}_r = \boldsymbol{\eta}$ and *not* by the direction of $\mathbf{q}$.

Graphite is a very convenient case for further analysis because for small $\mathbf{q}_r$ and $\mathbf{G}_0 = (0, 0, 2)$, the coupling element $\epsilon_{\mathbf{0}\mathbf{G}_0}(\mathbf{q}_r, \omega)$ dominates by far all other off-diagonal elements $\epsilon_{\mathbf{G}\mathbf{G}'}(\mathbf{q}_r, \omega)$. Neglecting the latter, the inversion of ϵ reduces to the inversion of a simple 2×2 dielectric matrix [24] and one obtains (the ω dependence is omitted)

$$\epsilon^{-1}_{\mathbf{G}_0\mathbf{G}_0}(\mathbf{q}_r) = \frac{1}{\epsilon_{\mathbf{G}_0\mathbf{G}_0}(\mathbf{q}_r)} + \frac{\epsilon_{\mathbf{G}_0\mathbf{0}}(\mathbf{q}_r)\epsilon_{\mathbf{0}\mathbf{G}_0}(\mathbf{q}_r)}{[\epsilon_{\mathbf{G}_0\mathbf{G}_0}(\mathbf{q}_r)]^2}\epsilon^{-1}_{\mathbf{00}}(\mathbf{q}_r).$$

This result is similar to the two-plasmon-band approximation [25]. The first term corresponds to the result without LFE. The second term leads to the reappearance of the spectrum $\epsilon^{-1}_{\mathbf{00}}(\mathbf{q}_r, \omega)$ weighted by the coupling element. Whenever the second term is strong, the spectrum for large $\mathbf{q} = \mathbf{q}_r + \mathbf{G}_0$ will also depend on the one for the reduced component $\mathbf{q}_r$, and hence on its anisotropy.

Still, it remains to be understood why this coupling to $\mathbf{q} \to \mathbf{0}$ appears *neither* for in-plane deviations $\mathbf{q} = (\eta, 0, 2)$, *nor* around $\mathbf{G}_0 = (0, 0, 1)$. To this end, we can make use of general properties of the dielectric function in semiconductors. In the limit of high frequencies, the coupling element can be approximated as [26]

$$\epsilon_{\mathbf{0}\mathbf{G}_0}(\mathbf{q}_r, \omega) = \frac{4\pi}{\omega^2}\frac{\mathbf{q}_r \cdot (\mathbf{q}_r + \mathbf{G}_0)}{q_r^2}n(-\mathbf{G}_0),$$

where $n(-\mathbf{G}_0)$ denotes the Fourier coefficient of the electron density. A similar expression has been found by Sturm and Oliveira [25] in the framework of a quasifree electron gas. First, we see from this equation that the coupling between density fluctuations with momentum $\mathbf{q}_r$ and $\mathbf{q}_r + \mathbf{G}_0$ is proportional to the cosine of the enclosed angle α' [see Fig. 2(b)]. The prefactor $\epsilon_{\mathbf{G}_0\mathbf{0}}\epsilon_{\mathbf{0}\mathbf{G}_0}/\epsilon^2_{\mathbf{G}_0\mathbf{G}_0} \propto \cos^2\alpha'$ enforces the anisotropy of the spectra: in particular, for a small in-plane $\mathbf{q}_r$, one has $\alpha = 90° \approx \alpha'$, which explains the absence of strong LFE in the spectrum for $\alpha = 90°$ [Fig. 2(a), top panel]. Second, the coupling element vanishes whenever the crystal structure factor, which is proportional to $n(-\mathbf{G}_0)$ becomes zero; i.e., whenever the Bragg reflection at $\mathbf{G}_0$ is forbidden. For graphite in Bernal stacking, this is the case for all $\mathbf{G}_0 = (0, 0, 2m + 1)$ where m is an integer. LFE around (0, 0, 1) stem hence only from a mixing with other *nonvanishing* $\mathbf{G} \neq \mathbf{0}$ beyond the 2×2 model. They do not introduce any significant dependence on the direction of $\mathbf{q}_r$ since $\mathbf{G} + \mathbf{q}_r \approx \mathbf{G}$. Instead, for $\mathbf{G}_0 = (0, 0, 2m)$, the two graphite planes A and B in the unit cell contribute in a constructive way (analogous to the constructive interference in the case of the Bragg reflection), which leads to the strong effect.

With these explanations in mind, let us come back to the results shown in Fig. 1(b). Since $\mathbf{q}_r$ is still reasonably small, the above arguments hold. In particular, we can explain the drastic spectral changes near (0, 0, 2) by the fact that (i) the spectrum from the first Brillouin zone reappears, which strongly depends on the direction of $\mathbf{q}_r$ (angle α) due to the anisotropy of graphite, and that (ii) the coupling and hence the strength of the recurring spectra is proportional to $|\mathbf{q}_r \cdot \mathbf{q}|^2 \propto \cos^2\alpha'$.

One may wonder whether such a spectacular effect can actually be observed, or whether it is masked either by

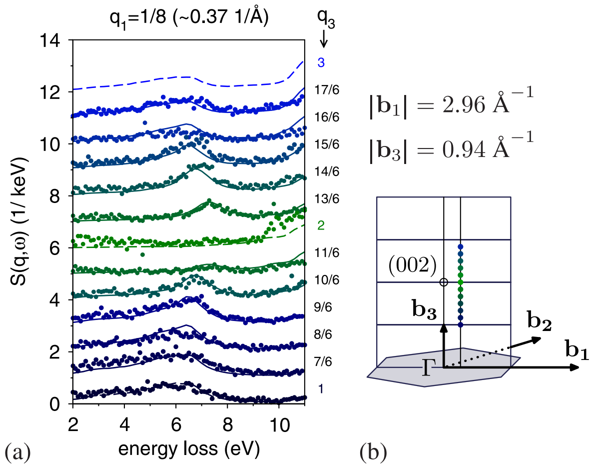

FIG. 3 (color online). (a) Comparison of the structure factor $S(\mathbf{q}, \omega)$ measured by IXS-experiments (dots) and calculated in RPA (lines; dashed for integer q_3) for $\mathbf{q} = (\frac{1}{8}, 0, q_3)$. The elastic tail has been removed from the raw experimental data and a uniform scaling has been applied. (b) Measured $\mathbf{q}$-points in reciprocal space.

exchange-correlation effects that are neglected in RPA, or by experimental conditions like a strong elastic tail near the Bragg reflection. Therefore, we have conducted inelastic x-ray scattering measurements for momentum transfers $\mathbf{q} = (\frac{1}{8}, 0, \frac{n}{6})$ covering the range between $\mathbf{q} = (0, 0, 1)$ and $(0, 0, 3)$. The in-plane component $|q_1 \mathbf{b}_1| = 0.37$ Å^{-1} is still small enough to create the desired effect [see Fig. 1(b)], but large enough to avoid the Bragg reflection. The measurements were carried out at the Taiwan inelastic scattering beam line in SPring-8 (BL12XU). The graphite sample was a plate having a surface of 2×3 mm^2 and a thickness of 100 μm [27]. The x-ray Laue photograph showed very nice spots, indicating that the sample was not Highly Oriented Pyrolitic Graphite but a single crystal. The energy resolution was 140 meV. A Si 400 four-bounce monochromator and a Si 444 spherical crystal analyzer were used. The momentum resolutions were approximately 0.15 Å^{-1} along the horizontal and the vertical axes. In order to subtract the tails of the elastic lines for the spectra, glass was measured as a reference. Figure 3(a) shows the measured spectra (dots) together with the corresponding calculated results (lines). The agreement is very good; in particular, the predicted peak shift is clearly seen in the measurements, as well as the abrupt change from a peaked spectrum for $\mathbf{q} = (\frac{1}{8}, 0, \frac{13}{6})$ to a completely flat one at $\mathbf{q} = (\frac{1}{8}, 0, 2)$, and the difference between $q_3 = \frac{13}{6}$ and $\frac{11}{6}$ due to the different angles α' [see Fig. 2(b)]. Hence, our measurements give unambiguous support to the presented theoretical predictions.

Beyond our studies of graphite, we expect similar results for other anisotropic crystals with strong LFE, especially for layered or quasi 1D structures. The exact reappearance of spectra from other Brillouin zones might however be obscured by the coupling factor, which is in general frequency dependent and complex valued, or the need to go beyond the two-plasmon-band approximation.

In conclusion, our RPA calculations and IXS measurements revealed and explained a striking discontinuity in the dynamic structure factor $S(\mathbf{q}, \omega)$ of graphite at momentum transfers $\mathbf{q}_r + \mathbf{G}_0$ close to Bragg allowed reciprocal-lattice vectors $\mathbf{G}_0$: infinitesimal changes in the momentum transfer induce strong changes in the resulting spectra. No discontinuity is observed when the crystal structure factor vanishes. It is hence a consequence of the Bernal stacking of the graphene layers that no changes occur at $\mathbf{G}_0 = (0, 0, 1)$. The theoretically predicted and experimentally observed effect has important consequences for measurements of $S(\mathbf{q}, \omega)$ close to an allowed Bragg reflection, as the resulting spectra can be *extremely sensitive* to the chosen momentum transfer. It is also an important step forward in the understanding of the dynamic structure factor of anisotropic systems, that may have broad applications including the description of strongly correlated systems.

This work was supported by the EU's FP7 through the ETSF-I3 project (Contract No. 211956) and by the ANR (Project NT05-3 43900). The experiment was carried out under an approval of SPring-8 and NSRRC (Proposal No. C04B12XU-1510N). Y. C. and N. H. are grateful to Professor Hiroyoshi Suematsu for providing us with the single crystal of graphite. R. H. thanks the Dr. Carl Duisberg-Stiftung and C'Nano IdF (IF07-800/R).

---

*Current address: National Synchrotron Light Source II, Brookhaven National Laboratory, Upton, NY 11973.

[1] N. Hiraoka *et al.*, Phys. Rev. B **72**, 075103 (2005).
[2] Y. Q. Cai *et al.*, Phys. Rev. Lett. **97**, 176402 (2006).
[3] W. Schülke and A. Kaprolat, Phys. Rev. Lett. **67**, 879 (1991).
[4] S. L. Adler, Phys. Rev. **126**, 413 (1962).
[5] N. Wiser, Phys. Rev. **129**, 62 (1963).
[6] S. Waidmann *et al.*, Phys. Rev. B **61**, 10149 (2000).
[7] A. G. Marinopoulos *et al.*, Phys. Rev. B **69**, 245419 (2004).
[8] S. Botti *et al.*, Phys. Rev. Lett. **89**, 216803 (2002).
[9] K. Zeppenfeld, Z. Phys. A **211**, 391 (1968).
[10] K. Zeppenfeld, Z. Phys. A **243**, 229 (1971).
[11] A. G. Marinopoulos *et al.*, Phys. Rev. Lett. **89**, 076402 (2002).
[12] P. B. Visscher and L. M. Falicov, Phys. Rev. B **3**, 2541 (1971).
[13] D. Grecu, Phys. Rev. B **8**, 1958 (1973).
[14] A. L. Fetter, Ann. Phys. (N.Y.) **88**, 1 (1974).
[15] C. S. Huang, M. F. Lin, and D. S. Chuu, Solid State Commun. **103**, 603 (1997).
[16] M. F. Lin, C. S. Huang, and D. S. Chuu, Phys. Rev. B **55**, 13961 (1997).
[17] E. Runge and E. K. U. Gross, Phys. Rev. Lett. **52**, 997 (1984).
[18] X. Gonze *et al.*, Comput. Mater. Sci. **25**, 478 (2002).
[19] We used 6144 k-points and an energy cutoff of 28 hartree.
[20] N. Troullier and J. L. Martins, Phys. Rev. B **43**, 1993 (1991).
[21] http://www.dp-code.org; V. Olevano *et al.* (unpublished).
[22] K. Sturm, W. Schülke, and J. R. Schmitz, Phys. Rev. Lett. **68**, 228 (1992).
[23] K. Höppner, A. Kaprolat, and W. Schülke, Eur. Phys. J. B **5**, 53 (1998).
[24] Indeed, we have verified that results of calculations neglecting all other off-diagonal elements are very close to the full ones.
[25] K. Sturm and L. E. Oliveira, Phys. Rev. B **22**, 6268 (1980).
[26] F. Bechstedt, Phys. Status Solidi B **112**, 9 (1982).
[27] H. Suematsu and S. Tanuma, J. Phys. Soc. Jpn. **33**, 1619 (1972).

5.3 Oxides

Transition metal oxides are a big class of materials, with an even larger variety of applications. TiO_2 is known for its applications in photo-catalysis, HfO_2 is a prominent high-κ material for resistive memories, optical coating, etc.), CuO is a building block of cuprate high-temperature superconductors and is today discussed as a potential photo-voltaic material. These are only examples of some systems I have been studying in the last years, thanks to the projects of several post-docs in the group. In all these examples, there's a strong common denominator: the strong connection with experiments. In all the cases in fact, we have conducted not only the theoretical work, but also the experimental counterpart (clearly in collaboration with our experimentalist colleagues): for TiO_2 we have conducted IXS experiments at the GALAXIES beamline in SOLEIL (thanks to the collaboration with Jean-Pascal Rueff and James Ablett), while for CuO the experiments were carried out mostly at the ESRF in Grenoble (with Simo Huotari); the EELS experiments for HfO_2, originally an ETSF user project, were conducted in Minatec Grenoble (with Cyril Guedj).

PLEASE REFER TO THE ATTACHED ARTICLE

APPLIED PHYSICS LETTERS **105**, 222904 (2014)

Evidence for anisotropic dielectric properties of monoclinic hafnia using valence electron energy-loss spectroscopy in high-resolution transmission electron microscopy and *ab initio* time-dependent density-functional theory

C. Guedj,[1,2] L. Hung,[3,4] A. Zobelli,[5] P. Blaise,[1,2,4] F. Sottile,[3,4] and V. Olevano[1,4,6]
[1]*University Grenoble Alpes, F-38000 Grenoble, France*
[2]*CEA, LETI, MINATEC Campus, F-38054 Grenoble, France*
[3]*LSI, CNRS, CEA, École Polytechnique, F-91128 Palaiseau, France*
[4]*European Theoretical Spectroscopy Facility (ETSF)*
[5]*LPS, CNRS and University Paris Sud, F-91405 Orsay, France*
[6]*CNRS, Institut Néel, F-38042 Grenoble, France*

(Received 12 September 2014; accepted 7 November 2014; published online 2 December 2014)

The effect of nanocrystal orientation on the energy loss spectra of monoclinic hafnia (m-HfO_2) is measured by high resolution transmission electron microscopy (HRTEM) and valence energy loss spectroscopy (VEELS) on high quality samples. For the same momentum-transfer directions, the dielectric properties are also calculated *ab initio* by time-dependent density-functional theory (TDDFT). Experiments and simulations evidence anisotropy in the dielectric properties of m-HfO_2, most notably with the direction-dependent oscillator strength of the main bulk plasmon. The anisotropic nature of m-HfO_2 may contribute to the differences among VEELS spectra reported in literature. The good agreement between the complex dielectric permittivity extracted from VEELS with nanometer spatial resolution, TDDFT modeling, and past literature demonstrates that the present HRTEM-VEELS device-oriented methodology is a possible solution to the difficult nanocharacterization challenges given in the International Technology Roadmap for Semiconductors. © *2014 AIP Publishing LLC*. [http://dx.doi.org/10.1063/1.4903218]

With the downscaling of microelectronic and optoelectronic devices, accurate metrology at the nanoscale has become an important objective for the microelectronic industry. At the same time, the International Technology Roadmap for Semiconductors categorizes the "measurement of complex material stacks and interface properties, including physical and electrical properties" as a "difficult challenge" for ~16 nm CMOS technology nodes. The characterization of high-κ gate stacks (mostly based on hafnia-based dielectrics) is particularly complicated due to the length scales at which electronic properties are determined. These new challenges for characterization and metrology arise not only from the introduction of thinner and more complex materials and stacks but also from the need to discern physical properties at an increasing spatial resolution. To develop nanocharacterization protocols that are independent of materials stacks and integration design, even more advanced methods are required. Valence electron energy-loss spectroscopy (VEELS) is the only technique capable of measuring dielectric and optical properties[1] (complex refractive index), and chemical properties[2] (composition, atomic bonding) at the same time and with nanometer spatial resolution, when all effects are properly taken into account.[3,4]

In this paper, we use the energy filtered TEM-VEELS technique (also known as EFTEM SI),[8] in a high-resolution transmission electron microscope (HRTEM) to simultaneously obtain the structural and spectroscopic properties of $P2_1/c$ m-HfO_2 with nanometric spatial resolution. HfO_2 is a prominent high-κ material used in various applications like MIM capacitors,[5] resistive memories (OxRRAM),[6] or optical coatings.[7] To this purpose, the dielectric properties of m-HfO_2 corresponding to the different crystal configuration and orientations that can be grown in an electronic device must be precisely measured, a task for which HRTEM-VEELS is particularly suited. After detailed nanostructural modeling of HRTEM measurements using quantitative image simulations, we obtained VEELS spectra for various well identified m-HfO_2 crystal orientations. For the same momentum-transfer directions, we also calculate *ab initio* time-dependent density-functional theory (TDDFT)[11] energy-loss spectra. For the calculated TDDFT spectra, we use the random-phase approximation (RPA) and also include local-field effects.[13,14] This level of theory allows us to reproduce, interpret, and even predict experimental energy-loss spectra.[15] With its reliability and predictivity, TDDFT is a valuable complement to experimentally applied research on high-κ materials for electronic or optical devices.

For the dielectric properties and spectra of m-HfO_2, we find a significant dependence on the crystal direction. The analysis of the main oscillators of the EELS spectra shows that the change in lattice orientation mostly affects the strength of the main bulk plasmon excitation at ~16 eV. A significant anisotropy of ~10% has been found also on the dielectric constant.

HfO_2 films are grown by atomic layer deposition (ALD) on 200 mm p-Si(100) wafers. Before deposition, substrates are treated with a diluted HF solution to remove any native oxides. ALD takes place in an ASM Pulsar 2000^{TM} module at 350 °C using alternating pulses of $HfCl_4$ and H_2O, with N_2 as a carrier gas. The introduction of H_2O vapor is used to desorb HCl at the growing surface, and the cycles are repeated sequentially to reach a thickness sufficient to maximize the crystal quality and to minimize the surface losses.

A final annealing at 650 °C is performed to crystallize HfO_2 and minimize the amount of oxygen vacancies. A high Tauc-Lorentz[18,19] band gap (∼5.9) is measured by spectroscopic ellipsometry and VEELS, which is consistent[20] with a low level of oxygen vacancies of this fully oxidized HfO_2 layer. This layer is therefore representative of a good quality dielectric material used in the microelectronic industry. Additional measurements are performed on high grade m-HfO_2 powders for verification.

Cross-sectional electron microscopy and diffraction experiments are performed in a JEOL 2010 FEF transmission electron microscope (TEM) operated at 200 kV at a magnification of 800 k, with an energy step of 0.1 eV between each image acquisition. The lowest achievable collection and convergence angles are used (few mrads) to minimize experimental momentum dispersion. The measured energy resolution is typically around 1.4 eV. For verification, complementary results are obtained with the Cs-corrected Titan microscope operated at 200 keV in STEM and TEM modes. About 80×10^6 spectra are acquired over 16 different samples to check the consistency of the results and to optimize the protocols of data acquisition and analysis. Samples are prepared with a Strata$^{\text{TM}}$ 400 DualBeam$^{\text{TM}}$ FIB/STEM system using Ga+ ions energies ranging from 30 keV down to 2 keV. An improvement in the quality of HRTEM-VEELS data is obtained by selective lift-off of superficial amorphous species by HF etching. Experimental data are corrected using the guidelines provided by Schaffer *et al.*[21] TEM lamella thickness is optimized (<40 nm) to avoid the need for multiple scattering deconvolution processing, but not too thin (>15 nm) to avoid excessive surface effects. Quantitative spectra are extremely difficult to obtain because of the numerous sources of variability due to instrumentation, sample preparation, and data analysis. The zero-loss (elastic) contribution is removed from a reference VEELS spectrum acquired simultaneously in the vacuum region closest to the measured region of interest. The quality and reproducibility of the deconvolution process are verified by bandgap analysis of millions of spectra. The TEM approach is particularly convenient for absolute comparison of 2 neighbour grains with different orientations, because the data acquisition is simultaneous for both nanocrystals and the sources of instrumental variability can be deconvoluted more efficiently. Fortunately, m-HfO_2 appears to be very stable under e-beam irradiation. The Kramers-Kronig analysis[22] is then performed on the single scattering distributions using classical routines available in the Digital Micrograph$^{\text{TM}}$ environment to provide complex permittivities,[23] energy-loss, and surface-loss functions versus local nanostructure.

Numerical calculations[17] are carried out within the framework of density-functional theory (DFT) using a plane-wave and pseudopotential implementation in a two-step approach: First, the ground state atomic structure and electronic density of m-HfO_2 is computed by static DFT[10] using the local-density approximation (LDA)[12] and the code ABINIT.[16] The calculated m-HfO_2 lattice parameters are in good agreement with our and literature[9] experimental values. We use a Hf pseudopotential that includes semicore 4*f*, 5*s*, and 5*p* electrons in valence since they contribute to excitations in the studied energy range. Second, the energy-loss and the dielectric function are calculated by linear-response TDDFT[11] using the DP code. The inclusion of local-field effects has been found to be crucial to correctly reproduce the HfO_2 energy-loss function. To compare with VEELS, TDDFT spectra are convoluted with a broadening of 1.5 eV, of the order of the experimental energy resolution.

A careful analysis of the crystal structure is necessary since hafnia has several phases depending on pressure[24] or growth method.[26–29] The monoclinic phase[25] is the most stable in ambient conditions.

The simulated diffraction patterns of the different phases are often very similar; therefore, the distinction between the HfO_2 phases is difficult. The comparison between experimental and simulated defocus-thickness series usually provides an identification of the phase and orientation of hafnia. In the worse cases, an unambiguous identification is provided by exit wave reconstruction techniques using the True Image FEI ®Software.[30]

VEELS spectra of single crystalline m-HfO_2 measured at negligible transferred momentum oriented along five different directions are presented in the top left of Fig. 1. The spectra usually display ten apparent features labelled from A to I, and, respectively, located at around 10, 16, 20, 23, 27, 35, 38, 44, and 47 eV, although some peaks overlap and could be considered as a broader degenerate contribution. Similar features are obtained for the polycrystalline case

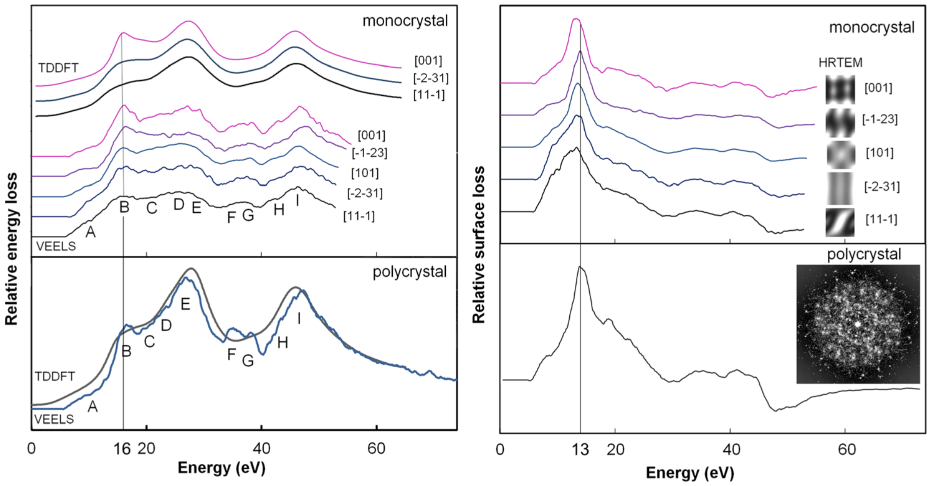

FIG. 1. Valence bulk energy loss (left) and surface-loss spectra (right) deconvoluted from measured VEELS spectra of m-HfO_2 in the case of monocrystals (top) and polycrystals (bottom) at several momentum-transfer directions, in comparison with *ab initio* TDDFT simulations. The TEM images of monocrystals and the selected area diffraction pattern of the polycrystal are also provided. Experimental curves in top panels are vertically shifted to facilitate comparison.

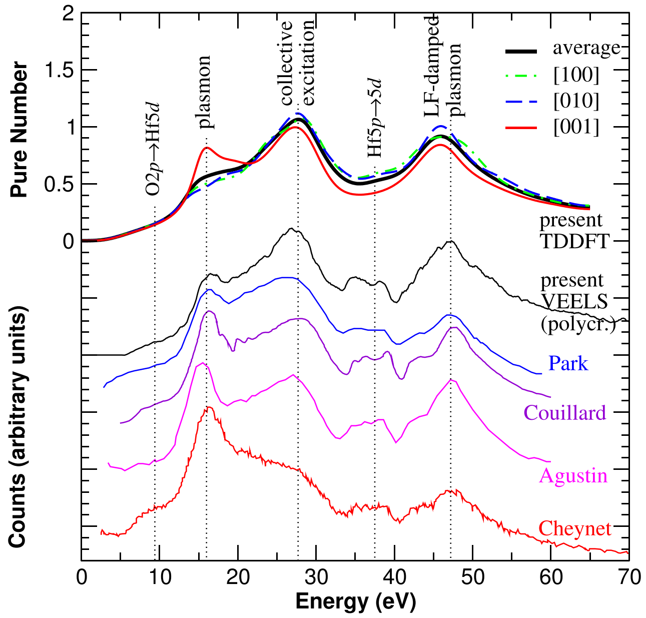

FIG. 2. Energy-loss spectra of monoclinic HfO_2. From top to bottom: TDDFT RPA with local fields calculation as in the [100] (dot-dashed green), [010] (dashed blue), and [001] (thin solid red) directions and their average (thick solid black line); VEELS spectra as measured by us (polycrystalline, black), by Park and Yang (blue),[31] Couillard *et al.* (violet),[32] Agustin *et al.* (magenta),[33] and Cheynet *et al.* (red).[34] Experimental curves are vertically shifted to facilitate comparison.

(bottom). The TDDFT calculation displays 5 main features (especially evident at smaller broadening) at 8, 16, 27, 38, and 46 eV, at positions close to the peaks A, B, E, I, and FG by less than 2 eV (see also Fig. 2). TDDFT reveals that the shoulder A is due to single particle transitions (O 2*p* → Hf 5*d*), like also F and G (Hf 5*p* → 5*d*); peak B is the only real bulk plasmon, while E and I are collective excitations. Local-field effects severely damp peak I, which would otherwise be the main total plasmon. Details about the theoretical calculation and interpretation will be provided elsewhere. Our TDDFT calculations with local-field effects can be considered the best-available simulated energy-loss spectra, with net improvement in agreement with experiment compared to previous DFT calculations[31] (which did not predict the damping of the I collective excitation).

We now analyze differences in spectra measured along different crystal directions. The most evident change is a modulation of the oscillator strengths of the shoulder A and, in particular, of the plasmon B. To correctly interpret this finding, it is important to deconvolute the surface loss functions (right), since the most intense feature of the surface losses is located around 13 eV, close to the position of the bulk plasmon. Strong differences in surface losses may therefore contribute to the lack of perfect congruence among literature data.

When all parameters are well controlled, the comparison between experiment and the TDDFT is good. Although less pronounced than in the experiment, TDDFT confirms the directional modulation of the plasmon. In both TDDFT and experiment, this is the most evident effect of anisotropy, the other changes being less obvious.

This is also evident in the TDDFT spectra shown in Fig. 2 (top curves), where we plot the energy-loss along the three main crystallographic directions, as well as a directional averaged spectrum. The most important anisotropy effect is observed once again on the bulk plasmon at 16 eV, with minor modifications on the rest of the spectrum. The plasmon appears as a well separated peak in the [001] direction, while it reduces to a shoulder in the other directions.

The anisotropy in the dielectric properties and spectroscopy of m-HfO_2 has not been reported so far. This can shed new light on the interpretation of VEELS spectra previously measured. In Fig. 2, we report the measured VEELS spectra of m-HfO_2 published in Refs. 31–34. We also show our measured VEELS (polycrystalline sample). It is evident that the measured VEELS presents some disagreements among them. We observe in particular, a different attribution of the intensity of the plasmon at ∼16 eV, which is the most intense peak, e.g., in Cheynet *et al.*,[34,35] while it is less intense than the collective excitation at ∼27 eV in Park and Yang.[31] We observe different intensities also on the 47 eV LF-damped plasmon. In light of our findings, the effect of anisotropy could partially contribute to explain the differences among previously measured VEELS spectra, even if many additional experimental factors, like sample thickness, roughness, and defectivity, could also affect the result. Performing absolute and perfectly quantitative measurements is indeed a real challenge. Current stability, convergence and collection angle, energy resolution, type of measurement (EFTEM vs. STEM), and the zero-loss removal method might have an impact on the resulting spectra, even if perfect single scattering configurations and highly accurate corrections of anisochromaticity and spatial drifts are used. The data analysis could also impact the Kramers-Kronig process significantly. Nevertheless, when limiting the influence of these factors, anisotropies in m-HfO_2 can be clearly observed, in agreement with TDDFT calculations.

The real and imaginary parts of the dielectric permittivity are represented in Fig. 3. Again, the overall agreement between experiment and simulation is good, in spite of the complexity of m-HfO_2. In particular, the real permittivity passes zero near 15 eV, indicating that peak B is a proper bulk plasmon, in agreement with TDDFT. Overall, we find good agreement between experiment and TDDFT-RPA (with local-field effects) even in the 20–70 eV range, which improves on previous DFT calculations.[31] It is important to note that some residual discrepancies are still present, especially in the intensity of the first plasmon peak, which is particularly sensitive to transitions possibly involving defect levels. But, the theoretical description can be already considered satisfactory in order to interpret and describe the correct physics in m-HfO_2.

Finally, we report our TDDFT calculated dielectric constants for m-HfO_2. Here, again we find significant anisotropies. TDDFT predicts a dielectric constant of 5.0 in the [100] and [010] directions, but only 4.6 in the [001] *z* direction, a difference of around 10%. The same 10% difference is confirmed also using the TDDFT adiabatic LDA approximation.[12] This anisotropy in the dielectric properties, both in the static regime and also at the bulk plasmon frequency, might have possible technological applications.

We have measured VEELS spectra of m-HfO_2 in correspondence to well defined momentum-transfer crystallographic

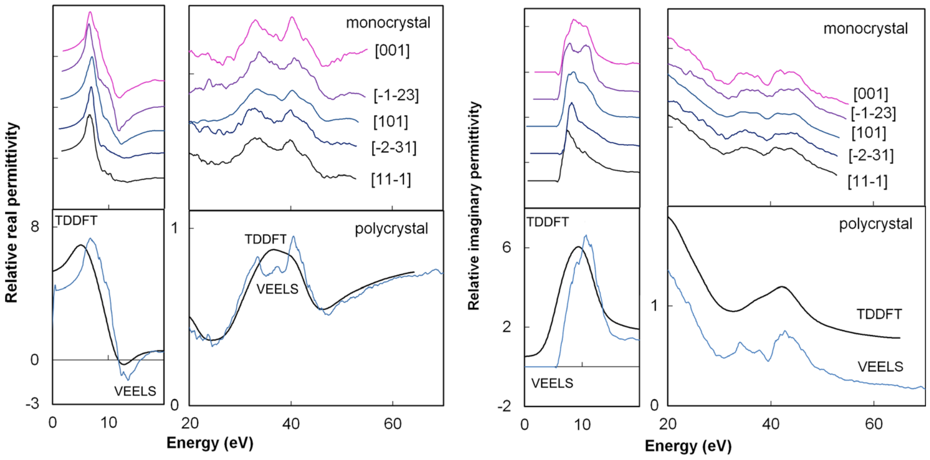

FIG. 3. Real (left) and imaginary (right) permittivity of m-HfO_2 measured in the case of monocrystals at several momentum-transfer directions (vertically shifted to ease comparison, top), and polycrystal in comparison with *ab initio* TDDFT (bottom).

directions. We have compared the experimental spectra to TDDFT calculated, finding a good agreement. This has allowed us to correctly interpret and understand the dielectric properties of polycrystalline or monocrystalline m-HfO_2. We have found a significant anisotropy in the dielectric properties, mostly on the bulk plasmon at ∼16 eV and on the dielectric constant. This can impact the behaviour of (opto)electronic devices based on this important high-κ material.

We acknowledge support from ETSF for simulations and the nanocharacterisation platform (PFNC, http://www.minatec.org/pfnc-plateforme-nanocaracterisation) for experiments, and Cezus (Areva) for providing m-HfO_2 powder. Computer time has been provided by the French GENCI supercomputing center (projects i2012096-655 and 544).

[1] M. Stöger-Pollach, Micron **39**, 1092 (2008).
[2] J. Wang, X. F. Wang, Q. Li, A. Hryciw, and A. Meldrum, Philos. Mag. **87**, 11 (2007).
[3] M. Stöger-Pollach, A. Laister, and P. Schattschneider, Ultramicroscopy **108**, 439 (2008).
[4] R. Erni and N. D. Browning, Ultramicroscopy **108**, 84 (2008).
[5] F. Mondon and S. Blonkowski, Microelectron. Reliab. **43**, 1259 (2003).
[6] D. B. Strukov, G. Snider, D. R. Stewart, and R. S. Williams, Nature **453**, 80 (2008); H. Y. Lee, P. S. Chen, T. Y. Wu, Y. S. Chen, C. C. Wang, P. J. Tzeng, C. H. Lin, F. Chen, C. H. Lien, and M.-J. Tsai, Tech Dig. - Int. Electron. Devices Meet. **2008**, 297.
[7] M. Gilo and N. Croitoru, Thin Solid Films **350**, 203 (1999).
[8] J. Verbeeck, D. Van Dyck, and G. Van Tendeloo, Spectrochim. Acta B **59**, 1529 (2004).
[9] J. Wang, H. P. Li, and R. Stevens, J. Mater. Sci. **27**, 5397 (1992); J. Adam and M. D. Rogers, Acta Crystallogr. **12**, 951 (1959).
[10] P. Hohenberg and W. Kohn, Phys. Rev. **136**, B864 (1964); W. Kohn and L. J. ShamPhys. Rev. **140**, A1133 (1965).
[11] E. Runge and E. K. U. Gross, Phys. Rev. Lett. **52**, 997 (1984); E. K. U. Gross and W. Kohn, Phys. Rev. Lett. **55**, 2850 (1985).
[12] A. Zangwill and P. Soven, Phys. Rev. A **21**, 1561 (1980).
[13] S. L. Adler, Phys. Rev. **126**, 413 (1962).
[14] N. Wiser, Phys. Rev. **129**, 62 (1963).
[15] H.-C. Weissker, J. Serrano, S. Huotari, E. Luppi, M. Cazzaniga, F. Bruneval, F. Sottile, G. Monaco, V. Olevano, and L. Reining, Phys. Rev. B **81**, 085104 (2010).
[16] X. Gonze, G.-M. Rignanese, M. Verstraete, J.-M. Beuken, Y. Pouillon, R. Caracas, F. Jollet, M. Torrent, G. Zerah, M. Mikami *et al.*, Z. Kristall. **220**, 558 (2005).
[17] The DFT calculation is converged at a kinetic energy cut-off of 150 Ha. In the TDDFT calculation, we used 300 bands, 9475 plane waves to represent wavefunctions and 329 for polarizability and dielectric matrices. We sampled the Brillouin zone by a 4 × 4 × 4 shifted k-points grid.
[18] M. Di, E. Bersch, A. C. Diebold, S. Consiglio, R. D. Clark, G. J. Leusink, and T. Kaack, J. Vac. Sci. Technol., A **29**, 041001 (2011).
[19] G. E. Jellison, Jr. and F. A. Modine, Appl. Phys. Lett. **69**, 371 (1996).
[20] E. Hildebrandt, J. Kurian, M. M. Müller, T. Schroeder, H.-J. Kleebe, and L. Alff, Appl. Phys. Lett. **99**, 112902 (2011).
[21] B. Schaffer, G. Kothleitner, and W. Grogger, Ultramicroscopy **106**, 1129 (2006).
[22] R. F. Egerton, *Electron Energy-loss Spectroscopy in the Electron Microscope* (Plenum, New York, 1996).
[23] A. N. Saxena and K. L. Mittal, J. Appl. Phys. **46**, 2788 (1975).
[24] J. M. Léger, A. Atouf, P. E. Tomaszewski, and A. S. Pereira, Phys. Rev. B **48**, 93 (1993).
[25] D. M. Adams, S. Leonard, D. R. Russel, and R. J. Cernik, J. Phys. Chem. Solids **52**(9), 1181 (1991); D. M. Adams, S. Leonard, and D. R. J. Russell, J. Phys. Chem. Solids **52**, 1181 (1991); J. E. Jaffe, R. A. Bachorz, and M. Gutowski, Phys. Rev. B **72**, 144107 (2005); R. Ruh and P. W. R. Corfield, J. Am. Ceram. Soc. **53**, 126 (1970); V. I. Khitrova and Z. G. Kiseleva, Sov. Phys. Crystallogr. **20**, 239 (1975); R. E. Hann, P. R. Suitch, and J. L. Pentecost, J. Am. Ceram. Soc. **68**, C285 (1985); A. M. Gavrish, B. Y. Sukharevskii, P. P. Krivoruchko, and E. I. Zoz, Inorg. Mater. **5**, 459 (1969).
[26] D. Taylor, Trans. J. Br. Ceram. Soc. **83**, 32 (1984); V. N. Parfenenkov, R. G. Grebenshchikov, and A. I. Domanskii, Inorg. Mater. **10**, 919 (1974); V. D. Kushkov, A. V. Mel'nikov, and A. M. Zaslavskii, Russ. J. Inorg. Chem. **34**, 1548 (1989); D. Kim, S. Hyun, S. Kim, and M. Yashima, J. Am. Ceram. Soc. **77**, 597 (1994); S. G. Popov, M. V. Paromova, Z. Y. Kulikova, O. N. Rozanova, and S. F. Pashin, Inorg. Mater. **26**, 843 (1990); L. Passerini, Gazz. Chim. Ital. **60**, 762 (1930); N. G. Gorashchenko, V. I. Ivanovskaya, A. A. Maier, N. I. Markov, N. R. Miftyakhetdinova, V. A. Myzina, V. V. Osiko, and V. M. Tatarintsev, Inorg. Mater. **21**, 1323 (1985); M. A. Caravaca and R. A. Casali, J. Phys. Condens. Matter **17**, 5795 (2005).
[27] J. P. Coutures and J. Coutures, J. Am. Ceram. Soc. **70**, 383 (1987); E. N. Isupova, V. B. Glushkova, and E. K. Keler, Inorg. Mater. **4**, 334 (1968).
[28] M. Hirabayashi, S. Yamaguchi, and T. Arai, J. Phys. Soc. Jpn. **35**, 473 (1973).
[29] O. Ohtaka, T. Yamanaka, S. Kume, N. Hara, H. Asano, and F. Izumi, J. Am. Ceram. Soc. **78**, 233 (1995); O. Ohtaka, T. Yamanaka, and S. Kume, J. Ceram. Soc. Jpn. **99**, 826 (1991); R. Suyama, H. Horiuchi, S. Kume, and Y. Kyokaishi, J. Ceram. Assoc. Jpn. **95**, 567 (1987); J. Haines, J. M. Leger, S. Hull, J. P. Petitet, A. S. Pereira, C. A. Perottoni, and J. A. H. Da Jornada, J. Am. Ceram. Soc. **80**, 1910 (1997); J. Tang, M. Kai, Y. Kobayashi, S. Endo, O. Shimomura, T. Kikegawa, and T. Ashida, Geophys. Monogr. **101**, 401 (1998); L.-G. Liu, J. Phys. Chem. Solids **41**, 331 (1980).
[30] W. M. J. Coene, A. Thust, M. Op de Beek, and D. van Dyck, Ultramicroscopy **64**, 109 (1996); A. Thust, W. M. J. Coene, M. Op de Beek, and D. van Dyck, Ultramicroscopy **64**, 211 (1996); A. Thust, M. H. F. Overwijk, W. M. J. Coene, and M. Lentzen, Ultramicroscopy **64**, 249 (1996).
[31] J. Park and M. Yang, Micron **40**, 365 (2009).

[32]M. Couillard, M. Kociak, O. Stephan, G. A. Botton, and C. Colliex, Phys. Rev. B **76**, 165131 (2007).

[33]M. P. Agustin, L. R. C. Fonseca, J. C. Hooker, and S. Stemmer, Appl. Phys. Lett. **87**, 121909 (2005).

[34]M. C. Cheynet, S. Pokrant, F. D. Tichelaar, and J.-L. Rouviere, J. Appl. Phys. **101**, 054101 (2007).

[35]C. C. Ahn, O. Krivanek, R. P. Burgner, M. M. Disko, and P. R. Swann, *EELS Atlas* (Gatan, Warrendale, 1983).

PHYSICAL REVIEW B **91**, 045102 (2015)

Quasiparticle excitations in the photoemission spectrum of CuO from first principles: A GW study

Claudia Rödl, Francesco Sottile, and Lucia Reining
Laboratoire des Solides Irradiés, École Polytechnique, CNRS, CEA-DSM, 91128 Palaiseau cedex, France
and European Theoretical Spectroscopy Facility (ETSF)

(Received 5 October 2014; revised manuscript received 4 December 2014; published 5 January 2015)

We present *ab initio* quasiparticle calculations for electronic excitations and the fundamental band gap of the strongly correlated transition-metal oxide CuO using the GW approximation of many-body perturbation theory. Problems related to the suitability of the method for strongly correlated materials and issues of self-consistency are addressed. We explain why quasiparticle self-consistent GW strongly overestimates the band gap of CuO. Apart from the band gap, electron addition and removal spectra in the quasiparticle approximation including lifetime and matrix-element effects are found to be in excellent agreement with the quasiparticle excitations in direct and inverse photoemission data.

DOI: 10.1103/PhysRevB.91.045102 PACS number(s): 71.15.−m, 71.27.+a, 71.45.Gm, 79.60.−i

I. INTRODUCTION

Cupric oxide (CuO), also known as tenorite, features a vast range of applications: it has been used as a pigment in glass and ceramics [1] for thousands of years and is nowadays discussed as a potential absorber material in photovoltaic devices [2] due to its room-temperature band gap of ∼1.4 eV [3,4]. Furthermore, CuO constitutes the building block and parent compound of the cuprate high-temperature superconductors [5]. It is assumed [6] that superconductivity in the cuprates is due to electron-correlation effects in the CuO_2 layers where the Cu ions exhibit the same square-planar coordination with O as it occurs in CuO. Recently, the possibility of high-temperature multiferroicity in CuO has been brought up [7]. All these applications are closely linked to specific properties of the electronic structure. However, surprisingly little is known about the electronic excitations in CuO from a theoretical point of view. This might be due to the fact that the band gap and all electronic excitations in its vicinity are governed by an intricate interplay between itinerant O $2p$ and localized Cu $3d$ electrons which renders the theoretical description notoriously difficult.

CuO crystallizes in a monoclinic face-centered structure (space group: $C2/c$) with four atoms per unit cell [8]. The near degeneracy of several competing equilibrium states in this material is illustrated by the existence of two antiferromagnetic orderings with different Néel temperatures T_{N} [9,10]. Below $T_{\mathrm{N}}^{(1)} = 213$ K, CuO exhibits the magnetic ordering that is shown in Fig. 1(a) with local magnetic moments in the range of $0.65 \ldots 0.69\mu_{\mathrm{B}}$ at the Cu atoms [9,10]. In this magnetic structure, each O atom is surrounded by a slightly distorted tetrahedron of four Cu atoms. Three of the surrounding Cu atoms have parallel local magnetic moments, whereas the local moment of the fourth Cu atom points in the opposite direction [9]. Between 213 K and $T_{\mathrm{N}}^{(2)} = 231$ K, the magnetic ordering exhibits a helical structure [10], before the system finally becomes paramagnetic at higher temperatures.

First-principles calculations of the electronic ground state using the non-spin-polarized local-density approximation (LDA) of density-functional theory (DFT) predict CuO to be metallic [11], whereas the experimental direct band gap extrapolated to zero temperature amounts to 1.67 eV [12]. Also spin-polarized LDA calculations do not yield a nonvanishing band gap [13]. Attempts have been made to correct one of the major deficiencies of the LDA, the self-interaction, by removing the corresponding term from the energy functional [13–15]. Even though an insulating ground state can be obtained in this way, the resulting densities of states (DOS) are in qualitative and quantitative contradiction to photoemission data [4,16], since the binding energy of the Cu $3d$ states is seriously overestimated.

Many-body perturbation theory is the method of choice to calculate electron addition and removal spectra from first principles. The GW approximation [17,18] to the electronic self-energy has been proven to be successful in the prediction of quasiparticle (QP) band gaps and DOS for semiconductors and other so-called weakly correlated systems [19]. Its applicability to strongly correlated systems, such as transition-metal oxides with open d shells, was contested until a few years ago. However, various groups [20–24] have shown that this "failure" of the GW approximation for the magnetically ordered phase of transition-metal oxides is in many cases due to solving the GW QP equation in first-order perturbation theory on top of an LDA Kohn-Sham electronic structure. This perturbational approach is applicable to systems with rather delocalized electrons where LDA and QP wave functions can be assumed to be similar [25]. Whenever the spatial distribution of strongly localized orbitals governs the electronic structure—e.g., in transition-metal oxides—nonlocal screened exchange becomes essential and affects also the one-particle wave functions. It can be accounted for by hybrid functionals [26], local exchange-correlation functionals with an additional nonlocal d-d on-site interaction U [27,28], or static approximations to the GW self-energy (COHSEX) [17] which may serve as advanced starting points [21–24] for a perturbative solution of the QP equation. Alternatively, the QP equation may be solved self-consistently [20].

Wu *et al.* [29] and Heinemann *et al.* [30] employed hybrid functionals and DFT+U to calculate Kohn-Sham band structures and DOS for CuO. However, these works investigate magnetic orderings different from the magnetic ground state. Rocquefelte *et al.* [31] used a PBE0-derived hybrid functional adjusting the admixture of Fock exchange to recover the experimental values for the local magnetic moments and the band gap. Lany [32] proposed to use an empirical attractive potential for both occupied and unoccupied d states to obtain a GW band gap in agreement with experiment.

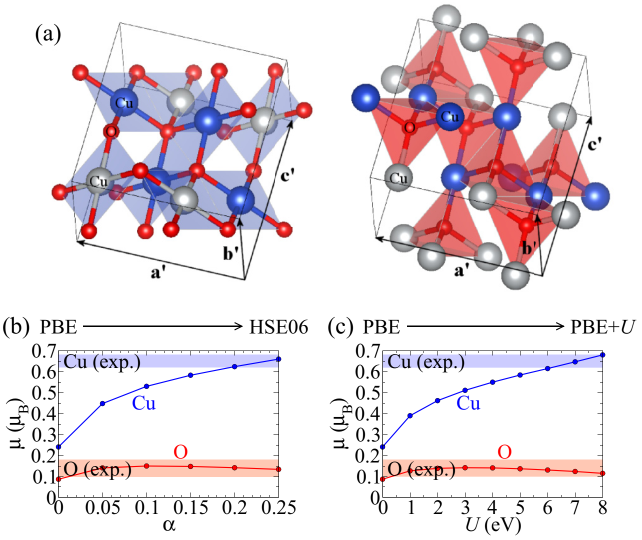

FIG. 1. (Color online) Magnetic ordering and local magnetic moments in CuO. The magnetic unit cell illustrating the ground-state magnetic ordering is displayed in (a). Big white and blue balls represent Cu atoms of opposite spin directions. Small red balls depict O atoms. The approximately square-planar coordination of the Cu atoms (left panel) and the tetrahedral coordination of the O atoms (right panel) are highlighted. The figures have been produced with VESTA [33]. The local magnetic moments μ that occur both at the Cu and O atoms are shown in dependence on the fraction of screened exchange α in the hybrid functional (b) or as a function of the on-site interaction U in the PBE+U approach (c). Experimental values [9] including their error bars are displayed as shaded areas.

Here, we aim to understand the QP excitations in the electron addition and removal spectrum of CuO from first principles. We calculate the band gap and the QP DOS within the GW approximation. The performance of various (partially) self-consistent GW iteration schemes is critically evaluated for this strongly correlated oxide. We find the band gap to be extremely sensitive to the chosen level of approximation. In particular, the dielectric screening employed in the respective GW iteration scheme has a strong impact on the QP gap. The most sophisticated self-consistent solution of the QP equation leads to a huge band-gap overestimation in the case of CuO. Hence, the momentum- and frequency-dependent dielectric function emerges to be a key quantity for describing and understanding the electron addition and removal properties of CuO. Furthermore, we calculate the QP DOS including lifetime and matrix-element effects and compare to direct and inverse photoemission data.

The paper is organized as follows. In Sec. II, the computational details and convergence parameters are summarized. The ground-state properties of CuO and electronic excitations in a DFT framework are briefly discussed in Sec. III. Section IV focuses on a detailed comparison of established GW self-consistency schemes. The band-gap problem and the influence of the electronic screening in the GW self-consistency cycle are addressed. In Sec. V, the resulting QP spectra are compared to experimental photoemission data. Finally, a summary is given and conclusions are drawn in Sec. VI.

II. COMPUTATIONAL DETAILS

Since structural and electronic degrees of freedom are closely entangled in CuO, experimental lattice parameters [8] are used throughout all calculations to avoid spurious effects that may result from deviations between experimental and calculated crystal structures. The experimentally observed antiferromagnetic ordering [9] is described within an eight-formula-unit cell whose lattice vectors are related by $\mathbf{a}' = \mathbf{a} + \mathbf{c}$, $\mathbf{b}' = \mathbf{b}$, and $\mathbf{c}' = -\mathbf{a} + \mathbf{c}$ to the lattice vectors of the conventional face-centered monoclinic chemical unit cell of CuO [see Fig. 1(a)].

DFT and GW calculations are performed using VASP [34–37] with the projector-augmented wave method and a plane-wave cutoff of 450 eV. The Cu $4s$, Cu $3d$, O $2s$, and O $2p$ electrons are considered as valence states. The Brillouin zone (BZ) is sampled with $3 \times 6 \times 3$ Γ-centered $\mathbf{k}$ points. In the hybrid-functional calculations, the HSE06 functional [26,38] with an inverse screening length $\mu = 0.2\ \text{Å}^{-1}$ and a fraction $\alpha = 1/4$ of short-range Fock exchange is used unless otherwise stated. For the DFT+U calculations, we apply the rotationally invariant scheme [28] on top of the PBE exchange-correlation functional [39]. The choice of the value of U is discussed below. The dielectric screening has been calculated for several functionals using VASP and DP [40].

The HSE06 and PBE+U electronic structures serve as starting points for QP calculations in various well-established GW schemes [20,25,37,41]. In all GW calculations, the screening is evaluated at 200 frequency points taking into account plane waves up to a cutoff of 200 eV. Both in the computation of the correlation self-energy and the electronic screening, 384 bands [corresponding to energies up to ∼80 eV above the valence-band maximum (VBM)] are included. To reduce the computational workload and render self-consistent calculations feasible, the BZ sampling is reduced to a mesh of $2 \times 3 \times 2$ $\mathbf{k}$ points in the self-consistent GW calculations which does not have a significant impact on the band gap or the DOS.

Recently, concerns have been raised about the notoriously slow convergence of GW band gaps with the number of empty bands in the self-energy and the plane-wave cutoff in the screening function, especially when the orbital characters of the lowest conduction band and the highest valence band are distinct, e.g., s and p states [43–45]. Even though in CuO the influence should be minor, since both VBM and conduction-band minimum (CBM) feature mixed pd character, the robustness of our results has been tested in this respect. We performed perturbative G_0W_0 calculations with norm-conserving PAW pseudopotentials [46] including only the Γ point but up to 6144 bands (∼640 eV above the VBM) and plane waves up to a cutoff of 500 eV in the screening matrix. The results indicate that the GW band gaps of CuO are converged for the set of parameters specified earlier. Indeed, we observe that both the VBM and CBM shift slowly to lower energies when the numbers of bands is increased for a fixed high cutoff in the screening matrix. Including more plane waves allows for a more accurate description of the localized states as well as their overlap with plane-wave-like high-lying conduction states in the screening matrix. The improved description of the correlation self-energy leads to a lowering in energy of the d-like states in the valence and low conduction

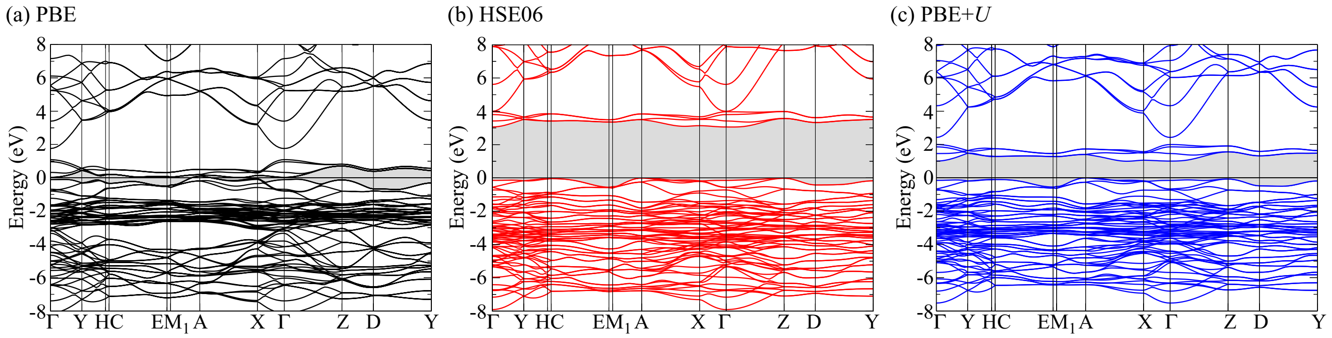
(a) PBE (b) HSE06 (c) PBE+U

FIG. 2. (Color online) Kohn-Sham band structures calculated with the PBE (a), HSE06 (b), and PBE+U ($U = 4$ eV) (c) functionals. The VBM is set to zero and the band gap is highlighted as shaded area. The nomenclature of the high-symmetry points follows Ref. [42].

bands [43,46]. However, in CuO, the difference between the CBM and the VBM, i.e., the band gap, converges much faster thanks to error cancellations that are due to the identical orbital character (see Sec. III A) of the gap-forming states.

III. GROUND STATE AND ELECTRONIC EXCITATIONS WITHIN DFT

Before discussing the excitation spectra, we briefly characterize the ground-state properties of CuO to illustrate the mechanisms that lead to an insulating ground state with magnetic moments as found in experiment.

A. Band structures and DOS

In Fig. 2, the DFT Kohn-Sham band structures of CuO calculated with the PBE, HSE06, and PBE+U (with $U = 4$ eV) functionals are displayed. As has been shown before [11,29], (semi)local density functionals yield a metallic ground state with a closely entangled band complex of O $2p$ and Cu $3d$ states around the Fermi energy [see Fig. 2(a)]. In particular, the highest valence band in the vicinity of the A point of the BZ is unoccupied, i.e., it exhibits a hole pocket. Contrary to the metallic PBE band structure, the HSE06 and PBE+U band structures feature indirect band gaps of 3.1 and 1.1 eV, respectively (see Table I). It is worthwhile to investigate the mechanism of gap formation in more detail.

TABLE I. Indirect (ind.) and direct (dir.) QP band gaps calculated in various flavors of the GW approximation starting from HSE06 and PBE+U ($U = 4$ eV) electronic structures. Furthermore, the band gaps obtained in the self-consistent COHSEX approximation are given. In all cases, the fundamental gap is indirect. If indirect and direct gap happen to have the same value, this is due to rounding on one decimal place.

Gap (eV)		DFT	G_0W_0	G_nW_0	G_nW_n	scG_nW_0	scG_nW_n
HSE06	ind.	3.1	3.5	3.7	3.8	3.7	4.1
	dir.	3.2	3.6	3.8	3.9	3.8	4.2
PBE+U	ind.	1.1	1.7	1.9	2.2	2.2	3.9
	dir.	1.2	1.8	2.0	2.3	2.2	4.1
COHSEX	ind.						4.0
	dir.						4.0

The band gap in DFT is given by the Kohn-Sham band gap and the discontinuity of the exchange-correlation potential upon electron addition and removal [47,48]. Generalized Kohn-Sham functionals that include nonlocal exchange account for a good fraction of the discontinuity already in the generalized Kohn-Sham band gap [49]. The failure of LDA and related functionals to open a gap can be partially traced back to the complete absence of the discontinuity in the exchange-correlation potential. Several orbital-dependent functionals have been proposed to improve the eigenvalue band gaps upon (semi)local Kohn-Sham functionals [49–51]: (i) hybrid functionals with a fraction α of (short-range) exchange, where the inverse of α can be related to the static electronic dielectric constant; (ii) self-interaction-corrected density functionals; (iii) density functionals with an additional on-site interaction U which is inspired by the multiband Hubbard model. In principle, U represents the screened on-site interaction in a solid which can be much smaller than the corresponding atomic value. Even though several schemes for the determination of U exist [51,52], it is often chosen such that it reproduces the experimental value of a specific property of the electronic structure (e.g., the band gap).

In Fig. 3(a), the evolution of the orbital-resolved DOS with increasing fractions of short-range screened exchange α in the HSE hybrid exchange-correlation functional is shown. The parameter α is varied between 0 (PBE) and 0.25 (HSE06). It becomes immediately clear from Fig. 3(a) that the Cu $3d_{xy}$, $3d_{yz}$, $3d_{zx}$, and $3d_{z^2}$ states do not take part in the band-gap formation. These orbitals, which are more or less degenerate in energy and hybridize only weakly with the O $2p$ states, are occupied for both spin directions and lie, rather independent of the value of α, in the energy range between 2 and 4 eV below the VBM. The Cu $3d_{x^2-y^2}$ states, on the other hand, strongly hybridize with the O $2p$ states. In the PBE approach, they form one band complex 4 to 8 eV below the VBM and a second one around the Fermi level. Increasing the fraction of Fock exchange leads to an imbalance between the spin-up and spin-down channels which goes along with the formation of a magnetic moment at the Cu atoms (see below). While the $d_{x^2-y^2}$ orbital becomes unoccupied for one spin direction, thus forming the CBM, the $d_{x^2-y^2}$ state in the opposite spin direction contributes, due to its hybridization with the O $2p$ states, to the bottom as well as the top valence states. The details of the crystal structure and the size of the band gap are intimately linked via this hybridization.

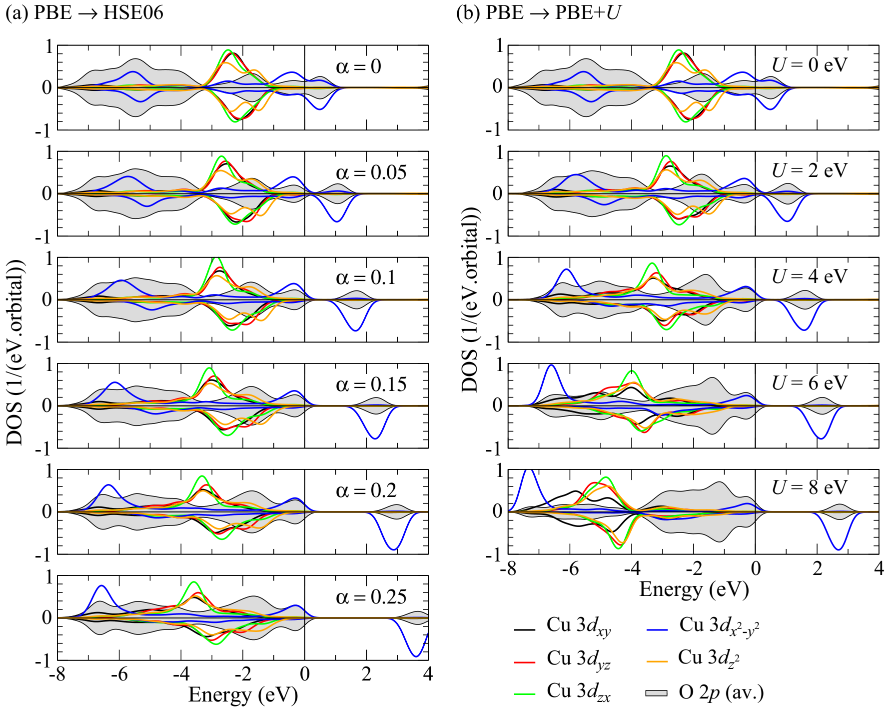

FIG. 3. (Color online) Orbital-projected DOS calculated with the hybrid functional for varying α (a) or with the PBE+U functional for varying U (b). The spin-up (positive values) and spin-down (negative values) contributions of the individual Cu 3d orbitals and the O 2p orbitals are shown. The local coordinate system at the Cu atoms is oriented such that the z axis is perpendicular to the Cu-O coordination square and the x axis parallel to a Cu-O bond. For the O 2p partial DOS, the average contribution per O atom is shown. The VBM is set to zero and all DOS are convoluted with a Gaussian of 0.5 eV full width at half maximum (FWHM).

If, instead of a fraction of short-range Fock exchange, one adds a d-d on-site interaction U to the PBE exchange-correlation functional [see Fig. 3(b)], a very similar behavior of the electronic states is observed for small $U \lesssim 4$ eV. Also in this case, the minority-spin $d_{x^2-y^2}$ state becomes unoccupied, while the majority-spin $d_{x^2-y^2}$ orbital hybridizes with the O 2p states. If, however, the on-site term is increased further, the occupied $d_{x^2-y^2}$ orbital moves to the bottom valence, whereas the O 2p orbitals form the top-valence states. Since the on-site interaction acts on all 3d orbitals, also the inert Cu 3d_{xy}, 3d_{yz}, 3d_{zx}, and 3d_{z^2} states shift to lower energies which does not happen if a hybrid functional is employed.

The band gap is sensitive to the details of the antiferromagnetic ordering. Several previous studies [29,30] did not investigate the experimentally observed ground-state magnetic ordering but other antiferromagnetic structures. Consequently, they find band gaps that are significantly lower. For instance, in Ref. [30], an indirect HSE06 band gap of 2.7 eV has been reported. Reproducing the HSE06 calculation with the magnetic ordering used in Ref. [30], we obtain an indirect gap of 2.5 eV significantly lower than the 3.1 eV we find for the ground-state magnetic ordering.

B. Magnetic moments

The calculated magnetic moments at the Cu and O atoms are shown in Figs. 1(b) and 1(c) in comparison to data from neutron-diffraction experiments [9]. The screening parameter α and the on-site interaction U have been varied in these plots to illustrate their influence on the value of the local magnetic moment. Best agreement with experiment is obtained for $\alpha = 0.25$ and $U \sim 7$ eV. However, modelling the complex many-body interaction by tuning a single scalar parameter cannot capture all effects of the electronic self-energy. The optimal choice of the respective parameter depends on the quantity that is calculated. In particular, it may be different for ground-state (lattice constants, magnetic moments) and excited-state properties (band structures, densities of states). For instance, the frequency dependence of the U parameter has been illustrated by mapping the full dynamical screened Coulomb interaction to local orbitals [52]. For reasons explained in Sec. IV B, we will later on choose the electronic structure computed with $U = 4$ eV as one of the starting points for the calculation of excitation properties. Here, we give results for both values $U = 4$ eV and $U = 7$ eV.

A peculiarity of CuO is the occurrence of a local magnetic moment not only at the transition-metal atoms, but also at the O atoms which is a consequence of the interplay between the complex magnetic ordering and the crystal structure: each O atom is embedded in a tetrahedral environment of four Cu atoms whereof one exhibits a magnetic moment pointing in the direction opposite to the magnetic moments of the three other Cu atoms [see Fig. 1(a)], which leads to a magnetic polarization of the electrons in the vicinity of the O atom. At the O atoms, we find local magnetic moments of $0.13\mu_B$ (HSE06), $0.14\mu_B$ (PBE+U, $U = 4$ eV), and $0.12\mu_B$ (PBE+U, $U = 7$ eV) that are in line with experiment ($0.14 \pm 0.04\mu_B$, Ref. [9]) and previous calculations [15,31]. The Cu magnetic moment amounts to $0.66\mu_B$ (HSE06), $0.55\mu_B$ (PBE+U, $U = 4$ eV), and $0.65\mu_B$ (PBE+U, $U = 7$ eV), which agrees well with experimental values of $0.65 \pm 0.03\mu_B$ [9] and $0.69 \pm 0.05\mu_B$ [10].

IV. ELECTRONIC EXCITATIONS WITHIN THE *GW* APPROACH

Band gaps calculated from Kohn-Sham electronic structures are not directly comparable to experimental gaps. The Kohn-Sham gap differs from the QP gap by the contribution arising from the derivative discontinuity of the exchange-correlation energy which accounts for electron addition and removal [47,48]. Generalized Kohn-Sham functionals, such as the HSE06 hybrid functional, take this term partially into account already in the eigenvalue gap [49] but are still suffering from the fact that the exact exchange-correlation potential is unknown. Green's function methods, such as the GW approach, on the other hand, include the electron addition and removal aspect by construction.

The GW self-energy $\Sigma_{GW}(12) = i\hbar G(12)W(12)$ is the product of the one-particle Green's function $G(12)$ and the screened Coulomb interaction $W(12) = \int d3\varepsilon^{-1}(13)v(3-2)$, with the inverse dielectric function $\varepsilon^{-1}(12)$ and the bare Coulomb interaction $v(1-2) = \frac{1}{4\pi\varepsilon_0}\frac{e^2}{|\mathbf{r}_1-\mathbf{r}_2|}\delta(t_1-t_2)$. In these expressions, numbers are used as shorthand for the set of space, spin, and time coordinates, i.e., $1 \equiv \mathbf{r}_1, s_1, t_1$. Usually, the screened interaction is calculated in the random-phase approximation (RPA), i.e., neglecting the electron-hole interaction [17,18].

QP states $|\psi_i\rangle$ can be obtained by solving the QP equation [18]

$$[T + V + V_{\mathrm{H}} + \Sigma_{GW}(\varepsilon_i)]|\psi_i\rangle = \varepsilon_i|\psi_i\rangle \tag{1}$$

self-consistently. Here, T denotes the kinetic energy, V the external potential, V_{H} the Hartree potential of the electrons, and $\Sigma_{GW}(\omega)$ the GW self-energy in frequency space, which has to be taken at the energy of the QP excitation ε_i. Usually, the QP equation is solved starting from Kohn-Sham eigenvalues $\varepsilon_i^{(0)}$ and wave functions $|\varphi_i\rangle$ either in first-order perturbation theory or applying (partially) self-consistent iteration schemes.

Assuming that Kohn-Sham wave functions $|\varphi_i\rangle$ and QP wave functions $|\psi_i\rangle$ are identical and, hence, that both the QP Green's function and the difference between self-energy and exchange-correlation potential are approximately diagonal in these wave functions, the QP equation reduces to

$$\varepsilon_i = \mathrm{Re}\langle\varphi_i|[T + V + V_{\mathrm{H}} + \Sigma_{GW}(\varepsilon_i)]|\varphi_i\rangle. \tag{2}$$

Keeping the wave functions fixed and iterating only over the eigenvalues [25,37], the QP energies in the $(n+1)$th iteration step are then given by

$$\varepsilon_i^{(n+1)} = \varepsilon_i^{(n)} + Z_i^{(n)} \times \left(\mathrm{Re}\langle\varphi_i|\left[T + V + V_{\mathrm{H}} + \Sigma_{GW}^{(n)}\left(\varepsilon_i^{(n)}\right)\right]|\varphi_i\rangle - \varepsilon_i^{(n)}\right), \tag{3}$$

with the QP renormalization factor

$$Z_i^{(n)} = \left(1 - \frac{\partial\ \mathrm{Re}\langle\varphi_i|\Sigma_{GW}^{(n)}(\omega)|\varphi_i\rangle}{\partial\omega}\bigg|_{\hbar\omega=\varepsilon_i^{(n)}}\right)^{-1}. \tag{4}$$

In this expression, the self-energy has been linearized around the QP pole. The matrix elements of the GW self-energy $\langle\varphi_i|\Sigma_{GW}^{(n)}(\omega)|\varphi_i\rangle$ are recalculated in each step using the Kohn-Sham wave functions and the QP eigenvalues obtained in the previous iteration. Depending on whether the energy eigenvalues that enter Σ_{GW} are updated in G only or both in G and W, the iteration scheme is called G_nW_0 or G_nW_n, respectively. In the simplest approach, only one iteration is performed and the energy eigenvalues are corrected in first-order perturbation theory (G_0W_0).

Alternatively, one can try to solve Eq. (1) directly which allows one to obtain also QP wave functions. However, the frequency-dependent self-energy operator $\Sigma_{GW}(\omega)$ renders this equation non-Hermitian and nonlinear which results in QP excitations with finite lifetime and renormalized intensity. Several procedures known as QP self-consistent GW have been proposed to construct an eigenvalue problem with a Hermitian Hamiltonian from Eq. (1) [20,41,53,54]. The resulting QP eigenvalues differ only marginally between these procedures [41]. In all of these GW schemes, the Green's function retains its noninteracting form and lifetime effects are neglected. Here, we follow the approach presented in Ref. [41]. We refer to it as scG_nW_0 or scG_nW_n depending on whether G only or both G and W are recalculated with the new set of eigenstates in each self-consistency step. The numerical implementation of this scheme yields band gaps in good agreement with experiment for weakly correlated materials. For transition-metal oxides and f-electron systems, however, d-d or f-f gaps are systematically overestimated [20,53,55]. It has been proposed to scale the self-energy with a prefactor of 0.8 in order to mimic the effects of vertex corrections empirically [55]. For instance, the rescaling of the self-energy compensates for the systematically underestimated dielectric constants in the scG_nW_n iteration scheme. Shishkin *et al.* [41] suggested to either include an exchange-correlation kernel in W to account for the excitonic effects or to keep W fixed on the DFT RPA level.

All of these flavors of GW self-consistency have been applied to a large variety of materials in the past. Here, we investigate how the different approaches perform for the DOS and band gap in the case of CuO. We analyze and discuss shortcomings of the methods that are expected to be characteristic for materials similar to CuO.

A. Perturbative G_0W_0

In Sec. III, it has been shown that both hybrid functionals and PBE+U yield insulating electronic structures for CuO. Here, we consider these electronic structures as possible starting points for GW calculations in the perturbative G_0W_0 approach.

In Fig. 4(a), the DOS calculated within the G_0W_0 approximation are shown in comparison to the subjacent hybrid-functional calculation for various values of the screening parameter α. We notice that the general line shape of the DOS barely changes if G_0W_0 corrections are added. This finding holds for the whole range of investigated parameters α. Only the band gap opens significantly—even for values of α where the hybrid functional already overestimates the experimental gap [cf. Fig. 4(c)]. Moreover, the band gap increases linearly with increasing screening parameter α.

On the one hand, this illustrates the strong starting-point dependence of non-self-consistent GW calculations. On the other hand, it yields valuable insight into the mechanisms that govern the band-gap formation in CuO within the GW framework, i.e., a picture of QPs screened by electron-hole excitations. It indicates that the hybrid-functional ansatz already captures most of the many-body effects that govern the energetic ordering of the states but fails in a similar way as the subsequent G_0W_0 calculation to predict the band gap.

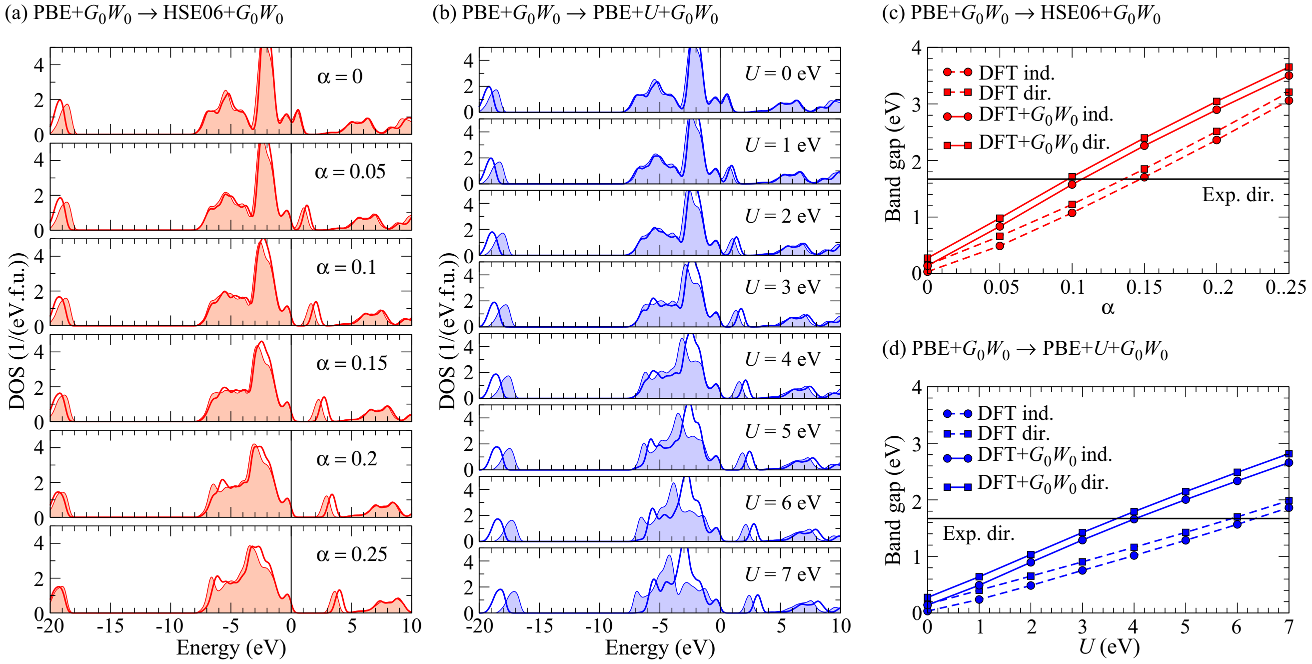

FIG. 4. (Color online) DOS as well as indirect (ind.) and direct (dir.) band gaps calculated in the G_0W_0 one-shot approach on top of the hybrid functional for varying α [(a),(c)] and the PBE+U functional for varying U [(b),(d)]. The respective DFT DOS is shown as shaded area, whereas the G_0W_0 DOS is indicated by a thick solid line. The VBM is set to zero. A Gaussian broadening of 0.5 eV is applied to the DOS. In (c) and (d), the experimental direct band gap at zero temperature [12] (cf. Table II), represented by a black horizontal line, is given for reference.

In particular, there does not seem to be a mechanism in G_0W_0 that compensates a band-gap overestimation in the subjacent hybrid-functional calculation.

Indeed, the HSE hybrid functional can be seen as a static approximation to the GW self-energy with the parameter α as inverse electronic static dielectric constant $1/\varepsilon_\infty$. The range-separation parameter which cuts down the Fock exchange for large distances acts as a screening length. Thus the HSE06 hybrid functional mimics already the important static screened-exchange contribution to the GW self-energy. This explains why setting $\alpha = 1/4$ (HSE06) yields good band gaps for intermediate-gap semiconductors with dielectric constants in the range of $\sim 2\ldots 6$ (see compilations in Refs. [56–58]) and why it is less accurate for strongly polarizable materials like Si with $\varepsilon_\infty = 11.94$ [59]. For CuO, a band gap of 1.42 eV was obtained by setting $\alpha = 0.15$ in a hybrid functional with infinite screening length (PBE0-derived functional) [31]. For $\alpha = 0.15$ and an inverse screening length of $\mu = 0.2$ Å^{-1}, we obtain an indirect gap of 1.7 eV and a direct gap of 1.9 eV (see Fig. 4). This observation is in line with the interpretation of α as inverse dielectric constant which amounts to $\varepsilon_\infty = 6.2\ldots 6.6$ in CuO [60–62].

In Fig. 4(b), we choose, instead of a hybrid functional, a PBE+U electronic structure as starting point for the G_0W_0 calculation. We find that, in particular for large values of U, the QP shifts are significantly bigger for some states compared to the QP shifts obtained for the hybrid functional starting point. For instance, the G_0W_0 corrections shift the O 2s states in the vicinity of -19 eV to significantly higher binding energies. G_0W_0 also tries to correct back the energetic position of the occupied Cu 3d states that are shifted to too high binding energies by large values of U in PBE+U. All in all, this indicates that PBE+U, in general, is a less good approximation to the GW self-energy which is intuitively clear, since it mostly affects the d states and does not provide an advanced description of exchange and correlation for the s and p states.

As expected, we find the PBE+U band gaps to increase linearly with U illustrating the d-d character of the highest valence and lowest conduction states [cf. Fig. 4(d)]. However, the G_0W_0 band gap increases with an even higher slope in dependence on U. For large U [e.g., $U = 7$ eV in Fig. 4(d)], where the gap is already overestimated, the band-gap opening due to G_0W_0 QP shifts is largest demonstrating the sensitivity of the results on the input electronic structure.

B. Eigenvalue self-consistent GW

Since self-consistent GW calculations are numerically very demanding, we focus on the comparison between two starting electronic structures from now on: (i) HSE06 ($\alpha = 1/4$) and (ii) PBE+U with $U = 4$ eV. These two starting points feature the peculiarity that their (state-projected) DOS are basically identical (see Fig. 3) except for strongly deviating band gaps which amount to 3.1 eV in the case of HSE06 and 1.1 eV for PBE+U (cf. Table I). In particular, the HSE06 band gap is almost twice as large as the experimental gap (see Table II), which is unusual for a 3d transition-metal monoxide [23,64]. A comparison between these two starting points may thus be helpful to understand the origin of the GW band-gap overestimation in CuO.

As we have seen in Sec. III, the energetic position of the Cu 3$d_{x^2-y^2}$ peaks and, in particular, the size of the band gap strongly depend on the choice of the exchange-correlation functional which cannot be cured by G_0W_0 QP corrections.

TABLE II. Available indirect (ind.) and direct (dir.) experimental gap values and their temperature dependence.

Gap (eV)	300 K	7 K	0 K
ind.	1.35 ± 0.02[a] 1.4 ± 0.3[b]		
dir.	1.34[c]	1.60[d]	1.67[e]

[a] Reference [3]; electrochemical determination of the photocurrent in p-type CuO.

[b] Reference [4]; x-ray photoemission and bremsstrahlung-isochromat spectroscopy.

[c] Reference [12]; reflectance and transmittance.

[d] Reference [63]; optical absorption, 7 K.

[e] Reference [12]; reflectance and transmittance, extrapolated to 0 K removing zero-point motion.

This underlines the need for a starting-point independent approach. QP calculations that keep the wave functions fixed but iterate the one-particle eigenvalues constitute a first step towards self-consistency.

In Table I, the indirect and direct QP band gaps of CuO are compiled for various self-consistent GW schemes. It is evident that, keeping the wave functions fixed, the band gap changes only very little compared to a G_0W_0 calculation. Convergence of the band gap is obtained after a few iteration steps (see Fig. 5). This holds likewise for the G_nW_0 and the G_nW_n iteration scheme and is independent of the starting point. However, the resulting values for the band gaps are strongly starting-point dependent. The PBE+U+G_nW_0/G_nW_n band gaps overestimate the experimental value only slightly, whereas the HSE06+G_nW_0/G_nW_n gaps are by more than a factor of 2 too large. Hence it can be concluded that wave-function self-consistency is highly important in CuO and, concomitantly, that QP and Kohn-Sham wave functions differ significantly in this material for the chosen generalized Kohn-Sham schemes.

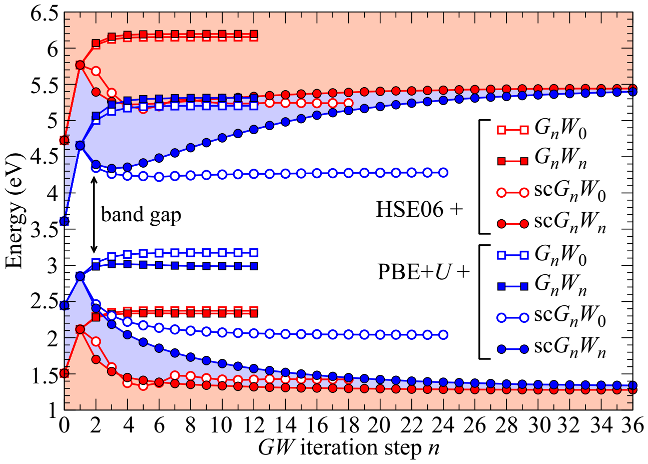

FIG. 5. (Color online) Convergence of the highest valence band and lowest conduction band at Γ with the number of iteration steps n in various flavors of the GW approximation. Results are given for HSE06 and PBE+U starting electronic structures. The zeroth iteration step corresponds to the DFT eigenvalues.

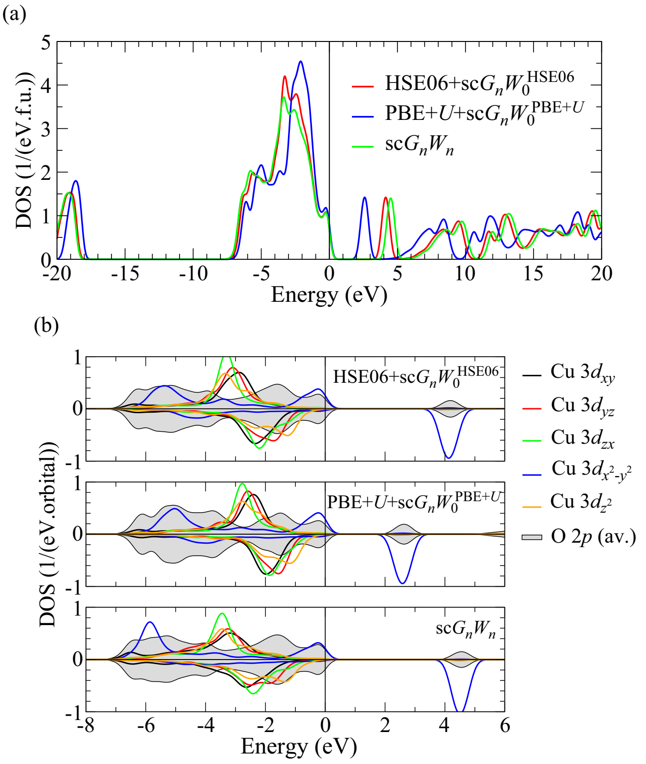

FIG. 6. (Color online) Full (a) and orbital-resolved (b) DOS of CuO for various self-consistent GW schemes. The screened Coulomb interaction W is either fixed (W_0) to the subjacent DFT starting point (HSE06 and PBE+U) or iterated to self-consistency (W_n). In the latter case, the resulting DOS is independent of the starting point. The DOS are broadened with a Gaussian of 0.5 eV (FWHM) and the VBM is set to zero.

C. Quasiparticle self-consistent GW

A self-consistent solution of the Hermitianized and linearized QP equation (1) should be essentially independent of the starting electronic structure. Indeed, we find that applying the scG_nW_n scheme to both starting points the electronic QP structures converge—even though slowly—to the same solution. This is illustrated for the VBM, the CBM, and, hence, the band gap in Fig. 5. The remaining deviations in the scG_nW_n gaps for the two starting points in Table I are due to the finite number of iteration steps. In Fig. 6, the resulting DOS as well as the orbital-projected DOS are plotted only once, since the curves for the two starting points are indistinguishable. We do not find the starting-point dependence that Liao *et al.* [65] observed for Fe_2O_3. However, we want to emphasize that convergence is hard to achieve and that in self-consistency cycles errors may accumulate.

Despite the line shape of the DOS being still very similar to the DFT results, the resulting band gap of more than 4 eV overestimates the experimental value by a factor of 2.5 (see Tables I and II). Even though a slight band-gap overestimation seems to be inherent to this approach, the discrepancy between scG_nW_n band gap and experimental band gap is striking for CuO.

D. Influence of the screening

The dramatic gap overestimation for CuO within the scG_nW_n scheme asks for a more detailed understanding. Let us assume for the moment that $\Sigma(12) = i\hbar G(12)W(12)$ is a good approximation for the full self-energy which reads $\Sigma(12) = -i\hbar \int d(34)G(13)W(14)\Gamma(324)$, with Γ being the vertex function that describes, for instance, electron-hole interactions in the screening or particle-particle interactions in the self-energy [18]. This means that, in the GW approximation, vertex corrections in the self-energy and thus contributions that are of second or higher order in the screened interaction (e.g., T-matrix diagrams) are neglected. However, the vertex function occurs also in the dielectric function $\varepsilon(12) = \delta(1-2) - i\hbar \int d(345)v(1-3)G(35)G(43)\Gamma(542)$ whose inverse governs the dynamically screened Coulomb interaction.

In the original formulation of Hedin's equations [17,18], the dielectric screening that enters the GW self-energy has to be evaluated in RPA, $\varepsilon(12) = \delta(1-2) + i\hbar \int d3v(1-3)G(32)G(23)$. Indeed, it has been shown that a screened Coulomb interaction calculated in RPA with independent-particle Green's functions constructed from a Kohn-Sham electronic structure yields results that are in good agreement with experiment for many semiconductors (see, e.g., Ref. [19]). This is due to an error cancellation between the neglected QP corrections in the Green's functions and the omission of the electron-hole attraction, i.e., excitonic effects.

The scG_nW_n scheme, on the other hand, updates wave functions and eigenvalues in W which corresponds to an inclusion of QP shifts, whereas the electron-hole interaction is still omitted. This leads to a systematic underestimation of the dielectric screening and, consequently, to too high band gaps [41]. The same effect can be observed already in the self-consistent static COHSEX (Coulomb hole plus screened exchange) approximation [17] to the GW self-energy. Even neglecting completely the frequency dependence of the screening throughout the self-consistency cycle, the strong band-gap overestimation can be reproduced. Self-consistent COHSEX yields a gap of 4.0 eV comparable to the scG_nW_n gap (cf. Table I).

In Fig. 7, the evolution of the macroscopic electronic static dielectric constant ε_∞ of CuO with the number of iteration steps in the G_nW_n and scG_nW_n schemes is shown. The respective values of ε_∞ for the iteration schemes where W is not subject to changes (G_nW_0 and scG_nW_0) correspond to the zeroth iteration. The dielectric constant of 10.3 in PBE+U+G_0W_0 (iteration step $n = 0$) is by far higher than the experimental values of 6.45 [61], 6.2 [60], and 6.6 [62]. The G_nW_n iteration scheme reduces ε_∞ to 7.6, whereas it decreases even well below the experimental value in the scG_nW_n approach. For the HSE06 starting point, on the other hand, changes are minor, since already in the G_0W_0 step $\varepsilon_\infty = 4.7$, which is further reduced to 4.5 (G_nW_n) or 4.1 (scG_nW_n). These values underestimate the experimental screening constant which is in line with the observed band-gap overestimation.

Little is known about the wave-vector and frequency dependence of the dielectric screening from experiment. Recently, the low-energy d-d excitations have been measured for high momentum transfers [66,67]. The only available data in a wide frequency range is the loss function $-\mathrm{Im}\,\varepsilon^{-1}(\mathbf{q},\omega)$ for vanishing momentum transfer $\mathbf{q} = 0$ (see Fig. 8). In Fig. 8, loss functions calculated in the RPA with the HSE06, PBE+U, and scG_nW_n electronic structures are compared to momentum-integrated electron-energy loss spectra [68] and inverted spectroscopic ellipsometry data [61]. In the literature, loss functions are most often calculated from electronic

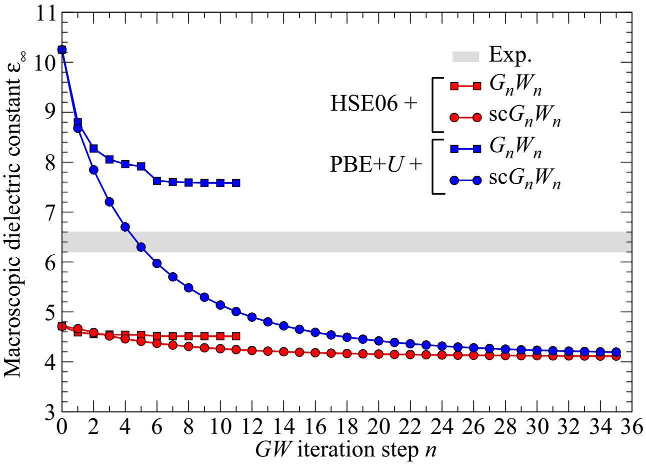

FIG. 7. (Color online) Convergence of the macroscopic electronic static dielectric constant ε_∞ (averaged over directions) with the number of iteration steps n in various flavors of the GW approximation. Results are given for HSE06 and PBE+U starting electronic structures. The zeroth iteration step corresponds to the macroscopic dielectric constant ε_∞ deduced from W_0. The range of available experimental values as the high-frequency limit of infrared [60,62] and the low-frequency limit of optical [61] spectroscopy is given as shaded area.

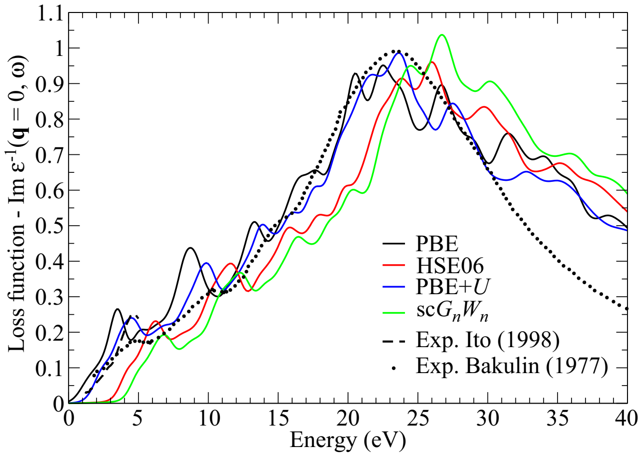

FIG. 8. (Color online) Frequency-dependent loss function of CuO for vanishing momentum transfer $\mathbf{q} = 0$ averaged over Cartesian directions. The loss function $-\mathrm{Im}\,\varepsilon^{-1}(\mathbf{q} = 0,\omega)$ is calculated in RPA using the DFT electronic structures of the two GW starting points (HSE06 and PBE+U) and the self-consistent scG_nW_n QP electronic structure. The direction-averaged loss function is compared to experimental data from spectroscopic ellipsometry [61] and electron-energy loss [68]. For completeness, the loss function calculated in RPA using the metallic PBE electronic structure is also given.

structures that have been obtained with a (semi)local density functional. For this reason, we provide also the loss function computed from PBE wave functions and eigenvalues for comparison, keeping in mind that PBE predicts CuO to be a metal.

The experimental loss data shown in Fig. 8 exhibit a broad plasmon peak around 23 eV and some fine structure at lower energies. The PBE, HSE06, PBE+U, and scG_nW_n calculations all recover the general line shape of the experimental loss spectrum; only the absolute peak positions are subject to a rigid energy shift that depends on the band gap of the respective electronic structure. The discrepancies between measured and calculated spectra at energies above the main plasmon are attributed to the $\mathbf{q}$ integration in the experimental loss spectrum which is due to its limited momentum resolution (cf., e.g., Ref. [69]). Both the main plasmon peak and the fine structure in the loss spectrum at low energies, in particular the pronounced peaks near 5 and 10 eV, are best described within the PBE+U approach.

E. Self-consistent *GW* with fixed screening

1. Fixed RPA electronic screening

The GW formalism links the dielectric screening, that is experimentally accessible through loss experiments, to quantities like the photoemission band gap or the QP DOS. Here, we investigate how changes in the screening affect the QP energies and the band gap. In the previous section, it has been shown that the PBE+U RPA screening compares excellently to experiment for small $\mathbf{q}$, i.e., in the long range which is usually dominant in the GW approach. In this spirit, we start from the PBE+U electronic structure and solve the QP equation (1) self-consistently without changing the matrix elements of W throughout the iteration (PBE+U+sc$G_nW_0^{\mathrm{PBE}+U}$). For the purpose of comparison, the same procedure is carried out for the HSE06 starting point.

The resulting band gaps can be found in Table I and Fig. 5. Of course, the result cannot be starting-point independent anymore. Using the HSE06 screening, we obtain an indirect band gap of 3.7 eV only marginally smaller than in the scG_nW_n approach. This is not unexpected considering the blueshift of all loss peaks in the HSE06 dielectric function (see Fig. 8). If, however, the PBE+U screening—which agrees much better with experiment for the available $\mathbf{q} = 0$ spectrum (cf. Fig. 8)—is used, we find a band gap of 2.2 eV which is already much closer to experiment, though still a little too high.

2. Estimate of polaronic screening contributions

The remaining difference between experimental and theoretical band gap might well be due to details of the screening, but it also raises the question whether other physical effects such as polarons contribute to the discrepancy. Taking into account polaronic excitations affects the band gap in two ways. (i) At nonzero temperatures, phonon states above the ground state will be occupied resulting in smaller band gaps. Thus the calculated band gaps have to be compared to experimental gaps at 0 K. (ii) Polarons may be excited during the photoemission experiment (even at zero temperature) and contribute to the screening of the Coulomb interaction which leads to a band-gap shrinkage.

In Table II, we compare the available experimental gap values for different temperatures. High-resolution optical data have been measured between 10 and 300 K and extrapolated to 0 K removing also the zero-point motion [12]. The resulting direct gap is found to be 1.67 eV at 0 K. An absorption study [63] conducted at 7 K reported the direct gap to be 1.60 eV (including zero-point motion) which is consistent with the other experiment. The indirect band gap, however, has been measured only at room temperature and was found to be 1.35 ± 0.02 eV [3] or 1.4 ± 0.3 eV [4]. Assuming that the gap-forming bands are essentially flat due to their d character, this is consistent with the room-temperature direct gap of 1.34 eV reported in Ref. [12].

Botti *et al.* [70] have shown recently that polaronic screening may reduce GW band gaps by about 15% in strongly polarizable materials like MgO. However, it is unlikely that polaronic screening can explain our results. The biggest gap renormalization due to polaronic screening is expected for materials with a small electronic static screening constant ε_∞ and a big static screening constant ε_0 [since the polaron coupling constant is proportional to $(1/\varepsilon_\infty - 1/\varepsilon_0)$] as well as large longitudinal optical phonon frequencies ω_{LO} [71,72]. For instance, in MgO, the dielectric constants amount to $\varepsilon_\infty = 2.94$ and $\varepsilon_0 = 9.83$, while ω_{LO} is 89 meV [73].

In CuO, the electronic static dielectric constant amounts to $\varepsilon_\infty = 6.6$ (averaged over directions, Ref. [62]), whereas the static dielectric screening constant including lattice polarizability is $\varepsilon_0 = 11.1$ (averaged over directions, derived from the fit parameters given in Ref. [62]). The longitudinal optical phonon frequencies lie in the energy range between 19 and 78 meV [62]. From these values, one can expect polaronic screening contributions in CuO to be lower than in MgO. Taking into account these considerations, the overestimation of the experimental band gap of 2.2 eV by about 30 % in the PBE+U+sc$G_nW_0^{\mathrm{PBE}+U}$ approach seems to be too large to be explained solely by polaronic effects.

3. Towards more realistic screening

We noticed in the previous section that the macroscopic dielectric constant ε_∞ calculated in RPA with the PBE+U functional is significantly higher than the experimental value, despite the fact that the peak positions and relative intensities of the PBE+U loss function match well the available experimental data. In principle, an overestimated dielectric constant should go along with an underestimation of the band gap—the opposite of what we find. This observation may be interpreted as a hint that details of the dielectric function must be crucial for the screening mechanisms in CuO. For instance, short-range contributions to the screening might be particularly important for the localized d electrons.

It is, hence, not clear whether the failure of the GW formalism to predict the band gap of CuO is due to a deficient description of the screening function or whether higher-order terms, i.e., vertex corrections, have to be included in the self-energy. However, before resorting to more complicated theories demanding even more involved calculations, it would be desirable to obtain state-of-the-art experimental data for the

TABLE III. Local magnetic moments μ at the Cu and O atoms calculated for flavors of the GW approximation where the QP wave functions change with respect to the HSE06 and PBE+U ($U = 4$ eV) starting electronic structures. Furthermore, the magnetic moments in the self-consistent COHSEX approximation are given.

μ (μ_B)		DFT	scG_nW_0	scG_nW_n
HSE06	Cu	0.66	0.69	0.70
	O	0.13	0.12	0.12
PBE+U	Cu	0.55	0.64	0.70
	O	0.14	0.13	0.12
COHSEX	Cu			0.67
	O			0.12

wave-vector- and frequency-dependent dielectric function in a wide spectral range in order to have a better comparison between theory and experiment. This will allow one to understand the mechanisms that reign the screening in CuO.

4. Local magnetic moments

In Table III, the local magnetic moments at the Cu and O atoms are listed for the DFT starting electronic structures and those flavors of the GW approximation which allow for a change in the wave functions and, concomitantly, the local magnetic moments. While the magnetic moments of the O atoms are almost independent of the approach, the local moments at the Cu atoms increase with increasing band gap. We attribute this to a stronger separation between the spin-up and spin-down channels of the Cu $3d_{x^2-y^2}$ orbital with increasing band gap [see also Fig. 6(b)]. However, all of the GW results are within the error bars of the experimentally determined magnetic moments which amount to $0.65 \pm 0.03\mu_B$ [9] and $0.69 \pm 0.05\mu_B$ [10].

V. COMPARISON TO PHOTOEMISSION SPECTRA

The band gap is just one characteristic of the electronic excitation spectrum of an insulator which contains too little information to draw conclusions about the electronic structure as a whole. Thus, we now focus on the comparison between the calculated QP DOS and available photoemission spectra. In Fig. 9(a), the QP electronic structures obtained within the HSE06+sc$G_nW_0^{\text{HSE06}}$, PBE+U+sc$G_nW_0^{\text{PBE}+U}$, and scG_nW_n schemes are compared to x-ray photoemission spectroscopy [4,16] (XPS) and bremsstrahlung-isochromat spectroscopy [4] (BIS) data. To this end, we go beyond the assumption of a noninteracting shape for the QP Green's function and introduce instead the renormalized QP Green's function

$$G(\omega) = \sum_i Z_i \frac{|\psi_i\rangle\langle\psi_i|}{\hbar\omega - \varepsilon_i - i\hbar/\tau_i \operatorname{sgn}(\mu - \varepsilon_i)} \tag{5}$$

that is weighted by the QP renormalization factor Z_i and contains the intrinsic widths of the QP peaks, which are the inverses of the QP lifetimes

$$\tau_i = \frac{\hbar}{Z_i |\langle\psi_i| \operatorname{Im} \Sigma_{GW}(\varepsilon_i)|\psi_i\rangle|}. \tag{6}$$

The chemical potential is denoted by μ. In this approximation, the peak widths are given by the product of the QP renormalization factor Z_i and the imaginary part of the self-energy at the QP excitation. Consequently, the sum over δ functions in the QP DOS is replaced by a sum over non-normalized Lorentzians with widths corresponding to the intrinsic QP lifetime of each excitation,

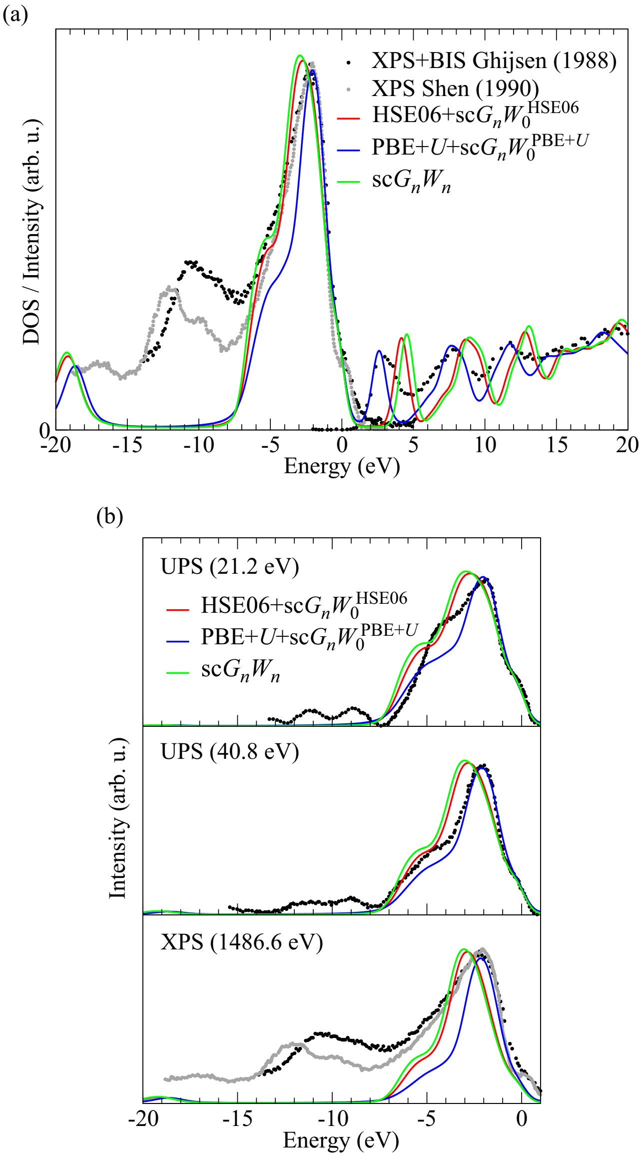

FIG. 9. (Color online) QP DOS of CuO compared to data from UPS, XPS, and BIS experiments. (a) QP DOS including intrinsic QP lifetimes are plotted together with XPS [4,16] (taken at an incident photon energy of 1486.6 eV) and BIS [4] data. A Gaussian broadening of 1.0 eV (FWHM) is applied to the calculated spectra to mimic temperature and instrumental broadening effects. In (b), the QP DOS are additionally weighted with the photoionization cross sections [74] of each orbital to facilitate comparison with photoemission spectra for various incident photon energies. Experimental data from Ghijsen *et al.* [4] and Shen *et al.* [16] are shown as black and gray dots.

$$\text{DOS}(\hbar\omega) = \sum_i \frac{Z_i}{\pi} \frac{\hbar/\tau_i}{(\hbar\omega - \varepsilon_i)^2 + (\hbar/\tau_i)^2}. \tag{7}$$

TABLE IV. QP renormalization factors Z for the highest valence (Γ_{VBM}) and lowest conduction band (Γ_{CBM}) at Γ calculated in various flavors of the GW approximation starting from HSE06 and PBE+U ($U = 4$ eV) electronic structures.

Z		G_0W_0	G_nW_0	G_nW_n	scG_nW_0	scG_nW_n
HSE06	Γ_{VBM}	0.74	0.73	0.74	0.73	0.76
	Γ_{CBM}	0.71	0.70	0.72	0.70	0.73
PBE+U	Γ_{VBM}	0.65	0.64	0.69	0.64	0.75
	Γ_{CBM}	0.62	0.62	0.67	0.60	0.73

Further, the DOS are convoluted with a Gaussian of 1.0 eV (FWHM) to take into account instrumental and temperature broadening effects.

In Table IV, the QP renormalization factors are given for the highest valence and lowest conduction band at the Γ point. The Z factors essentially follow the trend of the band gaps in the electronic structure used to calculate the screened Coulomb interaction. A high band gap in W shifts the onset of the imaginary part of the self-energy away from the QP poles, thus resulting in a more pronounced QP peak. Consequently, the QP renormalization factors are closest to one for the scG_nW_n scheme and depend strongly on the W employed, whereas they are basically insusceptible to self-consistency in G. A comparison between Figs. 6(a) and 9(a) shows that in particular the valence Cu 3d peak which is more pronounced in the PBE+U+sc$G_nW_0^{\mathrm{PBE}+U}$ approach is reduced to the same intensity as the equivalent peak in the HSE06+sc$G_nW_0^{\mathrm{HSE06}}$ or scG_nW_n approaches due to the smaller Z factors in the former GW scheme.

Comparing theory and experiment in Fig. 9(a), we find very good agreement for the peak positions, widths, and relative intensities in the range of QP valence excitations between −8 and 0 eV. Differences between the theoretical approaches in the valence-band region are too small to rule out one or more of the theoretical schemes. However, the PBE+U+sc$G_nW_0^{\mathrm{PBE}+U}$ approach seems to perform slightly better concerning the general line shape. The satellite structures that occur in the vicinity of −10 eV can, by definition, not be captured in our QP framework. The O 2s states around −19 eV are strongly broadened by lifetime effects.

The conduction-band region is dominated by a distinct peak at low energies that stems from the empty Cu 3$d_{x^2-y^2}$ band in the minority spin channel. All three theoretical approaches agree very well with the experimental BIS data regarding peak widths and relative intensities. Only the band gap differs significantly (see discussion in Sec. IV). The PBE+U+sc$G_nW_0^{\mathrm{PBE}+U}$ iteration scheme actually yields also peak positions that match the experimental inverse-photoemission peaks. Notably, the edge of the first conduction-band peak agrees well with the first BIS peak, even though the gap of 1.4 ± 0.3 eV deduced from experiment in Ref. [4] deviates from our gap value of 2.2 eV. It cannot be excluded that, apart from temperature effects, also different procedures to determine the gap are, to some extent, responsible for the discrepancy.

Photoemission spectra for CuO have been measured at various incident photon energies [see Fig. 9(b)]. This allows us to extract information about the orbital character of the valence states, since the photoionization cross sections of different orbitals vary with the incident photon energy. At high photon energies, primarily d states are probed, whereas at lower photon energies, in the UV, p and d states are excited with roughly the same probabilities. In Fig. 9(b), the calculated QP DOS weighted by photoionization cross sections [74] are compared to photoemission data taken at different energies. With increasing photon energy, the shoulders found around −5 eV and near the VBM in the experimental data decrease in intensity relative to the main photoemission peak. This behavior is due to the O 2p orbital contribution to these peaks [mixed with Cu 3$d_{x^2-y^2}$ states; see Fig. 6(b)] which is suppressed at higher incident energies. Despite the intense background in the experimental data for 1486.6 eV incident photon energy, also the strongly damped O 2s peak is visible. As in the case of the loss function, details of the photoemission spectra are thus very well described besides a constant shift of the conduction states that stems from the band-gap problem.

VI. SUMMARY AND CONCLUSIONS

We performed state-of-the-art many-body calculations in the GW approximation to compute the electronic QP excitation spectrum of the strongly correlated oxide CuO. In a first step, DFT was used to calculate starting electronic structures using the HSE06 and PBE+U exchange-correlation functionals. These functionals already account for large parts of the static screened exchange on the open Cu 3d shell and yield—apart from the band gap—almost identical DOS.

Subsequently, the performance of various recently proposed GW self-consistency schemes has been investigated. Aside from the general line shape of the QP DOS, the comparison focuses on the band gap as a characteristic quantity of each insulator. We find the band gap of CuO to be extremely sensitive to the details of the GW iteration scheme. Non-self-consistent and eigenvalue-self-consistent GW schemes are strongly starting-point dependent, since they do not update the one-particle wave functions. QP self-consistent GW, on the other hand, which updates also the wave functions, overestimates the band gap of CuO dramatically, since it removes the error cancellation between neglected QP effects and neglected excitonic effects in the dielectric screening by including only QP corrections in the self-consistency cycle.

That is why we resort to a QP self-consistent GW scheme where the screened Coulomb interaction compares well to the inverse dielectric function found in loss experiments and is kept fixed during the iteration. We find that the fundamental gap is still, albeit much less, overestimated within this approach. Our results indicate that the clue to the understanding of the electronic structure of CuO, and in particular the band gap, lies in the details of the screening. Therefore, momentum- and frequency-resolved experimental data for the dielectric function of CuO are urgently needed.

Apart from the gap, excellent agreement of the calculated QP spectra with the QP excitations in direct and inverse photoemission experiments is found, in particular when intrinsic QP lifetimes and matrix-element effects are taken into account.

ACKNOWLEDGMENTS

We are grateful for valuable discussions with G. Kresse, S. Huotari, P. Schattschneider, F. Bechstedt, M. Gatti, and X. Rocquefelte. Financial support has been provided by the European Commission Marie Curie Actions within the framework of the CEA Eurotalents program and the European Research Council under the European Union's 7th Framework Program (ERC Grant Agreement No. 320971). This work has benefited from collaboration with the Maison de la Simulation. Computer time has been provided by GENCI (Project No. 544).

[1] M. Heck and P. Hoffmann, Archaeometry **42**, 341 (2000).
[2] B. K. Meyer, A. Polity, D. Reppin, M. Becker, P. Hering, P. J. Klar, T. Sander, C. Reindl, J. Benz, M. Eickhoff, C. Heiliger, M. Heinemann, J. Bläsing, A. Krost, S. Shokovets, C. Müller, and C. Ronning, Phys. Status Solidi B **249**, 1487 (2012).
[3] F. P. Koffyberg and F. A. Benko, J. Appl. Phys. **53**, 1173 (1982).
[4] J. Ghijsen, L. H. Tjeng, J. van Elp, H. Eskes, J. Westerink, G. A. Sawatzky, and M. T. Czyzyk, Phys. Rev. B **38**, 11322 (1988).
[5] J. G. Bednorz and K. A. Müller, Z. Phys. B **64**, 189 (1986).
[6] A. J. Leggett, Nat. Phys. **2**, 134 (2006).
[7] T. Kimura, Y. Sekio, H. Nakamura, T. Siegrist, and A. P. Ramirez, Nat. Mater. **7**, 291 (2008).
[8] S. Åsbrink and L.-J. Norrby, Acta Crystallogr. B **26**, 8 (1970).
[9] J. B. Forsyth, P. J. Brown, and B. M. Wanklyn, J. Phys. C **21**, 2917 (1988).
[10] B. X. Yang, T. R. Thurston, J. M. Tranquada, and G. Shirane, Phys. Rev. B **39**, 4343 (1989).
[11] W. Y. Ching, Y.-N. Xu, and K. W. Wong, Phys. Rev. B **40**, 7684 (1989).
[12] F. Marabelli, G. B. Parravicini, and F. Salghetti-Drioli, Phys. Rev. B **52**, 1433 (1995).
[13] A. Svane and O. Gunnarsson, Phys. Rev. Lett. **65**, 1148 (1990).
[14] Z. Szotek, W. M. Temmerman, and H. Winter, Phys. Rev. B **47**, 4029 (1993).
[15] A. Filippetti and V. Fiorentini, Phys. Rev. Lett. **95**, 086405 (2005).
[16] Z.-X. Shen, R. S. List, D. S. Dessau, F. Parmigiani, A. J. Arko, R. Bartlett, B. O. Wells, I. Lindau, and W. E. Spicer, Phys. Rev. B **42**, 8081 (1990).
[17] L. Hedin, Phys. Rev. **139**, A796 (1965).
[18] L. Hedin and S. Lundqvist, in *Solid State Physics. Advances in Research and Applications*, edited by F. Seitz, D. Turnbull, and H. Ehrenreich (Academic Press, New York, 1969), Vol. 23, p. 1.
[19] W. G. Aulbur, L. Jönsson, and J. W. Wilkins, *Solid State Physics. Advances in Research and Applications*, edited by H. Ehrenreich and F. Spaepen (Academic Press, San Diego, 1999), Vol. 54, p. 1.
[20] S. V. Faleev, M. van Schilfgaarde, and T. Kotani, Phys. Rev. Lett. **93**, 126406 (2004).
[21] F. Bruneval, N. Vast, and L. Reining, Phys. Rev. B **74**, 045102 (2006).
[22] M. Gatti, F. Bruneval, V. Olevano, and L. Reining, Phys. Rev. Lett. **99**, 266402 (2007).
[23] C. Rödl, F. Fuchs, J. Furthmüller, and F. Bechstedt, Phys. Rev. B **79**, 235114 (2009).
[24] H. Jiang, R. I. Gomez-Abal, P. Rinke, and M. Scheffler, Phys. Rev. B **82**, 045108 (2010).
[25] M. S. Hybertsen and S. G. Louie, Phys. Rev. B **34**, 5390 (1986).
[26] J. Heyd, G. E. Scuseria, and M. Ernzerhof, J. Chem. Phys. **118**, 8207 (2003).
[27] V. I. Anisimov, J. Zaanen, and O. K. Andersen, Phys. Rev. B **44**, 943 (1991).
[28] S. L. Dudarev, G. A. Botton, S. Y. Savrasov, C. J. Humphreys, and A. P. Sutton, Phys. Rev. B **57**, 1505 (1998).
[29] D. Wu, Q. Zhang, and M. Tao, Phys. Rev. B **73**, 235206 (2006).
[30] M. Heinemann, B. Eifert, and C. Heiliger, Phys. Rev. B **87**, 115111 (2013).
[31] X. Rocquefelte, M.-H. Whangbo, A. Villesuzanne, S. Jobic, F. Tran, K. Schwarz, and P. Blaha, J. Phys.: Condens. Matter **22**, 045502 (2010).
[32] S. Lany, Phys. Rev. B **87**, 085112 (2013).
[33] K. Momma and F. Izumi, J. Appl. Crystallogr. **44**, 1272 (2011).
[34] G. Kresse and J. Furthmüller, Comput. Mater. Sci. **6**, 15 (1996).
[35] G. Kresse and D. Joubert, Phys. Rev. B **59**, 1758 (1999).
[36] M. Shishkin and G. Kresse, Phys. Rev. B **74**, 035101 (2006).
[37] M. Shishkin and G. Kresse, Phys. Rev. B **75**, 235102 (2007).
[38] A. V. Krukau, O. A. Vydrov, A. F. Izmaylov, and G. E. Scuseria, J. Chem. Phys. **125**, 224106 (2006).
[39] J. P. Perdew, K. Burke, and M. Ernzerhof, Phys. Rev. Lett. **77**, 3865 (1996).
[40] V. Olevano, L. Reining, and F. Sottile, http://dp-code.org.
[41] M. Shishkin, M. Marsman, and G. Kresse, Phys. Rev. Lett. **99**, 246403 (2007).
[42] W. Setyawan and S. Curtarolo, Comput. Mater. Sci. **49**, 299 (2010).
[43] B.-C. Shih, Y. Xue, P. Zhang, M. L. Cohen, and S. G. Louie, Phys. Rev. Lett. **105**, 146401 (2010).
[44] M. Stankovski, G. Antonius, D. Waroquiers, A. Miglio, H. Dixit, K. Sankaran, M. Giantomassi, X. Gonze, M. Côté, and G.-M. Rignanese, Phys. Rev. B **84**, 241201 (2011).
[45] C. Friedrich, M. C. Müller, and S. Blügel, Phys. Rev. B **83**, 081101 (2011).
[46] J. Klimeš, M. Kaltak, and G. Kresse, Phys. Rev. B **90**, 075125 (2014).
[47] J. P. Perdew and M. Levy, Phys. Rev. Lett. **51**, 1884 (1983).
[48] L. J. Sham and M. Schlüter, Phys. Rev. Lett. **51**, 1888 (1983).
[49] A. Seidl, A. Görling, P. Vogl, J. A. Majewski, and M. Levy, Phys. Rev. B **53**, 3764 (1996).
[50] J. P. Perdew, Adv. Quantum Chem. **21**, 113 (1990).
[51] M. Cococcioni and S. de Gironcoli, Phys. Rev. B **71**, 035105 (2005).
[52] F. Aryasetiawan, M. Imada, A. Georges, G. Kotliar, S. Biermann, and A. I. Lichtenstein, Phys. Rev. B **70**, 195104 (2004).
[53] M. van Schilfgaarde, T. Kotani, and S. Faleev, Phys. Rev. Lett. **96**, 226402 (2006).
[54] R. Sakuma, T. Miyake, and F. Aryasetiawan, Phys. Rev. B **80**, 235128 (2009).
[55] A. N. Chantis, M. van Schilfgaarde, and T. Kotani, Phys. Rev. B **76**, 165126 (2007).

[56] J. Heyd, J. E. Peralta, G. E. Scuseria, and R. L. Martin, J. Chem. Phys. **123**, 174101 (2005).

[57] F. Fuchs, J. Furthmüller, F. Bechstedt, M. Shishkin, and G. Kresse, Phys. Rev. B **76**, 115109 (2007).

[58] M. A. L. Marques, J. Vidal, M. J. T. Oliveira, L. Reining, and S. Botti, Phys. Rev. B **83**, 035119 (2011).

[59] K. V. Rao and A. Smakula, J. Appl. Phys. **37**, 2840 (1966).

[60] G. Kliche and Z. V. Popovic, Phys. Rev. B **42**, 10060 (1990).

[61] T. Ito, H. Yamaguchi, T. Masumi, and S. Adachi, J. Phys. Soc. Jpn. **67**, 3304 (1998).

[62] A. B. Kuz'menko, D. van der Marel, P. J. M. van Bentum, E. A. Tishchenko, C. Presura, and A. A. Bush, Phys. Rev. B **63**, 094303 (2001).

[63] T. Masumi, H. Yamaguchi, T. Ito, and H. Shimoyama, J. Phys. Soc. Jpn. **67**, 67 (1998).

[64] C. Rödl, F. Fuchs, J. Furthmüller, and F. Bechstedt, Phys. Rev. B **77**, 184408 (2008).

[65] P. Liao and E. A. Carter, Phys. Chem. Chem. Phys. **13**, 15189 (2011).

[66] W. B. Wu, N. Hiraoka, D. J. Huang, S. W. Huang, K. D. Tsuei, M. van Veenendaal, J. van den Brink, Y. Sekio, and T. Kimura, Phys. Rev. B **88**, 205129 (2013).

[67] S. Huotari, L. Simonelli, C. J. Sahle, M. Moretti Sala, R. Verbeni, and G. Monaco, J. Phys.: Condens. Matter **26**, 165501 (2014).

[68] E. A. Bakulin, M. M. Bredov, E. G. Ostroumova, and V. V. Shcherbinina, Fiz. Tverd. Tela (Leningrad) **19**, 1307 (1977) [Sov. Phys. Solid State **19**, 760 (1977)].

[69] N. Vast, L. Reining, V. Olevano, P. Schattschneider, and B. Jouffrey, Phys. Rev. Lett. **88**, 037601 (2002).

[70] S. Botti and M. A. L. Marques, Phys. Rev. Lett. **110**, 226404 (2013).

[71] G. D. Mahan, *Many-Particle Physics*, 2nd ed. (Plenum Press, New York, 1990).

[72] F. Bechstedt, K. Seino, P. H. Hahn, and W. G. Schmidt, Phys. Rev. B **72**, 245114 (2005).

[73] *Springer Handbook of Condensed Matter and Materials Data*, edited by W. Martienssen and H. Warlimont (Springer, Berlin, 2005).

[74] J. J. Yeh and I. Lindau, At. Data Nucl. Data Tables **32**, 1 (1985).

Chapter 6

Qualitatively new Phenomena

FINALLY, it is very rewarding when one's theoretical developments (together with numerical implementation, algorithm optimization, etc.) leads to the description of new physics, or shed a new light on a long-standing debate. The latter case is illustrated by the study of plasmonic satellites, a joint experimental-theoretical work in which we could finally disprove the existence of a plasmaron in Silicon putting a final word on a long debate. The first case (description of new effects and prediction of experimental results) is instead illustrated by the inclusion of a new dimension, the momentum transfer, in the description of excitonic properities of materials, predicting the excitonic features of solid Argon.

6.1 Plasmon Satellites

We have seen in Sec.1.1, that photoemission spectroscopy can be described by Green's function methods. It worths underlining that today most calculations aim at describing only the band-gap of semiconductors and insulators. Only very few attempts go beyond this observable, and try to look at the spectral function. This was however the aim of Matteo Guzzo in his PhD thesis, under my supervision. As we have already mentioned, a PES spectrum is not as simple as it seems (the photo-electron scatter with the other electrons; the final state of the electron is not always the same; the hole left in the systems create other excitations (that tend to screen the hole left behind); the photo-electron and the hole interact; all these things mix together, giving rise of the so-called extrinsic and interferences effects). The aim of the thesis was indeed to go beyond band-structure calculations and check how all these (beyond quasi-particle) effects act on the spectral function. The work was conducted in strict collaboration with some experimentalists of the Synchortron SOLEIL (beamline TEMPO). The results can be resumed in a very effective description of the PES, giving rise both of the quasi-particle peaks (the 'simple' part) and the satellites (all the extra screening effects aforementioned). The correct description of the plasmon satellite comes from two effects: 1) on a qualitative level, the possibility of describing the satellite (and multiple satellites as well) comes from the introduction of a cumulant-like formula, that permits to remove part of the weight from the quasiparticle peak and move it to satellite part; 2) on a quantitative level, the agreeement with the experiment is possible only once the so-called extrinsic and intereferences effects are taken into account: this was possible thanks to a collaboration with John Rehr and his group. This work is also one of the most clear example of "a PES spectrum is more than the spectral function".[1] Matteo's thesis has been awarded of the best thesis at the Ecole Polytechnique and its outcomes published in three articles [12, 111, 112].

PLEASE REFER TO THE ATTACHED ARTICLE

---

[1] This is also a notable exception to the well-known Duck Test, coined by James Whitcomb Riley, that could be paraphrased like *If I see a spectrum that looks like a spectral function and has the dimension of a spectral function, than I call it a spectral function.*

PRL **107,** 166401 (2011) PHYSICAL REVIEW LETTERS week ending 14 OCTOBER 2011

Valence Electron Photoemission Spectrum of Semiconductors: *Ab Initio* Description of Multiple Satellites

Matteo Guzzo,[1,2,*] Giovanna Lani,[1,2] Francesco Sottile,[1,2] Pina Romaniello,[3,2] Matteo Gatti,[4,2] Joshua J. Kas,[5]
John J. Rehr,[5,2] Mathieu G. Silly,[6] Fausto Sirotti,[6] and Lucia Reining[1,2,†]
[1]*Laboratoire des Solides Irradiés, École Polytechnique, CNRS, CEA-DSM, F-91128 Palaiseau, France*
[2]*European Theoretical Spectroscopy Facility (ETSF)*
[3]*Laboratoire de Physique Théorique, CNRS, Université Paul Sabatier, F-31062 Toulouse, France*
[4]*Departamento Física de Materiales, CSIC-UPV/EHU-MPC and DIPC, Universidad del País Vasco, E-20018 San Sebastián, Spain*
[5]*Department of Physics, University of Washington, Seattle, Washington 98195, USA*
[6]*Synchrotron-SOLEIL, BP 48, Saint-Aubin, F91192 Gif sur Yvette CEDEX, France*
(Received 1 July 2011; published 12 October 2011)

The experimental valence band photoemission spectrum of semiconductors exhibits multiple satellites that cannot be described by the *GW* approximation for the self-energy in the framework of many-body perturbation theory. Taking silicon as a prototypical example, we compare experimental high energy photoemission spectra with *GW* calculations and analyze the origin of the *GW* failure. We then propose an approximation to the functional differential equation that determines the exact one-body Green's function, whose solution has an exponential form. This yields a calculated spectrum, including cross sections, secondary electrons, and an estimate for extrinsic and interference effects, in excellent agreement with experiment. Our result can be recast as a dynamical vertex correction beyond *GW*, giving hints for further developments.

DOI: 10.1103/PhysRevLett.107.166401 PACS numbers: 71.45.Gm, 71.10.−w, 71.15.Qe

Photoemission is a prominent tool to access information about electronic structure and excitations in materials. Modern synchrotron sources can provide detailed insight, thanks to their high intensity and broad photon energy range. But the interpretation of the experimental data is far from obvious, and theory is an essential complementary tool. However, *ab initio* calculations typically focus on bulk band structure [1,2]; thus surface effects are ignored, and satellites are not included. The latter are a pure many-body effect due to coupling to excitations of the material. Such many-body effects are contained in approaches developed for correlated materials [3,4]; however, these are usually based on models with short-range interactions, whereas satellites such as plasmons involve long-range effects. Plasmon satellites have been extensively studied in core-level experiments [5]. There they can be described by a theoretical model where a single dispersionless fermion couples to bosons. The resulting exact Green's function has an exponential form given by the so-called cumulant expansion (CE). A Taylor expansion of the exponential leads to a well-defined quasiparticle (QP) peak followed by a decaying series of plasmon satellites at energy differences given by the plasmon energy, consistent with experimental observations [6–10]. In the valence region, plasmon satellites are much less studied, though *ab initio* approaches can provide a good starting point. At high photoelectron energies the photoemission spectrum is approximately proportional to the intrinsic spectral function $A(\omega) = -(1/\pi)\mathrm{Im}\mathcal{G}(\omega)$, where $\mathcal{G}$ is the one-particle Green's function. The latter is typically calculated using the widely used *GW* approximation (GWA) [7,11,12]. In principle, the GWA contains correlation effects beyond the quasiparticle approximation. However, these additional features are rarely calculated due to computational complexity and, more importantly, the serious discrepancies between GWA and experiment (see, e.g., [13–16]). The CE has also been used for homogeneous electron gas [17] and simple metals [14,15], yielding an improved description of satellites over *GW*. Silicon [16] and graphite [18] were also studied, but no plasmon satellite series were observed. However, these results are not conclusive due to difficulties of interpreting the experimental data. This leaves a series of important questions: (i) Do materials generally exhibit intrinsic satellites in the valence band region following a cumulant like distribution, or are the extrinsic plasmon peaks, due to losses incurred by the escaping photoelectron, dominant? (ii) If such series are seen, how bad are *ab initio GW* calculations? what is the reason for their failure? and (iii) how can they be improved? Answering these questions would be a crucial step towards a better understanding of correlation effects in electronic excitations and a predictive *ab initio* approach to photoemission.

In this Letter we focus on plasmon satellites using silicon as a prototypical example. We have obtained valence band photoemission data at high photon energy (XPS) that constitute a reliable and well resolved benchmark. Analysis of the data allows us to elucidate the failure of *GW* in describing the satellites. Then, starting from the fundamental equations of many-body perturbation theory (MBPT), we show how the failure can be overcome by using a decoupling approximation that leads to an exponential representation of the one-particle Green's function. Together with an estimate for extrinsic and interference effects, we obtain results for the quasiparticle peaks and satellites in excellent agreement with experiment. Our theoretical results can be expressed in terms of a dynamical vertex correction, a powerful basis for further modeling.

Angular resolved valence photoemission (ARPES) measurements were performed at the UHV photoemission experimental station of the TEMPO beam line [19] at the SOLEIL synchrotron radiation source. Linearly polarized photons from the Apple II type Insertion Device (HU44) were selected in energy using a high resolution plane grating monochromator with a resolving power $E/\Delta E = 5000$. The end-station chamber (base pressure 10^{-10} mbar) is equipped with a modified SCIENTA-200 electron analyzer with a delay-line 2D detector which optimizes the detection linearity and signal/background ratio [20]. The overall energy resolution was better than 200 meV. The photon beam impinges on the sample at an angle of 43°, and photoelectrons were detected around the sample surface normal with an angular acceptance of ±6°. An n-type ($N_D \simeq 2 \times 10^{-18} P\,\mathrm{atoms/cm^3}$) Si(001) wafer was cleaned from the native oxide by flash annealing at 1100 °C after prolonged degassing at 600 °C in ultrahigh vacuum. The silicon surface was annealed at 300 °C to prevent surface etching, and hydrogenated in a partial pressure of activated hydrogen about 2×10^{-8} mbar for 20 min. The ARPES was measured along the Σ direction. At 800 eV kinetic energy the Si Brillouin zone is observed with an emission angle slightly smaller than 5°. The measured photoemission map was integrated over the spectral intensity originated by two Brillouin zones. The Fermi level was obtained by measuring a clean Au(111) surface. The experimental data (crosses) are summarized in Fig. 1. One can distinguish the quasiparticle peaks between the Fermi level at zero and the bottom valence at −12 eV, followed by two prominent satellite structures, each at a mutual distance of about 17 eV, as well as a more weakly visible third satellite between −52 and −60 eV. These structures are obviously related to the 17 eV silicon bulk plasmon [21,22].

The exact one-electron Green's function $\mathcal{G}$ is described by an equation of motion with the form of a functional differential equation [23],

$$\mathcal{G} = \mathcal{G}_0 + \mathcal{G}_0 V_H \mathcal{G} + \mathcal{G}_0 \varphi \mathcal{G} + i \mathcal{G}_0 v_c \frac{\delta \mathcal{G}}{\delta \varphi}. \qquad (1)$$

Here $\mathcal{G}_0$ is the noninteracting Green's function, φ is a fictitious external perturbation that is set to zero at the end of the derivation, v_c is the bare Coulomb interaction, and all quantities are understood to be matrices in space, spin, and time. The Hartree potential V_H gives rise to screening to all orders. Linearizing V_H with respect to φ yields [24]

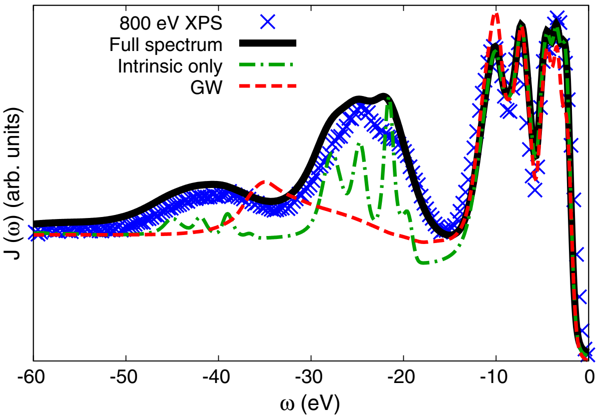

FIG. 1 (color online). Experimental XPS spectrum of Si at 800 eV photon energy (blue crosses), compared to the theoretical intrinsic $A(\omega)$ calculated from G_0W_0 (red dashed line), and from Eq. (4) (green dot-dashed line). On top of the latter the black solid line also includes extrinsic and interference effects. All spectra contain photoabsorption cross sections, a calculated secondary electron background and 0.4 eV Gaussian broadening to account for finite k-point sampling and experimental resolution. The Fermi energy is set to 0 eV.

$$\mathcal{G}(t_1t_2) = \mathcal{G}^0_H(t_1t_2) + \mathcal{G}^0_H(t_1t_3)\bar{\varphi}(t_3)\mathcal{G}(t_3t_2) + i\mathcal{G}^0_H(t_1t_3)\mathcal{W}(t_3t_4)\frac{\delta \mathcal{G}(t_3t_2)}{\delta \bar{\varphi}(t_4)}, \qquad (2)$$

where $\bar{\varphi}$ is equal to φ screened by the inverse dielectric function, $\mathcal{W}$ is the screened Coulomb interaction, and $\mathcal{G}^0_H$ is the Green's function containing the Hartree potential at vanishing $\bar{\varphi}$; only time arguments are displayed explicitly and repeated indices are integrated. This linearization preserves the main effects of $\mathcal{W}$ and hence of plasmons. With the additional approximation $\frac{\delta \mathcal{G}(t_3t_2)}{\delta \bar{\varphi}(t_4)} \simeq \mathcal{G}(t_3t_4)\mathcal{G}(t_4t_2)$ one obtains the Dyson equation $\mathcal{G} = \mathcal{G}^0_H + \mathcal{G}^0_H \Sigma \mathcal{G}$ in the GWA for the self-energy Σ. However this approximation can be problematic. For the following analysis we use the standard G_0W_0 approach, where $\mathcal{G}_0$ is taken from a local-density approximation calculation and $\mathcal{W}_0$ is the screened interaction in the random phase approximation. Figure 2 shows the G_0W_0 spectral function $A(\omega) = \frac{1}{\pi}|\mathrm{Im}\Sigma(\omega)|/\{[\omega - \varepsilon_H - \mathrm{Re}\Sigma(\omega)]^2 + [\mathrm{Im}\Sigma(\omega)]^2\}$ of Si [25] at the Γ point, for the top valence (solid line) and bottom valence (dashed), respectively. The top valence shows a sharp quasiparticle peak followed by a broad, weak satellite structure at about −21 eV. This peak stems from the prominent peak in ImΣ (full circles) at about −18 eV, itself due to the plasmon peak in Im$\mathcal{W}$. It is a typical plasmon satellite, though (cf. [7]), the QP-satellite spacing is slightly overestimated because the term $\omega - \varepsilon_H - \mathrm{Re}\Sigma$ (full squares) in the denominator of the expression for $A(\omega)$ is not constant. However the GWA has a more severe problem: for the bottom valence, the satellite structure at about −36 eV is much too far from the QP

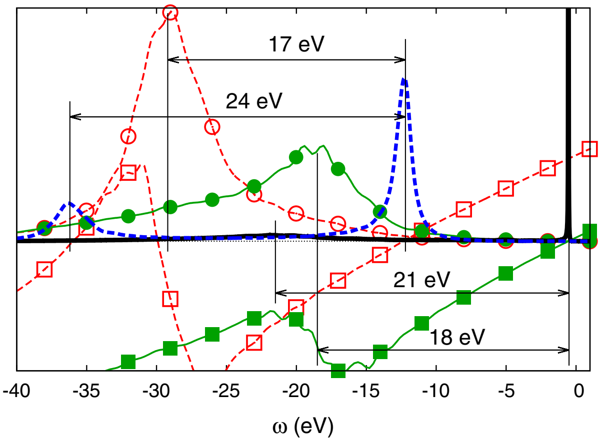

FIG. 2 (color online). G_0W_0 spectral function of bulk silicon for the top and bottom valence bands at the Γ point (black solid and blue dashed lines, respectively). The corresponding imaginary parts of the self-energy (red empty circles and dashed line, and green full circles and solid-line) and $\omega - \varepsilon_H - \mathrm{Re}\Sigma$ (red empty squares and dashed line, and green full squares and solid line) are also shown. The Fermi energy is set to 0 eV.

peak at about −12 eV, and much too sharp. This satellite does not correspond to a plasmon peak in ImΣ (empty circles), but to a zero in $\omega - \varepsilon_H - \mathrm{Re}\Sigma$ (empty squares) in the denominator of $A(\omega)$, as for a QP peak. It has been interpreted in the HEG as a *plasmaron*, a coupled hole-plasmon mode [26], but as noted below it is an artifact of the GWA [27,28]. Figure 1 compares the total *GW* spectral function (dashed red line) summed over all valence bands and *k* points, with our XPS data. The effects of cross sections are included by projecting on angular momenta in atomic spheres using the atomic data of Ref. [29]. The secondary electrons' background at energy ω was determined by integrating the calculated intrinsic spectral intensity between ω and the Fermi level, similar to [22]. A constant scaling factor was set such that the measured photoemission intensity at the highest binding energy (60 eV), where primary electrons intensity is absent, is reproduced. As expected, the dominant QP spectrum is well described by *GW*, but the satellite is dominated by the plasmaron around −36 eV, in complete disagreement with experiment. The experimental plasmon satellite at about −25 eV appears only as a weak shoulder in the GWA. Thus the plasmaron peak is responsible for the GWA failure [27,28] in silicon.

Vertex corrections are required to go beyond the GW self-energy. However, adiabatic vertex corrections (see, e.g., [30]) only lead to renormalization of energies and do not create new structures. Thus alternatively, we concentrate here on dynamical effects, and we choose to approximate directly Eq. (2), without passing through a self-energy.

We decouple Eq. (2) approximately by supposing that $\mathcal{G}$ and $\mathcal{G}_H$ are diagonal in the same single particle basis. Equation (2) is then applicable separately for every single matrix element of $\mathcal{G}$ and each state couples independently to the neutral excitations of the system through $\mathcal{W}$ [31]. The latter can now be understood as the screened intra-orbital Coulomb matrix element for the chosen state. Such a decoupling approximation can be optimized [27,28] by adding and subtracting a self-energy correction, hence by using a QP Green's function $\mathcal{G}_\Delta$ obtained from a good QP self-energy instead of $\mathcal{G}_H$. Since the GWA is currently the state-of-the art for QP properties, we suppose that for every decoupled state k, $\mathcal{G}_\Delta^k(\tau) = i\theta(-\tau)e^{-i\varepsilon_k\tau}$ is determined from $\Sigma^{GW}(\varepsilon_k)$, where $\varepsilon_k = \varepsilon_k^0 + \Sigma^{GW}(\varepsilon_k)$ is the (complex) *GW* quasiparticle energy and $\tau = t_1 - t_2$. Now Eq. (2) can be solved exactly for each state. Briefly the main steps are: (i) solve the noninteracting ($\mathcal{W} = 0$) version of (2), which leads to an explicit solution $\mathcal{G}_\Delta^\varphi$; (ii) iterate the result $\mathcal{G} = \mathcal{G}_\Delta^\varphi - \mathcal{G}_\Delta^\varphi \Delta \mathcal{G} + i\mathcal{G}_\Delta^\varphi \mathcal{W} \frac{\delta\mathcal{G}}{\delta\bar{\varphi}}$ starting from $\mathcal{G}^{(0)} = \mathcal{G}_\Delta^\varphi$. Here Δ compensates for the self-energy insertion used for the optimized decoupling; (iii) use the exact relation $\frac{\delta\mathcal{G}_\Delta^\varphi(t_3t_2)}{\delta\bar{\varphi}(t_4)} = \mathcal{G}_\Delta^\varphi(t_3t_4)\mathcal{G}_\Delta^\varphi(t_4t_2) = i\mathcal{G}_\Delta^\varphi(t_3t_2)\theta(t_2 - t_4)\theta(t_4 - t_1)$ to derive

$$\mathcal{G}(t_1t_2) = \mathcal{G}_\Delta(\tau)e^{i\Delta\tau}e^{i\int_{t_1}^{t_2} dt'[\bar{\varphi}(t') - \int_{t'}^{t_2} dt'' \mathcal{W}(t't'')]}. \qquad (3)$$

The equilibrium solution is obtained setting $\bar{\varphi} = 0$.

In silicon, where the peaks in the loss function are well defined, it is justified to use a single plasmon pole model $\mathcal{W}(\tau) = -i\lambda_k\{e^{-i\tilde{\omega}_k\tau}\theta(\tau) + e^{i\tilde{\omega}_k\tau}\theta(-\tau)\}$ with plasmon energy $\tilde{\omega}_k$ and intrinsic strengths λ_k for each matrix element of $\mathcal{W}$. Besides $\bar{\varphi}$, the total exponent becomes then $a_k[e^{i\tilde{\omega}_k\tau} - 1]$ with $a_k = \lambda_k/\tilde{\omega}_k^2$ obtained from the corresponding *GW* results. We find that a_k varies around 0.3. Taylor expansion of the exponential leads then to the spectral function

$$A_k(\omega) = \frac{e^{-a_k}}{\pi} \sum_{n=0}^{\infty} \frac{a_k^n}{n!} \frac{\Gamma_k}{(\omega - \epsilon_k + n\tilde{\omega}_k)^2 + \Gamma_k^2}, \qquad (4)$$

where $\epsilon_k = \mathrm{Re}[\varepsilon_k]$ and $\Gamma_k = \mathrm{Im}[\varepsilon_k]$. Equation (4) is similar to the plasmon pole version of the CE (cf. Ref. [13]). However here the exponential solution arises from a straightforward approximation to the fundamental differential equation (1): the linearization of the Hartree potential reveals the boson of the model (i.e., the plasmon *via* peaks in $\mathcal{W}$), and the diagonal approximation of $\mathcal{G}$ gives rise to each isolated fermion. Our results are summarized in Fig. 1. The dot-dashed line gives the result of this procedure together with the cross sections and the secondary electron background. The shapes of the QP peaks change little with respect to *GW*, but now the full series of satellites is present. The internal structure of the satellites which originate from the multiple valence bands, is also reproduced. This validates the decoupling approximation in the dense valence band region where, contrary to the case of an isolated core level, its success is *a priori* far from obvious. However, the intensity of the observed satellites is significantly underestimated. This discrepancy is similar to that found for the CE in simple metals, where extrinsic losses were suggested as a likely cause [14]. These might also be reduced by interference effects [32]. To check this possibility we estimated the contributions from both effects to the satellite strengths a_k using Eq. (32) and (36) of Ref. [33]. This approach uses a plasmon pole model, Inglesfield fluctuation potentials, and an average over hole position that takes account of the photoelectron mean free path λ [33]. We observe that the averaged total satellite line shape in this model is similar to that for the intrinsic part, with a width $\gamma \approx 2$ eV due to plasmon dispersion. Thus we can approximate the extrinsic and interference effects by renormalizing the intrinsic satellite intensity, i.e., by the replacement $\bar{a}_k = a_k + a^{\text{ext}} + a^{\text{inf}}$ in Eq. (4). These quantities are evaluated with $\omega_p = 16.7$ eV and $\lambda = 17.5$ Å at 800 eV for Si, yielding $a^{\text{ext}} = 0.63$ and $a^{\text{inf}} = -0.11$. This also modifies the strength $Z_k = e^{-\bar{a}_k}$ of the QP peaks, but preserves overall normalization. The broadening of the satellites must also be increased, $\Gamma \rightarrow \Gamma + n\gamma$. The total spectrum thus obtained (black line) is in unprecedented agreement with experiment. We stress that this result contains no fit parameters besides the two scaling factors (for spectrum and background) due to the arbitrary units of the experiment.

The success of our present approach stresses the need to go beyond the GWA. The exponential representation of $\mathcal{G}$ implicitly corresponds to a vertex correction $\tilde{\Gamma} = -\frac{\delta \mathcal{G}^{-1}}{\delta \bar{\varphi}}$ to the self-energy. Since our derivation yields $\mathcal{G}$ as a function of the screened potential $\bar{\varphi}$ (3), this functional derivative can be performed explicitly, using $-\frac{\delta \mathcal{G}^{-1}}{\delta \bar{\varphi}} = \mathcal{G}^{-1} \frac{\delta \mathcal{G}}{\delta \bar{\varphi}} \mathcal{G}^{-1}$. From Eq. (3), a straightforward derivative of $\mathcal{G}$ contains a series of satellite contributions. The two inverse Green's functions lead to a significant complication, because they contain the inverse of this series. This clearly illustrates the difficulty of modeling $\tilde{\Gamma}$ in order to treat dynamical effects. It suggests rather to concentrate on modeling $\frac{\delta \mathcal{G}}{\delta \bar{\varphi}}$, where the various contributions are simply summed, and hence to search for a self-energy of the form $\Sigma = -i \mathcal{W} \frac{\delta \mathcal{G}}{\delta \bar{\varphi}} \mathcal{G}^{-1}$ instead of $\Sigma = i \mathcal{G} \mathcal{W} \tilde{\Gamma}$. In conclusion, on the basis of our experimental XPS data we have analyzed the failure of *GW* to reproduce plasmon satellites and linked this failure to the appearance of an artificial plasmaron peak. On the other hand, *GW* results are fair when the imaginary part of Σ, hence the intensity of the corresponding plasmon, is small enough so that no sharp plasmaron is created. Thus surprisingly, one might expect *GW* to work better in describing satellites stemming from local plasmon or interband excitations close to the Fermi level in "strongly correlated" materials than for the strong plasmon structures in conventional semiconductors. Starting from the fundamental equations of MBPT we have derived an exponential solution to the one-particle Green's function, analogous to that from the CE, that overcomes the drawbacks of the GWA. Comparison to new photoemission data shows that this yields a very good description of the spectral function of bulk silicon, including the satellites series. By calculating the secondary electron background, cross section corrections as well as a correction for extrinsic and interference effects, we achieve an agreement between theory and experiment that can be considered as a benchmark. Our derivation also suggests how the results can be improved in cases where the presently used approximations are inadequate. Finally, by accessing an expression for the vertex function, our approach yields precious hints for directions to take in modeling dynamical effects beyond the GWA.

We acknowledge support by ANR (NT09-610745), St Gobain R&D (091986), and Triangle de la Physique (2007-71). J. J. R. and J. J. K. are also supported in part by DOE BES Grant DE-FG03-97ER45623 and DOE CMCSN. Computer time was granted by IDRIS (544). We thank F. Bechstedt for fruitful discussions.

---

*matteo.guzzo@polytechnique.edu
†lucia.reining@polytechnique.fr

[1] F. Aryasetiawan and O. Gunnarsson, Rep. Prog. Phys. **61**, 237 (1998).
[2] W. G. Aulbur, L. Jonsson, and J. W. Wilkins, Solid State Phys. **54**, 1 (2000).
[3] A. Georges, G. Kotliar, W. Krauth, and M. J. Rozenberg, Rev. Mod. Phys. **68**, 13 (1996).
[4] G. Kotliar *et al.*, Rev. Mod. Phys. **78**, 865 (2006).
[5] F. Offi *et al.*, Phys. Rev. B **76**, 085422 (2007).
[6] L. Hedin, Phys. Scr. **21**, 477 (1980).
[7] L. Hedin, J. Phys. Condens. Matter **11**, R489 (1999).
[8] P. Nozières and C. De Dominicis, Phys. Rev. **178**, 1097 (1969).
[9] D. Langreth, Phys. Rev. B **1**, 471 (1970).
[10] F. Bechstedt, *Principles of Surface Physics* (Springer, New York, 2003), Chap. 5, pp. 199–201.
[11] L. Hedin, Phys. Rev. **139**, A796 (1965).
[12] L. Hedin and S. Lundqvist, *Solid State Physics* (Academic Press, New York, 1969), Vol. 23.
[13] F. Aryasetiawan, Phys. Rev. B **46**, 13 051 (1992).
[14] F. Aryasetiawan, L. Hedin, and K. Karlsson, Phys. Rev. Lett. **77**, 2268 (1996).
[15] M. Vos *et al.*, Phys. Rev. B **66**, 155414 (2002).
[16] A. S. Kheifets *et al.*, Phys. Rev. B **68**, 233205 (2003).
[17] B. Holm and F. Aryasetiawan, Phys. Rev. B **56**, 12 825 (1997).
[18] M. Vos, A. S. Kheifets, E. Weigold, and F. Aryasetiawan, Phys. Rev. B **63**, 033108 (2001).
[19] F. Polack *et al.*, AIP Conf. Proc. **1234**, 185 (2010).
[20] N. Bergeard *et al.*, J. Synchrotron Radiat. **18**, 245 (2011).
[21] J. Stiebling, Z. Phys. B **31**, 355 (1978).
[22] L. Ley, S. Kowalczyk, R. Pollak, and D. A. Shirley, Phys. Rev. Lett. **29**, 1088 (1972).
[23] L. P. Kadanoff and G. Baym, *Quantum Statistical Mechanics* (W. A. Benjamin Inc., New York, 1964).

[24] G. Lani, P. Romaniello, and L. Reining, arXiv:1103.1630.

[25] A. Fleszar and W. Hanke, Phys. Rev. B **56**, 10 228 (1997).

[26] B. Lundqvist, Z. Phys. B **6**, 193 (1967); Phys. Kondens. Mater. **7**, 117 (1968).

[27] C. Blomberg and B. Bergersen, Can. J. Phys. **50**, 2286 (1972).

[28] B. Bergersen, F. Kus, and C. Blomberg, Can. J. Phys. **51**, 102 (1973).

[29] J. Yeh and I. Lindau, At. Data Nucl. Data Tables **32**, 1 (1985).

[30] R. Del Sole, L. Reining, and R. W. Godby, Phys. Rev. B **49**, 8024 (1994).

[31] In a similar spirit the equation of motion for the Green's function is decoupled in: C.-O. Almbladh and L. Hedin, *Handbook on Synchrotron Radiation* (North-Holland, Amsterdam, 1983), Chap. 8.

[32] F. Bechstedt, K. Tenelsen, B. Adolph, and R. DelSole, Phys. Rev. Lett. **78**, 1528 (1997).

[33] L. Hedin, J. Michiels, and J. Inglesfield, Phys. Rev. B **58**, 15 565 (1998).

Eur. Phys. J. B (2012) 85: 324
DOI: 10.1140/epjb/e2012-30267-y

THE EUROPEAN
PHYSICAL JOURNAL B

Regular Article

Plasmon satellites in valence-band photoemission spectroscopy

Ab initio study of the photon-energy dependence in semiconductors

M. Guzzo[1,a,b], J.J. Kas[2], F. Sottile[1,b], M.G. Silly[3], F. Sirotti[3], J.J. Rehr[2], and L. Reining[1,b]

[1] Laboratoire des Solides Irradiés, École Polytechnique, CNRS, CEA-DSM, 91128 Palaiseau, France
[2] Department of Physics, University of Washington, Seattle, 98195 WA, USA
[3] Synchrotron-SOLEIL, BP 48, Saint-Aubin, 91192 Gif sur Yvette Cedex, France

Received 27 March 2012 / Received in final form 15 June 2012

Abstract. We present experimental data and theoretical results for valence-band satellites in semiconductors, using the prototypical example of bulk silicon. In a previous publication we introduced a new approach that allows us to describe satellites in valence photoemission spectroscopy, in good agreement with experiment. Here we give more details; we show how the the spectra change with photon energy, and how the theory explains this behaviour. We also describe how we include several effects which are important to obtain a correct comparison between theory and experiment, such as secondary electrons and photon cross sections. In particular the inclusion of extrinsic losses and their dependence on the photon energy are key to the description of the energy dependence of spectra.

1 Introduction

Photoemission spectroscopy (PES) is an established tool for the analysis of the electronic structure of solids and molecules. Its increasing capability in energy-resolution and flexibility has made more urgent the need for advanced theoretical approaches able to cope with the huge range of systems being measured and with the high precision needed to match the experiment [1]. One powerful and commonly used framework is based on the one-particle Green's function $G(\mathbf{x}, \mathbf{x}', t, t')$ [2], which describes the propagation of one particle in the system. A popular approximation for the propagator is the GW approximation [3], which has proven to be successful in a variety of systems calculations of photoemission band gaps [4,5]. The quantity to be compared with experiment is the one-particle spectral function $A(\omega)$ which is proportional to the imaginary part of G. The main features of the spectral function $A(\omega)$ are quasiparticle (QP) peaks with finite lifetime. In addition, the spectral function shows incoherent satellite structures. In *sp* semiconductors these satellites are mainly due to the excitation of plasmons (both surface and bulk). Satellites in photoemission spectroscopy have been extensively studied for core-level spectra [6–8], while for valence-band spectroscopy there has been much less effort [9–11]. Still, valence-band satellites have been measured in a number of systems and are at the center of the debate around some highly interesting systems like transition metal oxides. In a previous work [12] we introduced a new method to describe satellites with an improved description of the intrinsic spectral function, including effects beyond the latter. In particular our method includes the dependence of the spectrum on photon energy. In this paper we present details of the method. We also show how the photoemission spectrum of silicon depends on the photon energy and we give a prediction for the trend at very high photon energies.

1.1 The sudden approximation and the three-step model

When making comparisons between theory and experiment, it is worth noting that there is not a complete coincidence between the spectral function $A(\omega)$ and the PES spectrum. This is because $A(\omega)$ only describes the propagation of the hole created by the incoming photon, while completely neglecting the losses of the photoelectron before it leaves the system. The use of $A(\omega)$, within these limits, to describe PES is known as the *sudden approximation*. While this approximation simplifies the description of PES, it is safe to say that it is never actually true. In fact it turns out that the losses of the outgoing photoelectrons are roughly the same at all photon energies. This is the result of two competing processes [6]:

(i) the reduction of the inelastic scattering cross section of electrons as their kinetic energy increases. As the photon energy increases, the average kinetic energy

---

[a] e-mail: `matteo.guzzo@polytechnique.edu`

[b] European Theoretical Spectroscopy Facility (ETSF), `http://www.etsf.eu`

of the electrons in the solid will increase. With it, the average loss probability per electron will decrease;

(ii) the increase of the mean free path of electrons as their kinetic energy increases. A larger mean free path will correspond to a greater maximum depth of a hole for which the corresponding photoelectron is fast enough to reach the surface and be detected. This implies that, on average, electrons will have to travel through a thicker layer of atoms before escaping the material. This way, the energy-loss probability will increase.

These two phenomena make the losses of the photoelectrons non-negligible at any photon energy. The good news is that the effect of these losses on the QP part of the spectrum is often only an overall renormalization of the peaks, which explains the success of the sudden approximation for the description of QP band structures. However, an appropriate calculation and interpretation of satellite structures in photoemission spectra requires one to go beyond the sudden approximation. A more complete, yet simplistic way of modeling the photoemission process is to divide it in three independent sequential steps:

1. optical excitation of the electron in the bulk;
2. travel of the excited electron to the surface;
3. escape of the photoelectron into vacuum.

This is known as the *three-step* model, as first proposed by Berglund and Spicer [13]. The total photoemission intensity is then given by the product of the probabilities of the three different processes. The first step is described by the one-particle spectral function $A(\omega)$. Losses coming from $A(\omega)$ are called *intrinsic* [6]. Step two is described by the electron energy-loss spectrum of the system and, along with step three, is considered part of the *extrinsic* losses. At this point, to get the total intensity, it would be sufficient to convolute $A(\omega)$ with the energy-loss spectrum. This case is referred to as the *sudden limit* [6]. However, this condition is met only at very high photon energies that are rarely accessed in usual PES conditions. In fact, there is quantum-mechanical interference between intrinsic and extrinsic losses, which is due to the interaction between the outgoing photoelectron and the hole it has left behind. The changes occurring in the photoemission spectrum following this kind of process, are referred to as *interference effects*. To describe this kind of processes one should in principle make use of a two-particle propagator [14], but it is possible to treat this effect in an approximate way retaining at the same time a good deal of physical insight. Within this picture, we use an optimized three-step model that attempts to overcome the shortcomings of its original formulation.

2 Theoretical framework

Our method is based on the exact equation of motion of the fully-interacting 1-particle electronic Green's function $G_\sigma(\mathbf{x}, \mathbf{x}', t, t')$. The equation reads [15]

$$G = G_0 + G_0 V_H G + G_0 \varphi G + i G_0 v_c \frac{\delta G}{\delta \varphi}, \tag{1}$$

where G_0 is the non-interacting Green's function, φ is a fictitious external perturbation that is set to zero at the end of the derivation, v_c is the bare Coulomb interaction, and all quantities are understood to be matrices in space, spin, and time. The Hartree potential V_H gives rise to screening to all orders. Spin only gives rise to a factor of 2, since we are interested here in non-magnetic systems where G is spin-diagonal.

2.1 Decoupling approximation for the Green's function

Linearizing V_H with respect to φ and assuming G and G^H diagonal on the same discrete basis yields a scalar equation for each matrix element $\mathcal{G} = G_{ii}$ which corresponds to a single state of the system [12,16]:

$$\begin{aligned}\mathcal{G}(t_1 t_2) = \mathcal{G}_H^0(t_1 t_2) + \mathcal{G}_H^0(t_1 t_3)\bar{\varphi}(t_3)\mathcal{G}(t_3 t_2) \\ + i\mathcal{G}_H^0(t_1 t_3)\mathcal{W}(t_3 t_4)\frac{\delta \mathcal{G}(t_3 t_2)}{\delta \bar{\varphi}(t_4)},\end{aligned} \tag{2}$$

where $\mathcal{G}_H^0$ is the Hartree Green's function in the limit of vanishing external potential; $\bar{\varphi} = \varepsilon^{-1}\varphi$ is the screened external perturbation potential;

$$\mathcal{W}(t_3 t_4) = \int drdr' |\phi(r)|^2 |\phi(r')|^2 W(rr' t_3 t_4) \tag{3}$$

is a diagonal matrix element of the screened Coulomb interaction W; ϕ is the single-particle wavefunction of the corresponding state; and ε^{-1} is the inverse microscopic dielectric function. It is worth noting that in equation (2) the approximation $\delta G/\delta\bar{\varphi} = GG$ – which corresponds to the Random-Phase Approximation (RPA) for the response to the screened external potential $\bar{\varphi}$ – gives back the GW approximation [3], which is hence included in the current approximation. The solution of equation (2) at vanishing φ, for a single occupied state, is

$$\mathcal{G}(t_1 t_2) = \mathcal{G}_H^0(t_1 t_2) \exp\left[-i\int_{t_1}^{t_2} dt' \int_{t'}^{t_2} dt'' \mathcal{W}(t't'')\right]. \tag{4}$$

We assume that $\mathcal{W}$ can be represented by a sum of N_p poles $\tilde{\omega}_j$ with strength λ_j, which is exact for infinite N_p:

$$\mathcal{W}(\tau) = \sum_j^{N_p} \lambda_j \left[e^{i\tilde{\omega}_j \tau}\theta(-\tau) + e^{-i\tilde{\omega}_j \tau}\theta(\tau)\right], \tag{5}$$

where $\tau = t - t'$. Using equation (5), the double integration of $\mathcal{W}$ in equation (4) is then analytically feasible. Once this is carried out, the matrix elements of the Green's function read

$$\mathcal{G}(\tau) = i\theta(-\tau)e^{-i(\epsilon + i\Gamma)\tau} \exp\left[\sum_j^{N_p} a_j (1 - e^{i\tilde{\omega}_j \tau})\right], \tag{6}$$

with $a_j = \lambda_j / \tilde{\omega}_j^2$. In equation (6), the first exponent $\epsilon + i\Gamma$ is the *complex* QP energy within the GW approximation. The GW correction to the Hartree energy naturally emerges from the integral of $\mathcal{W}$ in equation (4), provided that the same level of approximation is used for $\mathcal{W}$ in the GW self energy. The second exponential term provides for renormalization and formation of satellites at all orders. After having expanded and Fourier-transformed the latter, $A(\omega) = 1/\pi|\,\mathrm{Im}\mathcal{G}(\omega)|$ becomes

$$\begin{aligned} A(\omega) = \frac{\Gamma}{\pi} e^{-\sum_j^{N_p} a_j} \Bigg[& \frac{1}{(\omega - \epsilon)^2 + \Gamma^2} \\ & + \sum_j^{N_p} \frac{a_j}{(\omega - \epsilon + \tilde{\omega}_j)^2 + \Gamma^2} \\ & + \frac{1}{2} \sum_{jk}^{N_p} \frac{a_j a_k}{(\omega - \epsilon + \tilde{\omega}_j + \tilde{\omega}_k)^2 + \Gamma^2} \\ & + \frac{1}{6} \sum_{jkl}^{N_p} \frac{a_j a_k a_l}{(\omega - \epsilon + \tilde{\omega}_j + \tilde{\omega}_k + \tilde{\omega}_l)^2 + \Gamma^2} + \ldots \Bigg]. \end{aligned} \tag{7}$$

Equation (7) shows how the spectral function can be expanded as a sum of poles, which are regrouped here in different terms following the corresponding order. The zeroth order (first term) is the QP peak, centered at the QP energy ϵ. The following terms are centered at $\omega - n\tilde{\omega}_j$ (at order n, giving rise to the n-th satellite replica for that frequency) with a weight decreasing exponentially with n. In general, the weights a_j are of the order of $0.1/N_p$.

The electron energy-loss function of bulk silicon has a well-defined single-peaked shape, centered at 16.7 eV. This fact justifies the use of a single plasmon-pole model which is equivalent, in the above formulation, to the case $N_p = 1$.

2.2 Calculation of extrinsic losses and interference effects

In order to take the extrinsic and interference terms into account, we use the theoretical formalism of Hedin, Michiels, and Inglefield [6], which includes all three effects, i.e., intrinsic, extrinsic, and interference. In addition, the theory is based on a semi-infinite model of the system, and thus the satellite spectrum depends on the average distance traveled by the photo-electron through the surface. However, these calculations use a rather crude approximation for the valence electrons, treating them as localized states. The strategy is thus to use this complete model to calculate the extrinsic and interference terms only, replacing the intrinsic contribution with the more rigorous calculations detailed in the previous section. One might worry that the intrinsic spectrum would then not include effects due to the semi-infinite model. However, we find that the intrinsic spectrum is quite insensitive to distance from the surface. The theory accounts for the satellites in the PES spectrum in terms of a spectral function $A(\omega)$ of exponential form consistent with equation (7), which allows us to combine the two approaches. In this approach the photocurrent is given by

$$\langle J_k(\omega)\rangle = \sum_i |M_{ik_0}|^2 \int_0^\infty e^{-a} \int_{-\infty}^\infty e^{i(\omega_0 - \epsilon_k + \epsilon_i)t} \tag{8}$$

$$\times \exp\left[\int \gamma_{ik}(\omega)(e^{-i\omega t} - 1)\, d\omega\right] dt\, dz_c, \tag{9}$$

where

$$a \approx \int d\omega\, \gamma_{ik}(\omega) = 2z_c \mathrm{Im}\tilde{k} + a^i_{int}. \tag{10}$$

Here ω_0 is the photon-frequency, $k_0 = \sqrt{2(\omega_0 + \epsilon_i)}$ is the photo-electron momentum at threshold, and we have made the approximation that the matrix elements $M_{ik} = \langle i|d|k\rangle$ are roughly constant over the range of photo-electron energies of interest, i.e., from a few multiples of the plasmon energy below the photon energy to threshold where $\epsilon_k = \omega$. The function $\gamma_{ik}(\omega)$ characterizes the losses due to the excitation of single plasmons of energy $\omega_{\mathbf{q}}$ and can be split into intrinsic, extrinsic and interference contributions,

$$\gamma_{ik}(\omega) = \sum_{\mathbf{q}} |g_{\mathbf{q}}|^2 \delta(\omega - \omega_q) = \gamma_i^{int} + \gamma_k^{ext} + \gamma_{ik}^{inf}. \tag{11}$$

We calculate the extrinsic and interference terms by assuming that the intrinsic amplitude is independent of the initial (valence) state, which gives the amplitudes,

$$|g_{\mathbf{q}}| = \left| \frac{V^{\mathbf{q}}(z_c)}{\omega} + \frac{i}{\kappa} \int_{-\infty}^{z_c} e^{i(\tilde{k} - \kappa)(z - z_c)} V^{\mathbf{q}}(z) dz \right| \tag{12}$$

where the solid occupies the space $z > 0$. The first term gives the intrinsic amplitude, while the second term gives the extrinsic, and the cross terms give the interference, i.e.,

$$|g_q|^2 = |g_q^{\mathrm{int}}|^2 + |g_q^{\mathrm{ext}}|^2 + 2\mathrm{Re}[g_q^{\mathrm{int}} g_q^{\mathrm{ext}}]. \tag{13}$$

The complex wave numbers κ and $\tilde{k}$ are given by

$$\kappa = \sqrt{2(\omega_0 + \phi + \epsilon_F + i\Gamma(\omega + \epsilon_k)) - |\mathbf{Q} + \mathbf{K}|^2}, \tag{14}$$

$$\tilde{k} = \sqrt{k^2 + 2(\phi + \epsilon_F + i\Gamma(\epsilon_k)}, \tag{15}$$

and correspond to a time-inverted LEED state,

$$|\tilde{k}\rangle = e^{i\mathbf{K}\cdot\mathbf{R}} \left[\theta(z) e^{-i\tilde{k}^* z} + \theta(-z) e^{-ikz}\right]. \tag{16}$$

Here ϵ_F is the Fermi energy and ϕ is the work function. Further, bold capitals denote components of the vector perpendicular to the z direction (parallel to the surface). With the above definitions, $\epsilon_k = k^2$, and ω is measured relative to the valence binding energy so that the first detectable photo-electron comes at $\omega = \epsilon_k = 0$.

In order to evaluate the relative weights of various contributions to the PES signal, we use the Inglesfield fluctuation potential inside the solid (contributions outside being negligible) [6]. We then calculate the weight of the extrinsic and interference $a^{extinf}(\omega_0) = a^{ext}(\omega_0) + a^{inf}(\omega_0)$

Table 1. Values of the correction term a^{extinf} including extrinsic losses and interference effects and relative width (inverse lifetime) η for a set of photon energies ω_0.

ω_0 (eV)	a^{extinf}	η
200	0.432	2.882
480	0.479	1.085
800	0.530	0.570
1200	0.568	0.341
2000	0.609	0.178
5000	0.669	0.066
10000	0.703	0.027

contributions to the PES due to plasmons of energy $\omega_p = 16.7$ eV, at a given photon energy ω_0, i.e.,

$$a^{\text{extinf}}(\omega_0) = \int dk \gamma_k^{\text{ext}}(\omega_0) + \gamma_k^{\text{inf}}(\omega_0). \tag{17}$$

We incorporate these contributions in our total spectral function correcting the intrinsic contribution of Section 2.1 with the addition of $a^{extinf}(\omega_0)$ i.e.,

$$\bar{a}_i = a_i^{int} + a^{extinf}(\omega_0), \tag{18}$$

where i denotes the valence state, a_i^{int} is the intrinsic weight of the pole as it appears in equation (7) for the case $N_p = 1$. We can also calculate the width of the extrinsic + interference satellites and account for this by replacing the widths Γ in equation (7), i.e.

$$\Gamma \rightarrow \Gamma + n\,\eta(\omega_0), \tag{19}$$

η being the width (related to the dispersion of the plasmon) of the extrinsic plasmon peak at a given photon energy ω_0 and n the number of plasmon excitations involved, i.e. the order of the expansion in equation (7). Values of ω_0, a^{extinf} and η are listed in Table 1.

2.3 Additional effects

2.3.1 Lifetime of intrinsic plasmons

We must include a correction for the finite lifetime of intrinsic plasmons, which is infinite in (7) because of the plasmon-pole model we are using for the intrinsic part. Therefore, an additional width of 1.5 eV [17] is added to the inverse lifetime of extrinsic plasmons η.

2.3.2 Photon cross sections

Photon cross sections are taken from references [18,19]. For each element, the tables give the relative photon cross section of the atomic orbitals, calculated within the Hartree-Fock approximation. We have to use the atomic data for bulk silicon; since we are in a solid, the atomic character is mixed. The four valence bands of silicon contain two s electrons and two p electrons. The character of each band is calculated by projecting the wavefunctions onto spherical harmonics inside a sphere centered on the Si ion. The s and p character of each band sum up to one. We have then the following values:

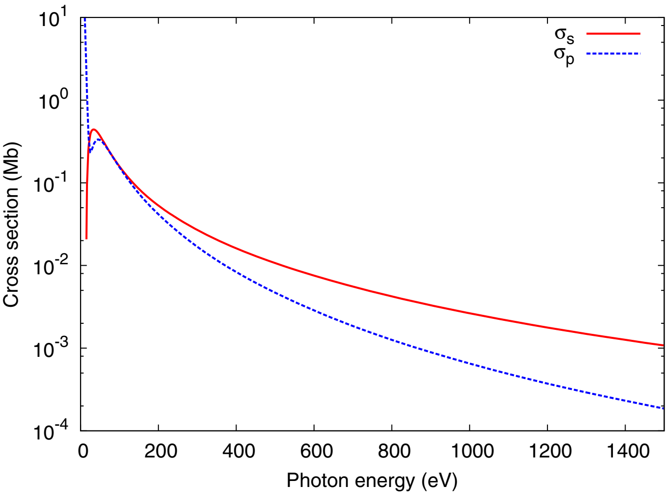

Fig. 1. (Color online) Photon cross sections, from reference [18]. Red solid line shows the values for the 3s electrons, while the blue dashed line shows the 3p electrons cross sections.

Band	#1	#2	#3	#4
s-type	0.95	0.75	0.25	0.05
p-type	0.05	0.25	0.75	0.95

In this picture, the relative weight of a photoemission peak will be the consequence of the s_k and/or p_k character of the corresponding state k. To include this effect in the spectral function, we can define an effective $\tilde{A}$ so that

$$\tilde{A}(\omega) = \sum_k (s_k\sigma_s + p_k\sigma_p)A_k(\omega), \tag{20}$$

where A_k is the (intrinsic or corrected) spectral function of a single state k and σ_s and σ_p are the photon cross sections for s and p electrons, tabulated in references [18,19] and shown in Figure 1 up to 1500 eV. The inclusion of cross-section effects is very important to reproduce the relative weight of s and p peaks in the photoemission spectrum (which can differ by an order of magnitude) and the respective changes at different photon energies.

2.3.3 Secondary electrons

The background of secondary electrons is calculated using the effective intrinsic spectral function $\tilde{A}(\omega)$, assuming that each peak in the intrinsic spectrum produces a constant flux of secondary electrons (i.e. a step function) at all binding energies greater than the quasiparticle energy ϵ. This is commonly known as a *Shirley* background [20]. The calculation of the background is achieved by the following integration of $\tilde{A}(\omega)$:

$$\mathcal{B}(\omega) = \int_\omega^\mu d\omega' \tilde{A}(\omega'), \tag{21}$$

where $\mathcal{B}$ is the background of secondary electrons. The final quantity that has to be compared with experimental data is given by the photocurrent $J(\omega)$ defined as:

$$J(\omega) = \alpha \tilde{A}(\omega) + \beta \mathcal{B}(\omega), \tag{22}$$

where α and β are two parameters that must be fixed to match the signal/background ratio in the experimental data. β is to be determined using the high binding-energy limit (where $\tilde{A}(\omega) \sim 0$) and then we fix α so as to match the QP peak intensity. The calculated background could also be subtracted from the experimental curves, in case one wishes e.g. to evaluate the intensity of satellites (see below).

3 Experimental setup

Valence PES measurements were performed at the UHV photoemission experimental station of the TEMPO beamline [21] at the SOLEIL synchrotron radiation source. Linearly polarized photons from the Apple II type Insertion Device (HU44) were selected in energy using a high resolution plane grating monochromator with a resolving power $E/\Delta E = 5000$. The end-station chamber (base pressure 10^{-10} mbar) is equipped with a modified SCIENTA-200 electron analyzer with a delay-line 2D detector which optimizes the detection linearity and signal/background ratio [22]. The overall energy resolution was better than 200 meV. The photon beam impinges on the sample at an angle of 43°, and photoelectrons were detected around the sample surface normal with an angular acceptance of ±6°. A doped n^+-type Si(001) wafer ($N_D \simeq 2 \times 10^{-18} P$ atoms/cm^3) was cleaned from the native oxide by flash annealing at 1100 °C after prolonged degassing at 600 °C in ultra-high vacuum. The silicon surface annealed at 300 °C to prevent surface etching was then hydrogenated in a partial pressure of activated hydrogen about 2×10^{-8} mbar for 20 min. At 800 eV kinetic energy the Si Brillouin zone (BZ) is observed with an emission angle slightly smaller than 5°. The Fermi level was obtained by measuring a clean Au(111) surface. The measured photoemission map at 800 eV was integrated over the spectral intensity originated by two BZ. For lower photon energies it was not possible to have a complete integration of the BZ. Considering the ratio between satellites and QP peaks – which is a key quantity for our analysis – independent of the integration on the BZ (as our theory assumes), justifies the use of photon energies lower than 800 eV for comparison with theory.

4 Results

We have measured PES data for several photon energies between 200 and 800 eV. Using our procedure we have calculated the photoemission spectra for a range of photon energies between 200 eV and 10 keV. A standard *GW* calculation was performed using the ABINIT code [23]. The *GW* calculation was used to evaluate the parameters of equation (7), under the assumption that $\mathrm{Im}W \sim 1/\pi\, \mathrm{Im}\Sigma$ [24], hence using an RPA screening. We calculated the correction paramenters for extrinsic losses and interference effects as described earlier in Section 2.2, and eventually included cross-section effects as in equation (20). The graph in Figure 2 shows the calculated photoemission spectra $\tilde{A}(\omega)$ for a number of selected photon energies, from 200 eV to 10 keV. In this figure the intensity of the curves has been scaled so that the spectra match in the QP region. Varying the photon energy, there is a small change in the QP part of the spectrum – between −15 and 0 eV from the Fermi energy – due to cross-section effects[1]. The most apparent change is in the satellite part, i.e. below −15 eV, where three satellites are visible. Our calculations show that with increasing photon energy the satellites have a tendency to show more structures. More importantly, the relative weight of satellites increases as the photon energy increases. This trend is the same as the one found in the experimental data, as reported in Figure 3. In this figure we also include data from reference [25]. We assume a complete integration of the BZ. The ratio between the weight of the first satellite – taken between −33 and −15 eV – and the QP peaks has been calculated, both in the theoretical and experimental case, evaluating the integral under the curves. The calculated background has been removed from the experimental curves before the evaluation of the integrals. The set of experimental values is small with respect to what would be needed to perform an exhaustive comparison with theory. For smaller photon energies (between 200 and 400 eV), the ratios are systematically overestimated. Partial integration of the BZ, caused by the low photon energy used, is probably the cause of the overestimation

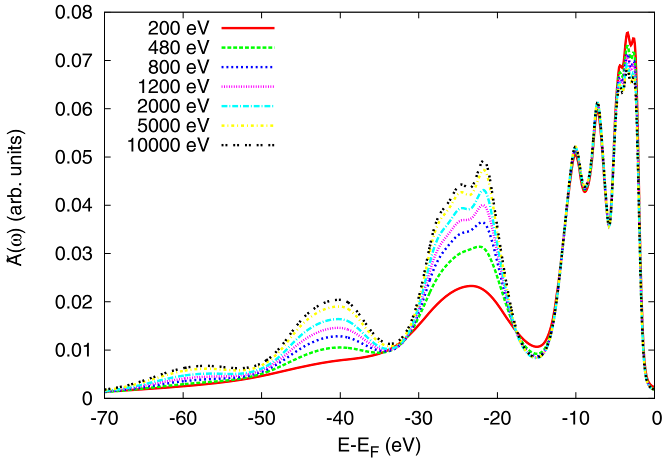

Fig. 2. (Color online) Calculated spectrum $\tilde{A}(\omega)$ for several photon energies between 200 eV and 10 keV. The spectra include the effect of cross sections and extrinsic losses. The curve intensities are aligned to match in the QP region, between −15 and 0 eV, to highlight the relative change of the satellite spectral weight, i.e. below −15 eV. The Fermi energy is at 0 eV.

---

[1] Additional variations related to different integrations of the BZ (found in experiment) are here neglected.

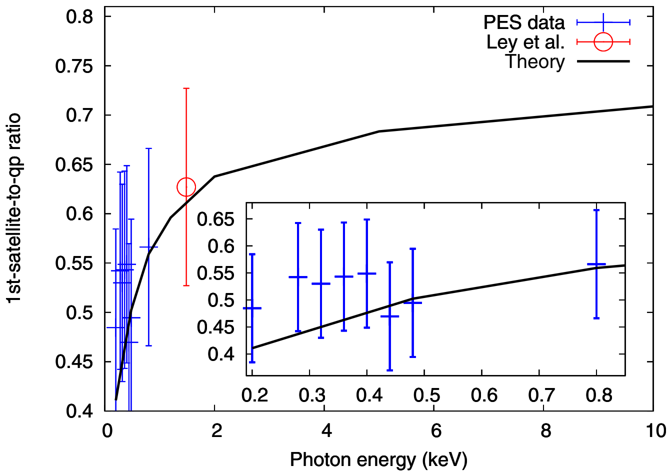

Fig. 3. (Color online) Intensity ratio between the first satellite and the QP part of the spectrum as a function of the photon energy. Our experimental data (blue crosses) are compared to theoretical calculation (black solid line). An additional point (red circle) taken from [25] has also been included for comparison. The inset shows a detail of the same plot.

of the satellite/QP ratio in these cases. In fact, the lower the photon energy, the smaller the portion of BZ measured for the same emission angle [1]. In our theory, we assume that QP states do not mix and each QP state has its own plasmons. This is a good approximation if done to evaluate a total spectrum, which is the result of a sum over all the states, i.e. over the whole BZ. Moreover our background is calculated assuming a uniform integral over the full BZ. Taken into account this and the inherent difficulty to precisely determine the points that define the QP region and the first satellite, our experimental points have an absolute error of ±0.1.

Theory allowed us to calculate spectra at high values of photon energies that we could not reach in experiment. Figure 3 shows how the satellite/QP ratio increases significantly from 0 up to 1−2 keV and how above 5−10 keV there is a sort of saturation effect. However, the satellite shape continues to sharpen (show more structure) as the photon energy increases. The origin of this sharpening is to be found in the width of extrinsic plasmon peak (see Tab. 1), which decreases as the photon energy increases and changes more than the intensity of plasmons, hence being the crucial quantity in the equation that determines most changes in the shape of satellites, as it appears from our analysis. The behavior of the satellite/QP ratio is more complicated due to the inelastic mean free path (IMFP) of the photoelectron, which increases with energy. This increase in IMFP gives rise to two competing effects: (i) the increased IMFP allows electrons from deeper in the material to escape, which increases the strenth of the extrinsic plasmon peak; (ii) the IMFP is (inversely) a measure of the probability of scattering plasmons, thus a larger IMFP means that the contribution to the plasmon peak from each hole is lowered.

5 Conclusion

In conclusion we have shown how to describe ab initio satellites in valence-band photoemission spectroscopy. Our method is able to describe multiple excitation of plasmons including lifetimes. This gives an accurate description of the intrinsic part of the spectrum. A number of effects that are not removable from experiment have to be added to the theoretical calculations to obtain an appropriate comparison with experimental data. The photon-energy dependence of satellites was studied including, in the spectral function $A(\omega)$, correcting terms for the intensity and width of extrinsic plasmon peaks, also taking into account interference effects. We compared the theoretical results with our experimental photoemission data, taken at several photon energies, between 200 and 800 eV. Using our theoretical approach, we could give a prediction on a larger range of energies. We evaluated the ratio between the weight of the first satellite and of the QP peaks. Satellites grow bigger with respect to QP peaks as the photon energy increases, until the sudden limit is reached, above 5−10 keV. The measured data are in agreement with the theoretical curve. The main physical process behind the increase of satellite weight appears to be the variation of the IMFP of photoelectrons. The evaluation of extrinsic and interference effects could be done in a relatively straightforward way thanks to the formulation we introduced for the Green's function and the spectral function. The same would not have been possible if one stayed within the *GW* approximation, where spurious plasmaron excitations spoil the satellite spectra [12] and multiple satellites are absent.

We acknowledge ANR (project #: NT09-610745) for funding, IDRIS and CCRT for computer time (GENCI-544 project). J.J. Rehr and J.J. Kas acknowledge the support of US Department of Energy, Basic Energy Sciences, Grant No. DE-FG03-97ER45623.

References

1. A. Damascelli, Z. Hussain, Z.-X. Shen, Rev. Mod. Phys. **75**, 473 (2003)
2. A.L. Fetter, J.D. Walecka, *Quantum theory of Many-Particle Systems* (MacGraw-Hill, New York, 1971)
3. L. Hedin, Phys. Rev. **139**, A796 (1965)
4. W. Aulbur, L. Jonsson, J. Wilkins, Solid State Phys. **54**, 1 (2000)
5. F. Aryasetiawan, O. Gunnarsson, Rep. Prog. Phys. **61**, 237 (1998)
6. L. Hedin, J. Michiels, J. Inglesfield, Phys. Rev. B **58**, 15565 (1998)
7. F. Bechstedt, *Principles of Surface Physics* (Springer, 2003), Chap. 5, pp. 199–201
8. F. Offi et al., Phys. Rev. B **76**, 085422 (2007)
9. L. Hedin, J. Phys.: Condens. Matter **11**, R489 (1999)
10. C.-O. Almbladh, L. Hedin, *Handbook on Synchrotron Radiation* (North-Holland, Amsterdam, 1983), Chap. 8
11. A.S. Kheifets et al., Phys. Rev. B **68**, 233205 (2003)

12. M. Guzzo, G. Lani, F. Sottile, P. Romaniello, M. Gatti, J.J. Kas, J.J. Rehr, M.G. Silly, F. Sirotti, L. Reining, Phys. Rev. Lett. **107**, 166401 (2011)
13. C.N. Berglund, W.E. Spicer, Phys. Rev. **136**, A1030 (1964)
14. F. Bechstedt, K. Tenelsen, B. Adolph, R. DelSole, Phys. Rev. Lett. **78**, 1528 (1997)
15. L.P. Kadanoff, G. Baym, *Quantum Statistical Mechanics* (W.A. Benjamin Inc., New York 1964)
16. G. Lani, P. Romaniello, L. Reining, New J. Phys. **14**, 013056 (2012)
17. B. Arnaud, S. Lebègue, M. Alouani, Phys. Rev. B **71**, 035308 (2005)
18. J. Yeh, I. Lindau, At. Data Nucl. Data Tables **32**, 1 (1985)
19. J.H. Scofield, *Theoretical photoionization cross sections from 1 to 1500 kev*, Tech. Rep. UCRL-51326, Lawrence Livermore National Laboratory, 1973
20. D.A. Shirley, Phys. Rev. B **5**, 4709 (1972)
21. F. Polack et al., AIP Conf. Proc. **1234**, 185 (2011)
22. N. Bergeard et al., J. Synch. Rad. **18**, 245 (2011)
23. X. Gonze, G.-M. Rignanese, M. Verstraete, J.-M. Beuken, Y. Pouillon, R. Caracas, F. Jollet, M. Torrent, G. Zerah, M. Mikami, P. Ghosez, M. Veithen, J.-Y. Raty, V. Olevano, F. Bruneval, L. Reining, R. Godby, G. Onida, D. Hamann, D. Allan, Z. Kristallogr. **220**, 558 (2005)
24. F. Aryasetiawan, L. Hedin, K. Karlsson, Phys. Rev. Lett. **77**, 2268 (1996)
25. L. Ley, S. Kowalczyk, R. Pollak, D.A. Shirley, Phys. Rev. Lett. **29**, 1088 (1972)

PHYSICAL REVIEW B **89**, 085425 (2014)

Multiple satellites in materials with complex plasmon spectra: From graphite to graphene

Matteo Guzzo,[1,2,*] Joshua J. Kas,[3] Lorenzo Sponza,[1,2] Christine Giorgetti,[1,2] Francesco Sottile,[1,2] Debora Pierucci,[4]
Mathieu G. Silly,[4] Fausto Sirotti,[4] John J. Rehr,[2,3] and Lucia Reining[1,2,†]
[1]*Laboratoire des Solides Irradiés, École Polytechnique, CNRS, CEA-DSM, F-91128 Palaiseau, France*
[2]*European Theoretical Spectroscopy Facility (ETSF)*
[3]*Department of Physics, University of Washington, Seattle, Washington 98195, USA*
[4]*Synchrotron-SOLEIL, BP 48, Saint-Aubin, F91192 Gif sur Yvette CEDEX, France*
(Received 15 February 2013; revised manuscript received 23 January 2014; published 27 February 2014)

The photoemission spectrum of graphite is still debated. To help resolve this issue, we present photoemission measurements at high photon energy and analyze the results using a Green's function approach that takes into account the full complexity of the loss spectrum. Our measured data show multiple satellite replicas. We demonstrate that these satellites are of intrinsic origin, enhanced by extrinsic losses. The dominating satellite is due to the $\pi + \sigma$ plasmon of graphite, whereas the π plasmon creates a tail on the high-binding energy side of the quasiparticle peak. The interplay between the two plasmons leads to energy shifts, broadening, and additional peaks in the satellite spectrum. We also predict the spectral changes in the transition from graphite towards graphene.

DOI: 10.1103/PhysRevB.89.085425 PACS number(s): 73.22.Pr, 71.45.Gm, 71.10.−w, 71.15.Qe

I. INTRODUCTION

Photoemission is a prominent experimental tool to access the electronic structure of materials. Angular-resolved photoelectron spectroscopy (ARPES) is frequently used to extract the band structure and quasiparticle (QP) lifetimes of a large variety of systems [1]. However, in a photoemission spectrum, besides the QP peaks and incoherent background, satellite peaks often appear. In the intrinsic spectral function, within the three-step model [2], these satellites can be understood in terms of coupling of a QP to additional excitations of the system.

Their nature is often debated. In simple metals plasmon satellite replicas are observed [3], but it is difficult to discern experimentally to which extent these are *intrinsic* features [4], or due to losses of the outgoing photoelectron (called *extrinsic*). In nickel, the satellite at 6 eV below the QP peak cannot be explained with the plasmon spectrum, but is due to a bound hole-hole state [5,6]. Recently a satellite in doped graphene was interpreted as a *plasmaron*, a strongly coupled electron-plasmon excitation [7]. In $3d$ and $4f$ systems, satellites have been ascribed to strong electron-electron interaction within a Mott-Hubbard picture [8]. In other materials, e.g., graphite, the very existence of intrinsic satellite features has been questioned. In this system observed valence-band satellite structures have been attributed to extrinsic losses and subtracted from the measured spectrum [9,10]. These debates, even for supposedly simple materials, are in part due to the lack of a widely applicable theoretical approach for the description of satellites. *Ab initio* calculations typically ignore satellites and concentrate on QP properties, often using the GW approximation for the self-energy in the framework of many-body perturbation theory [11]. In this approach the dynamically screened Coulomb interaction W that multiplies the one-body Green's function G contains plasmon excitations that may lead to satellites. However, GW is believed to fail in predicting the satellite spectra [4], although it performs well for QP energies. Satellites are rarely computed, so that much of the information obtained from experiment is wasted. Our aim is to push this limit.

In the present work we focus on plasmon satellites, which occur in most materials, from metals to insulators. Plasmons lead to multiple satellites, forming a decaying series of peaks below the QP. These structures can be explained with a spectral function derived from an exponential (also referred to as *cumulant*) form of the one-particle Green's function, itself a solution of an electron-boson coupling model [4,12,13]. In the present case the plasmon plays the role of the boson, though the cumulant form is more general. The plasmon contribution has been derived in several ways, e.g., starting from GW [4,13,14], or as a linear response contribution of the Hartree potential [15]. The combination of the cumulant solution with the GW calculation (GW + C) and the same method with additional extrinsic and interference contributions (GW + C*) yielded excellent agreement with experiment for bulk silicon [15,16]. The GW approximation alone, instead, gave rise to a spurious plasmaron solution in silicon, similarly to the homogeneous electron gas [17–19]. Hence, GW + C* appears to be the method of choice for plasmon satellites.

In this article we address the layered material graphite and its building block graphene. We generalize the approach used in Refs. [15,16] that was based on the use of a single plasmon pole approximation for W, to materials with an arbitrarily complex excitation spectrum. Our computational results are compared to new bulk sensitive photoemission data for graphite. The excellent agreement between theory and experiment allows us to address several important questions: (i) does graphite have *intrinsic* satellites? (ii) Does the GW approximation create a spurious plasmaron also in this material? (iii) Are there any new effects in the XPS spectrum caused by the more complex plasmon spectrum, and in particular by the existence of two main plasmon peaks? Finally, it allows us to make predictions for the satellite structure in graphene.

---

[*] matteo.guzzo@polytechnique.edu; present address: Physics Department, Humboldt-Universität zu Berlin, Zum Großen Windkanal 6, D-12489 Berlin, Germany.

[†] lucia.reining@polytechnique.fr

We start describing the experimental setup for the XPS measurements and the computational details of the calculations in Sec. II. Results are discussed in Sec. III. We analyze the shortcomings of the GW approximation in graphite and discuss the absence of a plasmaron in this particular case in Sec. III B. We give the interpretation of the XPS spectrum of graphite on the basis of our $\mathrm{GW}+\mathrm{C}^*$ calculations in Sec. III C. Then we calculate the $\mathrm{GW}+\mathrm{C}^*$ spectral function of undoped graphene showing how and why this differs from its graphite counterpart in Sec. III D. Conclusions are drawn in Sec. IV.

II. TECHNICAL DETAILS

A. Experimental setup

ARPES measurements were performed at the UHV photoemission station of the TEMPO beamline [20] at the SOLEIL synchrotron radiation source. Linearly polarized photons from the Apple II type Insertion Device (HU44) were selected in energy using a high resolution plane grating monochromator with a resolving power $E/\Delta E = 5000$. The end-station chamber (base pressure 10^{-10} mbar) is equipped with a modified SCIENTA-2002 electron analyzer with a delay-line 2D detector which optimizes the detection linearity and signal/background ratio [21]. The overall energy resolution was better than 200 meV. The photon beam impinged on the sample at an angle of 43°, and photoelectrons were detected on an angular range of 12°. Highly oriented pyrolytic graphite (HOPG) was cleaved in the introduction stage of the UHV system exposing a new surface immediately before the transfer to UHV. At 800 eV kinetic energy the Brillouin zone (BZ) is observed with an emission angle of about 8°. The measured photoemission map was integrated over the spectral intensity originated by one BZ. The Fermi level was obtained by measuring a clean Au(111) surface.

B. Computational details

We performed *ab initio* calculations using a plane-wave basis. We used the ABINIT code for all ground-state and GW calculations [22], using experimental values for lattice constants. The Brillouin zone of graphite was sampled using a $9 \times 9 \times 2$ Monkhorst-Pack grid [23], yielding 162 points in the full BZ. We have used Troullier-Martins norm-conserving pseudopotentials [24] available in the ABINIT code library. The plane-wave cutoff for the LDA ground-state calculation was fixed at 30 Ha. The full frequency dependence of the self-energy for the eight valence bands was calculated using a contour-deformation technique, and with partial self-consistency, namely on the quasiparticle energies in the Green's function (GW_0 calculations). W was calculated including 160 bands and using 997 plane waves for the wave functions. The dielectric matrix was calculated using 287 G vectors, 4 frequencies on the imaginary axis, and 60 frequencies on the real axis, with a maximum value fixed at 2 Ha. The self-energy was calculated using 250 bands, 1385 plane waves for the wave functions, 287 G vectors for the dielectric matrix, and 585 plane waves for the exchange term. The self-energy of graphite was calculated for 50 frequencies/Ha for a range of 65 eV below the Fermi energy.

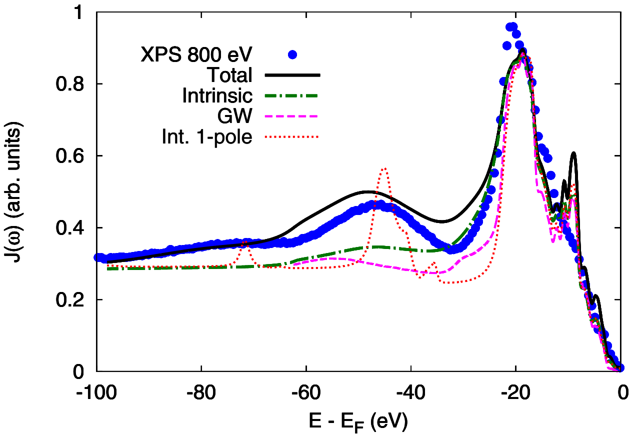

FIG. 1. (Color online) XPS spectrum of HOPG at 800 eV photon energy. The experimental data collected at normal emission (blue dots) are compared to the spectral function $A(\omega)$ calculated from GW (magenta dashed line) and from a multipole version of Eq. (1) (green dot-dashed line). On top of the latter the black solid line also includes extrinsic and interference effects. The result for $A(\omega)$ in the single plasmon pole approximation ($N_p = 1$) for Eq. (1) (red dotted line) is shown for comparison. All curves are scaled to match the intensity of the main QP peak at -20 eV. All theoretical spectra contain photoabsorption cross sections, the calculated secondary electron background, and 0.4 eV Gaussian broadening to account for finite BZ sampling and experimental resolution.

The GW_0 spectral function of graphene was calculated using equivalent parameters on a slightly different k-point grid ($12 \times 12 \times 1$). We set up a supercell in real space with 38 bohrs of vacuum on the z direction.

III. RESULTS

A. Experiment

The experimental result is shown by the blue dots in Fig. 1. The QP band structure is found between the Fermi level and 25 eV binding energy. A tail extends down to about -30 eV, followed by a broad satellite in the range [-65;-30] eV and a washed out structure below -65 eV. The average distance between the main satellite and the QP region is close to the energy of the $\pi + \sigma$ plasmon ($\sim$27 eV) in the loss spectrum of graphite. There is no clear structure that one could assign to the π plasmon (7 eV in the loss spectrum). Overall there is too much broadening to draw reliable conclusions only from the data. In previous experimental studies [10,25], features beyond the QP peaks have been attributed to extrinsic background effects and subtracted from the raw data in order to obtain an "intrinsic" spectrum. Our work suggests a revision of this hypothesis, as we show below.

B. Graphite–GW

We first look at the results of a GW calculation. The full frequency dependence of the self-energy is calculated with the ABINIT code [22], using a contour-deformation technique. The calculation involves a partial degree of self-consistency, namely on the real part of the QP energies, while W is kept fixed. The total GW spectral function (magenta dashed curve

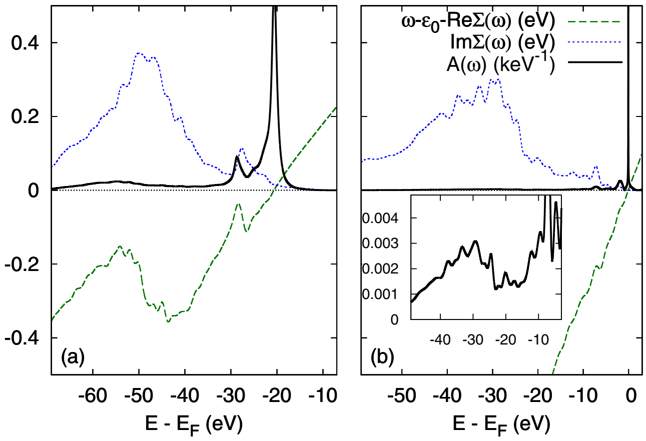

FIG. 2. (Color online) GW spectral function $A(\omega)$ (solid black line) with imaginary (dotted blue line) and shifted real (dashed green line) parts of the GW self-energy. (a) Lowest valence state at $k = (0.0,0.0,0.25)$. (b) Highest valence state at $k = (0.33,0.33,0.25)$. Inset: Zoom on $A(\omega)$.

in Fig. 1) well describes the QP part of the spectrum.[1] Moreover, it exhibits a small bump due to the π plasmon that may explain the tail located around -25 eV in the experiment and a second structure in correspondence with the first experimental satellite that can be attributed to the $\pi+\sigma$ plasmon. Overall the GW result is sufficiently good for a qualitative discussion, in striking contrast to, e.g., the case of silicon.

In order to understand this point, and to exclude a simple coincidence, we analyze the GW self-energy in a single plasmon-pole model.[2] The correlation part of the self-energy for a hole is then approximatively $\Sigma_c(\omega) = \lambda/[\omega - \epsilon + \omega_p - i\gamma]$, with γ, ω_p, and λ, respectively, the inverse lifetime, the plasmon frequency, and the strength; ϵ is the self-consistently calculated QP energy. This model describes the GW self-energy around each plasmon satellite, as one can see by qualitative comparison with the full *ab initio* calculation: The latter is shown in Fig. 2.

Figures 2(a) and 2(b) show the imaginary ImΣ (blue dotted line) and shifted real (green dashed line) $\omega - \varepsilon_0 - \mathrm{Re}\Sigma(\omega)$ parts of the *ab initio* GW self-energy for two valence states (ε_0 is the single-particle energy). The imaginary parts exhibit two structures, associated with the π and $\pi+\sigma$ plasmons, and the real parts have the dispersion resulting from the Kramers-Kronig relation. The satellites in the spectral function (black solid line) are in correspondence with the local maxima $\omega_{\max}$ of the real part of the self-energy.

To first order in γ, the model yields $\omega_{\max} \approx \epsilon - \omega_p - \gamma$: The GW satellites are close to the expected position $\epsilon - \omega_p$. For larger values of γ, the shift towards larger binding energy introduced by the GW approximation becomes significant. This explains the *quantitative* discrepancy with the experimental positions, as observed in Fig. 1. Still, the origin of the plasmon satellite remains unchanged. Instead, the model predicts that the spectrum becomes *qualitatively* worse when the oscillation in the real-part term is so strong that the curve crosses zero around $\omega_{\max}$: The satellite position is then no longer determined by $\omega_{\max}$, but by the left zero-crossing point, analogously to the QP. This crossing leads to a sharp peak, the so-called *plasmaron*, and is a spurious effect of the GW approximation [19]. The plasmaron spoils the satellite spectra of silicon [15] and the homogeneous electron gas, and is the origin for the bad reputation of GW satellites. Our model shows that such a crossing occurs for $\lambda > 2\gamma\omega_p$: It is favored by a large plasmon intensity and coupling, a small plasmon energy, and small broadening. This condition is not fulfilled in graphite: The π plasmon has small intensity, and the intense $\pi+\sigma$ plasmon has large broadening. This explains why GWA can be used in graphite to analyze plasmon satellites, contrary, e.g., to the case of silicon.

However, the remaining discrepancy still does not allow definite conclusions. It is hence important to compare to the more advanced GW + C*.

C. Graphite–GW + C*

We have first applied the single plasmon pole model as used in Refs. [15,16], reproducing the dominant $\pi+\sigma$ plasmon. The resulting intrinsic GW + C spectral function (red dotted curve in Fig. 1) shows two satellites at -50 and -75 eV, in very good correspondence with the experimental ones. They are however too sharp, and the tail on the QP peak is missing, contrary to the GW result, evaluated with the full energy dependence of W. We therefore include the full W also in GW + C, by adopting a multipole representation with a number of poles N_p [16,26]. The positions ω_j and strengths a_j are fitted to the results of a GW calculation [15,16].

The final results presented here were calculated using $N_p = 150$. However, already $N_p = 2$ (one pole for the π and $\pi+\sigma$ plasmon, respectively) represents the main features, and it eases the interpretation. For a given state, the spectral function $A(\omega) = 1/\pi|\,\mathrm{Im}G(\omega)|$ then becomes

$$
\begin{aligned}
A(\omega) = \frac{\Gamma}{\pi} e^{-(a_1+a_2)}\Bigg[&\frac{1}{(\omega-\epsilon)^2+\Gamma^2} + \frac{a_1}{(\omega-\epsilon+\omega_1)^2+\Gamma^2} \\
&+ \frac{a_2}{(\omega-\epsilon+\omega_2)^2+\Gamma^2} + \frac{1}{2}\frac{a_1^2}{(\omega-\epsilon+2\omega_1)^2+\Gamma^2} \\
&+ \frac{1}{2}\frac{a_2^2}{(\omega-\epsilon+2\omega_2)^2+\Gamma^2} \\
&+ \frac{a_1 a_2}{(\omega-\epsilon+\omega_1+\omega_2)^2+\Gamma^2} + \cdots\Bigg],
\end{aligned}
\tag{1}
$$

where $\epsilon + i\Gamma$ is the QP energy including lifetime broadening. The a_j and ω_j are the intensities and frequencies, respectively, associated with the plasmons. The spectral function shows a peak at the QP energy ϵ, followed by a series of satellite peaks. Their distance from the QP peak corresponds to sums of plasmon pole energies; for a peak of order n, one finds peaks at a distance of n (equal or different) plasmon energies from ϵ. The weight of each peak is the product of the corresponding a_j and a prefactor due to the expansion.

---

[1] The QP peak at -10 eV is too sharp, which may be due to the approximate inclusion of cross-section effects and to domains in the sample.

[2] The energetic distance of the two plasmons in graphite is large enough to qualitatively justify such a simplification for the present discussion.

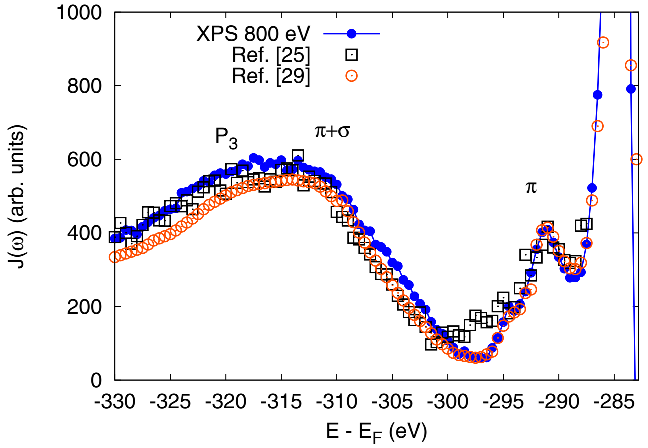

FIG. 3. (Color online) C 1s XPS spectrum of HOPG at 800 eV photon energy as measured in the present work (blue line with points), Ref. [25] (black squares), and in Ref. [27] (orange circles). Signatures of the π and $\pi + \sigma$ plasmons are clearly visible, as well as the feature termed P_3 in Refs. [25,27].

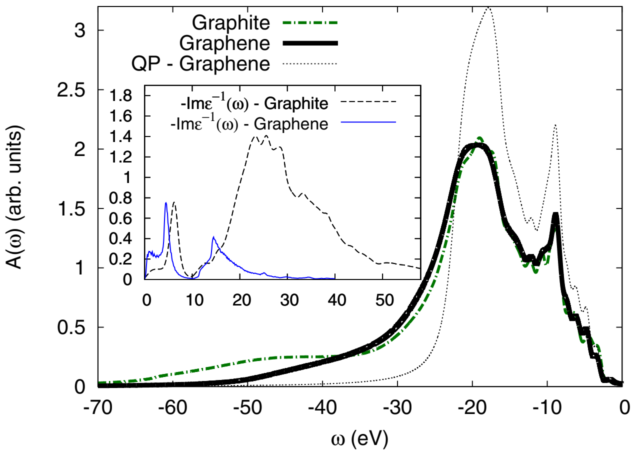

FIG. 4. (Color online) Comparison of graphite (dot-dashed green line) and graphene (solid black line) spectral functions using GW + C. The QP part of graphene (dotted black line) is reported for comparison. The QP and satellite tail at −30 eV do not change going from graphite to graphene, while most of the satellite weight below −40 eV disappears. This change stems from the differences in the loss functions. Inset: The calculated loss function $-\mathrm{Im}\,[\varepsilon^{-1}]$ (arbitrary units vs eV) of graphite (dashed black line) is compared to graphene (solid blue line). The curves are scaled to match the intensity of the π plasmon peak.

Equation (1) yields a first decaying series of plasmon satellites at a distance from the QP peak of multiples of ω_1, and a second series from ω_2. Moreover, a new series of multiple satellites results from the sum of multiples of ω_1 and ω_2, with the smallest being $\omega_1 + \omega_2$; the intensity of this peak is proportional to $a_1 a_2$. It is significantly more intense than the smaller second-order peak of the two because $a_1 a_2 > a_1^2/2$ for $a_1 < 2a_2$. Higher orders form additional structures centered at $n\omega_1 + m\omega_2$ with intensity $na_1 m a_2$. Since these mixed peaks have no one-to-one correspondence with the loss spectrum, their interpretation needs the support of theory.

The resulting spectral function $A(\omega)$ (green dot-dashed curve in Fig. 1), calculated for $N_p = 150$, shows the closest agreement in peak positions with the experimental result, much better than both the GW and the single pole ones. The tail below the QP region is well reproduced, the first satellite is in the correct position, and there is significant broadening as found in experiment. The second satellite at −75 eV is washed out. Contrary to a previous hypothesis, at least the first-order part of the satellite spectrum of graphite has hence a significant intrinsic contribution. To further add extrinsic and interference contributions, following [2,16], we renormalize the coefficients a_j and add a lifetime broadening to the plasmon energies. All parameters are calculated, not fitted, for 800 eV photon energy. We also include in all spectra the calculated secondary electron background and cross sections as described in Ref. [16]. The GW + C* result (black continuous curve in Fig. 1) is in excellent agreement with experiment, confirming the validity of the approach and the resulting analysis.

Satellites are resolved especially well in core-level spectra. Figure 3 shows our measured carbon 1s spectrum together with previous experimental results [25,27]. Both the signature of the π plasmon and the presence of at least one additional structure on the $\pi + \sigma$ plasmon satellite are clearly visible. The additional structure has been termed P_3, and measured in various carbon based materials [25] (see also, e.g., [27]), but could never be explained to our knowledge. However, for all measured materials it appears to be situated approximatively at the sum of the materials-dependent energies of the first two main plasmon peaks [25]. We can therefore identify it with the the $\omega_1 + \omega_2$ peak predicted by our Eq. (1).

The superposition of states in the valence broadens the spectrum, so that the π plasmon satellite close to the QP only shows up as a tail. Moreover, the $\omega_1 + \omega_2$ peak on the $\pi + \sigma$ satellite cannot be resolved. However, the position of the center of mass of the $\pi + \sigma$ satellite in the full spectrum in Fig. 1 shows a shift of ∼2 eV to higher binding energy as compared to the single pole calculation, which can be ascribed to the $\omega_1 + \omega_2$ contribution (see the Appendix for quantitative details). We can conclude that this mixed term leads in graphite to a shift of the main valence plasmon satellite and to an additional broadening. It contributes to the excellent agreement between our final result (black continuous curve) and experiment. Thus the approach allows us to fully describe and understand the XPS of graphite and to conclude the long standing debate about the nature of observed incoherent structures.

D. Graphene

These convincing results allow us to extend the calculations to graphene. It is important to produce benchmark results for ideal freestanding graphene, because experimental photoemission results are obtained on substrates, which complicates the interpretation. The transition from graphite to graphene, from three to two dimensions, is also interesting from a purely fundamental point of view.

Figure 4 shows the result of our calculations. The green dot-dashed curve is the graphite intrinsic spectral function (same as Fig. 1, without secondary-electron background). The black continuous curve is the GW + C result for graphene. In the QP region the two materials are extremely similar: Indeed,

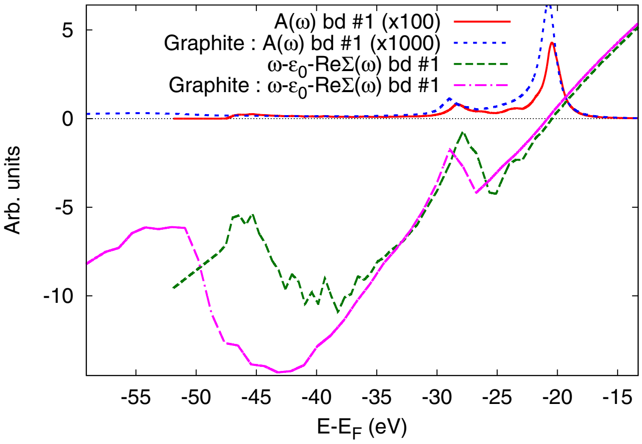

FIG. 5. (Color online) Γ-point GW_0 spectral function $A(\omega)$ for graphene (solid red line) and graphite (dotted blue line), along with the shifted real-part term of the self-energy for the lowest valence band of graphene (dashed green line) and graphite (dot-dashed magenta line), respectively.

the charge density on the graphene layers changes only a little when the sheets are brought together to form graphite, with weak hybridization and a similar band structure. However, satellites are due to plasmon excitations which involve the long-range Coulomb interaction. This long-range interaction "detects" the presence of additional layers even at far distances. The plasmon spectra of graphite and graphene are therefore completely different (see inset in Fig. 4). In particular the $\pi + \sigma$ plasmon in graphene disappears, with only a small contribution remaining at much lower energies (~15 eV), which explains the fading of the corresponding satellite in photoemission. The π plasmon is more stable and indeed, the corresponding tail on the QP peak remains intact. As our work confirms, this tail is an intrinsic feature of graphite and graphene.

For more detailed comparison, we also look at single bands including the corresponding self-energy contributions. Plasmaron solutions are defined as crossing of the $\omega - \varepsilon_0 - \mathrm{Re}\Sigma(\omega)$ curve with the horizontal axis, at higher binding energies than the QP peak. Figure 5 shows that there are no plasmaron solutions either in graphite or graphene. The behavior of the self-energy is similar in the two cases, as it is shown in Fig. 5. However, the shifted real-part term in graphite has a relatively steep slope stemming from the $\pi + \sigma$ plasmon, which leads to significant screening of the π plasmon structure. In graphene instead, the $\pi + \sigma$ plasmon is strongly suppressed, hence the structure in the real-part term due to the π plasmon is closer to zero. Still, our GW calculation shows no plasmaron solution for undoped graphene. Instead, doping creates carriers that lead to additional plasmon excitations at very low energies (small ω_p). The observed satellite lines [7] related to these excitations are sharp (small γ). In this parameter range our model predicts that a GW calculation yields a spurious plasmaron, which can be cured by GW + C*, as it has been demonstrated by recent *ab initio* calculations [28].

IV. CONCLUSION

We have conducted a joint experimental and theoretical study to understand plasmon satellites in materials very different from the homogeneous electron gas, using graphite as a prototype case. We have extended the calculation of the photoemission spectra based on GW + C* to the case of a material with more than one dominant collective excitation. The comparison to state-of-the art photoemission data over a wide range of binding energies confirms the predictive power of our approach. We can explain in detail the photoemission spectrum of graphite, and in particular demonstrate that it contains an intrinsic satellite contribution caused by the $\pi + \sigma$ plasmon, while the π plasmon leads to a tail on the QP peak. The interplay of the two plasmons causes an additional broadening and shift of the main satellite, and explains additional structures in cases of better resolution, e.g., core levels. We also discuss the problem of the spurious plasmaron in GW calculations, showing that, and why, the problem does not occur in undoped graphite, nor in undoped graphene, and why additional excitations due to doping create a more critical scenario.

ACKNOWLEDGMENTS

We acknowledge support by ANR (NT09-610745) and the RTRA Triangle de la Physique. J.J.R. and J.J.K. are also supported in part by DOE BES Grant DE-FG03-97ER45623 and DOE CMCSN. Computer time was granted by GENCI (544).

APPENDIX: PEAK-SHIFTING EFFECT IN SPECTRA WITH MULTIPLE SATELLITES

Here we describe in detail how one can estimate the shift of the first main satellite in the photoemission spectrum of graphite (roughly located at −50 eV) due to the two-plasmon structure of the energy-loss spectrum of graphite. The spectral function for $N_p = 2$ is given by (1). Our aim is to compare the position of the main satellite stemming from the $\sigma + \pi$ plasmon (ω_2 with weight a_2) to the average position that is obtained when also the first mixed satellite ($\omega_1 + \omega_2$ with weight $a_1 a_2$) is taken into account.

The calculated parameters concerning the intrinsic (superscript int) and total, i.e., intrinsic plus extrinsic and interference (superscript eff) contributions at ω_1 and ω_2 are

ω_j (eV)	a_j^{int}	a_j^{eff}
7.78	0.205	0.331
29.85	0.156	0.872

hence for $\omega_1 + \omega_2 = 37.63$ we have weights $a_1^{\mathrm{int}} a_2^{\mathrm{int}} = 0.032$ and $a_1^{\mathrm{eff}} a_2^{\mathrm{eff}} = 0.289$. These values are averaged over the Brillouin zone. To first approximation the center of mass of the structure composed by the $\pi + \sigma$ and the first mixed satellite is

$$\bar{\omega} = \frac{a_1 a_2(\omega_1 + \omega_2) + a_2 \omega_2}{a_1 a_2 + a_2}. \tag{A1}$$

The deviation from the main $\sigma + \pi$ peak is defined as $\Delta\omega = |\bar{\omega} - \omega_2|$. We obtain

$$\Delta\omega^{\mathrm{int}} = 1.3, \quad \Delta\omega^{\mathrm{eff}} = 1.9 \tag{A2}$$

for the purely intrinsic and for the total shift, respectively.

[1] A. Damascelli, Z. Hussain, and Z.-X. Shen, Rev. Mod. Phys. **75**, 473 (2003).

[2] L. Hedin, J. Michiels, and J. Inglesfield, Phys. Rev. B **58**, 15565 (1998).

[3] P. Steiner, H. Höchst, and S. Hüfner, *Topics in Applied Physics: Photoemission in Solids II* (Springer, Heidelberg, 1979).

[4] F. Aryasetiawan, L. Hedin, and K. Karlsson, Phys. Rev. Lett. **77**, 2268 (1996).

[5] C. Guillot, Y. Ballu, J. Paigné, J. Lecante, K. P. Jain, P. Thiry, R. Pinchaux, Y. Pétroff, and L. M. Falicov, Phys. Rev. Lett. **39**, 1632 (1977).

[6] A. Liebsch, Phys. Rev. Lett. **43**, 1431 (1979).

[7] A. Bostwick, F. Speck, T. Seyller, K. Horn, M. Polini, R. Asgari, A. H. MacDonald, and E. Rotenberg, Science **328**, 999 (2010).

[8] A. K. McMahan, K. Held, and R. T. Scalettar, Phys. Rev. B **67**, 075108 (2003).

[9] M. Vos, A. S. Kheifets, E. Weigold, and F. Aryasetiawan, Phys. Rev. B **63**, 033108 (2001).

[10] T. Sattler, T. Tschentscher, J. R. Schneider, M. Vos, A. S. Kheifets, D. R. Lun, E. Weigold, G. Dollinger, H. Bross, and F. Bell, Phys. Rev. B **63**, 155204 (2001).

[11] L. Hedin, Phys. Rev. **139**, A796 (1965).

[12] D. C. Langreth, Phys. Rev. B **1**, 471 (1970).

[13] L. Hedin, J. Phys.: Condens. Matter **11**, R489 (1999).

[14] C.-O. Almbladh and L. Hedin, *Handbook on Synchrotron Radiation* (North-Holland, Amsterdam, 1983).

[15] M. Guzzo, G. Lani, F. Sottile, P. Romaniello, M. Gatti, J. J. Kas, J. J. Rehr, M. G. Silly, F. Sirotti, and L. Reining, Phys. Rev. Lett. **107**, 166401 (2011).

[16] M. Guzzo, J. Kas, F. Sottile, M. Silly, F. Sirotti, J. Rehr, and L. Reining, Eur. Phys. J. B **85**, 324 (2012).

[17] L. Hedin, B. Lundqvist, and S. Lundqvist, Solid State Commun. **5**, 237 (1967).

[18] B. I. Lundqvist, Phys. Kondens. Mater. **9**, 236 (1969).

[19] C. Blomberg and B. Bergersen, Can. J. Phys. **50**, 2286 (1972).

[20] F. Polack, M. Silly, C. Chauvet, B. Lagarde, N. Bergeard, M. Izquierdo, O. Chubar, D. Krizmancic, M. Ribbens, J.-P. Duval, C. Basset, S. Kubsky, and F. Sirotti, AIP Conf. Proc. **1234**, 185 (2010).

[21] N. Bergeard, M. Silly, D. Krizmancic, C. Chauvet, M. Guzzo, J. Ricaud, M. Izquierdo, L. Stebel, P. Pittana, R. Sergo, G. Cautero, G. Dufour, F. Rochet, and F. Sirotti, J. Synch. Rad. **18**, 245 (2011).

[22] X. Gonze, G.-M. Rignanese, M. Verstraete, J.-M. Beuken, Y. Pouillon, R. Caracas, F. Jollet, M. Torrent, G. Zerah, M. Mikami, P. Ghosez, M. Veithen, J.-Y. Raty, V. Olevano, F. Bruneval, L. Reining, R. Godby, G. Onida, D. Hamann, and D. Allan, Z. Kristallogr. **220**, 558 (2009).

[23] H. J. Monkhorst and J. D. Pack, Phys. Rev. B **13**, 5188 (1976).

[24] N. Troullier and J. L. Martins, Phys. Rev. B **43**, 1993 (1991).

[25] F. R. McFeely, S. P. Kowalczyk, L. Ley, R. G. Cavell, R. A. Pollak, and D. A. Shirley, Phys. Rev. B **9**, 5268 (1974).

[26] J. J. Kas, A. P. Sorini, M. P. Prange, L. W. Cambell, J. A. Soininen, and J. J. Rehr, Phys. Rev. B **76**, 195116 (2007).

[27] J. Leiro, M. Heinonen, T. Laiho, and I. Batirev, J. Electron Spectrosc. Relat. Phenom. **128**, 205 (2003).

[28] J. Lischner, D. Vigil-Fowler, and S. G. Louie, Phys. Rev. Lett. **110**, 146801 (2013).

6.2 Exciton Dispersion

One of the most important elementary excitations is represented by excitons, collective low-energy excitations involving the creation of electron-hole (e-h) pairs, of paramount importance in elucidating the role of light absorption in, for example, the photovoltaic or photocatalytic process. Traditionally, excitons have been modeled following basic approximations, namely, the Frenkel and Wannier exciton models, which describe the two limiting cases of tightly and weakly bound e-h pairs, respectively. The Bethe-Salpeter equation has instead provided on one side the ab initio framework to study all kind of excitons (also the intermediate cases), and on the other a powerful tool for analysis. Optical absorption spectroscopy probes the long-wavelength limit $\mathbf{q} \to 0$. Thus, modern theoretical approaches for excitons have primarily focused on this limit. However, excitons can carry a finite momentum $\mathbf{q}$ and form a band structure as a function of $\mathbf{q}$. The study of excitons at finite $\mathbf{q}$ and the determination of their band structure are interesting not only from an academic perspective. Indeed, for both weakly and tightly bound excitons, their $\mathbf{q}$ dispersion determines the way the e-h pairs propagate inside the crystal and transport their excitation energy. This property is of crucial relevance for all applications involving light harvesting, and also provides fundamental knowledge about exciton mobility and migration.

The recent progress of scattering experiments such as electron energy-loss spectroscopy (EELS) or inelastic x-ray scattering (IXS), both in its resonant (RIXS) and nonresonant (NIXS) versions, makes it possible to probe electronic excitations at finite, even large, momentum transfer $\mathbf{q}$. Increasing $\mathbf{q}$ corresponds with a reduction in the probed length scale in real space. In fact, IXS and EELS are unique tools to measure electronic excitations that are dipole forbidden and thus not visible in optics. Typical examples are intra-atomic d-d excitations in strongly correlated transition-metal oxides or longitudinal p-like excitons in sp cubic crystals. In addition, the new electron microscopes are able today to reach very high spatial resolution (well under 1 nm) for the loss spectroscopy, which, in order to be investigated from the theoretical point of view, requires the knowledge of the dielectric function not at just $\mathbf{q} = 0$, but at many q's, in order to Fourier transform back in real space. There has been then a crucial need for a theoretical counterpart, an ab initio theory to describe large momentum transfer excitons. This sort of gap, between experiment and theory, has been closed thanks to our very recent work, in which (together with M.Gatti) I show how to extend the ab initio many-body approach to finite (and big) momentum transfer. We have published an article with all the theory (plus some theoretical predictions for solid argon) and a comparison with available NIXS data for large momentum tranfers [113]. Not only the agreement with the experiment is quantitatively good, but our theoretical aproach permits one to fully analyse the whole set of features of the spectra, describe the exciton character (via the plot of the excitonic wave-function), and characterize the full excitonic band-structure. Most recently we have tackled the problem of molecular solids [114], in order to compare with small variation of momentum transfer, normally achieved with the electron microscope, but also to show that the method can be easily applied to realistic (and big) systems (more than 90 atoms in the unit cell). This work is now the topic of a two post-docs here at Polytechnique under my supervision (G.Fugallo on hBN and F. Da Pieve for developement of RIXS within her Marie-Curie fellowship). Low dimensionality exciton dispersion is also on the way, notably with 2D systems, like hBN and Graphane (with P.Cudazzo).

PLEASE REFER TO THE ATTACHED ARTICLE

PHYSICAL REVIEW B **88**, 155113 (2013)

Exciton dispersion from first principles

Matteo Gatti[1,2,3,4] and Francesco Sottile[1,2]
[1]*Laboratoire des Solides Irradiés, École Polytechnique, CNRS-CEA/DSM, F-91128 Palaiseau, France*
[2]*European Theoretical Spectroscopy Facility (ETSF)*
[3]*Nano-Bio Spectroscopy Group, Departamento Física de Materiales, Universidad del País Vasco, Centro de Física de Materiales CSIC-UPV/EHU-MPC and DIPC, Avenida Tolosa 72, E-20018 San Sebastián, Spain*
[4]*Synchrotron SOLEIL, L'Orme des Merisier, BP 48 Saint-Aubin, 91192 Gif sur Yvette, France*

(Received 27 May 2013; revised manuscript received 19 September 2013; published 11 October 2013)

We present a scheme to calculate exciton dispersions in real materials that is based on the first-principles many-body Bethe-Salpeter equation. We assess its high level of accuracy by comparing our results for LiF with recent inelastic x-ray scattering experimental data on a wide range of energy and momentum transfer. We show its great analysis power by investigating the role of the different electron-hole interactions that determine the exciton band structure and the peculiar "exciton revival" at large momentum transfer. Our calculations for solid argon are a prediction and a suggestion for future experiments. These results demonstrate that the first-principles Bethe-Salpeter equation is able to describe the dispersion of localized and delocalized excitons on equal footing and represent a key step for the *ab initio* study of the exciton mobility.

DOI: 10.1103/PhysRevB.88.155113 PACS number(s): 71.35.−y, 77.22.−d, 79.20.Uv

I. INTRODUCTION

The study of elementary excitations is one of the most powerful ways to understand, predict, and tune the properties of materials. In particular, excitons, i.e., collective low-energy excitations involving the creation of electron-hole (e-h) pairs, are of paramount importance in elucidating the role of light absorption in, for example, the photovoltaic or photocatalytic process.[1] Traditionally, excitons have been modeled following basic approximations, namely, the Frenkel and Wannier exciton models, which describe the two limiting cases of tightly and weakly bound e-h pairs, respectively.[2,3] In most cases, however, interesting situations are intermediate between these two limits and model descriptions rapidly become very involved.[2–4] In the last couple of decades, instead, great advances have been obtained in the description of excitons thanks to many-body perturbation theory (MBPT).[5] In particular, the Bethe-Salpeter equation (BSE),[6] which is an effective two-particle equation for the polarizability, can nowadays be solved in an *ab initio* framework,[7–9] allowing one to obtain absorption spectra in excellent agreement with experiments, to perform accurate analysis, and to successfully predict experimental results.[10,11]

Optical absorption spectroscopy probes the long-wavelength limit $\mathbf{q} \to 0$. Thus, modern theoretical approaches for excitons have primarily focused on this $\mathbf{q} \to 0$ limit. However, excitons can carry a finite momentum $\mathbf{q}$ and form a band structure as a function of $\mathbf{q}$. The study of excitons at finite $\mathbf{q}$ and the determination of their band structure are interesting not only from an academic perspective. Indeed, for both weakly and tightly bound excitons, their $\mathbf{q}$ dispersion determines the way the e-h pairs propagate inside the crystal and transport their excitation energy. This property is of crucial relevance for all applications involving light harvesting,[12,13] and also provides fundamental knowledge about exciton mobility and migration.[14]

The recent progress of scattering experiments such as electron energy-loss spectroscopy (EELS) or inelastic x-ray scattering (IXS), both in its resonant (RIXS) and nonresonant (NIXS) versions, makes it possible to probe electronic excitations at finite, and even large, momentum transfer $\mathbf{q}$ with great accuracy.[15,16] Increasing $\mathbf{q}$ corresponds with a reduction in the probed length scale in real space. In fact, IXS and EELS are unique tools to measure electronic excitations that are dipole forbidden and thus not visible in optics. Typical examples are intra-atomic *d-d* excitations in strongly correlated transition-metal oxides[17–19] or longitudinal *p*-like excitons in *sp* cubic crystals.[2,3,9] In addition, the new electron microscopes are able today to reach very high spatial resolution (well under 1 nm) for the loss spectroscopy,[20–22] which, in order to be investigated from the theoretical point of view, requires the knowledge of the dielectric function not at just $\mathbf{q} = 0$, but at many $\mathbf{q}$'s, in order to Fourier transform back in real space. Concerning theory, however, *ab initio* simulations lie a long way behind experiments. Besides a few pioneering examples dealing with a small $\mathbf{q}$ range or core excitations,[23–31] excitons in the range of large momentum transfers remain largely unexplored by first-principles approaches.

The present work closes the gap with experiment. The extension of the Bethe-Salpeter equation to finite momentum transfers makes it possible to describe and understand the exciton dispersion well beyond the first Brillouin zone. In order to illustrate the accuracy and the great power of analysis of the BSE, we have considered two prototypical materials displaying bound excitons: lithium fluoride, for which recent high-quality experiments are available,[23,32–34] and solid argon, for which our spectra represent a prediction for future measurements. We show that, beyond model approaches, the *ab initio* BSE is able to simultaneously deal with strongly and weakly bound excitons, in a range of $\mathbf{q}$ vectors well beyond the optical limit. Moreover, the BSE formalism allows us to understand in a simple manner the exciton dispersion in terms of competing effects deriving from the electron band dispersion and the e-h interactions. The agreement with experiments in LiF is very good across the whole momentum-energy range, including the peculiar "exciton revival" at large $\mathbf{q}$, which we explain as a genuine many-body effect. In summary, these results illustrate the accuracy and the power of the BSE to study the exciton dispersion in a wide variety of materials, as well as to support and guide new experiments. The article is organized as follows: in Sec. II, we present the formula involved in the BSE (with finite momentum transfer) and, in Sec. III, the computational details; Sec. IV shows results and analysis for LiF, while Sec. V presents predictions for solid argon.

II. BETHE-SALPETER EQUATION AT FINITE MOMENTUM TRANSFER

The Bethe-Salpeter equation (BSE), based on the GW approximation (GWA) of the self-energy, reads[5]

$$\begin{aligned} L(1,2,3,4) &\\ = L_0(1,2,3,4) &+ \int d5678 L_0(1,2,5,6)[v(5,7)\delta(5,6)\delta(7,8) \\ &- W(5,6)\delta(5,7)\delta(6,8)]L(7,8,3,4), \end{aligned} \tag{1}$$

where (1) is a shorthand notation for position, time, and spin $(\mathbf{r}_1,t_1,\sigma_1)$, L is the two-particle correlation function, L_0 is its independent-particle version, v is the bare Coulomb interaction, and W is its statically screened version calculated in the random-phase approximation.

The Dyson-like Eq. (1) can be reformulated[10,11] as an eigenvalue problem by introducing the excitonic Hamiltonian H_{exc} written on a basis of electron-hole transitions[35] t : $(n_1\mathbf{k}_1) \rightarrow (n_2\mathbf{k}_2)$. According to the band index n being an occupied state (v) or an occupied state (c), these are classified as resonant transitions, $(v,\mathbf{k}-\mathbf{q_r}) \rightarrow (c,\mathbf{k})$, or antiresonant transitions, $(c,\mathbf{k}) \rightarrow (v,\mathbf{k}+\mathbf{q_r})$, where the momentum transfer $\mathbf{q_r}$ belongs to the first Brillouin zone. The matrix elements are then

$$\langle t|H_{\text{exc}}|t'\rangle = E_t\delta_{t,t'} + \langle t|v - W|t'\rangle, \tag{2}$$

where E_t is the energy associated to the transition (calculated in GWA), and

$$\begin{aligned} \langle t|v|t'\rangle &= \langle n_1\mathbf{k}_1 n_2\mathbf{k}_2|v|n'_1\mathbf{k}'_1 n'_2\mathbf{k}'_2\rangle \\ &= 2\delta_M \int d\mathbf{r}d\mathbf{r}' \phi^*_{n_2\mathbf{k}_2}(\mathbf{r})\phi_{n_1\mathbf{k}_1}(\mathbf{r})v(\mathbf{r},\mathbf{r}')\phi_{n'_2\mathbf{k}'_2}(\mathbf{r}')\phi^*_{n'_1\mathbf{k}'_1}(\mathbf{r}'), \end{aligned} \tag{3}$$

$$\begin{aligned} \langle t|W|t'\rangle &= \langle n_1\mathbf{k}_1 n_2\mathbf{k}_2|W|n'_1\mathbf{k}'_1 n'_2\mathbf{k}'_2\rangle \\ &= \int d\mathbf{r}d\mathbf{r}' \phi^*_{n_2\mathbf{k}_2}(\mathbf{r})\phi_{n'_2\mathbf{k}'_2}(\mathbf{r})W(\mathbf{r},\mathbf{r}')\phi_{n_1\mathbf{k}_1}(\mathbf{r}')\phi^*_{n'_1\mathbf{k}'_1}(\mathbf{r}') \end{aligned} \tag{4}$$

are the repulsive exchange electron-hole (e-h) interaction and the direct e-h attractive interaction, respectively. In Eq. (3), $\delta_M = 1$ for the singlet channel and $\delta_M = 0$ for the triplet. In this basis, H_{exc} takes a block matrix form,

$$H_{\text{exc}} = \begin{pmatrix} R & K^{R,A} \\ K^{A,R} & A \end{pmatrix}. \tag{5}$$

When the off-diagonal coupling terms K are set to 0, the Tamm-Dancoff approximation (TDA) is retrieved.

In the long-wavelength limit $\mathbf{q_r} \rightarrow 0$, $A = -R^*$ and $K^{A,R} = -[K^{R,A}]^*$. The diagonal blocks A and R are Hermitian and the coupling blocks K are symmetric. For a generic momentum transfer $\mathbf{q_r} \neq 0$, the antiresonant block A can no longer be obtained from the resonant block R $(A \neq -R^*)$ and the coupling terms are no longer symmetric. This doubles the computational cost of calculating H_{exc}.

From the solution of the eigenvalue problem,

$$H_{\text{exc}}(\mathbf{q_r})A_\lambda(\mathbf{q_r}) = E_\lambda(\mathbf{q_r})A_\lambda(\mathbf{q_r}), \tag{6}$$

where we have made explicit the dependence on the momentum transfer $\mathbf{q_r}$, one can obtain the inverse macroscopic dielectric function ϵ_M^{-1}. In the TDA, one has

$$\epsilon_M^{-1}(\mathbf{q},\omega) = 1 + \frac{8\pi}{q^2}\sum_\lambda \frac{\left|\sum_t A^t_\lambda(\mathbf{q_r})\tilde{\rho}^t(\mathbf{q})\right|^2}{\omega - E_\lambda(\mathbf{q_r}) + i\eta}, \tag{7}$$

where $\mathbf{q} = \mathbf{q_r} + \mathbf{G}_0$ is the desired momentum transfer, $\mathbf{G}_0$ is a reciprocal lattice vector, and $\tilde{\rho}_t(\mathbf{q}) = \langle\phi_{v\mathbf{k}-\mathbf{q_r}}|e^{-i\mathbf{qr}}|\phi_{c\mathbf{k}}\rangle$ is the oscillator strength. The loss function $-\text{Im}\epsilon_{\text{M}}^{-1}$ can be compared with EELS or IXS spectra.

Alternatively, if the Coulomb interaction v in the BSE is replaced by a modified interaction $\bar{v}$ that in the reciprocal space is equal to v for all the $\mathbf{G}$ components but $\mathbf{G}_0$ for which $\bar{v}(\mathbf{G}_0) = 0$, then from the solution of the excitonic eigenvalue problem, one obtains the macroscopic dielectric function ϵ_M:

$$\epsilon_M(\mathbf{q},\omega) = 1 - \frac{8\pi}{q^2}\sum_\lambda \frac{\left|\sum_t A^t_\lambda(\mathbf{q_r})\tilde{\rho}^t(\mathbf{q})\right|^2}{\omega - E_\lambda(\mathbf{q_r}) + i\eta}. \tag{8}$$

For simplicity, the notation is not modified with respect to Eq. (7), but here it is understood that A_λ and E_λ are the solution of the BSE with a modified Coulomb interaction $\bar{v}$. The long-range component of v that is omitted in $\bar{v}$ is responsible for the splitting at $\mathbf{q} = 0$ between longitudinal and transverse excitons in *sp* cubic crystals.[2,3,9] In the $\mathbf{q} \rightarrow 0$ limit, $\text{Im}\epsilon_{\text{M}}$ calculated from Eq. (8) gives the absorption spectrum (in which only transverse excitons are visible). At large momentum transfer, the long-range component of v becomes less and less important, since increasing $\mathbf{q}$ means probing a shorter length scale in real space. Moreover, at large momentum transfer,

$$\begin{aligned} -\text{Im}\epsilon_{\text{M}}^{-1}(\mathbf{q},\omega) &= \frac{\text{Im}\epsilon_{\text{M}}(\mathbf{q},\omega)}{[\text{Re}\epsilon_{\text{M}}(\mathbf{q},\omega)]^2 + [\text{Im}\epsilon_{\text{M}}(\mathbf{q},\omega)]^2} \\ &\rightarrow \text{Im}\epsilon_{\text{M}}(\mathbf{q},\omega), \end{aligned} \tag{9}$$

since $\text{Re}\epsilon_{\text{M}} \rightarrow 1$ and $\text{Im}\epsilon_{\text{M}}$ is small compared to 1.

Besides the spectrum, the solution of the BSE allows a straightforward analysis, for instance by visualizing the exciton wave function of the e-h pair in real space, e.g., for $\mathbf{q} = 0$:

$$\Psi_\lambda(\mathbf{r}_h,\mathbf{r}_e) = \sum_t A^t_\lambda \phi_{v\mathbf{k}}(\mathbf{r}_h)\phi_{c\mathbf{k}}(\mathbf{r}_e). \tag{10}$$

A. Comparison with the independent-particle picture

In order to have a clear idea about how the excitonic effects (or the many-body effects) are taken into account in a theory that uses an independent-particle basis [such as density-functional theory (DFT) Kohn-Sham], it is useful to write the analogous equation of Eq. (8) for an independent-particle system:

$$\epsilon_M(\mathbf{q},\omega) = 1 - \frac{8\pi}{q^2}\sum_t \frac{|\tilde{\rho}^t(\mathbf{q})|^2}{\omega - \epsilon_t + i\eta}. \tag{11}$$

The similarity is striking: in the latter formula, the (independent) transitions are summed up in a simple way, and their contribution to the final spectrum can only be in the energy range of the energy transition. In Eq. (8), instead, the transitions do not add up in a simple way, but they are mixed all together, via the eigenvectors of the excitonic Hamiltonian $A_\lambda^t(\mathbf{q_r})$, giving contribution to every exciton (every λ).

III. COMPUTATIONAL DETAILS

We have calculated the ground state of LiF and Ar using density-functional theory[36] within the local-density approximation (LDA),[37] using norm-conserving Troulliers-Martins pseudopotentials[38] in a plane-wave approach. In LiF, the energy cutoff is 40 Hartree, and we use a $12 \times 12 \times 12$ Γ-centered **k**-point grid. In Ar, the cutoff is also 40 Hartree and a finer grid with 4000 inequivalent **k** points is needed. In LiF, we have corrected the LDA band structure with a scissor operator of 6.05 eV for the band gap, and stretching the valence-band energies by 15% and conduction bands by 2%. These corrections bring the LDA band structure into agreement with photoemission.[8,24] Analogously, the scissor correction is 6.6 eV in Ar.[39] BSE spectra are converged with 20 bands for LiF and 10 bands for Ar. The TDA that is employed for those spectra (see Sec. II) has no influence on the bound excitons. The effect of the coupling is mainly visible for the plasmon peak and becomes more important at larger **q**. In the analysis of the exciton band dispersion in Fig. 4, a $4 \times 4 \times 4$ **k**-point grid is used with three occupied and one unoccupied bands.

IV. LITHIUM FLUORIDE

NIXS measures the dynamic structure factor $S(\mathbf{q},\omega)$ that is proportional to the loss function $-\mathrm{Im}\epsilon_M^{-1}(\mathbf{q},\omega)$ (the latter can be equivalently obtained also by EELS):[40] $S(\mathbf{q},\omega) = -q^2/(4\pi^2 n)\mathrm{Im}\epsilon_M^{-1}(\mathbf{q},\omega)$ (n is the average electron density). The inverse of macroscopic dielectric function ϵ_M^{-1} can be directly calculated from the BSE, as seen in Sec. II.

In Fig. 1, we compare our BSE calculations (right panel) with experiment[32] (left panel) for the dynamic structure factor of LiF over a wide range of energies (vertical axis) and momentum transfers (horizontal axis) along the ΓX direction.[41] We observe (i) a tightly bound exciton, dispersing around 14 eV (the quasiparticle band gap lies between 14.98 and 16.17 eV) with a modulation in intensity until $\sim 6\Gamma X$, and (ii) the valence plasmon at $\sim$23 eV, which fades out with increasing **q**. The agreement between theory and experiment is very good, both for the main features and for the fine structures in the spectra, generalizing previous results at selected $\mathbf{q} < 1.5\Gamma X$.[23,24] Here we focus on the bound exciton, which is mainly formed by e-h pairs from the three F $2p$ valence bands and the first Li $2s$ conduction band. In the optical limit, the two degenerate transverse excitons are seen in the absorption spectrum.[8,9,42] The third longitudinal exciton is visible in IXS at finite **q** along ΓX. The diagonalization of the excitonic Hamiltonian can also be achieved along different **q** directions, giving rise to a full description of the exciton band structure, as we show in Fig. 2. Thus, BSE calculations can complement experiments and obtain the band dispersion even for the excitons that are not visible in the spectra, but can be important, e.g., as deexcitation channels. For example, this is the case of the transverse excitons along ΓX. In other less symmetric directions such as ΓW, we find that both longitudinal and transverse branches become visible at the same time, confirming previous expectations[2] and very recent results.[33]

Inspection of the exciton wave function $\Psi(\mathbf{r}_e,\mathbf{r}_h)$ [see Eq. (10)] at $\mathbf{q} = 0$ reveals that, consistently with the large binding energy, each e-h pair is confined in a small volume of the crystal. We plot in Fig. 3 the wave function of the first exciton of LiF at $\mathbf{q} = 0$. This is defined as the probability distribution for the electron when the hole has been placed in $\mathbf{r}_h$. We report here the singlet (confirming the picture obtained, e.g., in Refs. 9 and 42) and the triplet low-lying excitation. It is worth highlighting three points: (i) even though the exciton is centered on the fluorine atom where the hole is fixed, it is delocalized over several primitive cells; (ii) the electron distribution, in addition, is not only localized on the same fluorine atom, but also on the nearest- and second-nearest-neighboring fluorine atoms, avoiding the lithium atoms, even though the empty $2s$ state of lithium is available, which shows how the physical picture can be counterintuitive if we rely only

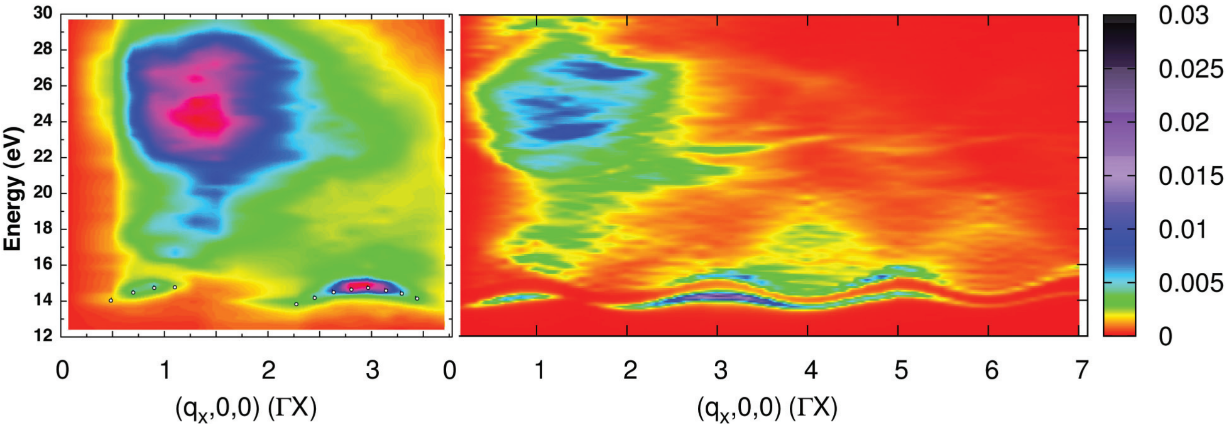

FIG. 1. (Color online) Dynamic structure factor of LiF as a function of energy (vertical axis) and momentum transfer **q** (horizontal axis) along ΓX in units of ΓX. Left panel: Experimental data from Ref. 32. Right panel: Bethe-Salpeter calculations. The absolute scale for theoretical data is reported, but none is available for experimental data.

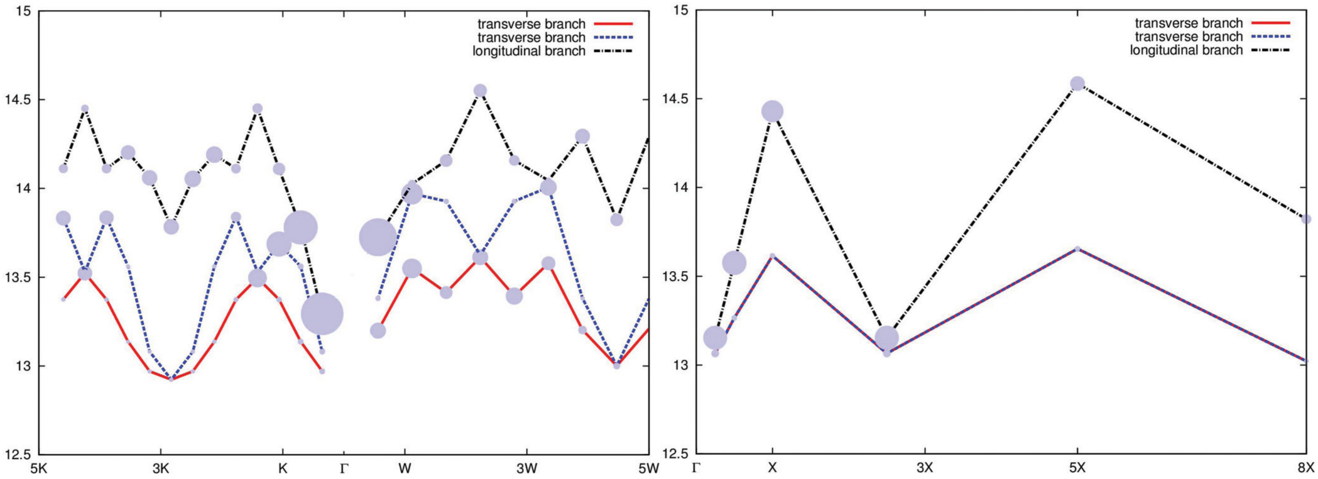

FIG. 2. (Color online) Exciton band structure of LiF. Three directions are investigated: ΓX, ΓK, and ΓW.

on a one-particle approximation; and (iii) the triplet exciton wave function shows a very similar picture as the singlet, with the electron distribution again localized on F atoms and not on Li atoms. This shows that the exchange electron-hole interaction is not qualitatively affecting the nature of the exciton.

In order to get a deeper understanding of the excitonic interactions at play in LiF, we can have a critical look at the energy-momentum map of $S(\mathbf{q},\omega)$ in Fig. 1 in the exciton region ($13 < \omega < 15$ eV), and ask the following series of questions: (i) Why does the dynamical structure factor fade for high $\mathbf{q}$? (ii) What is the origin of the exciton dispersion? (iii) Why does the intensity of the exciton increase with $\mathbf{q}$ up to $1\Gamma X$, disappear, and come back stronger than before up to $3\Gamma X$, to finally decay? It is easy to first answer question (i), for the decay of the independent-particle oscillator strengths $\tilde{\rho}^t(\mathbf{q})$ with increasing $\mathbf{q}$.

Question (ii) requires a deeper analysis, which is summarized in Fig. 4(a). The top-left panel represents the full *ab initio* calculation within a minimal model that includes F $2p$ and Li $2s$ bands; the top-right panel is a calculation in which we have artificially suppressed the band dispersion (same energy for every $\mathbf{k}$). The latter situation corresponds to the description that would be given by the simple Frenkel exciton model. Bottom panels are the equivalent triplet calculations, i.e., there is no e-h exchange interaction [v term in Eq. (2)]. Finally, in the bottom-right spectrum, the exciton dispersion is given only by e-h direct interaction W. Such dispersion, though small, precludes considering the overlap between wave functions localized on different atoms negligible in LiF.[43] The biggest contribution to the final exciton dispersion derives from the true electronic band dispersion [which gives $E_\lambda(\mathbf{q})$ a curvature that is opposite to the one obtained with the "flat bands" model], as can be seen by comparing the two top panels. This also implies that the necessary condition for simplified models to properly describe the exciton dispersion in LiF is to take into account (implicitly or explicitly) the electronic band dispersion.[4,32,33] It is interesting to compare also the triplet with the singlet, in order to directly evaluate the e-h exchange term, which has the effect of tempering the exciton dispersion, which otherwise would become too big. The final bandwidth of the exciton is 0.67 eV. Our *ab initio* calculations directly reproduce the experimental results and provide the tools for their analysis. It is worth noting that this analysis would be

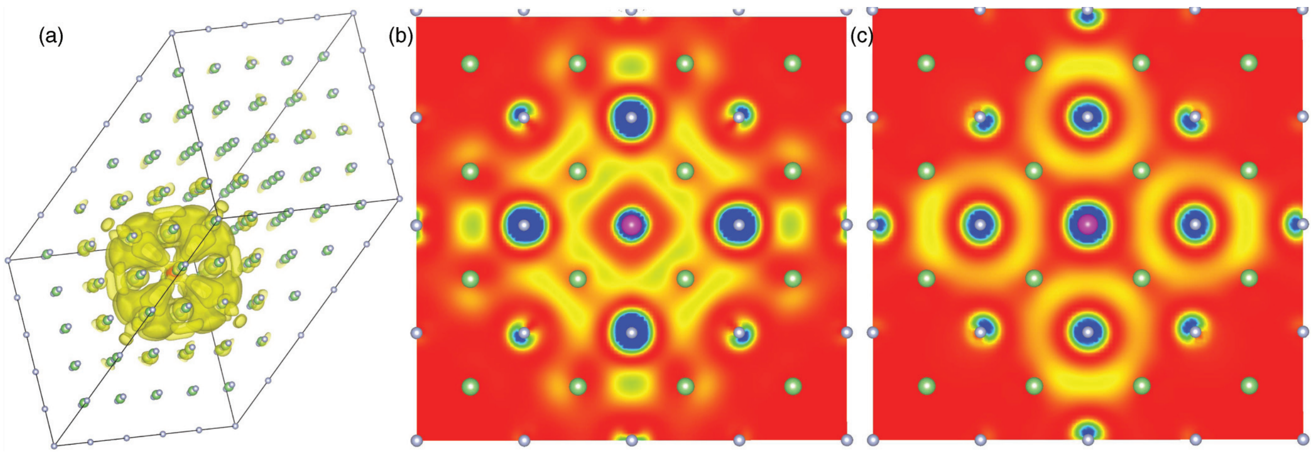

FIG. 3. (Color online) (a) Exciton wave function of LiF, when the hole is on top of the fluorine atom (violet in the center of the cell). (b) Cut along the [111] direction of the exciton wave function. (c) Same as (b), but for the triplet excitation. The physical picture is unchanged.

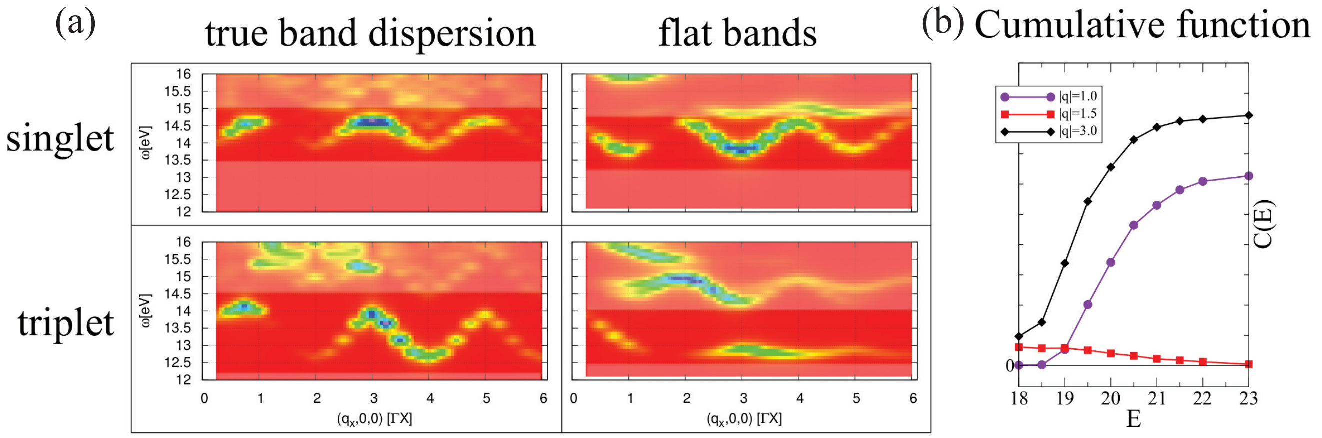

FIG. 4. (Color online) (a) Exciton dispersion in LiF in a minimal F $2p$ and Li $2s$ model with "flat bands" or with the full band dispersion for the singlet and the triplet. (b) Cumulative function $C^{\mathbf{q}}_{\lambda}(E)$ for the bound exciton in LiF as a function of the e-h transition energy E (see text) for the intensity maxima at $\mathbf{q} = \Gamma X$ and $3\Gamma X$, and for the minimum at $\mathbf{q} = 1.5\Gamma X$ (see Fig. 1).

very difficult by using simple models, such as Frenkel (that would hardly capture the band dispersion, which is the main cause of the exciton dispersion) or Wannier (that would impose the same parabolic dispersion to all excitons).

We can now tackle question (iii), which involves the important modulation of the exciton intensity (see Fig. 1). The exciton peak has a maximum at $\mathbf{q} \sim \Gamma X$; then it almost disappears before having a second and stronger maximum at $\mathbf{q} \sim 3\Gamma X$ (beyond this point the intensity decreases until the exciton definitively disappears). In order to explain this "exciton revival" at large $\mathbf{q}$, we analyze the numerator of Eq. (7). The modulation in intensity for $\mathbf{q} < 3\Gamma X$ cannot be explained by considering separately $\tilde{\rho}^t(\mathbf{q})$ and the eigenvectors $A^t_\lambda(\mathbf{q})$. In fact, their behavior does not show a clear pattern as a function of $\mathbf{q}$. Instead, we find that only by analyzing the $\tilde{\rho}^t A^t_\lambda(\mathbf{q})$ product as a whole is it possible to understand such an exciton revival. Indeed, the intensity of the exciton peak is determined by the constructive coherent superposition of the oscillator strengths from the different e-h configurations that form the excitonic state. To visualize explicitly the building up of the exciton as a function of the e-h transitions of energies E_t, in Fig. 4(b) we represent the cumulative function[44]

$$C^{\mathbf{q}}_{\lambda}(E) = \int_0^E d\omega \sum_t A^t_\lambda(\mathbf{q})\tilde{\rho}^t(\mathbf{q})\delta(\omega - E_t), \qquad (12)$$

for three representative $\mathbf{q} = \Gamma X$, $1.5\Gamma X$, and $3\Gamma X$. First of all, we realize that to quantitatively reproduce the intensity of the calculated spectrum, we have to take into account transitions spanning a wide energy range of at least ∼5 eV. Moreover, for the two maxima of spectral intensity at $\mathbf{q} = \Gamma X$ and $3\Gamma X$, we see that different e-h transitions are always summing up constructively and, as a consequence, $C^{\mathbf{q}}_{\lambda}(E)$ is an increasing function of the energy E. Instead, for the minimum at $\mathbf{q} = 1.5\Gamma X$, the superposition of the different e-h configurations is constructive up to $E = 18$ eV, but then it becomes destructive for e-h transitions at higher energies, which leads to a reduction in the final intensity of the peak. This analysis illustrates once more the many-body character of a collective excitation such as an exciton, which cannot be captured by any independent-particle picture.

V. ARGON

In view of the very good agreement with experiment for LiF, we now move to solid argon for which our calculations (see Sec. III) represent a prediction for future measurements. Argon is a textbook material that has been studied extensively in the past[2,39,45–50] for its absorption spectrum that shows a hydrogenlike bound-exciton series in which the $n = 1$ exciton has a strongly localized character and the higher excitons $n \geqslant 2$ are more delocalized.[51] The energy-momentum dispersion map represented in Fig. 5 fully discloses the richness of the excitation spectrum beyond what can be seen in the optical limit. First of all, we see that from the experimental point of view, one should preferably make the measurement at $\mathbf{q} = 3\Gamma X$, where the peaks are the most intense. At this momentum transfer, there are two prominent excitons at 13.8 and 15.4 eV, i.e., inside the band gap (which is marked by the white line in Fig. 5) and in the e-h excitation continuum,

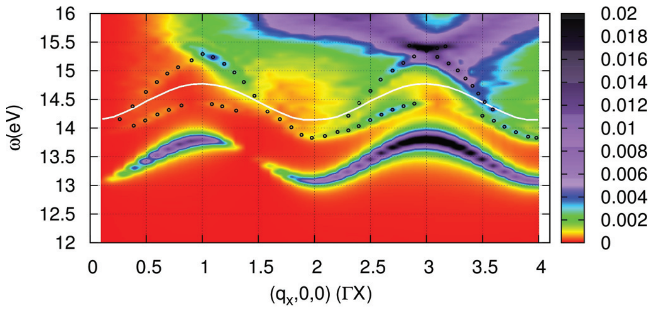

FIG. 5. (Color online) Dynamic structure factor of solid argon as a function of energy (vertical axis) and momentum transfer $\mathbf{q}$ (horizontal axis) along ΓX in units of ΓX: predictions from the Bethe-Salpeter equation. The white line is the quasiparticle direct band gap as a function of $\mathbf{q}$. The dots mark the dispersion of two excitons located between the two most prominent peaks.

respectively. The bound exciton, which corresponds to most intense $n = 1$ peak in the absorption spectrum, has a dispersion that recalls that of the lowest-energy exciton in LiF, while the dispersion of the resonant exciton at higher energies has an opposite curvature and is more intense outside the first Brillouin zone. In the energy range between these two excitons, several other weaker features appear (some of them are dipole forbidden and hence not visible in the absorption spectrum). In Fig. 5, the most intense among them are marked by the small dots. We find that the various exciton branches have a large bandwidth (up to 1 eV) and they show different dispersions. This is in contrast to the simple Wannier model in which the exciton energy levels of the Rydberg series should all have the same dispersion. We thus see that the first-principles BSE is able to describe at the same time the dispersion of a large variety of excitons, as shown here in solid Ar, from the more localized $n = 1$ exciton to the more delocalized resonant excitons. This would be very hard to achieve using a single model.

VI. CONCLUSIONS

In conclusion, we have shown how the *ab initio* Bethe-Salpeter equation is able to accurately describe the dispersion of plasmons and localized and delocalized excitons on equal footing. We have calculated the band structure of visible and dark excitons in LiF and analyzed its behavior in terms of competing electron-hole interactions. Our results for solid argon are a prediction for future experiments. This work opens the way for a large variety of applications, from the investigation of vertex corrections beyond the GW approximation for spectral properties to the study of dispersion of orbiton excitations in transition-metal oxides,[52] and represents a fundamental step towards an *ab initio* analysis of exciton propagation in real materials.[13]

ACKNOWLEDGMENTS

We thank Lucia Reining, Pina Romaniello, Pierluigi Cudazzo, Angel Rubio, and Simo Huotari for fruitful discussions, and Joanne Oates for critical reading. We thank Jean-Pascal Rueff and Peter Abbamonte for providing us with the corrected results from Ref. 32. We acknowledge financial support from Triangle de la Physique 2013-0013T IXST, the ERC Advanced Grant DYNamo (No. ERC-2010-AdG-267374), Spanish Grants (No. 2010-21282-C02-01 and No. PIB2010US-00652), Grupos Consolidados UPV/EHU del Gobierno Vasco (Grant No. IT578-13) and European Commission projects CRONOS (Grant No. 280879-2 CRONOS CP-FP7). Computational time was granted by GENCI (Project No. 544) and by the CNANO-SIMULEE-2009 project. Ground-state calculations are carried out with the ABINIT package,[53] while the dynamical structure factor, and all exciton analyses, are calculated with the EXC code.[54]

---

[1] A. Fujishima, X. Zhang, and D. A. Tryk, Surf. Sci. Rep. **63**, 515 (2008).

[2] R. S. Knox, *Theory of Excitons* (Academic, New York, 1963).

[3] F. Bassani and G. P. Parravicini, *Electronic States and Optical Transitions in Solids* (Pergamon, New York, 1975).

[4] See, e.g., M. Altarelli and B. F. Bassani, J. Phys. C **4**, L328 (1971).

[5] G. Strinati, Rivista del Nuovo Cimento **11**(12), 1 (1988).

[6] W. Hanke and L. J. Sham, Phys. Rev. Lett. **43**, 387 (1979).

[7] S. Albrecht, L. Reining, R. Del Sole, and G. Onida, Phys. Rev. Lett. **80**, 4510 (1998).

[8] L. X. Benedict, E. L. Shirley, and R. B. Bohn, Phys. Rev. Lett. **80**, 4514 (1998).

[9] M. Rohlfing and S. G. Louie, Phys. Rev. Lett. **81**, 2312 (1998).

[10] M. Rohlfing and S. G. Louie, Phys. Rev. B **62**, 4927 (2000).

[11] G. Onida, L. Reining, and A. Rubio, Rev. Mod. Phys. **74**, 601 (2002).

[12] G. Trinkunas, O. Zerlauskiene, V. Urbonien, J. Chmeliov, A. Gall, B. Robert, and L. Valkunas, J. Phys. Chem. B **116**, 5192 (2012).

[13] D. A. Wheeler and J. Z. Zhang, Adv. Mater. **25**, 2878 (2013).

[14] R. M. Hochstrasser and J. D. Whiteman, J. Chem. Phys. **56**, 5945 (1972).

[15] W. Schülke, *Electron Dynamics by Inelastic X-ray Scattering* (Oxford University Press, Oxford, UK, 2007).

[16] F. J. García de Abajo, Rev. Mod. Phys. **82**, 209 (2010).

[17] B. C. Larson, J. Z. Tischler, W. Ku, C. C. Lee, O. D. Restrepo, A. G. Eguiluz, P. Zschack, and K. D. Finkelstein, Phys. Rev. Lett. **99**, 026401 (2007).

[18] N. Hiraoka, H. Okamura, H. Ishii, I. Jarrige, K. D. Tsuei, and Y. Q. Cai, Eur. Phys. J. B **70**, 157 (2009).

[19] F. Iori, F. Rodolakis, M. Gatti, L. Reining, M. Upton, Y. Shvyd'ko, J.-P. Rueff, and M. Marsi, Phys. Rev. B **86**, 205132 (2012).

[20] S. Mazzucco, O. Stéphan, C. Colliex, I. Pastoriza-Santos, L. Liz-Marzan, F. J. García de Abajo, and M. Kociak, Eur. Phys. J. Appl. Phys. **54**, 33512 (2011).

[21] A. Rivacoba, N. Zabala, and J. Aizpurua, Prog. Surf. Sci. **65**, 1 (2000).

[22] F. J. García de Abajo and M. Kociak, Phys. Rev. Lett. **100**, 106804 (2008).

[23] W. A. Caliebe, J. A. Soininen, E. L. Shirley, C.-C. Kao, and K. Hämäläinen, Phys. Rev. Lett. **84**, 3907 (2000).

[24] J. A. Soininen and E. L. Shirley, Phys. Rev. B **61**, 16423 (2000).

[25] S. Galambosi, J. A. Soininen, K. Hämäläinen, E. L. Shirley, and C.-C. Kao, Phys. Rev. B **64**, 024102 (2001).

[26] A. Marini, R. Del Sole, and A. Rubio, Phys. Rev. Lett. **91**, 256402 (2003).

[27] H. K. Mao, E. L. Shirley, Y. Ding, P. Eng, Y. Q. Cai, P. Chow, Y. Xiao, J. Shu, R. J. Hemley, C. Kao, and W. L. Mao, Phys. Rev. Lett. **105**, 186404 (2010).

[28] C.-C. Lee, H. C. Hsueh, and W. Ku, Phys. Rev. B **82**, 081106 (2010).

[29] S. Sharma, J. K. Dewhurst, A. Sanna, A. Rubio, and E. K. U. Gross, New J. Phys. **14**, 053052 (2012).

[30] K. Hämäläinen, S. Galambosi, J. A. Soininen, E. L. Shirley, J.-P. Rueff, and A. Shukla, Phys. Rev. B **65**, 155111 (2002).

[31] J. Vinson, J. J. Rehr, J. J. Kas, and E. L. Shirley, Phys. Rev. B **83**, 115106 (2011).

[32] P. Abbamonte, T. Graber, J. P. Reed, S. Smadici, C.-L. Yeh, A. Shukla, J.-P. Rueff, and W. Ku, Proc. Natl. Acad. Sci. USA **105**, 12159 (2008).

[33] C.-C. Lee, X. M. Chen, C.-L. Yeh, H. C. Hsueh, P. Abbamonte, and W. Ku, arXiv:1205.4106v1.

[34] W. A. Caliebe, Ph.D. thesis, Kiel Universität, Germany, 1997, http://www.ieap.uni-kiel.de/solid/ag-press/r/pd/diss1.htm

[35] For simplicity, here we drop the spin index. H_{exc} can be easily generalized to spin-polarized systems.[10]

[36] P. Hohenberg and W. Kohn, Phys. Rev. **136**, B864 (1964).

[37] W. Kohn and L. J. Sham, Phys. Rev. **140**, A1133 (1965).

[38] N. Troullier and J. L. Martins, Phys. Rev. B **43**, 1993 (1991).

[39] F. Sottile, M. Marsili, V. Olevano, and L. Reining, Phys. Rev. B **76**, 161103 (2007).

[40] Throughout the paper, atomic units are used if not mentioned otherwise.

[41] The original figure in Ref. 32 contains an error that has been corrected by shifting the energy axis by 1.0 eV. J.-P. Rueff and P. Abbamonte (private communication).

[42] P. Puschnig and C. Ambrosch-Draxl, Phys. Rev. B **66**, 165105 (2002).

[43] P. Cudazzo, M. Gatti, and A. Rubio, Phys. Rev. B **86**, 195307 (2012).

[44] L. Yang, J. Deslippe, C.-H. Park, M. L. Cohen, and S. G. Louie, Phys. Rev. Lett. **103**, 186802 (2009).

[45] G. Baldini, Phys. Rev. **128**, 1562 (1962).

[46] R. Haensel, G. Keitel, E. E. Koch, M. Skibowski, and P. Schreiber, Phys. Rev. Lett. **23**, 1160 (1969).

[47] V. Saile, M. Skibowski, W. Steinmann, P. Gürtler, E. E. Koch, and A. Kozevnikov, Phys. Rev. Lett. **37**, 305 (1976).

[48] W. Andreoni, M. Altarelli, and F. Bassani, Phys. Rev. B **11**, 2352 (1975).

[49] S. Baroni, G. Grosso, L. Martinelli, and G. Pastori Parravicini, Phys. Rev. B **20**, 1713 (1979).

[50] S. Galamic-Mulaomerovic and C. H. Patterson, Phys. Rev. B **72**, 035127 (2005).

[51] Each exciton is additionally split into doublets for the effect of the spin-orbit coupling, which is neglected in the calculation.

[52] J. Schlappa, K. Wohlfeld, K. J. Zhou, M. Mourigal, M. W. Haverkort, V. N. Strocov, L. Hozoi, C. Monney, S. Nishimoto, S. Singh, A. Revcolevschi, J.-S. Caux, L. Patthey, H. M. Ronnow, J. van den Brink, and T. Schmitt, Nature (London) **485**, 82 (2012).

[53] X. Gonze, B. Amadon, P.-M. Anglade, J.-M. Beuken, F. Bottin, P. Boulanger, F. Bruneval, D. Caliste, R. Caracas, M. Ct, T. Deutsch, L. Genovese, P. Ghosez, M. Giantomassi, S. Goedecker, D. Hamann, P. Hermet, F. Jollet, G. Jomard, S. Leroux, M. Mancini, S. Mazevet, M. Oliveira, G. Onida, Y. Pouillon, T. Rangel, G.-M. Rignanese, D. Sangalli, R. Shaltaf, M. Torrent, M. Verstraete, G. Zerah, and J. Zwanziger, Comput. Phys. Commun. **180**, 2582 (2009).

[54] L. Reining, V. Olevano, F. Sottile, S. Albrecht, and G. Onida, The exc code (unpublished), http://www.bethe-salpeter.org/

PHYSICAL REVIEW B **88**, 195152 (2013)

Frenkel versus charge-transfer exciton dispersion in molecular crystals

Pierluigi Cudazzo,[1,2,*] Matteo Gatti,[1,2,3,4] Angel Rubio,[1,2,5] and Francesco Sottile[2,3]
[1]*Nano-Bio Spectroscopy Group, Departamento Física de Materiales, Universidad del País Vasco, Centro de Física de Materiales CSIC-UPV/EHU-MPC and DIPC, Avenida Tolosa 72, E-20018 San Sebastián, Spain*
[2]*European Theoretical Spectroscopy Facility (ETSF)*
[3]*Laboratoire des Solides Irradiés, École Polytechnique, CNRS-CEA/DSM, F-91128 Palaiseau, France*
[4]*Synchrotron SOLEIL, L'Orme des Merisiers, B.P. 48 Saint-Aubin, 91192 Gif-sur-Yvette, France*
[5]*Theory Department, Fritz-Haber-Institut der Max-Planck-Gesellschaft, Faradayweg 4-6, D-14195 Berlin-Dahlem, Germany*
(Received 26 June 2013; revised manuscript received 3 October 2013; published 27 November 2013)

By solving the many-body Bethe-Salpeter equation at finite momentum transfer, we characterize the exciton dispersion in two prototypical molecular crystals, picene and pentacene, in which localized Frenkel excitons compete with delocalized charge-transfer excitons. We explain the exciton dispersion on the basis of the interplay between electron and hole hopping and electron-hole exchange interaction, unraveling a simple microscopic description to distinguish Frenkel and charge-transfer excitons. This analysis is general and can be applied to other systems in which the electron wave functions are strongly localized, as in strongly correlated insulators.

DOI: 10.1103/PhysRevB.88.195152 PACS number(s): 71.35.−y, 71.15.Qe, 78.40.Me

Excitons are neutral electronic excitations that dominate the low-energy part of the optical spectra in insulators and semiconductors. They consist of bound electron-hole (e-h) pairs that can be excited in several ways: by absorption of light and by relaxation of free electrons and holes after optical or electrical pumping. They play an essential role in many semiconductor applications (e.g., for light-emitting diodes, lasers, and photovoltaic cells) and give rise to the rich field of Bose-Einstein exciton condensates.[1–3] In all these cases it is fundamental to understand the decay rate and the propagation of the excitons. The latter is directly related to their energy dispersion as a function of momentum transfer. Recent advances in loss spectroscopies make it possible to map out the full momentum-energy exciton dispersion.[4–7] On the other hand, the interpretation of these experimental spectra requires first-principles theoretical approaches able to describe and analyze excitons at finite momentum transfer. The Bethe-Salpeter equation (BSE) from many-body perturbation theory has become the most accurate framework to describe excitonic effects in the optical spectra of many materials.[8,9] However optical spectroscopy probes the zero-momentum-transfer limit only. Therefore first-principles analysis of the exciton dispersion is still an important goal to reach.

Molecular crystals represent a textbook case[10,11] that clearly illustrates the need for advanced theoretical tools to understand the exciton dispersion. Typically, the lowest-energy excited states in these materials are strongly localized Frenkel (FR) excitons, where the interacting e-h pairs are localized on the same molecular unit. Charge-transfer (CT) excitons, in which e-h pairs are delocalized on different units, usually appear at higher energies in the spectra. However, when the molecular units are large enough, the effective interactions for e-h pairs localized on the same site or on two different sites become comparable and either CT or FR excitons can occur. Under these conditions many-body effects become crucial to set the character of the excitons and an *ab initio* treatment of the e-h interactions is thus required.

In the present work we solve the BSE at finite-momentum transfer[12–14] to investigate two prototypical isoelectronic molecular crystals: picene and pentacene (see Fig. 1). By switching on the different e-h interactions step by step and analyzing their effects, we are able to draw a general picture of the exciton dispersion. We show that while the dispersion of FR excitons is set by the exchange e-h interaction, the dispersion of CT states is mainly related to the electronic band structure. Our conclusions have a general validity that holds in all systems in which the electron wave functions are strongly localized.

The BSE excitonic Hamiltonian in the basis of wave functions localized on the molecular units can be written as

$$\hat{H}_{\mathrm{ex}} = \sum_{\mathbf{R}i,\mathbf{S}j} h^{e}_{\mathbf{R}i,\mathbf{S}j} a^{\dagger}_{\mathbf{R}i} a_{\mathbf{S}j} - \sum_{\mathbf{R}i,\mathbf{S}j} h^{h}_{\mathbf{R}i,\mathbf{S}j} b^{\dagger}_{\mathbf{R}i} b_{\mathbf{S}j} + \sum_{\mathbf{R}i,\mathbf{S}j,\mathbf{P}l,\mathbf{Q}m} \left(2\bar{v}^{\mathbf{S}j,\mathbf{P}l}_{\mathbf{Q}m,\mathbf{R}i} - W^{\mathbf{S}j,\mathbf{P}l}_{\mathbf{Q}m\mathbf{R}i}\right) a^{\dagger}_{\mathbf{R}i} b^{\dagger}_{\mathbf{Q}m} b_{\mathbf{S}j} a_{\mathbf{P}l}. \quad (1)$$

Here $a^{\dagger}$ (a) and $b^{\dagger}$ (b) are creation (annihilation) operators for electrons and holes, and the boldface and italic letters indicate the lattice vector and the molecular unit in the primitive cell, respectively. h^{e} and h^{h} are the one-particle Hamiltonians for the motion of free electrons and holes, which are described by the band structure calculated in the *GW* approximation.[15] The BSE kernel is given by the sum of $2\bar{v}$, which includes only the $\mathbf{G} \neq 0$ reciprocal-space components of the bare Coulomb interaction v and the statically screened Coulomb interaction W. The matrix elements of $\bar{v}$ and W enter the BSE kernel as exchange and direct e-h interactions, respectively.

Due to the strong localization of the electronic wave functions on the molecular units, it is possible to neglect the overlap integrals between wave functions localized on different molecules. Under this condition the excitonic Hamiltonian $\hat{H}_{\mathrm{ex}}$, Eq. (1), takes a simple block form, being the sum of three terms: $\hat{H}_{\mathrm{FR}}$ and $\hat{H}_{\mathrm{CT}}$, which describe FR and CT excitons, respectively, plus a coupling term, $\hat{H}_{\mathrm{CT\text{-}FR}}$, which originates from hopping processes of independent e-h pairs and is related

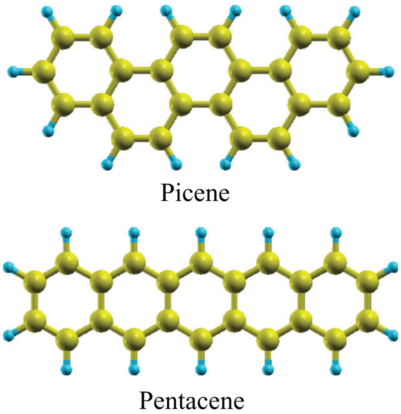

FIG. 1. (Color online) Molecular units of picene and pentacene.

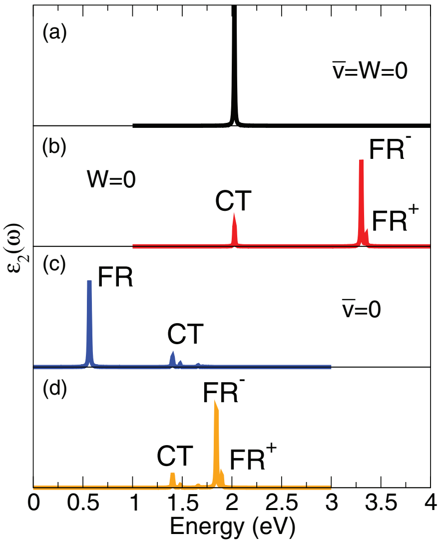

FIG. 2. (Color online) Absorption spectrum of pentacene (along a^*) where only transitions between HOMO-LUMO bands with zero dispersion are considered. The BSE is solved by (a) neglecting both the direct and the exchange e-h interactions ($\bar{v} = W = 0$); (b) including only the exchange e-h interaction ($W = 0$); (c) including only the direct e-h interaction ($\bar{v} = 0$); (d) and including both the direct and the exchange e-h interactions W and $\bar{v}$.

to the band dispersion.[16] Since $\hat{H}_{\text{CT-FR}}$ is responsible for scattering processes of an electron (or a hole) from site to site, it gives rise to a mixing between FR and CT states.

In the first stage, we neglect $\hat{H}_{\text{CT-FR}}$ by setting the band dispersion to 0. The two Hamiltonians $\hat{H}_{\text{FR}}$ and $\hat{H}_{\text{CT}}$ are thus completely decoupled. In pentacene the lowest excited state involves mainly bands deriving from HOMO-LUMO molecular levels. Considering only these bands, the excitonic Hamiltonian simplifies further, becoming diagonal in the band indexes. Excitons in this case can be described using a simple two-level tight-binding model with two molecules in the unit cell.[16] The eigenstates of the excitonic Hamiltonian consist of pure FR and CT states which can be symmetric or antisymmetric (±) with respect to the exchange of an e-h pair between two inequivalent molecules. The energy of FR excitons is

$$E_{\text{ex}}^{\text{FR}\pm}(\mathbf{q}) = \Delta\epsilon - \mathcal{W} + \mathcal{I}(\mathbf{q}) \pm |\mathcal{J}(\mathbf{q})|. \tag{2}$$

Here $\Delta\epsilon$ is the GW HOMO-LUMO gap, $\mathcal{W}$ is the on-site term of the direct e-h interaction W, and $\mathcal{I}$ and $\mathcal{J}$ are the excitation transfer integrals[17] stemming from the exchange e-h interaction $\bar{v}$ and are related to scattering processes of an e-h pair between two equivalent and inequivalent molecules, respectively. On the other hand, the energy of CT excitons is given by

$$E_{\text{ex}}^{\text{CT}\pm}(\mathbf{q}) = \Delta\epsilon - \tilde{\mathcal{W}}, \tag{3}$$

where $\tilde{\mathcal{W}}$ are the attractive intersite contributions to the direct e-h interaction W.

In order to confirm the validity of this simple model description, we solve the *ab initio* BSE in pentacene,[18] considering only transitions between HOMO-LUMO bands in which we artificially set the dispersion to 0. We relax these constraints later. We calculate the optical absorption spectrum, given by the imaginary part of the dielectric function $\epsilon_2(\omega)$ in the $\mathbf{q} \to 0$ limit. In the absence of e-h interactions [$\bar{v} = W = 0$ in Eq. (1)], the spectrum has only a single peak located at the HOMO-LUMO gap $\Delta\epsilon$ [see Fig. 2(a)]. In a molecular picture this means that all the e-h excitations become degenerate, and for a given position of the hole, the electron is delocalized everywhere. The effect of the repulsive exchange e-h interaction $\bar{v}$, when $W = 0$, is to shift the FR states at higher energies and to remove the degeneracy between symmetric and antisymmetric FR states [see Fig. 2(b)], i.e., to induce a Davydov splitting. In particular, we see that along a^* the more intense FR^- peak is located at a lower energy than FR^+[11]. On the contrary, CT states do not feel the exchange e-h interaction [see Eq. (3)] and their energy remains unchanged [compare Figs. 2(a) and 2(b)]. If instead we take into account only the direct e-h interaction W with $\bar{v} = 0$ in Eq. (1), all the peaks are red-shifted with respect to the noninteracting case [compare Figs. 2(a) and 2(c)]. Since the on-site $\mathcal{W}$ is always larger than $\tilde{\mathcal{W}}$, the FR exciton has a lower energy than the CT excitons [see Fig. 2(c)]. Moreover, the CT excitons are no longer degenerate: in fact the direct e-h interaction W depends on the e-h separation and thus different CT excitons are determined by different intersite matrix elements $\tilde{\mathcal{W}}$. On the contrary, since $\bar{v} = 0$ the degeneracy between symmetric and antisymmetric states is preserved. Finally, we take into account both W and $\bar{v}$ [see Fig. 2(d)]. The exchange e-h interaction $\bar{v}$ is felt only by the FR exciton, hence the energy difference between FR and CT states is reduced. In pentacene the exchange e-h interaction is so strong that when $\bar{v}$ is added to W, both symmetric and antisymmetric FR excitons skip above the lowest CT exciton [compare Figs. 2(c) and 2(d)]. As a consequence, in pentacene the lowest-energy excited state in the absence of hopping is a pure CT exciton. This does not happen in picene, for instance, where the exchange e-h interaction is not large enough to compensate for the effect of the direct on-site $\mathcal{W}$ and the lowest-energy excited state is a pure FR exciton.

In the tight-binding picture the exciton dispersion is caused by the scattering of the e-h pair from site to site. In general, scattering processes are induced by hopping through the interaction of an electron (or a hole) with the crystal field or through the effective e-h interaction. However, when the

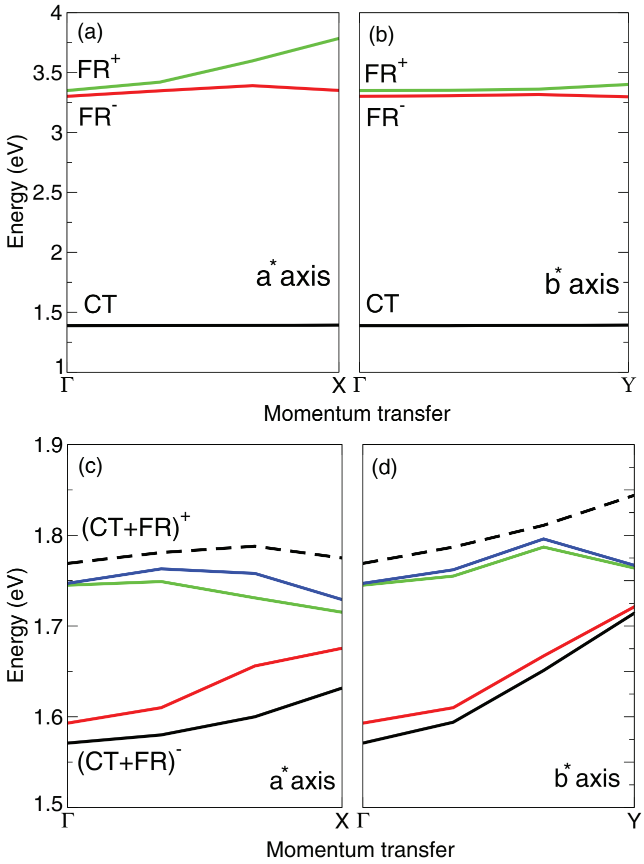

FIG. 3. (Color online) Exciton dispersion in pentacene: (a, b) without hopping and (c, d) including the full band dispersion. Solid and dashed black lines in (c) and (d) refer to excitons related to the coupling between the FR and the lowest CT states. Red, green, and blue lines are other excitons related to the coupling between the FR and the higher-energy CT states.

overlap between wave functions localized on different sites is negligible, the direct e-h interaction W cannot induce site-to-site scattering processes. Indeed in Eqs. (2) and (3) both $\mathcal{W}$ and $\tilde{\mathcal{W}}$ are independent of the momentum transfer $\mathbf{q}$. Therefore, in the absence of hopping the exciton dispersion is set only by the exchange e-h interaction $\bar{v}$. This is confirmed by solving the BSE in pentacene with zero hopping as a function of the momentum transfer $\mathbf{q}$ [see Figs. 3(a) and 3(b)]. Since they are not affected by the exchange e-h interaction $\bar{v}$, pure CT excitons do not disperse. On the contrary, both symmetric and antisymmetric FR excitons have a finite dispersion. Therefore the exciton dispersion provides an immediate way to distinguish FR from CT excitons. In particular, for $\mathbf{q}$ along the reciprocal-lattice axis a^* the FR$^+$ state has an exciton bandwidth of ~0.4 eV, which is ~0.1 eV for the FR$^-$ state [see Fig. 3(a)]. This suggests that the exchange e-h processes involving equivalent and inequivalent molecules compensate each other in the antisymmetric state, $\mathcal{I}(\mathbf{q})$ and $\mathcal{J}(\mathbf{q})$ having opposite signs for FR$^-$ excitons [see Eq. (2)]. On the other hand, for $\mathbf{q}$ along b^* [see Fig. 3(b)] the dispersion is negligible.

To investigate the effects of hopping of free electrons and holes, we relax the constraint of flat bands and we solve the BSE including the full dispersion of the HOMO-LUMO bands. First, through its $\mathbf{q}$ dependence, the hopping induces a finite dispersion of CT states [which otherwise is 0; see Figs. 3(a) and 3(b)] and modifies the intrinsic dispersion of FR excitons given by $\mathcal{I}(\mathbf{q})$ and $\mathcal{J}(\mathbf{q})$ [see Eq. (2)]. Moreover, switching on the hopping induces a mixing of FR and CT states (the coupling term $\hat{H}_{\text{CT-FR}}$ is no longer 0): in a real material the excited states are always a mixture of the two excitonic solutions. The hopping hence removes the degeneracy between symmetric and antisymmetric CT states, giving rise to two mixed excitons, with symmetric $(\text{CT}+\text{FR})^+$ and antisymmetric $(\text{CT}+\text{FR})^-$ character. The mixing between CT and FR excitons is stronger when the hopping is larger and when the energy difference between pure CT and FR states is lower. The e-h exchange interaction, through the terms $\mathcal{I}(\mathbf{q})$ and $\mathcal{J}(\mathbf{q})$ in Eq. (2), changes the energy difference between pure FR and CT excitons as a function of $\mathbf{q}$. In turn, this variation of their separation modulates the mixing effect due to hopping (which is larger when the excitons get closer in energy). We thus see that the exchange e-h interaction, through hopping, also has an (indirect) effect on CT excitons.

Therefore, from this general analysis we can conclude that the exciton dispersion in molecular crystals arises from the interplay between hopping and the exchange e-h interaction. The *ab initio* BSE results confirm these conclusions. We find [see Figs. 3(c) and 3(d)] that the lowest exciton in pentacene, at 1.55 eV at $\mathbf{q}=0$, is a $(\text{CT}+\text{FR})^-$ state. It is related to the lowest CT exciton in Figs. 3(a) and 3(b). The corresponding symmetric $(\text{CT}+\text{FR})^+$ state is at 1.76 eV at $\mathbf{q}=0$, giving a Davydov splitting of 0.2 eV. Between these two excitons, other combinations of FR and CT excitons appear. The width of the dispersion of these $(\text{CT}+\text{FR})^\pm$ states varies between 0.05 and 0.20 eV, which is rightly the order of magnitude of the HOMO-LUMO bandwidths. In particular, the exciton dispersion is larger along the b^* axis [see Fig. 3(d)], where the first exciton has a bandwidth of 0.14 eV, which is about twice as large as the dispersion along a^* [see Fig. 3(c)]. This difference is an indirect effect of the exchange e-h interaction. Because of it, along a^* FR excitons have an intrinsic finite dispersion, which is instead negligible along b^* [see Figs. 3(a) and 3(b)]. Therefore, as $\mathbf{q}$ increases, FR and CT get farther apart along a^*, reducing their coupling induced by hopping, while this does not occur along b^*.

Finally, in Figs. 4(a) and 4(b) we report the spectra of ϵ_2 as a function of $\mathbf{q}$ for pentacene, solving the BSE for a converged set of bands (so we relax the last constraint about using only HOMO and LUMO bands). For the lowest-energy peaks we find the same results as obtained by considering only the HOMO-LUMO bands [see Figs. 3(c) and 3(d)], confirming that the HOMO-LUMO bands make by far the most important contribution to these excitons. The lowest $(\text{CT}+\text{FR})^-$ state is visible for a polarization along the a^* axis, while its $(\text{CT}+\text{FR})^+$ counterpart is visible only along the b^* axis. Both excitons remain visible up to the Γ point of the second Brillouin zone, where their oscillator strengths drop to 0 and the spectral weight is transferred to higher-energy $(\text{CT}+\text{FR})$ states. Interestingly, at high momentum transfer along the b^* axis a new peak appears at an energy lower than that of the $(\text{CT}+\text{FR})^+$ state that determines the onset at $\mathbf{q}=0$. This new peak corresponds to the lowest $(\text{CT}+\text{FR})^-$ exciton,

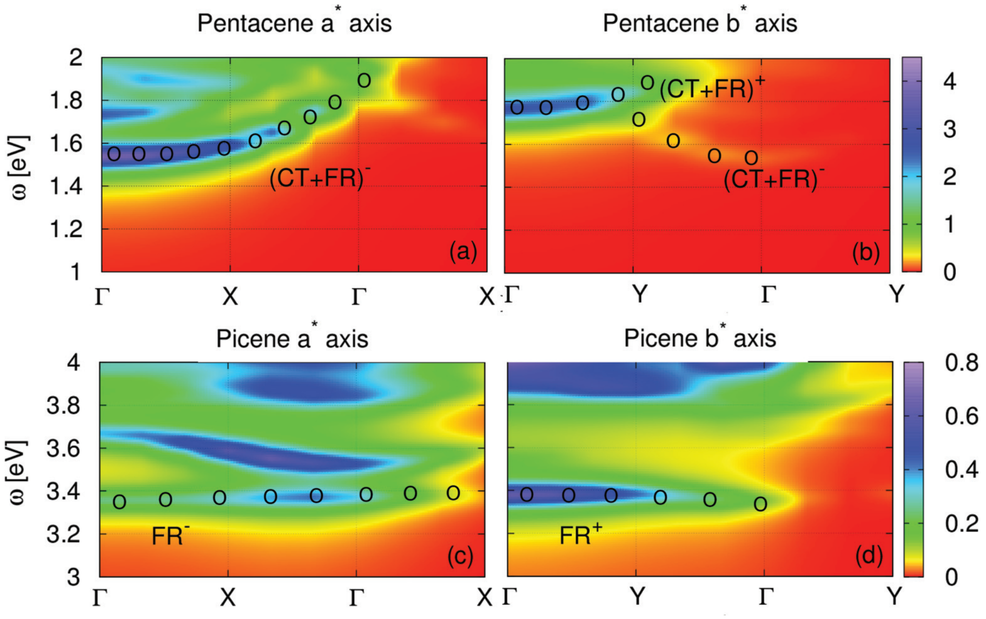

FIG. 4. (Color online) Map of the imaginary part of the macroscopic dielectric function ϵ_2 evaluated as a function of the energy (vertical axis) and momentum transfer (horizontal axis) along (a) the a^* axis and (b) the b^* axis of pentacene and along (c) the a^* axis and (d) the b^* axis of picene. Black circles are guides for the eye for the lowest-energy excitons.

which is dipole forbidden at low momentum transfer along the b^* axis but becomes visible at larger $\mathbf{q}$.

We can now compare pentacene with picene [see Figs. 4(c) and 4(d)], in which the lowest excited states are localized FR excitons. In particular, at $\mathbf{q} = 0$ the symmetric and antisymmetric FR$^+$ and FR$^-$ states are visible along the b^* and a^* axis, respectively, with a Davydov splitting of about 0.02 eV, which is one order of magnitude smaller than in pentacene. These lowest excitons, in contrast to pentacene, involve the contributions of several bands besides the HOMO-LUMO transitions. The mixing of HOMO-LUMO transitions with higher-energy excitations makes the contributions from the direct e-h interaction W larger, while it does not affect the kinetic term in Eq. (1). As a result, the exciton binding energy is also increased, giving rise to a strongly localized FR exciton, well separated in energy from the CT ones. As a consequence, the mixing with higher-energy CT excitons is negligible in picene. The lowest excited state thus preserves its intrinsic FR character and its dispersion is set by the exchange e-h interaction only. In Figs. 4(c) and 4(d) we see that for small $\mathbf{q}$ belonging to the first Brillouin zone, the FR$^-$ exciton has a positive dispersion, while the FR$^+$ state has a negative dispersion. For both excitons the bandwidth is about 0.02 eV, which is one order of magnitude smaller than in pentacene, suggesting that in the two systems the mechanism of the exciton dispersion is completely different.

The traditional interpretation of electroabsorption experiments[26,27] suggests that the lowest excited state in pentacene is an FR exciton, in seeming contrast with our analysis. In fact, the electroabsorption signal shows different behavior for FR and CT states. Its shape thus identifies unequivocally the exciton character when this is a pure FR or CT state. However, the interpretation of the electroabsorption spectra is rather complicated in real materials, where the excitons are always a mixture of the two configurations. On the other hand, our results are in good quantitative agreement with recent electron energy-loss spectroscopy (EELS) experiments.[28,29] While an exciton band structure with bandwidths of about 100 meV has been observed for pentacene, picene has not shown a measurable dispersion for $\mathbf{q}$ belonging to the a^*b^* plane. The present work thus provides the tools for interpretation of these recent experimental results also.

In conclusion, by combining *ab initio* many-body BSE calculations for picene and pentacene with a simple model interpretation, we have drawn a general picture of the exciton dispersion in molecular crystals. We have shown that the exciton dispersion is the result of the interplay between two mechanisms: electron and hole hopping and the electron-hole exchange interaction. The investigation of the exciton dispersion provides valuable insights into the nature of the excitons, allowing one to tell the difference between localized FR excitons and delocalized CT excitons. This analysis is of general validity and can be exploited to describe other strongly correlated insulators with localized electronic wave functions.

The authors acknowledge financial support from the European Research Council Advanced Grant DYNamo (ERC-2010-AdG-267374), Spanish grants (2010-21282-C02-01 and PIB2010US-00652), Grupos Consolidados UPV/EHU del Gobierno Vasco (IT578-13), European Commission projects CRONOS (Grant No. 280879-2 CRONOS CP-FP7), and the Maison de la simulation for technical support. Computational time was granted by GENCI (Project No. 544) and by the CNANO-SIMULEE-2009 project. This work was carried out under the HPC-EUROPA2 project, with the support of the European Community–Research Infrastructure Action of the FP7.

[*] pierluigi.cudazzo@ehu.es

[1] L. V. Butov *et al.*, Nature (London) **417**, 47 (2002).

[2] D. W. Snoke *et al.*, Nature (London) **418**, 754 (2002).

[3] J. Kasprzak *et al.*, Nature (London) **443**, 409 (2006).

[4] P. Abbamonte *et al.*, Proc. Natl. Acad. Sci. USA **105**, 12159 (2008).

[5] K. Yang *et al.*, Phys. Rev. Lett. **98**, 036404 (2007).

[6] W. Schülke, *Electron Dynamics by Inelastic X-Ray Scattering* (Oxford University Press, New York, 2007).

[7] F. J. García de Abajo, Rev. Mod. Phys. **82**, 209 (2010).

[8] S. Albrecht, L. Reining, R. Del Sole, and G. Onida, Phys. Rev. Lett. **80**, 4510 (1998); L. X. Benedict, E. L. Shirley, and R. B. Bohn, *ibid.* **80**, 4514 (1998); M. Rohlfing and S. G. Louie, *ibid.* **81**, 2312 (1998).

[9] G. Onida, L. Reining, and A. Rubio, Rev. Mod. Phys. **74**, 601 (2002).

[10] A. Davydov, *Theory of Molecular Excitons* (McGraw–Hill, New York, 1962).

[11] V. M. Agranovich, *Excitations in Organic Solids* (Oxford University Press, New York, 2008).

[12] M. Gatti and F. Sottile Phys. Rev. B **88** 155113 (2013).

[13] W. A. Caliebe, J. A. Soininen, E. L. Shirley, C.-C. Kao, and K. Hämäläinen, Phys. Rev. Lett. **84**, 3907 (2000).

[14] A. Marini, R. Del Sole, and A. Rubio, Phys. Rev. Lett. **91**, 256402 (2003).

[15] L. Hedin, Phys. Rev. **139**, A796 (1965).

[16] P. Cudazzo, M. Gatti, and A. Rubio, Phys. Rev. B **86**, 195307 (2012).

[17] F. Bassani and G. Pastori Parravicini, *Electronic States and Optical Transitions in Solids* (Pergamon Press, Oxford, 1975).

[18] For picene and pentacene we have used the experimental crystal structures of Refs. 19 and 20. In both cases, converged BSE spectra have been obtained with a $6 \times 6 \times 4$ grid of $\mathbf{k}$ points, 53 occupied and 29 empty bands. The coupling between resonant and antiresonant transitions, beyond the Tamm-Dancoff approximation adopted here, does not qualitatively modify our conclusions regarding the dispersion of the lowest-energy excitons and their nature. See also Ref. 21. Ground-state and *GW* band-structure calculations follow those in Refs. 16, 22, and 23 and were performed with the ABINIT[24] code. For the BSE at finite $\mathbf{q}$ we used the EXC code.[25]

[19] A. De, R. Ghosh, S. Roychowdhury, and P. Roychowdhury, Acta Crystallogr. C **41**, 907 (1985).

[20] O. D. Jurchescu, Ph.D. thesis, Rijksuniversiteit Groningen (2006); http://dissertations.ub.rug.nl/faculties/science/2006/o.d.jurchescu.

[21] C. Ambrosch-Draxl, D. Nabok, P. Puschnig, and Ch. Meisenbichler, New J. Phys. **11**, 125010 (2009).

[22] F. Roth, M. Gatti, P. Cudazzo, M. Grobosch, B. Mahns, B. Büchner, A. Rubio, and M. Knupfer, New J. Phys. **12**, 103036 (2010).

[23] P. Cudazzo, M. Gatti, F. Roth, B. Mahns, M. Knupfer, and A. Rubio, Phys. Rev. B **84**, 155118 (2011).

[24] X. Gonze *et al.*, Z. Kristallogr. **220**, 558 (2005).

[25] See http://www.bethe-salpeter.org/.

[26] L. Sebastian, G. Weiser, and H. Bässler, Chem. Phys. **61**, 125 (1981).

[27] L. Sebastian, G. Weiser, G. Peter, and H. Bässler, Chem. Phys. **75**, 103 (1983).

[28] F. Roth, B. Mahns, B. Büchner, and M. Knupfer, Phys. Rev. B **83**, 165436 (2011).

[29] F. Roth, R. Schuster, A. König, M. Knupfer, and H. Berger, J. Chem. Phys. **136**, 204708 (2012).

Chapter 7

Software-related Management Coordination

ALONGSIDE with the research activity, the coordination (and active development) of the two ab initio codes DP and EXC, also represents a big portion of my everyday work. In particular, together with the developement of new features to be implemented, I extensively worked for the porting of the codes on massively parallel machines. The complexity of Teraflop/s (and today Petaflop/s) system architectures and the simulations who should exploit it represent a real challenge.

It is not possible to tackle this challenge without a multi-scale interdisciplinary approach. As a scientist, I have to create synergy with HPC (High Performance Computing) computer scientists and numerical analysts. To achieve that I have adopted a triple strategy: i) on one side I have established a (now long-standing) collaboration with the Maison de la Simulation, a laboratory of five partners (CEA, CNRS, INRIA, University of Orsay and University of Versailles-St.Quentin) whose aim is to support and stimulate the scientific community in order to get the best out of supercomputers; ii) on the other, we work with the most important European partnership, like PRACE, for the development of codes working on parallel machines, Graphics accelarator, MIC, etc.; iii) finally, we apply for national and regional grant in order to buy and maintain a local cluster, crucial for our work, highly centered on fundamental developement.

The outcomes of the first strategy was the establishement of a collaboration between the Maison de la Simulation and our group, useful for our next projects. This collaboration permitted a 2-years post-doc (who benefited of the EuroTalent grant) to work on spectroscopic properties of CuO, and, also thanks to 18-months enginneer time, the porting of DP and EXC codes on the GENCI machines (national supercomputing centres).

The second strategy lead to the Preparatory Access project (pa20101148) that I have coordinated and whose aim was the porting of the DP code to the new generation GPU's graphic processors. Main goal of this PRACE project was to evaluate how GPU could speed up Linear Response TDDFT code DP. Profiling analysis of the code has been done to identify computational bottlenecks to be delegated to the GPU. Results showed that one can reasonably expect about 10 times speedup on the total execution time, depending on the structure of the input and the size of used datasets, and speedups up to 16 have been observed for some cases [69]. More details about it can be found in the Appendix B.

The third action, culminated in 2 regional grants, CNANO SIMULEE and OXYMORE ES-GPU, that have permitted to buy a local cluster (which today counts more than 800 cores, 25 Terabyte of storage, and 4400 Gb of RAM) and to invest in the new generation NVIDIA GPUs machine.

Part III

Perspectives and projects

Chapter 8

Frontiers Emerging from Exciton Dispersions

STATE of the art for the calculation of band structures in a wide range of materials (from sodium to uranium) is today the GW approximation (GWA) of many-body perturbation theory (MBPT) [17, 115]. In this framework, the self-energy $\Sigma(\mathbf{r}, \mathbf{r}', \omega)$, which is a non-local, non-hermitian and frequency-dependent potential taking into account exchange and correlation (xc) effects, is approximated by the convolution of the Green's function $G(\mathbf{r}, \mathbf{r}', \omega)$ and the dynamically screened Coulomb interaction $W(\mathbf{r}, \mathbf{r}', \omega) = \epsilon^{-1}(\mathbf{r}, \mathbf{r}', \omega)v(\mathbf{r}, \mathbf{r}')$. Here v is the bare Coulomb interaction and ϵ is the dielectric function, which in the GWA is calculated at the level of the random-phase approximation (RPA). Since the 1980s the application of the GWA to real materials has followed a first-order perturbative scheme based on Kohn-Sham (KS) ingredients [116]. This standard scheme, known as G_0W_0, improves considerably the results for the band gaps of semiconductors, which are strongly underestimated using semilocal KS xc functionals [116]. In the last years, the G_0W_0 scheme has been largely revisited in order to get rid of the dependency on the KS starting point (unavoidable in any perturbative approach). An approximate procedure to reach self-consistency within the GW framework has been proposed: the quasiparticle self-consistent GW ($QSGW$) method [117, 118]. $QSGW$ allows one to solve most of the flaws of G_0W_0 at a moderate calculation cost. In particular, situations in which the KS starting point is not adequate (e.g. for small band-gap semiconductors and some transition-metal oxides [119]) are then cured, bringing a clear improvement with respect to G_0W_0. However, band gaps are systematically overestimated by the $QSGW$ method [118]. These errors have been ascribed to the missing electron-hole interactions in the calculation of W: it was empirically found that by rescaling by 0.8 the screened interaction W to mimic excitonic effects, the results were improved with respect to experiment [118, 120, 121]. Different ways of improving upon the GW results (called "vertex corrections" in the MBPT jargon) have been much debated in literature [41, 122].

8.1 Band-gaps from vertex-corrected W

This issue will constitute part of my next-future work. I plan to systematically investigate, beyond the state-of-the-art GW approximation, the role of excitonic effects in the screening of the Coulomb interaction W on band structures and band gaps. This will be possible thanks to the solution of the Bethe-Salpeter equation (BSE) [115] for the calculation of ε^{-1}. The BSE nowadays can be solved in an ab initio framework, allowing one to accurately model excitons and to obtain absorption spectra (i.e. for vanishing momentum transfer $\mathbf{q} \rightarrow 0$) in excellent agreement with experiments [115]. Recently we have demonstrated its high level of accuracy and great power of analysis also for the calculation of ε^{-1} in a wide range of energy and momentum transfers and for the study of exciton dispersions well beyond the dipole approximation [113]. Being completely parameter free, it is able to predict the full IXS and EELS spectra of materials, without any experimental input [113, 114].

This important achievement now gives us the opportunity to explore and advance novel frontiers of ab initio simulations. In fact, besides extending the applicability of the BSE to high momentum transfers, our recently developed method allows a careful analysis of whole spectrum of excitations entering W. On this basis we expect that a BSE calculation of W will provide a quantitative evaluation of the improvements with respect to the GWA.

The most immediate perspective is then to confirm or dismiss the expectations about the role played by excitonic effects in W for band structure calculations.

8.2 Addressing fundamental questions to progress our knowledge

Let's now discuss, on a more qualitative level, about a long-standing debate that has been animating the discussions in the electronic structure community: What is the "best" screened interaction W that we should consider in an electronic system? There are several possibilities, due to the wide range of approximation that naturally appears in the long procedure to finally describe the screening, but we can cut out to two main opposite ideas: is it better to construct a screening which is completely consistent with the level of approximation used, using the self-consistence scheme for instance, or to rely on the best possible screening, as it would be described by IXS or EELS experiments? The question is delicate: in the first case we maintain a certain coherence in the theory, we avoid double counting and the operative procedure is easy to implement; the second possibility instead relies on the description of the screening not in a self-consistent scheme, but rather in a one-shot description that however has to be the best possible, with all effects included. The debate is still very alive, and many partial answers can be given for one or the other solution [118, 119, 121, 123]. However, very recently, we have carried out a joint work with a group of experimentalists that gives major hints about the latter solution [124, 125], suggesting that indeed the best screening to use should be the experimental one. The future work will prove this insight on the basis of numerical results.

8.3 Reducing dimensionality

The recent work on exciton dispersion has opened the way to the study of a new class of materials for photovoltaics, i.e. system with reduced dimensionality. We plan then to analyze and discuss in details the exciton dispersion in those systems, in particular layered systems and nanotubes. It has been recently shown [126–129] that the low dimensionality of the carbon nanotubes can lead to theoretical record efficiency of 42%. At the same time, today controllable doping gradient has permitted to layered materials like MoS_2 to emerge as new and promising materials for solar cell devices [130, 131], thanks to the their large area-to-volume ratio (this makes them effectively 2D systems) and the foreseen mobility (which will make them much better than polycrystalline or amorphous systems as today used in silicon technology). Our objective is then to carry out a careful study of exciton dispersion and mobility of systems with reduced dimensionalities, starting indeed from the very promising 2D MoS_2 and 1D carbon nanotubes. This is ongoing work with the post-doc Pierluigi Cudazzo and Giorgia Fugallo.

8.4 Discovering new phenomena

Finally let's now discuss about qualitatively new phenomena. The cumulant expansion of G combined with the GWA for Σ allows one to accurately describe plasmon satellites in PES spectra [111, 113, 132]. Satellites are a genuine signature of many-body dynamical correlation in the PES spectra, beyond the one-particle picture of the band structure. Plasmon satellites are due to the coupling between the hole created in the photoemission process and plasmons that are additionally excited in the electronic system. We now intend to investigate the possible existence of "exciton satellites", i.e. many-body fingerprints in PES spectra of the coupling between the photohole and additional excitons in the system. This new kind of satellites could not be univocally identified so far for the lack of adequate computational approaches. While plasmons can be calculated in the RPA used for W in the GWA, excitons can be described only thanks to the BSE. In a work already started with I.Reshetnyak (PhD student in the group), we will make this identification possible. We will calculate exciton satellites in the spectral function of prototypical excitonic materials, which will be verified by photoemission experiments that we are going to propose to experimentalists.

Chapter 9

Bootstrap-like (series of) kernel(s)

So far, we have constructed a scalar exchange correlation kernel (it is essentially a number). Since the bootstrap kernel has the correct long-range $\frac{1}{|\mathbf{q}|^2}$ behaviour, it could be seen as an *ab initio* way to find the parameter in the long-range kernel $\frac{\alpha}{|\mathbf{q}|^2}$. It is indeed the case and, while it doesn't manage to find the best possible α for Silicon, it still find a very reasonble value for the insulators, for which a trial an errors would be lengthy and not efficient (contrary to the case of semiconductors where a rough estimate can be guessed on the basis of the dielectric constant [133]). The reason for this choice (after all the exchange-correlation kernel is a frequency dependent matrix in $\mathbf{G}, \mathbf{G}'$) is threefold: i) the original formulation concerned mainly a scalar kernel [74]; ii) it is much simpler to implement and test; iii) it permitted to avoid the iteration scheme proposed in [74] and propose a one shot kernel. There are however important reasons to further develop this, so far, simple kernel:

- the description of the optical absorption of insulators is still unsatisfactory. Even when a bound exciton is found (not obvious) the binding energy is too small.

- a scalar kernel cannot capture at the same time optical absorption and plasmonic features. If the scalar kernel can be viewed, in fact, as an *ab initio* version of the long-range kernel, it cannot work for both optical and loss function, in which the weight of the excitonic effect is not comparable. For instance, in Silicon, the value of the parameter for the optical absorption is $\alpha = -0.15$, while for the plasmon is $\alpha = -2.0$ (more than on order of magnitude of difference). It is not possible then for just one number to have two different values. This requires a matrix extension.

- a scalar (and frequency independent) kernel cannot capture a series of bound excitons. In fact, being just a number, it cannot create more than one pole inside the band-gap. The BSE manages this thanks to a complex matrix $\varepsilon^{-1}_{\mathbf{G},\mathbf{G}''} v(\mathbf{G}'', \mathbf{G}')$. The Nanoquanta kernel [95] do the same but at the price of a BSE-like computational time. The idea here is to try to obtain the same, using a bootstrap-like idea. In parallel , Sangeeta Sharma and co-workers are dealing with the very same problem following a different approach. Rather than go towards a more complex matrix formalism, they are investigating a scalar but frequency dependent kernel, which is also, in principle, able to obtain more than one bound excitons (thanks to Sangeeta for the private communication on this subject).

For all these reasons we are working to a matrix extension of this kernel, which however has to be conducted in a prudent and careful manner, analysing what it means in this iterative procedure, ingredient by ingredient. For instance, a simple replacement of the matrices in all the ingredients (rather than the macroscopically averaged counterpart) simplty destroys the spectrum.

Chapter 10

Resonant Inelastic X-ray Scattering

New generation synchrotrons permitted what is called today a new renaissance of x-ray physics, and the first beneficiary of this renaissance has incontroversly been the Resonant Inelastic X-ray Scattering (RIXS). In the last decade, in fact, RIXS advances have been remarkable, thanks to its unique capability of probing elementary excitations by measuring their energy, polarization, momentum. The microscopic picture of RIXS can be summarized as follows: i) an incoming photon promotes a core electron to a conduction (empty) state; ii) afterwards, a different electron from the valence region decays and annihilates the core-hole. The net result is a final state with an electron-hole excitation, whose energy and momentum are defined by the respective conservation laws. Compared to other spectroscopic techniques, RIXS has numerous advantages, confirmed by an exponentially increasing number of applications in the last years, namely: huge scattering phase-space, bulk sensitivity, chemical specificity, polarization sensitivity, small sample volumes. The main disadvantage of RIXS, with respect to other techniques, like Angle Resolved Photo-Emission Spectroscopy (ARPES) is the need of an intense incident flux in order to obtain enough scattered photons and so having the claimed energy and momentum resolution. This was the only problem that has limited RIXS experiments in the past. Today, however, many progresses in RIXS instrumentation have strongly changed the situation and generalized the range of materials and energies where to perform RIXS experiments. As an example, the energy resolution of RIXS at the L edge of Cu in La_2CuO_4 was about 1.6 eV in 1996, 0.8 eV in 2003, 0.13 eV in 2008 [134]. Of course, great progress in the experimental RIXS requires and stimulate great advances also in the theoretical description. Unfortunately the theoretical and numerical counterpart has not known, in the recent years, the advances required for a profound comprehension of the scattering process and of the dynamic correlation that this experimental technique probes. The basic theoretical foundation of RIXS has been established long ago [135], relying on the second- and third-order expansion of the matter-radiation Dirac equation, which ends in a set of very schematic equations, the Kramers-Heisenberg (KH) equations (see Eq.(1.19)). These equations look schematically like the Fermi Golden rule for a second-order process of absorption+emission of a photon. However, though schematically simple, the solution of these equations, which involve the calculation of scattering amplitudes between many-body wave-functions, is impossible for a realistic system, crucially asking for clever strategies, fast algorithms, efficient approximations, and, above all, deep understanding of the elementary physical processes involved. Another important characteristic, often underlined as an advantage, of RIXS is its extreme versatility in probing a large class of different excitations of the system under study, inter-band and intra-band transitions, collective excitations, plasmons, orbital excitations, magnetic excitations, electron-phonon coupling, etc. This certainly can be an advantage, but also implies huge interpretation problems, for many elementary excitations participate and compete to the same RIXS spectrum. Without a powerful analysis tool, capable of disentangling different contributions, or of switching off/on a kind of excitation, the interpretation of an experiment and, in last analysis, a deep understanding of the

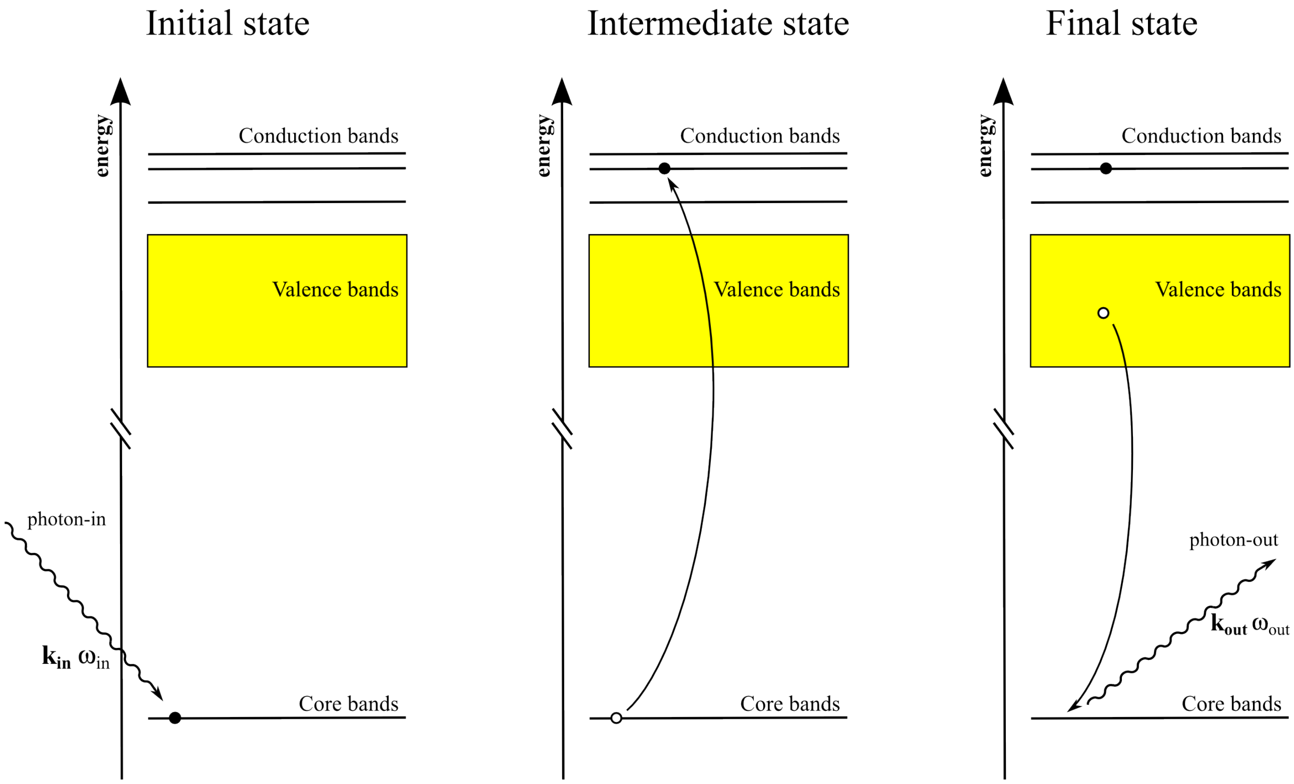

Figure 10.1: Schematic view of the Resonant Inelastic X-ray Scattering. An X-ray of energy ω_{in} and momentum $\mathbf{k_{in}}$ impinges on the system in its initial ground-state, causing the excitation of a core-electron. The empty core of the system in its intermediate excited state is filled up by a valence electron, emitting another X-ray of energy ω_{out} and momentum $\mathbf{k_{out}}$, leaving the system in its final excited state. This scheme describes the so-called direct RIXS, which is only a part of the total phenomena covered by the KH formula. See Ref.[136] for more details.

material is impossible.

Most of RIXS data are today obtained at transition metal and Oxygen edges. The reason for this is an extreme interest in the so-called strongly correlated transition metal oxides, both for their intrinsic complexity that makes their study intellectually challenging and for the prospect of novel applications (high-Tc superconductors, colossal magneto-resistance, transparent conducting oxides, etc). If, on one side, this historical attention has been very beneficial for the transition metal oxides and related fields, on the other side, it worths underlining the huge potential for application of RIXS (both experimentally and theoretically) on other materials and fields.

One of the axes of my future work is then centered on the RIXS. It has already started with a Marie-Curie Fellowship post-doc, Fabiana da Pieve, whose project (RESCOR, I am the scientific responsible) aim is to make a new, qualitative jump towards the predictive description of RIXS experiments, over a whole range of materials and energies, where theory (and numerical simulation) is needed to add values beyond the mere reproduction of a spectrum.

This requires on one hand the evaluation of the basic equations which describe RIXS within the Bethe-Salpeter formalism, a very promising approach in light of recent developments and results; on the other hand it crucially demands the improvement of the currently used approximations to correlation in order to treat the so-called strongly correlated materials, to which RIXS experiments have been mainly devoted due to the incredible richness of their properties. To reach this goal we will: i) combine the advantages of different theoretical approaches (Hubbard model Hamiltonian, Density Functional Theory, Green's Function Many-Body Theory and Bethe-Salpeter equation) to obtain both an accurate and efficient tool to analyse and predict RIXS spectroscopies; the use of the Hubbard model (used in the large DMFT community) to receive hints, insights about the physics of the local problem will be formalized within an ab initio framework (so going beyond any parameter approach), based on the Density Functional Theory, GW and Bethe-Salpeter equation; ii) develop new methods and new strategies to tackle the daunting problem of the description, within an ab initio framework, of strongly correlated systems.

This, still very vague, project will be tackled from different angles, and putting together the knowledge and advances acquired in the last years:

- the finite momentum developments will permit to tackle the KH formula beyond the dipole approximation
- recent developments in Projector Augmented Waves techniques (able to tackle core electrons) will be used to obtain the ingredients (one-particle eigenvalues and wavefunctions) entering the RIXS theory, analogously to what is done in the code OCEAN [137], by the group of John Rehr, with whom we collaborate on the RIXS project.
- new developments in the group (notably within the MC project of Pierluigi Cudazzo) concerning the dynamical BSE [79, 138], will be of particular help in the specific indirect channel of RIXS.

Appendix A

Linear Response Theory

A linear response function χ to an applied external field F is defined through the relation:

$$\delta \langle p \rangle = \langle p \rangle - p_0 = \chi F \tag{A.1}$$

where p_0 is the value of the operator p when $F = 0$.[1] So $\delta \langle p \rangle$ is the response of the system to an applied field F, and χ is the *response function*, which is in the $F \to 0$ limit, independent of the applied field. More in detail, for any measurable property $p(\mathbf{r}, t)$:

$$\delta \langle p(\mathbf{r}, t) \rangle = \int d\mathbf{r}' \int dt' \chi\left(\mathbf{r}, \mathbf{r}'; t - t'\right) F(\mathbf{r}', t')$$

where the *causality* condition is used in the time integral.
The Fourier transform of χ is a complex function $\chi(\omega) = \chi_1 + i\chi_2$:

$$\chi(\omega) = \int dt \chi(t) e^{-i\omega t}$$

for a response function to a purely time-dependent applied field $F(t) = F_0\, e^{-i\omega t}$. The causality condition implies that $\chi(\omega)$ is analytic in the upper half plane of the complex plane[2], with precise relations between real and imaginary part of χ, namely the Kramers-Kronig [139, 140] relations:

$$\chi_1(\omega) = \frac{2}{\pi} \mathrm{P} \int_0^\infty d\omega' \frac{\omega' \chi_2(\omega')}{\omega'^2 - \omega^2} \quad ; \quad \chi_2(\omega) = -\frac{2\omega}{\pi} \mathrm{P} \int_0^\infty d\omega' \frac{\chi_1(\omega')}{\omega'^2 - \omega^2}.$$

If $F(\mathbf{r}, t)$ is the external perturbation, the corresponding term that has to be added to the system's Hamiltonian is

$$H_1(t) = \int g(\mathbf{r}) F(\mathbf{r}, t) d\mathbf{r}$$

where $g(\mathbf{r})$ is the coupling variable between the perturbation and the system, and H_1, the perturbing contribution to the Hamiltonian, is expressed in the interaction picture. Within this scheme it is possible to derive the linear response function in terms of ground state quantities. First order time-dependent perturbation theory yields the Kubo formula (see, e.g. Ref. [65]) for the response function:

$$\chi\left(\mathbf{r}, \mathbf{r}', t - t'\right) = -i \langle N | \left[g(\mathbf{r}, t), g(\mathbf{r}', t')\right] | N \rangle \, \Theta(t - t')$$

with $|N\rangle$ many-body ground state ($|N\rangle = \varphi^0$).

In summary, we have to consider the following two criteria for χ to be considered the response function of the system, related to the perturbation F:

---

[1] p can be, for example, the macroscopic magnetisation of a sample subject to a magnetic field (F). χ, the response function, plays then the role of the magnetic susceptibility.

[2] Or the lower half plane if, by convention, we let the field to oscillate as $e^{i\omega t}$ instead of $e^{-i\omega t}$.

a) In writing $\delta \langle p \rangle = \chi F$, the quantity F has to be a truly *perturbing* potential, something that can be changed at will without any influnce from the medium.

b) The influence on the medium has to be described as an additional Hamiltonian $H_1 = -gF$

The first requirement implies the causality condition, the second introduce the dynamics of the influence, and define a truly response function (sometimes also called generalized susceptibility).

Important response functions are for instance the density-density, density-current and current-current response functions,

$$\chi_{\rho\rho}(\mathbf{r},\mathbf{r}',\omega) = -i\int_0^\infty d\tau e^{i(\omega+i\eta)\tau} \langle N|\left[\rho(\mathbf{r},t),\rho(\mathbf{r}',t')\right]|N\rangle = \frac{\delta\rho(\mathbf{r},\omega)}{\delta V_{\text{ext}}(\mathbf{r}',\omega)} \tag{A.2}$$

$$\chi_{\rho\mathbf{j}}(\mathbf{r},\mathbf{r}',\omega) = -i\int_0^\infty d\tau e^{i(\omega+i\eta)\tau} \langle N|\left[\rho(\mathbf{r},t),\mathbf{j}(\mathbf{r}',t')\right]|N\rangle = \frac{\delta\rho(\mathbf{r},\omega)}{\delta \mathbf{A}_{\text{ext}}(\mathbf{r}',\omega)} \tag{A.3}$$

$$\chi_{\mathbf{j}\rho}(\mathbf{r},\mathbf{r}',\omega) = -i\int_0^\infty d\tau e^{i(\omega+i\eta)\tau} \langle N|\left[\mathbf{j}(\mathbf{r},t),\rho(\mathbf{r}',t')\right]|N\rangle = \frac{\delta\mathbf{j}(\mathbf{r},\omega)}{\delta V_{\text{ext}}(\mathbf{r}',\omega)} \tag{A.4}$$

$$\chi_{\mathbf{jj}}(\mathbf{r},\mathbf{r}',\omega) = -i\int_0^\infty d\tau e^{i(\omega+i\eta)\tau} \langle N|\left[\mathbf{j}(\mathbf{r},t),\mathbf{j}(\mathbf{r}',t')\right]|N\rangle = \frac{\delta\mathbf{j}(\mathbf{r},\omega)}{\delta \mathbf{A}_{\text{ext}}(\mathbf{r}',\omega)} \tag{A.5}$$

representing the observables in TDDFT or BSE.

Appendix B

Porting DP over GPU's

The collaboration with the Maison de la Simulation started in occasion of the post-doc work of Claudia Rödl. The idea was to study the spectral properties of correlated materials, starting from a prototype for high-Tc cuprate superconductors: CuO. Already fot this system, the computational requirements were important. The collaboration with engineers and technicians from the Maison de la Simulation promised fast advances in the optimization of our codes. During one of the meetings, the crucial part of the TDDFT calculation, as implemented in the DP code, was recognised as possible candidate for GPU porting. This had implied a lot of work and involvement from both sides. We managed to obtain, for this specific projet, a preparatory access PRACE grant. The final result is promising, but prude Here follows the report of such activity.

Available on-line at www.prace-ri.eu

Partnership for Advanced Computing in Europe

GPU Implementation of Linear Response TDDFT algorithm in DP code

F.Sottile[a], C.Roedl[a], V.Slavnic[b], P.Jovanovic[b],
D.Stankovic[b], P.Kestener[c], F.Houssen[c]

[a]Laboratoire des Solides Irradiés, Ecole Polytechnique, CNRS, CEA , UMR 7642, 91128 Palaiseau cedex, France
[b]Institute of Physics Belgrade, Serbia
[c]Commissariat à l'Énergie Atomique

Abstract

Main goal of this PRACE project was to evaluate how GPU could speed up Linear Response TDDFT code – DP. Profiling analysis of the code has been done to identify computational bottlenecks to be delegated to the GPU. In order to speed up this code using GPUs, two different strategies have been developed: a local one and a global one. Both strategies have been implemented with cuBLAS and/or CUDA C. Results showed that one can reasonably expect about 10 times speedup on the total execution time, depending on the structure of the input and the size of used datasets, and speedups up to 16 have been observed for some cases.

Project ID: PA1148

---

1. Presentation of the DP code

The DP code [1] is an ab initio TDDFT linear response code, working in reciprocal space, on a plane-waves basis, and in frequency domain. Its main purpose (not the only one) is to calculate the electronic polarizability of a wide range of materials, being 0D (like atoms or clusters), 1D (nanotubes and nanowires), 2D (graphene, surfaces, and layered systems) or bulk. The code is written in Fortran 90, with some insertion of C (essentially for parsing the input file and dealing with the operative system). The testing suite is written in PERL. The post-processing tools are written in Fortran and in Python.

The structured of the code is the following:

- Initialization part: reading of a ground state electronic structure file and creation of all possible energy transistions N_t(from valence/occupied to conduction/empty states).
- Creation of the polarizability

  $$\chi^0(g, g', \omega) = \sum_{t=1}^{N_t} \tilde{\rho}_t(g) \times \tilde{\rho}_t^*(g') \times \mathrm{den}_t(\omega)$$

  where for any transition t there is $\tilde{\rho}_t(g)$, a vector of dimension N_g (the number of plane waves), and $\mathrm{den}_t(\omega)$, a vector of dimension N_ω (number of energies in which the polarizability is evaluated), to be calculate. The CPU times grows linearly with N_t and quadratically with N_g, while the memory occupancy goes like $N_g^2 \times N_\omega$ (the dimension of χ^0). This is the most cumbersome part of the calculation, especially for what concerns the CPU time, but also, in most cases, for what concerns the memory occupancy. The evaluation of χ^0 gives also the scaling of the whole code, which goes as N_{at}^4, with N_{at} = number of atoms.
- Creation of the macroscopic dielectric function via the formula

  $$\epsilon^{-1} = 1 + v(g)\left(1 - \chi^0 v\right)^{-1}_{gg''} \chi^0(g'', g', \omega)$$

  which involves a matrix inversion. This term does not gives particular problems: each energy ω can be treaten in an independent way and is easily and efficiently parallelized.
- Writing down the output and spectra.

After a preliminary analysis, it has been confirmed that the evaluation of the polarizability χ^0 and in particular the time spent in the matrix creation, through the library method `cgerc`, is the most time consuming part and will the object of the present parallelization project.

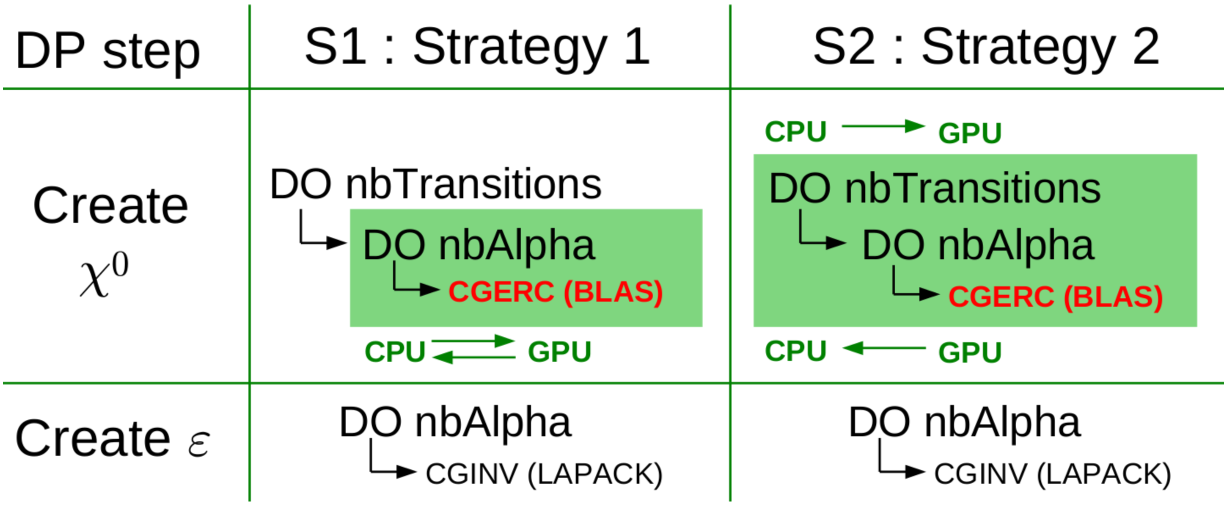

Fig. 1: GPU strategies for DP

2. GPU strategies

The structure of the DP code is illustrated by the Figure 1. In DP, the typical parameter magnitudes are as follow : the number of transitions is about 1 000 000, the number of alpha is about 500. The code is made of 2 major parts : the first one is "create χ^0", the second one is "create ε". A profiling analysis made, first with "GNU gprof" [2], then with "Scalasca" [3], confirmed that there are 2 hot spots :

- The first hot spot is an intensive call to CGERC (BLAS method) in "create χ^0" : CGERC is called about 500 000 000 times ($nbTransitions \times nbAlpha$ according to the notations of the Figure 1).
- The second hot spot is a repeated call to CGINV in "create ε" : CGINV is called about 500 times ($nbAlpha$ according to the notations of the Figure 1). CGINV calls CGETRF and CGETRI (LAPACK methods).

From profiling results, it turns out that CGINV takes (in average) 1000 times more time than CGERC : roughly speaking, finally there is still a factor 1000 between CGERC and CGINV. On overall, the CGERC operation is more costly than CGINV : this is why CGERC is found to be the first hot spot. This is illustrated by the Figure 2 where one can clearly see that the χ^0 step is much more time consuming than the ε step. As a consequence, speeding up "create ε" with a classical MPI approach works pretty well. Nevertheless, speeding up "create χ^0" with a classical MPI approach may not be that efficient : one could expect GPU to do things faster.

To port the DP code to GPU, one can use 2 strategies. The first strategy is local and has been implemented by "la Maison de la Simulation" (CEA, France) : the idea is to delegate to GPU only a subpart of the "create χ^0" step. The second strategy is global and has been implemented by the Institute of Physics Belgrade (IPB, Serbia) : the idea is to delegate to GPU the whole "create χ^0" step. Before activities on GPU implementation started, MPI version of DP, which was able to distribute the work over several MPI processes, was already available, and it was used as a starting point in porting activities.

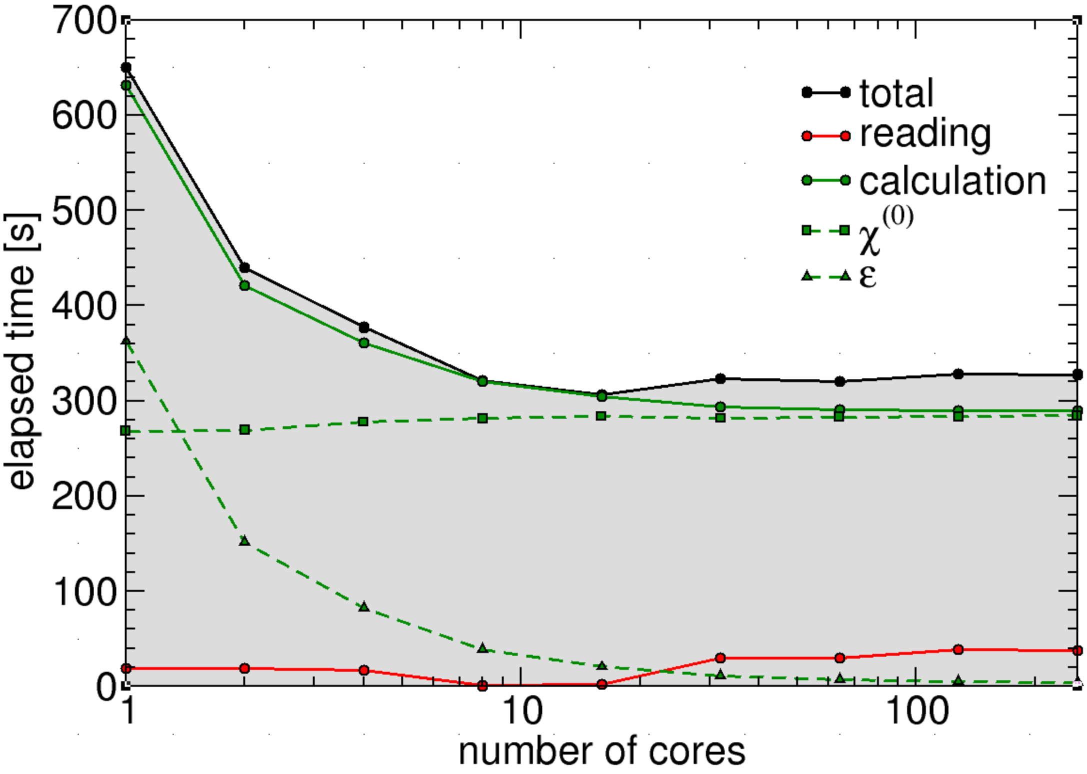

Fig. 2: Profiling of a typical DP run

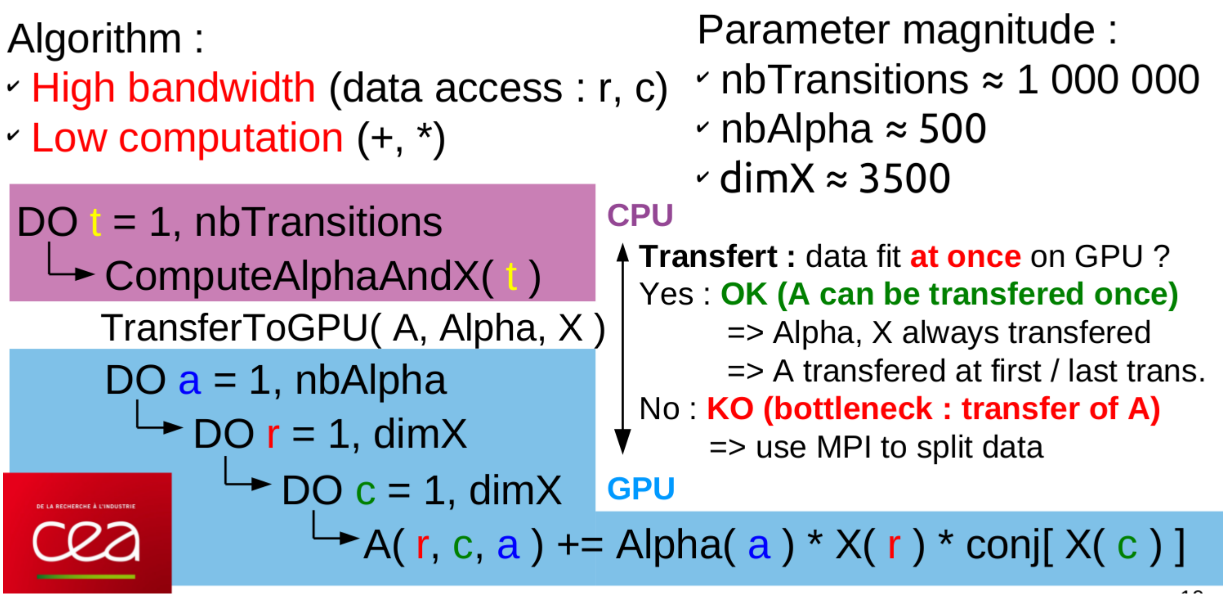

Algorithm :
- ✓ High bandwidth (data access : r, c)
- ✓ Low computation (+, *)

Parameter magnitude :
- ✓ nbTransitions ≈ 1 000 000
- ✓ nbAlpha ≈ 500
- ✓ dimX ≈ 3500

```
DO t = 1, nbTransitions
  └→ ComputeAlphaAndX( t )
     TransferToGPU( A, Alpha, X )
     DO a = 1, nbAlpha
       └→ DO r = 1, dimX
            └→ DO c = 1, dimX
                 └→ A( r, c, a ) += Alpha( a ) * X( r ) * conj[ X( c ) ]
```

CPU

Transfert : data fit at once on GPU ?

Yes : **OK (A can be transfered once)**
=> Alpha, X always transfered
=> A transfered at first / last trans.

No : **KO (bottleneck : transfer of A)**
=> use MPI to split data

GPU

Fig. 3: Strategy 1 - Presentation

2.1. *Strategy 1*

2.1.1. *Presentation*

The first strategy is local : basically, the idea is to delegate CGERC to GPU. This is the very first and most simple idea one can have. The main drawback of this approach will clearly be CPU / GPU transfers that are known to be bottlenecks. The Figure 3 illustrates the algorithm. For sake of clarity, we recall that CGERC (BLAS method) perform the following operation :

$$A(i,j) \mathrel{+}= \alpha \times X(i) \times \overline{X(j)} \tag{1}$$

where A is a complex 2D matrix, α is a scalar and X a complex vector. In DP, CGERC is called a lot of times so that α is actually a vector. Finally, the work to delegate on GPU looks like :

$$A(i,j,k) \mathrel{+}= \alpha(k) \times X(i) \times \overline{X(j)} \tag{2}$$

where A is a complex 3D matrix, α is a vector and X a complex vector.
The 3 data to transfer from CPU to GPU are A, α and X. After the GPU computation is done, the only data to transfer back to CPU is A. α and X are updated by CPU at each iteration and must be transfered to GPU at each iteration : according to notations of Figure 3, α and X are transfered $nbTransitions$ times (the typical magnitude of $nbTransitions$ is 1 000 000). A is not modified at CPU side so that, when possible, A may be only transfered once to GPU (at CPU side, A is seen as a computational result needed to proceed to the following "create ε" step).

Clearly, one have 2 possible situations :

- A, α and X fit all at once on GPU memory. Here, A can be transfered once from CPU to GPU at the first iteration, and, A can be transfered back from GPU to CPU at the last iteration (A stays on GPU and is updated on GPU). One can expect significant speed up using GPU.
- A, α and X do **not** fit at once on GPU memory. Here, A will have to be transfered by chunk at each iteration. The GPU approach will be much slower than the initial full CPU code. In this case, the only way out is to use MPI to split the initial data into smaller pieces to distribute over several processus. A is a matrix whose elements are simple precision complex (2 * 4 bytes = 8 bytes). According to Figure 3, the size of A is $dimX^2 \times nbAlpha$ where $dimX$ is the size of the X vector and $nbAlpha$ is the size of the α vector. As a result, the rule of thumb to apply to be sure that data will fit on GPU, is to choose $dimX$ and $nbAlpha$ such that :
  $$8 \times dimX^2 \times nbAlpha \approx 0.8 * GPUMem \tag{3}$$
  where $GPUMem$ is the memory in bytes available on GPU (generally, $dimX$ is fixed and $nbAlpha$ is adjusted). Note that to know the value of $GPUMem$, the user has just to run DP during one iteration (one transition) using the verbose mode (to specify in the input file) : $GPUMem$ will be printed in DP output log. This rule enables to target 80 % occupancy on GPU (to get the best possible performance, GPU must be loaded enough).

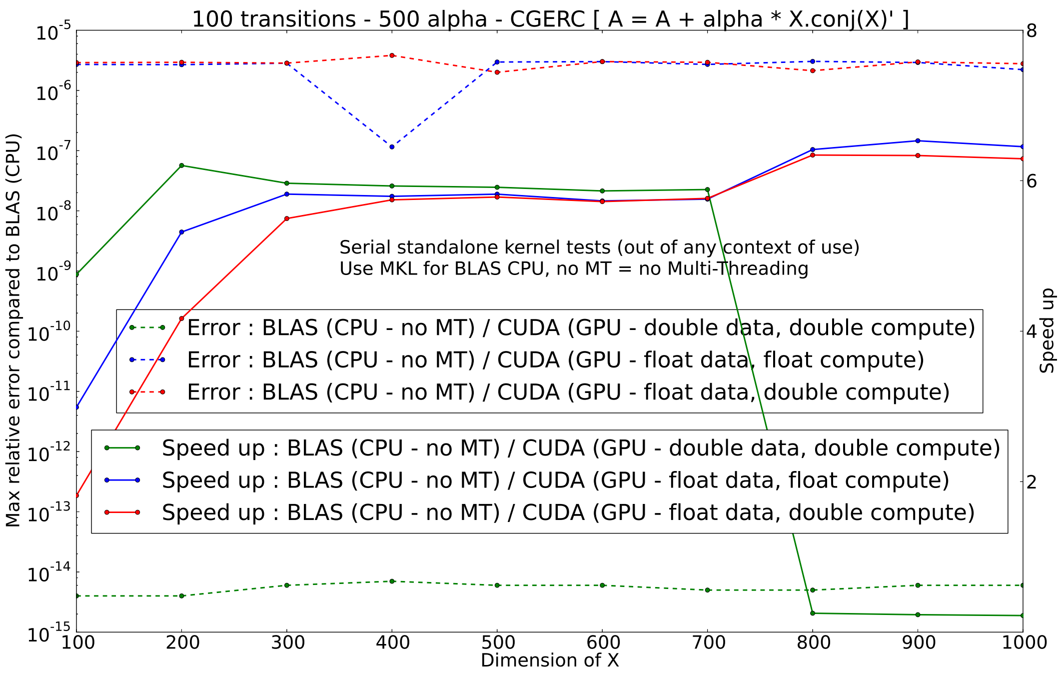

Fig. 4: Strategy 1 - Validation

In short, the first strategy can be wrapped-up this way : the (potentially large) data are split (in smaller pieces) and spread over several MPI processus (CPU), then each CPU is associated to a GPU, and finally each CPU delegates the job to his GPU. Once the GPU is done, the CPU will get results back and go over the "create ε" step. One can expect to overlap GPU computations with CPU to GPU transfer (X and α are updated at CPU side, so that they must be transfered to GPU at each iteration). Note that a verbose mode is available in the implementation. This verbose mode forces GPU synchronization (with CPU) to get reliable timing information (profiling information). As a result, the user should turn off the verbose mode for production runs (the verbose mode makes the CPU wait for the GPU at each iteration, so the transfer / computation overlap will not occur). Both a CUDA and a cuBLAS implementation have been done and compared (the cuBLAS version was used as a reference in terms of results and performance).

2.1.1. CUDA kernel validation

The CUDA kernel has been validated outside of any context of use (outside of DP). The Figure 4 illustrates the validation process. On GPU, floating point operations will not be run in the same order than on CPU. Moreover, the IEEE norm can not ensure commutativity. CPU results are taken to be the reference : to allow a fair comparison with GPU, some specific options have been set during compilation (nvcc options [4] : –ftz=false –prec-div=true –prec-sqrt=true). To validate the CUDA kernel, one had to use double precision complex and to perform every calculation with double precision : results show the relative error (compared to CPU results) is bounded by 10^{-14}. Note that using double data, we can observe here the transfer bottleneck that may occur if all data do **not** fit at once on GPU (Figure 4 for $dimX >= 800$) : speed up drops as A must be transfered by chunk at each iteration (transition). At this point a float version of the double kernel was derived : basically, double are replaced by float. The float kernel will be faster but the relative error magnitude will be about 10^{-5}. Hoping a better error / speed up tradeoff, an additional test has been performed using float data, converting float to double, and computing with double precision : results show that the benefit is only a potential error decrease (10^{-7}), while the speed up drops (tests showed one can expect error decrease when the data set is "small" enough, otherwise the number of operations will increases so much that at least one of them will cut the error back to the previous full float kernel). Using float data and performing double computation is not a good tradeoff. Finally, the float kernel will be used to speed up DP as the A matrix handled by DP is a simple precision complex matrix.

2.1.1. CUDA kernel optimization

The CUDA kernel has been optimized outside of any context of use (outside of DP). The Figure 5 and 6 illustrate the optimization process. The process is as follow : test several grid sizes to find the best one

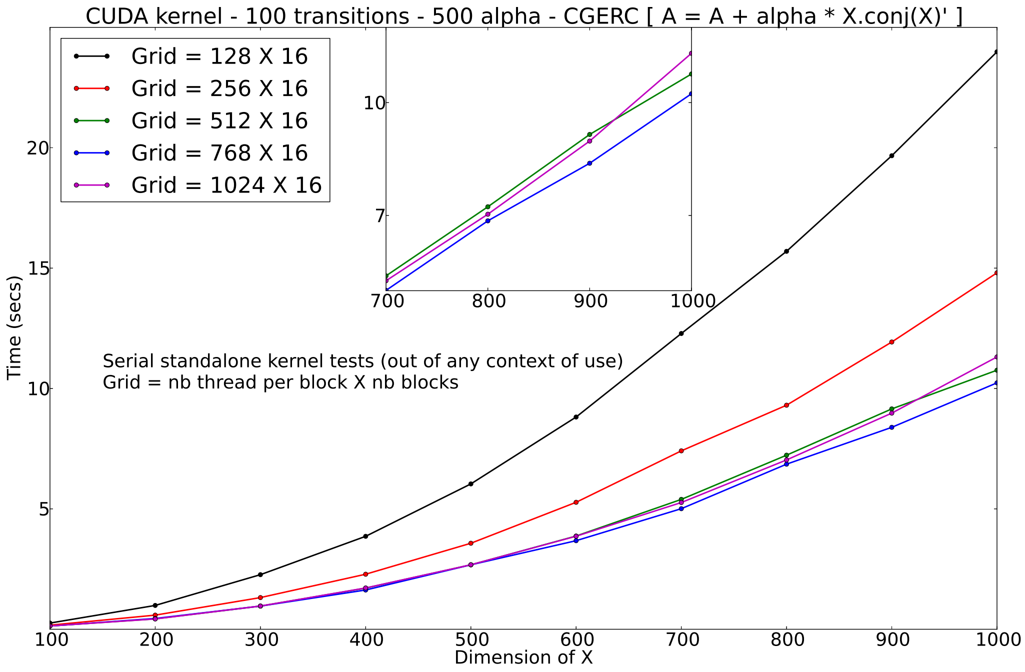
CUDA kernel - 100 transitions - 500 alpha - CGERC [A = A + alpha * X.conj(X)']

Serial standalone kernel tests (out of any context of use)
Grid = nb thread per block X nb blocks

Fig. 5: Strategy 1 - Grid sizing

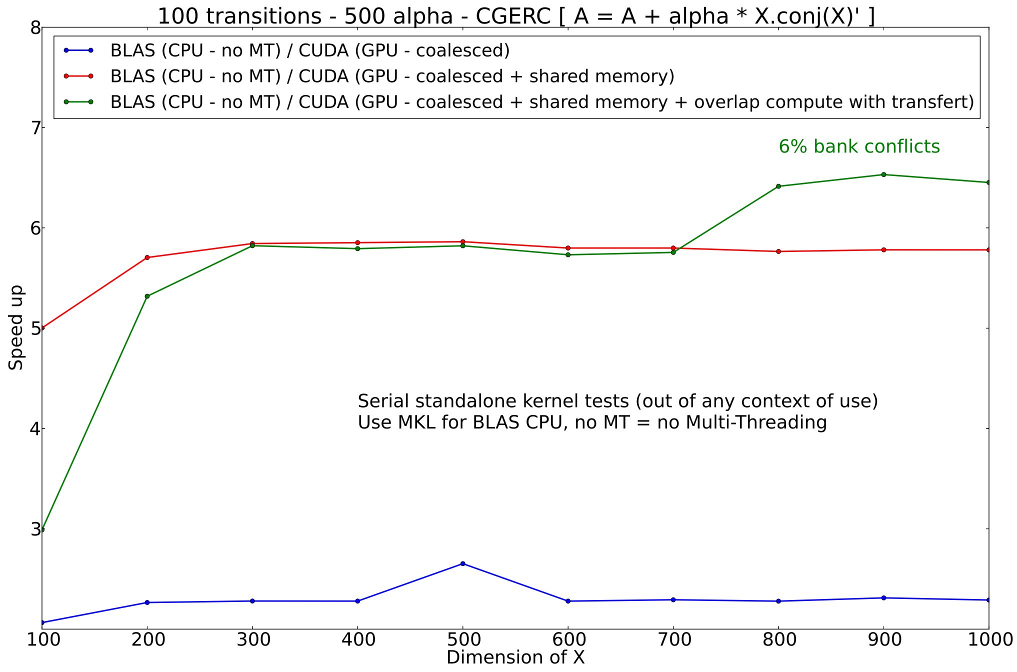
100 transitions - 500 alpha - CGERC [A = A + alpha * X.conj(X)']

6% bank conflicts

Serial standalone kernel tests (out of any context of use)
Use MKL for BLAS CPU, no MT = no Multi-Threading

Fig. 6: Strategy 1 - Optimization

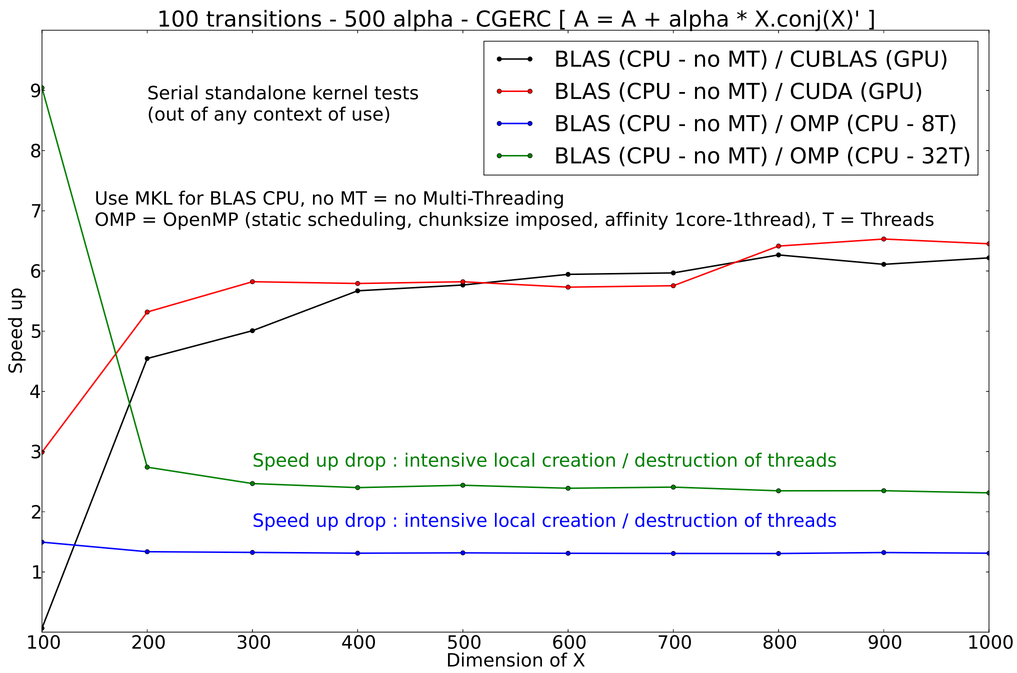

Fig. 7: Strategy 1 - Standalone results

(here, 768 X 16), and optimize step by step. First, to get the best possible performance, coalescing [5, 6] has to be ensured. Then, as the algorithm is highly bandwidth, use of shared memory has been added to the CUDA implementation and improves significantly performances (the first coalesced kernel was naive, and shared memory has been added after some optimizations so that the gap between the coalesced and shared memory version is not only, but mostly, due to shared memory [5, 6]). Finally, computations have been overlapped with transfers. At this step, a profiling analysis (using "nvvp", the Nvidia profiler) has shown there was only 6% bank conflict left so that the optimization has not been pushed further (actually, a kernel has been written to reduce bank conflicts down to 1%, but to achieve this, data have to be stored and accessed in a complex way so that the speed up drops).

2.1.1. Results

First, the strategy 1 has been tested outside of any context of use (outside of DP). The Figure 7 illustrates the first results. The cuBLAS implementation has been done so that it should be possible to overlap computations with transfer : as the CGERC method from cuBLAS has to be called progressively at each iteration (one call for each α), results are pretty much the same when there is no overlap. The CUDA implementation allows to compute directly the whole data set (one call for every α) and to overlap efficiently computations with transfer. The speed up is computed using a non multi-threaded CPU (1 thread, CGERC from MKL BLAS) as reference. For sake of completeness, GPU approaches have been compared with multi-threaded CPU approaches (several threads, CGERC implemented with OpenMP, ensuring static scheduling with imposed chunksize and 1core-1thread affinity to get best possible performances). It turns out that, as the strategy is local, threads have to be created and destroyed frequently so that multi-threaded CPU approaches are not efficient.

Then, the CUDA and cuBLAS implementations have been plugged into DP. The Figure 8 and 9 illustrate the speed up one can expect. First, a small test case (Argon) has been ran from 1 to 8 MPI processus. Then, a bigger test case (HFO2O) has been ran from 16 to 256 processus (on "Curie", 288 GPUs are available so that using 256 processus was the bigger possible test). In both case, strong and weak scalings have been performed. On "Curie", 2 queues are available : a full CPU one (xlarge) and a CPU / GPU one (hybrid). The xlarge nodes are made of 8 (quadricore) CPUs, while the hybrid nodes are made of 2 (quadricore) CPUs and 2 GPUs. To allow a fair comparison, the CPU runs have been performed ensuring 2 MPI process per node on the xlarge queue. Results show that, the more there is work to do, the more CUDA outperforms cuBLAS. To get the best possible performance, GPU must be fully loaded (target 80 % GPU occupancy), and, for big runs (128 MPI processus or more) the user must make sure enough RAM is available (otherwise the code swaps and the speed up drops). Depending on cases, one can expect a x10 to x14 speed up (on the total elapsed time).

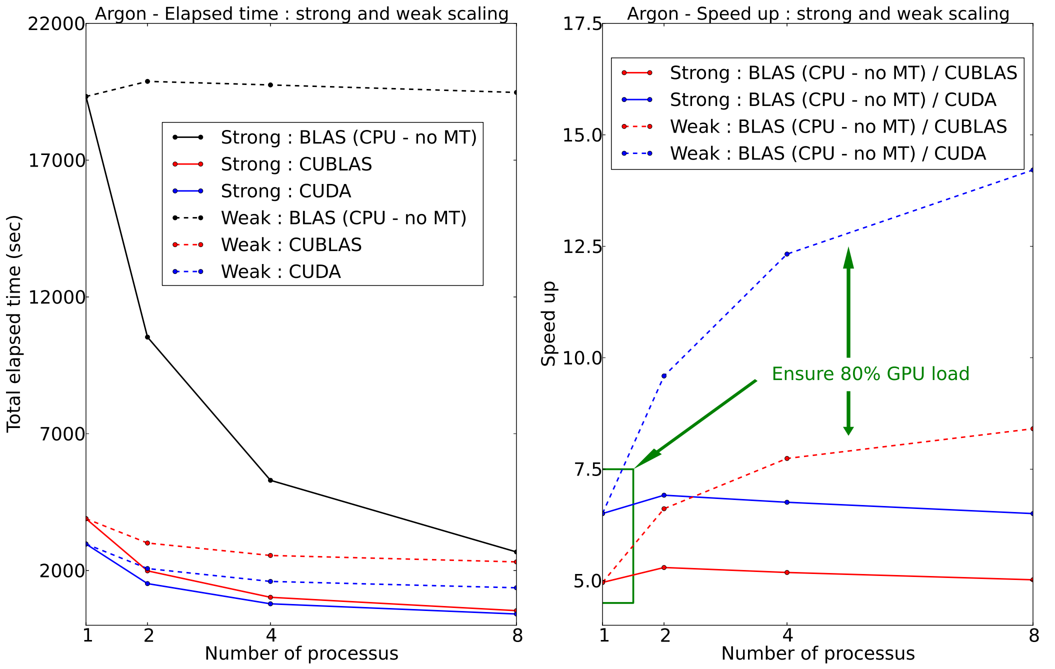

Fig. 8: Strategy 1 - Argon : small test case

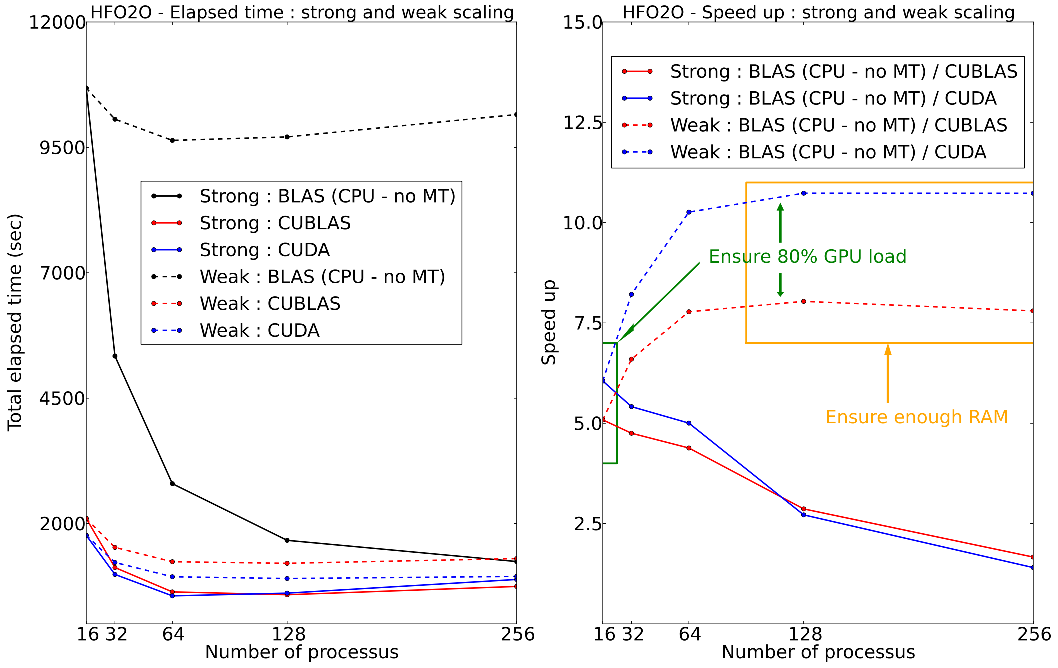

Fig. 9: Strategy 1 - HFO2O : typical test case

It should be stressed that for :

- The faster Argon CPU run (weak scaling over 8 procs), the initialization time (reading input files) was about 15 seconds while the computation time (χ^0 and ε steps) was about 19500 seconds. The ratio between initialization and computation time is about 1300.
- The faster HFO2O CPU run (weak scaling over 256 procs), the initialization time (reading input files) was about 170 seconds while the computation time (χ^0 and ε steps) was about 10150 seconds. The ratio between initialization and computation time is about 60.

As only the χ^0 step can benefit from GPU speed up, we can expect better speed up (than x10-x14) in cases where the ratio between initialization and computation time is higher (ratio ¿ 10000) than the ones presented in this document.

2.2. *Strategy 2*

2.2.2. *Presentation*

The main goal when designing strategy 2 of the GPU approach for the DP code was to minimize communication and data transfers between the CPU and the GPU. This communication has an impact on the performance, because in the algorithm presented in strategy 1 section, data has to be copied to the GPU for each transition (one iteration of the computational loop). When the number of transitions is large (which is often the case for some real inputs DP was designed for), it is expected that the memory transfer time can be a significant factor in the performance of the entire program.

To ensure that the data will be transferred only once to the GPU (and back to the CPU after all transitions have been processed), the whole loop which iterates through all transitions had to be ported to the GPU using CUDA technology. This can be seen on Figure 1, where the outline of the algorithm is presented.

However, because now both α and X vectors need to be computed directly on the GPU, all related data structures needed for their computation need to also reside in the GPU memory during all iterations of the transitions loop. To illustrate this, we will briefly present needed steps for computation of the X vector for one transition:

- We select 2 waveforms from the auxiliary data structure, which holds all waveforms for the input dataset, based on the index depending on the current transition.
- We perform FFT on them, multiply them together and perform inverse FFT on the resulting waveform vector. During the multiplication phase, elements of 2 waveforms to be multiplied in one step are selected using indexes stored in the table containing index mapping. Which column from the mapping table will be read, again depends on the current transition.
- We select a subset of the waveform calculated in the previous step to get the X vector which will be used together with α to update the A matrix.

Because the waveform structure and the mapping table described above also consume significant amount of memory, that means that the GPU memory now has to be shared between the A matrix and these structures. Also, the number of waveforms in the auxiliary structure grows linearly with the number of total transitions, so we can expect to reach the limits of the available GPU memory much faster than with strategy 1, as the size of the input test case grows (whether with more transitions or with larger A matrix).

Available memory limit can be overcame either implicitly with distributing computation among many MPI processes, or by explicitly managing data movement on the GPU card, so that the matrix is processed in parts. The MPI approach for division of the data is already present in the DP code, and when enough resources are not available, a modification of the strategy 2 for out-of-core solving of the problem was developed, and will be described later in this text.

Having in mind that now the entire body of the loop will be executed on the GPU, the strategy 2 approach has a risk of slowing down parts of the loop that are sequential or less parallel than updating of the matrix A, because in that case advantages of the GPU are lost or at least diminished (a single GPU core is much slower than the equivalent CPU core). However, because FFT operation is now also moved to the GPU (which is expected to be faster), and because for larger test cases, vectors that are being operated on inside the loop are also larger, in overall, less parallel loop parts are not expected to be a factor of slowing down of the algorithm when running on CUDA GPUs.

2.2.2. *Implementation details*

For the implementation of the strategy 2, CUDA C was used along with cuBLAS and cuFFT numerical libraries. CUDA code was split in multiple kernels, each corresponding to a single original FORTRAN routine called inside the loop. Each call to FFTW3 library routine was swapped with a call to cuFFT routine, and each MKL BLAS *cgerc* call was swapped with the corresponding cuBLAS call (*cublasCgerc*). One FORTRAN routine had to be split into 2 kernels, because there is a data dependency between the first and the second part of the routine, which couldn't be solved within a CUDA thread block. This initial GPU implementation works properly if the matrix A, all waveforms and index mapping tables can fit into GPU memory together.

Because kernels were developed in CUDA C, and could not be called directly from FORTRAN code, several wrapper C routines were created for initialization of the GPU memory, copying necessary data to the GPU, executing body of the computational loop, and copying the A matrix back to be further used in the create ε step. Custom kernel for updating the A matrix was not developed like it was done in strategy 1, because more focus had to be put on porting the entire loop on the GPU and on implementing modification for out-of-core execution when the input data sets are exceptionally large.

Even though it might look like performance-wise it could be better to put the entire loop in the single kernel, because some overhead related to starting multiple kernels from the CPU side could be alleviated, it was not done in this implementation. One of the reasons for this is that we wanted to keep using external FFT library (for simplicity, and better performance), and it was not possible to call cuFFT from inside the kernel. The other reason is that because waveforms are not always accessed in a linear fashion, but are instead sometimes indexed indirectly using values from the mapping table, a situation where synchronization of all threads executing the kernel in necessary can arise. This cannot be done efficiently in CUDA, because it was designed in a way that only threads in same blocks can directly synchronize and share data.

There are two independent tasks that need to be performed before the A matrix is updated:

- Calculation of the X vector, and
- Calculation of the α vector

Because there are no data dependencies between these tasks, they can be executed concurrently on the GPU. To achieve this, separate CUDA streams are created, one for each task, and each kernel is configured to run in a stream associated with the task they are a part of. Because FFT is a part of the X vector calculation, cuFFT library was configured to run in a first stream. This overlapping of computation on the GPU can be useful because there is a varying degree of parallelism between kernels (some operate on long vectors, some on shorter ones, and some even run with only a single thread), and it is possible that GPU won't be fully utilized running just a single task at a time. CUDA runtime can then select which kernels can be overlapped and help us gain a bit of performance.

For updating of matrix A using cuBLAS *cgerc* call, streams are also used to help in gaining performance. Increase in performance when using streams can especially be significant when the size of a single transform is not very large. Since in DP code many matrices need to be updated in every loop iteration (meaning that we can view A as a 3D structure, see Equation 2 in Section 2.1.1.), and cuBLAS allows for overlapped calls, we have used 30 separate streams to perform matrix updates. This helped us gain approximately 2-3 times the performance compared to sequential updating.

We have managed to avoid host to device synchronization entirely in this case, save for the points of memory transfers, which only happen twice. Streams were synchronized directly on the GPU, so that as soon as the computation of X and α was done, updating of the matrix starts. Because synchronization with the host is much more expensive than the synchronization between streams on the GPU, a potential overhead was successfully eliminated.

2.2.2. Offloading computation to CPUs

Even though it is expected that moving main DP computational loop to GPU will result in significant performance gains, it shouldn't be forgotten that CPUs on modern HPC systems have multiple cores and can contribute to calculation tasks to some extent. The advantage of the algorithm employed in the DP code is that iterations of the loop are independent and can be executed in parallel or out-of-order, and this can be used to offload some subset of iterations to be executed on CPUs.

Because there is already a routine in the DP code which equally splits transitions to MPI processes when DP is used with MPI parallelization, it was easy to modify that routine to take into account that both CPUs and GPUs will participate in calculating transitions. There is difference in performance between a GPU card and a CPU core, so that routine was modified to perform a weighted distribution instead. Once a MPI process knows its set of transitions, it can begin with the computation, regardless of whether it will be performed on the GPU or on a CPU core.

Each MPI process can either use a GPU or a CPU core for the execution of the computation loop. In this implementation, first 2 processes on each node were selected to use GPU for computations, because a CURIE hybrid node contains 2 GPU cards. DP already supports running performance tests with only a few iterations of the loop (used to estimate total time needed for simulation, *testrun* input parameter controls this), so this test was extended to run on both the CPU and the GPU. After a short test run has been performed, reported ratio between execution times on the CPU and the GPU can be used as an input to routine where transitions are split. In this way, it is expected that processes that run loop on the GPU and those who run it on the CPU will complete calculation for transitions assigned to them in roughly the same time.

2.2.2. Modifying strategy 2 for out-of-core approach

As previously described in the presentation of this strategy for GPU code implementation, instead of only storing the A matrix on the GPU during loop execution, some auxiliary structures also need to be stored, so that vectors α and X can be calculated directly on the GPU. A problem arises when combined size of these structures exceeds available memory on the GPU, because then it is no longer possible to run DP for this input case. To solve this problem, we had to manipulate data movement between CPU and GPU so that data is transferred only when absolutely needed, and kept and reused on the GPU for as long as possible, in order to reduce the penalty for needing to synchronize data on the main memory and on the GPU. Although the performance of the code for the out-of-core approach won't be optimal (because now there will be more communication than initially planned for the strategy 2 approach), we wanted to show that it can be used to solve problems that couldn't even be solved without it when not enough memory is available, and that the introduced overhead will still be within acceptable bounds.

Analysis of the access patterns of the structure holding all waveforms and the table containing index mapping showed that they exhibit very good locality. Waveform structure was accessed in a way that only a small part of it is used for some subset of N transitions (where N is significantly larger than the number of used waveforms), while mapping table was accessed so that a single column is reused multiple times, and then wasn't used again for a long time. Because of that, if we had enough space to hold the working set of waveforms on the GPU, and just a single column of the mapping table, we could ensure that data won't be copied between CPU and GPU more than necessary. In fact, for test cases we have used during development, after a part of the waveform structure was used, it was not needed again. If that is the case, then the total amount of data transferred to the GPU will be the same as when everything fits at once (only that now data transferring has to be done using multiple copy operations).

We implemented software caching of the waveform structure and the mapping table in the GPU memory, using FIFO replacement policy, so that data loaded the earliest is swapped first. One waveform or a mapping table column is transferred to the GPU when it is needed, and reused in subsequent transitions. That allowed us to have the number of "cache misses" equal to the total number of waveforms (meaning each one is loaded only once because of compulsory misses). Size of the waveforms cache was an order of magnitude (or more) smaller than the initial size of the waveform structure for our test cases, and only a single line was needed for caching mapping table entries, which allowed us to have more space for storing of the A matrix.

The situation is a bit different with the A matrix, because entire matrix has to be updated for each transition. That means that we can't make any use of caching, but instead have to resort to updating the matrix part by part. First, a part of the matrix is transferred to the GPU, then it is updated usign cuBLAS calls, and it is returned to the main memory. This is repeated until all parts have been processed. Downside of this is that the entire A matrix has to be transferred back and forth for each update. Because memory transfers take more time than the computation itself, this can slow down the algorithm by at least an order of magnitude.

To overcome this problem, internal structure of the loop had to be slightly modified. Main change is that now instead of computing one α and X vector and then using them to update the A matrix, many α and X vectors that correspond to subsequent transitions are computed in a batch, and then used to update parts of the A matrix, for many transitions at the time. These transformation of the computational loop don't affect algorithm correctness, because updates on the A matrix are linear and can be executed in any order. This is better illustrated by the following pseudo-code:

- Initial version of the loop:

```
do i=1, num_trans
  calculate X
  calculate alpha
  update_matrix(A, X, alpha)
end do
```

- Modified version of the loop for out-of-core execution:

```
batch_size = K
num_batches = num_trans / K
do i=1, num_batches
  do j=1, batch_size
    calculate X(j)
    calculate alpha(j)
  end do
  for each A part
    copy A_part to GPU
    do j=1, batch_size
      update_matrix_part(A_part, X(j), alpha(j))
    end do
    copy back A_part to CPU
  end for each
end do
```

As a consequence, now the entire matrix A doesn't have to be moved for each transition, but can instead be transferred only once for a batch of K transitions. This can greatly reduce time spent in copying data, and can help us get close to performance of the original algorithm if the batch size is large enough. At the same time, with large batch size, significant space on the GPU card has to be dedicated to storing of intermediate α and X vectors, and that space also plays a part in the memory management.

Managing memory space for all these structures might not be easy for each possible problem DP is used to solve, but for our test cases it could be done with very good efficiency. It was done with assumption that waveform structures and mapping vectors exhibit good access locality for input cases used with DP (this was true for all the cases we tested during development). Our approach to divide available memory between all these necessary structures can be summarized as:

- First analyze access patterns for waveform structure and mapping table, and allocate just enough space for their software caches, so that entire working set can fit at once. This ensures that no unnecessary swapping of some waveform will happen, even when it is still needed in the near future.
- Then we allocate space for the number of A matrices equal to at least twice the number of CUDA streams used for cuBLAS calls. This was done to ensure that there will be enough data to fully utilize computational capabilities of the GPU, and was selected more as an educated guess than a strict rule.

- The remaining space can then be used to store K pairs of temporary vectors.

Theoretically, if we can manage to fit temporary vectors for all transitions on the GPU, we should be able to match the performance of the original algorithm, even when using much less space on the GPU card. The only difference will then be that the large amount of data would be transferred using many separate calls to copying routines, instead in a single call, but assuming that the modification for out-of-core execution will be used for very large data sets, overhead associated with a routine call will be insignificant compared to the time spent in actually transferring the data.

2.2.2. Results

Strategy 2 for porting DP code to the GPU has been tested using the DP code already supporting MPI parallelization, with the computational loop moved to the GPU. Also, a modification of the strategy 2 where a part of the computation is offloaded to the CPU was tested. Separate testing was done using modified input (to create larger data structures) with the out-of-core modification, using only one GPU card, to show what kind of a performance drop we can expect if there is not enough memory to solve the problem in-core (where there are only 2 points of data movement – before and after the computation).

All development, verification and performance testing of the GPU strategy 2 of the DP code was done using CURIE supercomputer (specifically, CURIE hybrid nodes). Each hybrid node on CURIE consists of 2 Intel Westmere processors, each having 4 processing cores running on 2.66GHz, and 2 NVIDIA Tesla M2090 graphic processing units (GPUs).

First series of tests was performed with the MPI+GPU approach for the DP code, when the main computational loop was executed only on the GPU cards. Because each CURIE node has 2 Tesla cards, when running on more than one node, processes were spread over all nodes so that there are exactly 2 MPI processes executing on a single node. Also because there are 2 CPU sockets, and each GPU is connected to a bus local to the socket, each MPI process was bound to a separate socket. More details on this, and the explanation on how to control process scheduling can be found in CURIE best practices guide.

On Figure 10 we show execution times and speedups for test cases of Argon (small test case), and Hafnium oxide (larger production-ready input). We would like to stress that these inputs are not exactly the same as the ones reported with strategy 1 (see Section 2.1.1.), because there the input was modified in order to reach at least 80% memory occupancy on the GPU. This was not done here, because the emphasis when designing strategy 2 was not just to showcase the maximum performance of the “updating A” step, but instead to address the overall performance of the loop. Tests were conducted for configurations having from 1 to 256 MPI processes (on 1 to 128 nodes), with 1 GPU card per process. Execution time is split into initialization time (mostly reading input files from disk, completely unrelated to GPU implementation) and computation time for create χ^0 step, which was the focus of the GPU algorithm.

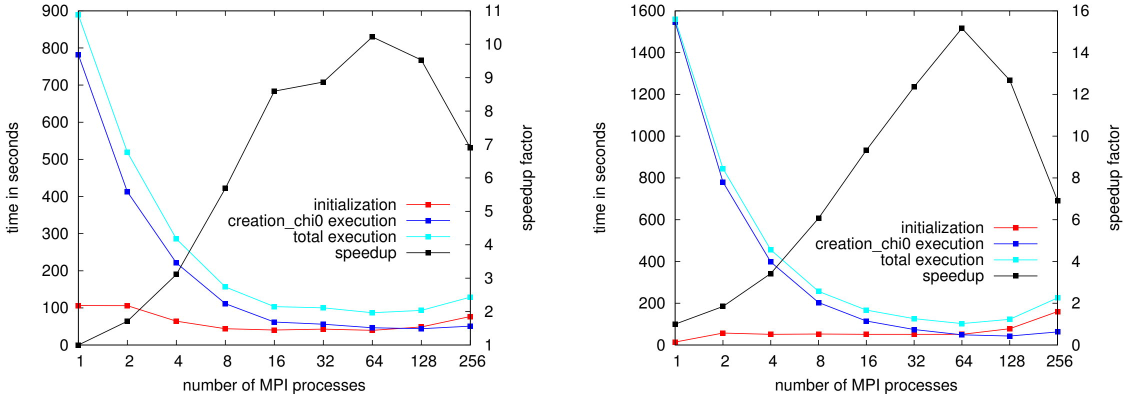

(a) (b)

Fig. 10: Performance and scaling of the GPU strategy 2 for the DP code, for 1 to 256 total GPU cards with 2 GPUs per CURIE node (time when running with 1 GPU used as a baseline for speedup): (a) Argon (small) test case; (b) Hafnium oxide (moderate) test case.

It can be seen that GPU implementation of strategy 2 for DP code scales reasonably well when a larger number of GPU cards is used in execution. For the small test case, it would be optimal to run with 16 MPI processes (using 16 GPUs), while for the larger input, scaling is very good for up to 64 processes. Since computing one transition is independent from others, when the total number of transitions is divided to more processes, time for the computation itself decreases in a linear fashion. Because of that, reasons for limitations in scaling DP CUDA code are in other parts of the code, that are either constant or even increase as the number of processes increase.

Time spent in DP initialization is unrelated to CUDA, and is roughly constant over the range of processes used for testing (with the exception for 256 processes, when its increase can be easily observed), so once that time becomes close to, or even surpasses the calculation time on the GPU cards, adding more and more card actually does very little for the performance. The figures also show that the execution time actually stops decreasing, as would be expected, and even increases at the end of the range. Reason for this is that the CUDA runtime initialization time is not constant, but instead starts to increase rapidly when the number of GPU cards used grows. This cannot be explained easily, and is probably related to the implementation of CUDA drivers. This time is spent at the first call to any CUDA routine during the execution, and we chose to present it here as a part of calculation time, because, as it can be seen, it is a realistic problem that can limit performance, and should be considered when running DP over a large set of GPU cards.

To compare GPU implementation execution times with CPU execution times, we tested the same cases for configurations with 1 to 256 MPI processes, but now without using GPU cards at all. MPI processes were distributed using by-socket discipline, so that inside of a node, processes were bound to CPU cores alternating between 2 sockets. On Figure 11 we report total execution times for all tests done using GPUs for computation, total execution times for all tests done using CPUs for computation, and their ratios (CPU/GPU time).

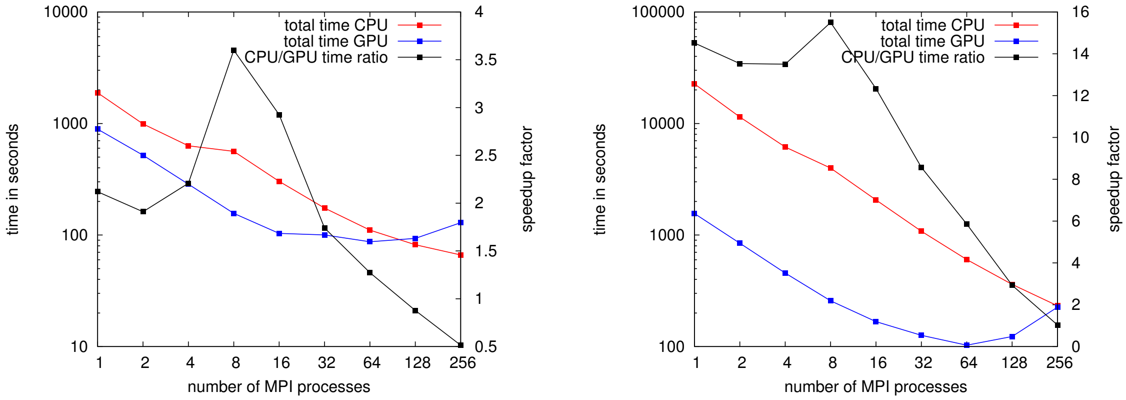

(a) (b)

Fig. 11: Performance of the GPU strategy 2 for DP code compared with the CPU only version, for 1 to 256 GPU cards (each MPI process controlling one GPU), and 1 to 256 CPU cores (each MPI process bound to a CPU core): (a) Argon (small) test case; (b) Hafnium oxide (large) test case.

Here we see that the expected speedup of the DP code when GPUs are used can be up to 3.5 for the smaller test, and up to 16 for the larger one. Actual numbers are even larger when comparing execution times of the single iteration, but since the emphasis here is on the real use-case presentation, execution times for the entire simulation are presented. In both cases, performance ratio peaks for the case with 8 MPI processes.

The first reason for this is that when code is executed only on CPUs, 8 processes saturate the entire node. Because CURIE node has NUMA architecture, by-socket process scheduling is used to ensure equal load-balancing of both memory sockets. But when a node is full, memory bandwidth starts to bottleneck execution performance a bit. Because of that, when code runs on 8 processes, it cannot be expected to be twice as fast as in the case with 4 processes. Since GPUs do not share memory, this situation doesn't show up when everything is calculated on the GPU. The second reason is in the above mentioned issue with CUDA initialization time, which reduces effectiveness of GPUs as the number of processes grows. Because this doesn't affect CPUs, it influences the drop in GPU code speedup when compared to the CPU.

To showcase the performance of our approach with offloading parts of the computation to CPUs, we selected the Argon test case. It was done because the GPU performance gain ratio on that test was lower than in the other case, which means that the performance gap between the GPU and a CPU core is not as wide. In cases like this, it is expected that the CPU will be able to contribute more to the computation, and that load-balancing will be closer to equal. To test the offloading, we constricted test configurations to multiples of 8 MPI processes (to fully saturate each CURIE node). 2 CPU cores were dedicated to controlling one GPU each, and the remaining 6 were used for computation. Weight parameter for load-balancing was selected based on previously presented tests, and was equal to 3.6. Results of offloading performance tests are shown in Figure 12, and it can be seen that using CPU to handle some subsets of transitions can give almost twice the computational performance as when using only GPUs, for suitable test cases. Although, because of the already described issues with DP initialization (IO related), and CUDA runtime initialization, overall performance gains are in fact not that large.

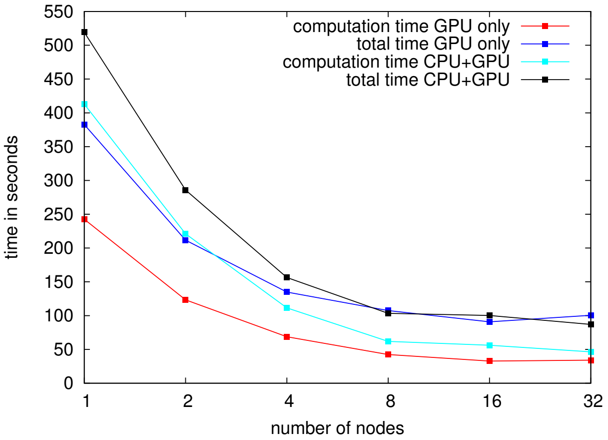

Fig. 12: Performance of the CPU offload modification of the GPU strategy 2 for DP compared to initial GPU implementation, for 1 to 32 CURIE nodes (6 CPU cores + 2 GPU cards per node for offload modification, 2 GPU cards per node for initial GPU implementation), for Argon test case.

Fig. 13: Placeholder for out-of-core

3. Conclusion

We have successfully ported the DP code to GPUs, with 2 different approaches to implementation of the main computational loop. Using the first strategy, we have obtained a speedup of 10 to 14 times compared to the CPU code. Moreover, one can expect even better speedup when the ratio between initialization and computation time is high, since initialization time cannot be made to scale. From a practical point of view, the main drawback is that the user must make sure that all the data can fit at once on GPUs. To do that, a rule of thumb must be applied (see Section 2.1.1.). Moreover, to get the best possible performance, the user must ensure that the GPU is loaded enough (target 80% memory occupancy on GPU).

When the second strategy is used, speedups of up to 16 times were observed using production-ready inputs, and good scaling for up to 64 GPU cards was achieved. Some modifications to the original strategy were also implemented, allowing us to use CPUs to help with the computation, and to solve problems that cannot fully fit into GPU memory, using out-of-core approach. CPU offload for Argon case showed that on a CURIE node, CPUs can contribute to computation almost as much as GPUs. The use of the out-of-core approach allows solving of problems of much greater sizes, without severely impacting the performance.

Based on the analysis of these two strategies, it is recommended to use strategy 1 when we have inputs that satisfy conditions regarding GPU memory usage, because it contains custom written kernels that employ CUDA shared memory and give very good performance when *cgerc* BLAS operation is performed in a way used in the DP code. On the other hand, strategy 2 gives better relative performance when larger inputs are used, but its performance does not depend on the size of the data as much, and it can be used to efficiently solve very large problems when out-of-core modification is used.

Acknowledgements

This work was financially supported by the PRACE project funded in part by the EUs 7th Framework Programme (FP7/2007-2013) under grant agreement no. RI-211528 and FP7-261557. The work is achieved using the PRACE Research Infrastructure resources [Curie, France].

References

1. V. Olevano, L.Reining, F.Sottile, *The DP code*, `http://etsf.polytechnique.fr/Software/DP`
2. GNU gprof profiler
   `http://www.cs.utah.edu/dept/old/texinfo/as/gprof_toc.html`
3. Scalasca performance analysis tool
   `http://www.scalasca.org/`
4. Precision and Performance Floating Point and IEEE 754 Compliance for NVIDIA GPUs, Whitehead N., Fit-Florea A., Nvidia, 2011
5. Optimizing Matrix Transpose in CUDA, Ruetsch G., Micikevicius P., Nvidia, 2009
6. CUDA C Best Practice Guide, Nvidia

References and Bibliography

[1] H. Hertz, Annalen der Physik **267**, 983 (1887), ISSN 1521-3889, URL `http://dx.doi.org/10.1002/andp.18872670827`.

[2] J. Thomson, Phil. Mag. **44**, 293 (1897).

[3] P. Lenard, Wien. Ber. **108**, 1649 (1899).

[4] A. Einstein, Annalen der Physik **322**, 132 (1905), ISSN 1521-3889, URL `http://dx.doi.org/10.1002/andp.19053220607`.

[5] S. Hüfner, *Photoelectron Spectroscopy: Principles and Applications* (Springer, Berlin, 2003).

[6] A. Damascelli, Physica Scripta **T109**, 61 (2004).

[7] A. Damascelli, Z. Hussain, and Z.-X. Shen, Rev. Mod. Phys. **75**, 473 (2003).

[8] L. Hedin, J. Michiels, and J. Inglesfield, Phys. Rev. B **58**, 15565 (1998), URL `http://link.aps.org/doi/10.1103/PhysRevB.58.15565`.

[9] C.-O. Almbladh and L. Hedin, in *Handbook on Synchrotron Radiation* (North-Holland, Amsterdam, 1983), vol. 1, p. 607.

[10] F. Aryasetiawan and O. Gunnarsson, Rep. Prog. Phys. **61**, 237 (1998).

[11] W. G. Aulbur, L. Jönsson, and J. W. Wilkins, Solid State Physics **54**, 1 (1999).

[12] M. Guzzo, G. Lani, **F. Sottile**, P. Romaniello, M. Gatti, J. J. Kas, J. J. Rehr, M. G. Silly, F. Sirotti, and L. Reining, Phys. Rev. Lett. **107**, 166401 (2011), URL `http://link.aps.org/doi/10.1103/PhysRevLett.107.166401`.

[13] M. Guzzo, Ph.D. thesis, École Polytechnique (2012), URL `http://etsf.polytechnique.fr/node/3215`.

[14] V. I. Anisimov, F. Aryasetiawan, and A. I. Lichtenstein, J.Phys.: Condens. Matter **9**, 767 (1997), URL `http://stacks.iop.org/0953-8984/9/767`.

[15] A. Georges and G. Kotliar, Phys. Rev. B **45**, 6479 (1992).

[16] G. Kotliar, S. Y. Savrasov, K. Haule, V. S. Oudovenko, O. Parcollet, and C. A. Marianetti, Rev. Mod. Phys. **78**, 865 (2006).

[17] L. Hedin, Phys. Rev. **139**, 796 (1965), URL `http://journals.aps.org/pr/abstract/10.1103/PhysRev.139.A796`.

[18] G. Strinati, H. J. Mattausch, and W. Hanke, Phys. Rev. B **25**, 2867 (1982).

[19] M. S. Hybertsen and S. G. Louie, Phys. Rev. Lett. **55**, 1418 (1985).

[20] R. W. Godby, M. Schlüter, and L. J. Sham, Phys. Rev. B **36**, 6497 (1987).

[21] F. Sottile, Ph.D. thesis, École Polytechnique (2003), URL `http://etsf.polytechnique.fr/node/1671`.

[22] F. Bruneval, Ph.D. thesis, École Polytechnique (2005), URL `http://etsf.polytechnique.fr/node/1670`.

[23] M. Gatti, Ph.D. thesis, École Polytechnique (2007), URL http://etsf.polytechnique.fr/node/1744.

[24] M. Nakatake, Y. Okamura, S. Akiyama, H. Namatame, and M. Taniguchi, Journal of Electron Spectroscopy and Related Phenomena **88**, 1027 (1998).

[25] A. Shukla, M. Calandra, M. Taguchi, A. Kotani, G. Vankó, and S.-W. Cheong, Phys. Rev. Lett. **96**, 077006 (2006).

[26] M. Budke, V. R, H. Liebl, G. Rangelov, and M. Donath, Review of Scientific Instruments **78** (2007).

[27] C. Colliex, *La Microscopie Electronique* (PUF, 1998).

[28] *Nobel prize in physics 1986*, URL http://www.nobelprize.org/nobel_prizes/physics/laureates/1986/ruska-bio.html.

[29] J. Hillier and R. Baker, J. Appl. Phys. **15**, 663 (1944).

[30] R. F. Egerton, Reports on Progress in Physics **72**, 016502 (2009).

[31] F. J. García de Abajo, Rev. Mod. Phys. **82**, 209 (2010), URL http://journals.aps.org/rmp/abstract/10.1103/RevModPhys.82.209.

[32] R. H. Ritchie and A. Howie, Phil.Mag. A **58**, 753 (1988).

[33] L. Zhang, R. Erni, J. Verbeeck, and G. Van Tendeloo, Phys. Rev. B **77**, 195119 (2008), URL http://link.aps.org/doi/10.1103/PhysRevB.77.195119.

[34] R. H. Ritchie, Phys. Rev. **106**, 874 (1957).

[35] P. M. Platzman and P. A. Wolff, *Waves and Interactions in Solid State Plasmas* (Academic Press. New York, 1973).

[36] E. K. U. Gross and W. Kohn, Phys. Rev. Lett. **55**, 2850 (1985).

[37] S. Botti, A. Schindlmayr, R. Del Sole, and L. Reining, REPORTS ON PROGRESS IN PHYSICS **70**, 357 (2007), ISSN 0034-4885.

[38] M. A. L. Marques, N. Maitra, F. Nogueira, A. Rubio, and E. K. U. Gross, eds., *Fundamentals of Time-dependent density functional theory* (Springer, Berlin, 2012).

[39] G. Strinati, Rivista del Nuovo Cimento **11**, 1 (1988), and references therein, URL http://dx.doi.org/10.1007/BF0272596.

[40] S. Albrecht, G. Onida, and L. Reining, Phys. Rev. B **55**, 10278 (1997).

[41] G. Onida, L. Reining, and A. Rubio, Rev. Mod. Phys. **74**, 601 (2002), URL http://journals.aps.org/rmp/abstract/10.1103/RevModPhys.74.601.

[42] R. Hambach, Ph.D. thesis, École Polytechnique (2010), URL http://etsf.polytechnique.fr/node/2695.

[43] T. P. Devereaux and R. Hackl, Rev. Mod. Phys. **79**, 175 (2007), URL http://link.aps.org/doi/10.1103/RevModPhys.79.175.

[44] E. Hippert, F.and Geissler, J. Hodeau, E. LeliÃÍvre-Berna, and J.-R. Regnard, eds., *Neutron and X-ray Spectroscopy* (Springer, 2006).

[45] W. Schülke, *Electron Dynamics by Inelastic X-ray Scattering* (Oxford University Press, 2007).

[46] F. E. Low, Phys. Rev. **96**, 1428 (1954).

[47] M. GellâĂŘMann and M. L. Goldberger, Phys. Rev. **96**, 1433 (1954).

[48] P. M. Platzman and N. Tzoar, Phys. Rev. B **2**, 3556 (1970).

[49] M. Blume, J. Appl. Phys **57**, 3615 (1985).

[50] J. C. Maxwell, Philos. Trans. Roy. Soc. London **155**, 459 (1865).

[51] F. Stern, Solid State Physics **15**, 299 (1965).

[52] J. D. Jackson, *Classical Electrodynamics* (John Wiley & Sons; 3rd edition, 1999).

[53] M. Gatti, F. Sottile, and L. Reining, accepted on Phys. Rev. B, URL http://journals.aps.org/prb/accepted/6e070Y41P8f16d4c24c5224314f28b68cf9d2b695.

[54] K. Riedling, *Ellipsometry for Industrial Applications* (Springer-Verlag Wein, New York, 1988).

[55] H. G. Tompkins, *A User's Guide to Ellipsometry* (Academic Press, New York, 1993).

[56] H. G. Tompkins and W. A. McGahan, *Spectroscopic Ellipsometry and Reflectometry: A User's Guide* (John Wiley & Sons, New York, 1999).

[57] Fujiwa, *Spectroscopic Ellipsometry - Principles and Applications* (Wiley, New York, 2007).

[58] S. D. George, T. Petrenko, and F. Neese, Inorganica Chimica Acta **361**, 965 (2008), ISSN 0020-1693, protagonists in Chemistry: Professor Edward I Solomon, URL http://www.sciencedirect.com/science/article/pii/S0020169307003374.

[59] R. Del Sole and E. Fiorino, Phys. Rev. B **29**, 4631 (1984).

[60] O. Dolgov and E. Maksimov, *The Dielectric Function of Condensed Systems* (Elsevier, 1989), chap. The Dielectric Function of Crystalline Systems, p. 221.

[61] S. L. Adler, Phys. Rev. **126**, 413 (1962).

[62] N. Wiser, Phys. Rev. **129**, 62 (1963).

[63] G. D. Mahan, *Many-particle physics* (Plenum, New York, 1981).

[64] A. L. Fetter and J. D. Walecka, *Quantum theory of many-particle systems* (McGraw-Hill, New York, 1971).

[65] A. A. Abrikosov, L. P. Gorkov, and I. E. Dzyaloshinski, *Methods of Quantum Field Theory in Statistical Physics* (Prentice-Hall, Englewood Cliffs, NJ, 1963).

[66] V. Olevano, L. Reining, and F. Sottile, the DP code, unpublished, URL http://dp-code.org.

[67] X. G. et al., Comp. Mat. Sci. **25** (2002), `http://www.abinit.org/`.

[68] P. Giannozzi, S. Baroni, N. Bonini, M. Calandra, R. Car, C. Cavazzoni, D. Ceresoli, G. L. Chiarotti, M. Cococcioni, I. Dabo, et al., Journal of Physics: Condensed Matter **21**, 395502 (19pp) (2009).

[69] F.Houssen, P.Kestener, and **F. Sottile**, pRACE preparatory access N.2010PA1148. Porting DP over massively parallel machines and GPUs.

[70] L. Reining, V. Olevano, A. Rubio, and G. Onida, Phys. Rev. Lett. **88**, 066404 (2002).

[71] F. Sottile, V. Olevano, and L. Reining, Phys. Rev. Lett. **91**, 56402 (2003).

[72] G. Adragna, R. Del Sole, and A. Marini, Phys. Rev. B **68**, 165108 (2003).

[73] R. Stubner, I. V. Tokatly, and O. Pankratov, Phys. Rev. B **70**, 245119 (2004).

[74] S. Sharma, J. K. Dewhurst, A. Sanna, and E. K. U. Gross, Phys. Rev. Lett. **107**, 186401 (2011), URL http://link.aps.org/doi/10.1103/PhysRevLett.107.186401.

[75] S. Sharma, J. K. Dewhurst, A. Sanna, A. Rubio, and E. K. U. Gross, New Journal of Physics **14**, 053052 (2012), URL http://stacks.iop.org/1367-2630/14/i=5/a=053052.

[76] S. Rigamonti, S. Botti, V. Veniard, C. Draxl, L. Reining, and F. Sottile, Phys. Rev. Lett. **114**, 146402 (2015), URL http://link.aps.org/doi/10.1103/PhysRevLett.114.146402.

[77] L. Hedin, Phys. Rev. **139**, A796 (1965).

[78] F. Bechstedt, K. Tenelsen, B. Adolph, and R. Del Sole, Phys. Rev. Lett. **78**, 1528 (1997).

[79] A. Marini and R. Del Sole, Phys. Rev. Lett. **91**, 176402 (2003).

[80] P. Romaniello, D. Sangalli, J. A. Berger, F. Sottile, L. G. Molinari, L. Reining, and G. Onida, The Journal of Chemical Physics **130**, 044108 (2009).

[81] D. Sangalli, P. Romaniello, G. Onida, and A. Marini, The Journal of Chemical Physics (2011), in press.

[82] L. Sponza, Ph.D. thesis, École Polytechnique (2013), URL http://etsf.polytechnique.fr/node/3336.

[83] F. Fuchs, C. RÃűdl, A. Schleife, and F. Bechstedt, Phys. Rev. B **78**, 085103 (2008).

[84] W. Press, S. Teukolsky, W. Vetterling, and B. Flannery, *Numerical Recipes - The art of scientific computing* (Cambridge University Press, 1992).

[85] P. H. Hahn, W. G. Schmidt, and F. Bechstedt, Phys. Rev. Lett. **88**, 16402 (2002).

[86] W. G. Schmidt, S. Glutsch, P. H. Hahn, and F. Bechstedt, Phys. Rev. B **67**, 85307 (2003).

[87] R. Haydock, Solid State Physics **35**, 215 (1980).

[88] R. Haydock, Comput. Phys. Commun. **20**, 11 (1980).

[89] F. Sottile, L. Reining, V. Olevano, S. Albrecht, and G. Onida, unpublished, URL http://www.bethe-salpeter.org/.

[90] M. Marsili, Ph.D. thesis, Universitá di Roma Tor Vergata, Roma (Italy) (2005), URL http://etsf.polytechnique.fr/node/3249.

[91] E. Runge and E. K. U. Gross, Phys. Rev. Lett. **52**, 997 (1984).

[92] J. P. Perdew, K. Burke, and M. Ernzerhof, Phys. Rev. Lett. **77**, 3865 (1996).

[93] **F. Sottile**, V. Olevano, and L. Reining, Phys. Rev. Lett. **91**, 056402 (2003).

[94] F. Sottile, K. Karlsson, L. Reining, and F. Aryasetiawan, Phys. Rev. B **68**, 205112 (2003).

[95] **F. Sottile**, M. Marsili, V. Olevano, and L. Reining, Phys. Rev. B **76**, 161103 (2007), URL http://link.aps.org/doi/10.1103/PhysRevB.76.161103.

[96] A. Marini, C. Hogan, M. GrÃijning, and D. Varsano, Computer Physics Communications **180**, 1392 (2009), ISSN 0010-4655.

[97] A. Gulans, S. Kontur, C. Meisenbichler, D. Nabok, P. Pavone, S. Rigamonti, S. Sagmeister, U. Werner, and C. Draxl, Journal of Physics: Condensed Matter **26**, 363202 (2014).

[98] G. Kresse and J. Furthmüller, Comp. Mat. Sci. **6** (1996).

[99] Z. Yang, F. Sottile, and C. A. Ullrich, sumitted to Phys. Rev. Lett. (2015), URL http://arxiv.org/abs/1501.05631.

[100] O. Pulci, M. Marsili, E. Luppi, C. Hogan, V. Garbuio, **F. Sottile**, R. Magri, and R. Del Sole, PHYSICA STATUS SOLIDI B-BASIC SOLID STATE PHYSICS **242**, 2737 (2005), URL http://dx.doi.org/10.1002/pssb.200541115.

[101] L. Caramella, G. Onida, F. Finocchi, L. Reining, and **F. Sottile**, Phys. Rev. B **75**, 205405 (2007), URL http://link.aps.org/doi/10.1103/PhysRevB.75.205405.

[102] L. Caramella, Ph.D. thesis, University of Milan (2009), URL http://arxiv.org/abs/1211.6270.

[103] J. A. Berger, L. Reining, and **F. Sottile**, Phys. Rev. B **82**, 041103 (2010), URL http://link.aps.org/doi/10.1103/PhysRevB.82.041103.

[104] J. Berger, L. Reining, and **F. Sottile**, The European Physical Journal B **85**, 326 (2012), URL `http://dx.doi.org/10.1140/epjb/e2012-30237-5`.

[105] J. A. Berger, L. Reining, and **F. Sottile**, Phys. Rev. B **85**, 085126 (2012), URL `http://link.aps.org/doi/10.1103/PhysRevB.85.085126`.

[106] A. Castro, M. A. L. Marques, D. Varsano, **F. Sottile**, and A. Rubio, Comptes Rendus de Physique **10**, 469 (2009), URL `http://dx.doi.org/10.1016/j.crhy.2008.09.001`.

[107] M. Palummo, C. Hogan, F. Sottile, P. Bagala, and A. Rubio, The Journal of Chemical Physics **131**, 084102 (2009).

[108] R. Hambach, C. Giorgetti, N. Hiraoka, Y. Q. Cai, F. Sottile, A. G. Marinopoulos, F. Bechstedt, and L. Reining, Phys. Rev. Lett. **101**, 266406 (2008), URL `http://link.aps.org/doi/10.1103/PhysRevLett.101.266406`.

[109] P. Cudazzo, M. Gatti, and A. Rubio, Phys. Rev. B **86**, 075121 (2012).

[110] G. Fugallo, M. Gatti, and F. Sottile, *Exciton dispersion in layered materials*, to be submitted.

[111] M. Guzzo, J. Kas, **F. Sottile**, M. Silly, F. Sirotti, J. Rehr, and L. Reining, Eur. Phys. J. B **85**, 324 (2012), URL `http://dx.doi.org/10.1140/epjb/e2012-30267-y`.

[112] M. Guzzo, J. J. Kas, L. Sponza, C. Giorgetti, **F. Sottile**, D. Pierucci, M. G. Silly, F. Sirotti, J. J. Rehr, and L. Reining, Phys. Rev. B **89**, 085425 (2014), URL `http://link.aps.org/doi/10.1103/PhysRevB.89.085425`.

[113] M. Gatti and M. Guzzo, Phys. Rev. B **87**, 155147 (2013).

[114] P. Cudazzo, M. Gatti, A. Rubio, and **F. Sottile**, Phys. Rev. B **88**, 195152 (2013), URL `http://link.aps.org/doi/10.1103/PhysRevB.88.195152`.

[115] G. Onida, L. Reining, and A. Rubio, REVIEWS OF MODERN PHYSICS **74**, 601 (2002), ISSN 0034-6861.

[116] M. S. Hybertsen and S. G. Louie, Phys. Rev. B **34**, 5390 (1986).

[117] S. V. Faleev, M. van Schilfgaarde, and T. Kotani, Phys. Rev. Lett. **93**, 126406 (pages 4) (2004), URL `http://link.aps.org/abstract/PRL/v93/e126406`.

[118] M. van Schilfgaarde, T. Kotani, and S. Faleev, Phys. Rev. Lett. **96**, 226402 (2006), URL `http://journals.aps.org/prl/abstract/10.1103/PhysRevLett.96.226402`.

[119] M. Gatti, F. Bruneval, V. Olevano, and L. Reining, Phys. Rev. Lett. **99**, 266402 (2007), URL `http://journals.aps.org/prl/abstract/10.1103/PhysRevLett.99.266402`.

[120] A. Svane, N. E. Christensen, M. Cardona, A. N. Chantis, M. van Schilfgaarde, and T. Kotani, Phys. Rev. B **81**, 245120 (2010).

[121] A. Svane, N. E. Christensen, M. Cardona, A. N. Chantis, M. van Schilfgaarde, and T. Kotani, Phys. Rev. B **84**, 205205 (2011), URL `http://journals.aps.org/prb/abstract/10.1103/PhysRevB.84.205205`.

[122] A. Grüneis, G. Kresse, Y. Hinuma, and F. Oba, Phys. Rev. Lett. **112**, 096401 (2014), URL `http://link.aps.org/doi/10.1103/PhysRevLett.112.096401`.

[123] S. V. Faleev, M. van Schilfgaarde, and T. Kotani, Phys. Rev. Lett. **93**, 126406 (2004), URL `http://journals.aps.org/prl/abstract/10.1103/PhysRevLett.93.126406`.

[124] C. Rödl, **F. Sottile**, and L. Reining, Phys. Rev. B **91**, 045102 (2015), URL `http://link.aps.org/doi/10.1103/PhysRevB.91.045102`.

[125] C. Rödl, K. O. Ruotsalainen, L. Reining, A.-P. Honkanen, J. M. Ablett, J.-P. Rueff, F. Sirotti, R. Verbeni, A. Al-Zein, S. Huotari, et al., to be submitted.

[126] B. J. Landi, R. P. Raffaelle, S. L. Castro, and S. G. Bailey, Progress in Photovoltaics: Research and Applications **13**, 165 (2005), URL `http://dx.doi.org/10.1002/pip.604`.

[127] S. Cataldo, P. Salice, E. Menna, and B. Pignataro, Energy Environ. Sci. **5**, 5919 (2012), URL `http://dx.doi.org/10.1039/C1EE02276H`.

[128] J. S. Lee, M. W. Kim, and T. W. Noh, New Journal of Physics **7**, 147 (2005).

[129] Z. Li, V. P. Kunets, V. Saini, Y. Xu, E. Dervishi, G. J. Salamo, A. R. Biris, and A. S. Biris, ACS Nano **3**, 1407 (2009), URL `http://pubs.acs.org/doi/abs/10.1021/nn900197h`.

[130] M. Fontana, Nature Scientific Reports **3**, 1634 (2012).

[131] S. Sutar, P. Agnihotri, E. Comfort, T. Taniguchi, K. Watanabe, and J. U. Lee, Appl. Phys. Lett. **104**, 122104 (2014).

[132] F. Aryasetiawan, L. Hedin, and K. Karlsson, Phys. Rev. Lett. **77**, 2268 (1996), URL `http://journals.aps.org/prl/abstract/10.1103/PhysRevLett.77.2268`.

[133] S. Botti, F. Sottile, N. Vast, V. Olevano, L. Reining, H.-C. Weissker, A. Rubio, G. Onida, R. Del Sole, and R. W. Godby, Phys. Rev. B **69**, 155112 (2004), URL `http://link.aps.org/doi/10.1103/PhysRevB.69.155112`.

[134] L. Braicovich, J. van den Brink, V. Bisogni, M. M. Sala, L. J. P. Ament, N. B. Brookes, G. M. De Luca, M. Salluzzo, T. Schmitt, V. N. Strocov, et al., Phys. Rev. Lett. **104**, 077002 (2010).

[135] H. H. Kramers and W. Heisenberg, Z. Phys. **31**, 681 (1925).

[136] J. van den Brink and M. van Veenendaal, Europhys. Lett. **73**, 121 (2006).

[137] J. Vinson, J. J. Rehr, J. J. Kas, and E. L. Shirley, Phys. Rev. B **83**, 115106 (2011), URL `http://link.aps.org/doi/10.1103/PhysRevB.83.115106`.

[138] G. Strinati, Phys. Rev. B **29**, 5718 (1984).

[139] H. A. Kramers, Nature **117**, 775 (1926).

[140] R. de L. Kronig, J. Opt. Soc. Am. **15**, 547 (1926).